



**HAL**  
open science

# Tracking past climate and environmental change across continental Eurasia

Christian Laag

► **To cite this version:**

Christian Laag. Tracking past climate and environmental change across continental Eurasia. Climatology. Université Paris Cité, 2023. English. NNT : 2023UNIP7099 . tel-04557398

**HAL Id: tel-04557398**

**<https://theses.hal.science/tel-04557398>**

Submitted on 24 Apr 2024

**HAL** is a multi-disciplinary open access archive for the deposit and dissemination of scientific research documents, whether they are published or not. The documents may come from teaching and research institutions in France or abroad, or from public or private research centers.

L'archive ouverte pluridisciplinaire **HAL**, est destinée au dépôt et à la diffusion de documents scientifiques de niveau recherche, publiés ou non, émanant des établissements d'enseignement et de recherche français ou étrangers, des laboratoires publics ou privés.



Thèse préparée à Université Paris Cité,  
Institut de physique du globe de Paris  
École doctorale Sciences de la Terre et de l'environnement  
et physique de l'Univers STEP'UP n°560  
Équipes de Paléomagnétisme

# Tracking past climate and environmental change across continental Eurasia

par Christian Laag

Thèse de doctorat de Sciences de la Terre et de l'environnement

- dirigée par  
France LAGROIX  
et Yohan GUYODO
- présentée et soutenue publiquement le  
31 mars 2023
- devant un jury composé de  
Joshua FEINBERG, Professeur, University of Minnesota (rapporteur)  
Christine HATTÉ, DR-CEA, Laboratoire des Sciences du Climat et de  
l'Environnement (rapporteur)  
Simo SPASSOV, Research Scientist, Centre de Physique du Globe de l'Institut  
Royal Météorologique (examineur)  
Magali ADER, Professeur, IPGP-UPC (examineur)  
Yohan GUYODO, CRHC-CNRS, IPGP (co-directeur de thèse)  
France LAGROIX, DR-CNRS, IPGP (directrice de thèse)



## Content

Abstract in English .....	V
Résumé en Français .....	VII
Résumé substantiel en Français .....	IX
1. Introduction .....	1
1.1. Historical overview of the origin and growth of loess research .....	1
1.2. The definition of loess, its distribution and processes resulting in loess-paleosol sequences .	9
1.3. Earth's climate history – how far can we go from a loess point of view?.....	15
2. Studying loess-paleosol sequences.....	16
2.1. Magnetism .....	18
2.1.1. Environmental magnetism.....	18
2.1.2. Hysteresis loops and isothermal remanent magnetization experiments .....	19
2.1.3. Magnetic susceptibility.....	21
2.1.4. Anhyseretic remanent magnetization .....	26
2.1.5. Isothermal remanent Magnetization acquisition experiments and unmixing .....	26
2.1.6. Magnetic parameter ratios.....	27
2.1.7. FORC analysis.....	30
2.2. Colorimetry .....	33
2.2.1. The CIE 1931 color system .....	34
2.2.2. Tristimulus values .....	34
2.2.3. The Lab color System.....	34
2.2.4. DRS Diffuse reflectance spectrometry .....	35
2.2.5. Colour contrast enhancement – indications for an easier accessible soil classification?	39
2.3. Granulometry.....	40
2.3.1. Methods .....	40
2.3.2. Grain size spectra .....	40
2.3.3. Standard Grain size variables .....	41
2.4. Attenuated total reflectance Fourier Transform Infrared Spectrometry (ATR-FTIR) .....	43
2.5. Determining ages in loess-paleosol sequences .....	45
2.5.1. Absolute.....	45
2.5.2. Correlative .....	46
2.5.3. Tephrostratigraphy vs. Tephrochronology .....	46
2.6. Climate variability from orbital to millennial time scales .....	50
2.6.1. Orbital Forcing .....	50
2.6.2. Millennial timescale climate change .....	52

3. General objectives of the PhD Thesis .....	56
4. Publications .....	61
4.1. A detailed magnetic record of Pleistocene climate and distal ash dispersal during the last 800 kyrs - The Suhia Kladenetz quarry loess-paleosol sequence near Pleven (Bulgaria).....	61
4.2. Measuring and evaluating colorimetric properties of samples from loess-paleosol sequences .	77
4.3. A multiproxy analysis of the Pleven LPS, in preparation .....	98
5. Synthesis.....	160
5.1. Mid Brunhes climate transition (MBT).....	160
5.2. The total time cover of the Pleven LPS – two solutions .....	162
5.3. Identification of millennial scale climate variability .....	166
5.4. Multi-proxy (Crypto-)tephra identification in Pleven .....	167
5.5. Future work .....	175
5.5.1. Pleven .....	175
5.5.2. Nussloch P9.....	177
5.5.3. Zmajevac .....	178
References .....	181
Acknowledgements .....	204
Appendix .....	208
Appendix A: Supplement for Chapter 4.1.....	208
Appendix B: Supplement for Chapter 4.3.....	222
Appendix C: Conversions of Colorimetry.....	244
Appendix D: Publication Zemun.....	245
Appendix E: Publication Zmajevac.....	270
Appendix F: R-package LESLIE .....	291
The LESLIE R Package.....	292
The LESLIE R-shiny application .....	295
Objectives of LESLIE .....	296
Appendix G: R-code VSM haRvester.....	297
Structure and working process of the code.....	297
Objectives of the VSM harvester .....	303
Appendix H: Contributions to international conferences .....	304
Data availability statement .....	307

To my beloved wife Assoumpta Laag-Uwimanzi

## Abstract in English

The cyclical nature of glacial and interglacial cycles caused by the Earth's orbital parameters (Milanković cycles) leads to changes in emission, transport and deposition of mineral dust as well as in the formation of loess and intercalated soils. Loess covers 10 % of the Earth's continental surfaces and 20% of Europe's. In Eastern Europe, loess deposits span up to 1 million years and are valuable paleoclimate archives. This thesis aims to contribute knowledge of past climate change on orbital to millennial timescales archived in loess and paleosol sequences. The aims of this thesis are reached by implementing multiple approaches (environmental magnetism, colorimetry, mid-infrared spectrometry, granulometry and tephrostratigraphy) leading to interpretations derived from the integration of the multi-disciplinary data sets.

A new loess and paleosol sequence (LPS), located in the Lower Danube basin and exposed in the Suhia Kladenetz quarry near the city of Pleven in northern Bulgaria (43°27'24.0"N, 24°41'26.7" E), was studied. The sedimentary sequence was described, sampled, and analyzed over two field seasons (2018 & 2021) along two profiles (SK18 & PL21). The Pleven LPS is ~27 m thick and composed of seven loess units, six buried soil complexes (paleosol) below the present day topsoil, and one 20-cm thick volcanic ash (tephra) layer. Bulk material was sampled continuously at a 2-cm depth resolution resulting in 1336 sampling depths. The main contributions of this thesis are summarized as follows:

Building an initial correlative age model for the Pleven LPS based on the correlation of magnetism-based proxies of pedogenesis and detrital dust with the  $\delta^{18}\text{O}$  LR04 and the Antarctic ice core dust flux records. Refining the age model with magnetism- and colorimetry-derived proxies of pedogenesis correlation to Greenland  $\delta^{18}\text{O}$  NGRIP record and  $\delta^{18}\text{O}$  LR04 stack for different age intervals. The age model indicates dust accumulated continuously at Pleven starting between 850 and 950 ky ago.

Developing goethite and maghemite content derived paleoprecipitation proxies. Demonstrating their validity by comparing to precipitation dependent  $\delta^{13}\text{C}$  records and model data. Quantifying mean annual precipitation (MAP) values for the last ~800 ky and comparing to modeled MAP data.

Improving the methodology of color spectra analysis for semi-quantitative goethite and hematite contents and a coded routine to enhance color contrast. Combining colorimetry derived goethite and hematite contents and mineral magnetic data, millennial timescale climate

variations are detected in the last glacial (MIS 4-2) loess, in the penultimate glacial (MIS 6) loess, and for the first time in MIS12 glacial loess.

Characterizing a multi-parameter signature of tephra material and identifying the occurrence of several cryptotephra layers throughout the Pleven LPS. Age model assigned ages of the outcropping tephra and identified cryptotephra find counterparts in other regional tephrochronological records radiometrically dated, providing independent validation of the correlative age model and valuable stratigraphic markers for regional correlations.

Observing the demise of the mid-Pleistocene transition (1200 – 700 ka) and the mid-Brunhes climate event (~430 ka) characterized in variations of smectite and kaolinite contents derived from mid-infrared spectroscopy, hematite content derived from colorimetry and various magnetic parameters.

In summary, the new high-resolution Pleven LPS, investigated using a diverse set of approaches, is a comprehensive record of climate change over the most part of the last million year and provides a benchmark for stratigraphic correlations. Furthermore, the developed goethite-based paleoprecipitation proxy identifies millennial timescale variations during periods of increased loess accumulations for the last glacial, the penultimate glacial and MIS 12 glacial periods.

**Key words:** Loess-paleosol sequence, Quaternary, Environmental Magnetism, Colorimetry, Infrared Spectroscopy, Granulometry, Tephra, Mid-Brunhes Climate Event, Mid-Pleistocene Climate Transition, Millennial scale climate change

## Résumé en Français

La succession cyclique de périodes glaciaires et interglaciaires (cycles de Milanković) entraîne des variations dans l'émission, le transport et le dépôt de poussières minérales, favorisant la formation de loess et de sols intercalés. Le loess recouvre 10% des surfaces continentales mondiales et 20% de l'Europe. La thèse présentée ici vise à améliorer nos connaissances des changements paléoclimatiques sur les échelles orbitales à millénaires archivées dans les séquences de loess et de paléosols de l'Europe de l'Est, sur l'essentiel du dernier million d'années. Une approche multidisciplinaire est suivie, utilisant le magnétisme environnemental, la colorimétrie, la spectroscopie infrarouge, la granulométrie et la téphrostratigraphie.

Une nouvelle séquence de loess et de paléosols (LPS), située dans le bassin du Bas-Danube au sein de la carrière de Suhia Kladenetz près de Plevén en Bulgarie (43°27'24.0"N, 24°41'26.7"E), a été étudiée. La séquence sédimentaire a été décrite, échantillonnée et analysée le long de deux profils (SK18 et PL21) lors de deux campagnes de terrain (2018 et 2021). La séquence de 27 m est composée de sept unités de loess, de six complexes de paléosols et d'une couche de 20 cm de cendres volcaniques (téphra). Le sédiment a été échantillonné (en vrac) en continu avec une résolution stratigraphique de 2 cm, donnant 1336 profondeurs d'échantillonnage. Les principales contributions de cette thèse sont résumées comme suit :

Élaboration d'un premier modèle d'âge corrélatif pour la LPS de Plevén, à partir de la corrélation de plusieurs indicateurs magnétiques avec l'enregistrement du flux de poussières en Antarctique et la compilation  $\delta^{18}\text{O}$  LR04. Le modèle d'âge est affiné avec d'autres indicateurs de pédogenèse dérivés du magnétisme et de la colorimétrie, corrélés aux  $\delta^{18}\text{O}$  de NGRIP et de LR04 pour différents intervalles d'âge. Le modèle d'âge indique que la poussière s'est accumulée de manière continue à Plevén depuis 850 ou 950 ka.

Développement d'indicateurs de paléoprécipitation dérivés de la teneur en goéthite et maghémite. Démonstration de leur validité en les comparant à des modèles et à des enregistrements de  $\delta^{13}\text{C}$  dépendants de la précipitation. Quantification des valeurs de précipitation annuelle moyenne (MAP) sur les derniers ~800 ky et comparaison avec des modèles de MAP.

Amélioration de la méthode d'analyse des spectres de couleur pour obtenir des teneurs semi-quantitatives en goéthite et hématite et écriture d'un code optimisant le contraste des couleurs. En combinant les teneurs en goéthite et hématite issues de la colorimétrie et du magnétisme, des variations climatiques millénaires sont détectées dans le loess des deux dernières glaciations (MIS 4-2, MIS 6) et pour la première fois dans le loess du MIS12.

Mise en évidence d'une signature multi-paramètres des tephres et identification de plusieurs cryptotephres à Pleven. Les âges assignés par le modèle d'âge à ces tephres et cryptotephres permettent de trouver leurs homologues dans d'autres enregistrements téphrochronologiques régionaux datés radiométriquement, fournissant à la fois une validation indépendante du modèle d'âge corrélatif et de nouveaux marqueurs stratigraphiques régionaux.

Observation de la fin de la transition du Pléistocène moyen (1200-700 ka) et de l'événement climatique Mid-Brunhes (~430 ka) caractérisés par les teneurs en smectite et en kaolinite dérivées de la spectroscopie infrarouge, et en hématite dérivées de la colorimétrie et de divers paramètres magnétiques.

En résumé, la nouvelle LPS de Pleven, étudiée à l'aide d'un ensemble diversifié d'approches, est un enregistrement complet des changements climatiques du dernier million d'années et fournit une référence pour des corrélations stratigraphiques. De plus, l'indicateur de paléoprécipitation basé sur la goethite identifie des variations à l'échelle millénaire du dépôt de loess durant les deux dernières périodes glaciaires, ainsi que pour la période glaciaire du MIS 12.

**Mots clés :** Séquence de loess-paléosol, Quaternaire, Magnétisme environnemental, Colorimétrie, Spectroscopie Infrarouge, Granulométrie, Téphra, Événement climatique du Mid-Brunhes, Transition climatique du Pléistocène moyen, Variabilité climatique à l'échelle millénaire.

## Résumé substantiel en Français

L'alternance des conditions glaciaires et interglaciaires, rythmée par les variations des paramètres orbitaux de la Terre (paramètres de Milanković d'excentricité, d'obliquité et de précession), favorise l'émission, le transport et le dépôt de loess (limon éolien) et le développement des sols à des latitudes moyennes. Le loess recouvre 10% des surfaces continentales mondiales et 20% de l'Europe. En Europe de l'Est, les séquences de loess et de paléosols s'étendent généralement sur une échelle de temps couvrant le dernier million d'années, de manière continue. Ainsi, les séquences loess-paléosol sont des archives sédimentaires importantes pour étudier les changements climatiques du passé.

Durant le Quaternaire (les 2,6 millions d'années passées), il y a eu des changements majeurs de la tendance climatique à long terme, ainsi que de grands événements ou des transitions substantielles, tels que la transition climatique du Pléistocène moyen et l'événement climatique du Mid-Brunhes. La transition du Pléistocène moyen (1250 à 700 ka) marque le passage d'une périodicité dominante de 41 ka (obliquité) à une périodicité dominante de 100 ka (excentricité) dans l'alternance des cycles glaciaires et interglaciaires. L'événement climatique du Mid-Brunhes (~430 ka), qui est notamment présent dans les carottes de glace de l'Antarctique (par exemple, EPICA), indique un passage d'interglaciaires plus doux à des interglaciaires très chauds et humides. Par ailleurs, des changements climatiques à l'échelle des millénaires sont bien documentés dans les carottes de glace du Groenland (par exemple, NGRIP), ainsi que dans les spéléothèmes et d'autres archives climatiques à haute résolution. Ces changements climatiques millénaires sont composés de cycles de Dansgaard-Oeschger (durée moyenne de 1500 ans, interstadias chauds et humides), d'événements de Heinrich (durée moyenne de 500 ans, décharges de débris de délestage par les icebergs dans l'océan Atlantique nord) et de cycles de Bond (durée de 10 à 15 mille ans, couvrant plusieurs cycles de Dansgaard-Oeschger). Les cycles climatiques plus courts (plus rapides) sont documentés dans les séquences de loess-paléosol en Europe pour le dernier glaciaire, peu confirmés pour l'avant-dernier glaciaire et pas encore attestés pour les glaciaires plus anciens dans les séquences de loess-paléosol en Europe. Pour identifier les changements climatiques du passé à l'échelle orbitale et millénaire, un modèle d'âge robuste de l'archive étudiée est nécessaire pour permettre ensuite une comparaison avec d'autres archives paléoenvironnementales bien établies.

Obtenir un modèle d'âge robuste pour les séquences de loess-paléosol est un défi. Afin d'étudier les variations climatiques à l'échelle orbitale à millénaire, différentes techniques de datation (absolues et corrélatives) sont applicables aux séquences de loess-paléosol. Cependant, les



techniques de datation absolues couramment utilisées telles que le  $^{14}\text{C}$  et la datation par luminescence atteignent leurs limites de datation à environ 50 ka et 250 ka, respectivement. Les incertitudes des déterminations d'âge basées sur la luminescence sont généralement de l'ordre de plusieurs dizaines de milliers d'années, ce qui est trop important pour permettre des corrélations robustes avec les changements climatiques millénaires. Le potentiel des niveaux de cendres volcaniques (tephra) intégrés dans les séquences de loess et de paléosol pour surmonter ces défis chronologiques a, jusqu'à présent, reçu peu d'attention. Dans les milieux marins et lacustres, les tephras sont des marqueurs chronologiques et stratigraphiques importants ; l'empreinte géochimique des éjectas de verre volcanique joue un rôle clé. Dans les dépôts de loess-paléosol, un facteur limitant est la préservation de ces éjectas sans altération, qui est une condition nécessaire à la bonne identification de leur empreinte géochimique. Dans les bassins des Carpates et du Danube inférieur, quatre niveaux de cendres volcaniques sont reconnues de manière régionale, se produisant sous la forme de couches distinctes observables sur le terrain (tephra proprement dit) ou à travers des observations ou analyses de laboratoire (cryptotephra).

Ma thèse se présente sous la forme d'une compilation de mes contributions, visant à mieux comprendre les changements climatiques passés à l'échelle orbitale et millénaire à partir de leurs empreintes dans une séquence de loess-paléosols située dans la vallée inférieure du Danube (nord de la Bulgarie). Cette séquence archive plusieurs couples d'unités de loess et de paléosols reflétant de multiples cycles glaciaires et interglaciaires. Les objectifs de cette thèse sont atteints en adoptant une approche multidisciplinaire utilisant le magnétisme environnemental, la colorimétrie, la spectroscopie infrarouge, la granulométrie et la téphrostratigraphie.

La thèse est construite avec la structure suivante :

Dans le premier chapitre, une perspective historique sur les recherches conduites sur les loess est présentée. Plusieurs personnages clés ont mené à l'origine éolienne actuellement acceptée du loess et à d'autres caractéristiques clés définissant le loess. Les idées et hypothèses sur le loess en tant qu'accumulation de poussière minérale éolienne peuvent être retracées jusqu'à un premier point de départ datant de plus de 2000 ans. Un second point de départ, celui de la recherche européenne sur le loess, peut être trouvé en 1726. Plusieurs controverses et débats sur l'origine, la formation, la distribution, la définition et la pertinence du loess dans les études paléo-environnementales ont existé et sont examinés sur une ligne de temps quasi continue de

1726 jusqu'à la première étude magnétostratigraphique fiable présentée en 1982. À partir de ces années, un développement rapide et une grande quantité de publications peuvent être trouvés dans le domaine de la recherche sur le loess.

Le Chapitre 2 comprend une vue d'ensemble de certains aspects fondamentaux de différentes méthodes appliquées pour étudier les séquences loess-paléosol. La revue se concentre sur les méthodes appliquées dans le cadre de cette thèse, telles que le magnétisme environnemental, la colorimétrie, la granulométrie, la réflectance totale atténuée en spectroscopie infrarouge à transformée de Fourier, ainsi que les différentes techniques de datation appliquées aux séquences loess-paléosol.

Dans le Chapitre 3, les objectifs généraux de la thèse sont énoncés et peuvent être résumés comme suit :

- Combien de temps est couvert par la séquence loess-paléosol de Pleven ?
- Pouvons-nous bâtir un jeu de données permettant de définir des indicateurs fiables des paléoenvironnements/systèmes climatiques prédominants ?
- Pouvons-nous quantifier les paramètres paléo-environnementaux ?
- Pouvons-nous détecter des niveaux de tephra servant de points d'ancrage pour améliorer un modèle d'âge corrélatif pour cette séquence loess-paléosol ?
- Pouvons-nous détecter des changements climatiques à l'échelle millénaire ?

Pour répondre à ces questions, une nouvelle séquence de loess et de paléosol exposée dans la carrière Suhia Kladenetz (SK) près de la ville de Pleven dans le nord de la Bulgarie a été étudiée. Cette séquence couvre 27 m d'accumulation de poussière continue et a été étudiée avec une résolution de 2 cm de profondeur. Un jeu de données multidisciplinaire de haute résolution acquis à partir de 1336 profondeurs d'échantillonnage comprend des mesures magnétiques et colorimétriques (toutes les profondeurs d'échantillonnage), une spectrométrie infrarouge (ATR-FTIR ; 719 profondeurs d'échantillonnage) et des analyses de distribution de la granulométrie (249 profondeurs d'échantillonnage). Les principales contributions de cette thèse sont présentées dans trois chapitres clés et les principales conclusions des chapitres 4.1, 4.2 et 4.3 sont résumées ci-après.

Le chapitre 4.1 présente initialement la séquence de loess-paléosol de Pleven. Un premier jeu de données acquises sur des échantillons provenant de la séquence de Pleven a été utilisé pour obtenir des premières connaissances sur la variabilité du climat ancien et pour construire un modèle d'âge corrélatif afin d'identifier la durée totale de la séquence de 27 m de Pleven. Deux modèles d'âge corrélatifs ont été construits à partir d'indicateurs magnétiques du degré de développement pédogénique (la valeur absolue de la dépendance en fréquence de la susceptibilité magnétique,  $\Delta\chi$ ) et de la dynamique des vents (le rapport de l'aimantation rémanente isotherme acquise dans un champ de 2 Tesla et de la susceptibilité magnétique en champ faible,  $IRM_{2T}/\chi_{lf}$ ). La variabilité de la pédogenèse ( $\Delta\chi$ ) a été comparée à la compilation de  $\delta^{18}O$  de foraminifères benthiques LR04 et les variations de la dynamique des vents ( $IRM_{2T}/\chi_{lf}$ ) ont été comparées à l'enregistrement du flux de poussières de l'Antarctique EPICA Dome C. Les deux modèles d'âge corrélatif sont en accord et indiquent que le dépôt de poussières à Pleven s'est poursuivi sans interruption sur les derniers 830 mille ans. Les taux de sédimentation calculés sont les plus élevés lors des stades isotopiques marins MIS 6 (dernière période glaciaire) et MIS 12, qui sont tous les deux connus comme les périodes glaciaires avec les conditions les plus rudes du dernier million d'années.

À Pleven, il existe une couche de tephra d'une épaisseur de 20 cm stratigraphiquement située dans l'avant dernier stade glaciaire MIS 6. En se basant sur les paramètres magnétiques des échantillons provenant de ce niveau de tephra (en particulier les anomalies dans les paramètres magnétiques dépendants de la concentration et de la taille des grains), des échantillons similaires révélant également ces anomalies magnétiques ont été trouvés dans trois autres niveaux stratigraphiques à Pleven. De plus, des observations au microscope optique ont confirmé la présence d'éjectas de verre volcanique. Les modèles d'âge corrélatifs ont permis une attribution d'âge provisoire à ces niveaux de cryptotephra et ont été comparés à des niveaux de tephra datés préservés dans des archives environnementales riches en tephras telles que le lac Ohrid, Tenaghi Philippon et le bassin de Fucino.

En outre, les paramètres magnétiques montrent une bipartition de la séquence de Pleven, qui sépare les paléosols plus vieux S5 et S6 des paléosols plus jeunes S4 vers le sol holocène en haut du profil. Les données magnétiques acquises dans le but de contraindre la minéralogie magnétique indiquent que la magnétite est le principal porteur de l'aimantation rémanente anhystérétique (ARM) pour les paléosols plus vieux S5 et S6, tandis que la maghémite est le principal porteur pour les unités S4 vers le haut. Les âges de cette bipartition provenant de modèles d'âge corrélatifs coïncident avec l'événement climatique du Mid-Brunhes.

Le chapitre 4.2 présente un protocole méthodologique détaillé pour une extraction efficace des spectres colorimétriques de minéraux indicatifs du climat passé, tels que la goethite et l'hématite. La goethite et l'hématite se forment sous différents climats et environnements prédominants, mais la détermination de leur concentration est difficile à établir avec des méthodes magnétiques. La spectroscopie de réflexion diffuse (DRS) est une méthode grâce à laquelle certains de ces défis peuvent être levés. Cependant, jusqu'à présent, aucun protocole détaillé n'a été publié pour rationaliser cette procédure. Un biais systématique dans le signal, qui se produit lors de la mesure de propriétés colorimétriques à travers des boîtes en plastique (dans lesquelles les échantillons de loess sont généralement stockés), est ainsi mis en évidence et un protocole développé pour l'éliminer. De plus, une nouvelle routine R "LESLIE" est présentée permettant d'améliorer le contraste des couleurs dans les séries stratigraphiques, afin d'identifier les changements subtils des nuances de couleur invisibles à l'œil nu.

Dans le chapitre 4.3, une évaluation de toutes les données multidisciplinaires acquises au cours de mon travail sur cette thèse est présentée. Les données comprennent les résultats en magnétisme environnemental, colorimétrie (suivant la méthodologie présentée au chapitre 4.2), granulométrie et en spectroscopie infrarouge. Ce chapitre fournit la première preuve multidisciplinaire / multi-proxy de l'interaction interglaciaire-glaciaire préservée à Plevel. Le modèle de datation corrélatif présenté au chapitre 4.1 est affiné avec les variations de concentrations en goethite et hématite dérivées de la colorimétrie. Les variations des contenus semi-quantitatifs de goethite montrent une forte variabilité pendant les glaciaires. Cette variabilité a été trouvée pour ressembler à la variabilité à l'échelle millénaire préservée dans la carotte de glace du Groenland NGRIP pour le dernier cycle interglaciaire-glaciaire (les derniers ~ 130 mille ans).

En outre, les abondances de goethite et d'hématite déterminées à partir de la spectroscopie DRS ajoutées à la corrélation  $\Delta\chi$  ont permis d'identifier la fin de chaque interglaciaire, ce qui n'était pas possible uniquement avec les données magnétiques présentées dans le chapitre 4.1. Le modèle corrélatif affiné présenté dans le chapitre 4.3 a corrélé les variations de goethite à la  $\delta^{18}\text{O}$  NGRIP pour les derniers 130 mille ans et l'hématite, la goethite et  $\Delta\chi$  disposés en compromis par point d'ancrage corrélés à la compilation  $\delta^{18}\text{O}$  LR04. Les données magnétiques, colorimétriques et de spectroscopie infrarouge ainsi intégrées ont favorisé la mise en évidence de climats différents avant et après l'événement climatique du Mid-Brunhes (430 ka) à Plevel. Contrairement aux compilations mondiales, qui indiquent que les conditions climatiques étaient plutôt extrêmes lors des plus récents interglaciaires (MIS 11-Holocène), tous les indicateurs tels

que l'hématite, la goethite, les abondances de kaolinite et de smectite ainsi que les changements de tailles des grains magnétiques et des abondances minérales reflètent à Pleven que la température, la saisonnalité, les précipitations et l'intensité d'altération étaient considérablement augmentées pendant les interglaciaires plus anciens préservés sous la forme des paléosols S5 et S6.

Dans ce chapitre, je présente une preuve combinée de la variabilité à l'échelle des millénaires provenant des contenus semi-quantitatifs de goethite et des indicateurs magnétiques tels que l'aimantation rémanente isotherme dite « dure » (HIRM). La corrélation susmentionnée avec NGRIP est rendue possible par une ressemblance remarquable entre les cycles humides et chauds de Dansgaard Oeschger dans NGRIP et les augmentations à court terme de goethite, qui est démontrée suivre la précipitation. Les variations de goethite à Pleven ne ressemblent pas seulement à l'intensité de différents cycles de Dansgaard Oeschger, mais dans plusieurs cas également au motif en dent-de-scie des événements D-O. Les événements de Heinrich, qui sont des événements courts, secs et froids, coïncident avec une réduction de la précipitation à Pleven, indiquée par une réduction des contenus en goethite. Quelques études effectuées sur des séquences européennes de loess-paléosols ont trouvé une variabilité climatique à l'échelle des millénaires pour le dernier cycle glaciaire/interglaciaire, beaucoup moins pour l'avant dernier glaciaire (MIS6). Pour la première fois dans des séquences européennes de loess-paléosols, les variations de goethite indiquent une variabilité climatique à l'échelle des millénaires pour MIS 4-2, MIS 6 et MIS 12. Pour d'autres glaciaires, la vitesse de sédimentation à Pleven n'était pas assez élevée pour identifier cette variabilité.

Puisque la précipitation est un élément clé des reconstructions de paléoclimats, un test de quantification de la précipitation a été effectué. Des études récentes effectuées sur le Plateau de Loess en Chine ont établi un lien entre la néoformation de maghémite et la précipitation, fournissant ainsi une fonction climatique. Des expériences de susceptibilité magnétique à haute température ont été effectuées sur 81 échantillons répartis de manière plutôt continue sur la séquence de loess-paléosols de Pleven. Les teneurs en maghémite ont été déterminées à partir de ces expériences et ont été calculées à l'aide de la fonction climatique donnée en valeurs de précipitations annuelles moyennes. De plus, les valeurs de paléo-précipitations dérivées de la maghémite de S4 à l'Holocène ont été corrélées avec les teneurs en goethite. Comme indiqué dans le chapitre 4.1, la maghémite est le principal porteur de rémanence dans cet intervalle plus jeune. Une régression de second ordre a été construite par la suite pour transformer toutes les valeurs de goethite en valeurs de précipitations annuelles moyennes. Enfin, ces valeurs MAP

ont été comparées à des données modélisées valides pour la région de Plevén. Les valeurs MAP modélisées et re-calculées concordent bien et fournissent ainsi la première courbe de précipitations annuelles moyennes absolues pour les séquences de loess-paléosols d'Europe de l'Est pour les derniers 830 mille ans.

Dans ce chapitre, les couches de tephra et de cryptotephra présentées dans le chapitre 4.1 sont réexaminées à partir de l'intégration de données magnétiques supplémentaires acquises, de données dérivées de DRS et de teneurs en smectite dérivées d'expériences en spectroscopie infrarouge. Des caractéristiques de distinction supplémentaires sont observées pour le tephra et les 3 couches de cryptotephra présentées dans le chapitre 4.1, ce qui a permis d'identifier 51 candidats supplémentaires de cryptotephra préservés dans le LPS de Plevén. L'identification des candidats cryptotephra a été effectuée avec différents paramètres magnétiques indiquant des changements rapides de la taille, de la concentration et de la minéralogie des grains magnétiques ainsi que d'augmentations de la teneur en smectite. Des estimations d'âge dérivées du modèle d'âge corrélatif ont été déterminées pour chaque cryptotephra. Les occurrences de tephra dans les archives environnementales riches en tephra situées régionalement ont été compilées et recherchées pour trouver des correspondances. Cinquante et une des couches de cryptotephra ont trouvé des équivalents qui coïncident dans le temps avec une différence absolue d'âge inférieure à 2 mille ans. Cela pourrait être un premier pas vers un cadre de référence tephro-stratigraphique pour les séquences de loess-paléosol de l'Est de l'Europe et pourrait améliorer les défis géochronologiques à l'avenir.

En résumé, la séquence de loess-paléosol de Plevén, d'une résolution élevée et archivant en continu la plus grande partie des derniers millions d'années et étudiée à l'aide d'une variété d'approches, est un enregistrement unique et précieux des changements climatiques et environnementaux et fournit une référence pour les corrélations stratigraphiques. De plus, des variations à l'échelle des millénaires d'un marqueur de paléoprécipitation basé sur la goethite sont mises en évidence lors de périodes d'accumulations accrues de loess pendant la dernière glaciation, la glaciation antérieure et la glaciation MIS 12.

## 1. Introduction

### 1.1. Historical overview of the origin and growth of loess research

# 1

Searching for the very beginning of loess research leads to two potential starting points. China is very likely one starting point, however it is very poorly documented in western literature (Smalley et al., 2001). Sources such as (Liu, 1988) provide some initial summary of ancient Chinese loess research and detail initial assumptions about loess genesis and its origin. The second starting point is Europe, for which contributions to loess research are well documented from the mid-17<sup>th</sup> century. (Smalley et al., 2001) provides a broad and detailed overview of the first 175 years of European and Chinese loess research. The journey, key personalities, and growth of knowledge of loess research, from 1823 to the most recent milestones is recounted next.

#### **Huangtu**

Neither sand nor mud, are some characteristics associated to the Chinese term “Huangtu”, which translates roughly to “yellow earth” and appeared in Chinese literature about 2000 years ago (Liu, 1988). The great historian Ban Gu (A.D. 32-92) indicates with his work “The Books of the Western Han Dynasty (Wuxingzhi, vol. III) that a principal property of Huangtu is its airborne origin: “in the morning of one day in the fourth month of the third year of Yuanfeng, Jianshi, in the sovereignty of the Emperor Cheng Di, Han Dynasty (78 B.C.), strong winds blew from the northwest. Red and yellow thin, floating clouds were hanging over the sky and yellow dust (Huangtu) fell on the ground from morning till night” (Liu, 1988). Fundamental characteristics of loess that hold true today such as an airborne (dust storm) origin, a dominance of silt size particles, or a yellowish color, were already known 2000 years ago in China.

#### **Luigi Fernandino Marsigli**

The cornerstone of European loess research was established first by Count Luigi Ferdinando Marsigli in the late 17<sup>th</sup> century. He was born 1658, founded the Institute of Sciences in Bologna (Istituto delle Scienze) in 1714 (Vaccari, 2000), and four years before his death, in 1730, published the first drawing of a loess-paleosol sequence (Marsigli, 1726).

Along with the drawing of Figure 1, observations made by Marsigli over the years were reported comprehensively in a six-volume collection (Marsigli, 1726), dealing predominantly with the Danube River system. This body of work, presenting fundamental insights into loess research, came one century before the pioneering work of Karl Caesar von Leonhard.

## *DIVERSA TERRARUM ALVEI CON- STITUTIO.*

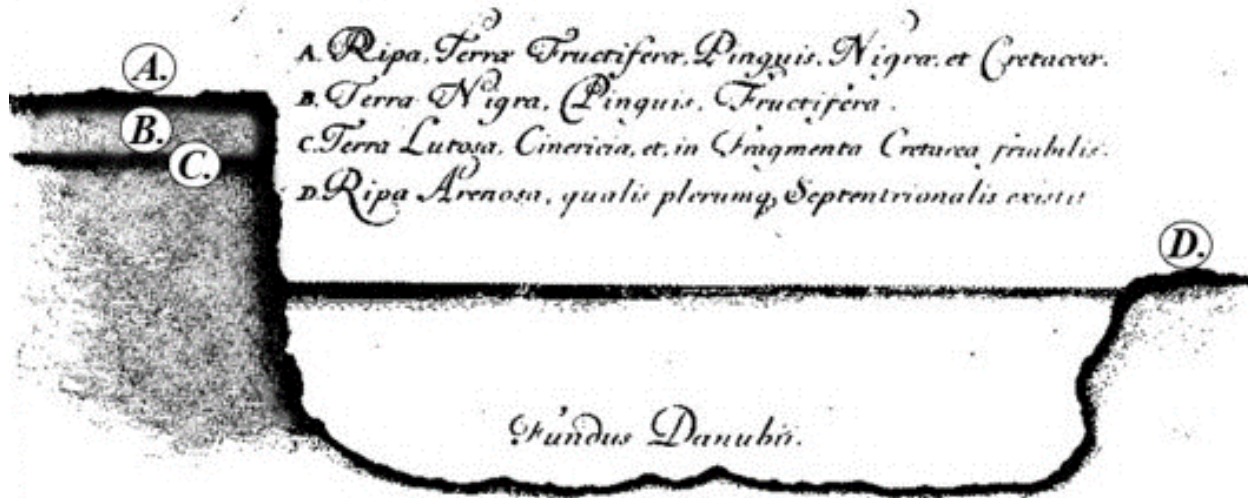


Figure 1: First drawing of a loess-paleosol sequence published in 1726 by Marsigli. Modified from its original and adapted from (Marković et al., 2009b). A: Ripa terra fructifera pinguis nigra et cretacea – a black fertile carbonate soil. B: Terra Nigra. Pinguis, Fructifera – a black fertile soil; C: Terra Lutosa, Cineriaria et in fragmenta Cretacea friabilis – a yellowish layer with carbonate fragments, which, today, is assigned as loess.

### **Karl Cäsar von Leonhard**

Karl Cäsar von Leonhard (1823/1824) is credited for having coined the term “loess” all the while ignoring the aeolian origin of loess (Liu, 1988). The early origin of the term loess stems from the German northern Baden dialect “loefs” spoken as “loesch”. Workers in brickyard quarries of northern Baden called the material they were mining “loesch” and Karl Cäsar von Leonhard simply took it over.

### **Charles Lyell places loess at the forefront**

Loess, the dusty material, began to receive international attention with the third volume of the textbook “Principles of Geology” by Charles Lyell (Lyell, 1833) and particularly the sub-chapter “Loess of the Valley of the Rhine”. It is assumed that Charles Lyell met Karl Cäsar von Leonhard in Heidelberg and that they visited together the Haarlass *locus typicus* (Smalley et al., 2001). Lyell acknowledges in his textbook that many authors have written about loess and makes many references to a M. Leonhard but it remains unclear whether he is referring to Karl Cäsar von Leonhard. Beginning on p. 151, Lyell exposes a hypothesis whereby loess would have had an alluvial origin resulting from a sudden deposition of flood or muddy waters. He also reports on M. Leonhard’s compositional description of loess as consisting ‘chiefly of



argillaceous matter combined with a sixth part of carbonate of lime and a sixth of quartzose and micaceous sand'. Despite there being documentation of observations made of loess, a comprehensive compilation of these, enabling to recount Europe's contributions to our early understanding of the origin of loess is lacking. Some of Lyell's observations included description of numerous land shells, a yellowish-grey pulverulent loam, and calcareous sandy concretions up to the size of a man's head. He also reports on the thickness of loess deposits, up to "several hundred feet", the absence of visible stratification and remains of marine origin, and the frequent occurrence of land mammal remains such as mammoth, horse and other quadrupeds. However, another hypothesis is resulting from further characteristics Lyell lists. A key observation resulting from Lyell's geographically widespread investigations throughout the Rhine valley alluvial plain is that mineral characteristics are identical in all loess deposits and that loess mantles the landscape including volcanic hills as observed in the Rodderberg volcanic mountain (located in Rheinland Pfalz), where about 20 m of loess is found in the Rodderberg crater based on borehole observations. All these observations suggested strongly that the origin of loess was not alluvial and led Lyell to hypothesize on an aeolian origin of loess.

In conclusion Charles Lyell placed loess at the forefront of international discussions, which in Europe fueled loess research for the following decades (1840-1900) targeting the origin and formation of loess.

### **Ferdinand von Richthofen on the aeolian origin of loess**

An aeolian origin of loess, is recognized first in European loess research by Ferdinand von Richthofen (Liu, 1988). In 1882, Richthofen identified 12 characteristics of loess, which were slightly modified by (Smalley et al., 2001):

- 1) Loess is petrographically, stratigraphically and faunally distinct compared to all previously described sediment deposits;
- 2) Loess has everywhere nearly perfect homogeneity in composition and structure;
- 3) The distribution of loess is independent of the altitude above sea level;
- 4) Large loess bodies have a peculiar shape;
- 5) Quartz grains in loess have almost exclusively an angular occurrence;
- 6) Loess is almost completely devoid of stratification
- 7) Loess often develops a capillary structure caused by the occurrence of innumerable tubes
- 8) Loess is frequently encrusted with calcium carbonates, having generally vertical traces which ramify downwards like root tracks;

- 9) Loess has the tendency to develop vertical cleavage;
- 10) Loess embeds land shells in large quantities;
- 11) Great quantities of mammal bones are found in loess
- 12) whenever a basin between hills is filled with loess, the slopes of these hills are covered in angular fragments of close by located rock, upon which the yellow soil lies.

Von Richthofen published in 1886 the first comprehensive German book about geomorphology (Liu, 1988) detailing observations made about the aeolian origin of loess during his extensive journeys to China (Liu, 1988). He compared properties of *huangtu* (Chinese loess) and loess and concluded that both materials were basically sharing the same common properties listed above (Liu, 1988).

### **John Hardcastle linking loess and climate**

John Hardcastle, from New Zealand, suggested, most likely for the first time, a link between loess and climate in “On the Timaru loess as a climate register” (Hardcastle, 1890; Smalley et al., 2001; Smalley and Fagg, 2015). In this work, Hardcastle’s observations point to the significance of glacial actions in supplying material for loess deposits (Smalley and Fagg, 2015) and concludes that loess deposits could record climate, thus a potential archive of how climate had evolved over time. Hardcastle’s work can be seen as pioneering of loess-related paleoclimatology.

### **Connecting loess genesis to glaciers (Pavel Tutkovskii)**

Pavel Apollonovich Tutkovskii was born in 1858 in Vinnitsa Oblast (formerly Lipovets) and died in 1930 in Kiev. He was a geologist and researcher of the Academy of Sciences of the Ukraine SSR (1919) and the Academy of Sciences of the Byelorussian SSR (1928). His important contributions connected distinct glacial deposits and structures, including the genesis of loess, to environmental conditions (Smalley et al., 2001) building on initial speculations by Hardcastle, which received rather low worldwide recognition (Smalley et al., 2001). Tutkovskii’s work also took time to propagate across scientific communities but this all changed in 1900 when he published his observations in English (Tutkovskii, 1900) in addition to his native Russian language (Tutkovskii, 1899), and in 1910 after presenting his work at the 11<sup>th</sup> international Geological Congress in Stockholm (Smalley et al., 2001) in German (Tutkovskii, 1910).

### **Vladimir Afanas'evich Obruchev and desert loess**

Vladimir Afanas'evich Obruchev (1863 - 1956) was a Russian loess researcher and the pioneer of desert-loess related research with a study published in 1911 (Obruchev, 1911). His ideas of desert-loess and its aeolian transport were developed initially from observations in the region around the city of Tomsk (Tomsk oblast, located in Western Siberia and Mid-Russia) (Smalley et al., 2019) and published in 1952 in the seminal work "Loess and its significance" in the journal *Nouyi Mir* (Obruchev, 1952).

### **Lev Semenovich Berg's in-situ loess formation hypothesis**

Lev Semenovich Berg (born in 1876 in Bendery, Moldova, died in 1950 in Leningrad) proposed a very different process of loess formation. A process in which loess is a product of weathering and soil formation and excludes any means of sediment transport (Smalley et al., 2001). From the existing literature it is still not clear when L.S. Berg came up with the "in-situ" formation idea until he published initially his work in 1916 (Berg, 1916) in Russian and post mortem in an English translation (Berg, 1964) performed by the Israel program for scientific translations. What is known is that L.S. Berg worked on loess deposits in western Russia – in the Chernigov province (Smalley et al., 2001). L.S. Berg was not a supporter of an aeolian origin of loess. In his initial Russian publication and further English translation (Berg, 1964) p. 18) he stated: "According to the theory which I started developing in 1916, loess and loess-like rocks formed in-situ, from the most diverse material, composed of fine earth, rich in carbonates. As to the aeolian origin of loess, I flatly deny it." In addition to fueling controversy, Berg initiated discussions on a so-far not-recognized but essential process whereby accumulating mineral dust transforms into loess, which he called "loessification". He describes this process in his 1916 work as the transformation of non-loess-ground to loess ground (Berg, 1916, 1964) with weathering and pedogenesis as the main driving factors. Berg would pass away in 1950 still convinced that loess was not of an aeolian origin but having contributed to advancing loess research with the concept of loessification, a process recognized yet poorly understood in present-day. At present, loessification is not considered to be a pedogenic process but rather a means by which accumulating mineral dust is stabilized preventing further transport (Smalley et al., 2010; Smalley and Marković, 2014).

## **Rudolf Grahmann, the beginning of European loess cartography**

Rudolf Grahmann (born 1888 in Leipzig and died in 1962 in Koblenz, Germany) was a German geologist, at the University of Leipzig, with main interests in Quaternary research, hydrogeology and archeology. He presented the first European loess distribution map in 1932 (Grahmann, 1932) in collaboration with his colleagues B. Brandt, G. Dubois, G. Grötzinger, and F. Münichsdörfer. (Grahmann, 1932).

Updated European loess distribution maps were published thereafter in the Association française pour l'étude du Quaternaire (AFEQ) Bulletin in 1969 (Fink, 1969), in Petermanns Geographische Mitteilungen in 1977 (Fink et al., 1977), and in the International Union for Quaternary Research (INQUA) newsletter in 1983 (Haase et al., 1983).

Grahmann's work remained the foundation for the first modern digital loess distribution map presented by (Haase et al., 2007). The most recent European loess distribution map is presented in (Lehmkuhl et al., 2021) and is used throughout the present dissertation.

## **Richard Joel Russel – Adoption of the “in-situ” idea of loess**

Richard Joel Russell (1895 – 1971), professor at Louisiana State University in Baton Rouge (USA), served as president of the Geological Society of America (1955-1956) and was elected to the National Academy of Sciences in 1959 (Howe, 1971). As a supporter of Berg's ideas of loess formation through weathering and pedogenesis, his conviction (loess is not aeolian in origin) is based on research conducted with Harold N. Fisk during expeditions up the Mississippi, Ohio, and Tennessee Rivers and along the Atlantic Coastline (Howe, 1971; Smalley et al., 2001). Russel's arguments (Russell, 1944) included observations such as:

- 1) Loess being found on slopes facing all directions, making it difficult to determine a specific wind direction responsible for the observed distribution;
- 2) Consistently uniform grain size distributions of loess are unlikely (inconsistent) with wind or water driven depositional processes;
- 3) Observed loess layering appears more consistent with a colluvial process (soil that has been moved by gravity) rather than an aeolian (wind-related) process.

Many were in opposition with Russell's view providing counter-observations from (Doeglas, 1949) loess in both the Dutch region and the lower Mississippi Valley. A full bibliographic list of commentaries to (Russell, 1944) is reported in (Smalley, 1980).

## **Chinese Loess stratigraphy and Liu Tungsheng: “ordinary people doing extraordinary things”**

Liu Tungsheng (1917-2008) was a Chinese loess scientist and one of the most honored loess scientists worldwide (Zhang et al., 2018). Tungsheng stepped onto the international scene at the 6<sup>th</sup> INQUA meeting in Poland in 1961 (Smalley et al., 2001). Here, with collaborator Zhang Zong-hu (former Chang Tsung-hu), they presented the precise stratigraphy of a 120 m thick Chinese loess deposit from Wucheng, intercalated by multiple paleosols (Liu and Chang, 1964). Their detailed stratigraphic description supported the idea that different climatic periods/events were preserved in the loess and paleosol deposit. Liu’s contributions to loess research in the following decades (see below collaborations with F. Heller) and up to his death were outstanding and pathed the way for loess research.

## **Julius Fink and the INQUA loess commission**

Julius Fink founded the INQUA sub-commission on European loess stratigraphy in 1961. In 1969, the sub-commission reached full commission status and the focus extended to global loess stratigraphy. Julius Fink stayed at the helm of the commission until the 10<sup>th</sup> INQUA congress when replaced by Marton Pécsi, a member of the Hungarian Academy of Sciences (Smalley et al., 2001). Fink’s efforts to make loess stratigraphy an important cornerstone of the INQUA research interests also increased the importance of loess research in Quaternary studies foreseeing, knowingly or inadvertently, the potential of loess studies to reveal Quaternary history.

## **George Kukla: Reshaping the Quaternary with loess research**

George Kukla (1930-2014) was a Czech paleoclimatologist and loess researcher at the Lamont-Doherty Earth Observatory at the University of Columbia (USA). Kukla was the first loess researcher to investigate the famous terrestrial loess sequence of Krems-Schießstätte (or Krems riffle range site) and to correlate the terrestrial loess record successfully to deep sea sediment records of paleoclimatic variability (Kukla, 1970). Kukla shed light into Pleistocene and end of Pliocene climate variations and stated that all climate (terrestrial recorded) variations can be recognized in marine sediments. Kukla contributed significantly to European loess research, establishing a comprehensive continental wide loess stratigraphy (Kukla, 1975) and enhanced land-sea correlations summarizes in Figure 21 of (Kukla, 1977), and similarly for Chinese loess research (Kukla, 1987; Kukla and An, 1989). By recognizing the palaeoclimatological link between loess deposits and deep-water isotope, Kukla paved the way for future loess studies.

### **Friedrich Heller and Tungsheng Liu paving the way for loess magnetism research**

Pioneering studies performed by Friedrich Heller and Tungsheng Liu paved the way for magnetostratigraphic and paleoclimate studies of loess-paleosol sequences. In their first paper (Heller and Liu, 1982) they presented the first paleomagnetic stratigraphy for a 136m long borehole profile close to the key site Luochuan located in the Central Chinese Loess plateau. They were able to identify the Brunhes-Matuyama, the Jamarillo and the Olduvai geomagnetic events. Based on their identified polarity changes, they provided for the first time a paleomagnetically dated loess-paleosol sequence covering the last 2.4 Ma. The magnetic susceptibility data identified intercalated paleosols outlining 17-recorded glaciations. A similar number had been identified previously in European loess deposits by (Kukla, 1975, 1977) and correlated to the 17 glaciations recorded in deep sea sediment record from the Atlantic (van Donk, 1976). In (Heller and Liu, 1984), the Luochuan loess magnetic susceptibility record was refined by doubling the number of samples and correlated to the paleomagnetic age controlled V28-239  $\delta^{18}\text{O}$  record (Shackleton and Opdyke, 1976) of the Pacific. Spectral analysis of the magnetic susceptibility record identified the 41 ka astronomical obliquity period (Heller and Liu, 1986) improving the age model and enabling to deduce that the apparent sediment accumulation was reduced by 25 % during interglacial highlighting the significant difference in sedimentation accumulation between glacials and interglacials.

## 1.2. The definition of loess, its distribution and processes resulting in loess-paleosol sequences

### Common characteristics of loess as a sediment

Loess is an accumulation of aeolian mineral dust comprised dominantly of 50-70% silt sized (10-50 $\mu$ m) angular shaped particles of quartz (Muhs et al., 2014). Loess also contains more variable amounts of fine silt, clays and fine sands. The mineralogical assemblage is typically completed by feldspar, micas and carbonates as well as other magnesium and iron bearing mafic minerals and oxyhydroxides. Loess appears in a color range from pale yellow to brownish ochre yellow. One type locality (*locus typicus*) of loess accumulation is the Haarlass site, close to the city of Heidelberg, Germany (Fig. 2).



Figure 2: The Haarlass site type locality of loess accumulation, near Heidelberg (Germany). Photo provided and permission by Ludwig Zöller.

The mineralogy and isotopic composition of loess deposits worldwide are representative of the average composition of the upper continental crust (Chauvel et al., 2014; Gong et al., 2017). Despite these common characteristics of loess, local and temporal variations in grain size distributions, mineralogical assemblage and appearance (color, texture, ...) are observed and reflect variations of distances to source areas, distance of transport source-to-sink, and post-depositional processes (e.g. pedogenesis, diagenesis). These variations enclose information about prevailing environmental and climatic conditions of source and sink areas; where mineral dust is deflated and accumulates, respectively.

### **Its distribution worldwide**

Loess covers around 10% of the Earth's terrestrial surface (Pye, 1987; Pécsi, 1990) and is widespread especially in the northern hemisphere (Muhs and Bettis, 2003). A recent compilation (Li et al., 2020) of global loess-regions is shown in Figure 3. In Europe alone, loess covers about 20% of the terrestrial land mass (Haase et al., 2007; Vasiljević et al., 2014). The most recently updated loess- and loess like sediment distribution map (Lehmkuhl et al., 2021) is shown in Figure 4. Loess covers at the time of accumulation mostly steppe or semi-steppe regions, where arid or semi-arid environmental conditions are maintained due to higher potential evaporation than precipitation (Pye, 1987; Muhs and Bettis, 2003). In these regions, the thickest loess deposits can also be found (see Fig. 3 taken from (Li et al., 2020)). The three most prominent loess-covered areas are the Chinese loess plateau, the Russian plains, and the Great Plains of Northern America and within the Mississippi Basin (Evans and Heller, 2003).



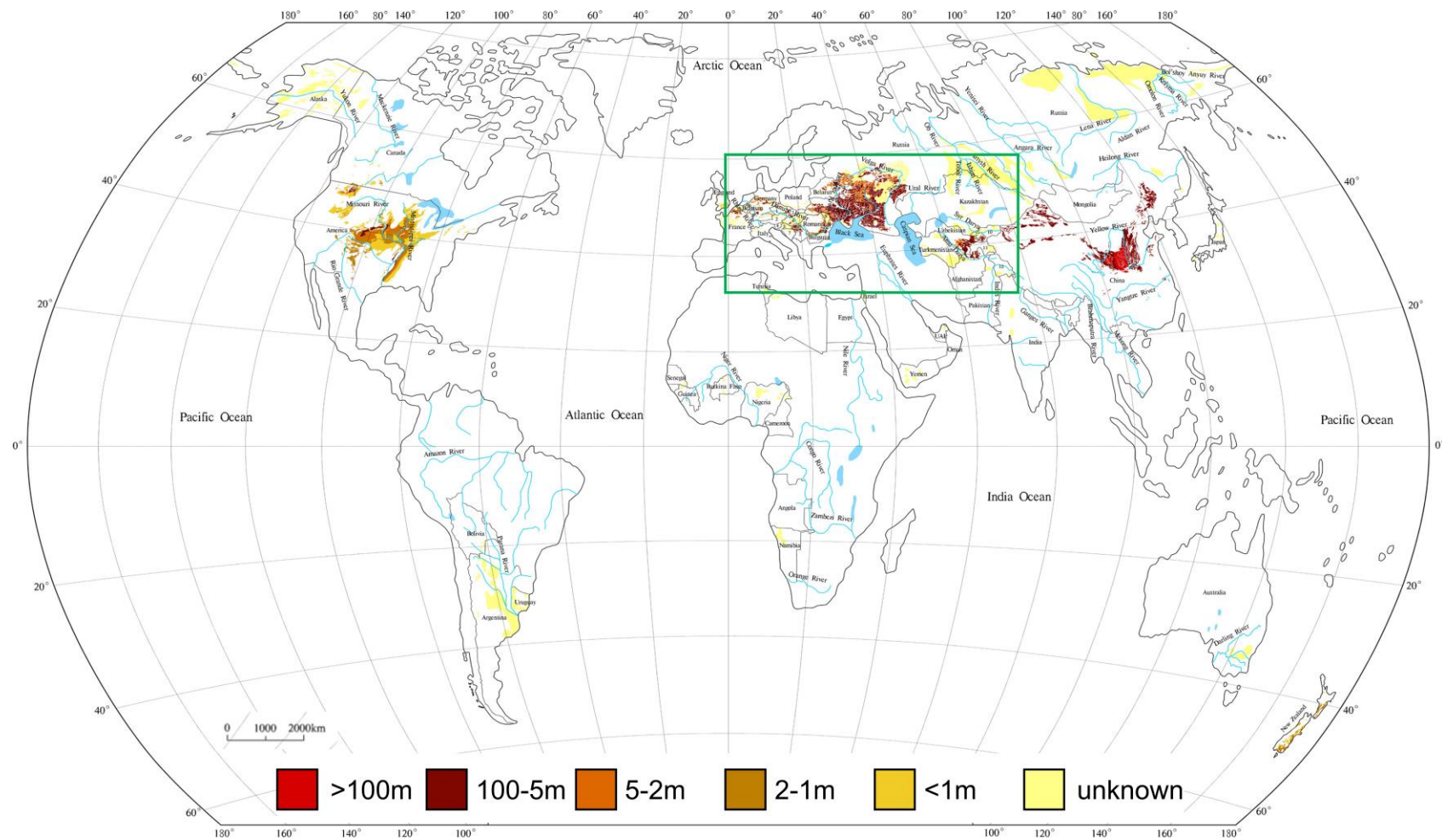


Figure 3: Global loess distribution adapted and modified from (Li et al., 2020). The color scale indicates the thickness of loess accumulation. The green rectangle delimits the area from which loess-paleosol sequences or loessite sequences presented in the core chapters or appendix of the present thesis were investigated.

Figure 3 confirms that the thickest loess distributions are preserved in the northern hemisphere and the thickest are found in the central part of the Chinese loess plateau. In addition to the three “hotspots” mentioned previously, the European loess belt, distributed between 40° and 60° latitude north (Fig. 4) contains significant deposits spatially spread nearly continuously from Western Europe to Eastern Europe and thickening eastward. Other regions, because of lower or lack of data availability (Li et al., 2020), are not shown in Figures 3 and 4, such as loess in Japan, Armenia (e.g., the Matmata Basin (Mettig, 2020), the northeastern Iranian (Kehl et al., 2005, 2021; Vlaminck et al., 2016; Lauer et al., 2017) in northwestern Turkey and Kashmir (Dar and Zeeden, 2020; Zeeden et al., 2021; Mir et al., 2022). However, studies have been presented or published for these, which could be incorporated in future maps, as envisioned by (Li et al., 2020).

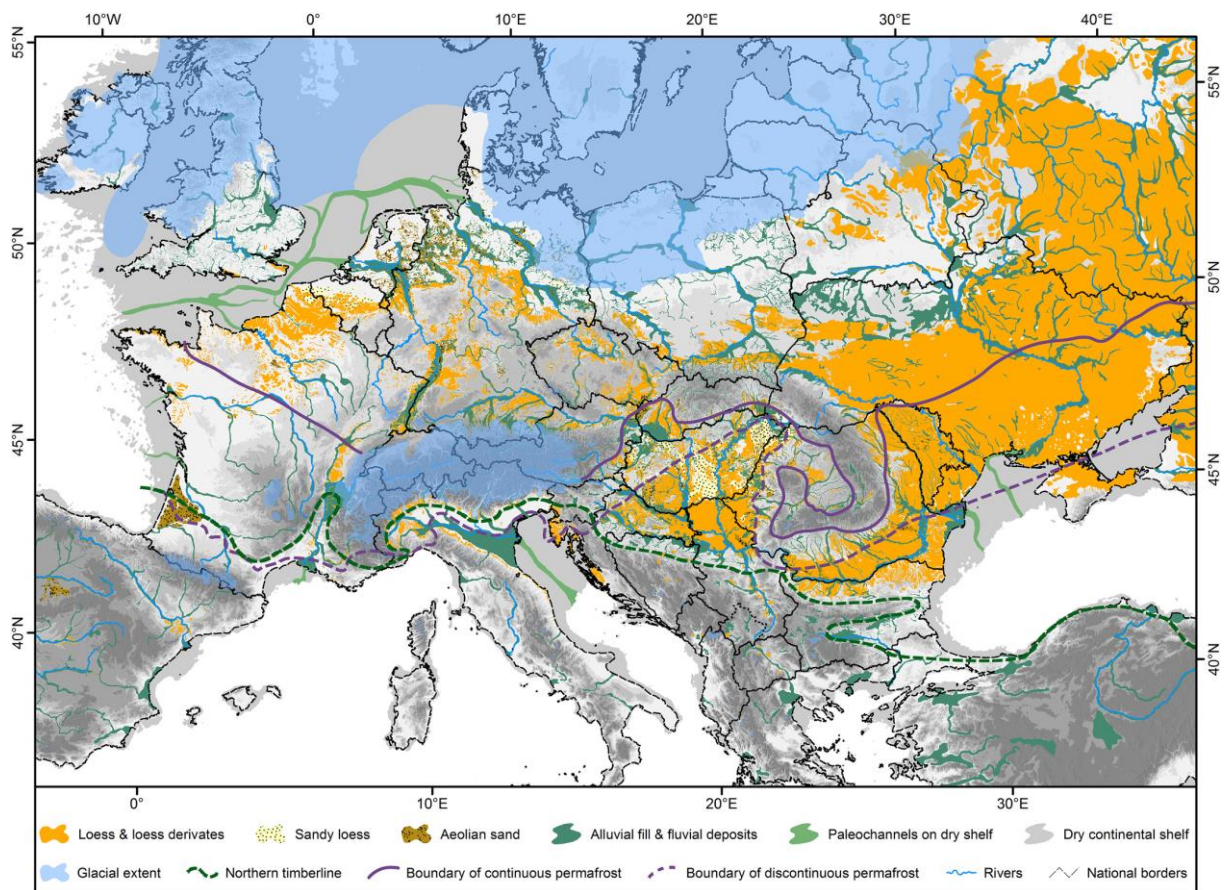


Figure 4: Most recent loess distribution map for Europe (Lehmkuhl et al., 2021).

### **Distinguishing different types of loess**

Loess deposits can be further divided into glacial loess and desert loess based on the genesis of the mineral dust and characteristics of the sediment pathway. Glacial loess, as its name implies, originates from the production of mineral dust formation by glacial grinding. Source areas of loess are proglacial sander and gravel surfaces, periglacial river valleys, with feral rivers, frost soils, pediments and alluvial fans in (semi-) arid areas, intra-montane basins of dry regions, glacial-eustatically dry-fallen shelves. (Zöller, 2017) underlined especially the latter mentioned importance and long-time neglected significance of shelves from the British-French channel and the North Sea as source areas for European loess deposits. Furthermore, (Zöller, 2017) mentioned the importance of source areas for Western-, Middle-, and Eastern loess deposits as former periglacial regions.

### **From mineral dust to loess to a loess-paleosol sequence**

Loessification is considered as the process whereby mineral dust is diagenetically transformed to loess (Zöller, 2017) and can be viewed as a universal process (Pécsi, 1990) because occurring in all continental environments where mineral dust accumulates. A first step of loessification is trapping the mineral dust particles preventing it from being further deflated and transported. (Svirčev et al., 2013) mentions a biological loess crust which aids in trapping particles. A persistent vegetation cover consisting of grasses and shrubs in the sink area may also trap dust. The neo-formation of carbonate bridges between particles or cementation is another process involved in the formation of loess (Zöller, 2017) and increasing the structural stability of loess leading to the observed loess cliffs, for example, along the Danube River. The initial or primary stages of loessification are distinct from a pedogenic process (Sprafke and Obreht, 2016). However the later or secondary stages of loessification during which the initial loess-like structures stabilizing mineral dust particles are enhanced lead to the incorporation of loess into the lithosphere and/or the pedosphere (Sprafke and Obreht, 2016).

Relatively thick loess accumulations appear in the field to be layered due to non-weathered loess being intercalated by weathered loess units. Glacial conditions, characterized by cold and dry climate conditions, reduced vegetation cover, lower sea-level and strong winds, favor an increase in mineral dust supply by facilitating deflation, uptake, and transportation by wind and the deposition of mineral dust over widespread areas. Under interglacial conditions, characterized by warm and humid conditions, increased vegetation cover, higher sea-level and lower velocity winds, mineral dust availability decreases entraining less deflation, less uptake and transport of lesser mineral dust from sources to sinks. The reduced mineral dust

accumulation in combination with prevailing moist and warm climate conditions allow surface soil formation (or pedogenic alteration) of previously accumulated mineral dust. The rate of mineral dust accumulation and climatic conditions predominantly dictate the development of a loess – paleosol sequence, whether the pedogenic process will be accretional, top-down or a combination of both (e.g. Jordanova and Jordanova, 2020), and consequently how one reads and interprets the physical properties archived in a loess – paleosol record.

### 1.3. Earth's climate history – how far can we go from a loess point of view?

The loess deposits the Chinese Loess Plateau (CLP) have thicknesses as great as 300 m (Liu, 1988), which is much thicker than European LPSs. The central and southern parts of the CLP provides the most complete LPSs recording up to 34 loess – paleosol couplets (Yang and Ding, 2010). Therefore, LPS of the CLP can provide insights into the paleoclimatology of the Quaternary Period (last ~ 2.6 Ma) (Liu et al., 1999) and as far as 6 or 7 Ma into the Pliocene and Late Miocene epochs if the underlying red clays are considered (Ding et al., 1999b; Nie et al., 2016).

Across the European loess belt, the thickest deposits are found in Eastern Europe within the Carpathian Basin and Lower Danube area (see review of (Marković et al., 2015)). Here, loess and paleosol sequences archive up to the last 1 Ma of Earth's climate history at key locations in Hungary (Paks and Udvari U2-A borehole (Pécsi et al., 1995; Frechen et al., 1997; Sartori, 2000; Thiel et al., 2014; Sümegi et al., 2018)), Czech Republic (Forster et al., 1996), Titel-Stari Slankamen composite (Marković et al., 2011, 2015), Batajnica (Marković et al., 2009a, 2011, 2015), Mošorin (Marković et al., 2011, 2015), Viatovo, Koriten, Lubenovo (Jordanova et al., 2007, 2008), Lunca (Necula, 2006; Constantin et al., 2015), Zimnicea (Radan, 2012), and Ukraine (Hlavatskyi and Bakhmutov, 2020, 2021). Several glacial/ interglacial cycles can be studied going as far back as the glacial marine isotope stage 20 (MIS 20).

## 2. Studying loess-paleosol sequences

To study loess-paleosol sequences, a broad palette of analytical methods are already commonly applied. These methods aim to provide geochronological, sedimentological and or palaeoclimatological constrains derived from LPSs. Geochronological approaches can be of absolute or correlative nature. Absolute dating techniques often applied in LPSs are  $^{14}\text{C}$  (e.g., (Lang et al., 2003)) and luminescence dating (Duller, 2008). These techniques are rather costly and time consuming but provide (below their dating limits) absolute ages for the LPS of interest. In contrary, correlative geochronological approaches aim to identify common patterns of climatic fluctuations preserved in indicative paleoclimatic proxies (Marković et al., 2015). This method allows age assignment for all investigated samples but care must be taken by understanding correlated proxies from a loess-paleosol sequence compared to another (not identical) proxy. A sub-discipline of correlative age modeling is cyclostratigraphy. Cyclostratigraphy is applied on long-time covering sedimentary series which uses tuning approaches of in sedimentary series imprinted parameter variations by insolation changes, which are combined effects of the Earth's orbital eccentricity, obliquity and precession (Strasser et al., 2007). A combined correlative and absolute dating technique is the investigation of oriented samples for reconstruction of the Earth's magnetic field strength and direction. The reconstruction of the Earth's magnetic field strength allows a correlation to the Virtual Axial Dipole Moment and identification of geomagnetic reversals or excursions provide absolute dates (Channell et al., 2020). Sedimentological/micromorphological approaches aim with aid of thin sections to investigate microfeatures preserved in sediments. These microfeatures indicate prevailing conditions during erosion, transport and post depositional diagenesis (Menzies and Meer, 2018). Paleoclimate proxies derived from different disciplines provide detailed insights into prevailing climate regimes and environmental evolution (Obrecht et al., 2019), and thus allow e.g., qualitative and/or quantitative temperature, precipitation, vegetation composition reconstructions. Grain size distributions provide insights into wind intensity, wind direction and pedogenesis intensity (Újvári et al., 2016). Rock magnetic studies allow to investigate soil sediment humidity, intensity of pedogenesis, weathering, wind direction reconstruction (Lagroix and Banerjee, 2002), magnetic fabric, magnetic mineral concentration, composition and grain size indicative for past climate conditions during or after loess accumulation (Maher, 2011; Liu et al., 2012). X-ray fluorescence can identify the provenance of loess as well as weathering intensity (Liang et al., 2012). Colorimetric investigations applied to LPS in order to identify hematite and goethite

2



provide with these mineral abundances insights into precipitation, temperature, seasonality and winter mildness (Liu et al., 2011; Jiang et al., 2022). Investigations regarding mollusk assemblages provide insights into vegetation, humidity and summer temperatures (Moine, 2014; Wu et al., 2018). Stable carbon isotopes  $\delta^{13}\text{C}$  provide information about C3/C4 vegetation type domination as well as indications of prevailing temperatures and precipitation (Hatté et al., 2013; Zech et al., 2013). Less commonly applied are approaches to investigate N-alkanes, which allow the reconstruction of vegetation compositions (Zech et al., 2007, 2013; Schatz et al., 2011). Analyses of branched glycerol dialkyl glycerol tetraethers (brGDGT) allow hence temperature reconstructions (Zech et al., 2012; Schreuder et al., 2016).

In the frame of this thesis, some of the aforementioned methods are used and partly improved. The loess-paleosol sequence of Plevén was investigated with an environmental magnetism approach, spectroscopic techniques such as diffuse reflectance spectroscopy as well as mid-infrared spectrometry. Granulometric measurements were conducted as well as a correlative age modelling approach. The following chapters will present a state-of-the-art overview about the employed disciplines.

## 2.1. Magnetism

### 2.1.1. Environmental magnetism

Environmental magnetism comprises the utilization of rock and mineral magnetism experiments to investigate the formation, transportation, deposition and post-depositional alterations of magnetic minerals under the influences of a wide range of environmental processes (Liu et al., 2012). Over the past decades a broad palette of magnetic experiments was developed leading to a multitude of different magnetic parameters, their ratios and other techniques such as IRM acquisition unmixing and first order reversal curves. These experiments are in loess- investigations commonly applied to gain insights into the magnetic mineralogy, the magnetic concentration and the magnetic grain size. These information are used to disentangle past climate changes, the characterization of e.g., paleosols and loess units. A more recent approach targets the identification and characterization of important marker horizons which are in Eastern loess-paleosol sequences represented as crypto-tephra layers (volcanic ash deposits invisible to the naked eye). These crypto-tephra layers are valuable stratigraphic markers since radiometric (e.g.,  $^{14}\text{C}$ ) and dosimetric (luminescence dating) reach their dating limits at ca. 50 ka and 250 ka, respectively.

Many studies performed on Eastern European Loess Paleosol sequences evidenced (e.g., via paleomagnetic dating) that more than 800 to sometimes 1000 ka are continuously preserved in Eastern Europe. However, paleomagnetic dating is sometimes difficult to apply since sampling is rather difficult and measurement time and evaluation is rather long. This hinders from a high-resolution magnetic stratigraphy so far. Further Paleomagnetic dating can be a combination of relative paleointensity (representing the strength of the Earth's magnetic field) correlations to well established RPI stacks such as PISO-1500 (Channell et al., 2009) and SINT-800 (Guyodo and Valet, 1999), or SINT-2000 (Valet et al., 2005), and the identification of geomagnetic reversals (such as the Brunhes-Matuyama Boundary) serving as an important marker point in the Quaternary and especially in Eastern European LPSs since in several LPSs the recording time is up to 1 -1.1 Ma ( (Marković et al., 2015; Song et al., 2018b; Sümegi et al., 2018; Hlavatskyi and Bakhmutov, 2020, 2021).



### 2.1.2. Hysteresis loops and isothermal remanent magnetization experiments

Hysteresis loops and isothermal remanent magnetization experiments provide a strong toolbox to magnetically derive insights into magnetic mineralogy, concentration and magnetic grain size. Hysteresis loops alone provide multiple parameters and are intensified by their outcome with distinct isothermal remanent magnetization experiments. Three main experiments that are usually conducted on the vibrating sample magnetometer are: the hysteresis loop, the acquisition of an isothermal remanent magnetization (IRM), and the backfield direct current demagnetization of the IRM (allowing further the determination of the coercivity of remanence ( $H_{CR}$ ), the s-ratio and the HIRM). A hysteresis loop is generally obtained by cycling the applied magnetic field from a strong positive field (for instance 1.5T), to the opposite field (i.e., -1.5T in this case), then back to the maximum field. Hysteresis loops provide the following parameters: coercivity ( $H_C$ ), saturation magnetization ( $M_S$ ), saturation remanent magnetization ( $M_{RS}$ ), and high-field magnetic susceptibility ( $\chi_{hifi}$ ).

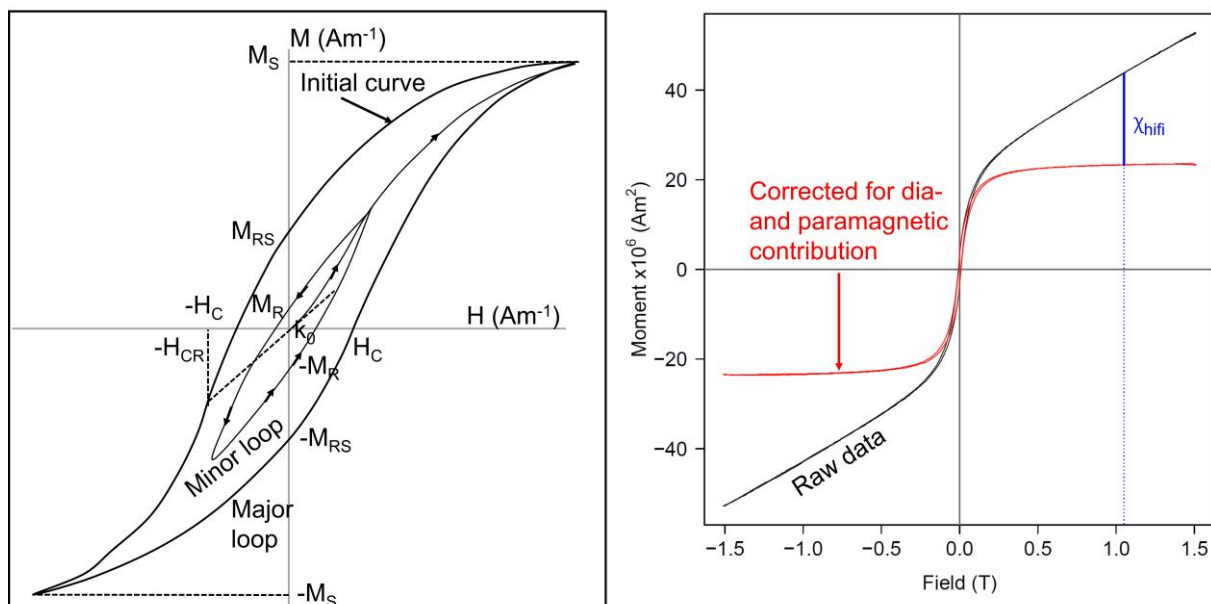


Figure 5. Left: schematic hysteresis loop with hysteresis parameters. Right: Hysteresis loop before and after correction for dia- and paramagnetic contribution.

#### Saturation Magnetization ( $M_S$ )

The saturation magnetization ( $M_S$ ) represents the magnetization of ferromagnetic grains in the maximum applied field, when all magnetic moments are parallel to the applied field.  $M_S$  is related to the type and content of magnetic minerals, but independent of the magnetic grain size (Liu et al., 2012).

### **Saturation Remanent Magnetization ( $M_{RS}$ ) – concentration dependent**

In this PhD thesis work and setting of experimental settings, the saturation magnetization of remanence ( $M_{RS}$ ) is equivalent to the SIRM.  $M_{RS}$  is generally used as an approximation of total mineral magnetic concentration with grain size larger than the superparamagnetic (SP) / single domain (SD) threshold (Zhang et al., 2007). (Thompson and Oldfield, 1986) stated in their study, that unlike the low-field magnetic susceptibility ( $\chi_{lf}$ ),  $M_{RS}$  is not influenced by (super) para- and diamagnetic minerals.  $M_{RS}$  vs.  $\chi_{lf}$  shows in Chinese loess a clear separation of loess and paleosol samples (e.g. (Zhang et al., 2007). Both higher  $M_S$  and  $M_{RS}$  values indicate an increase in ferrimagnetic minerals like magnetite and maghemite. Simultaneously, lower  $M_S$  and  $M_{RS}$  values indicate the absence of strongly ferrimagnetic minerals. The ratio of  $M_{RS}/M_S$  is declared as grain size dependent (Dunlop, 2002a, 2002b) for (synthetic) magnetite grains, but remains difficult to interpret for natural sedimentary samples (e.g., stemming from loess-paleosol sequences) since these natural samples are mixtures of different magnetic minerals in varying concentrations and different grain sizes. Many studies performed in the eastern European LPSs employing the Day-Dunlop plot indicate that the natural bulk samples reflect magnetic grain sizes in the pseudo-single-domain state (PSD).

### **Coercivity ( $H_C$ )**

The coercivity ( $H_C$ ) is the value of the applied field necessary to obtain a null induced magnetization, returning from saturation. Loess or paleosol samples with high contents of strong magnetic minerals such as hematite and goethite will increase  $H_C$ .

### **Coercivity of Remanence ( $H_{CR}$ )**

The coercivity of remanence ( $H_{CR}$ ) is the value of the backfield necessary to remove the remanent magnetization of the sample after saturation ( $M_{RS}$ ). Since  $H_{CR}$  is a grain size indicating parameter, the detection of tephra layers stems beside other parameters on very low values of  $H_{CR}$ .

### **Addressing magnetic grain sizes**

Several attempts were done in the past decades to employ environmental magnetic parameters to detect changes in magnetic grain sizes. (King et al., 1983) proposed the utilization of the ratio of the susceptibility of anhysteretic remanent magnetization  $\chi_{ARM}$  vs. the low field magnetic susceptibility  $\chi_{lf}$  as a grain size proxy. Criticism was later mentioned by a study of artificial magnetite grains performed by (Maher, 1988) stating that  $\chi_{lf}$  is influenced by paramagnetic contributions. She advocated an exchange of  $\chi_{lf}$  by the SIRM (in this thesis

equivalent to  $M_{RS}$ ) since the SIRM is not affected by paramagnetic contributions and moreover sensitive to particles within the multi-domain (MD) grain size range. However, caution must be paid for possible occurring magnetic interactions of magnetite particles which affects the grain size dependence of mentioned magnetic parameters in case of densely packed artificial samples. The validity of applying magnetic parameters tested on artificial grain size assemblages is proved by good correlations and nearly equivalent magnetic behavior of natural sediment assemblages. The magnetic discrimination of magnetic grains of the fine SP grain size can be identified utilizing the magnetic grain size spectrum via  $\chi_{fd}\%$  or  $\Delta\chi$  and  $\chi_{ARM}/SIRM$  and the comparison to coarse MD contents (Maher, 1988).

### 2.1.3. Magnetic susceptibility

The most commonly applied magnetic parameter to receive stratigraphical information for separating different geomorphological / geological units inside a stratigraphic column is the low field magnetic susceptibility (hereafter labelled as  $\chi_{lf}$ ).  $\chi_{lf}$  is defined as the ratio between the magnetic response (or the induced magnetization,  $M$ ) of a material to an applied magnetic field ( $H$ ):  $\chi_{lf} = M/H$ . It is noteworthy, that all magnetic minerals inside a natural sample contribute to  $\chi_{lf}$ . Differences occur in intensity of contribution based on different kinds of magnetic behavior, different magnetic minerals and differences in concentration and regarding magnetic grain size.

Paramagnetic minerals like silicates and clays as well as diamagnetic materials like quartz and carbonates contribute but in a significantly lower amount than ferrimagnetic (magnetite, maghemite) and antiferromagnetic (hematite, goethite) to the bulk  $\chi_{lf}$  signal. A relative increase in the concentration of ferrimagnetic minerals or an increase of the ratio of magnetically soft to hard minerals result in an increase of  $\chi_{lf}$ . Thus,  $\chi_{lf}$  is widely accepted as an indicator of weathering and pedogenic modification of parent material (Zhou et al., 1990; An et al., 1991a; Verosub et al., 1993; Heller and Evans, 1995; Verosub and Roberts, 1995; Liu et al., 2012; Ye et al., 2020). Additionally, has been used as a proxy for monsoon precipitation intensity (e.g. (Zhao et al., 2020)).

### Frequency dependence of magnetic susceptibility

The frequency dependence of magnetic susceptibility (Eyre, 1997; Worm, 1998) as absolute values

$$\Delta\chi = \chi_{lf} - \chi_{hf}$$

Or as a percentage which indicates the relative proportion of abundance of super-paramagnetic grains compared to the bulk magnetic susceptibility (Mullins, 1977; Dearing et al., 1996, 1997):

$$\chi_{fd}(\%) = \frac{\chi_{lf} - \chi_{hf}}{\chi_{lf}} \times 100$$

The frequency dependence of magnetic susceptibility considers domain theory derived magnetic grain size behavior into account. In very small magnetic particles like so-called SD (single domain) magnetic grains, only a uniform magnetization is possible. This implies that a SD magnetic grain has a common magnetic alignment direction. When magnetic grains become larger in grain size, the aforementioned domain splits into further domains, so-called multi domains (MDs, e.g., (Worm et al., 1991)), which are separated by domain walls (Liu et al., 2012). The resulting magnetization in a SD particle is uniform and in an MD particle divers. An increase in measured magnetic susceptibility of SD grains of the same mineral will be therefore larger than measured on MD-only containing samples (Maher, 2016). Furthermore, the resulting / measured remanence of MD grains is lower than that of SD grains. The same holds true for the coercivity of SD grains which is higher than for MD grains comparing same mineralogical equivalent grains (Maher, 2016). Pseudo-Single Domain (PSD) grain sizes show mixed effects, because they have magnetic grain ranging in the SD area but contain multi-domains. Applying grain size dependent and coercivity dependent magnetic experiments, PSDs reflect rather low coercivities simultaneously increased remanence. PSD magnetic grain sizes serve as a main recorder of paleomagnetic variations (Maher, 2016). However, besides aforementioned magnetic grain size classes there is the super-paramagnetic (SP) magnetic grain size class which is a sub-class of the SD grains with a grain size smaller than 0.03  $\mu\text{m}$  (Banerjee et al., 1993). Absolute grain sizes depend thus on experimental conditions such as e.g., temperature (Stephenson, 1971). Stable single domains (SSDs), another subclass of single domain (SD) grains reflect a higher susceptibility, which is in comparison to MD and PSDs higher. SD particles have in general regarding magnetite and maghemite grains a average grain size of 20-75 nm (Roberts et al., 2017).

In combination with hysteresis loop measurements,  $\chi_{lf}$  can be further divided into the ferrimagnetic component (hereafter labelled as  $\chi_{ferri}$ ) and the dia-and paramagnetic component (hereafter named as  $\chi_{hifi}$ ).

The high-field slope susceptibility (hereafter assigned as  $\chi_{\text{hifi}}$ ) is a magnetic susceptibility derived from the high field slope of a hysteresis loop, stemming from the high field linear segment of the loop, after saturation (i.e., closing of the loop).  $\chi_{\text{hifi}}$  is seldomly discussed as a magnetic parameter, e.g. (Liu et al., 2012; Taylor et al., 2014), because many factors could influence this magnetic parameters.  $\chi_{\text{hifi}}$  is in general the nonferrimagnetic contribution to the bulk magnetic susceptibility, or, in other words, combined paramagnetic and diamagnetic contributions to the (low-) field magnetic susceptibility  $\chi_{\text{lf}}$  (Liu et al., 2012). Fluctuations of  $\chi_{\text{hifi}}$  can be caused by changes in concentration of mineral composition of the paramagnetic component of the bulk magnetic susceptibility or the unsaturated (or high-coercivity) ferromagnetic component (Taylor et al., 2014) or a mixture of both. In the case that all ferromagnetic material is perfectly saturated,  $\chi_{\text{hifi}}$  should be the dia- and paramagnetic contribution of the whole signal. In the maximum applied field, it is possible that not all iron oxides contained in the measured bulk sample will be saturated. This will be indicated by the not perfectly linear part of the loop, indicating that there are unsaturated magnetic minerals contributing to the high field slope of the loop, such as hematite. Goethite will also contribute to  $\chi_{\text{hifi}}$ . These two minerals can either be present as individual grains or as coatings on detrital silicate grains. At Pleven, a saw-tooth pattern has been observed in the  $\chi_{\text{hifi}}$  stratigraphic record, similar to patterns in analyzed grain size variations for shorter time periods (interstadials and stadials) reflecting changes in aeolian deposition, but with coarser grain sizes in cool phases (Antoine et al., 2009a). In glacials, the balance shifting to increased aeolian input (with respect to pedogenic input) is expected. A general increase of the material content at the onset of an interglacial will lead to higher amounts of hematite and goethite possibly affecting in the high-field slope. Therefore, different methods should be combined to disentangle the contributors to the high field slope. In case that goethite is contained in the high-field slope, low-temperature magnetic measurements can be very useful. The contribution of hematite can be tested by the comparison between the high-field slope and the faction acquired between 1.0 and 1.5 T.

The ferrimagnetic susceptibility component  $\chi_{\text{ferri}}$  is considered to be a mildly grain size dependent parameter owing to the effects of complex spin structures that depend on the size and shape of the investigated magnetic particles (Liu et al., 2012). The ferrimagnetic susceptibility component is calculated as the difference between the bulk magnetic low-field magnetic susceptibility and the high-field magnetic susceptibility:

$$\chi_{\text{ferri}} = \chi_{\text{lf}} - \chi_{\text{hifi}}$$

This leads to the fact that all ferrimagnetic grain sizes are included as well as anything else not taken out by the high-field slope.

High temperature magnetic susceptibility experiments are usually performed in an apparatus with a furnace, a cooling unit, and a magnetic susceptibility measuring unit. In the majority of conducted experiments, an argon atmosphere is used to prevent as much as possible the oxidation of the heated magnetic grains. The result of a heating cycle (usually between room temperature and 700°C) produce heating up and cooling down curves hereafter named  $\chi$ -T curves. These  $\chi$ -T curves are able to track changes in magnetic mineralogy during heating and are thereafter considered to be mineralogy dependent. Several studies employed  $\chi$ -T curves to disentangle mineralogy compositions in loess-paleosol sequences, e.g. (Deng et al., 2001, 2005; Liu et al., 2005, 2010). An example from a study from the Chinese Loess Plateau focusing on the Red Clay unit from (Zhao et al., 2020) shows in  $\chi$ -T curves a high initial magnetic susceptibility in combination with a “hump” at 320 – 450°C, which is declared as indicative for the relative abundance of fine-grained maghemite and furthermore the presence of hematite and goethite. The abundance of maghemite as a relative proportion of the decreasing signal towards higher temperatures was employed by (Gao et al., 2019) before to reconstruct quantitative values of paleoprecipitation based on a transect of mean annual precipitation gradients across the Chinese loess plateau.

Mainly, the reversibility or non-reversibility of a heating and cooling curve of high-temperature magnetic susceptibility measurements give assumptions about the organic content of the analyzed material. In the study of (Makaroğlu et al., 2018), irreversibility of thermomagnetic curves is associated with organic rich material. Furthermore, with respect to the cooling curves, if they show a sharp increase from 580°C towards ~ 300°C, an indication of a mineralogical transformation from paramagnetic minerals during the heating stage is present (Hrouda, 1994; Sagnotti et al., 1998). However,  $\chi$ -T curves in combination with prior CBD treatment (citrate-bicarbonate-dithionite) can show reduced values in their initial susceptibility and in combination with a non-visible variation up to 580°C and a constant behavior between 580°C and 700°C the CBD treatment removed maghemite, fine grained magnetite and hematite (Deng et al., 2000, 2005; Dunlop and Özdemir, 2013). Recent studies investigated high-temperature magnetic susceptibility measurements for the thermally forced transition of unstable maghemite to hematite.  $\chi_{300-450}$  is assumed in several studies a valuable indicator for the relative abundance of maghemite (Deng et al., 2001; Liu et al., 2005; Zhao et al., 2017, 2020) which is

sensitive for changes in paleo-precipitation and used for latter mentioned ability in Chinese loess deposits e.g. (Gao et al., 2019).

The more recent parameter  $\chi_{T_{max}}$  is considered to be grain size dependent and is defined as the temperature at which the magnetic susceptibility reaches a peak during heating. The expression of this peak depends mainly on the gradual unblocking of fine-grained SD-particles. These particles are in the single domain magnetic state at room-temperature but become unblocked at higher temperatures (Zhao et al., 2020). With increasing grain size,  $\chi_{T_{max}}$  also increases (Liu et al., 2005).  $\chi_{T_{max}}$  is possibly also affected by the reduction of hematite to magnetite associated with the combustion of organic matter. Another reason could be the neo-formation of minor ferrimagnetic phases during heating (Oches and Banerjee, 1996; Deng et al., 2004).

#### 2.1.4. Anhysteretic remanent magnetization

Anhysteretic remanent magnetization is the magnetization acquired by a sample with aid of a laboratory induced alternating field of 100 mT and a superimposed DC field of 0.05 mT (the standard protocol of paleomagnetism studies) and 0.1 mT as it is the standard for environmental magnetic studies. Small particles are more efficient acquiring remanence (e.g. anhysteretic remanent magnetization, hereafter abbreviated ARM), and yield higher values of ARM (Maher, 1988; Dunlop, 1995; Evans and Heller, 2003). ARM is sensitive to SD grains, with a grain size of  $\sim 0.02\text{-}0.06\ \mu\text{m}$ , and follows two different power laws with changing behavior above and below  $\sim 1\ \mu\text{m}$  with a steeper slope for smaller grains. This leads to higher ARM/SIRM ratios for samples containing a higher fraction of SD-PSD particles (Evans and Heller, 2003). The widely used susceptibility of the ARM is the ratio of the mass-normalized ARM (with the unit  $\text{Am}^2\text{kg}^{-1}$ ) divided by the applied bias field given as  $H$  and having the unit A/m. The resulting unit for the susceptibility of ARM ( $\chi_{\text{ARM}}$ ) is then  $\text{m}^3\text{kg}^{-1}$ , as in the case of  $\chi_{\text{f}}$ .

$\chi_{\text{ARM}}$  is an excellent measure for single domain (SD) grains because SD grains acquire easier a remanence compared to particles having several domain walls. This leads to lower magnetostatic energy configurations to acquire remanence (Evans and Heller, 2003). An example for that is the study by (Maher, 1988) where she compares two synthetic magnetite grain size powders with two different main grain size compositions. The first powder has mean grain size diameters around  $0.05\ \mu\text{m}$  and leads to a  $\chi_{\text{ARM}}$  of  $\sim 8 \times 10^{-3}\ \text{m}^3\text{kg}^{-1}$ . In contrast to that, the second powder with mean grain size diameters of  $1.0\ \mu\text{m}$  leads to  $8 \times 10^{-4}\ \text{m}^3\text{kg}^{-1}$  (note the one order lower  $\chi_{\text{ARM}}$ ) (Maher, 1988).

#### 2.1.5. Isothermal remanent Magnetization acquisition experiments and unmixing

Highly resolved Isothermal remanent magnetization experiments provide valuable information about mineral magnetic assemblages and magnetic grain sizes. The component separation enabled earlier but utilized here by (Maxbauer et al., 2016) provides further insights into past climate change. Since all loess or paleosol samples are represent a mixture of different magnetic mineral contributions and different coercivities, their unmixing helps to get insights in these variations.



#### 2.1.6. Magnetic parameter ratios

Magnetic parameter ratios are valuable proxies to either track changes in magnetic grain sizes or magnetic mineralogy. The ratios presented below does not compile all ratios but rather the ones which are utilized in this study.

##### **Grain size dependent ratios:**

Grain sizes vary because of either changes of pedogenesis (which favors neo-formation of super-paramagnetic particles) or intensified harsher glacial conditions where intensified wind velocities and dust storms allow the uptake and deposition of coarser magnetic grains. The ratio between  $\chi_{\text{ferri}}$  and  $M_S$  can be used to track variations in the relative concentration of superparamagnetic (SP) particles, assuming a constant magnetic mineral assemblage (Hunt et al., 1995; Liu et al., 2003, 2012), because  $\chi_{\text{lf}}$  or  $\chi_{\text{ferri}}$  are higher for SP than for SD grains. The anhysteretic remanent magnetization normalized by the low field magnetic susceptibility ( $\text{ARM}/\chi_{\text{lf}}$ , or better  $\chi_{\text{ARM}}/\chi_{\text{lf}}$ ) is a reliable tool to discriminate SP (assumed to be neoformed during pedogenesis) from larger single domain grains (SD), as SP grains cannot carry a remanence, while both SP and SD grains respond well to external field (high susceptibility, with that of SP grains being larger).

$H_{\text{CR}}/H_C$ , the so-called coercivity ratio which is the ratio of the coercivity of remanence to coercive force is grain size sensitive if magnetite is the dominant carrier of remanence. Values for this ratio of up to three indicate rather SD sized magnetite whereas larger values rather reflect the presence of PSD or MD grains (Day et al., 1977; Dunlop, 2002a, 2002b).

$M_{\text{RS}}/M_S$  is the ratio of saturation remanence and saturation magnetization and grain size dependent.  $M_{\text{RS}}/M_S$  is like  $H_{\text{CR}}/H_C$  sensitive for magnetite as remanence carrier. SD magnetite has average values of 0.5, whereas smaller values are indicative for coarser grains of magnetite like MD and PSD grains (Day et al., 1977; Dunlop, 2002a, 2002b).

$\chi_{\text{ARM}}/\chi$  increases with decreasing grain size and indicates changes in the magnetite grain size if the magnetic mineralogy is dominantly magnetite and significant amounts of SP particles are absent (King et al., 1982; Evans and Heller, 2003).

$\text{ARM}/\text{SIRM}$  is a sensitive indicator for grain size changes of magnetite. Smaller magnetite grains which have a grain size below 1  $\mu\text{m}$  rather present SD to PSD particles increase the  $\text{ARM}/\text{SIRM}$  ratio (Evans and Heller, 2003)

$SIRM/\chi_{lf}$  is the ratio of the saturation isothermal remanence and the low-field magnetic susceptibility. (Thompson and Oldfield, 1986; Peters and Dekkers, 2003) stated that under the precondition of a uniform magnetic mineralogy, and no significant presence of paramagnetic minerals,  $SIRM/\chi_{lf}$  tracks grain size variations of SD grain size, where higher values stem from the presence of smaller SD grains.

$IRM_{100}/M_S$  did not find application yet in studies performed on loess-paleosol sequences but provides a promising proxy for crypto-tephra identification. In general,  $IRM_{100}/M_S$  cannot be considered as a pure grain size dependent magnetic proxy. Overall, the ratio rather can be tentatively assigned as a efficiency of remanence carrier parameter which is only indirectly related to grain size of ferrimagnetic minerals. Stable single domain (SSD) grain sizes up to pseudo-single domain grain sizes are expressing the highest efficiency in remanence acquisition and are therefore often target of paleomagnetic studies. Coarser magnetic grain sizes in the SSD-SD-PSD grain size range are being expected from highly explosive volcanic eruptions.

### **Magnetic mineralogy:**

IRMs (Isothermal remanent magnetizations) applied in different field steps (e.g., as applied here in 100mT steps towards the backfield maximum of -1.5T) are the remanent magnetizations (i.e., measured in zero field) of a sample after applying direct current magnetic fields of increasing absolute values. The S-Ratio (King and Channell, 1991) is a valuable ratio to discriminate between soft and hard magnetic minerals (Frank and Nowaczyk, 2008). another mineralogical remanence based parameter  $IRM_{100}/IRM_{300}$  will put further evidence of tephra identification. The  $IRM_{100}/IRM_{300}$  parameter is in this thesis assumed to present the relative abundance of magnetite and maghemite. It is here assumed that only the magnetite acquires a IRM in fields up to 100 mT. Maghemite is here assumed that only and all maghemite acquires a IRM between 100 and 300 mT. The resulting ratio, including aforementioned pre-conditions provides a relative proportion of magnetite carried remanence compared to magnetite and maghemite carried remanence.

### **Identifying crypto-tephras utilizing expected magnetic characteristics**

Volcanogene ash layers (tephras) are widespread in European and Iranian loess-paleosol sequences (Poucllet et al., 1999; Horváth, 2001; Wacha et al., 2011; Fitzsimmons et al., 2013; Marković et al., 2015; Laag et al., 2018, 2021a, 2021b; Antoine et al., 2019; Kehl et al., 2021; Scheidt et al., 2021). Unfortunately, tephra layers are mixed with aeolian dust and are invisible

to the naked eye (then called crypto-tephras) and often identified after sample investigation in the laboratory, commonly indicated by standardly applied magnetic susceptibility as sharp but pronounced peaks. Highly explosive silicic volcanic eruptions are identified as the origin of crypto-tephra layers which are in LPSs accompanied by volcanic glass shards rather than volcanogene rock fragments or volcanogene minerals (Lowe et al., 2017). Based on the volcanic eruption process tephra layers are expected to have different grain size and mineralogical characteristics which differentiate them from bracketing loess.

Before a volcanic eruption, the magma is a fluid with high pressure prevailing before eruption. Metal-oxides crystallize first and are composed of oxides of Titanium (Ti), Iron (Fe) and Nickel, whereas Nickel-oxides are rather seldom and can be neglected. However, the elements Titanium and Iron have very similar ion-radiuses and are therefore incorporated into alloys equivalently. However, the statistical of Titanium incorporation into alloys is higher when higher pressures are present compared to Iron oxides. During the eruption, the afore present pressure decreases rapidly. The silicate-rich melt erupting is still fluid, which is contrary to already crystallized Fe- and/or Ti-oxide alloys. This leads to a kind of crystalline order of resulting mineral complexes. Higher order crystallization of silicates leads to higher amounts of volcanic glass shards. This leads to either silicate poor tephras, which contain high amounts of metal ions in the volcanic debris, whereas silicate-rich eruptions provide only small amounts of iron-bearing minerals. One can imagine a soup (molten material) in which are peas contained (already crystalized iron and titanium oxides). This soup hardens during the eruption immediately since the loss of pressure is present. This process leads to the incorporation of Fe- or Ti- oxide minerals inside volcanic glass shards which transform immediately from fluid to solid. The wind transportation of these magnetic grains incorporated in volcanic glass shards are leading to the deposition in Eastern Europe, accompanied by the mineral dust accumulation and hence environmental factors prevailing at the location of accumulation which directly influences the preservation of magnetic grains in grain size classes comprising the smallest SP towards larger MD particles. The incorporation of diverse magnetic grain sizes leads to a kind of protection of these grains when confronted with weathering conditions. Different scenarios are leading to different grain sizes present in tephra-bearing samples. For example, SP grains, which are highly sensitive to weathering and less volcanic glass shards present will lead to a lower preserved amount of SP grains but larger SD and larger grains able to carry remanence. High amounts of provided glass shards containing SP grains will lead to crypto-tephra layers indicating a higher preserved SP abundance which does not indicate pedogenesis but

preservation of volcanogene SP grains due to higher amounts of weathering protecting volcanic glass shards. This explanation might provide a better understanding of tephra-bearing samples which indicate a paleoclimatic signal with the presence of SP particles which stem not of paleoclimatic variability but volcanic activity. However, as (Till et al., 2011) showed in her study, that magmatic ejections resulting in tephra layers have in general coarser magnetic grain sizes since these layer represent rapidly cooled “frozen” magma at the time of eruption, which provides high amounts of SD and PSD sized magnetic particles in a ferrimagnetic low-coercivity magnetite / titanomagnetite mineralogy bracketed in loess. These rather large magnetic grains are less sensitive to weathering and are therefore assigned tentatively as a common characteristic of magnetic behavior preserved in LPSs regrading crypto-tephra samples. Having in mind grain size dependent and mineralogical magnetic parameters such as  $H_{CR}$ ,  $\chi_{lf}$ ,  $\chi_{ferri}$ , and thus  $IRM_{100}/M_S$ . Taking all aforementioned ideas into account, crypto-tephra layers shall have a magnetic character of: Low  $H_{CR}$ , high  $\chi_{lf}$ ,  $\chi_{hifi}$ ,  $\chi_{ferri}$ ,  $IRM_{100}/M_S$ ,  $IRM_{100}/IRM_{300}$ , S-ratio, with variable amounts of  $\Delta\chi$ .

#### 2.1.7. FORC analysis

First Order Reversal Curve (FORC) measurements enable a closer focus on magnetic grain sizes and found application on several LPSs in the past decades (Necula et al., 2013; Hu et al., 2015; Namier et al., 2021), with an increasing trend of continuous application over stratigraphical series in more or less high resolution. FORC analysis is rather time consuming but simultaneously very valuable. While grain size investigations utilizing hysteresis derived magnetic ratios such as  $M_{RS}/M_S$  and  $H_{CR}/H_C$  of bulk samples from loess-paleosol sequences always lead to Pseudo-Single Domain dominated mixture, FORC diagrams provide insight into coercivity distributions as well as particles interactions.

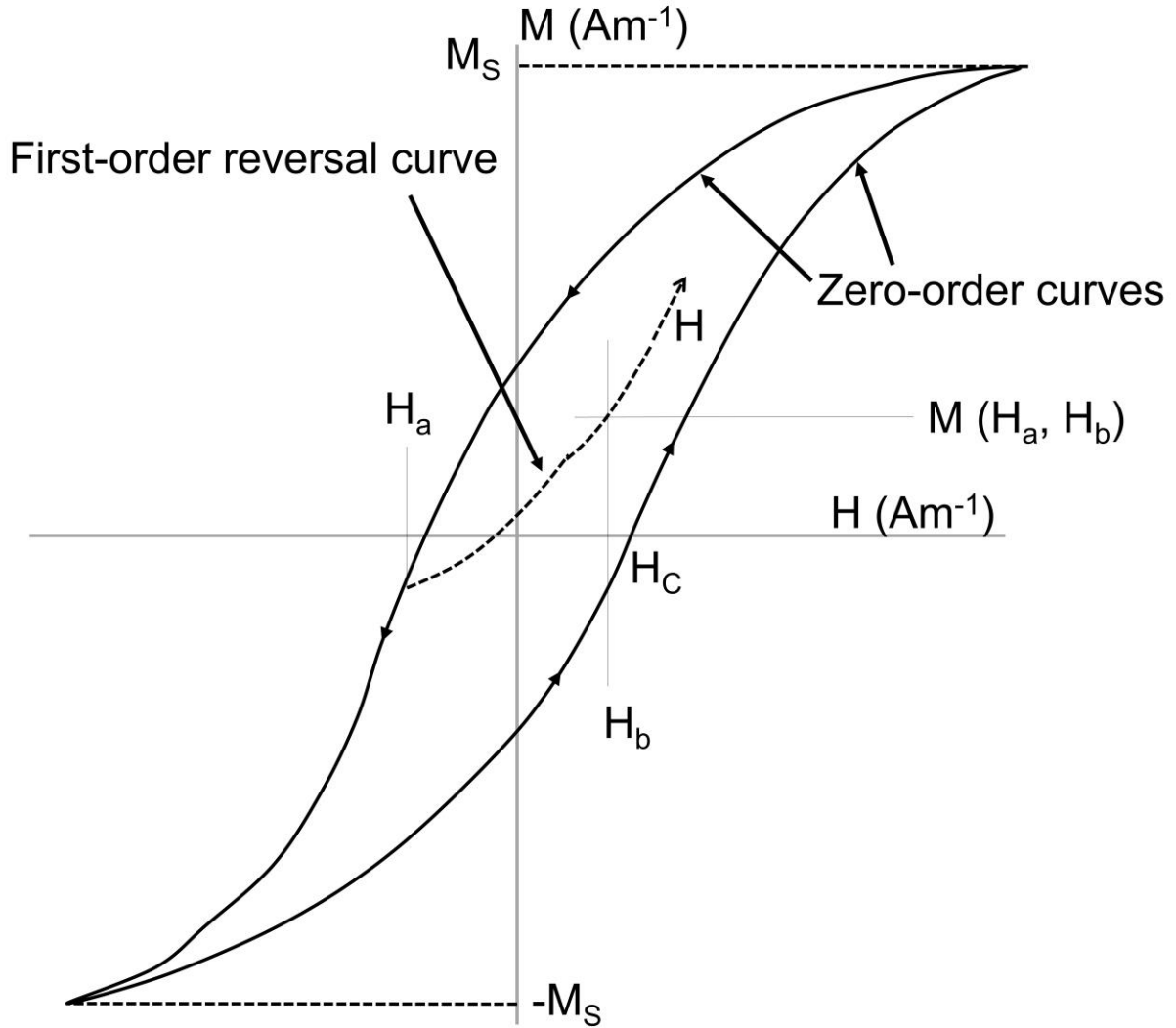


Figure 3: Scheme of a FORC measurement.

FORC measurements (Roberts et al., 2000, 2014; Pike et al., 2001; Egli and Winklhofer, 2014) stem from hysteresis measurements. A FORC measurement starts with a saturation of the sample in a large magnetic field. Then, the field is decrease to reach a reversal field ( $H_a$ ), and subsequently increased back up. A series of FORCs, generally more than a hundred, is thus generated, thus exploring the inside of the main hysteresis loop. The suite of FORCs can be used to determine the FORC distribution, which for any magnetization at field  $H_b$  ( $M(H_a, H_b)$ ) is expressed as:

$$p(H_a, H_b) = -\frac{\delta^2 M(H_a, H_b)}{\delta H_a \delta H_b}$$

In practice, it is convenient to plot the FORC distribution using the new coordinates

$$H_C = \frac{H_a - H_b}{2}$$

and

$$H_U = \frac{H_a + H_b}{2}$$

representing the coercivity and bias field, respectively. Contour plots of the FORC distribution using  $H_C$  and  $H_U$  as horizontal and vertical axes are called FORC diagrams.

## 2.2. Colorimetry

The relationship of colorimetric variations in soils and paleoclimatic changes is discussed and known since the past decades, e.g. (Carter, 1956; Kász and Werner, 1962; Schädel and Werner, 1963). Munsell color charts for the identification of distinct colors were applied over the past decades e.g., (Deng et al., 2004). However, alpha-numerical values for colors reflected by samples investigated are hardly to process and even harder to evaluate statistically. Attempts e.g., by (Torrent et al., 1980) to convert these alpha-numerical values into graphically and statistically representative displays such as the redness rating (RR) calculated as:

$$RR = (10 - H) \times \frac{C}{V}$$

Where C and V stand for the numerical values of the Munsell derived chroma and value and H which is representing the hue, where YR (yellow-red) hue ratings were considered by their afore notated decimals, but reddish ( R ) skips the scale from e.g., 10 to 0.

However, recent developments inside e.g., the R programming language (R Core Team, 2023) allows an user friendly approach to re-calculate in-field taken Munsell color values, in times, where spectrophotometers were not invented or available. This allows not only to visualize investigator derived Munsell color values (which are in literature always presented in stratigraphical tables or expressed as a result of rather complex formulas, e.g., RR) and it is for a reader only possible to study the Munsell color charts by the given alphanumerical values during reading the text of the manuscript. Here, we underline this possibility to statistically re-evaluate the massive amount of Munsell color data presented in older literature (and still current literature such as e.g., (Mahmoudian et al., 2022; Sun et al., 2022)), covert it with aid of the R-package “aqp” (Beaudette et al., 2022) into RGB values. These RGB values can be further converted to CIE-Lab values and allow then a stratigraphical visualization as performed in (Zeeden et al., 2017) and thus to perform colorimetric enhancement based on an idea of (Sprafke et al., 2020). Aforementioned color spaces such as the CIE-Lab color space and DRS derived mineralogical qualitative contents are more described in the following paragraphs.

### 2.2.1. The CIE 1931 color system

The CIE 1931 color system is a color space that was created by the International Commission on Illumination (CIE) in 1931. It is based on the human visual system's response to color and is used as a standard for representing colors numerically. The CIE 1931 color space is a two-dimensional representation of color, with the x-axis and y-axis representing the chromaticity coordinates of the color. The chromaticity coordinates describe the hue and saturation of a color, but not its brightness or luminance. The CIE 1931 color space is used as a reference for specifying colors in many fields, including color printing, television, and computer graphics.

### 2.2.2. Tristimulus values

The CIE 1931 color space is based on the concept of tristimulus values, which are a way of quantifying the human visual system's response to color. Tristimulus values are the amounts of three primary colors (red, green, and blue) that are needed to match a given color. The CIE 1931 color space defines a set of standard tristimulus values, known as the CIE standard observer, which are used to determine the tristimulus values for any given color.

The chromaticity coordinates (x, y) can then be plotted on a graph, known as the chromaticity diagram, to represent the color in the CIE 1931 color space. The chromaticity diagram is divided into a series of curves, known as the spectral locus, which represent the colors that can be produced by monochromatic light sources (i.e., light sources that produce light of a single wavelength). The chromaticity coordinates of a color can be used to determine its position on the chromaticity diagram and, therefore, its hue and saturation.

### 2.2.3. The Lab color System

The Lab color system spans a three-dimensional sphere with three axis. The Luminance ( $L^*$ ) is the vertical (y) axis, defining the brightness of the material of investigation.  $L^*$  ranges from 0 to 100 % where 0 defines black and 100 white. The two horizontal axis x and y assign redness ( $a^*$ ) and blueness ( $b^*$ ) in a range of negative and positive values.  $a^*$  is negative green and positive red,  $b^*$  is negative blue and positive yellow.

The use of the Lab color system in comparison to widely used Munsell color charts for characterization of soil and loess colours is the throughout numerical appearance of the measured data which is easily to be statistically analyzed, manipulated, compared/correlated to other e.g. magnetic or granulometric data and easily to display and enhanced in graphs. Several studies performed on loess-paleosol sequences utilized redness-rating (RR) or redness ( $a^*$ ) derived from spectrophotometers as either a indicator for the presence of hematite and/or a



indicator for the degree of weathering.  $b^*$  providing with more positive values rather yellowish colors is assumed to indicate the presence of goethite. Stemming from these implications, the ratio of  $a^*/b^*$  is in several studies employed as a hematite/goethite ratio. However, the provided  $L^*a^*b^*$  data is determined rather complex and integrates over several DRS-single nm wavelengths.

Since  $a^*$  is rather targeting red colors, it was and still utilized as a parameter reflecting redness which is in paleoenvironmental studies referred as hematite since it has in its pigmenting grain size a very reddish color. In the contrary,  $b^*$  is expressing rather yellowish colors which as then assigned as the goethite content. Resulting of these assumptions, the ratio of  $a^*/b^*$  was assumed to represent the ratio of hematite and goethite. However, these parameters integrate several wavelengths and might be misleading. Several other studies employed the co-measured diffuse reflectance spectra and their derivatives to extract physically better explained qualitative estimates of hematite and goethite based on their absorbance characteristics.

#### 2.2.4. DRS Diffuse reflectance spectrometry

Diffuse reflectance spectrometry (DRS) employs the reflectance and after transformation absorbance spectra as a function of the wavelength, most commonly applied in the visible light range between 400 and 700 nm. Different magnetic minerals such as hematite and goethite reflect different intensities of absorbance at specific wave intervals which stem from their mineral characteristics. In the past decades it became modern to investigate especially thick paleoenvironmental archives such as marine and limnic, as well as loess-paleosol sequences in a high-resolution utilizing DRS. This procedure finds its motivation since the initial studies performed targeting hematite and goethite contents via first and second derivatives (Kosmas et al., 1984, 1986). In the following years, extensive measurements of DRS spectra were exploited to access mineralogical constrains reflecting past climates (Ji et al., 2001, 2002), and finds application and methodological improvement until today (Lepre and Olsen, 2021; Cao et al., 2022; Jiang et al., 2022).

### **Indicative 1 derivative and 2 derivative values to disentangle hematite and goethite**

To disentangle qualitative goethite and hematite contents, several studies performed aiming in identifying these minerals qualitatively utilized different protocols of data evaluation. What these studies have in common is the application of the Kubelka-Munk function (Kubelka and Munk, 1931), which transforms diffuse reflectance values of a visible light spectrum into absorbance values. However, several studies only employ either the first derivative (Deaton and Balsam, 1991; Guo et al., 2022) of the resulting absorbance spectrum and some studies employ the second derivative (Kosmas et al., 1984, 1986; Scheinost et al., 1998; Jiang et al., 2022). Not mentioned in all studies are the measurement conditions and settings used for measurements (such as observer angle, open width of the device oculus) and if the samples were homogenized and measured under laboratory conditions (artificial light of a day-light shielded room) or if measurements were performed on boxed material or bare material.

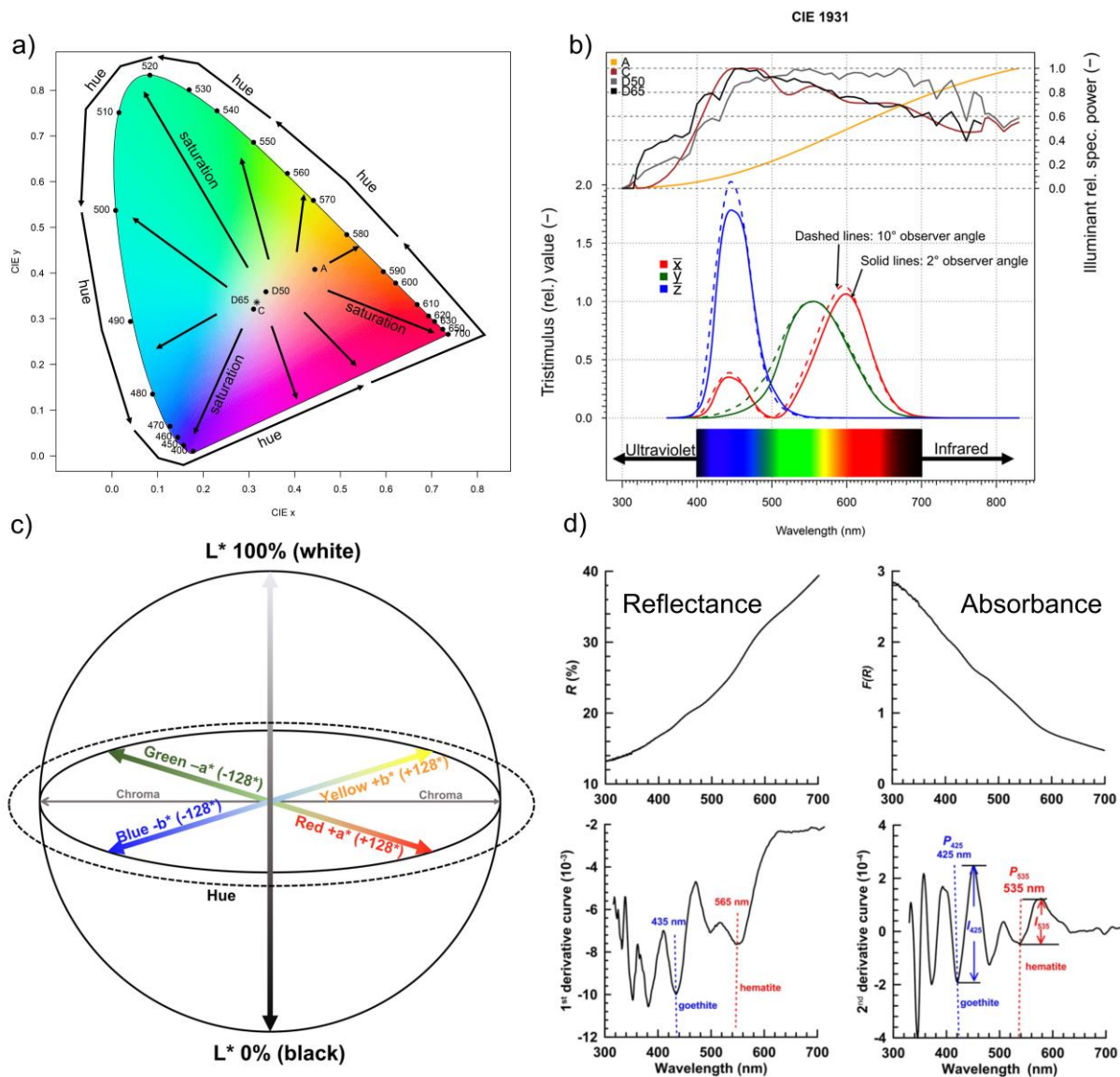


Figure 4: a) A two-dimensional representation of the CIE1931 color system. Wavelengths (in nm) later employed to identify semi-quantitative amounts of hematite and goethite, stemming from diffuse reflectance spectra (DRS) are indicated as well as white-values for different selected illuminant standards (A, D50 and C). The standard illuminant D65 is used in this thesis. B) Top: The Illuminant relative spectral power as a function of the wavelength. Middle: Relative tristimulus values on a wavelength scale and the 2° and 10° observer angle in comparison. Bottom: Visualized visible and invisible light range between 300 and 850nm. C) Schematic representation of the spheric L\*a\*b\* color system. Absolute numerical limit values of the x- and z-axis are theoretical and might be impossible to be visualized with colors. D) Extract of figure 9 from Jiang et al., 2022 (modified). Panel on top left shows the raw reflectance spectrum, panel on the top right the applied Kubelka-Munk function resulting in the absorbance spectrum. Bottom left represents the first derivative of the absorbance spectrum and panel on the bottom right the second derivative. Goethite and hematite wavelengths and discriminative peaks or lows are indicated.

### **Implications and limitations of colorimetric values to discriminate magnetic minerals**

The application of DRS spectral analysis to gain insights into magnetic minerals such as hematite and goethite found broad presence in several studies employing these minerals as proxies for paleoenvironmental and paleoclimatic change on various time scales. However, most applied relatively spectrophotometers provide a resolution of 10nm inside the visible light spectrum (400-700nm) where absorbance spectra indicate the qualitative presence or absence of hematite and goethite. However, a multitude of minerals is present in bulk samples stemming from loess-paleosol sequences which might contribute to absorbance spectra of hematite and goethite. One indication for that is the clay mineral montmorillonite, which has a spectral absorbance peak around 520 nm (Szeberényi et al., 2020). Measurements conducted with higher resolution spectrophotometers (e.g., allowing a resolution of 0.5 nm) will better discriminate between different minerals contributing to the DRS spectra. Coupled with mid-, near and far infrared methods, this approach could be significantly strengthened in its outcome. With only applied DRS spectral analysis will not be a straightforward method disentangling the mineral assemblage of samples taken from loess-paleosol sequences.

### **Enhanced and detailed DRS investigations of hematite and goethite**

Spectrophotometers which a higher resolution (e.g., 0.5-1.0 nm) allow a more detailed investigation of hematite and goethite. Several factors can influence the absolute waveband positions for hematite and goethite and provide therefore further insights into, e.g., past climate change, change of source material. Controlling factors of color properties of hematite and goethite are identified as variations in grain size e.g., (Morris et al., 1985), aluminum (Al) substitution and specific surface area (SSA) (Torrent and Barrón, 2003), and crystal shape. (Liu et al., 2011) further confirmed that in their study the overall controlling factor for shifts in waveband peak positions is Al-substitution. An increased Al-substitution results in a shift towards smaller DRS waveband positions of hematite and goethite by 1-3nm (Liu et al., 2011). However, Al-substitution is a valuable paleoenvironmental indicator, which increases due to higher pedogenesis intensity coupled to higher acidity during interglacials, providing larger amounts of Al<sup>3+</sup> in the sediment. Hence, the width of the absorption band could indicate with enlargement a rather aeolian-hematite signal compared to a narrow opening and higher-in-amplitude of the spectrum-waveband absorbance location for hematite, which indicates rather pedogenic neof ormation of hematite. Further XRD analysis evidencing the absence/presence of Al might indicate a rather grain size influenced shift of DRS peaks of hematite such as

investigated by (Lepre and Olsen, 2021). They conclude that a shift towards smaller wavebands (535-550nm) indicated rather smaller hematite particles.

However, disentangling different factors controlling the waveband positions of hematite and goethite are challenging with no further (e.g., XRD) experiments since Al-content, grain size, SSA and crystal shape co-vary (Liu et al., 2011). Additionally, commonly applied spectrophotometers such as utilized in this thesis have a resolution of 10nm, which hinders subtle changes of waveband positions of peak values of 1-3 nm as identified by (Liu et al., 2011).

#### 2.2.5. Colour contrast enhancement – indications for an easier accessible soil classification?

Colorimetric parameters stemming from the Lab color system can be translated to the commonly known RGB color system. Employing this process allows to visualize measured colours graphically and allows to follow stratigraphical changes systematically by perception. Unfortunately, this procedure was not often employed even several years after presenting the approach by (Zeeden et al., 2017) and most times remained as line graphs restricted to  $L^*a^*b^*$  values (Panin et al., 2021). Visualizations of Lab colours by translations to RGB colors in loess research was initially done by (Zeeden et al., 2017) by using an available R-package provided by the R-core team (R Core Team, 2023) named “grDevices”. Pushing that state-of-the-art forward, the initial code stemming from (Zeeden et al., 2017) was modified for automatic borders of minimal and maximal axis as well as the possible complementation into stratigraphic depth (or age) scales for the resulting plot or for the implementation into stratigraphic parameter fluctuations incorporated into that colorimetric summary of a sequence of loess and intercalated paleosols. Transforming Lab values into RGB values sometimes misses important stratigraphical information or hints for the appearance of paleosols since the colorimetric changes are very soft and on badly calibrated PC-screens barely to see by eye. Therefore, for example, Sprafke developed a Excel sheet for contrast enhancement of resulting Lab colours after translation to RGB colours within his work about a Austrian LPS (Sprafke et al., 2020).

## 2.3. Granulometry

### 2.3.1. Methods

The identification of grain size compositions and changes over a stratigraphical column was found valuable to provide insights about pedogenic processes (e.g., the formation of clays), changing wind intensities and the detection of distinct storm events providing stratigraphically distinct layers of coarse grain sizes, respectively. In the early beginnings, pipette method employing Stokes' law was the method of choice for investigations of grain size compositions. With rising technological process, laser diffraction grain size measurement devices found place in many sedimentological laboratories. Most common is the Beckman-Coulter series of products, on which also Plevén samples in the Laboratory Géographie Meudon and Zmajevac samples at the LIAG in Hannover were measured. For avoiding aggregate formation and most efficient separation of single grains, different methods can be applied prior to measurement.

At the LIAG in Hannover (Novothy et al., 2011; Wacha et al., 2018, 2021) the samples are typically placed in a overhead rotator for at least 8 hours in a solution of ammonium hydroxide. The average values of three successive measurements are then obtained. In the case of Plevén, samples were not chemically treated, as carbonate contents were too high.

Similar to the LIAG Hannover protocol, the Meudon protocol also skips the chemical treatment prior to measurement. However, during sample preparation, a measured amount of material is filled in plastic tubes with a hexameta phosphate sodium solution, and rotated in an overhead rotator for at least 24 hours for the same purpose of grain size separation thus avoiding the formation of aggregates. After that step, wet sieving is performed with a 160 micron sieve to remove large carbonate concretions and snail shells and other organic matter. After that, the measurement is conducted, always comparing different measurements with each other and the resulting error, when error too high, the measurement of a single measurement was repeated. The leftovers > 160 microns are dried in an oven at 40°C and weighted, and sealed for further investigations of the composition of the coarse grain size fraction. With noted initial sample weight for the grain size analysis and the left-over mass after drying, the relative percentage of coarse grain material can be calculated.

### 2.3.2. Grain size spectra

Grain size spectra in loess can provide different information, for example about changing sources of the material or (like in Wacha et al., 2018) presented additional inputs of volcanic ashes (hereafter referred as tephra layers). Several studies employing grain size spectra show a uni-modal behavior, one peak at the silt section and a varying amount of clay content, thus a

varying coarse grain size content. Double peaks in the grain size spectra were discussed e.g., in (Machalett et al., 2008) which were identified in the silt size range. Identifying different end members for contributing for the whole grain size spectra, statistical analysis such as the end member modelling performed by (Dietze and Dietze, 2019) and MatLab based packages provided by (Paterson and Heslop, 2015) were used in past studies. In the following thesis, the approach by (Paterson and Heslop, 2015) was utilized to discriminate between different grain size end members. Paterson and Heslop's approach enables the application of diverse distributions such as the Weibull distribution, which is for the limiting lower grain size range of clays and sieving at 160  $\mu\text{m}$  more realistic than assuming for these grain size classes a rather normally distributed behavior.

### 2.3.3. Standard Grain size variables

Grain size parameters of loess samples are commonly calculated to gain insight into past wind dynamics (such as wind speed), and distances to potential dust sources varying from millennial to glacial/interglacial cycles. Further influencing conditions potentially modifying grain sizes at a site are vegetation cover at the source area as well as the precipitation regime at the sink and source areas.

The U-ratio is the ratio of the coarse silt and medium silt grain size fractions and is calculated as:

$$U - ratio = \frac{\text{vol\% of coarse silt}}{\text{vol\% of fine silt}} = \frac{16 - 44 \mu\text{m}}{5.5 - 16 \mu\text{m}}$$

And was proposed (Vandenberghe et al., 1985, 1997; Vandenberghe and Nugteren, 2001) as proxy a rather glacial conditions with highly dynamic aeolian environment with high U-ratio values and interglacial conditions with lower U-ratios.

In 2008, (Machalett et al., 2008) introduced the concept of the "twin peak" (TP) ratio. This ratio is calculated by dividing the volume percentage of very coarse silt (30.1-63.4  $\mu\text{m}$ ) by the volume percentage of medium to coarse silt (11.8-27.4  $\mu\text{m}$ ):

$$TP - ratio = \frac{\text{vol\% of very coarse silt}}{\text{vol\% of medium to coarse silt}} = \frac{30.1 - 63.4 \mu\text{m}}{11.8 - 27.4 \mu\text{m}}$$

Variations in the individual peaks of a bimodal dominated grain size spectrum are thought to reflect the effects of aeolian dust transport and wind strength at a local or regional level. High TP-ratios indicate colder periods with stronger winds that transport coarser particles, while low TP-ratios reflect more interglacial conditions with weaker winds.

Initial studies presented by (Liu et al., 1989; Ding et al., 1992) employed ratios of <2µm/10-50 µm and <2 µm/ > 10 µm grain size ratios to gain insights into past wind intensity variations. The concept of the commonly applied grain size index (GSI) was later introduced by (Rousseau et al., 2002). The GSI is an indicator that generally reflects the changes in the efficiency of the processes that involve picking up, moving and laying down of both coarse and fine dust particles, which is directly influenced by the variations in the wind velocity. This concept was first introduced by (Rousseau et al., 2007) and used to correlate the German LPS Nussloch successfully towards the NGRIP dust record on a millennial timescale (Rousseau et al., 2007; Antoine et al., 2009b).

This index (modified in absolute grain sizes by application of laser particle size granulometric measurements) is widely regarded as a dependable measure of wind activity and an appropriate indicator for atmospheric dust.

$$GSI = \frac{\textit{coarse silt}}{\textit{fine silt \& clay}} = \frac{26 - 52.6 \mu m}{< 26 \mu m}$$

In comparison with the U-ratio, the GSI includes the clay grain size fraction too. Higher grain size index values display increased frequency and intensity of dust storms which result during glacials into high sedimentation rates. However, the GSI seems to be rather a integrative proxy displaying not only wind strength but also other environmental factors such as combined wind and precipitation factors (Újvári et al., 2016). Mean grain sizes and median grain sizes are hence commonly applied grain size related parameters and underly the assumption that the overall / average/ median grain size is a function of wind speed/strength and therefore often applied to LPSs to trace these environmental variations (An et al., 1991b; Derbyshire et al., 1995; Chen et al., 1997). During the late 90s and early 00s, several researchers brought additional environmental states contributing to the median and mean grain sizes such as changes in aridity in the source area (An et al., 1991b), or also the increasing and decreasing extent of desert dust sources which might indicate the source to sink distance of loess in China (Ding et al., 1999a, 2005). (Sun et al., 2010, 2012) interpreted the loess grain size variations as a combination of the factors of winter monsoon strength, wind intensity, distance of source and sink areas of mineral dust as well as the aridity and extent of source areas but playing a minor role compared to wind intensity.



#### 2.4. Attenuated total reflectance Fourier Transform Infrared Spectrometry (ATR-FTIR)

ATR-FTIR is a method to examine the clay mineralogy of sediments (which is comparable to XRD analysis aiming the same goal). However, compared to XRD techniques, ATR-FTIR analysis are faster and cheaper to perform. Therefore, large sample numbers can be analyzed leading to a high-resolution record of clay mineral composition changes, which are displaying past climate changes. ATR-FTIR is a mid-infrared technique that is sensitive to water bearing minerals ( $\text{OH}^-$  and  $\text{H}_2\text{O}$ ) such as clay minerals and other sheet silicates (e.g., smectite, muscovite, kaolinite and chlorite). Sediments that were influenced by weathering processes lead to higher portions of these minerals and serve therefore as an indicator for weathering. Furthermore, ATR-FTIR can detect amorphous silicates which are a result of weathered tephra material (e.g., which is XRD analysis not capable for).

So far, only few studies were presented which employed ATR-FTIR experiments being applied on loess-paleosol sequences stratigraphically and in a high resolution to gain insights into past climate change. However, the discrimination between different clay minerals is not possible by magnetic, colorimetric or granulometric experiments so far, but provides additional information of paleoenvironmental/paleoclimatic variations since the neo-formation of different clay minerals is significantly influenced by e.g., rainfall, seasonality, temperature. (Udvardi et al., 2014) is one of seldomly performed studies employing ATR-FTIR analysis on loess-paleosol sequences and compiled a valuable and extensive table in which different clay minerals are identified by their qualitative abundance in loess-paleosol sequences. However, just listing different wavenumbers assigned to water-bearing minerals would be misleading but a measured spectrum of a sample stemming from a paleosol and one of a loess unit reflects remarkably the mineral abundances differences. (Udvardi et al., 2014) presented a mineral abundance table which might be not complete and is further enlarged by ATR-FTIR characteristics resulting in a peak for goethite at  $\sim 449/450 \text{ cm}^{-1}$  (Cornell and Schwertmann, 2003), which is close to the sensitivity range of ATR-FTIR experiments. Besides the initial study of (Udvardi et al., 2014) no study is known employing ATR-FTIR experiments in a fine resolution applied to loess-paleosol sequences of Eastern Europe to identify clay mineralogy and trace back past environmental and paleo-climatic change.

However, no other study showing the extraction mechanism of clay minerals performed on loess-paleosol samples is up to now and to our knowledge available. However, mineral specific wavenumbers (in  $\text{cm}^{-1}$ ) assigned for different (clay) minerals are compiled by (Udvardi et al.,

2014) and build on analysis performed by (Wada, 1967; Farmer, 1974; van der Marel and Beutelspacher, 1976; Hlavay, 1978; Madejová and Komadel, 2001; Cornell and Schwertmann, 2003; Vaculíková and Plevová, 2005; Jung et al., 2010). In frame of this thesis, analysis were performed on an Bruker Vector 22 mid-infrared spectrometer equipped with an ATR extension allowing the analysis of grinded dry sediment material.

## 2.5. Determining ages in loess-paleosol sequences

### 2.5.1. Absolute

Absolute dating methods aim to provide an absolute age (with errors) for an investigated sample. Different methods such as luminescence dating and  $^{14}\text{C}$  dating found wider application in loess-paleosol sequences. Commonly applied absolute (radiometric or dosimetric) dating techniques have advantages and obstacles. First of all,  $^{14}\text{C}$  dating is a reliable method to date loess deposits when charcoal or plant remains are present. Taking numerous calibration curves for  $^{14}\text{C}$  dating into account, this method is very precise and reliable (providing rather low age uncertainties) for the last 50.000 years. Luminescence dating can be split into thermally and optically stimulated luminescence methods which diffused in either quartz or feldspar assessments and mineral-dependent a various amount of different applied protocols. The largest obstacle when applying luminescence dating is the estimate of the water history in which the taken sample / sediment was taken. The water history massively changes the absolute dating outcome by more than 20% of the estimated / calculated absolute age. Luminescence dating experiments might provide reliably ages up to 160- 200 ka, luminescence experiments performed on feldspars allow an older absolute time determination potentially reliably for the last 250 ka only. One example given is the vast amount of luminescence age determinations performed on the Biały Kościół loess-paleosol sequence, located in last glacial ice margin close distance and the Croatian LPS Zmajevac. For Biały Kościół, (Zöller et al., 2022) proposed different luminescence protocols for a LPS (which most likely represents the last 140ka (the last interglacial/glacial cycle). Ages of the oldest samples diverge in their mean ages by about 100 to 200 kyrs, indicating with one protocol applied for Biały Kościół in the early Eemian but also provides ages of  $405 \pm 30\text{ka}$  for the same sample indicating the onset of the interglacial by more than 300 ka shifted. The same kind of age-uncertainty and large age discrepancy stemming from different applied protocols targeting different minerals (quartz & feldspars) and different grain size compositions puts question marks on the reliability of luminescence dating methods.

### 2.5.2. Correlative

Corelative age models have been applied in various paleoclimatic / paleoenvironmental reconstruction studies. Terrestrial archives lack in a commonly and robust and furthermore valid absolute chronology since many absolute dating techniques such as  $^{40}\text{Ar}/^{39}\text{Ar}$  dating cannot be applied to sedimentary archives and so the only available dosimetric dating stems from feldspar luminescence dating with errors up to 120ka or luminescence dating restricted reliably to the last 130ka with a median error of 10% (13ka). However, major glacial and interglacial shifts are recognized on marine and terrestrial archives, leading to the overall applied correlation of terrestrial archives towards globally distributed stacks of environmental change such as the famous LR04 stack ((Lisiecki and Raymo, 2005). As from the beginning of loess research identified e.g., by Kukla (Kukla, 1975, 1977), recorded interglacials and glacials in loess deposits stem from the same source, the orbital parameters of the Earth. These appearing changes are well known being preserved in the global sea level (see the model calculation by (Imbrie and Imbrie, 1980) and overall calculated orbital cycles such as presented by (Laskar et al., 2011).

### 2.5.3. Tephrostratigraphy vs. Tephrochronology

Any volcanic ash layer (visible or invisible in the field - leading to the label of tephra (visible) and crypto-tephra (non-visible by the naked eye in the field) is composed of rock-fragments, glass shards in highly variable amounts and other minerals or materials which are ejected into the air during a volcanic eruption. These marker horizons are preserved in Eastern European LPSs and based on prevailing westerly wind directions of the at least 800 ka might stemming from volcanic rich and highly active regions from the western Italian volcanic ridge. Other “close-by” potential volcanic sources of accumulated tephra material. It must be stated that there are different disciplines of tephra research in context of loess-paleosol sequences.

The term “tephrostratigraphy” comprises attempts to identify tephra materials via different methods such as magnetism, color, spectrometric methods and granulometry. The identification of (crypto-) tephra layers inside a stratigraphical column and a rather robust knowledge about the assigned age-related stratigraphy allows a comparison towards other records / LPSs where the potential tephra layers might have been also observed. However, tephra identification was performed in Eastern LPSs mostly thought significant peaks in magnetic low-field susceptibility or applied on in-field outcropping tephra deposits. A pedostratigraphic framework generated based on a field observation approach and coupled with low-field magnetic susceptibility records established a quasi-chronological framework, in

which tephra layers are tentatively identified and after that – under the condition that the stratigraphical position is quasi-comparable, the assignment done that it might be a tephra equivalent. However, this approach is highly speculative since hard evidence (e.g., geochemical fingerprinting of volcanic glass shards) is in most cases not applied. The bare identification of tephra layers and their stratigraphical position and following correlation is for this thesis summarized under the term “tephrostratigraphy”.

The term “tephrochronology” is valid to be employed when e.g., a geochemical analysis of non-weathered glass shards of tephra layers was performed.  $Ar^{40}/Ar^{39}$  dated other tephra rich records such as the Fucino Basin (Giaccio et al., 2019), Lake Ohrid ((Leicher et al., 2021) and Tenaghi Philippon (Tzedakis et al., 2006) provide for the tephra layers preserved detailed geochemical composition analysis of the preserved volcanic glass shards. The combination of reliable  $Ar^{40}/Ar^{39}$  dating with correlating geochemically fingerprinted volcanic glass shards which enables the determination of the individual volcano and outback is comprised under the term of tephrochronology.

So far, with respect to loess-paleosol sequences, a very limited number of studies was successful in determining the geochemistry of volcanic glass shards and trace it back to its individual origin/outbreak (Pouclet et al., 1999; Fitzsimmons et al., 2013). Examples for that are the discrimination of the wide-spread and catastrophic outbreak of the Phlegraean Fields (Italy) at 39.8 ka BP where volcanic ashes accumulated in Romania (LPS of Urluia) with multiple decameter thickness (having an absolute distance of more than 1500 km) (Fitzsimmons et al., 2013; Veres et al., 2013). This event falls hence timely together with the demise of the Neanderthals occupying large areas of the Eastern European region (Black et al., 2015) and the several hundreds of years arising population of the modern human. Severe volcanic eruptions like the just mentioned Campanian Ignimbrite/Y5 tephra underlines the prompt consequences of this kind of landscape instability and naturally occurring hazards. Other attempts in geochemically fingerprinting preserved tephra layer such as the far spread “Bag-tephra” were undertaken by (Pouclet et al., 1999), which is stratigraphically located on the demise of the interglacial corresponding to the marine isotope stage MIS11 and in loess stratigraphy stratigraphically located at the demise of the S4 paleosol (Pouclet et al., 1999; Horváth, 2001; Fu et al., 2019).

The correct assignment and correlation towards a widespread or macroscopically preserved tephra layer is still under debate since geochemical results are not allowing a precise

determination of the origin of the tephra. One attempt by Yu Fu, so far only presented as a poster (Fu et al., 2019) at the INQUA in Dublin 2019, employed  $\text{Ar}^{40}/\text{Ar}^{39}$  dating applied on the Bag Tephra conserved at the Feduvar section which is with its stratigraphical assignment part of the Titel Stari-Slankamen composite profile. However, their absolute dating approach failed to capture the eruption age of this tephra. But a pyroxene composition analysis as well as a glass composition analysis offers the reliably way to correlate it to the so-called Villa-Senni eruption which is located at the Alban Hills and dated between 351 and 357 ka. These geochemical analyses rely on the intact glass shards determined by the weathering degree, which allows a successful determination of the geochemical composition or even not.

In most older tephra layers (older than the CIY5) multiple LPSs fail to preserve a stable condition in which a tephra layer or more detailed expressed volcanic glass shards can be preserved. Some factors protecting highly fragile volcanic glass shards are essential such as a high accumulation of mineral dust acting as a protective layer against weathering factors and such exclusion of bioturbation. In nearly no eastern European LPSs both of these conditions are given leading to highly weathered volcanic glass shards not able being analyzed by standard geochemical conditions. One overcome of this problem is the study of rare Earth elements enabled by ICP-MS laser ablation method. This method uses, unfortunately, a rather broad in diameter laser beam to transform the glass shard into steam and analyses its spectrum. Saying this it is essential to mount individual grains to avoid the measurement of mixed signals. The necessary single glass shard mounting process is very difficult to be performed but e.g., the University laboratory of Cambridge Tephra studies (Christine Lane) is capable and developed this method further.

However, from this PhD and the employed mid-infrared spectra analysis (ATR-FTIR) via a PCA provide a potential bypass of problematics stemming from too weathered glass shards. The idea behind is the “fingerprinting” of remaining minerals AFTER weathering of volcanic glass shards. Why should be this fingerprint be not discriminable and allowing the characterization of different tephras as done with geochemistry fingerprinting of intact/non-weathered glass shards? Initial approaches employing the ATR-FTIR method coupled with a PCA shows remarkable results. The previous mentioned CI-Y5 tephra was analyzed with various samples stemming from marine cores (Vigliotti, 2015) and the terrestrial archive, the LPS of Urruia (Fitzsimmons et al., 2013), where geochemical glass shard investigations confirmed that it is the same tephra layer. The PCA shows quite clearly that with the ATR-FTIR approach the weathering remains and even more important, independent of the kind of

archive, the tephra samples for this eruption can be evidenced. Moreover, a significantly older tephra layer (L2-tephra) falls together with numerous preserved L2 tephra records spread at least over several loess containing this tephra layer (Laag et al., 2018). Both statements lead to a novel and unique approach to not search for intact preserved glass shards but bypass this approach to identify and characterize the weathering products by ATR-FTIR methods. This enables to perform tephrochronology even on older than the 39.8 ka tephra and moreover opens a reliable pathway for Eastern European loess chronology and with a step further direct EELP – vs. marine archive correlations. A more detailed data presentation and discussion about the application of ATR-FTIR can be found in the objectives chapter targeting the Pleven manuscript in preparation.

## 2.6. Climate variability from orbital to millennial time scales

### 2.6.1. Orbital Forcing

The Earth's climate is strongly dependent of the Earth's orbital parameters. These parameters fluctuate cyclic, also known under the term Milankovitch cycles (Milanković, 1941). The orbital cycles have a different periodicity and are the Eccentricity, Obliquity and Precession. The combined effect of these three orbital parameters are the insolation. Eccentricity is the orbit shape of the Earth around the sun. The Earth wanders around the sun on a non-perfect circle but rather an ellipse. The reason behind is the gravitational force of Jupiter and Saturn, which cause the divergence of the Earth's orbit from perfectly circular orbit. The change of the Earth's orbit causes a direct change of the Earth's distance to the sun. A change of the Earth's orbit influences therefore the total amount of solar radiation on the Earth. Having a rather elliptic orbit causes an increase in 23 % of solar radiation reaching the Earth's surface. The modern state of eccentricity is a rather circular shape. Eccentricity cycles have a duration of 100 ky and cause generally the alteration between interglacial/glacial cycles. Obliquity is the tilt of the Earth's axis and the angle of which this tilt diverges from the orbital plane. Obliquity is the cause for seasons on the Earth. The tilt varies between 22.1 and 24.5°. With a higher tilt, the seasonality (or the different between seasons) increases. The average duration of an obliquity cycle is 41 ky. Precession is the gradual change in orientation of the Earth's axis of rotation. In general, the Earth wobbles around its axis during rotation. There are two types of precession, the axial precession and the apsidal precession. The axial precession is the Earth's wobbling caused by tides, which are hence caused by gravitational forces of moon and sun. The axial precession has a direct impact on the difference of seasonality extremes either on the northern or southern hemisphere. The apsidal precession ascribes the overall wobble of the entire Earth's orbit around the sun, which is caused by combined effects of gravitational interactions of the Saturn and Jupiter. In contrary to axial precession, the apsidal precession modifies the orientation of the Earth's orbit in relation to its elliptic plane. Insolation is the integrated effect of eccentricity, obliquity and precession resulting in the total incoming solar radiation on the Earth. The overall combined effect resulting in the insolation triggers besides others temperature and precipitation changes. Based on the tilt of the Earth, insolation changes gradually over latitudes.



### **Mid-Pleistocene transition**

The mid-Pleistocene transition is a rather long-time covering climate transition which reflects that glacial cycles before that transition rather express a 41 ka cyclicity and afterwards a pure 100 ka cyclicity. This transition occurred between 1250 and 700 ka (Hönisch et al., 2009) and can be found in various climate archives. The most prominent archive reflecting this transition is the Lisiecki & Raymo  $\delta^{18}\text{O}$  record (Lisiecki and Raymo, 2005).

### **Mid-Brunhes climate transition**

The Mid-Brunhes climate transition (MBT) falling together with the MIS 12 – 430 ka termination is a globally observed transition from rather temperate to warmer interglacials occurring during the middle of the Brunhes geomagnetic polarity chron (Ao et al., 2020). and is characterized e.g., in the Antarctic ice cores by higher temperatures and higher atmospheric  $\text{CH}_4$  contents after the MBT (Jouzel et al., 2007). The MBT was firstly observed by (Jansen et al., 1986) who identified on the southern hemisphere a general transition to more humid conditions during interglacials, which is in agreement with a study by (Hodell et al., 2003) focusing on marine cores stemming from the subantarctic South Atlantic. They describe additionally an abrupt shift towards lower  $\delta^{18}\text{O}$  values, thus identifying during marine oxygen isotope stage (MIS) 11 similar global  $\text{pCO}_2$  levels compared to the Holocene (Hodell et al., 2003) assign further the timing of the MBT event caused by the 413 kyr- covering eccentricity periodicity. Hence, the MBT falls together with termination V (~ 430 ka), the changeover from MIS 12 to MIS 11, where the MIS 12 is demonstrated as the most intense glaciation for the time interval of the late Pleistocene and MIS 11 the warmest interglacial, e.g., (Burckle, 1993). Termination V is thus indicated by a sea level rise from MIS 12 to MIS 11 with approximately 160 m (Hodell et al., 2003). Termination V is the greatest amplitude climate change occurred during the last 500 kyrs (Howard, 1997). This rather intense change between interglacial stadial maximum  $\text{CO}_2$  and  $\text{CH}_4$  levels and their impacts on the Eastern Europe prevailing climates is not seen before in the Carpathian Basin and Lower Danube area since several terrestrial archives do not recognize them at all in e.g., the magnetic susceptibility records close to the investigated Pleven section such as the Lunca (Constantin et al., 2015) and the Titel-Stari-Slankamen LPSs (Song et al., 2018b) reflecting similar magnetic susceptibility amplitudes before and after the MBT. However, the Bulgarian LPS Lubenovo reflects rather smaller magnetic susceptibility amplitudes for the older paleosols. Evaluating several multi-disciplinary data we first evidence this severe paleoclimatic change evidenced by mineral

magnetism properties (revealing magnetic grain size, concentration and mineral abundance), diffuse reflectance spectrometry of the visible light range (DRS, indicating goethite and hematite variations), and clay mineralogy derived from mid-infrared spectrometry (ATR-FTIR experiments), indicating palaeoclimatological relevant smectite and kaolinite contents.

Our results show, that the time period before the MPT caused all magnetic, DRS and ATR-FTIR data reflecting a severe intense pedogenesis rather occurring during tropical environments, leading to the intensified neo-formation of hematite and goethite, witnessing wet and high-temperature environments coupled with strong seasonality as well as high smectite and kaolinite contents pointing towards rather extreme and rather Mediterranean climates before the occurrence of the MBT.

#### 2.6.2. Millennial timescale climate change

Millennial timescale climate changes are rather short living climate variabilities with rather pronounced and abrupt changes in temperature, precipitation and seasonality. These rather short climate changes can be sub-divided in Dansgaard-Oeschger cycles and Heinrich events. Bond cycles are rather a integration of several Dansgaard-Oeschger cycles, which end usually as a harsh stadial condition identified as a Heinrich event.

Dansgaard-Oeschger (DO) cycles are evidenced in the Greenland ice cores, which provide an annual to centennial resolution of climate change for the last c. 127 ka following the GICC05 timescale (Rasmussen et al., 2014) which reflects the last interglacial/glacial cycle. The driving factor behind these millennial scale DO-cycles is still under debate up to today. Recent studies included potentially volcanic eruptions which were identified occurring predominantly during the onset of DO-cycles (Lohmann and Svensson, 2022), however other stimulations based on combined orbital influences as insolation effects might be taken into consideration. Dansgaard-Oeschger cycles have a approximated mean duration of 1.450 ka. DO-cycles are further associated with rapid sea-surface temperature increases by 10-15°C. DO-cycles appear in Greenland ice core records with rather moist and warm climate conditions and are interrupted by rather cold and dry climatic conditions which are ascribed as Greenland stadials or in shorter intervals as Heinrich events.

Heinrich events are associated with discharge of ice rafted debris events in the Northern Atlantic. These events were recognized at the same timing in loess-paleosol sequences with intervals of coarser grain sizes in the Chinese loess paleosol sequences associated with more glacial and cold conditions (Song et al., 2018a). These events are used as important anchor

points for correlative age models. Heinrich event associated ice rafted debris layers are further poor in planktonic foraminifera (Heinrich, 1988). Heinrich events can be associated between the last 70 and 14 ka (Bond et al., 1992) and show thus in sedimentological archives a decrease in salinity. Heinrich events are further characterized by long lasting transport based on ice-related transport distances which can cover up to 3000 km from their origin. The causalities behind the occurrence of Heinrich events are up to date poorly understood and under debate. The time occurrence and frequency between 5 and 10 ka mismatches every orbital induced climate variability. However timely intervals of prevailing rather cold and harsh conditions were identified in the northern hemisphere. Evidence for Heinrich events recorded in terrestrial sedimental archives are scarce. However, Heinrich events recorded in the Biya River and Katun' river LPSs (both following the wind vigor model) from the Russian Plain, follow with high values in susceptibility (cold) the recorded Heinrich events from the north eastern African coast marine drill core ODP658C (Evans et al., 2003) where Heinrich events have been identified in reconstructed sea-surface temperatures derived from alkenone measurements on phytoplankton remains (Zhao et al., 1995). The conditions influencing reconstructed sea surface temperatures at Core ODP658C are complex and consist mainly hydrological processes which include the Canary Current, upwelling, seasonal river runoff and in situ tropical waters and a complex system of seasonal winds like the trade wind and the Saharan Air layer (Sarnthein et al., 1981; McIntyre et al., 1988; Pujos, 1992). Fluctuations of Sea surface temperatures (SSTs) might have for the Iberian Peninsula and even its dryer interior a higher severe impact on the geomorphic system and there is a strong relationship between loess deposition and Heinrich events during MIS 2. And Heinrich events have a stronger than thought effect on landscape evolution than expected on the Iberian Peninsula, not only on the coastal area but also on the much drier interior.

Millennial timescale climate variability is known being preserved in various ice core, and speleothem archives expressed as  $\delta^{18}\text{O}$  (combination of rather warm and moist circumstances) and  $\delta^{13}\text{C}$  (taken as a rather precipitation indicating proxy) on the northern and southern hemisphere. Most famous and intensely studied regarding millennial scale climate change variability is the NGRIP ice core and provides the most accurate timescale GICC05 (Rasmussen et al., 2014) for the last interglacial/glacial cycle. Deep Sea sediments such as stemming from the famous Iberian Margin (Hodell et al., 2013) and Northern Atlantic provide further evidence of Dansgaard-Oeschger (-like) cycles and Heinrich (-like) events exceeding the last glacial/interglacial cycle. A synthesis provided by (Sun et al., 2021) evidences, that

millennial scale climate change is a northern hemisphere-wide occurring phenomenon for (at least) the last 1.5 Ma. Since the NGRIP “hard” data does only provide the record of millennial timescale climate variability for the last interglacial/glacial cycle the work of (Barker et al., 2011) modelled millennial timescale climate variability for the last 800 kyrs. This synthetic data set is in overall agreement with robustly observed past millennial climate change derived from the Antarctica EPICA  $\delta D$  (Jouzel et al., 2007) as well as the Iberian Margin G. bulloides foraminifera  $\delta^{18}O$  record (Hodell et al., 2013). We compare Barkers’ modelled data for the last 700 ka with robust and hard data from foraminifera variations preserved in the Iberian Margin composite record (Hodell et al., 2013) and independently dated (via RPI and correlation towards LR04, (Lisiecki and Raymo, 2005)) ice rafted debris from Hudson Bay (Channell et al., 2012) falling with high values together with cold (Heinrich event-like) events (Channell et al., 2012) allowing a direct comparison for the 850-700 kyr period where only modelled data is available so far based on  $GL_{SYN}$   $\delta^{18}O$  predicted variations (Barker et al., 2011). Since our terrestrial archive is rather condensed and reflecting rather low sedimentation rates, however with field observation-derived evidence for un-interrupted accumulation, we focus on highest sedimentation rates such as reflected by MIS4-2, MIS6, and MIS12 and compare our multi-proxy data with records, stacks and synthetic data as aforementioned to provide the first time Eastern European LPS preserved millennial scale variability for MIS12 and ascertain for a few studies focusing on MIS 6 the ability of preserved MSCVs.

Precipitation sensitive parameters such as the qualitative goethite content (Zhang and Nie, 2017), derived from DRS-spectrometry indicate a constantly driven MSCV during the last interglacial, which mirrors in its frequency of small but consistent and pronounced precipitation events MIS12. Our target profile is not ideal to derive MSCVs since its rather low sedimentation rate compared to other close-by sections, but we are able to certainly evidence most like northern ice sheet instability driven as well as AMOC-influenced moisture variability preserved in this rather condensed profile. Doing so, and presenting our assessment of use of multi-proxy data we smoothen the path towards our methodology applied to higher resolved archives.

Small (millennial) timescale climate changes are seldomly conserved in Eastern European LPSs since the recording of the mentioned small climate changes require a rather high sedimentation rate and a constant deposition of material best stemming from the same source area. A few studies were successful to show the recording of the last and penultimate interglacial / glacial cycles to millennial scale climate variations (Shi et al., 2003; Rousseau et

al., 2020). In the famous Greenland ice cores, three types of millennial scale changes are recorded and precisely dated: The so-called Heinrich events and the Dansgaard-Oeschger cycles and the up to today debated Bond-cycles.

Only a few studies reported so far successfully recorded millennial timescale past climate change identified in loess of Ukraine (Stayky), (Rousseau et al., 2011) as also shown by (Veres et al., 2018).

### 3. General objectives of the PhD Thesis

Loess-paleosol sequences are mostly investigated in Eastern Europe utilizing single parameters (most commonly applied low-field magnetic susceptibility) and seldomly grain size and colorimetry. A throughout applied multi-proxy study performed in a high resolution is still missing and accompanied by several archives with erosional layers or sampling gaps. This thesis tries to overcome these issues to provide detailed insights into past climate change on orbital and millennial timescales applying a never afore conducted sampling resolution combined with a multi-disciplinary approach. The core of this PhD thesis focuses on the Pleven loess-paleosol sequence located in northern Bulgaria. The three main chapters are building on each other.

3

In the first chapter, the loess-paleosol sequence of Pleven was initially presented. This study contains an attempt to investigate the whole time cover with aid of an (initial) correlative age model, which tracks either pedogenesis intensity (with  $\Delta\chi$  indicating the neo-formation of SP-particles) which is favored during interglacial conditions. A commonly utilized correlation target is the LR04 benthic foraminifera  $\delta^{18}\text{O}$  record. We utilized a second indicator indicating magnetically variations in the coarse grain size fraction which is provided during harsh glacial conditions. These grain size variations were correlated towards the EPICA Dome C dust flux record. Both age models are in agreement and indicate that the interglacial/glacial variability either reflected by increased pedogenesis intensity for interglacials and increased coarse grain dust supply during glacials are in concert. Further detailed magnetic investigations identified and characterized the in-field outcropping L2 tephra and three other crypto-tephras which were partly preserved in other LPSs of the lower Danube and Carpathian Basin. Ages derived from both age models were tentatively assigned to the crypto-tephra layers and resulting potential equivalents in tephra-rich paleoclimatic archives are discussed. Detailed magnetic measurements indicated a change of prevailing climatic conditions which are contrasting before and after 430 ka, which might indicate the successful preservation of the Mid-Brunhes climate transition.

The second chapter comprises methodological advances I figured out during my experiments aiming to identify colorimetric / DRS quantitative abundances of hematite and goethite. Detailed protocols enabling hematite and goethite signatures and quantitative abundances are still missing regarding investigations performed on sedimentary accumulations and require independent evidence. In this study we most as possible detailed describe the way from raw DRS spectra utilizing second derivatives spectra and its evaluation, which is confirmed by

independently acquired ART-FTIR spectra. A comparison was done on 719 samples investigated by both methods providing evidence for the correct identification of goethite and calcite / dolomite indicated by the luminance ( $L^*$ ). This chapter further introduced a novel R-package enabling the application of loess-color contrast enhancement in order to detect subtle changes of color nuances invisible by the naked eye.

The third chapter includes all data measured during the time of my PhD composed of environmental magnetic, colorimetric, granulometric and mid-infrared spectroscopic data. The new findings of chapter 2 are incorporated into this study. Therefore, the third chapter provides the first multi-proxy evidence for multiple interglacial/glacial cycles preserved in Plevén. This multi-proxy study allowed the creation of a correlative age model which compares magnetic data  $\Delta\chi$  and colorimetric derived data (goethite and hematite semi-quantitative contents) correlated to NGRIP  $\delta^{18}\text{O}$  variability for the last interglacial/glacial cycle and  $\delta^{18}\text{O}$  benthic foraminifera variations stemming from LR04 for older age intervals. This multi-disciplinary correlative age model improved the age model presented in chapter 1 for the last 430 ka and changed onsets and demise of interglacials and glacials since magnetic data variation is smeared in the older part (onset of sedimentation towards 430 ka). It is still unclear when sedimentation had started at Plevén and studies performed on answering this question are rare. A discussion about the onset will be part of a further grant application and is discussed in chapter 5.2. The lower two paleosol complexes show that the mid-Brunhes transition is (as suggested in chapter 4.1.) successfully recorded as a diminished signal of pedogenesis indicative magnetic proxies which witnessed enhanced growth of SP particles present as larger grain sizes, the neo-formation of heat and precipitation sensitive goethite and hematite abundances as well as ATR-FTIR derived abundances of smectite and kaolinite which are influenced by heat, weathering intensity and seasonality. The paleosols formed before the Mid-Brunhes event have witnessed more intense pedogenesis and more extreme prevailing climate than interglacials after the mid-Brunhes event. This is contrary to the global interglacial characterization before and after the Mid-Brunhes climate event. Furthermore, colorimetrically determined semi-quantitative goethite and magnetically derived (HIRM) parameters show for MIS4 to present a remarkable millennial timescale climate change variability equivalent to  $\delta^{18}\text{O}$  variabilities (Dansgaard-Oeschger cycles and Heinrich events) preserved in NGRIP. Millennial timescale climate change was further confirmed for the penultimate glacial MIS6. For the first time, millennial scale climate change was evidenced for the harsh glacial MIS12 in Eastern European LPSs. Goethite and maghemite are presented as valuable paleo-

precipitation proxies. It is shown, that goethite is neoformed and not a source related signal, and a transfer function to calculate mean annual precipitation values stemming from the Chinese loess plateau was tested initially targeting the Holocene soil. 81 high-temperature magnetic susceptibility measurements were performed and the Chinese Loess-Plateau transfer function applied in depth. Resulting MAP values were compared to a recently published model for Plevén for the last 800 ky. Chapter 4.1. had as a result that maghemite is more present in the paleosols S5 to present and magnetite more present in the older paleosols S5 and S6. DRS-derived goethite contents were transformed into MAP values utilizing maghemite contents from the post-MBE, and Extended for the whole sequence. The comparison of modelled data and goethite recalculated MAP values are in excellent agreement for the last 850 ky and are a first attempt to quantify mean annual precipitation in Europe for the last 850 ky utilizing combined magnetic and colorimetric methods. Furthermore, the broad application of multidisciplinary experiments lead to the identification of common characteristics of tephra layers based on magnetic mineralogy, magnetic grain size and smectite contents which are either a pedogenesis indicator or a weathering product of volcanogene glass shards. The detailed investigation of magnetic and mid-infrared data compared to bracketing loess units allowed the identification of 55 (crypto-)tephra candidates never observed in loess from Eastern Europe. Given the improved age model presented here and comparison with other tephra-rich records enabled the identification of 51 of aforementioned crypto-tephra layers falling together with radiometrically dated tephtras. Geochemical glass shard characterization allowing for directly linking these tephra deposits in Plevén with tephra deposits e.g., from Lake Ohrid and the Fucino Basin are not available, since several factors such as weathering of glass shards hinder geochemical analysis. A future bypass focusing with mid-infrared methods coupled to multi-variate analysis presented initially in chapter 5.4. needs further focus.

All in all, the Plevén LPS comprises several interglacial/glacial cycles, provides evidence for detailed preservation of prevailing climate conditions, a record of the Mid-Brunhes climate event and potentially the demise of the Mid-Pleistocene transition (dependent on the absolute onset of sedimentation discussed in chapter 5.2.). Additionally, the Plevén LPS provides insights into millennial scale climatic change during MIS4-present, MIS 6 and for the first time for MIS12. The detailed multi-proxy approach enabled the identification of 55 tephra candidates where 51 are found as potential equivalent in other tephra-rich records. The combination of identified millennial scale climate changes and further investigations of preserved tephra layers will significantly strengthen lower Danube and Carpathian basin



located terrestrial stratigraphies, land-sea correlations and may allow over-regional quantifications of climatic parameters such as precipitation and temperatures.

Additionally, I was involved in several projects located from western south central France (Pfeifer et al., 2020) towards the most eastern LPS I studied and contributed to located in Kashmir, India (Zeeden et al., 2021; Mir et al., 2022), comprised locally by (Scheidt et al., 2021) in Romania, (Laag et al., 2021a) in Serbia, and (Wacha et al., 2021) in Croatia (the latter both studies presented in the appendix (D and E) and Zmajevac in the further work chapter 5.5.3. Hence, located north Biały Kościół (Laag et al., 2019a) towards southern Iranian (Kehl et al., 2021) and the Cameroon volcanic line (Schmidt et al., 2022). With respect to methodological improvements of luminescence dating, I contributed to two studies (Pagonis et al., 2020; Kreutzer et al., 2021). These studies are side-works and not shown in this thesis but enabled myself to gain further insights into other paleoenvironmental archives located on widely the northern hemisphere. These insights include insights into orbital and millennial scale climate change, the identification and characterization of crypto-tephra layers and differences of locally preserved sedimentation rates and provenances. Furthermore, studies focusing on luminescence derived age models increased my criticism about reliability in luminescence dating results. All localities (despite the Cameroon volcanic line locality) including so-far unpublished papers are indicated in the map shown below.

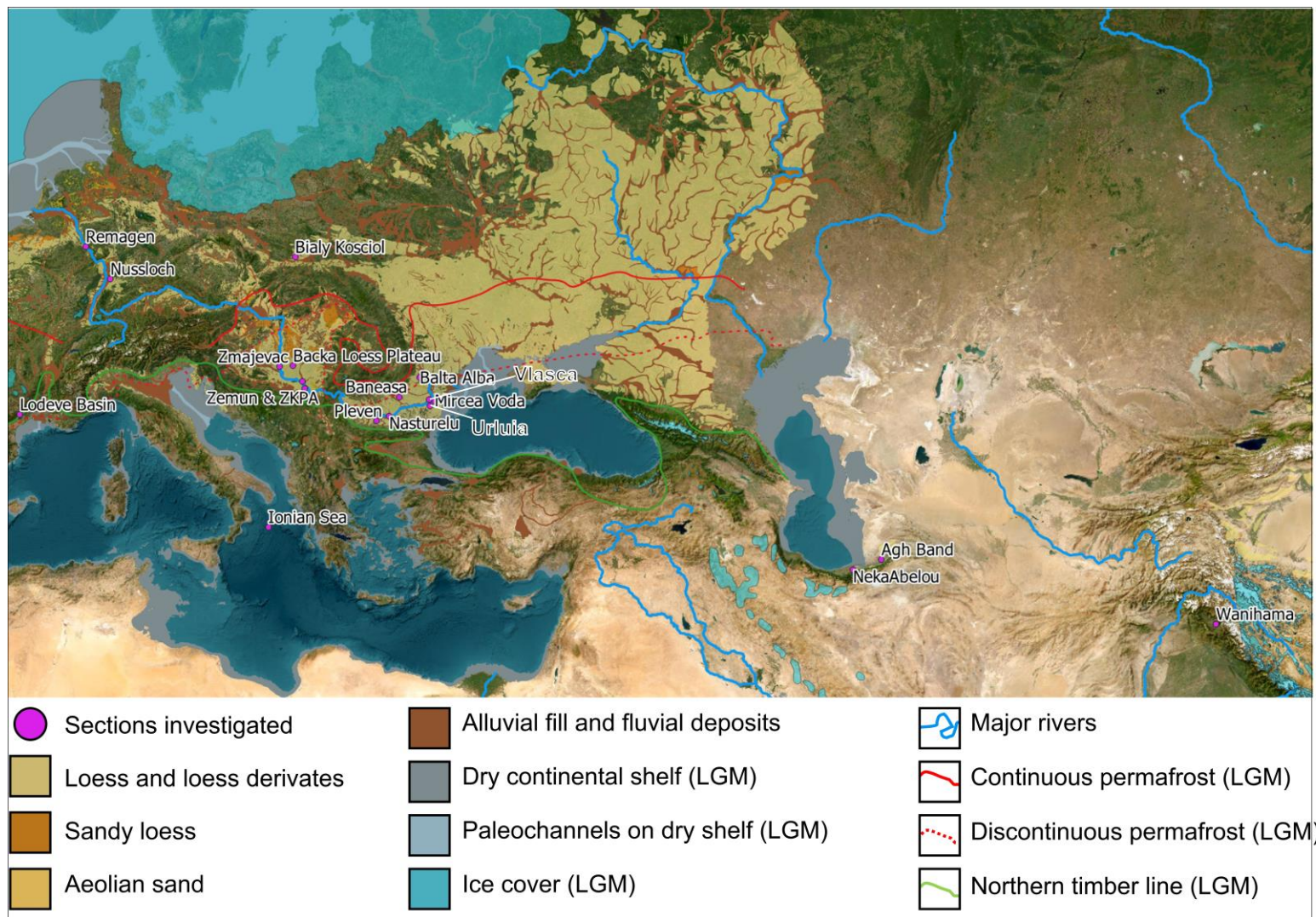


Figure 5: Figure 9: Map reflecting the loess distribution and last glacial ice cover over Eurasia. Data for loess distribution from (Lehmkuhl et al., 2021) and (Haase et al., 2007). Last glacial ice cover data stems from (Ehlers et al., 2011).

## 4. Publications

### 4.1. A detailed magnetic record of Pleistocene climate and distal ash dispersal during the last 800 kyrs - The Suhia Kladenetz quarry loess-paleosol sequence near Pleven (Bulgaria)

Diana Jordanova<sup>1</sup>, Christian Laag<sup>2</sup>, Neli Jordanova<sup>1</sup>, France Lagroix<sup>2</sup>, Bozhurka Georgieva<sup>1</sup>, Daniel Ishlyanski<sup>1</sup>, Yohan Guyodo<sup>2</sup>

<sup>1</sup> National institute of Geophysics, Geodesy and Geography, Bulgarian Academy of Sciences, Sofia, Bulgaria

<sup>2</sup> Université Paris Cité, Institut de physique du globe de Paris, Paris, France

#### Status :

- Submitted : 30.11.2021
- Received in revised form : 13.05.2022
- Accepted : 14.05.2022
- Available online : 19.05.2023
- Published in : Global and Planetary Change 214, 103840

#### Main findings:

- The Pleven LPS is a highly resolved paleoenvironmental archive which preserved the interplay of dust accumulation and soil formation for the last 800 ky
- Learning from an 20cm thick in-field outcropping tephra layer accumulated in the penultimate glacial (L2), concentration dependent parameters such as  $\chi_{lf}$ ,  $\chi_{ARM}$  and IRM enabled the identification of three cryptotephra layers, further evidenced by the presence of volcanogenic glass shards identified via microscopy observations
- Tentative age assignments were made based on the built age model, which builds on correlations of detrital dust input at Pleven (magnetic coarse grain fraction) which dust flux recorded in EPICA dome C (Antarctica) and pedogenesis indicating  $\Delta\chi$  correlated towards benthic foraminifera  $\delta^{18}O$  stack LR04
- There is a remarkable bi-partition of the Pleven LPS comparing pedogenesis indicating magnetic parameters from the older two paleosol complexes S6 and S5 towards younger pedocomplexes S4 towards the Holocene soil. Magnetic parameters addressing magnetic mineralogy reflect that magnetite is the main carrier for ARM below the L5 loess unit and maghemite for the younger part (S4 towards the top). This transition falls timely together with the mid-Brunhes climate event.

# 4



## A detailed magnetic record of Pleistocene climate and distal ash dispersal during the last 800 kyrs - The Suhia Kladenetz quarry loess-paleosol sequence near Pleven (Bulgaria)

Diana Jordanova<sup>a,\*</sup>, Christian Laag<sup>b</sup>, Neli Jordanova<sup>a</sup>, France Lagroix<sup>b</sup>, Bozhurka Georgieva<sup>a</sup>, Daniel Ishlyanski<sup>a</sup>, Yohan Guyodo<sup>b</sup>

<sup>a</sup> National Institute of Geophysics, Geodesy and Geography, Bulgarian Academy of Sciences, Acad. G. Bonchev str., block 3, 1113 Sofia, Bulgaria

<sup>b</sup> Université Paris Cité, Institut de Physique du Globe de Paris, CNRS, 1 rue Jussieu, 75005 Paris, France

### ARTICLE INFO

Editor: Zhengtang Guo

#### Keywords:

Mineral magnetism  
Loess  
Paleosols  
Cryptotephra  
Age model  
Lower Danube  
Middle and Upper Pleistocene

### ABSTRACT

Loess-paleosol sequences (LPS) from the Lower Danube area are valuable terrestrial archives of environmental change in SE Europe during the Pleistocene. A twenty-seven meters thick sequence has been sampled in Central North Bulgaria near the city of Pleven within the Suhia Kladenetz (SK) quarry. The sedimentary sequence consists of seven loess units and six interbedded paleosol complexes covering the last 800 kyrs. The continuous 2 cm resolution sampling depth interval enabled the recovery of several cryptotephra in addition to a ~ 20 cm thick tephra deposit observed in the field within the L<sub>2</sub> loess unit. All cryptotephra are clearly identified in laboratory analyses by their strong magnetic signal, particularly well expressed by concentration – dependent anhysteretic susceptibility ( $\chi_{ARM}$ ), isothermal remanence (IRM), low field magnetic susceptibility ( $\chi_{lf}$ ) and in some cases by frequency dependent magnetic susceptibility ( $\Delta\chi$ ), coercivity of remanence ( $B_{CR}$ ), and hard isothermal remanence ( $HIRM_{2.0-0.3T}$ ). Complementary optical and scanning electron microscope analyses of single grains from the tephra deposit and cryptotephra intervals reveal the presence of volcanogenic grains with smooth glassy surfaces and vesicular internal structure; fluidal grains with bulbous surfaces and dense irregular grains. Grain size sensitive magnetic ratios  $\chi_{ARM}/\chi_{lf}$ ,  $ARM/IRM_{100mT}$ ,  $IRM_{2T}/\chi_{lf}$  are not always discriminative, suggesting that (crypto)tephras do not have a single uniform source. Preliminary correlative age models are used to estimate ages for the (crypto)tephras and propose likely associated volcanic eruptions. Finally, strong pedogenic magnetic enhancement of the younger paleosols (S<sub>4</sub>, S<sub>3</sub>, S<sub>2</sub> and partly S<sub>1</sub>) contrasts with the smeared and low magnetic signal of the older paleosols (S<sub>6</sub> and S<sub>5</sub>). Moreover, an enhanced content of low-coercivity hematite observed from the upper part of the S<sub>5</sub> paleosol upwards to the present and a sharp increase in the concentration of maghemite at the expense of magnetite observed for the S<sub>3</sub>, S<sub>2</sub> and S<sub>1</sub> paleosols provides strong evidence for a significant paleoenvironmental change. The timing of this change, based on the SK LPS age models, is compatible with the mid-Brunhes climate transition.

### 1. Introduction

Loess-paleosol sequences (LPSs) of the European loess belt are valuable paleoenvironmental archives recording Earth's history during the Pleistocene glacial – interglacial cycles. The scientific literature demonstrates that high-resolution magnetic records from LPSs are sensitive markers of the evolution of Atlantic ocean circulation, global ice sheets volume, and sea surface temperatures (e.g. Marković et al., 2015; Obrecht et al., 2019; Rousseau et al., 2017; Zeeden et al., 2020).

Determining a high-resolution chronology for LPS remains a major challenge beyond the limits of radiocarbon dating. Correlative age modelling and the validity of such an approach was established early on by the works of Kukla (1977) on European LPS and Heller and Liu (1986) on Chinese LPS. At present, the approach is still relevant. The chronology of LPS is routinely constrained by correlating, for example, mineral magnetism-derived climate proxies to paleoclimate records of global ice volumes tracked by benthic foraminifera  $\delta^{18}O$  (e.g. Buggle et al., 2009; Marković et al., 2012a; Zeeden et al., 2016) or other

\* Corresponding author.

E-mail address: [diana\\_jordanova77@abv.bg](mailto:diana_jordanova77@abv.bg) (D. Jordanova).

<https://doi.org/10.1016/j.gloplacha.2022.103840>

Received 30 November 2021; Received in revised form 13 May 2022; Accepted 14 May 2022

Available online 19 May 2022

0921-8181/© 2022 Elsevier B.V. All rights reserved.



astronomically tuned proxy records (e.g. Heslop et al., 2002; Basarin et al., 2014).

Tephra and cryptotephra deposits are valuable regional chronostratigraphic markers (Lowe, 2011; Ponomareva et al., 2015). Site locations where (crypto)tephra deposits are preserved are highly valuable regional LPS records even when taking into account the high variability in thickness of volcanic ash deposits due to topographic and atmospheric factors (Poulidis et al., 2017; Watt et al., 2015). Therefore, tephra and cryptotephra deposit-bearing LPS records have an accrued value for regional correlations and potential for well-constrained chronology. Volcanic material can be dated directly by radiometric age determination and the geochemical properties of (crypto)tephras can be correlated to the geochemical signature of a specific volcanic edifice. Thus, tephras and cryptotephras preserved within a LPS may be indirectly dated by geochemical fingerprinting providing independent chronological tie-points.

The present study focuses on a new 27 m thick LPS from Central North Bulgaria (Lower Danube region). It reports a first stratigraphic description of the sequence and room temperature mineral magnetic data. Two age models are proposed from the correlation of magnetic proxy data indicative of pedogenesis and wind dynamics to paleoclimate records of ice sheet volumes and dust flux, respectively. These are then used to assign ages to the one outcropping tephra deposit and to the three cryptotephras identified in the laboratory from mineral magnetic data and microscopic observations. Finally, potential sources of the tephra and cryptotephras are discussed in light of geochemical and geochronological studies published on regional tephra-rich sedimentary archives such as the Fucino Basin (Giaccio et al., 2019), Lake Ohrid (Leicher et al., 2021) or Tenaghi Philippon (Vakhrameeva et al., 2018, 2019; Wulf et al., 2018).

## 2. Site description

The studied profile is situated in Central North Bulgaria (43°27'24.0"N, 24°41'26.7"E) near the city of Pleven (Fig. 1) within the Suhia Kladenetz (SK) quarry. The region is geomorphologically outlined by two of the largest Danube river tributaries originating from the Balkan range – the Vit and Osam rivers. The loess - paleosol sequence lays on a Pliocene denudation surface (PDS), shaped along the shoreline of the Dacian basin (Evlogiev, 2007). The PDS eroded down to the Brusarska sedimentary series of Romanian - Dacian age (~2.6–4.9 Ma) in the region of Pleven (Kojumdjieva and Popov, 1988). The Brusarska sediments are composed of yellow – rusty and greenish clays intercalated by thin sandy layers in the upper part and lenses of lignite coals at its base. After the waters within the lacustrine-fluvial Dacian basin regressed, eolian sedimentation started at about 800 kyrs in pace with Pleistocene glacial – interglacial cycles. Seven loess units ( $L_7$  to  $L_1$ ) and six interbedded paleosol complexes ( $S_6$  to  $S_1$ ) are observed below the Holocene soil ( $S_0$ ). The sampling site is located in an open active quarry where the clays of the Brusarska sedimentary series are being extracted (Fig. 1S). The present day relief in the area is undulating with an absolute altitude of 245 m (a.s.l.). Based on a phytoclimatic classification (Botti, 2018), the climate is subhumid temperate continental (SH3d). The long-term (50 year period between 1931 and 1980) mean annual temperature at Pleven meteorological station is 11.6 °C (Kjutchukova, 1983) and the mean annual precipitation is 578 mm (Koleva and Peneva, 1990). The monthly distribution of precipitation peaks in May–June and is lowest in February, while the mean monthly temperature is highest in July–August, and lowest in January (Fig. 2S). Preserved modern soils in the area are strongly leached Chernozems (Haplic Chernozems according to (IUSS Working Group WRB, 2015)).

The SK loess-paleosol sequence was sampled in 2018 on freshly cleaned vertical faces segmenting the larger quarry steps in two to three sub-sections (Fig. 3S). A continuous column of sediment was prepared and sampled at a 2 cm depth resolution. Slices of bulk sediment of about 10 × 6 × 2 cm in dimension (approx. 300 g of material) were taken per

sampling interval. The SK sequence is 26.72 m in total vertical thickness, which at a 2 cm continuous depth sampling resolution results in 1336 bulk sediment samples collected. The stratigraphy and lithological units are described in Table 1S and depicted in Figs. 2, 3, 4, 8 and 9. Munsell colors of wet material from each horizon were determined using the Munsell Soil Color Book (Munsell Color Company, 2009). A visible 20 cm thick tephra deposit, observed to be horizontally continuous across the quarry, outcrops over the 732–714 cm depth interval. This tephra serves as a remarkable textural boundary and stratigraphic marker within the second  $L_2$  loess unit (Fig. 4S).

## 3. Methodology

### 3.1. Magnetic measurements

Sample preparation and measurements were carried out at the NIGGG (Sofia, Bulgaria) and IPGP (Paris, France) paleomagnetic laboratories. All bulk sediment samples ( $n = 1336$ ) were air dried, crushed by hand in a porcelain crucible and sieved through a 2 mm mesh. Afterwards, three sub-samples per sampling interval were prepared. For sub-sample type 1, bulk sediment was packed in 10 cm<sup>3</sup> plastic cylinders and weighed. For sub-sample type 2, bulk sediment was packed in gelatin capsules and weighed. For sub-sample type 3, two grams of bulk sediment was mixed with gypsum and water and placed in a 8 cm<sup>3</sup> cubic mold. The mold is removed once the mixture is dry.

Magnetic susceptibility of the bulk sediment (sub-sample type 1) was measured at NIGGG on a MFK – 1A susceptibility bridge (AGICO, Czech Republic) in a 200 A/m field at 976 Hz and 15,616 Hz working frequencies. The mass-specific low-field magnetic susceptibility ( $\chi_{lf}$ ) reported herein is the low frequency measurement. The frequency-dependent magnetic susceptibility  $\Delta\chi$  is defined as the difference between the low frequency  $\chi_{976\text{Hz}}$  and high frequency  $\chi_{15616\text{Hz}}$  magnetic susceptibility values, and its percentage as  $\chi_{fd}\% = \frac{(\chi_{976\text{Hz}} - \chi_{15616\text{Hz}})}{\chi_{976\text{Hz}}} \times 100$  (%).

Hysteresis data were acquired on bulk sediment (sub-sample type 2) using a Vibrating Sample Magnetometer (Model 3900, Princeton Measurements Corporation, USA) at IPGP. Hysteresis loops were measured in a  $\pm 1.5$  T maximum applied fields in 5 mT field increments, 100 ms averaging time and in continuous sweep mode. The following parameters were derived: saturation magnetization ( $M_S$ ) after removal of the high-field slope defined over the 1.05 to 1.5 T segment, saturation remanent magnetization ( $M_{RS}$ ), and coercive force ( $B_C$ ). The mass specific high-field susceptibility ( $\chi_{\text{high}}$ ) corresponds to the linear slope of the high field segment between 1.05 and 1.5 T. The coercivity of remanence ( $B_{CR}$ ) was determined in a subsequent direct current (DC) demagnetization of the forward field isothermal remanent magnetization ( $IRM_{1.5T}$ ) over 70 backfield logarithmic steps up to  $-0.5$  T.

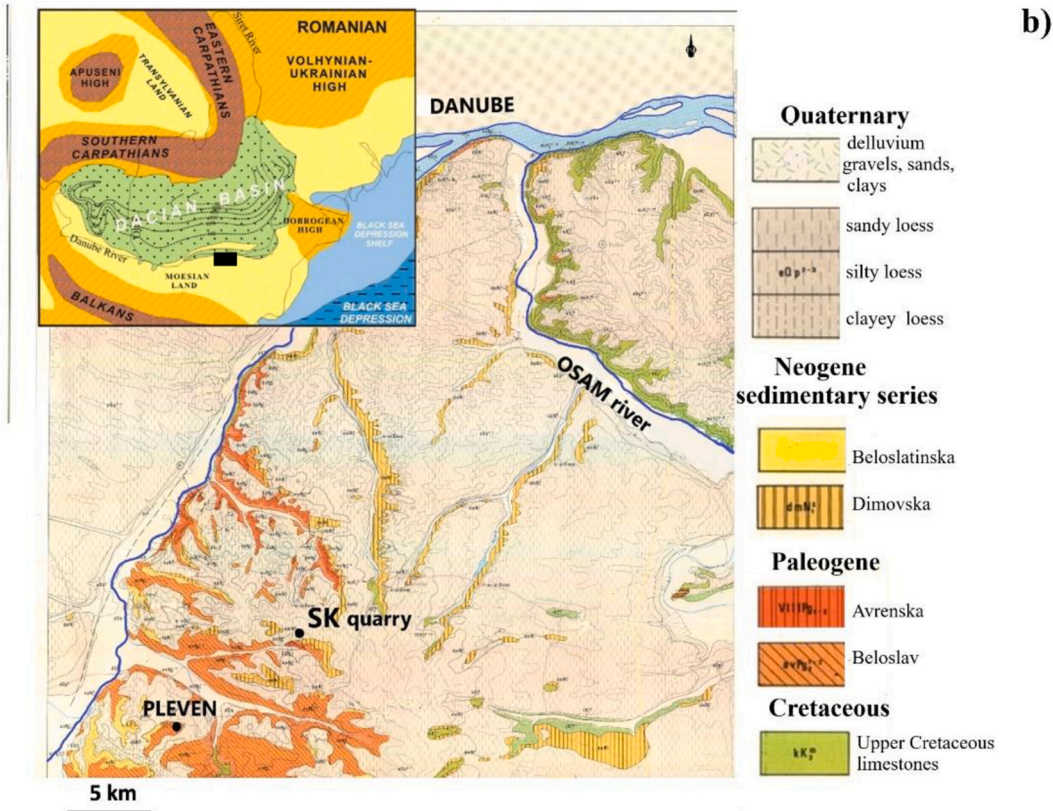
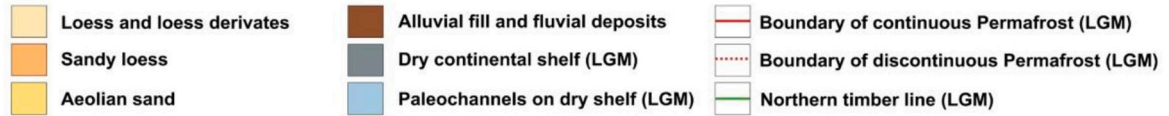
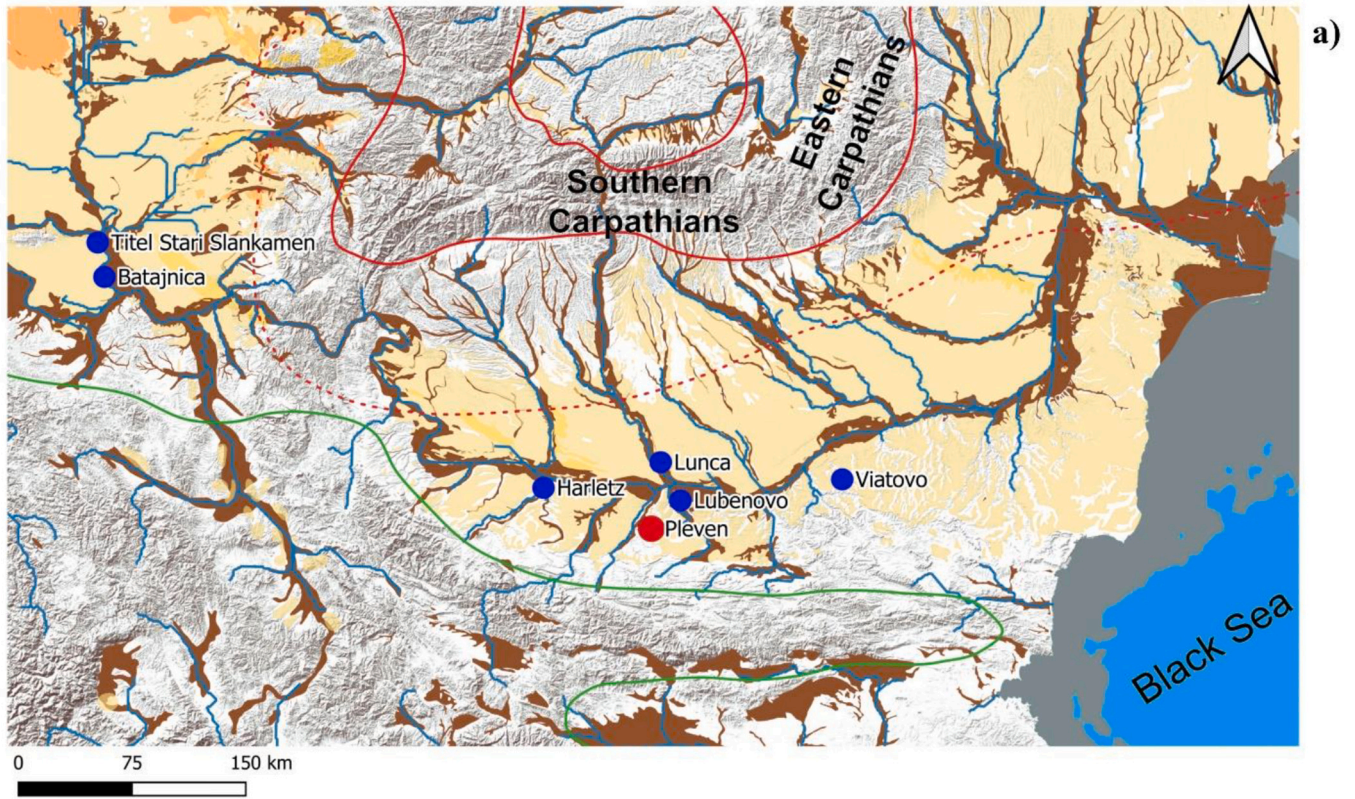
At NIGGG, various magnetic remanences, described below, were imparted in the laboratory on bulk sediment (sub-sample type 3) and measured using a JR-6A automatic spinner magnetometer (AGICO Ltd., Czech Rep.) with a sensitivity of  $2 \times 10^{-6}$  A/m.

Anhyseteric remanent magnetization (ARM) was imparted using a Molspin AF demagnetizer in a 100 mT peak AF field superimposed on a 0.1 mT DC field. Mass or volume normalized ARM and DC field normalized intensities ( $\chi_{\text{ARM}}$ ) are reported.

Isothermal remanent magnetizations (IRM) were imparted using a IM-10-30 pulse magnetizer (ASC Scientific, USA) in a 2 T forward field ( $IRM_{2T}$ ) and in 100 mT and 300 mT backfields ( $IRM_{0.1\text{mT}}$  and  $IRM_{0.3\text{mT}}$ ).

Lastly, a composite remanence was imparted along three orthogonal axes. Sequentially, an  $IRM_{2T}$  was imparted along the +z axis of the cubic sample, followed by an  $IRM_{0.2T}$  along the +y axis, and finally an  $ARM_{100\text{mT}}$  along the +x axis. The composite remanence was stepwise thermally demagnetized and used as a diagnostic tool for determining coercivity of remanences and unblocking temperatures ( $T_{\text{ub}}$ ) of the





(caption on next page)



**Fig. 1.** a) Map of the Middle- and Lower Danube loess areas (modified after [Lehmkuhl et al., 2021](#)) and location of the studied Plevn SK loess-paleosol profile in the context of other studied sites in the area: Plevn – Suhia Kladenetz (this study); Harletz ([Antoine et al., 2019](#)); Lubenovo borehole; Lunca profile ([Constantin et al., 2015](#)); Viatovo ([Jordanova et al., 2008](#)); Titel Stari-Slankamen ([Marković et al., 2012b](#); [Song et al., 2018](#)); b) geological map of the study area (from Geological map of Bulgaria, 1:100000) with the location of the Suhia Kladenetz (SK) quarry to the NE of the city of Plevn and inset figure of paleogeographic reconstruction of Dacian basin during Dacian period (after [Dinu et al. \(2007\)](#)). Black square depicts Plevn region.

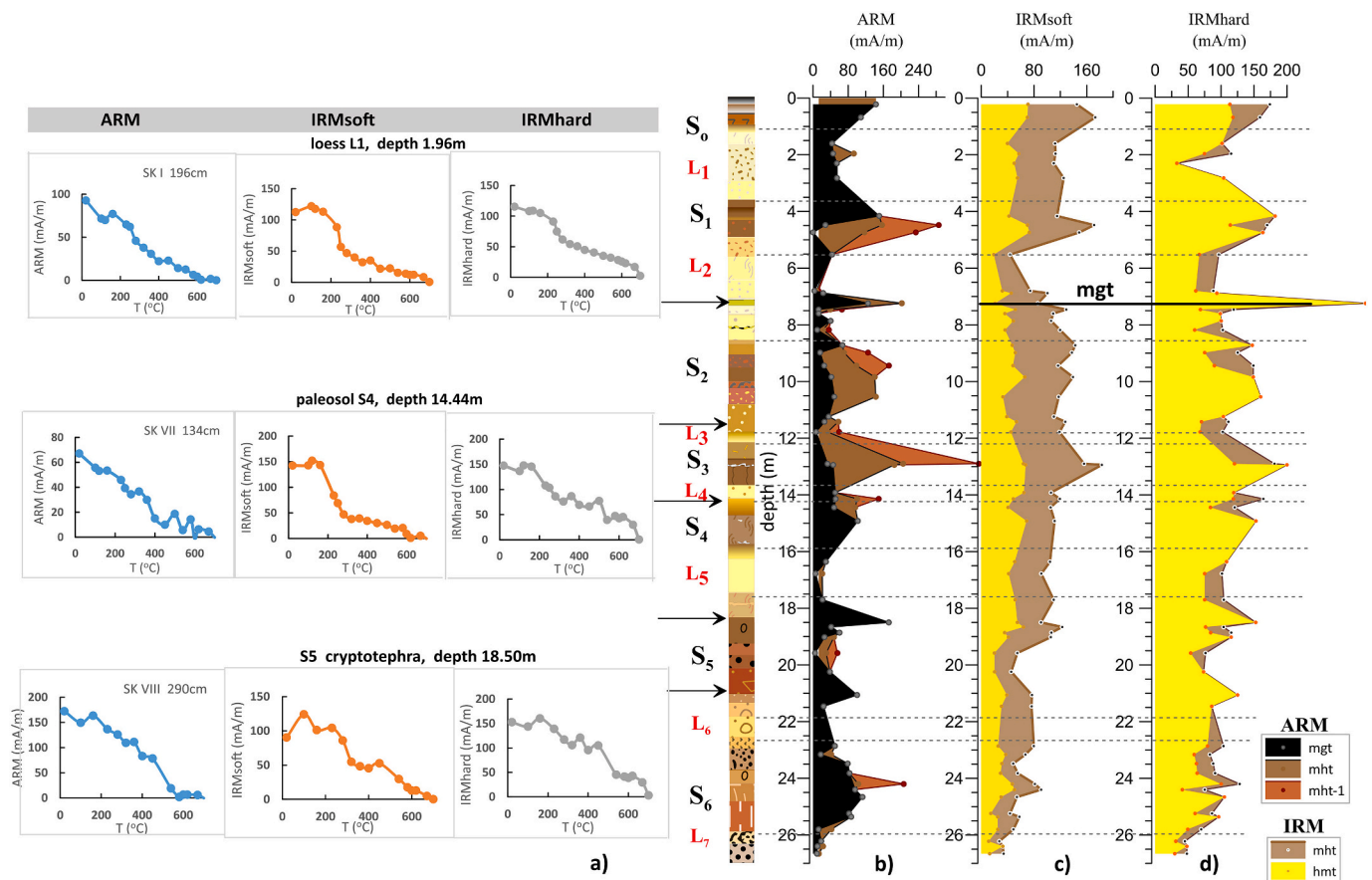


**Fig. 2.** a) Step-wise thermal demagnetization decay curves for the composite remanence's ARM component (left), IRM<sub>soft</sub> component (middle) and IRM<sub>hard</sub> component (right) of representative samples. See [section 3.1](#) for the experimental conditions of the composite remanence acquisition. b) Variations with depth of the ARM component intensities carried by magnetite (black area), maghemite with T<sub>ub</sub>s of (280–360 °C) (brown), and maghemite with T<sub>ub</sub> of 400 °C (dark red – brown). c) Variations with depth of IRM<sub>soft</sub>s, carried by maghemite (brown) and hematite (yellow). The single black bar at 7.2 m depth corresponds to the strong magnetite component identified only in the sample from L<sub>2</sub> tephra. d) Variations with depth of IRM<sub>hard</sub>s, carried by maghemite (brown) and hematite (yellow). Abbreviations: mgt – magnetite; mht – maghemite; hmt – hematite. See Table 1S for description of stratigraphic column. Arrows next to the column indicate depths of the tephra and cryptotephra deposits. (For interpretation of the references to color in this figure legend, the reader is referred to the web version of this article.)

major remanence carrying minerals. Thermal demagnetizations were carried out over 19 steps starting from room temperature up to 700 °C in air using a MMTD shielded furnace (Magnetic Measurements Ltd., UK).

### 3.2. Optical microscopy

Bulk sediments from selected sampling intervals identified as potentially bearing (crypto)tephra material were investigated microscopically. For each interval investigated, 10 g of bulk sediment was treated to remove organic matter and carbonates. First, the sediment was crushed, dispersed ultrasonically in distilled water and dried. The sediment was then treated with 50 ml of 5% HCl for 4 h at room temperature. The solution was centrifuged to remove the supernatant and the remaining sediment was treated with 50 ml of 10% H<sub>2</sub>O<sub>2</sub> in a 60 °C water bath for 10 min and left overnight at room temperature. Finally, the sediment was rinsed with distilled water and passed through a 250 μm and a 50 μm sieves. Single grains from the 50 μm < d < 250 μm fraction were investigated in polarized reflected light (RL) with a ZEISS AxioScope 5 optical microscope equipped with a ZEISS AxioCam 208

color camera.

### 3.3. Scanning Electron Microscopy (SEM)

Bulk sediment of the tephra deposit within the L<sub>2</sub> loess unit was treated following the same protocol described in [Section 3.2](#) and investigated for the presence of volcanic ash particles. Grains were dispersed on a conductive tape and carbon coated. SEM images and elemental contents were analyzed with a Scanning Electron Microscope JEOL JSM6390 coupled with EDX INCA Oxford analyzer in back scattered electrons mode.

### 3.4. Correlative age modelling

A first age-depth model is built from the correlation of the frequency dependent magnetic susceptibility ( $\Delta\chi$ ), a sensitive indicator for the presence of ultra-fine viscous superparamagnetic particles produced during pedogenesis ([Dearing et al., 1996](#); [Maher, 2011](#)) to the LR04 benthic foraminifera  $\delta^{18}\text{O}$  record ([Lisiecki and Raymo, 2005](#)). Coarse

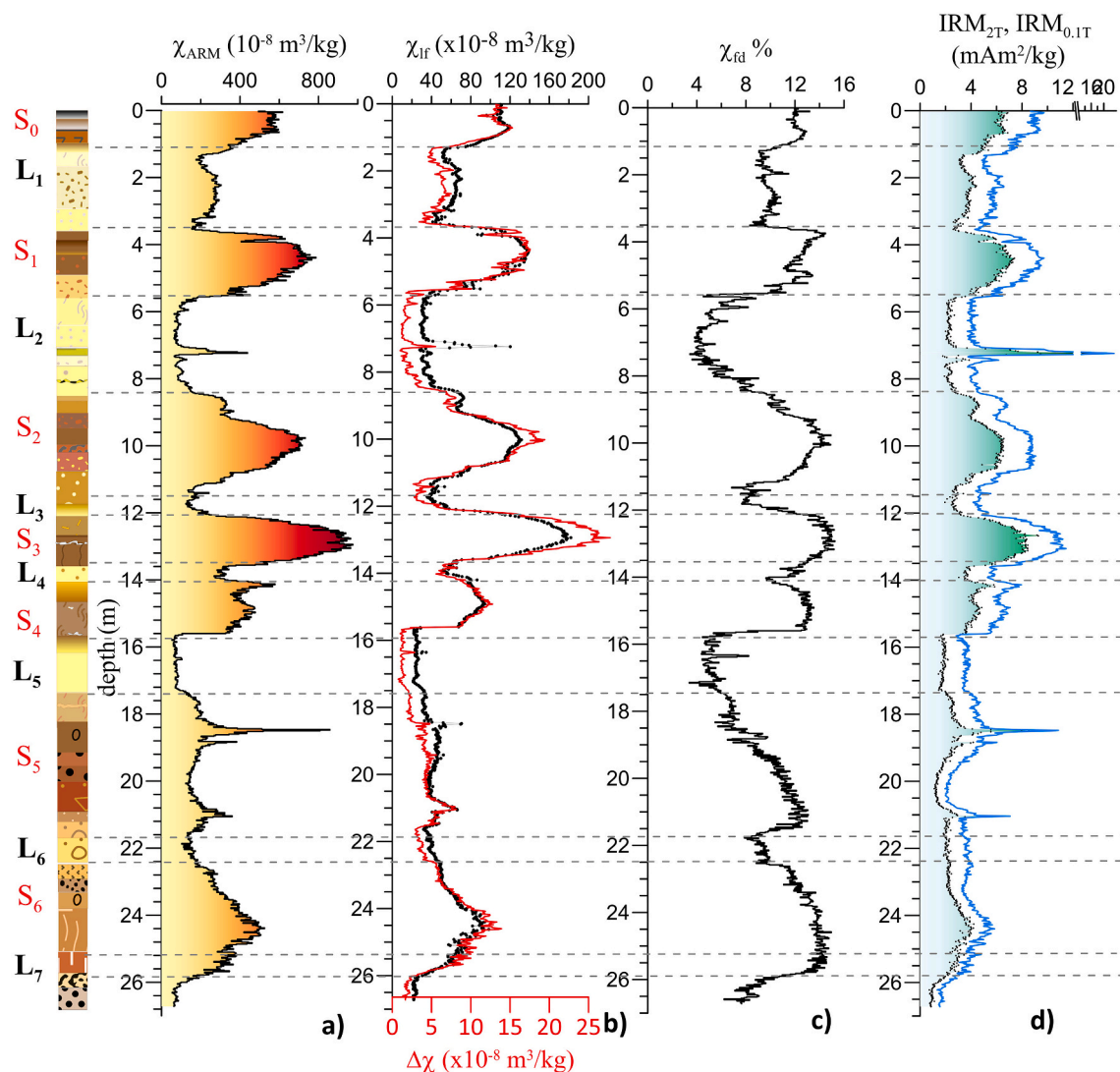


**Fig. 3.** Depth variations of concentration – dependent magnetic parameters along the SK profile: a) anhysteretic susceptibility  $\chi_{ARM}$ ; b) low field magnetic susceptibility  $\chi_{lf}$  and frequency dependent magnetic susceptibility  $\Delta\chi$  (red); c) percent frequency dependent magnetic susceptibility  $\chi_{fd}$  %; and d) isothermal remanence, acquired in fields of 0.1 T (shaded curve) and 2 T (blue line). (For interpretation of the references to color in this figure legend, the reader is referred to the web version of this article.)

tuning and age calculation was performed with QAnalyzeSeries (Kotov and Pálike, 2018). Interglacials are associated with low global ice sheet volumes and favorable climate conditions leading to soil formation on continental surfaces. Consequently, low  $\delta^{18}O$  values in the LR04 record are expected to be associated with high  $\Delta\chi$  values. The sharp  $\delta^{18}O$  signal associated with glacial terminations is favored for determining correlative tie-points with the  $\Delta\chi$  record.

A second age-depth model is built from the correlation of the  $IRM_{2T}/\chi_{lf}$  ratio, argued in section 5.1 as a magnetic proxy of wind dynamics, to the EPICA Dome C (EDC) dust flux record (Lambert et al., 2008, 2012). Here, marked changes in  $IRM_{2T}/\chi_{lf}$  and/or field observations are correlated to onsets or terminations of EDC peaks in dust flux.

For both age-depth model exercises, no time lag between records is assumed.

## 4. Results

### 4.1. Remanence-bearing magnetic mineralogy

Thermal demagnetization decay curves of the laboratory imparted composite remanence (see section 3.1) for selected representative

samples are shown in Fig. 2a and Figs. 5S, 6S and 7S. The ARM component thermal demagnetization curves display a progressive decrease with final unblocking temperatures ( $T_{ub}$ ) of 580–600 °C. An additional  $T_{ub}$  at 400 °C is observed within paleosols  $S_1$ ,  $S_2$ ,  $S_3$  (Fig. 6S) and the component carries a significant intensity (Fig. 2b). The thermal demagnetization of the soft IRM component ( $IRM_{soft}$ ) shows consistent unblocking behavior for all samples analyzed.  $IRM_{soft}$  components decay sharply at c. 250–320 °C and reach final demagnetizations at 700 °C (Figs. 2a, 5S, 6S, 7S). A few exceptions are observed with final  $T_{ub}$  at 600 °C ( $S_4$  in Fig. 2a,  $S_2$  in Fig. 6S, and  $L_2$  tephra and  $S_5$  cryptotephra in Fig. 7S). The hard IRM component ( $IRM_{hard}$ ) demagnetization curves define consistently for all samples a final  $T_{ub}$  at 700 °C. A lower  $T_{ub}$  at 250 °C is also observed for loess samples (Fig. 2a, 5S) and for  $S_1$  and  $S_3$  paleosols (Fig. 6S). Based on the observed  $T_{ubs}$  we attribute the phase components of each remanence type accordingly: ARM carriers are identified as magnetite / oxidized magnetite ( $T_{ub}$  of 580–600 °C) and maghemite with an  $T_{ub}$  or transformation temperature of 250–400 °C;  $IRM_{soft}$  carriers are attributed to hematite with  $T_{ub}$  of 700 °C, maghemite with  $T_{ub}$  (or transformation temperature) of 250–360 °C; and  $IRM_{hard}$  carriers are considered as maghemite for  $T_{ub}$  of 250 °C and hematite for  $T_{ub}$  of 700 °C (Dunlop and Özdemir, 2013). Variations with depth of the



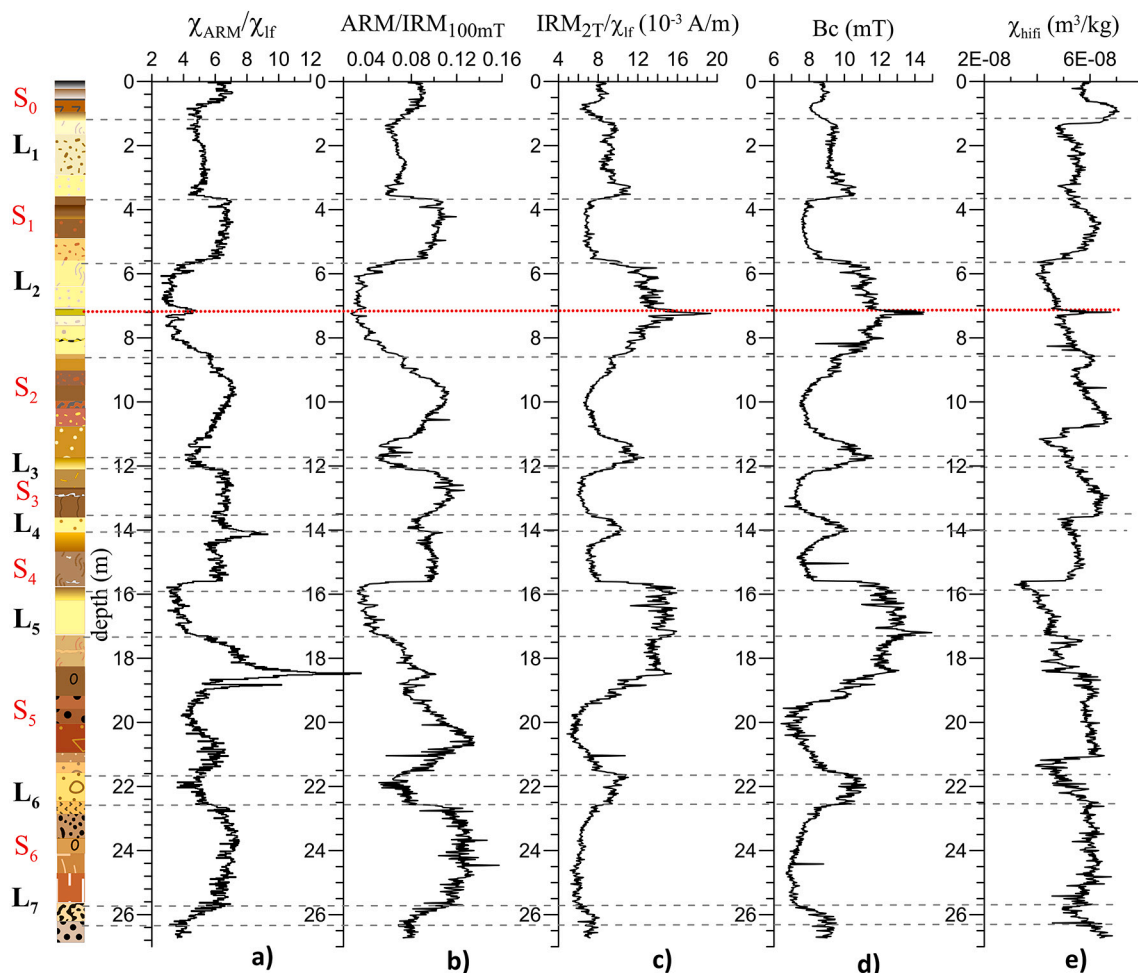


**Fig. 4.** Depth variations of grain-size dependent magnetic parameters along the SK profile: a) ratio of anhysteretic susceptibility to low-field magnetic susceptibility  $\chi_{ARM}/\chi_{lf}$ ; b) anhysteretic remanence normalized to the isothermal remanence, acquired in 0.1 T field  $ARM/IRM_{100mT}$ ; c) ratio of isothermal remanence, acquired in 2 T field to low-field magnetic susceptibility  $IRM_{2T}/\chi_{lf}$ ; d) coercive force ( $B_c$ ), and e) high-field magnetic susceptibility ( $\chi_{hif}$ ). Red line indicates the position of the visible tephra layer in the  $L_2$  loess unit. (For interpretation of the references to color in this figure legend, the reader is referred to the web version of this article.)

corresponding intensities of each of the above phases, contributing to ARM,  $IRM_{soft}$  and  $IRM_{hard}$  of the composite remanence signal are depicted in Figs. 2b, c, and d. ARM carried by magnetite ( $T_{ub}$  at 580–600 °C range) shows the highest intensities for  $S_0$ , upper part of  $S_1$ ,  $S_4$  and  $S_6$ , and for the  $L_2$  tephra and the cryptotephra within  $S_5$  (Fig. 2b). Maghemite or another alternative phase with an  $T_{ub}$  of 400 °C carries an important ARM signal in the upper part of  $S_3$  and  $S_2$  and the lower part of  $S_1$  (Fig. 2b). The intensity of the  $IRM_{soft}$  component carried by maghemite across the paleosols  $S_3$ ,  $S_2$  and  $S_1$  are greater than a factor of two the  $IRM_{soft}$  intensities carried by hematite (Fig. 2c). In older pedocomplexes  $S_5$  and  $S_6$ ,  $IRM_{soft}$  intensities carried by maghemite are still higher than  $IRM_{soft}$  intensities carried by hematite but by less than a factor of two. The strongest  $IRM_{soft}$  signal is carried by magnetite and is observed specifically for the  $L_2$  tephra deposit as indicated by the black bar in Fig. 2c. The  $IRM_{hard}$  component is carried mainly by hematite with observed higher intensities in paleosols and the  $L_2$  tephra deposit in comparison to less weathered loess units.

#### 4.2. Depth variations of rock magnetic parameters

Low-field mass specific magnetic susceptibility ( $\chi_{lf}$ ) reveals systematic strong magnetic enhancement of the upper three paleosols as compared to the loess horizons (Fig. 3b). Lower parts of the profile (depths 14–26 m) show smeared and low-amplitude  $\chi_{lf}$  variations

truncated by two sharp peaks at 18.48 m and 21.00 m.  $\Delta\chi$  varies similarly as  $\chi_{lf}$  with depth (Fig. 3b), while  $\chi_{fd}$  % displays a different variability, outlining pedogenic alterations in all paleosols by reaching values as high as 12–14% (Fig. 3c). Anhysteretic susceptibility ( $\chi_{ARM}$ ), which is a sensitive indicator for the presence of stable single domain ferrimagnets (Maher, 1988) varies significantly along depth (Fig. 3a). In addition to enhanced values in paleosols, sharp and high peaks are observed at depths of the visible tephra deposit (7.20 m depth) and several depth intervals from the lower part of the profile (14.10 m; 18.48 m; 18.80 m; 21.00 m). The same pattern is revealed in other parameters such as  $\Delta\chi$ ,  $IRM_{100mT}$  and  $IRM_{2T}$  (Fig. 3b, d, Fig. 9S).

Magnetic grain size dependent ratios ( $\chi_{ARM}/\chi_{lf}$ ,  $ARM/IRM_{100mT}$ ) exhibit a distinct character along the profile (Fig. 4a, b). The sensitivity of  $\chi_{lf}$  to the presence of superparamagnetic (SP) grains results in relatively low enhancement of  $\chi_{ARM}/\chi_{lf}$  ratio in paleosols compared to the strong sharp peaks caused by high  $\chi_{ARM}$  as revealed in Fig. 3a. Meanwhile, the ratio  $ARM/IRM_{100mT}$  varies strongly between loess and paleosols (Fig. 4b). Maxima are observed in the lower part of the profile (particularly in  $S_6$  and  $S_5$ ) contrasting with their relatively low susceptibilities. The ratio  $IRM_{2T}/\chi_{lf}$  (Fig. 4c) outlines loess units with high values and paleosols with low values. The coercive force ( $B_c$ ; Fig. 4d) varies analogously to  $IRM_{2T}/\chi_{lf}$ , while high field susceptibility ( $\chi_{hif}$ ) (Fig. 4e) exhibits saw-tooth variability with the sharp low to high transitions coinciding with the bases of  $S_5$  through  $S_1$  paleosols and  $S_0$

Holocene soil.

#### 4.3. Optical and scanning electron microscopy (SEM) observations

Microphotographs of single grains from the L<sub>2</sub> tephra are shown in Fig. 5 (a, c, e) together with results from energy-dispersive spectroscopy (EDS) elemental analyses (Fig. 5b, d, f). The particle in Fig. 5a resembles well the described morphology of angular blocky ash particles with internal bubbly texture (area outlined by the yellow rectangle), generated by phreatomagmatic eruptions (Pardo et al., 2014; Ross et al., 2022). EDS analyses reveal that the clast has aluminosilicate composition (Fig. 5b). Characteristic “stepped features” are also recognized from

SEM images of particle fragments (Fig. 10S a, b), as well as elongated porous grains (Fig. 10S c, d). Dense blocky grains with smooth walls and sharp edges were also frequently found (Fig. 5c). They are described in the literature as a result of fast magma cooling and glass fragmentation (Dürig et al., 2012; Cashman and Rust, 2016). EDS spectra of these dense grains show high content of Fe and Mn (Fig. 5 d, f). A cusped vesicle-wall shard imaged in Fig. 5e further affirms the volcanogenic origin of the grains examined from the L<sub>2</sub> tephra deposit.

Images stemming from the optical microscopy investigation of assumed cryptotephra at depths of 14.20 m, 18.48 m and 21.00 m are shown in Fig. 6. Like the L<sub>2</sub> tephra deposit (Fig. 6a), the cryptotephra at the top of S<sub>4</sub> paleosol (Fig. 6b) reveals irregular particles with smooth

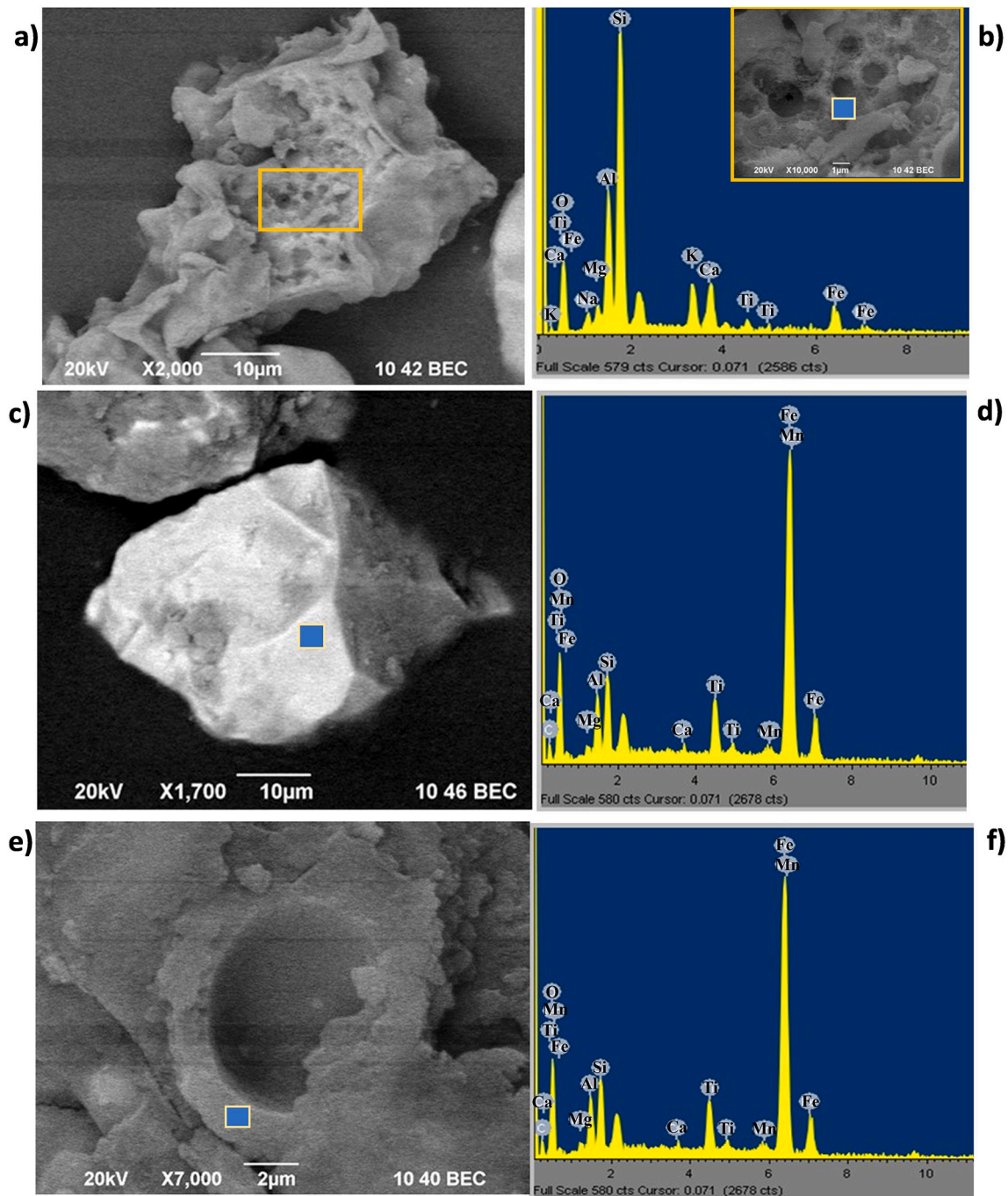


**Fig. 5.** SEM images (back scattered electrons mode) of (a) elongated clast, (c) dense particle, and (e) cusped vesicle-wall shard from the visible tephra layer at 7.2 m depth in L<sub>2</sub> loess unit. The corresponding EDS spectra, taken in the locations marked by blue squares are presented in b), d) and f). (For interpretation of the references to color in this figure legend, the reader is referred to the web version of this article.)

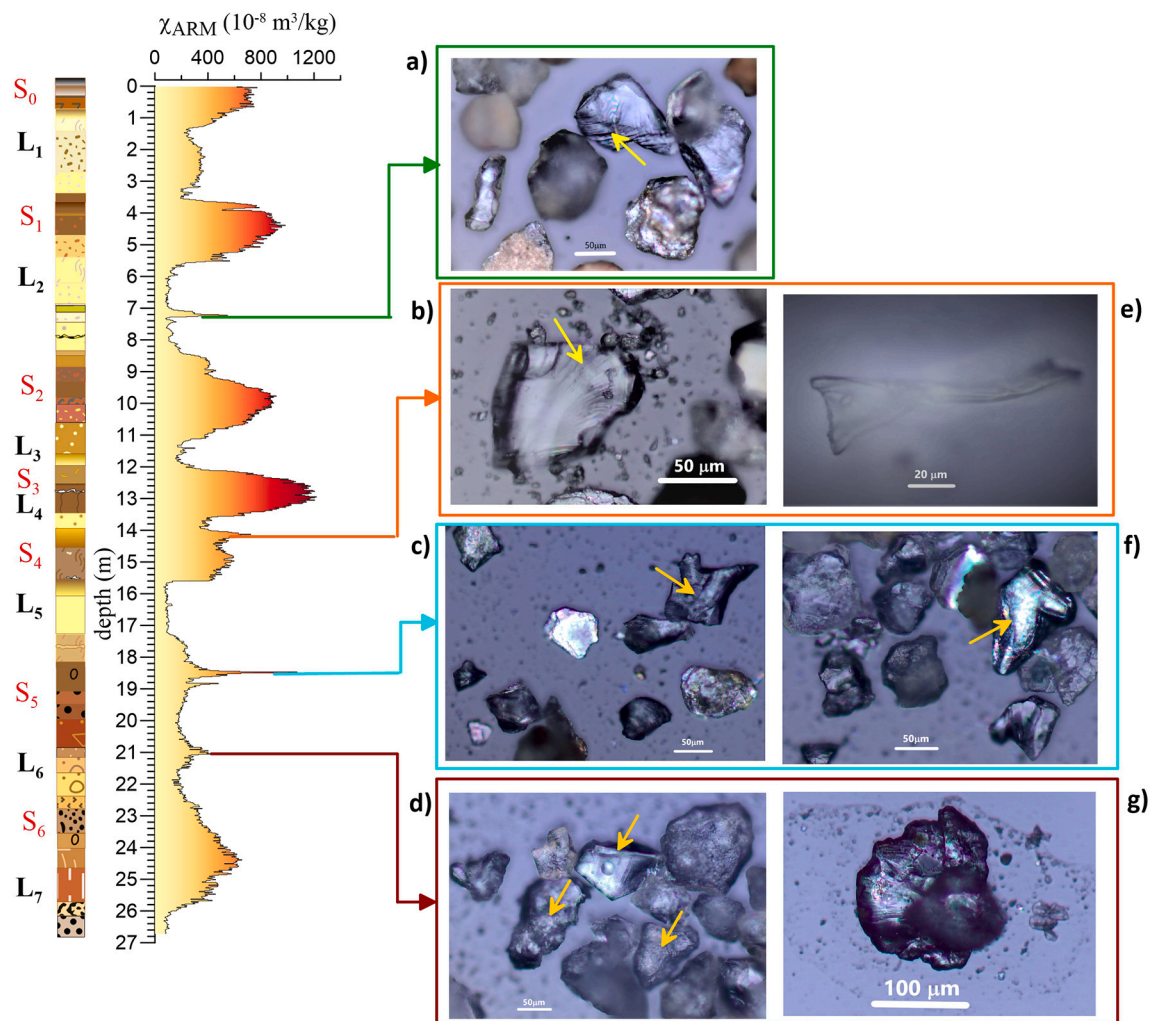


**Fig. 6.** Optical microphotographs (reflected light) of single grains separated from the  $50 \mu\text{m} < d < 250 \mu\text{m}$  size range, showing grains of supposed volcanogenic origin with various morphologies: smooth glassy irregular grains with well – expressed Hackle marks (a, b), dense blocky and fluidal particles with molten surface (c, d, f, g) and vesicle wall shard (e) from depth intervals, characterized by sharp maxima in anhysteretic susceptibility ( $\chi_{\text{ARM}}$ ) (left graph) argued as fingerprinting the presence of cryptotephra.

glassy surfaces and Hackle marks, indicative for brittle fragmentation of magmatic melt in ash particles (Dürig and Zimanowski, 2012). Grains investigated from the cryptotephra at the top and bottom of  $S_5$  paleosol (Fig. 6c, f, d, g) display different morphologies – a wealth of fluidal particles (Ross et al., 2022) with smooth, molten bulbous surfaces are observed. These surface properties are described as signs of hydrodynamic fragmentation of basaltic magma (so called passive particles, e.g. Zimanowski et al. (2015)). Small glass fragment of vesicle wall was found in the 14.20 m cryptotephra within  $S_4$  (Fig. 6e).

#### 4.4. Correlative age models

One basic assumption for building correlative age models is that dust accumulated continuously at variable rates with no erosional gaps. The absence of erosional gaps in the SK profile is supported by field observations (Table 1S). From the general onset of sedimentation on top of the PDS (Evlogiev, 2007), we expect a maximum age for the onset of sedimentation at the SK LPS of about 800 kyrs. Stratigraphically, the onset of sedimentation corresponds to the clay to loess transition at 26.12 m (Table 1S). This age is constrained by the stratigraphic position of the Matuyama-Brunhes (M/B) boundary observed in  $L_7$  loess at Viatovo LPS (Jordanova et al., 2008), some 125 km ENE of the SK LPS (see Fig. 1a). The uppermost 60 cm of the Holocene soil ( $S_0$ ) are excluded from the age

– depth correlation due to the observed 30 cm thick ploughed horizon at the top of the sequence (Table 1S). An additional 30 cm of reworking below were also excluded. An age estimate of 4.2 ka is ascribed to the profile depth of 60 cm, based on the proposed Holocene sub-division by Walker et al. (2012). Thus, following the above assumptions, the 26.12 m to 0.60 m depth interval is expected to have evolved from about 800 to 4.2 ka. A calculated time resolution per sampling interval (2 cm) is thus of  $\sim 0.62$  kyrs or  $\sim 3.2$  cm/kyr.

The correlative age model between  $\Delta\chi$  vs. LR04 shown in Fig. 7a based on 14 tie-points (Table 2S) has a correlation coefficient of 0.524. The age model comparing  $\text{IRM}_{2T}/\chi_{\text{lf}}$  with EDC (Fig. 7b) is constructed from 10 tie-points (Table 2S) and has a correlation coefficient of 0.350. Both age models are in good agreement (Fig. 8a) and comply with the proposed onset of sedimentation on the PDS with both age models rendering ages for the clay to loess boundary at 26.12 m depth of 810 ka. For the 60 cm depth interval at the top of the sequence, the  $\Delta\chi$  – LR04 and the  $\text{IRM}_{2T}/\chi_{\text{lf}}$  – EDC age models render ages of 0 ka and 7.7 ka, respectively. Both estimates are compatible with a projected age of 4.2 ka at 60 cm depth. Calculated sedimentation rates (SR) are expectedly higher in loess than in paleosols (Fig. 8b). The highest SRs (5.5 to 5.9 cm/kyr depending on age model) are derived for  $L_2$  loess deposition (MIS 6) but these are significantly lower than deduced SR ( $\sim 14$  cm/kyr; Antoine et al., 2019) for the  $L_2$  loess at Harletz, located 75 km WNW of



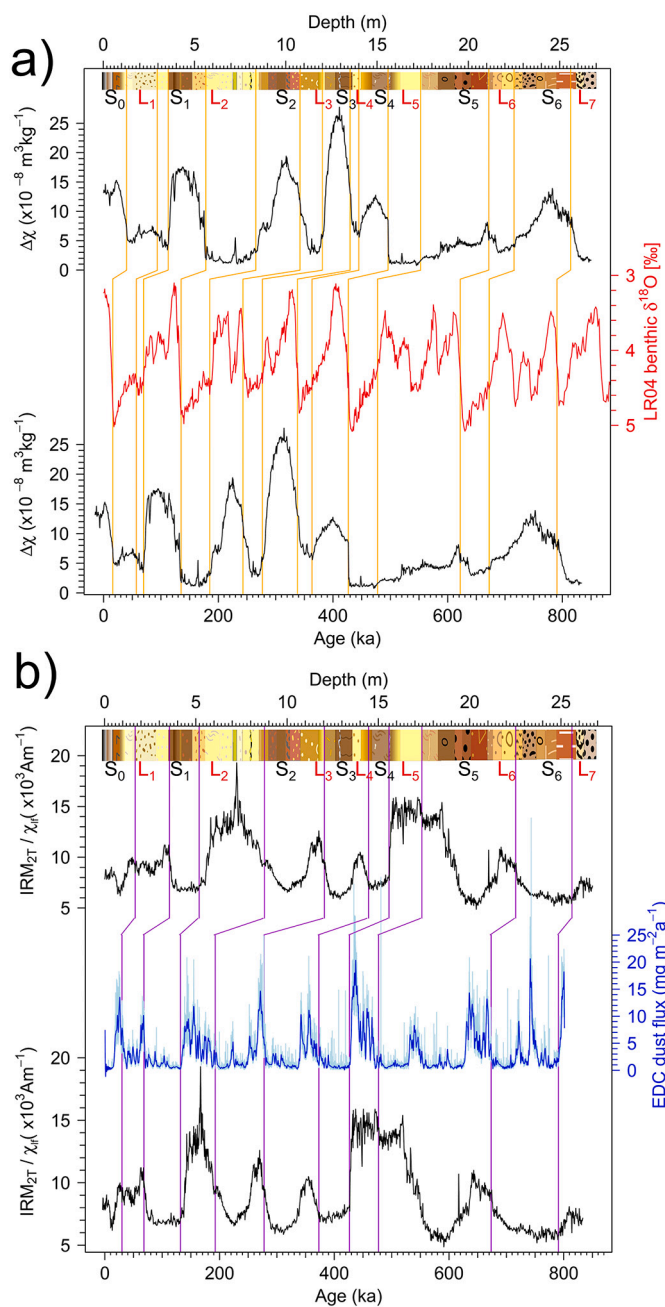


**Fig. 7.** The correlative age model between (a) the pedogenic proxy  $\Delta\chi$  and benthic foraminifera  $\delta^{18}\text{O}$  LR04 record (Lisiecki and Raymo, 2005) based on 14 tie-points (Table 2S) and (b) the wind dynamic proxy  $\text{IRM}_{2T}/\chi_{if}$  and the dust flux record of EPICA Dome C (Lambert et al., 2008, 2012) based on 10 tie-points (Table 2S).

the SK LPS. The  $L_5$  loess unit, corresponding to MIS 12, also results in relatively high SR values of 3.5 cm/kyr, in agreement with knowledge of glacial strengths over the last 800 kyr (e.g., Lang and Wolff, 2011).

The correlative age model exercise also results in age estimates of the visible tephra deposit in the MIS 6  $L_2$  loess (7.20 m) and the three identified cryptotephra at about 14.20 m, 18.48 m and 21.00 m (Fig. 8a).

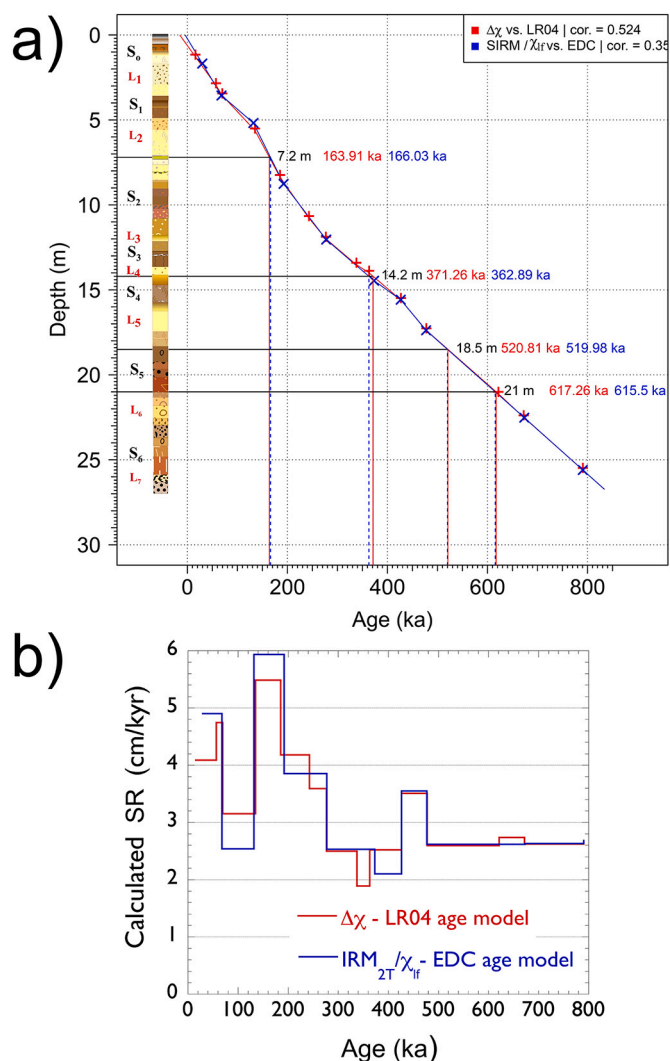


**Fig. 8.** (a) Comparison of the two correlative age models on an age-depth plot. Depths of (crypto)tephras and resulting age estimates are reported on the plot. (b) Calculated sedimentation rates resulting from the two age-models.

## 5. Discussion

### 5.1. Mineral magnetic response of loess-paleosol sedimentary sequence to paleoclimatic changes

Magnetic properties of loess-paleosol sequences are widely utilized as sensitive paleoenvironmental archives (Buggle et al., 2014; Fitzsimmons et al., 2012; Hao et al., 2008; Hu et al., 2015; Liu et al., 2005; Maher, 1998; Marković et al., 2011; Obrecht et al., 2019). The sensitivity is controlled by the strong influence of environmental factors on phase composition, concentration and grain size distribution of pedogenic iron oxides (Cornell and Schwertmann, 2003; Liu et al., 2012; Maher, 2016; Lagroix et al., 2016). Results from stepwise thermal demagnetization experiments of the composite remanence (Fig. 2, 5S, 6S, 7S) allow matching depth changes of high-resolution basic magnetic parameters to certain remanence-bearing mineral magnetic phases. The ARM intensity systematically shows a component with final  $T_{ubS}$  of 600 °C with the exception of very few intervals, indicative for the presence of low-temperature oxidation of the original magnetite (Dunlop and Özdemir, 2013). The second magnetic phase, identified through  $T_{ubS}$  of 250–320 °C (Fig. 8S), is considered as thermally unstable maghemite, which transforms upon heating to hematite in this temperature range (Cornell and Schwertmann, 2003; Machala et al., 2011). Even higher

transformation temperatures, up to 400 °C, can be ascribed to maghemite whose vacancies occupy tetrahedral sites (de Boer and Dekkers, 2001; Takei and Chiba, 1966). A similar increase in maghemite  $T_{ub}$  may also arise from surface inhomogeneity in nm-sized particles, metastable growth or defects (Grau-Crespo et al., 2010). Such specific tetrahedrally coordinated vacancies and surface inhomogeneities are favored in nm-sized maghemite particles (Coduri et al., 2020; Machala et al., 2011). Depth variations in the intensity of the ARM components carried by magnetite and maghemite (Fig. 2b) reveal that maghemite is generally restricted to the upper 13 m of the profile with strong contributions to the signal in the entire thickness of paleosols  $S_3$  and  $S_2$ , and the lower part of  $S_1$ .

Maghemite is also identified as a carrier of the  $IRM_{soft}$  component, showing lower intensities below 13 m depth, similar to ARM component carried by maghemite (Fig. 2b). However, unblocking or transformation temperatures of  $IRM_{soft}$ -bearing maghemite are systematically lower (280–300 °C) (Fig. 8S) compared to those of ARM.  $T_{ub}$  of the  $IRM_{hard}$ -maghemite carrying component are even lower - at 250 °C (Fig. 8S). Overall, the remanence intensities (and consequently the concentration) of maghemite are greatest in the uppermost 13 m of the sequence. The upper part of  $L_2$  and all of  $L_5$  show marked decrease of ARM intensity, suggesting that they are the least weathered loess units of the SK profile. Both of these intervals also coincide with the highest calculated SRs (Fig. 8b). The hard IRM component (Fig. 2d) is primarily carried by hematite with a sharp unblocking at  $T_{ub}$  of 700 °C (Fig. 8S). The intensity of this high-coercivity hematite component changes systematically with depth, showing enhancement in paleosols (Fig. 2d), which implies that this high-coercivity hematite is of pedogenic origin. Finer grained pedogenic hematite, which cannot carry remanence and exist in SP state, are also common in soils (Long et al., 2015; Jiang et al., 2018), developed under warmer climates (Cornell and Schwertmann, 2003; Long et al., 2015, 2016; Gao et al., 2018).

The concentration of hematite and maghemite carriers of  $IRM_{soft}$  component show a step-like increase at 19 m towards the top of the sequence (Fig. 2c) without any clear discrimination between loess and paleosol units. The lack of stratigraphic discrimination of loess-paleosol units by hematite  $IRM_{soft}$  component suggests that most probably it is of primary detrital origin, reflecting the mineralogy of the dust source areas. The grain size of this detrital hematite is expected to be coarser. The step - like change in the intensity of  $IRM_{soft}$  at depth of 19 m (Fig. 2c) implies that the change in the main dust source area or climate at the dust source area occurred at the timing of  $S_5$  formation (or deposition of its parent loess  $L_6$ ). Whether the  $S_5$  paleosol (and  $S_6$ ) developed uniquely as an accretionary soil or with some periods of down-building soil formation is an open question. It is an important point for which more detailed multi-disciplinary analyses such as grain size distribution and other proxy parameters for changes in wind speed are underway to provide an answer. Similar weaker intensities of  $IRM_{soft}$  are observed in the upper part of the second loess  $L_2$ , following tephra layer (Fig. 2c). It could signify a change in the dust source caused by changing general atmospheric circulation after large explosive eruptions (Sjolte et al., 2021).

Mostly parallel changes in the intensity of maghemite components in  $IRM_{soft}$  and ARM within the paleosol units  $S_3$ ,  $S_2$  and  $S_1$  support the hypothesis that they represent one population with a common pedogenic origin. A more important maghemite contribution to the pedogenic signal is observed in the upper 13 m of the sequence. Magnetite dominates the pedogenic signal of the lower parts of the sequence (paleosol  $S_4$  and especially  $S_6$ ). The marked contrast may be due to a major change in paleoenvironment such as mid-Brunhes climate transition (Ao et al., 2020; Barth et al., 2018).

The above changes in type and concentration of magnetic minerals carrying the pedogenic versus the parent material signal along the SK LPS determine also the contrast between magnetic enhancement of paleosols, (crypto)tephra deposits, and loess units. As seen in Fig. 3 (a, b), the Holocene soil  $S_0$  and the paleosols  $S_1$ ,  $S_2$  and  $S_3$ , characterized by

high maghemite content (Fig. 2b, c) exhibit strong magnetic enhancement compared to the weakly magnetic loess units. The magnetic expression of the visible tephra deposit in the  $L_2$  loess unit has a similar amplitude to that of the  $\chi_{lf}$  enhancement of  $S_2$  and  $S_1$ ,  $\chi_{ARM}$  that is lower than  $S_2$  and  $S_1$ , and IRM (acquired in 2 T and 100mT) values that exceed by far all other values. In contrast, older cryptotephra layers are best expressed as high spikes of  $\chi_{ARM}$  and IRM but have relatively low  $\chi_{lf}$  values (Fig. 3, levels 14.10 m; 18.48 m; 21.00 m). Clear distinction between pedogenically enhanced paleosols and cryptotephra levels is provided by the variability of frequency dependent magnetic susceptibility. Pedogenesis is intimately associated with high  $\Delta\chi$  and  $\chi_{fd}\%$ , while incorporation of volcanogenic ashes (tephra) within eolian dust and soil leads to no perceptible peak in  $\chi_{fd}\%$  (Fig. 3c). Similar magnetic expressions of cryptotephra material within sedimentary sequences are reported by Shin et al. (2020), McCanta et al. (2015), Makaroglu et al. (2018) and others. Cryptotephra detection in LPSs through its magnetic signature is favored by the weakly magnetic nature of loess material and generally magnetically enriched volcanic ash (Lagroix et al., 2004; Vigliotti et al., 2014). Within paleosols, the addition of ferrimagnetic minerals of pedogenic origins may mask or render more difficult the identification of ferrimagnetic minerals of volcanogenic sources. The predominantly single domain effective magnetic grain size of tephra-derived magnetite, excluding a superparamagnetic tail, facilitates the identification of cryptotephra deposit within paleosol horizons (Fig. 3a) using ARM signal. In favor of a good preservation of tephra deposited during interglacial conditions are the findings that thicker and more even layers are formed under dense (closed) shrub canopy (Cutler et al., 2016; Dugmore et al., 2020), which are realized better under interglacial conditions. Geochemical instability of the fresh volcanic ash in the soil environment is another issue (e.g., Kilian et al., 2006), but larger ash particles (the microscopically observed particles are with sizes  $d > 50 \mu m$ ) are not much affected due to their low area / volume ratio. The magnetic ratios (Fig. 4) reveal further peculiarities of the effective magnetic grain size variations along depth of the SK profile. The ratios  $\chi_{ARM}/\chi_{lf}$  and  $ARM/IRM_{100mT}$  are utilized as indicators for the relative abundance of stable single domain magnetite-like carriers (Geiss et al., 2008) in the bulk material. In the studied profile, paleosols show enhanced values of similar amplitudes compared to the parent loess. This cyclic smooth pattern is punctuated by two sharp peaks at 14.10 m; 18.48 m; indicative for cryptotephra occurrence. However, the other level (21.00 m) visible as an anomalous peak in concentration-dependent magnetic parameters (Fig. 3) is not discriminated by the grain size sensitive ratios (Fig. 4) similarly to the  $L_2$  tephra deposit. The magnetic ratio  $IRM_{2T}/\chi_{lf}$  (Fig. 4c) reveals significant variations along depth of SK profile, delineating loess units by high values and paleosols by low values. Ordinary use of the ratio as grain size proxy in dominantly magnetite - bearing sediments (Liu et al., 2012) is not applicable in our case because of the important contribution of hematite (see Fig. 2). The strong influence of hematite presence in binary mixtures at magnetite content less than 1 wt% is well established (Frank and Nowaczyk, 2008). Much lower contents of magnetite are reached in non-weathered loess at SK site. Even though we argue that detrital hematites are of lower coercivity (e.g. carriers of  $IRM_{soft}$ ), their dominance in the loess samples also causes an increase in  $IRM_{2T}/\chi_{lf}$  ratio. This is due to the weaker sensitivity of hematites' SIRM to grain size changes in SD - MD range (Özdemir and Dunlop, 2014). Consequently, the ratio  $IRM_{2T}/\chi_{lf}$  (Fig. 4c) in this particular case is considered as a proxy for changes in the relative proportion of detrital fraction, having mean grain size in the silt grain size region ( $2 < d < 50 \mu m$ ) according to the general characteristics of loess sediments (Muhs, 2013). Silt size fraction is the main component in the loess sediments, strongly dependent on a number of factors, including wind speed (Újvári et al., 2016). Thus, the ratio  $IRM_{2T}/\chi_{lf}$  can also serve as magnetic proxy for wind dynamics.

Fig. 9S provides a detailed view of a larger set of magnetic parameters across a 2 m depth interval centered on the visible tephra and cryptotephra. As the data in Figs. 3 and 4 suggested, each (crypto)

tephra is expressed by anomalous parameters with respect to the surrounding material but the set of characteristic anomalous parameters differs. Consequently, we infer that the volcanic sources of these ashes are either of different mineralogy or of different eruptive characteristics. SEM and optical microscopy observations of the L<sub>2</sub> tephra and grain size separates from cryptotephra (Figs. 5, 6, 10S) give further evidences on the occurrence and size range of volcanic ash particles in these deposits. The inspected particles are large with typical sizes of 50–100 μm. Since strong peaks in ARM characterize these (crypto)tephras, such large grains are likely not mono-mineral particles but contain strongly magnetic fine nm-sized inclusions, carrying strong ARMs. Such well crystalline nanolith magnetite growth has been observed in experimentally produced basaltic pumice as well as in natural basalts from Mt. Etna (Di Genova et al., 2020, 2018). The authors cited show that crystalline magnetite nanoliths (sizes about 10–20 nm up to 50 nm) represent less than 4% by volume but play an important role in increasing magma viscosity, promoting its fragmentation during cooling and ascent, and thus controlling the type of eruption.

The fluidal ash particles from the cryptotephra at 21.00 m depth

(Fig. 6d) have well expressed molten and bulbous morphologies. Distinct magnetic properties in concentration – dependent parameters are observed (Fig. 3) but not for magnetic grain size sensitive ratios (Fig. 4). This implies a less constricted grain size distribution (GSD) of the magnetic carriers in this tephra material. Broad GSD may indicate source-specific peculiarity or higher degree of alteration of the volcanogenic products due to, for example, microbially mediated secondary alterations in the paleosols (Badurina et al., 2020) or longer elapsed time since deposition (Cashman and Rust, 2016). Rare occurrence of silicate glass particles (Fig. 6e) is probably due to low thermodynamic stability of the volcanic glass in surface environments and its fast weathering and degradation with simultaneous synthesis of Fe-(oxy)hydroxides (Schindler et al., 2019).

## 5.2. Local and regional spatio-temporal patterns of paleoclimate and volcanic ash dispersal

Variations with depth of the magnetic parameters along the SK profile reveal detailed recording of environmental change during the

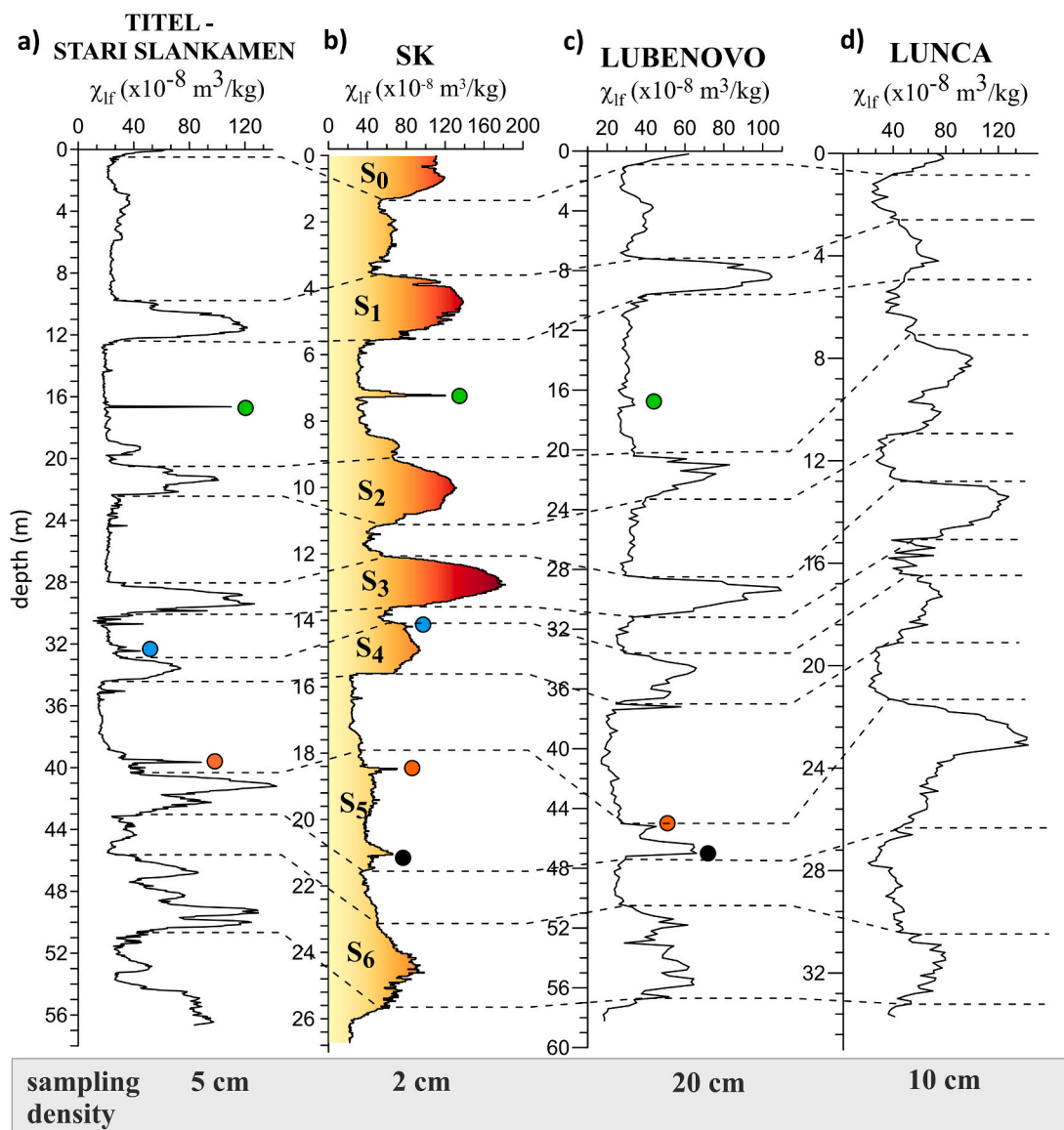


**Fig. 9.** Correlation of magnetic susceptibility record of the SK LPS (b) with published records from the region: a) Titel - Stari Slankamen stack (Song et al., 2018); c) Lubenovo borehole (Jordanova et al., 2007); d) Lunca (Constantin et al., 2015). Color dots indicate the position of (crypto)tephra deposits discussed in the text. Refer to Fig. 1a for the location of LPSs.



last ~800 kyrs. It represents a valuable archive, allowing for distinction of relatively short – term events on geological time scales. The best examples of such events are dust falls from volcanic eruptions, contributing occasionally to the total eolian dust flux. Various factors play role for establishment and preservation of detailed high-resolution LPSS (Lehmkuhl et al., 2021). One external, purely methodological factor is the sampling density (sampling interval). The observed clear discrimination of cryptotephra layers through their sharp maxima in  $\chi$ ,  $\chi_{ARM}$  and/or IRM variations along the SK LPS (Fig. 3) are smeared or indistinguishable in the magnetic susceptibility record along nearby Lubenovo borehole (Jordanova et al., 2007), drilled at ~25 km to the NE (Fig. 9c). It is important to note that the Lubenovo borehole is 64 m long and was sampled at 20 cm resolution. Consequently, even though the deposit at Lubenovo is nearly three times thicker than the SK deposit for the same time period, the continuous 2 cm sampling resolution undertaken for the SK LPS results in a time domain resolution that is approximately 3 times higher than for the Lubenovo profile. This is visible from the presented correlation between the two records in Fig. 9 (b, c). The L<sub>2</sub> tephra deposit with its strongly magnetic signal is identified in Lubenovo record only as a small  $\chi_{lf}$  increase in three sample levels (~ 60 cm). Another LPS from the region is Lunca profile (Constantin et al., 2015) (Fig. 9d). Magnetic susceptibility variations along Lunca, situated less than 80 km to the north across the Danube on Romanian territory, do not show any indications for the presence of cryptotephra. This might be explained by the lower sampling density at Lunca site (10 cm).

In LPSS from other Central and SE European locations, the tephra in L<sub>2</sub> loess is everywhere distinguished by its strongly magnetic signal (Antoine et al., 2019; Balescu et al., 2010; Laag et al., 2021; Marković et al., 2015; Obrecht et al., 2016; Panaiotu et al., 2001). The older cryptotephra layer detected in L<sub>4</sub> from sites in the Carpathian basin (Csonka et al., 2020; Horváth, 2001; Laag et al., 2021; Marković et al., 2015) reveals strong magnetic signal as well. Along the SK profile, this tephra is best manifested by the strong peaks in ARM and IRM at 14.10 m (Fig. 3, 9S) in the upper part of S<sub>4</sub> paleosol. Its stratigraphic position (marked by blue circle in Fig. 9) is similar to the observed tephra deposit in L<sub>4</sub> loess of the Feduvar section from the composite Titel – Stari Slankamen profile (Song et al., 2018) (Fig. 9a). Other peaks in the susceptibility record within S<sub>5</sub> paleosol (red and black circles in Fig. 9) can be correlated with similar signature of Titel loess (Marković et al., 2012b; Song et al., 2018). In a regional context, the magnetic susceptibility record of the SK LPS shows remarkable similarities with the Titel – Stari Slankamen LPS (Song et al., 2018) situated some 400 km NW upstream the Danube river. Both records, SK and Titel – Stari Slankamen, reveal the presence of several (crypto)tephra deposits. The relative pedogenic magnetic enhancement in S<sub>4</sub> to S<sub>1</sub> paleosols (Fig. 9a, b) also follows a similar trend. Importantly, the SK S<sub>5</sub> paleosol complex characterized by the occurrence of two cryptotephra susceptibility peaks - at its base and at its top - demonstrates much lower magnetic enhancement compared to the strong magnetic enhancement observed at Titel – Stari Slankamen and Lunca LPSS (Song et al., 2018; Constantin et al., 2015). The Lunca site is considered in this comparison among LPSS from low Danube area, having in mind its close proximity to SK and Lubenovo sites. The aim is to explore the possible effect of tephra additions on the establishment of the pedogenic magnetic enhancement under similar paleoclimate conditions. The comparison suggests that the presence of significant tephra material in paleosols at SK and Lubenovo LPSS may influence the pedogenic processes. Weathering products of basaltic tephra are usually halloysite, imogolite or allophane clays (Lowe, 1986) which, in combination with lowering of the pH (Kilian et al., 2006) could lead to potentially weaker magnetic enhancement, increased clay content and development of hydromorphic features. Identification of the sources of volcanic ashes (cryptotephra) requires further detailed microscopic and geochemical analyses and could serve for the establishment of a rigorous tephrochronological stratigraphy of the site.

### 5.3. Reviewing potential volcanic sources of (crypto)tephras

The absence of geochemical analyses prevents a rigorous tephrochronological stratigraphy of the SK profile to be established. Thus, we review below potential volcanic sources for the tephra and cryptotephra deposits based on the correlative age models age estimates and published literature. Age estimations stemming from the correlative age models inherit uncertainties from the paleoclimate records in addition to uncertainties associated to the correlation exercise itself. Lisiecki and Raymo (2005) report a 4 kyrs age uncertainty for the last 1 Myrs of  $\delta^{18}O$  benthic foraminifera LR04 record. Parrenin et al. (2007) report age uncertainties of EDC dust flux record varying from 1 to 6 kyrs depending on the time period and methods used. The age uncertainty associated to the correlation exercise is more difficult to quantify. Mathematically, the maximum age uncertainty would be equal to one half of the time period between two consecutive tie-points. However, the absence of erosional gaps and the approach undertaken to establish tie-points (i.e. times of sharp changes) significantly reduce the uncertainty inherent to the correlation exercise. Since the EDC record is characterized by increasing and decreasing dust fluxes that are not as sharp as glacial terminations in the LR04 record, age uncertainties due to the correlation exercise are expected to be higher for the IRM<sub>2T</sub>/ $\chi_{lf}$  – EDC age model than the  $\Delta\chi$  – LR04 age model.

Age estimates for the L<sub>2</sub> tephra deposit are of 163.9 ka and 166.0 ka resulting from the  $\Delta\chi$  – LR04 and the IRM<sub>2T</sub>/ $\chi_{lf}$  – EDC age models, respectively. Several volcanic eruptions recorded in Lake Ohrid, Fucino Basin and the Mediterranean Sea can be tentatively assigned to the L<sub>2</sub> tephra layer. From Lake Ohrid, OH-DP-0617 Vico B with  $162 \pm 6$ , OH-DP-0624 CF-V5 Pitigliano Tuff with  $163 \pm 22$  ka are possible equivalent candidates (Leicher et al., 2016). From the Ionian sea, three tephra layers of similar age range are reported: I-13/KC01B ( $161.9$  ka (Insinga et al., 2014)), P-12/KET82–22 ( $164$  ka (Paterne et al., 2008)), and I-14bottom/KC01B ( $167.2$  ka (Insinga et al., 2014)). Possible equivalent tephra from the Fucino Basin (Italy) could be TF-15 (Vico Ignimbrite C with an  $^{40}Ar/^{39}Ar$  age of a correlated tephra of  $153.5 \pm 4.6$  ka), TF-16 (Vico Ignimbrite B, with  $160.6 \pm 4.0$  ka), and TF-17 stemming from the Campanian Volcanic Zone (Taurano Ignimbrite with  $159 \pm 1.6$  ka) (Giaccio et al., 2019).

The cryptotephra at 14.10 m has age estimates of 371.3 ka and 362.9 ka from the  $\Delta\chi$  – LR04 and the IRM<sub>2T</sub>/ $\chi_{lf}$  – EDC age models, respectively. Based on its stratigraphical position, we correlate this cryptotephra with the suggested position of the Bag tephra at Mošorin profile and the Mošorin & Stari Slankamen synthetic (MSS) loess-paleosol sequence (Marković et al., 2015), and thus to the TF-85 Villa Senni eruption from the Colli Albani volcano with an age of  $367.5 \pm 1.6$  ka. A recent study of Monaco et al. (2021) provides evidence for an older age for the Bag tephra and correlate it to the tephra cluster TF-102/106 based on a phonotephritic-tephriphonolithic composition.

The identified cryptotephra at 18.50 m, at the top of S<sub>5</sub> paleosol (indicated by red circle in Fig. 9) can be correlated with the tephra deposit in the L<sub>5</sub> unit at Dukatar section, representing part of the lower portion of Titel – Stari Slankamen stack (Song et al., 2018). Based on resulting age estimation for the cryptotephra at 18.50 m depth of 520.8 ka and 520.0 ka from the  $\Delta\chi$  – LR04 and the IRM<sub>2T</sub>/ $\chi_{lf}$  – EDC age models, respectively, a potential equivalent may be the OH-DP-2060/ Tufo di Bagni Albule, dated to  $527 \pm 2$  ka within the Lake Ohrid record (Leicher et al., 2016; Marra et al., 2009). A similar age range is calculated and dated for the OH-DP-2017 stemming from the Acerno A11–12 eruption, dated to  $514 \pm 6$  ka (Petrosino et al., 2014) and re-calculated age by Leicher et al. (2016) of  $511 \pm 6$  ka. Since the Tufo Bagni Albule tephra is preserved in Italian tephra rich archives as well as in the Lake Ohrid, we consider it as widespread and assume a higher possibility that it be conserved in the SK LPS rather than the Acerno A11–12 tephra.

For the cryptotephra at 21.00 m depth, age estimates of 617.26 ka and 615.5 ka result from the two age models. No tephra deposit is found in this time window in the Fucino basin, Lake Ohrid or Tenaghi

Philippon records. The Tiber River composite record (Monaco et al., 2021) does have a tephra occurrence dated to  $614 \pm 3$  ka (Kamer and Renne, 1998) which could be a potential candidate. The lack of stratigraphically coeval cryptotephra occurrences in older than  $L_5$  deposits in other Middle and Lower Danube basin LPS is motivation for further, detailed analyses (microscopic, geochemical and magnetic) to confirm more rigorously the occurrence of a cryptotephra deposit at this depth interval.

## 6. Conclusions

The loess-paleosol sequence exposed in Suhia Kladenetz (SK) quarry from lower Danube loess area is a high-resolution proxy record with high sensitivity to the dynamic interplay between eolian dust sedimentation and soil formation, driven by climate oscillations over the last 800 kyrs. Concentration – dependent magnetic parameters of bulk sediment samples ( $\chi_{lf}$ ,  $\chi_{ARM}$ , IRM) show variations, allowing unambiguous identification of a number of cryptotephra deposits through their strong magnetic signal in addition to the visible  $\sim 20$  cm thick tephra within the  $L_2$  loess unit. Microscopy observations on single grains from the visible tephra and cryptotephra deposits confirm the presence of volcanogenic particles with surface topology closely resembling the ones of volcanic ash particles produced during fast magma cooling and glass fragmentation. Based on the correlative age-models, age estimates for the tephra and cryptotephra provide constraints enabling to propose likely correlations with tephra occurrences within well-dated tephra-rich records such as the Fucino Basin, Lake Ohrid and other Mediterranean Sea sediment cores.

The older paleosols,  $S_6$  and  $S_5$ , exhibit a markedly different pedogenic magnetic signature characterized by low magnetic enhancement with respect to  $S_4$  through  $S_0$  (paleo)sols yet with equivalent content of superparamagnetic pedogenic particles ( $\chi_{fd}$  %) and values of grain size dependent ratios. Magnetic mineralogy, deduced from stepwise thermal demagnetization of a composite remanence, reveals the dominant presence of magnetite as ARM carrier for lower (older) part of the sequence from  $L_7$  to  $S_4$  and maghemite - for the upper (younger) part of the sequence from  $L_4$  to  $S_0$ . Hematite is the dominant carrier of the  $IRM_{soft}$  component and shows a clear step-like increase in intensity above the  $S_5$  paleosol. These magnetic mineralogical observations coupled with the noteworthy change in amplitudes of concentration dependent magnetic parameters between paleosols and underlying loess units below  $\sim 16$  m depth and above, all point towards a significant paleoenvironmental change. The marked change at 16 m depth probably marks the occurrence of the mid-Brunhes climate transition within SK LPS.

Supplementary data to this article can be found online at <https://doi.org/10.1016/j.gloplacha.2022.103840>.

## Data availability

The magnetic data presented in this article will be made available on the Pangea data repository (<https://www.pangea.de/>) once accepted.

## CRediT authorship contribution statement

**Diana Jordanova:** Conceptualization, Writing – original draft, Supervision, Funding acquisition. **Christian Laag:** Conceptualization, Methodology, Formal analysis, Investigation, Writing – original draft, Visualization. **Neli Jordanova:** Conceptualization, Writing – review & editing, Methodology, Visualization. **France Lagroix:** Conceptualization, Formal analysis, Writing – review & editing, Visualization, Supervision. **Bozhurka Georgieva:** Investigation, Formal analysis. **Daniel Ishlyanski:** Investigation, Formal analysis. **Yohan Guyodo:** Methodology, Formal analysis, Writing – review & editing, Supervision.

## Declaration of Competing Interest

The authors declare that they have no known competing financial interests or personal relationships that could have appeared to influence the work reported in this paper.

## Acknowledgements

The study is financially supported by project No KP-06-N34/2 funded by the Bulgarian National Science Fund and benefitted from funds received through the INSU-CNRS SYSTER program. The authors are very thankful for the generous logistic support by the geologist of the quarry V. Mihajlova during the fieldwork. Prof. Dr. Cristian Panaiotu kindly provided susceptibility data for Lunca LPS, and Professor Qingzhen Hao - data of the Titel-Stari Slankamen record published in Song et al. (2018), for which they are sincerely acknowledged. The authors are thankful to the two anonymous reviewers. Their comments improved the manuscript.

## References

- Antoine, P., Lagroix, F., Jordanova, D., Jordanova, N., Lomax, J., Fuchs, M., Debret, M., Rousseau, D.-D., Hatté, C., Gauthier, C., Moine, O., Taylor, S.N., Till, J.L., Coutard, S., 2019. A remarkable late Saalian (MIS 6) loess (dust) accumulation in the lower Danube at Harletz (Bulgaria). *Quat. Sci. Rev.* 207, 80–100. <https://doi.org/10.1016/j.quascirev.2019.01.005>.
- Ao, H., Rohling, E.J., Stringer, C., Roberts, A.P., Dekkers, M.J., Dupont-Nivet, G., Yu, J., Liu, Q., Zhang, P., Liu, Z., Ma, X., Zhou, W., Jin, Z., Xiao, G., Wang, H., Sun, Q., Yang, P., Peng, X., Shi, Z., Qiang, X., An, Z., 2020. Two-stage mid-Brunhes climate transition and mid-Pleistocene human diversification. *Earth Sci. Rev.* 210, 103354. <https://doi.org/10.1016/j.earscirev.2020.103354>.
- Badurina, L., Šegvić, B., Mandić, O., Zanoni, G., 2020. Smectitization as a trigger of bacterially mediated Mn-Fe micronodule generation in felsic glass (Livno-Tomislavgrad Paleolake, Bosnia and Herzegovina). *Minerals* 10, 899. <https://doi.org/10.3390/min10100899>.
- Balescu, S., Lamothe, M., Panaiotu, Cristina, Panaiotu, Cristian, 2010. La chronologie IRSL des séquences lessiques de l'est de la Roumanie. *Quaternaire* 115–126. <https://doi.org/10.4000/quaternaire.5488>.
- Barth, A.M., Clark, P.U., Bill, N.S., He, F., Pisias, N.G., 2018. Climate evolution across the Mid-Brunhes transition. *Clim. Past* 14, 2071–2087. <https://doi.org/10.5194/cp-14-2071-2018>.
- Basarin, B., Bugge, B., Hambach, U., Marković, S.B., Dhand, K.O., Kovačević, A., Stevens, T., Guo, Z., Lukić, T., 2014. Time-scale and astronomical forcing of Serbian loess–paleosol sequences. *Glob. Planet. Chang.* 122, 89–106. <https://doi.org/10.1016/j.gloplacha.2014.08.007>.
- Botti, D., 2018. A phytoclimatic map of Europe. *Cybergeo: Eur. J. Geogr.* [online], *Environ. Nat. Paysage* document 867. doi:10.4000/cybergeo.29495.
- Bugge, B., Hambach, U., Glaser, B., Gerasimenko, N., Marković, S., Glaser, I., Zöller, L., 2009. Stratigraphy, and spatial and temporal paleoclimatic trends in Southeastern/eastern European loess–paleosol sequences. *Quat. Int.* 196, 86–106. <https://doi.org/10.1016/j.quaint.2008.07.013>.
- Bugge, B., Hambach, U., Müller, K., Zöller, L., Marković, S.B., Glaser, B., 2014. Iron mineralogical proxies and Quaternary climate change in SE-European loess–paleosol sequences. *CATENA* 117, 4–22. <https://doi.org/10.1016/j.catena.2013.06.012>.
- Cashman, K., Rust, A., 2016. Introduction: part 2: Volcanic Ash: generation and spatial variations. In: *Volcanic Ash: Hazard Observation*. Elsevier, pp. 5–22. <https://doi.org/10.1016/B978-0-08-100405-0.00002-1>.
- Coduri, M., Masala, P., Del Bianco, L., Spizzo, F., Ceresoli, D., Castellano, C., Cappelli, S., Oliva, C., Checchia, S., Allieta, M., Szabo, D.-V., Schlabach, S., Hagelstein, M., Ferrero, C., Scavini, M., 2020. Local Structure and Magnetism of Fe<sub>2</sub>O<sub>3</sub> Maghemite Nanocrystals: the Role of Crystal Dimension. *Nanomaterials* 10, 867. <https://doi.org/10.3390/nano10050867>.
- Constantin, D., Cameniță, A., Panaiotu, C., Necula, C., Codrea, V., Timar-Gabor, A., 2015. Fine and coarse-quartz SAR-OSL dating of last Glacial loess in Southern Romania. *Quat. Int.* 357, 33–43.
- Cornell, R.M., Schwertmann, U., 2003. *The iron Oxides: Structure, Properties, Reactions, Occurrences and Uses*. John Wiley & Sons.
- Csonka, D., Bradák, B., Barta, G., Szeberényi, J., Novothny, Á., Végh, T., Süle, G.T., Horváth, E., 2020. A multi-proxy study on polygenetic middle- to late pleistocene paleosols in the Hévízgyőr loess-paleosol sequence (Hungary). *Quat. Int.* 552, 25–35. <https://doi.org/10.1016/j.quaint.2019.07.021>.
- Cutler, N.A., Shears, O.M., Streeter, R.T., Dugmore, A.J., 2016. Impact of small-scale vegetation structure on tephra layer preservation. *Sci. Rep.* 6, 37260.
- de Boer, C.B., Dekkers, M.J., 2001. Unusual thermomagnetic behaviour of haematites: neoformation of a highly magnetic spinel phase on heating in air. *Geophys. J. Int.* 144, 481–494. <https://doi.org/10.1046/j.0956-540X.2000.01333.x>.
- Dearing, J.A., Dann, R.J.L., Hay, K., Lees, J.A., Loveland, P.J., Maher, B.A., O'Grady, K., 1996. Frequency-dependent susceptibility measurements of environmental materials. *Geophys. J. Int.* 124, 228–240.



- Di Genova, D., Caracciolo, A., Kolzenburg, S., 2018. Measuring the degree of “nanotilization” of volcanic glasses: Understanding syn-eruptive processes recorded in melt inclusions. *Lithos* 318–319, 209–218. <https://doi.org/10.1016/j.lithos.2018.08.011>.
- Di Genova, D., Brooker, R.A., Mader, H.M., Drewitt, J.W.E., Longo, A., Deubener, J., Neuville, D.R., Panara, S., Shebanova, O., Anzellini, S., Arzilli, F., Bamber, E.C., Hennet, L., La Spina, G., Miyajima, N., 2020. In situ observation of nanolite growth in volcanic melt: A driving force for explosive eruptions. *Sci. Adv.* 6, eabb0413. <https://doi.org/10.1126/sciadv.abb0413>.
- Dinu, C., Gradinaru, E., Stoica, M., Diaconescu, V., 2007. South Dobrogea 2007 Field Trip, Project SAP No 8460002354 Report. Univ. Bucharest.
- Dugmore, A.J., Thompson, P.I.J., Streeter, R.T., Cutler, N.A., Newton, A.J., Kirkbride, M.P., 2020. The interpretive value of transformed tephra sequences. *J. Quat. Sci.* 35 (1), 23–38.
- Dunlop, D.J., Özdemir, Ö., 2013. *Rock Magnetism: Fundamentals and Frontiers*, 1. Paperback ed. with corr., 2. ed., reprinted. ed. Cambridge studies in magnetism. Cambridge Univ. Press, Cambridge.
- Dürig, T., Zimanowski, B., 2012. “Breaking news” on the formation of volcanic ash: Fracture dynamics in silicate glass. *Earth Planet. Sci. Lett.* 335–336, 1–8.
- Dürig, T., Mele, D., Dellino, P., Zimanowski, B., 2012. Comparative analyses of glass fragments from brittle fracture experiments and volcanic ash particles. *Bull. Volcanol.* 74, 691–704.
- Evgoviev, Y., 2007. Evidence for the Aeolian Origin of Loess in the Danubian Plain. *Geol. Balcanica* 36, 31–39.
- Fitzsimmons, K.E., Marković, S.B., Hambach, U., 2012. Pleistocene environmental dynamics recorded in the loess of the middle and lower Danube basin. *Quat. Sci. Rev.* 41, 104–118. <https://doi.org/10.1016/j.quascirev.2012.03.002>.
- Frank, U., Nowaczyk, N.R., 2008. Mineral magnetic properties of artificial samples systematically mixed from haematite and magnetite. *Geophys. J. Int.* 175 (2), 449–461.
- Gao, X., Hao, Q., Wang, L., Oldfield, F., Bloemendal, J., Deng, C., Song, Y., Ge, J., Wu, H., Xu, B., Li, F., Han, L., Fu, Y., Guo, Z., 2018. The different climatic response of pedogenic hematite and ferrimagnetic minerals: evidence from particle-sized modern soils over the Chinese Loess Plateau. *Quat. Sci. Rev.* 179, 69–86.
- Geiss, C.E., Egli, R., Zanner, C.W., 2008. Direct estimates of pedogenic magnetite as a tool to reconstruct past climates from buried soils. *J. Geophys. Res.* 113, B11102. <https://doi.org/10.1029/2008JB005669>.
- Giaccio, B., Leicher, N., Mannella, G., Monaco, L., Regattieri, E., Wagner, B., Zanchetta, G., Gaeta, M., Marra, F., Nomade, S., Palladino, D.M., Pereira, A., Scheidt, S., Sottili, G., Wonik, T., Wulf, S., Zeeden, C., Ariztegui, D., Cavinato, G.P., Dean, J.R., Florindo, F., Leng, M.J., Macri, P., Niespolo, E., Renne, P.R., Rolf, C., Sadori, L., Thomas, C., Tzedakis, P.C., 2019. Extending the tephra and palaeoenvironmental record of the Central Mediterranean back to 430 ka: A new core from Fucino Basin, Central Italy. *Quat. Sci. Rev.* 225, 106003 <https://doi.org/10.1016/j.quascirev.2019.106003>.
- Grau-Crespo, R., Al-Baitai, A.Y., Saadoun, I., De Leeuw, N.H., 2010. Vacancy ordering and electronic structure of  $\gamma$  Fe<sub>2</sub>O<sub>3</sub> (maghemite): a theoretical investigation. *J. Phys. Condens. Matter* 22, 255401. <https://doi.org/10.1088/0953-8984/22/25/255401>.
- Hao, Q., Oldfield, F., Bloemendal, J., Guo, Z., 2008. The magnetic properties of loess and palaeosol samples from the Chinese Loess Plateau spanning the last 22 million years. *Palaeogeogr. Palaeoclimatol. Palaeoecol.* 260, 389–404. <https://doi.org/10.1016/j.palaeo.2007.11.010>.
- Heller, F., Liu, T.-S., 1986. Palaeoclimatic and sedimentary history from magnetic susceptibility of loess in China. *Geophys. Res. Lett.* 13, 1169–1172.
- Heslop, D., Dekkers, M.J., Langereis, C.G., 2002. Timing and structure of the mid-Pleistocene transition: records from the loess deposits of northern China. *Palaeogeogr. Palaeoclimatol. Palaeoecol.* 185 (1–2), 133–143.
- Horváth, E., 2001. Marker horizons in the loesses of the Carpathian Basin. *Quat. Int.* 76–77, 157–163. [https://doi.org/10.1016/S1040-6182\(00\)00099-9](https://doi.org/10.1016/S1040-6182(00)00099-9).
- Hu, P., Liu, Q., Heslop, D., Roberts, A.P., Jin, C., 2015. Soil moisture balance and magnetic enhancement in loess–palaeosol sequences from the Tibetan Plateau and Chinese Loess Plateau. *Earth Planet. Sci. Lett.* 409, 120–132. <https://doi.org/10.1016/j.epsl.2014.10.035>.
- Insinga, D.D., Tamburrino, S., Lirer, F., Vezzoli, L., Barra, M., De Lange, G.J., Tiepolo, M., Vallefuoco, M., Mazzola, S., Sprovieri, M., 2014. Tephrochronology of the astronomically-tuned KC01B deep-sea core, Ionian Sea: insights into the explosive activity of the Central Mediterranean area during the last 200 ka. *Quat. Sci. Rev.* 85, 63–84. <https://doi.org/10.1016/j.quascirev.2013.11.019>.
- IUSS Working Group WRB, 2015. World Reference Base for Soil Resources 2014, update 2015. In: *International Soil Classification System for Naming Soils and Creating Legends for Soil Maps*, FAO. World Soil Resources Reports, Rome, p. 106.
- Jiang, Z.X., Liu, Q.S., Roberts, A.P., Barron, V., Torrent, J., Zhang, Q., 2018. A new model for transformation of ferrihydrite to hematite in soils and sediments. *Geology* 46 (11), 987–990.
- Jordanova, D., Hus, J., Geeraerts, R., 2007. Palaeoclimatic implications of the magnetic record from loess/palaeosol sequence Viatovo (NE Bulgaria): Palaeoclimatic implications of the magnetic record. *Geophys. J. Int.* 171, 1036–1047. <https://doi.org/10.1111/j.1365-246X.2007.03576.x>.
- Jordanova, D., Hus, J., Evgoviev, J., Geeraerts, R., 2008. Palaeomagnetism of the loess/palaeosol sequence in Viatovo (NE Bulgaria) in the Danube basin. *Phys. Earth Planet. Inter.* 167, 71–83.
- Karner, D.B., Renne, P.R., 1998. 40Ar/39Ar geochronology of Roman volcanic province tephra in the Tiber River valley: Age calibration of middle Pleistocene Sea-level changes. *Geol. Soc. Am. Bull.* 110, 0740. [https://doi.org/10.1130/0016-7606\(1998\)110<0740:AAGORV>2.3.CO;2](https://doi.org/10.1130/0016-7606(1998)110<0740:AAGORV>2.3.CO;2).
- Kilian, R., Biester, H., Behrmann, J., Baeza, O., Fesq-Martin, M., Hohner, M., Schimpf, D., Friedmann, A., Mangini, A., 2006. Millennium-scale volcanic impact on a superhumid and pristine ecosystem. *Geology* 34 (8), 609–612. <https://doi.org/10.1130/G22605.1>.
- Kjutschukova, M., 1983. Reference book on climate of Bulgaria. In: *Volume III – Air Temperature, Soil Temperature, Frost*. Izkustvo Publisher, Sofia, Bulgaria, Nuaka i (in Bulgarian).
- Kojumdchieva, E., Popov, N., 1988. Lithostratigraphy of Neogene sediments from NW Bulgaria (in Bulgarian). *Paleontol. Stratigr. Lithol.* 25, 3–26.
- Koleva, E., Peneva, R., 1990. Climate handbook. In: *Precipitation in Bulgaria*. Bulgarian Academy of Sciences Publisher, Sofia (in Bulgarian).
- Kotov, S., Pälke, H., 2018. QAnalySeries – a cross-platform time series tuning and analysis tool (other). *Geology*. <https://doi.org/10.1002/essoar.10500226.1>.
- Kukla, G.J., 1977. Pleistocene land-sea correlations. I. Europe. *Earth. Sci. Rev.* 13, 307–374.
- Laag, C., Hambach, U., Zeeden, C., Lagroix, F., Guyodo, Y., Veres, D., Jovanović, M., Marković, S.B., 2021. A detailed paleoclimate proxy record for the Middle Danube Basin over the last 430 kyr: a rock magnetic and colorimetric study of the Zemun loess-palaeosol sequence. *Front. Earth Sci.* 9, 600086 <https://doi.org/10.3389/feart.2021.600086>.
- Lagroix, F., Banerjee, S.K., Jackson, M., 2004. Magnetic properties of the Old Crow tephra: Identification of a complex iron titanium oxide mineralogy. *J. Geophys. Res.* 109, B01104.
- Lagroix, F., Banerjee, S.K., Jackson, M.J., 2016. Geological Occurrences and Relevance of Iron Oxides. In: Faivre, D. (Ed.), *Iron Oxides*. From Nature to Applications. Wiley-VCH, Weinheim, pp. 9–29.
- Lambert, F., Delmonte, B., Petit, J.R., Bigler, M., Kaufmann, P.R., Hutterli, M.A., Stocker, T.F., Ruth, U., Steffensen, J.P., Maggi, V., 2008. Dust-climate couplings over the past 800,000 years from the EPICA Dome C ice core. *Nature* 452 (7187), 616–619.
- Lambert, F., Bigler, M., Steffensen, J.P., Hutterli, M., Fischer, H., 2012. Centennial mineral dust variability in high-resolution ice core data from Dome C, Antarctica. *Clim. Past* 8 (2), 609–623.
- Lang, N., Wolff, E.W., 2011. Interglacial and glacial variability from the last 800 ka in marine and terrestrial archives. *Clim. Past* 7 (2), 361–380.
- Lehmkuhl, F., Nett, J.J., Pötter, S., Schulte, P., Sprafke, T., Jary, Z., Antoine, P., Wacha, L., Wolf, D., Zerboni, A., Hošek, J., Marković, S.B., Obrecht, I., Sümege, P., Veres, D., Zeeden, C., Boemke, B., Schaubert, V., Viehweger, J., Hambach, U., 2021. Loess landscapes of Europe - Mapping, geomorphology, and zonal differentiation. *Earth Sci. Rev.* 215, 103496 <https://doi.org/10.1016/j.earscirev.2020.103496>.
- Leicher, N., Zanchetta, G., Sulpizio, R., Giaccio, B., Wagner, B., Nomade, S., Francke, A., Del Carlo, P., 2016. First tephrostratigraphic results of the DEEP site record from Lake Ohrid (Macedonia and Albania). *Biogeosciences* 13, 2151–2178. <https://doi.org/10.5194/bg-13-2151-2016>.
- Leicher, N., Giaccio, B., Zanchetta, G., Sulpizio, R., Albert, P.G., Tomlinson, E.L., Lagos, M., Francken, A., Wagner, B., 2021. Lake Ohrid’s tephrochronological dataset reveals 1.36 Ma of Mediterranean explosive volcanic activity. *Sci. Data* 8 (1), 14.
- Lisiecki, L.E., Raymo, M.E., 2005. A Pliocene-Pleistocene stack of 57 globally distributed benthic  $\delta^{18}O$  records. *Paleoceanography* 20. <https://doi.org/10.1029/2004PA001071>.
- Liu, Q., Torrent, J., Maher, B.A., Yu, Y., Deng, C., Zhu, R., Zhao, X., 2005. Quantifying grain size distribution of pedogenic magnetic particles in Chinese loess and its significance for pedogenesis. *J. Geophys. Res.* 110 <https://doi.org/10.1029/2005JB003726>.
- Liu, Q., Roberts, A.P., Larrasoana, J.C., Banerjee, S.K., Guyodo, Y., Tauxe, L., Oldfield, F., 2012. Environmental magnetism: Principles and applications. *Rev. Geophys.* 50, RG4002. <https://doi.org/10.1029/2012RG000393>.
- Long, X.Y., Ji, J.F., Balsam, W., Barron, V., Torrent, J., 2015. Grain growth and transformation of pedogenic magnetic particles in red Ferralsols. *Geophys. Res. Lett.* 42 (14), 5762–5770.
- Long, X.Y., Ji, J.F., Barron, V., Torrent, J., 2016. Climatic thresholds for pedogenic iron oxides under aerobic conditions: Processes and their significance in paleoclimate reconstruction. *Quat. Sci. Rev.* 150, 264–277.
- Lowe, D.J., 1986. Controls on the rates of weathering and clay mineral genesis in airfall tephra: A review and new Zealand case study (chapter 12). In: Colman, S.M., Dethier, D.P. (Eds.), *Rates of Chemical Weathering in Rocks and Minerals*. Academic Press, Orlando, FL (USA).
- Lowe, D.J., 2011. Tephrochronology and its application: A review. *Quat. Geochronol.* 6, 107–153.
- Machala, L., Tuček, J., Zbořil, R., 2011. Polymorphous Transformations of Nanometric Iron(III) Oxide: A Review. *Chem. Mater.* 23, 3255–3272. <https://doi.org/10.1021/cm200397g>.
- Maher, B.A., 1988. Magnetic properties of some synthetic sub-micron magnetites. *Geophys. J.* 94, 83–96.
- Maher, B.A., 1998. Magnetic properties of modern soils and Quaternary loessic paleosols: paleoclimatic implications. *Palaeogeogr. Palaeoclimatol. Palaeoecol.* 137, 25–54.
- Maher, B.A., 2011. The magnetic properties of Quaternary aeolian dusts and sediments, and their palaeoclimatic significance. *Aeolian Res.* 3, 87–144. <https://doi.org/10.1016/j.aeolia.2011.01.005>.
- Maher, B.A., 2016. Palaeoclimatic records of the loess/palaeosol sequences of the Chinese Loess Plateau. *Quat. Sci. Rev.* 154, 23–84. <https://doi.org/10.1016/j.quascirev.2016.08.004>.
- Makaroglu, O., Gagatay, M.N., Nowaczyk, N.R., Pesonen, L.J., Orbay, N., 2018. Discrimination of Holocene tephra units in Lake Van using mineral magnetic analysis. *Quat. Int.* 486, 44–56.

- Marković, S.B., Hambach, U., Stevens, T., Kukla, G.J., Heller, F., McCoy, W.D., Oches, E. A., Buggle, B., Zöller, L., 2011. The last million years recorded at the Stari Slankamen (Northern Serbia) loess-paleosol sequence: revised chronostratigraphy and long-term environmental trends. *Quat. Sci. Rev.* 30, 1142–1154. <https://doi.org/10.1016/j.quascirev.2011.02.004>.
- Marković, S.B., Hambach, U., Stevens, T., Basarin, B., O'Hara-Dhand, K., Gavrilov, M.M., Gavrilov, M.B., Smalley, I., Teofanov, N., 2012a. Relating the Astronomical Timescale to the Loess–Paleosol Sequences in Vojvodina, Northern Serbia. In: Berger, A., Mesinger, F., Sijacki, D. (Eds.), *Climate Change*. Springer Vienna, Vienna, pp. 65–78. [https://doi.org/10.1007/978-3-7091-0973-1\\_5](https://doi.org/10.1007/978-3-7091-0973-1_5).
- Marković, S.B., Hambach, U., Stevens, T., Jovanović, M., O'Hara-Dhand, K., Basarin, B., Lu, H., Smalley, I., Buggle, B., Zech, M., Svirčev, Z., Sümegi, P., Milojković, N., Zöller, L., 2012b. Loess in the Vojvodina region (Northern Serbia): an essential link between European and Asian Pleistocene environments. *Neth. J. Geosci.* 91, 173–188. <https://doi.org/10.1017/S0016774600001578>.
- Marković, S.B., Stevens, T., Kukla, G.J., Hambach, U., Fitzsimmons, K.E., Gibbard, P., Buggle, B., Zech, M., Guo, Z., Hao, Q., Wu, H., O'Hara Dhand, K., Smalley, I.J., Újvári, G., Sümegi, P., Timar-Gabor, A., Veres, D., Sirocko, F., Vasiljević, D.A., Jary, Z., Svensson, A., Jović, V., Lehmkuhl, F., Kovács, J., Svirčev, Z., 2015. Danube loess stratigraphy — Towards a pan-European loess stratigraphic model. *Earth Sci. Rev.* 148, 228–258. <https://doi.org/10.1016/j.earscirev.2015.06.005>.
- Marra, F., Karner, D.B., Freda, C., Gaeta, M., Renne, P., 2009. Large mafic eruptions at Alban Hills Volcanic District (Central Italy): Chronostratigraphy, petrography and eruptive behavior. *J. Volcanol. Geotherm. Res.* 179, 217–232. <https://doi.org/10.1016/j.jvolgeores.2008.11.009>.
- McCanta, M.C., Hatfield, R.G., Thomson, B.J., Hook, S.J., Fisher, E., 2015. Identifying cryptotephra units using correlated rapid, nondestructive methods: VSWIR spectroscopy, X-ray fluorescence, and magnetic susceptibility. *Geochim. Geophys. Res.* 16, 4029–4056. <https://doi.org/10.1002/2015GC005913>.
- Monaco, L., Palladino, D.M., Gaeta, M., Marra, F., Sottili, G., Leicher, N., Mannella, G., Nomade, S., Pereira, A., Regattieri, E., Wagner, B., Zanchetta, G., Albert, P.G., Arienzo, I., D'Antonio, M., Petrosino, P., Manning, C.J., Giaccio, B., 2021. Mediterranean tephratigraphy and peri-Tyrrhenian explosive activity reevaluated in light of the 430–365 ka record from Fucino Basin (Central Italy). *Earth Sci. Rev.* 220, 103706. <https://doi.org/10.1016/j.earscirev.2021.103706>.
- Muhs, D.R., 2013. The geologic records of dust in the Quaternary. *Aeolian Res.* 9, 3–48.
- Munsell Color Company, 2009. *Munsell Soil Color Charts: With Genuine Munsell Color Chips*. Munsell Color, Baltimore MD.
- Obrecht, I., Zeeden, C., Hambach, U., Veres, D., Marković, S.B., Böskén, J., Svirčev, Z., Bačević, N., Gavrilov, M.B., Lehmkuhl, F., 2016. Tracing the influence of Mediterranean climate on Southeastern Europe during the past 350,000 years. *Sci. Rep.* 6, 36334. <https://doi.org/10.1038/srep36334>.
- Obrecht, I., Zeeden, C., Hambach, U., Veres, D., Marković, S.B., Lehmkuhl, F., 2019. A critical reevaluation of palaeoclimate proxy records from loess in the Carpathian Basin. *Earth Sci. Rev.* 190, 498–520. <https://doi.org/10.1016/j.earscirev.2019.01.020>.
- Özdemir, Ö., Dunlop, D.J., 2014. Hysteresis and coercivity of hematite. *J. Geophys. Res. Solid Earth* 119, 2582–2594.
- Panaïotu, C.G., Panaïotu, E.C., Grama, A., Necula, C., 2001. Paleoclimatic record from a loess-paleosol profile in southeastern Romania. *Phys. Chem. Earth, Part A: Solid Earth Geodesy* 26, 893–898. [https://doi.org/10.1016/S1464-1895\(01\)00138-7](https://doi.org/10.1016/S1464-1895(01)00138-7).
- Pardo, N., Cronin, S.J., Németh, K., Brenna, M., Schipper, C.I., Breard, E., White, J.D., Procter, J., Stewart, B., Agustín-Flores, J., Moebis, A., Zernack, A., Kereszturi, G., Lube, G., Auer, A., Neall, V., Wallace, C., 2014. Perils in distinguishing phreatic from phreatomagmatic ash; insights into the eruption mechanisms of the 6 August 2012 Mt. Tongariro eruption, New Zealand. *J. Volcanol. Geotherm. Res.* 286, 397–414.
- Parrenin, F., Barnola, J.-M., Beer, J., Blunier, T., Castellano, E., Chappellaz, J., Dreyfus, G., Fischer, H., Fujita, S., Jouzel, J., Kawamura, K., Lemieux-Dudon, B., Loulergue, L., Masson-Delmotte, V., Narcisi, B., Petit, J.-R., Raisbeck, G., Raynaud, D., Ruth, U., Schwander, J., Severi, M., Spahni, R., Steffensen, J.P., Svensson, A., Udisti, R., Waelbroeck, C., Wolff, E., 2007. The EDC3 chronology for the EPICA Dome C ice core. *Clim. Past* 3, 485–497. <https://doi.org/10.5194/cp-3-485-2007>.
- Paterne, M., Guichard, F., Duplessy, J.C., Siani, G., Sulpizio, R., Labeyrie, J., 2008. A 90,000–200,000 yrs marine tephra record of Italian volcanic activity in the Central Mediterranean Sea. *J. Volcanol. Geotherm. Res.* 177, 187–196. <https://doi.org/10.1016/j.jvolgeores.2007.11.028>.
- Petrosino, P., Jicha, B.R., Mazzeo, F.C., Russo Ermolli, E., 2014. A high resolution tephratigraphical record of MIS 14–12 in the Southern Apennines (Acerno Basin, Italy). *J. Volcanol. Geotherm. Res.* 274, 34–50. <https://doi.org/10.1016/j.jvolgeores.2014.01.014>.
- Ponomareva, V., Portnyagin, M., Davies, S.M., 2015. Tephra without Borders: Far-reaching Clues into Past Explosive Eruptions. *Front. Earth Sci.* 3. <https://doi.org/10.3389/feart.2015.00083>.
- Poulidis, A.P., Takemi, T., Iguchi, M., Renfrew, I.A., 2017. Orographic effects on the transport and deposition of volcanic ash: A case study of Mount Sakurajima, Japan. *J. Geophys. Res. Atmos.* 122, 9332–9350. <https://doi.org/10.1002/2017JD026595>.
- Ross, P.S., Dürrig, T., Comida, P.P., Lefebvre, N., White, J.D., Andronico, D., Thivet, S., Eyche, J., Gurioli, L., 2022. Standardized analysis of juvenile pyroclasts in comparative studies of primary magma fragmentation; 1. Overview and workflow. *Bull. Volcanol.* 84 (1), 1–29.
- Rousseau, D.-D., Boers, N., Sima, A., Svensson, A., Bigler, M., Lagroix, F., Taylor, S., Antoine, P., 2017. (MIS3 and 2) millennial oscillations in Greenland dust and Eurasian aeolian records: a paleosol perspective. *Quat. Sci. Rev.* 169, 99–113.
- Schindler, M., Michel, S., Batchelder, D., Hochella, M.F., 2019. A nanoscale study of the formation of Fe-(hydr)oxides in a volcanic regolith: Implications for the understanding of soil forming processes on Earth and Mars. *Geochim. Cosmochim. Acta* 264, 43–66. <https://doi.org/10.1016/j.gca.2019.08.008>.
- Shin, J.Y., Kim, W., Hyeon, K., 2020. High potency of volcanic contribution to the ~400 kyr sedimentary magnetic record in the Northwest Pacific. *Front. Earth Sci.* 8, 300. <https://doi.org/10.3389/feart.2020.00300>.
- Sjölte, J., Adolphi, F., Guðlaugsdóttir, H., Muscheler, R., 2021. Major differences in regional climate impact between high- and low-latitude volcanic eruptions. *Geophys. Res. Lett.* 48, e2020GL092017.
- Song, Y., Guo, Z., Marković, S.B., Hambach, U., Deng, C., Chang, L., Wu, J., Hao, Q., 2018. Magnetic stratigraphy of the Danube loess: a composite Titel-Stari Slankamen loess section over the last one million years in Vojvodina, Serbia. *J. Asian Earth Sci.* 155, 68–80.
- Takei, H., Chiba, S., 1966. Vacancy Ordering in Epitaxially-Grown Single Crystals of  $\gamma$ -Fe<sub>2</sub>O<sub>3</sub>. *J. Phys. Soc. Jpn.* 21, 1255–1263. <https://doi.org/10.1143/JPSJ.21.1255>.
- Újvári, G., Kok, J.F., Varga, G., Kovács, J., 2016. The physics of wind-blown loess: Implications for grain size proxy interpretations in Quaternary paleoclimate studies. *Earth Sci. Rev.* 154, 247–278.
- Vakhrameeva, P., Koutsodendris, A., Wulf, S., Fletcher, W.J., Appelt, O., Knipping, M., Gertisser, R., Trieloff, M., Pross, J., 2018. The cryptotephra record of the Marine Isotope Stage 12 to 10 interval (460–335 ka) at Tenaghi Philippon, Greece: exploring chronological markers for the Middle Pleistocene of the Mediterranean region. *Quat. Sci. Rev.* 200, 313–333.
- Vakhrameeva, P., Wulf, S., Koutsodendris, A., Tjallingii, R., Fletcher, W.J., Appelt, O., Ludwig, T., Knipping, M., Trieloff, M., Pross, J., 2019. Eastern Mediterranean volcanism during marine isotope stages 9 to 7e (335–235 ka): insights based on cryptotephra layers at Tenaghi Philippon, Greece. *J. Volcanol. Geotherm. Res.* 380, 31–47.
- Vigliotti, L., Channell, J.E.T., Stockhecke, M., 2014. Paleomagnetism of Lake Van sediments: chronology and paleoenvironment since 350 ka. *Quat. Sci. Rev.* 104, 18–29. <https://doi.org/10.1016/j.quascirev.2014.09.028>.
- Walker, M.J.C., Berkelhammer, M., Björck, S., Cwynar, L.C., Fisher, D.A., Long, A.J., Lowe, J.J., Newham, R.M., Rasmussen, S.O., Weiss, H., 2012. Formal subdivision of the Holocene Series/Epoch: a discussion paper by a working group of INTIMATE (integration of ice-core, marine and terrestrial records) and the Subcommittee on Quaternary Stratigraphy (International Commission on Stratigraphy). *J. Quat. Sci.* 27 (7), 649–659.
- Watt, S.F.L., Gilbert, J.S., Folch, A., Phillips, J.C., Cai, X.M., 2015. An example of enhanced tephra deposition driven by topographically induced atmospheric turbulence. *Bull. Volcanol.* 77, 35. <https://doi.org/10.1007/s00445-015-0927-x>.
- Wulf, S., Hardiman, M.J., Staff, R.A., Koutsodendris, A., Appelt, O., Blockley, S.P., Lowe, J.J., Manning, J., Ottoloni, L., Schmitt, A.K., Smith, V.C., Tomlinson, E.L., Vakhrameeva, P., Knipping, M., Kotthoff, U., Milner, A.M., Christianis, K., Kalaitzidis, S., Tzedakis, P.C., Schmied, G., Pross, J., 2018. The marine isotope stage 1–5 cryptotephra record of Tenaghi Philippon, Greece: towards a detailed tephratigraphic framework for the Eastern Mediterranean region. *Quat. Sci. Rev.* 186, 236–262.
- Zeeden, C., Kels, H., Hambach, U., Schulte, P., Protze, J., Eckmeier, E., Marković, S.B., Klasen, N., Lehmkuhl, F., 2016. Three climatic cycles recorded in a loess-paleosol sequence at Semeac (Romania) - Implications for dust accumulation in South-Eastern Europe. *Quat. Sci. Rev.* 154, 130–142. <https://doi.org/10.1016/j.quascirev.2016.11.002>.
- Zeeden, C., Obrecht, I., Veres, D., Kaboth-Bahr, S., Hošek, J., Marković, S.B., Böskén, J., Lehmkuhl, F., Rolf, C., Hambach, U., 2020. Smoothed millennial-scale palaeoclimatic reference data as unconventional comparison targets: Application to European loess records. *Sci. Rep.* 10, 5455. <https://doi.org/10.1038/s41598-020-61528-8>.
- Zimanowski, B., Büttner, R., Dellino, P., White, J.D.L., Wohletz, K.H., 2015. Chapter 26 - Magma- water interaction and phreatomagmatic fragmentation. In: Sigurdsson, H. (Ed.), *The Encyclopedia of Volcanoes*, Second edition. Academic Press, Elsevier. ISBN 978-0-12-385938-9; pp. 473 - 484.

## 4.2. Measuring and evaluating colorimetric properties of samples from loess-paleosol sequences

Christian Laag<sup>1</sup>, France Lagroix<sup>1</sup>, Sebastian Kreutzer<sup>2,3</sup>, Stoil Chapkanski<sup>4</sup>, Christian Zeeden<sup>5</sup>, Yohan Guyodo<sup>1</sup>

<sup>1</sup> Université Paris Cité, Institut de Physique du Globe de Paris, CNRS, 1 rue Jussieu, Paris, France

<sup>2</sup> Institute of Geography, Ruprecht-Karl-University of Heidelberg, 69120 Heidelberg, Germany

<sup>3</sup> Archéosciences Bordeaux, UMR 6034, CNRS-Université Bordeaux Montaigne, Pessac, 33600, France

<sup>4</sup> University of Paris 1, Panthéon-Sorbonne, Laboratory of Physical Geography (LGP), UMR 8591, CNRS, 2 Rue Henri Dunant, 94320, Thiais - Paris, France

<sup>5</sup> LIAG - Leibniz Institute for Applied Geophysics, Stilleweg 2, 30655 Hannover, Germany

### **Status:**

- Manuscript submitted to MethodsX (Elsevier): 19.12.2022
- Reviews received 14.01.2023
- Revised Submission scheduled for 19.02.2023

### **Main findings:**

- Method found to eliminate plastic box signals, in which sedimentary samples are stored and investigated for diffuse reflectance spectral properties
- Improved protocol for hematite and goethite semi-quantitative extraction of diffuse reflectance spectra
- Protocol was validated via mid-infrared spectroscopic experiments
- A novel and user-friendly R-package “LESLIE” is presented, allowing loess-color contrast enhancement to detect subtle changes in stratigraphical color nuances invisible by the naked eye

## Measuring and evaluating colorimetric properties of samples from loess-paleosol sequences

Christian Laag<sup>1\*</sup>, France Lagroix<sup>1</sup>, Sebastian Kreuzer<sup>2,3</sup>, Stoil Chapkanski<sup>4</sup>, Christian Zeeden<sup>5</sup>, Yohan Guyodo<sup>1</sup>

<sup>1</sup> Université Paris Cité, Institut de Physique du Globe de Paris, CNRS, 1 rue Jussieu, Paris, France

<sup>2</sup> Institute of Geography, Ruprecht-Karl-University of Heidelberg, 69120 Heidelberg, Germany

<sup>3</sup> Archéosciences Bordeaux, UMR 6034, CNRS-Université Bordeaux Montaigne, Pessac, 33600, France

<sup>4</sup> University of Paris 1, Panthéon-Sorbonne, Laboratory of Physical Geography (LGP), UMR 8591, CNRS, 2 Rue Henri Dunant, 94320, Thiais - Paris, France

<sup>5</sup> LIAG - Leibniz Institute for Applied Geophysics, Stilleweg 2, 30655 Hannover, Germany

\*laag@ipgp.fr

### Keywords

Colorimetry, spectrophotometry, color enhancement, loess-paleosol sequence, goethite, hematite

### Abstract

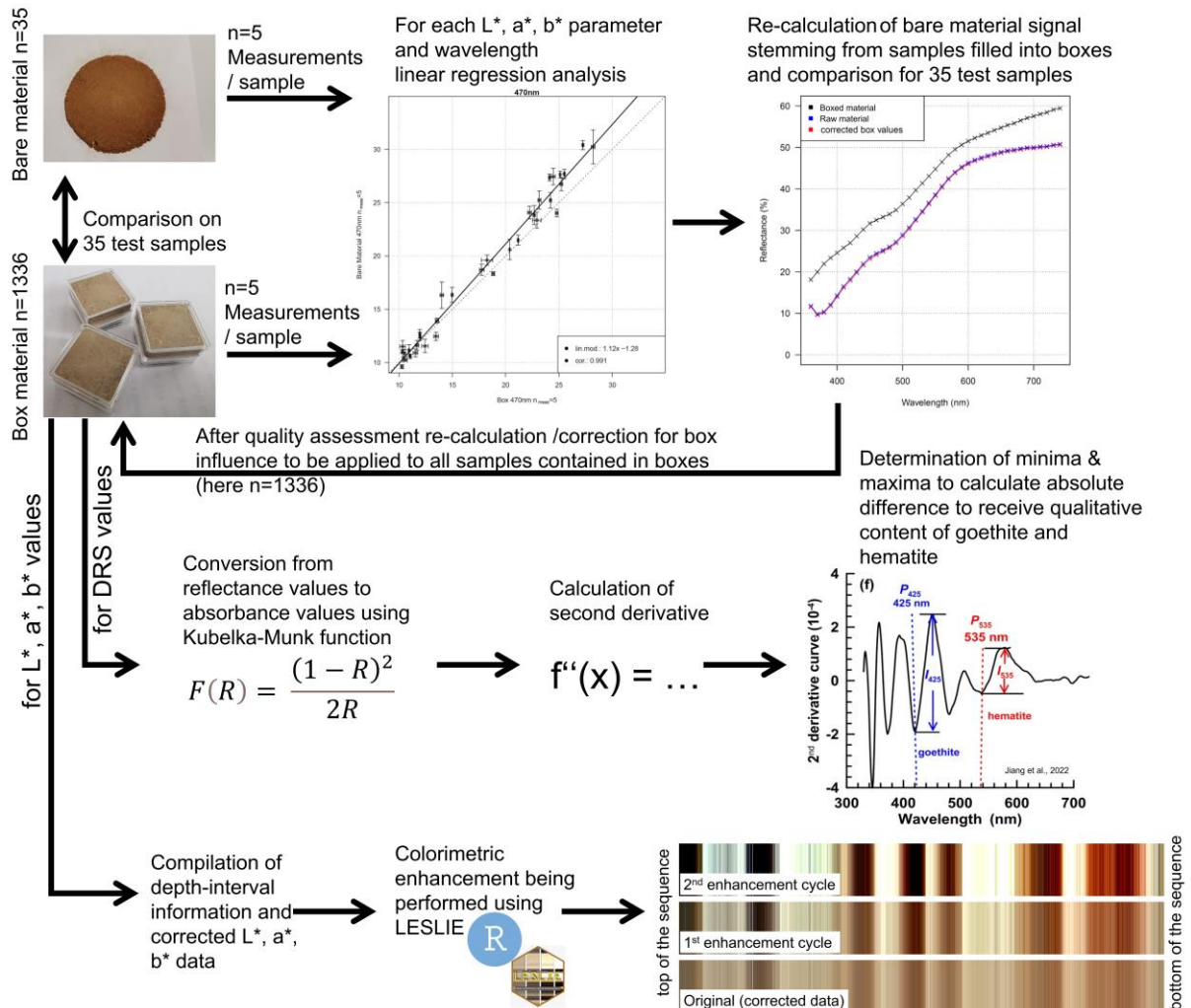
Colorimetric measurements performed on sediment archives such as loess-paleosol sequences provide valuable insight into paleoenvironmental changes. These measurements enable us to distinguish climate-sensitive minerals such as hematite and goethite, secondary carbonates, and overall observable changes in stratigraphic units influenced by paleoclimate variations. With commonly applied analytical tools, for example, pertaining to environmental magnetism, quantifying concentrations of individual minerals is challenging. Colorimetry overcomes this challenge allowing paleoenvironmental reconstructions from variations of climate-sensitive minerals formed *in situ* in response to paleoenvironmental conditions (e.g., precipitation, temperature).

In this article, we present:

- An easily reproducible and accurate protocol to perform colorimetric measurements and analyses for spectrophotometers;
- A solution to eliminating colorimetric data biases resulting from the plastic boxes in which many samples are prepared for analytical purposes or stored to facilitate subsequent investigations;

- A novel and user-friendly R package (LESLIE) to enhance measured colorimetric parameters, highlight subtle changes in color nuances, help characterize the stratigraphy and identify individual stratigraphic units.

### Graphical abstract





## Introduction

Colorimetric measurements performed on sediments such as loess-paleosol sequences are inexpensive and straightforward to apply. Paleoenvironmental studies are increasingly reporting colorimetry data providing a powerful complement to routinely presented environmental magnetism or granulometric analysis [1–3]. Magnetic measurements discriminating of hematite and goethite, important indicators for past climate conditions, are time-consuming and determine concentrations challenging because of their relatively weak magnetizations and grain-size dependent magnetic properties. Non-remanence bearing silicate and carbonate minerals such as calcite are not identifiable or concentrations are non-quantifiable via magnetic analytical methods. It has been demonstrated [4–6] that colorimetric measurements can estimate qualitative amounts of goethite and hematite and that Luminance ( $L^*$ ) can be a proxy for qualitative amounts of calcite. Thus, colorimetric measurements provide an inexpensive and non-time-consuming alternative to other methods, such as X-ray powder diffraction (XRD) and Fourier-transformed infrared spectroscopy (FTIR) experiments. Colorimetric measurements with spectrophotometers present many advantages over retrieving color codes from Munsell color charts. Munsell color observations are highly subjective, dependent on the light source, the observer's color perception, and sensitivity to slight differences in color-nuances. Moreover, the Munsell color system is non-continuous, urging the researcher to sort samples into color classes, inevitably leading to lower resolution and data loss.

The past decades of loess research underlined the clear benefits of examining colorimetric measurements to gain a deeper paleoclimate understanding of the archive studied [2,3,7–10]. Spectrophotometers measure color in a three-dimensional  $L^*a^*b^*$  color space (ISO/CIE 11664-4:2019) as well as diffuse reflectance spectra (DRS) in the visible light range from 400 nm to 700 nm at typically 0.5 nm to 10 nm interval. The  $L^*a^*b^*$  color space enables equipment-independent color representations. The defined color-sphere has a vertical y-axis, ranging from 0% (absolute black) to 100% (absolute white). The x-axis ( $a^*$ , redness value) has undefined limits ranging from negative (green) to positive (red). The z-axis ranges from negative (blue) to positive (yellow). Each colorimetric measurement is uniquely identified as a three-dimensional coordinate placed in the  $L^*a^*b^*$  color-sphere.

DRS values are of emerging importance for paleoclimatic studies. Several studies have successfully evidenced the ability to trace hematite and goethite contents qualitatively from loess-paleosol sequences from DRS data [5,11–13]. However, they lack a detailed description

of the measurement protocol used in the study, while many factors influence the measured colorimetric signal. The luminance ( $L^*$ ), for example, is massively influenced by the material's water content as well as grain/aggregate size. The luminance appears lower as water content increases. The same holds for non-homogenized samples, which produce larger shadow areas when light during measurement is applied. Therefore, colorimetric measurements are best performed under controlled laboratory conditions instead of in the field. Although traditionally in-field performed, alpha-numerical Munsell color values can be re-calculated and compared to spectrophotometer results.

In many laboratories, standard magnetic experiments are performed on sediment sample material stored in plastic boxes. Whether colorimetric measurements were acquired in an original study or not, sample storage in plastic boxes facilitates their subsequent investigation. However, plastic boxes (although transparent) bias colorimetric values. In this study, we present an easy way to remove the boxes' colorimetric signal from the sought sediment signal by performing a correction procedure. The correction procedure opens the broad potential to measure, or re-measure stored or archived sediment from previous studies, allowing new or more profound insights into past climatological and environmental conditions. Specifically, our study characterizes the colorimetric signal of non-scratched ultra-clear plastic box containers and how to remove this unwanted signal on bulk sediment colorimetric results. The correction procedure will allow institutes and laboratories studying loess-paleosol sequences and potentially other unconsolidated sediments to re-investigate archived sample material.

In addition, we present a new R [14] package providing a user-friendly colorimetric enhancement protocol to improve color contrasts across stratigraphy [15]. This procedure will help identify contacts and transitions between stratigraphical units, visually improve the color characteristics of different units and identify potentially alien material preserved in the profile of interest, e.g., crypto-tephra layers. Tephra and crypto-tephra layers are crucial age control points complementing direct dating methods, e.g.,  $^{14}\text{C}$  and luminescence dating, especially beyond their dating limits.

To provide independent validation of mineral down-depth relative abundances estimated by the colorimetric measurements, we performed Fourier Transformed Infrared Attenuated Total Reflection (ATR-FTIR) spectrometry analysis on 719 samples [16] (Fig. 1). ATR-FTIR allows spectroscopic measurements of the matter in the mid-infrared range between  $4000 - 400 \text{ cm}^{-1}$  ( $2.5\text{-}25 \text{ }\mu\text{m}$ ). ATR-FTIR is a rapid and non-destructive molecular-based tool for which the mineral absorbance depends on the interatomic bonds, the degree of crystallinity, as well as the

shape and size of mineral particles. Minerals such as silicates, carbonates, and iron-oxides may be identified by ATR-FTIR [17], and for some minerals, relative abundances can be predicted [18]. ATR-FTIR was chosen as an independent validation tool, rather than conventional X-ray diffraction, because it is rapid (~5 min/sample), can be performed on small (10-100 mg) samples, and does not require chemical treatments and radiation emission.

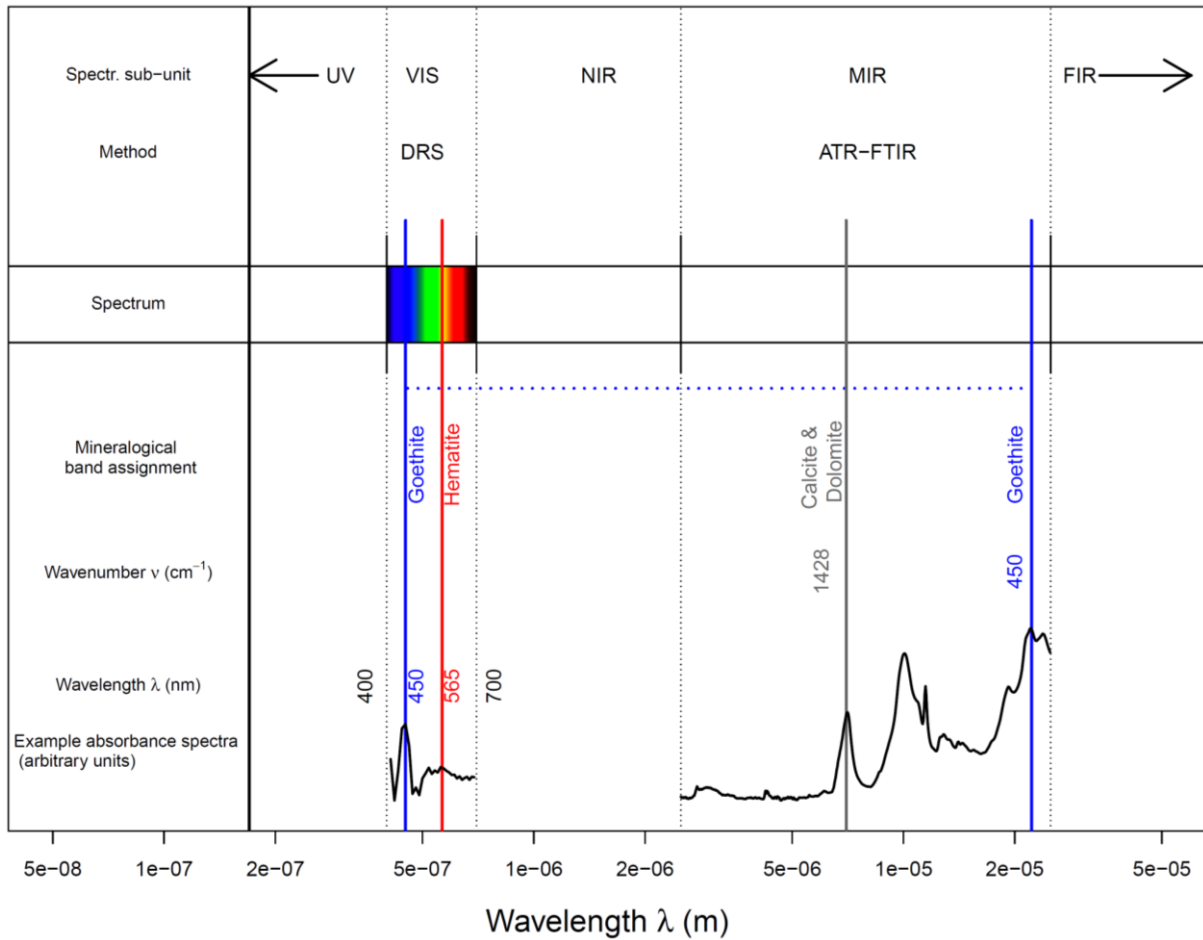


Figure 1: Overview of DRS and FTIR-ATR data spectra in relation to visible and non-visible wavelengths.



## Method details

### Measurement of colorimetric data

All colorimetric measurements were performed with a Konica Minolta 600d spectrophotometer. Before measurements, the spectrophotometer was calibrated with Konica Minolta-provided white and black standards. The resolution of DRS data is 10 nm in the visible light range from 400 nm to 700 nm. The measurements were performed with a 0.8 cm wide open oculus, a D65 norm light source, and an observer angle of 2° (CIE 1931 standard observer angle). Each sample was measured five times to calculate the mean and standard deviation.

### Measurements performed on bare material

For measurements carried out on raw material from 35 samples, approximately 20 g of material was placed on white paper and compressed with a massive (2 kg) plain surface stainless steel cylinder to avoid shadows and to simulate the compaction inside the plastic boxes. The five measurements were acquired at different positions of the compressed sample material (see Fig. 2a). Each time, the sample material was re-mixed and compressed again with the stainless-steel cylinder to avoid user-induced cracks of the material which would lead to artificially lower L\* values due to shadows between non-compressed material.

### Measurements performed on boxed material

Measurements through the boxes were carried out at five different positions (see Fig. 2b) on the same 35 sediment samples. The experiment was performed under day-time independent laboratory room light sources on homogenized, carefully hand-grinded, several weeks room-temperature dried bulk material to avoid water influence (decreasing, e.g., L\*). The comparison was made between reflectance data from measurements performed on boxed and bare materials, as shown in Fig. 2. Afterwards, this data was plotted for each wavelength in biplots to investigate their correlation and dependency. Linear models were calculated, and linear regression functions were determined and listed in Table 1.

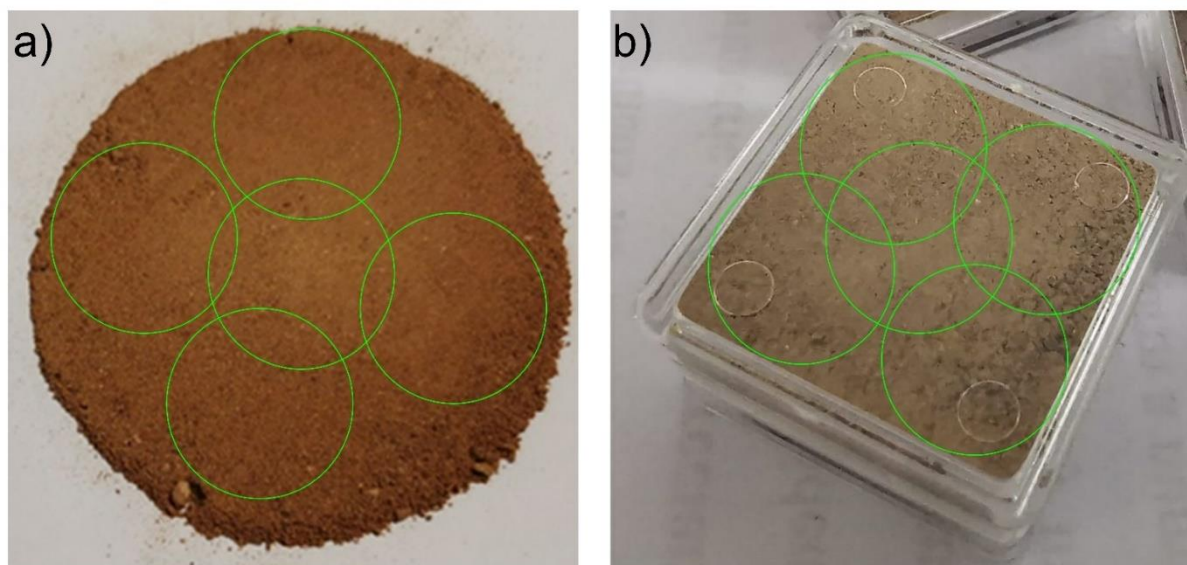


Figure 2: Measurement targets with a) raw material and b) boxed material.

The 35 sediment samples were selected from the Pleven LPS sequence in northern Bulgaria [19] and represent a mixture of end-member values such as high and low  $a^*$ , high and low  $L^*$ , and high and low  $b^*$  in colorimetric measurements to build robust regression functions. The samples were measured in plastic boxes. The boxes are made of non-magnetic ultra-clear plastic (Caubère reference 212 (19x19x10 mm, 4 cm<sup>3</sup>), material: crystal-clear polystyrene PS) and were stored using layer-wide wipes to avoid scratches from non-consolidated sample material. Note that the bare sediment to boxed sediment comparison regression functions should be considered plastic box brand and type dependent. The correction method developed in this study can be followed for other brands and types of plastic boxes.

#### Comparison of boxed and bare material

The first analyses evidenced that the boxes' colorimetric signal is not a fixed absolute value to be added or subtracted from the measured signal. Therefore, we considered calculating for each parameter ( $L^*$ ,  $a^*$ ,  $b^*$ , and all individual DRS wavelength-reflectance values) single regression functions to eliminate the box signal.

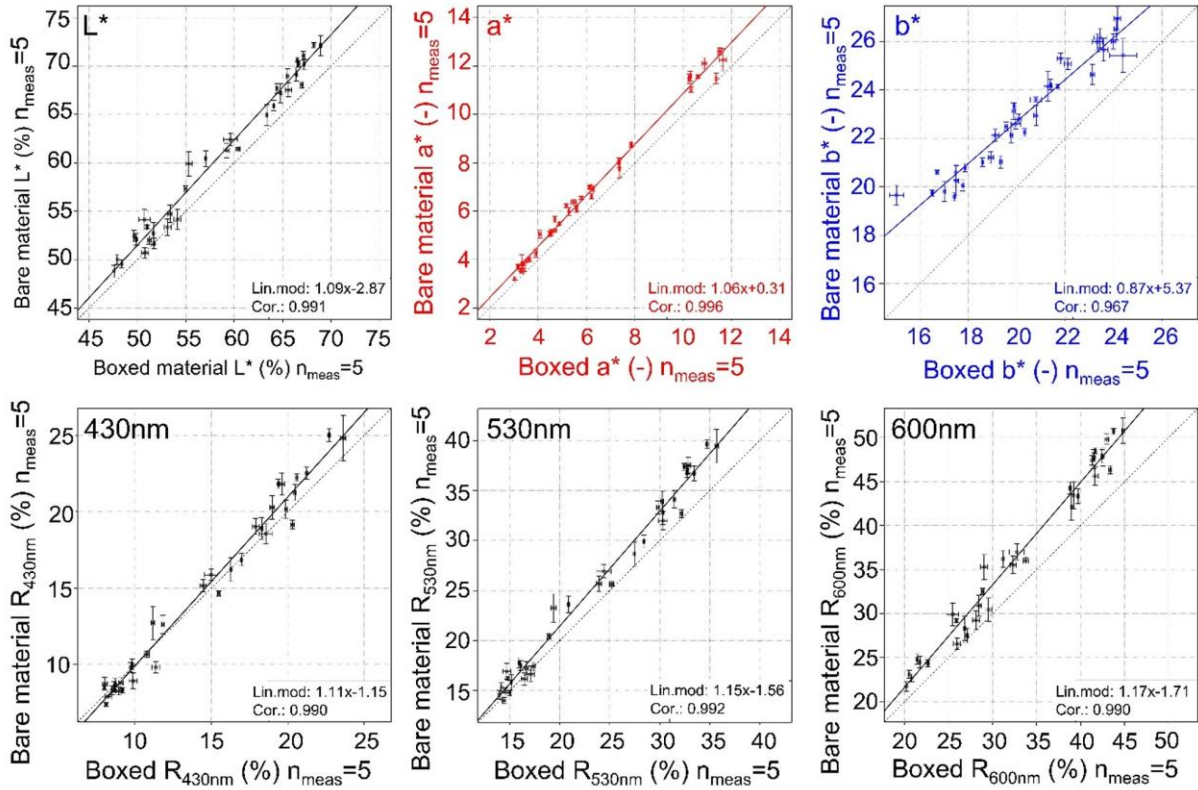


Figure 3: Comparison of 35 samples measured through the box (abscissa) and on raw material (ordinate).  $L^*$ ,  $a^*$ , and  $b^*$  values are shown in A-C and exemplary three wavelengths (430 nm, 530 nm, and 600 nm D-F). Standard deviations resulting from 5 measurements are shown as error bars. The solid line of each figure displays the linear regression model of datasets, and the dotted line represents a 1:1 ratio with a slope of 1. Linear model parameters are given together with  $r^2$  in the legend on each graph at the bottom right.

Figure 3 demonstrated that not all colorimetric regression parameters between boxed and bare materials are identical. Nevertheless, regressions are linear. To estimate the overall correlation, we compared the boxed and bare material color signal for each parameter ( $L^*$ ,  $a^*$ ,  $b^*$ , and all DRS wavelengths) and calculated the correlation parameters and coefficients (Fig. 3, Table 1).

Each regression function was then applied to the corresponding raw parameters to adjust the DRS spectra to represent bare material measured through a plastic box. A visual confirmation of validity is shown in Fig. 5.

#### Reflectance to absorbance transformation

In the next step, we transformed the DRS parameters from reflectance to absorbance values employing the Kubelka-Munk function [20] given from

$$F(R) = \frac{(1-R)^2}{2R}.$$

$R$  is the dimensionless (recalculated to decimal values since Konica Minolta values are provided as percentages) relative reflectance value (provided by Konica Minolta Instruments). We

investigated all correlation parameters for each DRS variable (Fig. 3, Table 1) to ensure that the investigation intervals for hematite and goethite are well-defined and robust (see Table 1).

#### Extraction of qualitative goethite and hematite concentrations

Subsequently, the second derivative of the DRS data was calculated following [21–23], and the absolute and true band amplitude (TBA) was identified following [7]. The TBA is the absolute peak height in the second derivative of the Kubelka-Munk (KM) absorbance transformed reflectance values and estimates the qualitative abundance of goethite and hematite. We considered the first minimum of the second derivative of the KM-recalculated absorbance of reflectance data for goethite between 410 nm and 430 nm and the maximum between 440 nm and 460 nm. The absolute difference of these reflectance values in the ordinate of the second derivative of the DRS data indicates the qualitative amount of hematite and goethite [21,24]. The TBA in this range is the qualitative goethite content determined for each of the five individual measurements of each sediment sample.

The same procedure was applied to qualitatively estimate the hematite content for each sample and its five measurements. To calculate the hematite TBA, a minimum of the second derivative absorbance spectrum between 510 nm and 530 nm was identified, and a maximum between 550 and 580nm. The ordinate difference of the absorbance values is considered qualitative hematite content. For each sample, the mean and standard deviation of the five individual measurements was calculated. Our procedure applies a range of maximum, and minimum search that deviates strategically from commonly applied fixed wavelength values. Cation substitutions (e.g., aluminum) and particle size of hematite and goethite are known to shift DRS peak positions [24,25]. Varying natures of hematite and goethite in LPS are expected, given that species of detrital, pedogenic, and diagenetic origins co-exist at the scale of the LPS and may co-exist at the scale of a sample. Therefore, a wavelength interval-based selection of absorbance values rather than a fixed value is justified. The resulting variable wavelength positions of the absorbance peak values are valuable information enabling the interpretation of processes as discussed in Laag et al. (in prep.).

Table 1: Linear model parameters and their correlations based on 35 samples measured through boxes and raw material. Blue and red-shaded table entries cover extraction areas for goethite (blue) and hematite (red).

Wavelength (nm)	Slope	Intersect (nm)	r <sup>2</sup>	Wavelength (nm)	Slope	Intersect (nm)	r <sup>2</sup>
<b>L*</b>	1.09	-2.87	0.991	<b>540</b>	1.16	-1.63	0.992
<b>a*</b>	1.06	0.31	0.996	<b>550</b>	1.16	-1.71	0.992
<b>b*</b>	0.87	5.37	0.967	<b>560</b>	1.16	-1.75	0.991
<b>400</b>	1.09	-1.10	0.988	<b>570</b>	1.17	-1.78	0.991
<b>410</b>	1.10	-1.11	0.988	<b>580</b>	1.17	-1.78	0.990
<b>420</b>	1.10	-1.13	0.989	<b>590</b>	1.17	-1.75	0.990
<b>430</b>	1.11	-1.15	0.990	<b>600</b>	1.17	-1.71	0.990
<b>440</b>	1.11	-1.19	0.990	<b>610</b>	1.16	-1.69	0.989
<b>450</b>	1.12	-1.24	0.991	<b>620</b>	1.16	-1.69	0.989
<b>460</b>	1.12	-1.26	0.991	<b>630</b>	1.16	-1.73	0.988
<b>470</b>	1.12	-1.28	0.991	<b>640</b>	1.16	-1.73	0.988
<b>480</b>	1.12	-1.30	0.991	<b>650</b>	1.16	-1.80	0.988
<b>490</b>	1.13	-1.32	0.991	<b>660</b>	1.16	-1.85	0.987
<b>500</b>	1.13	-1.36	0.991	<b>670</b>	1.15	-1.90	0.987
<b>510</b>	1.14	-1.43	0.992	<b>680</b>	1.15	-1.99	0.987
<b>520</b>	1.14	-1.50	0.992	<b>690</b>	1.15	-2.04	0.986
<b>530</b>	1.15	-1.56	0.992	<b>700</b>	1.15	-2.16	0.986

### Color contrast enhancement

Our contrast enhancement algorithm is motivated by two ideas presented in Zeeden et al. [26,27] (color values presented rectangles in stratigraphic order) and Sprafke et al. [28] (contrast enhancement) but seeks to simplify and strengthen the outcome. Zeeden et al. [26,27] provided an R-Script to represent colorimetric values as rectangles in stratigraphical order. Sprafke et al. [28] used contrast enhancement based on *MS Excel<sup>TM</sup>* to identify cold and warm periods, represented by rather “cold” and “warm” colors. Here, we combine both approaches to provide an enhanced stratigraphical overview in a documented R package called LESLIE (LoESs coLorimetry sIgnal Enhancement) [15] designed to take L\*, a\*, and b\* values only in its combination to be re-calculated to RGB values and hence allow to perform a user-defined number of enhancement cycles. The R package and its example data allow the user to adjust the data structure for the R package using the given example (prepare your data with depths in one column and L\*a\*b\* values in columns 2-4). Depth limits are user-defined or are calculated automatically if no depth interval for each sample is given. For usability reasons, we limited the user interaction to selecting a file, the number of enhancement cycles, and a few graphical adjustments parameters. We recommend two to three enhancement cycles, which we consider sufficient. However, users may want to test with more enhancement cycles. The re-calculated and enhanced values are returned as numerical values to be exported, e.g., as comma separated files (CSV) and used in different applications. Future work may entail a web application with LESLIE running in the background facilitating an easy-to-use graphical user interface.

### Validating goethite and calcite concentrations using mid-infrared spectrometry

Mid-infrared spectrometry, capable of tracking goethite and calcite concentrations qualitatively, was measured independently of qualitative DRS-derived goethite and calcite concentrations. A subset of 719 samples was measured with Fourier Transform Infrared Brucker Vector 22 spectrometer equipped with an Attenuated Total Reflection sampling accessory and diamond crystal. The samples were scanned (mean of 64 scans) from 4000 to 400  $\text{cm}^{-1}$  at an 8  $\text{cm}^{-1}$  resolution. Two band peak values were selected to calculate the mean signal value for calcite and goethite using the substation between minima and maxima of wavenumber absorbance. Wavenumbers were selected after [29] for goethite and [30] for calcite. The results were compared with the DRS goethite signals, and  $L^*$  values and correlations were evaluated. The overall agreement / high correlation of the two independent methods (DRS-derived goethite and luminance values and ATR-FTIR-derived goethite and calcite values) was used as an indicator of the validity of the identified goethite and calcite concentrations.

### Recalculating true color DRS values from boxed measurements

Scatterplots of bare and boxed material measurements (Fig. 3) indicate all individual wavelengths' linear behavior, allowing the application of linear regression models. Correlation coefficients indicate an overall excellent agreement, with the lowest correlation coefficient at  $r = 0.986$  by correlating box and bare material measurements of wavelengths at the end of the spectrum (690 nm and 700 nm) and the highest correlation coefficients at  $r = 0.992$  for the wavelengths of 510 nm to 550 nm. The scanning intervals for goethite (taking minimum and maximum into account) from 410 nm to 460 nm range with their  $r=0.988$  to  $r=0.991$ , for hematite (between 520 nm and 580 nm) between  $r = 0.990$  and  $r=0.992$ .



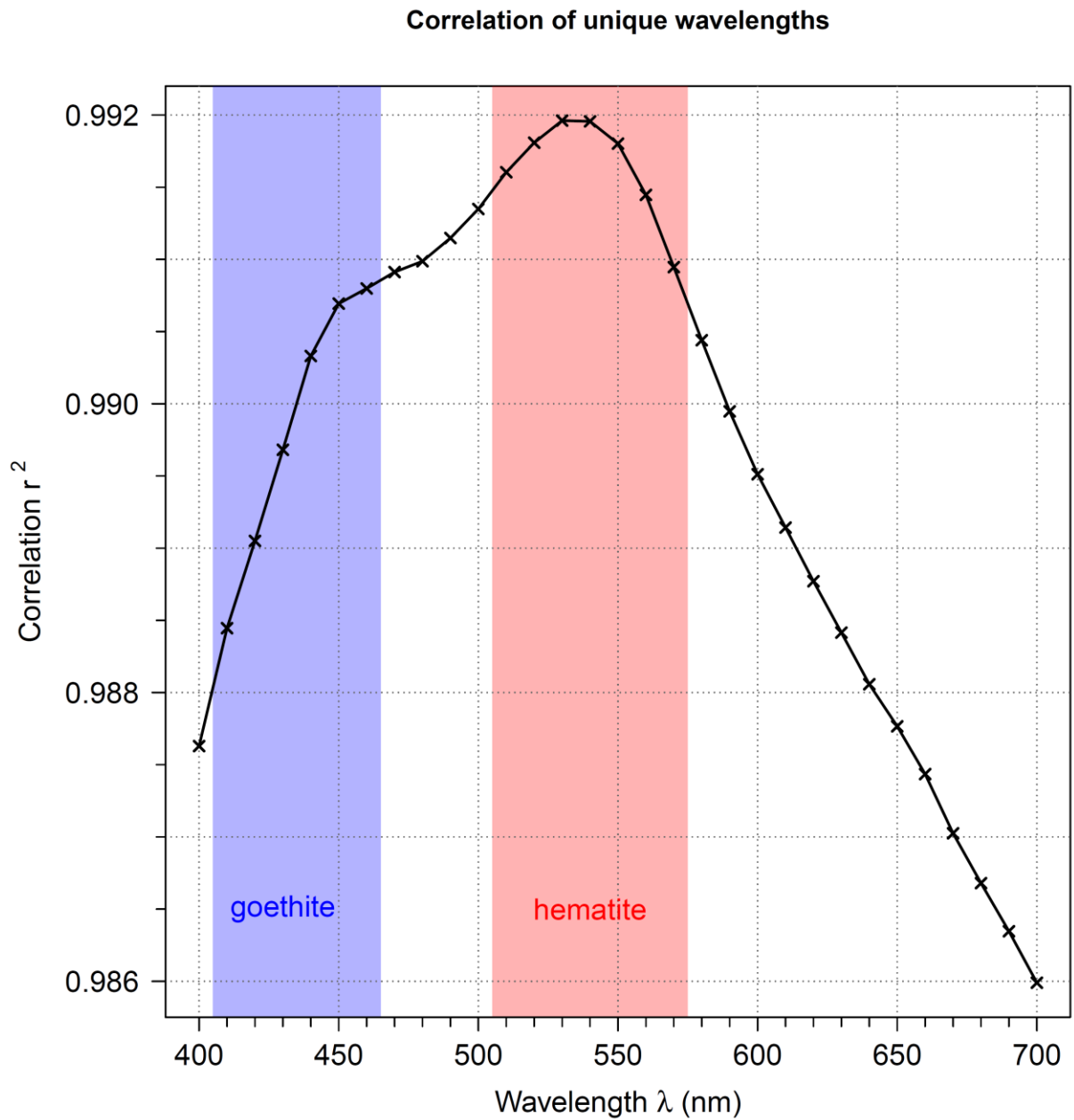


Figure 4: Compilation of correlation coefficients for each wavelength. The wavelength intervals where goethite and hematite are extracted are indicated in blue and red rectangles.

The slopes of the linear models were always positive ( $>1$ ) with a minimal negative y-axis intersection (Table 1). Slopes differ minimally for wavelengths in the lower end of the spectrum (400 nm and 410 nm) but remain  $> 1$ , whereas the highest slopes are reached around 550 nm and 580 nm. The mean and standard deviations of bare-material measurements are generally slightly higher than the mean and standard deviations calculated for boxed material. This observation may be due to the spreading/cracking of the compressed bare material (increasing mean and standard deviation) or, alternatively, a higher overlap of measurement areas of the boxed samples (decreasing mean and standard deviation), as shown in Fig. 2.

From the calculated linear models for each individual wavelength, a comparison was carried out between bare material, box material, and re-calculated bare material. In Fig. 5, all three spectra are plotted and compared. This figure shows the successful recalibration of the raw material from material contained in the boxes for four of the 35 samples.

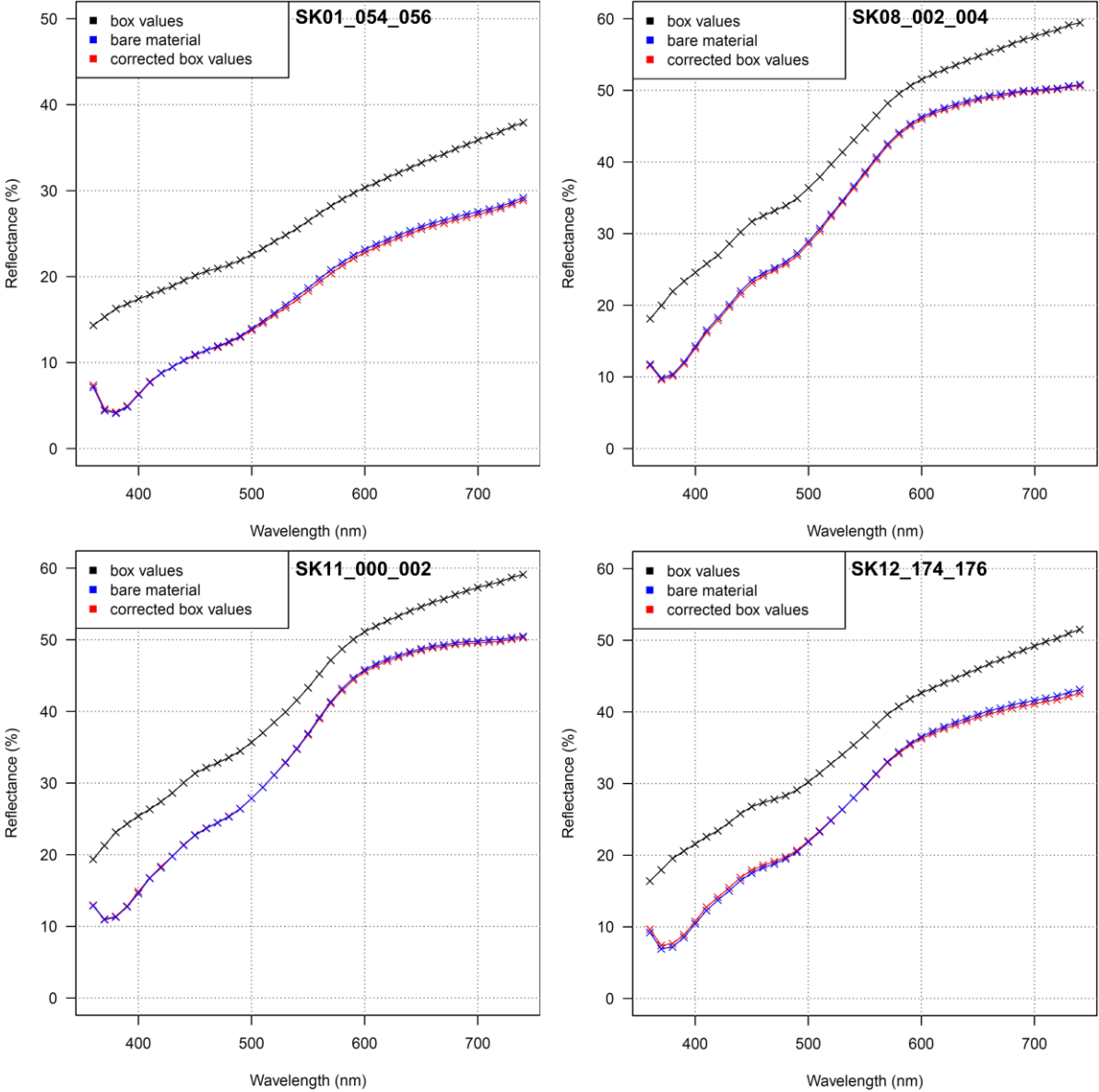


Figure 5: Representative samples spread over the whole Pleven SK18 profile [19]. Displayed are data of four samples: in black are the boxed material measurements, in blue are the un-boxed/raw material measurements, and in red are the boxed measurements applying the linear regression functions shown in Table 1 to match the unboxed material.



### Integrating color enhancement and box-correction

A comparison between the uncorrected (boxed material) and the corrected/recalculated spectra displaying the outcome of the colorimetric enhancement protocol is shown in Fig. 6 for two enhancement cycles of analyses obtained on all 1336 sample depths of the Pleven LPS (Laag et al., in prep.). Figure 6 shows, for each cycle,  $L^*a^*b^*$  values re-calculated as RGB values for the boxed sample before correction (left panels) and after correction (right panels).

The resulting RGB colors for the non-corrected  $L^*a^*b^*$  values are rather dim or muted, leading to less visible color changes in the stratigraphic plot.

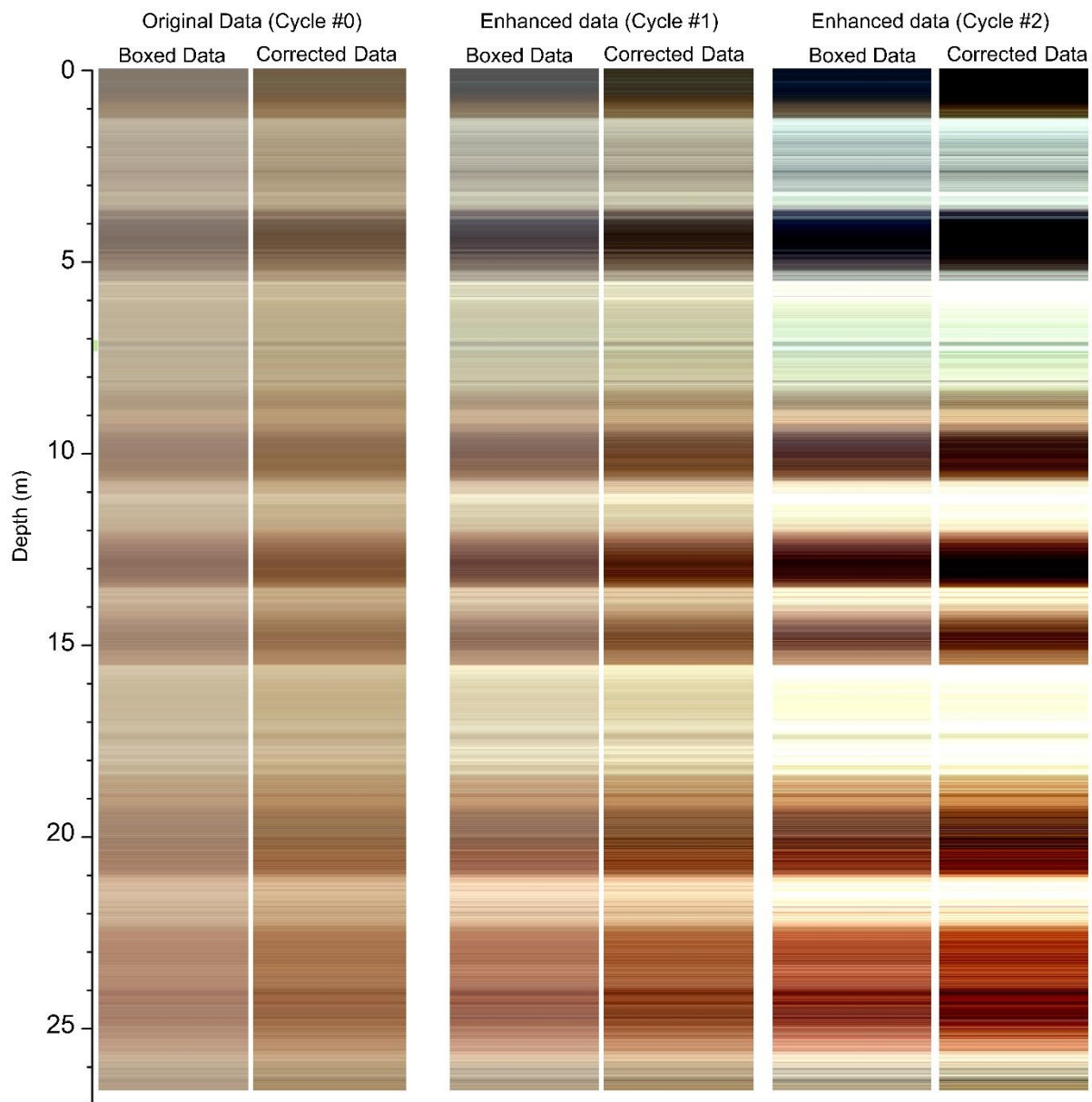


Figure 6: Comparison of the applied colorimetric enhancement cycles performed on boxed material (not corrected) and corrected samples Lab signals.

The right-panel figures of each sub-plot indicate a far clearer stratigraphic differentiation, and transitions from one stratigraphic unit to another are more easily identifiable. Thus, the colorimetric enhancement (cycle #0 being the original data and cycles #1 and #2 the enhanced values) adds value to the investigator's visual interpretation of the color column. In cycle #2 of the corrected data, one can observe a better-expressed reddening in the lower half of the stratigraphic column than in the original (corrected) data. This reddening was already observed in [19], further evidenced by increased DRS-derived hematite contents based on in-field measurements during the September 2021 field campaign and mineral magnetic data (Laag et al., in prep.).

## Method validation via ATR-FTIR

Independent validation of DRS-derived semi-quantitative goethite and calcite concentrations was conducted by comparison with acquired attenuated total reflection Fourier transform infrared (ATR-FTIR) spectrometry. For this purpose, the wavenumber (WN) 450  $\text{cm}^{-1}$  was selected to determine the goethite content following [29] and WN 1428  $\text{cm}^{-1}$  for calcite [31–34]. Calcite (in primary and/or secondary form) is a very bright, nearly white mineral, which clearly influences the overall luminance ( $L^*$ ). Previous LPS studies, e.g., [35], have demonstrated calcite content to correlate well to  $L^*$ . Moreover, during the 2018 Pleven LPS field work, HCl tests were conducted systematically at each sampling depth and attest to the occurrence of carbonates (see supplementary Table 1S of [19]).

Semi-quantitative goethite concentration was derived from both DRS and ATR-FTIR analyses for a total of 719 samples. The linear correlation coefficient between the two different analytical methods (DRS-derived goethite content and ATR-FTIR-derived goethite content) is  $r=0.84$  (Fig. 7), demonstrating a good agreement between these independently derived goethite concentrations. The significance of the correlations, evaluated from an F-test, is excellent, with  $p < 2 \times 10^{-16}$ . We calculated the same  $r$  for the relationship between DRS-derived luminance ( $L^*$ ) and ATR-FTIR-derived calcite content. The significance of the correlation is also excellent, with  $p < 2 \times 10^{-16}$ .

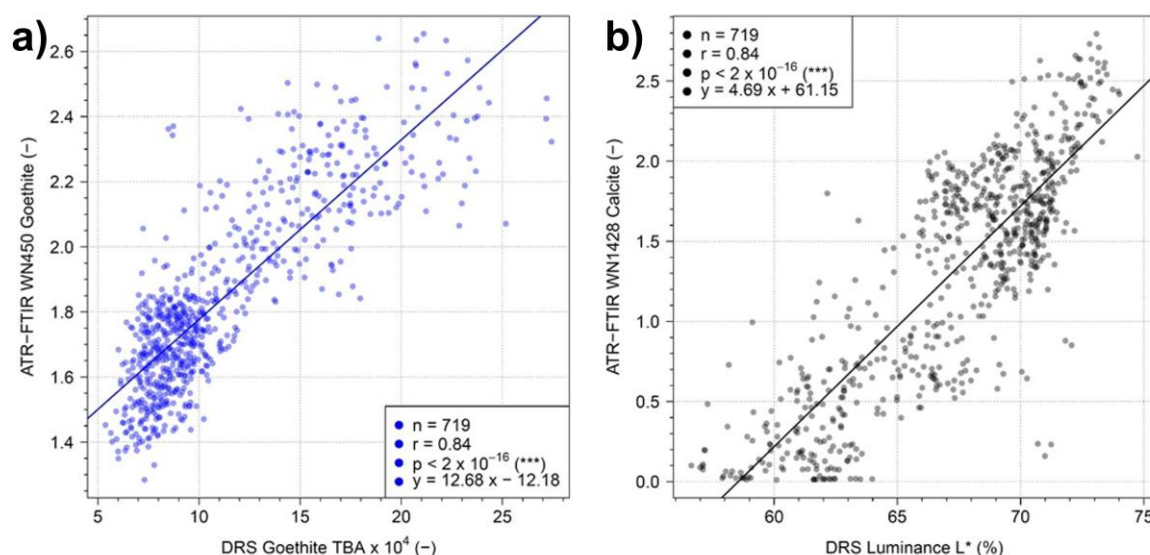


Figure 7: a) Comparison of DRS-derived qualitative goethite amounts with ATR-FTIR-derived goethite amounts. b) shows a comparison of  $L^*$  with ATR-FTIR-derived Calcite contents. Both comparisons follow a linear trend, correlate significantly well, and are based on 719 data points.

For calcite, at a wavenumber of  $1428 \pm 11 \text{ cm}^{-1}$ , the laser beam activates the stretching mode of  $\text{CO}_3$  in an asymmetrical behavior [31]. This causes a strong peak in the absorbance spectrum calculated from the ATR-FTIR measured spectra. However, the resulting peak wavenumber-position at  $1428 \text{ cm}^{-1}$  is experimentally considered and is accompanied by a standard deviation of  $\pm 11 \text{ cm}^{-1}$ . We tried to circumvent this possible deviation from a fixed wavenumber position by applying ranges of the absorbance signal's minimum- and maximum wavenumber position per sample, allowing for a standard deviation that does not influence the calculated absolute band amplitude.

## Conclusion and summary

The present study outlines and validates a method for correcting colorimetric measurements acquired on sediments prepared or stored in plastic containers. A detailed workflow is presented to estimate qualitative amounts of goethite, hematite, and calcite. We demonstrate that goethite and calcite concentrations determined by two independent methods (DRS and ATR-FTIR spectrometry) are coherent. Finally, a newly developed and user-friendly designed R-Package called “LESLIE” is presented. LESLIE enables laboratories to perform colorimetric enhancement of existing or new  $L^*a^*b^*$  data acquired with spectrophotometers and significantly better data interpretation, including the detection of crypto-tephra layers overlooked by other analytical methods (e.g., magnetic properties, mid-infrared spectrometry, granulometry).

## **CRedit author statement**

**Christian Laag:** Conceptualization, methodology, software, validity tests, data curation, original draft preparation, and editing. **France Lagroix:** Writing, original draft preparation, writing, reviewing and editing, investigation, supervision. **Sebastian Kreutzer:** Software, validity test, writing, reviewing, and editing. **Stoil Chapkanski:** methodology, reviewing and editing. **Christian Zeeden:** Writing, reviewing, and editing. **Yohan Guyodo:** Writing, original draft preparation, writing, reviewing and editing, investigation, supervision.

## **Acknowledgments**

We thank the Laboratoire de Géographie Physique: Environnements quaternaires et actuels (LGP), UMR 8591 CNRS - Université Paris 1 - UPEC, Thiais, France, for granting access to the spectrophotometer Konica Minolta CM 600d and the Fourier Transform Infrared Bruker Vector 22 spectrometer, equipped with Attenuated Total Reflection sampling accessory. The authors also thank Dr Tobias Sprafke for sharing the calculations for colorimetric contrast enhancement performed in MS Excel<sup>TM</sup>. This research did not receive any specific grant from public, commercial, or not-for-profit funding agencies.

## **Supplementary material and/or additional information**

The R Package “LESLIE” is available here: <https://doi.org/10.5281/zenodo.7257765>

## **References**

- [1] C. Laag, U. Hambach, C. Zeeden, F. Lagroix, Y. Guyodo, D. Veres, M. Jovanović, S.B. Marković, A detailed paleoclimate proxy record for the Middle Danube Basin over the last 430 kyr: a rock magnetic and colorimetric study of the Zemun loess-paleosol sequence, *Frontiers in Earth Science*. 9:600086 (2021). <https://doi.org/10.3389/feart.2021.600086>.
- [2] T. Lukić, B. Basarin, B. Buggle, S.B. Marković, V.M. Tomović, J.P. Raljić, I. Hrnjak, A. Timar-Gabor, U. Hambach, M.B. Gavrilo, A joined rock magnetic and colorimetric perspective on the Late Pleistocene climate of Orlovat loess site (Northern Serbia), *Quaternary International*. 334–335 (2014) 179–188. <https://doi.org/10.1016/j.quaint.2014.03.042>.
- [3] L. Wacha, C. Laag, A. Grizelj, S. Tsukamoto, C. Zeeden, D. Ivanišević, C. Rolf, A. Banak, M. Frechen, High-resolution palaeoenvironmental reconstruction at Zmajevac (Croatia) over the last three glacial/interglacial cycles, *Palaeogeography, Palaeoclimatology, Palaeoecology*. 576 (2021) 110504. <https://doi.org/10.1016/j.palaeo.2021.110504>.
- [4] J. Ji, W. Balsam, J. Chen, Mineralogic and Climatic Interpretations of the Luochuan Loess Section (China) Based on Diffuse Reflectance Spectrophotometry, *Quat. Res.* 56 (2001) 23–30. <https://doi.org/10.1006/qres.2001.2238>.
- [5] J. Ji, W. Balsam, J.U. Chen, L. Liu, Rapid and Quantitative Measurement of Hematite and Goethite in the Chinese Loess-paleosol Sequence by Diffuse Reflectance Spectroscopy, *Clays and Clay Minerals*. 50 (2002) 208–216. <https://doi.org/10.1346/000986002760832801>.
- [6] Q. Liu, J. Bloemendal, J. Torrent, C. Deng, Contrasting behavior of hematite and goethite within paleosol S5 of the Luochuan profile, Chinese Loess Plateau, *Geophys. Res. Lett.* 33 (2006) L20301. <https://doi.org/10.1029/2006GL027172>.

- [7] Z. Jiang, Q. Liu, A.P. Roberts, M.J. Dekkers, V. Barrón, J. Torrent, S. Li, The Magnetic and Color Reflectance Properties of Hematite: From Earth to Mars, *Reviews of Geophysics*. 60 (2022). <https://doi.org/10.1029/2020RG000698>.
- [8] J. Torrent, V. Barrón, Q. Liu, Magnetic enhancement is linked to and precedes hematite formation in aerobic soil, *Geophys. Res. Lett.* 33 (2006) L02401. <https://doi.org/10.1029/2005GL024818>.
- [9] J. Torrent, Q. Liu, J. Bloemendal, V. Barrón, Magnetic Enhancement and Iron Oxides in the Upper Luochuan Loess-Paleosol Sequence, Chinese Loess Plateau, *Soil Sci. Soc. Am. J.* 71 (2007) 1570–1578. <https://doi.org/10.2136/sssaj2006.0328>.
- [10] P. Hu, Q. Liu, J. Torrent, V. Barrón, C. Jin, Characterizing and quantifying iron oxides in Chinese loess/paleosols: Implications for pedogenesis, *Earth and Planetary Science Letters*. 369–370 (2013) 271–283. <https://doi.org/10.1016/j.epsl.2013.03.033>.
- [11] I. Obreht, C. Zeeden, U. Hambach, D. Veres, S.B. Marković, J. Böskén, Z. Svirčev, N. Bačević, M.B. Gavrilov, F. Lehmkuhl, Tracing the influence of Mediterranean climate on Southeastern Europe during the past 350,000 years, *Sci Rep.* 6 (2016) 36334. <https://doi.org/10.1038/srep36334>.
- [12] Z.L. Ding, V. Ranov, S.L. Yang, A. Finaev, J.M. Han, G.A. Wang, The loess record in southern Tajikistan and correlation with Chinese loess, *Earth and Planetary Science Letters*. 200 (2002) 387–400. [https://doi.org/10.1016/S0012-821X\(02\)00637-4](https://doi.org/10.1016/S0012-821X(02)00637-4).
- [13] P. Antoine, F. Lagroix, D. Jordanova, N. Jordanova, J. Lomax, M. Fuchs, M. Debret, D.-D. Rousseau, C. Hatté, C. Gauthier, O. Moine, S.N. Taylor, J.L. Till, S. Coutard, A remarkable Late Saalian (MIS 6) loess (dust) accumulation in the Lower Danube at Harletz (Bulgaria), *Quaternary Science Reviews*. 207 (2019) 80–100. <https://doi.org/10.1016/j.quascirev.2019.01.005>.
- [14] R Core Team, R: A Language and Environment for Statistical Computing, R Foundation for Statistical Computing, Vienna, Austria, (2022). <https://r-project.org>.
- [15] C. Laag, S. Kreutzer, LESLIE - LoESs coLorimetry sIgnal Enhancement: v0.1.0, (2022). <https://doi.org/10.5281/ZENODO.7257765>.
- [16] M.B. Toffolo, F. Berna, Infrared Absorption Spectroscopy (IR, FTIR, DRIFT, ATR), in: S.L. López Varela (Ed.), *The Encyclopedia of Archaeological Sciences*, John Wiley & Sons, Inc., Hoboken, NJ, USA, 2018: pp. 1–4. <https://doi.org/10.1002/9781119188230.saseas0325>.
- [17] Chapkanski, Stoil, Goiran, Jean-Philippe, Rosa, Carlo, Kay, Stephen, De Graauw, Arthur, Gallet, Xavier, D’Ottavio, Daniele, Key, Simon, INFRARED SPECTROSCOPIC INVESTIGATIONS OF THE NORTHERN MOLE OF PORTUS, THE ANCIENT HARBOUR OF ROME. INSIGHTS FOR STRATIGRAPHY AND PROVENANCE OF RAW MATERIALS FOR CONSTRUCTION, (2021). <https://doi.org/10.5281/ZENODO.5057562>.
- [18] S. Chapkanski, K. Jacq, G. Brocard, C. Vittori, M. Debret, A.U. De Giorgi, D. D’Ottavio, E.M. Giuffré, J.-P. Goiran, Calibration of Short-Wave InfraRed (SWIR) hyperspectral imaging using Diffuse Reflectance Infrared Fourier Transform spectroscopy (DRIFTS) to obtain continuous logging of mineral abundances along sediment cores, *Sedimentary Geology*. 428 (2022) 106062. <https://doi.org/10.1016/j.sedgeo.2021.106062>.
- [19] D. Jordanova, C. Laag, N. Jordanova, F. Lagroix, B. Georgieva, D. Ishlyamski, Y. Guyodo, A detailed magnetic record of Pleistocene climate and distal ash dispersal during the last 800 kyrs - The Suhia Kladenetz quarry loess-paleosol sequence near Pleven (Bulgaria), *Global and Planetary Change*. 214 (2022) 103840. <https://doi.org/10.1016/j.gloplacha.2022.103840>.
- [20] P. Kubelka, F. Munk, An article on optics of paint layers, *Technical Physics*. 12 (1931) 259–274.

- [21] A.C. Scheinost, A. Chavernas, V. Barrón, J. Torrent, Use and Limitations of Second-Derivative Diffuse Reflectance Spectroscopy in the Visible to Near-Infrared Range to Identify and Quantify Fe Oxide Minerals in Soils, Clays and Clay Minerals. 46 (1998) 528–536. <https://doi.org/10.1346/CCMN.1998.0460506>.
- [22] C.S. Kosmas, D.P. Franzmeier, D.G. Schulze, Relationship among Derivative Spectroscopy, Color, Crystallite Dimensions, and Al Substitution of Synthetic Goethites and Hematites, Clays and Clay Minerals. 34 (1986) 625–634. <https://doi.org/10.1346/CCMN.1986.0340602>.
- [23] C.S. Kosmas, N. Curi, R.B. Bryant, D.P. Franzmeier, Characterization of Iron Oxide Minerals by Second-Derivative Visible Spectroscopy, Soil Science Society of America Journal. 48 (1984) 401–405. <https://doi.org/10.2136/sssaj1984.03615995004800020036x>.
- [24] J. Torrent, V. Barrón, The visible diffuse reflectance spectrum in relation to the color and crystal properties of hematite, Clays and Clay Minerals. 51 (2003) 309–317. <https://doi.org/10.1346/CCMN.2003.0510307>.
- [25] C.J. Lepre, P.E. Olsen, Hematite reconstruction of Late Triassic hydroclimate over the Colorado Plateau, Proc. Natl. Acad. Sci. U.S.A. 118 (2021) e2004343118. <https://doi.org/10.1073/pnas.2004343118>.
- [26] C. Zeeden, L. Krauß, H. Kels, F. Lehmkuhl, Digital image analysis of outcropping sediments: Comparison to photospectrometric data from Quaternary loess deposits at Şanoviţa (Romania) and Achenheim (France), Quaternary International. 429 (2017) 100–107. <https://doi.org/10.1016/j.quaint.2016.02.047>.
- [27] C. Zeeden, L. Krauß, F. Lehmkuhl, H. Kels, Supplementary R script for manuscript “Digital image analysis of outcropping sediments: comparison to photospectrometric data from Quaternary Loess deposits at Sanovita (Romania) and Achenheim (France),” (2016). <https://doi.org/10.5880/SFB806.17>.
- [28] T. Sprafke, P. Schulte, S. Meyer-Heintze, M. Händel, T. Einwögerer, U. Simon, R. Peticzka, C. Schäfer, F. Lehmkuhl, B. Terhorst, Paleoenvironments from robust loess stratigraphy using high-resolution color and grain-size data of the last glacial Krems-Wachtberg record (NE Austria), Quaternary Science Reviews. 248 (2020) 106602. <https://doi.org/10.1016/j.quascirev.2020.106602>.
- [29] R.M. Cornell, U. Schwertmann, The iron oxides: structure, properties, reactions, occurrences and uses., John Wiley & Sons, 2003.
- [30] B. Udvardi, I.J. Kovács, P. Kónya, M. Földvári, J. Fűri, F. Budai, G. Falus, T. Fancsik, C. Szabó, Z. Szalai, J. Mihály, Application of attenuated total reflectance Fourier transform infrared spectroscopy in the mineralogical study of a landslide area, Hungary, Sedimentary Geology. 313 (2014) 1–14. <https://doi.org/10.1016/j.sedgeo.2014.08.005>.
- [31] V.C. Farmer, The infrared spectra of minerals, Mineralogical Society, London, 1974.
- [32] L. Vaculíková, E. Plevová, Identification of clay minerals and micas in sedimentary rocks., Acta Geodynamica et Geomaterialia. 2 (2005) 167–175.
- [33] H.W. van der Marel, H. Beutelspacher, Atlas of infrared spectroscopy of clay minerals and their admixtures, Elsevier Scientific Pub. Co, Amsterdam ; New York, 1976.
- [34] J. Hlavay, Characterization of the Particle Size and the Crystallinity of Certain Minerals by IR Spectrophotometry and Other Instrumental Methods—II. Investigations on Quartz and Feldspar, Clays and Clay Minerals. 26 (1978) 139–143. <https://doi.org/10.1346/CCMN.1978.0260209>.
- [35] J.A. Mir, R.A. Dar, M. Vinnepand, C. Laag, C. Rolf, C. Zeeden, Exploring the potential of high-resolution physical property data from Loess-Paleosol Sequences in Kashmir for paleoenvironmental reconstructions, Palaeogeography, Palaeoclimatology, Palaeoecology. in press (2022).

### 4.3. Pleven Laag et al., in prep.

#### **A multiproxy analysis of the Pleven LPS: Documenting the Mid-Brunhes Climate Transition and Millennial-Scale Climate Change in MIS 2-4, 6, and 12**

Christian Laag<sup>1</sup>, France Lagroix<sup>1</sup>, Yohan Guyodo<sup>1</sup>, Diana Jordanova<sup>2</sup>, Neli Jordanova<sup>2</sup>, Stoil Chapkanski<sup>3</sup>, Ségolène Saulnier-Copard<sup>3</sup>, Olivier Moine<sup>3</sup>, Bozhurka Georgieva<sup>2</sup>, Daniel Ishlyanski<sup>2</sup>, Pierre Antoine<sup>3</sup>

<sup>1</sup> Université Paris Cité, Institut de physique du globe de Paris, CNRS, Paris, France

<sup>2</sup> National Institute of Geophysics, Geodesy and Geography, Bulgarian Academy of Sciences, Sofia, Bulgaria

<sup>3</sup> Laboratoire de Géographie Physique: Environnements quaternaires et actuels (LGP), UMR 8591 CNRS - Université Paris 1 - UPEC, Thiais, France

#### **Status :**

- Manuscript in preparation
- Target Journal: Geochemistry, Geophysics, Geosystems

#### **Main findings:**

- Multi-proxy evidence for multiple interglacial/glacial cycles preserved in the Pleven LPS
- Transition from intense heat, precipitation and seasonality dominated interglacials before and milder interglacials after the mid Brunhes climate event
- First evidence for preserved millennial scale climate variability during MIS12, further confirmation for MIS 6 and MIS4-present.
- Goethite can be considered as a precipitation proxy
- Maghemite and Goethite utilized for a quantitative paleoprecipitation reconstruction for the last 850 ky at Pleven
- Multi-proxy evidence for 55 (crypto) tephra layers preserved in Pleven whose 51 radiometrically dated potential counterparts can be found in the tephra rich record Lake Ohrid



## **A multiproxy analysis of the Pleven LPS: Documenting the Mid-Brunhes Climate Transition and Millennial-Scale Climate Change in MIS 2-4, 6, and 12**

Christian Laag<sup>1</sup>, France Lagroix<sup>1</sup>, Yohan Guyodo<sup>1</sup>, Diana Jordanova<sup>2</sup>, Neli Jordanova<sup>2</sup>, Stoil Chapkanski<sup>3</sup>, Ségolène Saulnier-Copard<sup>3</sup>, Olivier Moine<sup>3</sup>, Bozhurka Georgieva<sup>2</sup>, Daniel Ishlyanski<sup>2</sup>, Pierre Antoine<sup>3</sup>

<sup>1</sup> Université Paris Cité, Institut de physique du globe de Paris, CNRS, Paris, France

<sup>2</sup> National Institute of Geophysics, Geodesy and Geography, Bulgarian Academy of Sciences, Sofia, Bulgaria

<sup>3</sup> Laboratoire de Géographie Physique: Environnements quaternaires et actuels (LGP), UMR 8591 CNRS - Université Paris 1 - UPEC, Thiais, France

### **Abstract**

Loess-palaeosol sequences (LPSs) located in Eastern Europe are excellent archives of past climate and environmental change. Eastern European LPSs can cover up to the last 1 Ma with alternating loess and paleosols units resulting from changes in prevailing climate conditions during glacial and interglacial conditions. Such paleoclimate records are most impactful and advance knowledge when a precise age model is associated. However, commonly applied dating techniques, such as <sup>14</sup>C and luminescence, have dating limits of c. 50 ka and 250 ka, and decrease in reliability with a systematic increase of errors with increasing sediment age. Overcoming this problem is routinely address by correlative dating methods towards global stacks (e.g., LR04) or other archives dated by more reliable absolute dating. Volcanic ash layers (tephras) are widespread over Eastern Europe and were employed in loess research as important stratigraphical marker horizons. However the detection and characterization of distinct tephra layers are difficult and with increasing weathering degree of volcanic glass shards geochemical “fingerprinted” becomes impossible.

At Pleven, two profiles were investigated and sampled. In 2018 the Suhia Kladenetz section (SK18, 27 m long) was investigated at a 2-cm continuous resolution leading to 1336 sampling depths. Environmental magnetism and colorimetric experiments were performed at all sample depths. Mid-infrared (ATR-FTIR), granulometric and other magnetic experiments performed continuously over the whole profile but at a lower resolution. In 2021, a second sampling campaign was carried out along a profile (PL21, 24m long) approximately at 200 m from SK18 within the same quarry during which further stratigraphic observations were made and 630 oriented samples collected to investigate anisotropy of magnetic susceptibility and perform paleomagnetic studies to reconstruct the Earth’s magnetic field strength and direction. Due to

the 15-month delay (Covid) of this field campaign, these investigations of the oriented samples are underway.

Due to the high resolution of the resulting data and integration of different methods and disciplines, the Pleven LPS provides detailed insights into past climate and environmental change for the last ~850 ky (MIS 20-present). For the first time in Eastern Europe, detailed mineralogical results evidence the successful recording of the Mid-Brunhes climate transition, which occurred at 430 ka (MIS12). In addition, we confirm previous observations of millennial scale climate change variability in loess through MIS4-present (65-3 ka), provide further evidence of millennial climate change preserved in MIS6 loess and evidence for the first time millennial scale climate variability preserved in MIS 12 (480-430ka) loess. Environmental magnetic and ATR-FTIR data confirm 4 (crypto)tephra layers reported for SK18 in a previous study, and support the identification of 51 additional cryptotephra candidate layers occurring over the whole profile. We derive ages for all cryptotephra candidates from our correlative age model. A comparison to other tephra rich paleo-archives such as Lake Ohrid and the Fucino Basin lead to a first and tentative tephrostratigraphic framework for the Pleven LPSs. The current approach is strictly tephro-stratigraphical since geochemical fingerprinting of extracted volcanic glass shards enabling a robust source tracking has yet to be done. However, with only four tephra layers reported in the literature for Eastern European LPSs, the innovative integration of multi-disciplinary data evidencing cryptotephra layers in the Pleven LPS is a step forward in addressing the geochronological challenges inherent to LPSs and strengthens the potential for regional limnic-sea-land stratigraphic correlations and regional paleoclimate reconstructions in Eastern Europe.

## Introduction

Loess-paleosol sequences (LPSs) are valuable terrestrial archives of past climate change, which in the geographical area of this study reach a time coverage of up to 1 million years (Jordanova et al., 2008; Marković et al., 2015; Sümegi et al., 2018; Hlavatskyi and Bakhmutov, 2020, 2021). LPSs provide, based on the methods applied, insights into past climate change (Bugge et al., 2013, 2014; Basarin et al., 2014; Marković et al., 2015; Schaetzl et al., 2018), paleo-wind-directions (Lagroix and Banerjee, 2002; Költringer et al., 2021), seasonality (Sun et al., 2003), and mollusk assemblages (Sümegi et al., 2018; Gavrilović et al., 2019). Several studies applied to LPSs were able to date these sequences based on recorded changes in the Earth's magnetic field paleointensity and paleodirections (e.g., (Ding et al., 1999; Deng, 2008; Hlavatskyi and Bakhmutov, 2021)), thus relying on a single proxy approach and missing the possible combination of time information provided by paleoenvironmental fluctuations likely preserved in these archives. In this study, for the first time in the case of eastern European LPSs, a broad set of in-depth applied environmental magnetic, colorimetric, granulometric, and mid-infrared-spectrometric data is presented, covering the last 850 thousand years.

Deep insights into the recorded occurrences of long time scale changes such as the Mid-Brunhes climate transition (Jansen et al., 1986; Hodell et al., 2003; Jouzel et al., 2007; Ao et al., 2020) are provided, as well as on millennial scale fluctuations such as Dansgaard-Oeschger (-like) cycles and Heinrich (-like) events (Heinrich, 1988; Bond et al., 1992; Shi et al., 2003; Rasmussen et al., 2014; Zeeden et al., 2018; Antoine et al., 2019; Rousseau et al., 2020; Heinrich et al., 2021). This study also permitted to describe vegetation dynamics in the Pleven region. Furthermore, integration of magnetic, colorimetric and mid-infrared experiments provide means of detecting potential crypto-tephra candidates, learning in particular from an outcropping tephra from the penultimate glacial L2-loess deposit as presented in (Jordanova et al., 2022) which is also recognized in single-parameter studies performed in close-by sections (Song et al., 2018; Antoine et al., 2019; Laag et al., 2021).

## Methods

### Site description and field work

The Suhia Kladenetz site (in the following abbreviated as SK18) is located in an active quarry in Central North Bulgaria ( $43^{\circ}27'24.0''\text{N}$ ,  $24^{\circ}41'26.7''\text{E}$ ) and was initially sampled in 2018 (see Fig. 1). Additional sampling, field measurements and stratigraphic description was conducted in September 2021 (assigned as PL21) with the aim to perform in-field colorimetric measurements as well as magnetic susceptibility measurements. Furthermore, oriented samples were taken to perform paleomagnetic and anisotropy of magnetic susceptibility measurements. Another aim of the field campaign conducted in 2021 was the continuous sampling of oriented samples allowing the investigation of magnetic fabric and the reconstruction of the Earth's magnetic field strength and direction as well as the improvement of the existing field-description presented in (Jordanova et al., 2022). However, paleomagnetic and anisotropy of magnetic susceptibility experiments are underway but the field description of PL21 is utilized in this study.

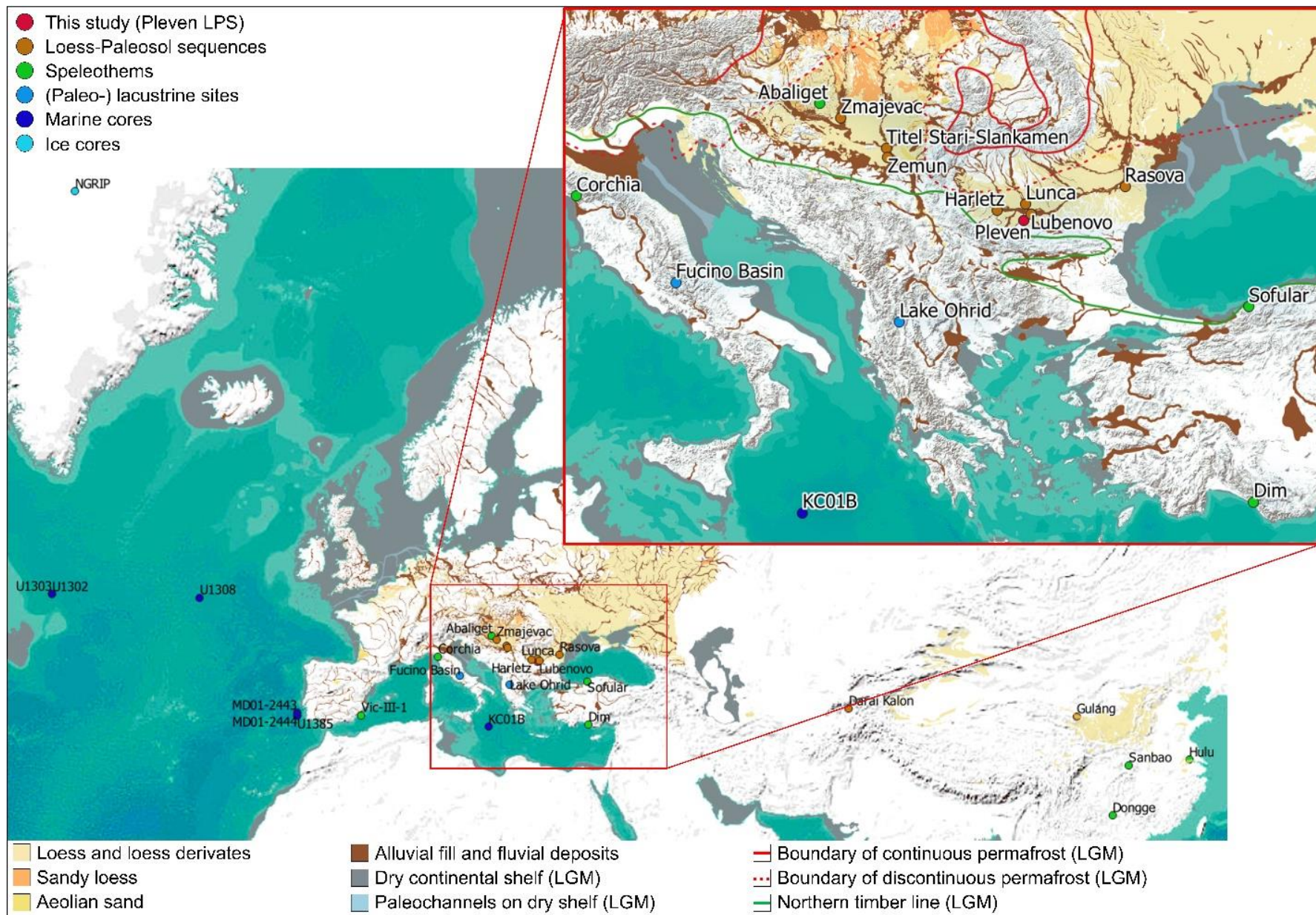




**Figure 1: Map of the distribution of mentioned paleoenvironmental archives categorized by their archive type on the northern hemisphere. Not shown: EPICA Dome C (Antarctica). Base-map stems from QGIS, loess distribution from (Lehmkuhl et al., 2021). The Pleven LPS is indicated in red, other mentioned locations in the text are categorized as LPSs and displayed in orange, speleothems in green, paleo-lacustrine sites in royal blue, marine cores in dark blue and ice cores in bright blue.**

The SK18 sequence is composed of twelve sub-profiles, which were carefully levelled during sampling, in order to ascertain correct merging of the samples into a composite profile. After cleaning the profile from weathered and unconsolidated material, slices were taken with the dimension of approximately 10 x 6 x 2 cm<sup>3</sup>, leading to an approximately 300 g bulk sediment sample. The SK18 composite profile has a total thickness of 26.72m and 1336 bulk samples. In-field measurements comprise HCl droppings on different stratigraphical units and evaluation of different units regarding their color with the aid of Munsell Color Charts (Jordanova et al., 2022).

The sampling conducted to establish the PL21 sequence was performed on four discrete steps, owing to improved quarry work and individual equipment. Sampling occurred several hundred meters away from the SK18 site since sampling location was dominantly restricted for security reasons (active quarry works and slope instabilities). As a consequence, the PL21 sampling unfortunately did not reach the full extent of SK18, and sampling was limited to 23.80 m. Taking into account magnetic susceptibility and DRS-based luminance (L\*) data from both profiles (for SK18 laboratory data and for PL21 in-field data), excellent agreement is found between the two profiles (see supplementary figure 1). This allows observations and data acquired from the PL21 and the SK18 profiles to be merged (supplementary data table 1).

The Pleven sequence (combining SK18 and PL21) is deposited and formed on the Pliocene denudation surface (PDS) and overlies in its deepest part on clayey material (assigned in following graphs as Clays – dark violet diamonds in bi-plots). Building on the clayey unit, a thin loess layer L7 formed (dark blue circles), stratigraphically followed by a reddish paleosol S6 (dark red squares). A pedogenetically overprinted loess layer sits on top and is assigned as L6 (marine blue circles). Right above L6, a strongly weathered horizon assigned as S5 (red squares). The rather thick interval between S5 and S4 is clearly identified in the field as L5 (light blue circles), which shows little indication for weathering. Compared to the rather reddish appearing paleosols S6 and S5, the S4 paleosol (orange squares) appears more reddish - brown.

Compared to L5, a rather thin, pedogenetically overprinted loess unit L4 (dark green circles) is archived followed by a very brown paleosol S3 (ochre squares). Loess L3 (intermediate green) appears somewhat unaltered and is followed by S2 paleosol (dark brown squares), which appears rather brownish. S2 is overlaid by a loess layer free of any observable indicators of pedogenesis – L2 (shiny green circles), which contains an outcropping tephra layer – named in following bi-plots as L2-tephra (orange triangles). S1 (pale brown squares), in contrast to L2-S4, expresses blackish colors, similarly to the Holocene soil S0 (black squares). This could indicate enhanced weathered organic material still preserved in S1 and S0. These two paleosols are intercalated by a rather whitish loess unit L1 (green-yellow circles). A tabulated detailed profile can be found in the supplementary data table 1.

### Laboratory sample preparation

Prior to sub-sampling into different sample types, bulk samples were dried at room temperature for several days. Sub-samples followed five different preparations: ultra-clear plastic boxes (8 cm<sup>3</sup>- Type A), gelatine capsules (Type B), half-height plastic boxes (4cm<sup>3</sup> – Type C) and threatened loose material and their coarse grain leftovers (for grain size analysis-Type D), and loose material (for mid-infrared spectrometry, Type E). The detailed description of each sample type can be found in the supplementary material a).

### Environmental Magnetism

#### Room temperature magnetic susceptibility

Room-temperature magnetic low- and high frequency susceptibility data were measured at NIGGG on a MFK-1A susceptibility bridge (AGICO, Czech Republic) in a 200 A/m field and working frequencies of 976 and 15,616 Hz and presented in (Jordanova et al., 2022). The frequency dependence of magnetic susceptibility ( $\Delta\chi$ ) as the absolute difference of low-frequency (976Hz) and high-frequency (15676 Hz) magnetic susceptibility, as well presented in (Jordanova et al., 2022) were used in this study, being compared with additional parameters from magnetic experiments conducted at IPGP as described in the following sections.

At IPGP, room temperature low-field magnetic susceptibility ( $\chi_{lf}$ ) was measured on bulk sediments filled in non-magnetic gelatine capsules (Type B) using a AGICO KLY3 operating at a frequency of 875 Hz and an applied field of 300 A/m. Measurements were carried out three times, allowing for the calculation of the mean and mass normalized. These  $\chi_{lf}$  values were later used to merge the SK18 and the PL21 profiles (see supplementary figure 1).

#### High-temperature dependence of magnetic susceptibility

High temperature magnetic susceptibility measurements were performed on 81 samples using a KLY3 susceptibility bridge (field frequency of 875 Hz and amplitude of 300 A/m) equipped with the CS-3 furnace at the Grubenhagen Paleo-and Environmental Magnetism Grubenhagen (outpost of the Leibniz-Institute for Applied Geophysics, Hannover, Germany). Magnetic susceptibility was measured at 6°C intervals upon heating to 700°C and cooling to 50°C. Measurements were performed in an argon atmosphere to prevent oxidation during the heating process. The diamagnetic background of the empty glass holder and furnace assembly was measured and subtracted from measured response. Each sample ranging from 1 to 2 g was homogenized, weighed, in order to report mass-specific magnetic susceptibility values.

The temperature dependent mass-specific magnetic susceptibility data was interpolated to a 0.1°C resolution employing Piecewise Cubic Hermite Interpolation Polynomials (or pchip). This interpolation was performed in R (R Core Team, 2023) and is a shape preserving piecewise cubic Hermite polynomial approach that attempts to determine slopes such that function values do not overshoot data values, which commonly occurs with spline interpolations. Unblocking temperatures were determined from the first derivatives of the pchip interpolated data in order to interpret the magnetic mineralogy.

#### Vibrating sample magnetometer (VSM) experiments

A series of experiments were conducted on all 1336 gelatine capsule samples of the SK18 profile using a Vibrating Sample Magnetometer (VSM, Model 3900 Princeton Measurement Corporation, USA) at IPGP. Hysteresis loops were measured in  $\pm 1.5$  T applied maximum fields. Measurements were acquired in continuous sweep mode at 5 mT field increments and with 100 ms averaging time. Saturation magnetization ( $M_S$ ) was determined after subtraction of the high-field slope between 1.05 and 1.5 T. The high-field slope was converted into a mass-specific high-field magnetic susceptibility ( $\chi_{\text{hifi}}$ ) and subsequently subtracted from the  $\chi_{\text{lf}}$  to isolate the ferrimagnetic component ( $\chi_{\text{ferri}}$ ) of the bulk magnetic susceptibility.

$$\chi_{\text{ferri}} = \chi_{\text{lf}} - \chi_{\text{hifi}}$$

Other hysteresis loop derived parameters are the saturation remanent magnetization ( $M_{\text{RS}}$ ), and the coercive force ( $B_C$ ). The coercivity of remanence ( $B_{\text{CR}}$ ) was determined by subjecting the forward field isothermal remanent magnetization ( $\text{IRM}_{1.5\text{T}}$ ) to 70 backfield steps logarithmically spaced up to -0.5 T. A forward field isothermal remanent magnetization



(IRM<sub>1.5T</sub>) was also subjected to linearly spaced 100 mT backfield steps from -0.1 T to -1.5 T providing a coarse coercivity distribution and data from which the S-ratio is calculated after (King and Channell, 1991) as:

$$S - ratio = \frac{IRM_{-0.3T}}{IRM_{-1.5T}}$$

The S-ratio can range from -1 to +1, where values close to +1 indicate a dominant contribution of soft-magnetic particles such as magnetite and maghemite to the IRM<sub>1.5T</sub>. With decreasing S-ratio values there is an increasing contribution of hard magnetic minerals such as hematite to the IRM<sub>1.5T</sub> (e.g. (Frank and Nowaczyk, 2008)). The contribution of hard magnetic mineral component (HIRM) to the total IRM<sub>1.5T</sub> is calculated after (Taylor and Lagroix, 2015; Liu et al., 2016) as:

$$HIRM = IRM_{-0.3T} - IRM_{-1.5T}$$

Highly resolved IRM acquisitions provide insights into granulometric and mineralogic characteristics of loess. IRM acquisitions were acquired on Type B sub-samples for 263 sample depths corresponding to all depths measured for their laser-granulometric properties (every 6<sup>th</sup> sample, 12cm resolution), and depths where cryptotephra layers were suspected (see supplementary figure 2). Stepwise IRM acquisition curves were measured from an initial field of 15  $\mu$ T to a final field of 1.5T in 300 logarithmically-spaced steps. Samples were initially demagnetized using the VSM DC demagnetization sub-routine from 1.6 T to zero at a 2 % field decay rate.

Unmixing coercivity distributions allows insights into individual components of the samples' magnetic mineralogy and magnetic grain size and identifies the relative contribution to the total acquisition of a single component. IRM acquisition curves were decomposed into individual coercivity spectra for every measured bulk sample, using the Max-Unmix R shiny web application (Maxbauer et al., 2016). A smoothing factor of 0.5 was applied on the raw data for all samples. Four components were selected for all 263 samples, and in some cases a 5<sup>th</sup> component when necessary which indicates the presence of tephra material. Starting component settings can be found in Table 1, which during the unmixing progress were slightly modified to reach the lowest possible resulting RSS error.

<b>Component</b>	<b>logBH (initial)</b>	<b>BH (initial) (mT)</b>	<b>Interpretation</b>
<b>C1 (blue)</b>	1.40	22	Magnetite/maghemite
<b>C2 (purple)</b>	1.95	85	Weakly magnetic / antiferromagnetic iron oxides likely partially magnetized goethite or finer grained hematite
<b>C3 (mint)</b>	0.69	5	Most likely fine grained ferrimagnetic/pedogenic and /or MD particles
<b>C4 (red)</b>	2.9	500	Weakly magnetic / antiferromagnetic iron oxides like partially magnetized goethite or finer grained hematite
<b>C5 (green)</b>	1.60	40	If required, then indicative for tephra layers

**Table 1: Individual IRM components and their interpretation.**

Afterwards data treatment was performed in R (R Core Team, 2023), where each components' percent contribution to the bulk signal ( $O_C$ ) was multiplied by  $M_{RS}$ , to have a more stratigraphical comparable log of the individual components.

First order reversal curves (FORC) were measured on 15 Type B samples over a  $H_U$  range of  $\pm 80$  mT and a  $H_C$  range from 0-100 mT. Multiple FORC's were measured on a given sample and an averaging time of 300 ms selected to reduce measurement noise. By choosing a rather narrow field increment of ca. 2mT 198 FORCs were measured per series element. The number of elements measured inside a FORC series is reported on each resulting FORC diagram. The program FORCinel (Harrison and Feinberg, 2008) was used for analysis of the raw FORCs. FORC diagrams were produced after drift and high-field slope corrections, subtraction of the lower branch of 30 FORCs, and removal of the first data point. Afterwards, the FORCinel option to average multiple FORCs was used. The VARIFORC approach presented in (Egli, 2013) was employed to smooth resulting FORC diagrams. Different combinations of smoothing factors were tested before deciding a final smoothing factor set for the individual sample, taking noise and measurement artefacts into account. To gain insights about the general coercivity distribution, irreversible coercivity distributions were extracted (Harrison and Feinberg, 2008) by integrating over the whole  $H_U$  range. This approach, as opposed to

extracting at  $H_U=0$ , has the advantage of considering maximum intensities that may be slightly above or below the central ridge position of  $H_U=0$  that would otherwise be missed..

### Colorimetry

Spectrophotometers provide numerical color values following the CIE-Lab color system (ISO/CIE 11664-4:2019) as well as diffuse reflectance values (R%).  $L^*$ ,  $a^*$ , and  $b^*$  values span a 3-dimensional sphere where luminance (brightness) ranges from 0% (black) to 100% (white).  $a^*$  and  $b^*$  span two horizontal axes orthogonal to each other, where  $a^*$  is negative green and positive red, and  $b^*$  (yellowness) is negative blue and positive yellow.

Colorimetric measurements were performed at the Laboratoire de Géographie Physique (LGP) in Meudon (France) with a Konica Minolta CM600d spectrophotometer. Measurements were done at 10 nm intervals across the visible light spectrum (400-700 nm) on all 1336 Type C sub-samples. The spectrophotometer was used with a 0.8 cm open oculus and an observer angle set to  $10^\circ$ . Five measurements per sample were conducted, leading to 6680 individual spectra and  $L^*$ ,  $a^*$  and  $b^*$  values. Their means and standard deviations were calculated after all data manipulation and reported in this study as error-bars/polygons.

Subsequently, it became apparent that the plastic of the boxes through which the analyses were conducted, following procedures recommended by Konica Minolta, produced a non-negligible signal. A method was developed to eliminate the plastic box signal without requiring the re-analysis of 1336 samples. The complete demonstration of this correction method is provided in (Laag et al., 2022). Goethite and hematite extraction and colorimetric enhancement strategies were also developed and available in an R-package called LESLIE (Laag and Kreutzer, 2022).

The following calculations were then performed for all DRS (box corrected) spectra. The Kubelka-Munk theory (Kubelka and Munk, 1931) was applied to calculate transferred reflectance values  $F(R)$ :

$$F(R) = \frac{(1 - R)^2}{2R}$$

Where  $R$  is the reflectance (converted in a decimal value) for a thick sample layer. The second derivative ( $f''$ ) values of the  $F(R)$  spectra were calculated following (Kosmas et al., 1984, 1986; Scheinost et al., 1998). Peak positions (minima and maxima) were then identified for each resulting  $f''(F(R))$  to receive “true” band amplitudes (denoted as “TBA”) as described in (Jiang et al., 2022). To account for shifts in wavelength of peak positions, a range of wavelengths was scanned to identify the TBA. The lower 10 nm resolution of the spectrophotometer used in this

study may favor shifts in observed peak positions in comparison to higher resolution spectrophotometers used in other studies quoted here. For goethite, the wavelength range between 420 and 450 nm was scanned to identify TBA minima and maxima. While for hematite, the 530 to 580 nm wavelength range was scanned. The following spectrophotometer-derived data are provided in this study:  $L^*$ ,  $a^*$ ,  $b^*$ ,  $TBA_{Goeth}$  and  $TBA_{Hema}$  for the true band amplitudes of goethite, and hematite, respectively.

To visualize  $L^*$ ,  $a^*$ , and  $b^*$  values, LESLIE (Laag and Kreutzer, 2022) a modified R code from (Zeeden et al., 2017) was used to transform  $L^*$ ,  $a^*$  and  $b^*$  data into visible RGB values resulting in a colorimetry contrast enhancement function comparable to (Sprafke et al., 2020). Colorimetric enhancement allows detecting small changes in colorimetric properties, invisible by observations made on non-enhanced data.

### Granulometry

Sediment grain size distributions were analyzed at the Laboratoire de Géographie Physique (Meudon, France) using a Beckman Coulter LS 13320 PID230 laser diffraction grain size analyzer. Every 6<sup>th</sup> sample from SK18, for a total amount to 249 samples, was analyzed (see supplementary figure 2). The bulk material was not treated to remove carbonates. Three to four grams of bulk material was transferred into a plastic tube with approximately 90 ml of hexametaphosphate sodium in solution and dispersed for 24 hours in a spinning and overturning rotator. Thereafter, the dispersed sediment was wet sieved through a 160  $\mu\text{m}$  mesh. The <160 $\mu\text{m}$  fraction was measured for grain size distribution on the laser diffractometer and the >160 $\mu\text{m}$  fraction was dried at 30°C for several days in an oven. The mass of the >160 $\mu\text{m}$  dried sediment was measured and the weight percent of the initial sample calculated.

For each analyzed sample, three to five measurements were carried out and averaged. In this study, we consider the laser diffraction upper grain size limit of clay to be 6  $\mu\text{m}$  based on findings in (Antoine et al., 2019). In their study, the standard Robinson sieving and pipette method was used on sediment from the nearby Harletz loess and paleosol sequence (see Fig.1) to determine the corresponding laser diffraction upper grain size limit of clay. Moreover, the present study conducted the grain size analyses on the same apparatus as in (Antoine et al., 2019). Other grain size fraction considered are: fine silt (FSI, 6-20  $\mu\text{m}$ ) content, coarse silt (CS, 20-63  $\mu\text{m}$ ), fine sand (FSA, 63-160  $\mu\text{m}$ ). Grain size index (GSI) and Coarse Silt Index (CSI) are calculated following (Antoine et al., 2019). Unmixing of acquired grain size spectra was performed with aid of the AnalySize software package (Paterson and Heslop, 2015) using a

underlying Weibull distribution. Initial tests were performed on individual grain size spectra stemming from different units to identify the most accurate number of end-members.

#### Mid-Infrared Spectrometry (ATR-FTIR)

At the LGP in Meudon a Bruker Vector 22 ATR-FTIR device was used, operating with the OPUS software. The background signal was measured initially and after every ~20th samples and subtracted from the acquired spectra. Grinded and homogenized sample material (e.g., 4-5 mg) was placed on the surface of a diamond. A compression apparatus was then closed and with aid of a resistance dependent screw (allowing always the same pressure of the samples material towards the diamond) was tightened. Measurements were conducted in absorbance mode, using a  $8\text{ cm}^{-1}$  resolution and 64 measurements were applied per sample in order to increase the quality of the spectra. To identify the mineral assemblage of the bulk sample, no discrimination between clay and silt fractions was carried out. This was willingly avoided because potentially preserved volcanic glass shards may have larger grain sizes than the commonly used clay or fine silt fraction, in which case would be overlooked. To identify different mineral compositions, discriminative wavenumbers were obtained in the literature (Cornell and Schwertmann, 2003; Udvardi et al., 2014) compiled for a representative paleosol, loess and tephra sample in supplementary figure 3. Before qualitative mineral abundance determination, a baseline correction was performed, where each spectrum was subtracted at each wavenumber by its absorbance intensity at  $4000\text{ cm}^{-1}$ . A schematic procedure of qualitative mineral abundance identification is visualized for calcite and dolomite in supplementary figure 3. Similar to DRS-derived hematite and goethite extractions, a range of minima and maxima absorbance intensities was identified. The absolute difference between these values was taken as the individual qualitative mineral abundance where single peaks are addressing per wavenumber one individual mineral. Table 2 shows which minerals were extracted at which wavenumber.

Mineral (composition)	Wavenumber (cm <sup>-1</sup> )	Reference
Dolomite and Calcite	1428	(Farmer, 1974; van der Marel and Beutelspacher, 1976; Vaculíková and Plevová, 2005)
Smectite	1650	(van der Marel and Beutelspacher, 1976)
Kaolinite	3696	(Wada, 1967; Farmer, 1974; Madejová and Komadel, 2001; Vaculíková and Plevová, 2005; Jung et al., 2010)
Goethite	450	(Cornell and Schwertmann, 2003)

**Table 2: ATR-FTIR minerals extracted in this study and their wavenumber positions.**

### Improving the correlative age model

The correlative age model in (Jordanova et al., 2022) for SK18 holds true for the Pleven LPS indicating it covers the last ~ 800 kyrs (MIS 20-MIS0). However, with the high-resolution colorimetry-derived qualitative hematite and goethite contents acquired in this study, attempt to improve the correlative age model is made. The starting correlative age model uses tiepoints from (Jordanova et al., 2022). Tiepoints were adjusted iteratively considering in addition to increases of  $\Delta\chi$  increases, increases in  $TBA_{Hema}$  and  $TBA_{Goeth}$  to identify glacial terminations. Additional tiepoints were introduced to increase overall running correlation if additional tiepoints did not result in significant changes in correlative age of tiepoints in (Jordanova et al., 2022). Finally, age-depth conversion was performed using the QAnalySeries software (Kotov and Pälke, 2018).

## Results

### Environmental magnetism

From concentration dependent magnetic parameters displayed in Figure 2 alongside the stratigraphy, the 4 youngest paleosols (S4 to S1) and the recent Holocene soil (S0) show systematically high values in  $\chi_{lf}$ ,  $\chi_{ferri}$ ,  $\chi_{hifi}$ ,  $M_s$  and  $M_{RS}$ . Compared to paleosols S3-S0, S4 shows the lowest magnetic concentrations.



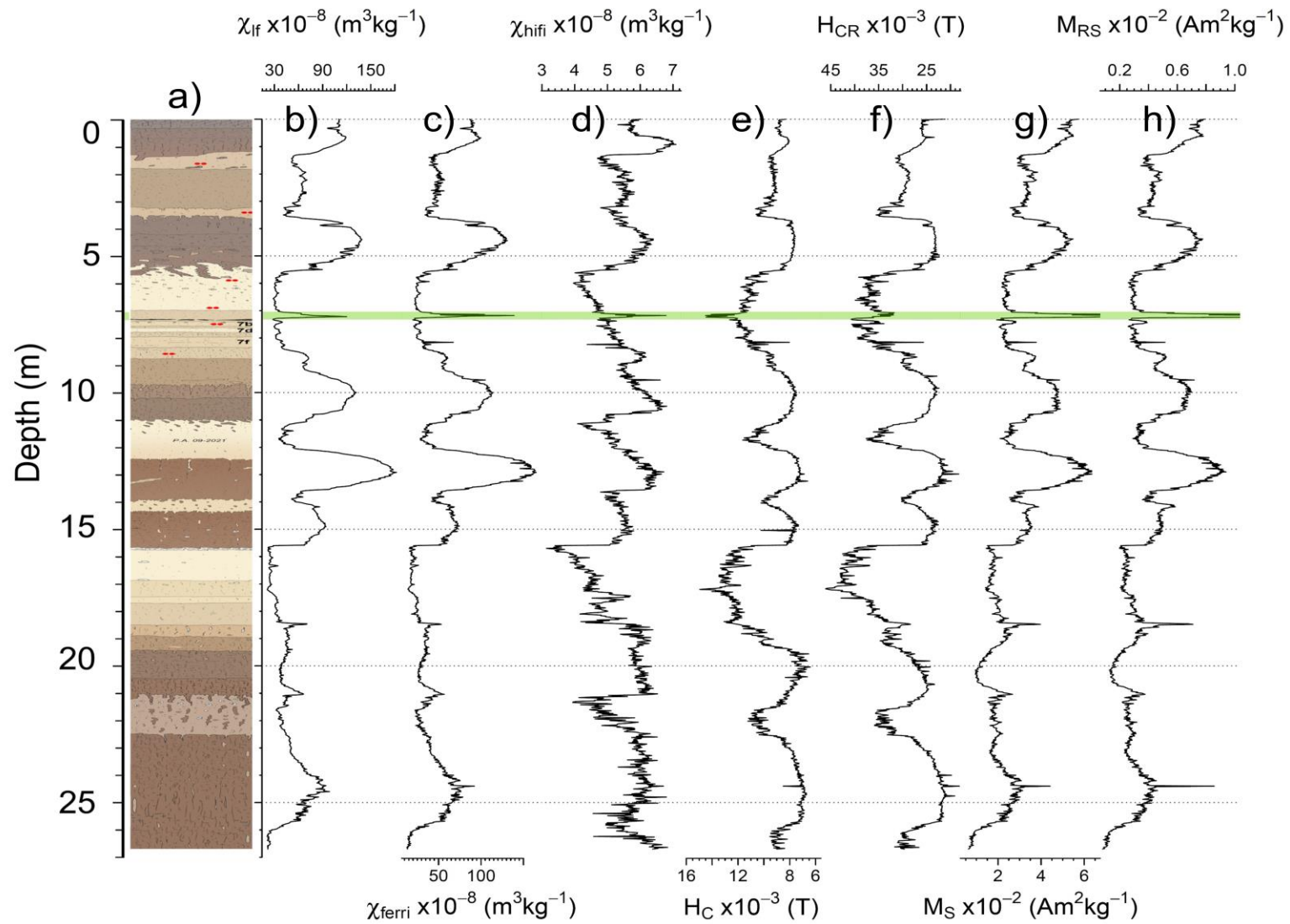


**Figure 2: Magnetic susceptibility parameters and coercivity and magnetization parameters on depth scale. a) displays the stratigraphic drawing, b) the low-field magnetic susceptibility, c) the ferrimagnetic susceptibility, d) the high-field magnetic susceptibility, e) the coercivity force, f) the coercivity of remanence, g) the saturation magnetization, and h) the remanent saturation magnetization. As a horizontal green bar, the in-field outcropping L2 tephra is indicated.**

The older part of the Pleven LPS reflects a significant change in the magnetic concentration with amplitudes of variations significantly subdued in comparison to the upper half of the profile. An exception is  $\chi_{\text{hifi}}$ , which shows variations of similar or greater amplitude, similarly to  $H_C$  and  $H_{CR}$ .

The outcropping L2 tephra layer (indicated in Fig. 2 with a green horizontal bar) displays a sharp and well-pronounced peak in all concentration dependent parameters. For  $H_{CR}$  a weaker local maximum is observed, while  $H_C$  shows a sharp local minimum. Elsewhere throughout the profile, several sharp peaks of different magnetic parameters can be observed.

Figure 3 compiles magnetic grain size dependent ratios.  $\chi_{\text{lf}}$  is shown providing a stratigraphy reference frame of the profile. The absolute frequency dependence of magnetic susceptibility  $\Delta\chi$  is a reliable indicator of pedogenetically neo-formed magnetic particles with a narrow grain size overlapping the unstable single domain (superparamagnetic, SP) to stable single domain grain sizes. The threshold between SP and SD particles at room temperature is about 30nm (Moskowitz, 1980), where ferrimagnetic minerals such as the low coercivity magnetite and maghemite minerals play an overall role.  $\Delta\chi$ ,  $\chi_{\text{lf}}$  and  $\chi_{\text{ferri}}$  co-vary suggesting that soft-magnetic ferrimagnetic minerals dominates the superparamagnetic fraction. In the lower part of the profile (profile base up to 16 m)  $\Delta\chi$  suggest minimal SP content while  $\chi_{\text{ferri}}/M_S$ , which also tracks SP concentration if assuming a single magnetic mineral assemblage, shows significant maxima through S6 and S5. In a mixed mineral assemblage, a significant increase in the relative proportion of a low  $M_S$  mineral (e.g. hematite) with respect to a high  $M_S$  mineral (e.g. magnetite) would lead to  $\chi_{\text{ferri}}/M_S$  increasing. The similar variations of  $\Delta\chi$  and  $\chi_{\text{ferri}}/M_S$  above 16 m suggest that  $\chi_{\text{ferri}}/M_S$  is tracking changes in SP concentration (relative proportions of the magnetic mineral assemblage remains constant). Contrasting variations of  $\Delta\chi$  and  $\chi_{\text{ferri}}/M_S$  below 16 m suggest a major change in paleosol magnetic mineral assemblage likely to a more hematite rich assemblage relative to the soft ferrimagnetic component, which is also supported by the S-ratio. The ratio of the anhysteretic remanent magnetization (ARM) normalized by the

low-field magnetic susceptibility ( $\chi_f$ ) can be an indicator for SD-magnetic grain sizes. Paleosols have higher SD abundances than loess units. A slight trend of increasing SD contribution with time is observed from the base of the profile to its top.

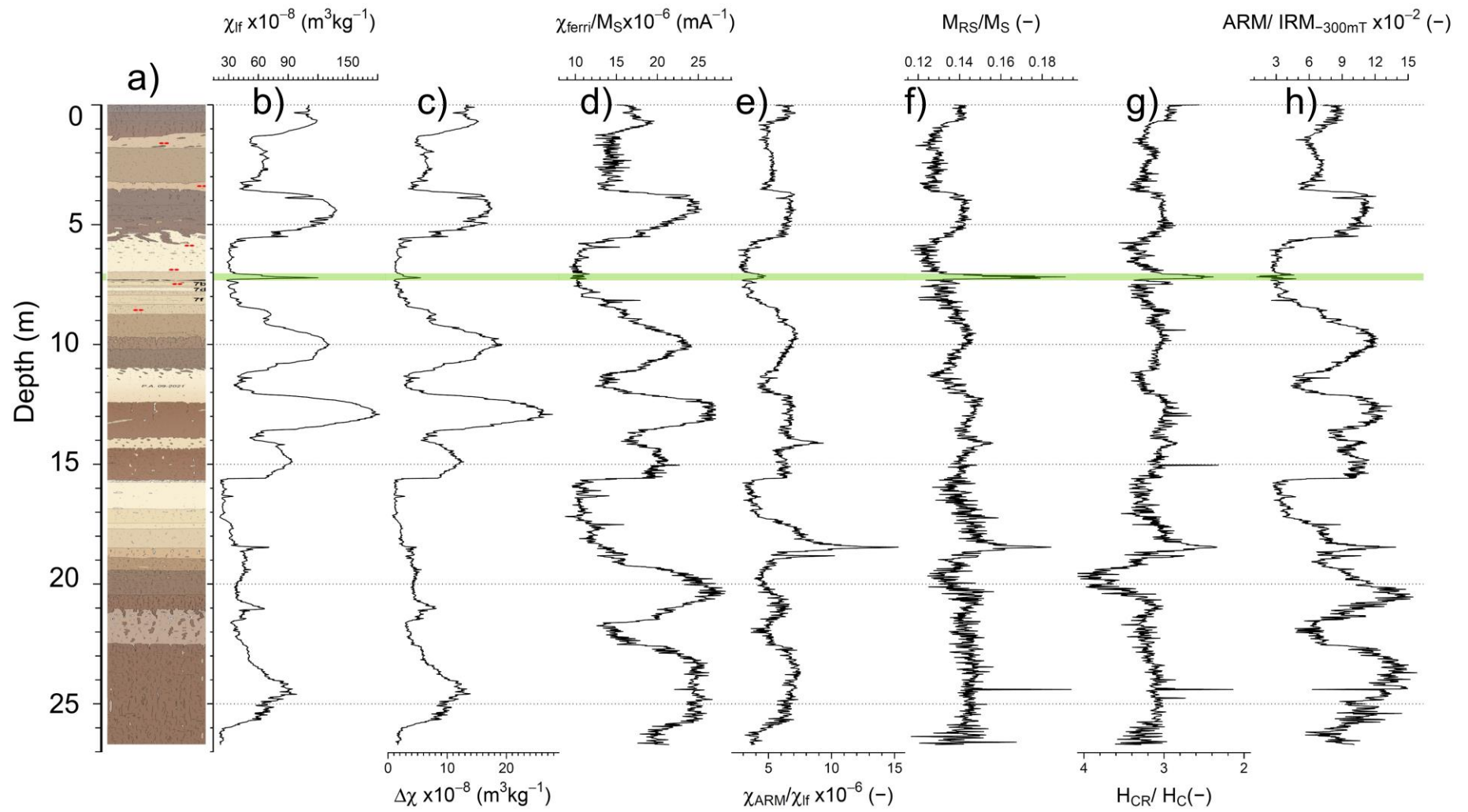


**Figure 3: Grain size dependent magnetic parameters on depth scale. A) and b) display the stratigraphical drawing and the low-field magnetic susceptibility as orientation. Panel c) shows the frequency dependence of magnetic susceptibility with high values indicating the presence of more SP particles. Panel d) displays with  $\chi_{\text{ferri}}/M_S$  another magnetic ratio sensitive for SP particles under the assumption, that MS is mono-mineralic. Divergence of  $\Delta\chi$  and  $\chi_{\text{ferri}}/M_S$  indicates mineralogical change of SP particles for older paleosols below 16m. Panels e)-h) display other grain size sensitive magnetic proxies indicating with higher values more coarser grain sizes.**

In (Jordanova et al., 2022), peaks in SD magnetic grain size concentration, interpreted from peak values of both  $\chi_{\text{ARM}}$  and  $\chi_{\text{ARM}}/\chi_{\text{lf}}$ , are associated major (crypto)tephra layers for which there occurrence is confirmed optically. Relatively coarser magnetic grain sizes contained in (crypto)tephra layers appears supported by other grain size dependent parameters such as  $M_{\text{RS}}/M_S$ .

Low-field magnetic susceptibility ( $\chi_{\text{lf}}$ ) and its comparison to its absolute frequency dependence ( $\Delta\chi$ ) provide the general magnetic behavior of the Pleven LPS with respect to the magnetic enhancement model, where paleosols have increased  $\chi_{\text{lf}}$  and  $\Delta\chi$  values. Figure 4 a) shows a commonly applied magnetic enhancement plot, where the paleosols S4 – S0 show both enhanced  $\chi_{\text{lf}}$  and simultaneously enhanced  $\Delta\chi$  values. The background susceptibility ( $\chi_{\text{B}}$ ) represented by the y-axis ( $\chi_{\text{lf}}$ ) intercept value indicates a  $\chi_{\text{B}}$  detrital susceptibility of  $18.61 \pm 0.31 \times 10^{-8} \text{ m}^3\text{kg}^{-1}$ . This value is low compared to other LPSs of eastern Europe, e.g., Zemun (SRB) where  $\chi_{\text{B}}$  is  $24.6 \times 10^{-8} \text{ m}^3\text{kg}^{-1}$  (Laag et al., 2021), Sedlec and Zemechy with 22 and  $23 \times 10^{-8} \text{ m}^3\text{kg}^{-1}$  (Forster et al., 1996), yet higher than  $\chi_{\text{B}}$  for Asian and Chinese loess with  $17 \pm 2 \times 10^{-8} \text{ m}^3\text{kg}^{-1}$  (Forster et al., 1994), and Romanian loess at Semlac with  $10 \times 10^{-8} \text{ m}^3\text{kg}^{-1}$  (Zeeden et al., 2016). The overall correlation between  $\chi_{\text{lf}}$  and  $\Delta\chi$  is  $r^2 = 0.96$ . The highest magnetic enhancement is observed in S3 paleosol, followed by S2 and S1 in decreasing magnitude. The lowest magnetic enhancement is found in the loess units L7, L5 and L2. The generally lower magnetic enhancement in loess units compared to paleosol units is typical for LPSs. Thus, L2 and L5, representing MIS 6 and MIS 12, experienced the harshest glacial conditions significantly limiting the neo-formation of SP-particles. Outlier samples from the L2 loess unit are associated to tephra layers and show the same magnetic behavior as observed for the L2 and Bag tephra of the Zemun LPS (Laag et al., 2021). Reduced  $\Delta\chi$  and higher  $\chi_{\text{lf}}$  is also

observed from the Iranian LPS Neka for a tephra layer in-depth evidenced by geochemical data of glass shard (Kehl et al., 2021). Figure 4a suggests that magnetic enhancement is limited in the older paleosols S5 and S6 compared to younger paleosols. However,  $\chi_{\text{ferri}}/M_s$  and S-ratio provide strong evidence that hematite dominates the pedogenic mineral assemblage in S5 and S6 instead of magnetite and maghemite which dominate the younger paleosols' pedogenic mineral assemblage.

Figure 4c shows a King-Plot (King et al., 1982), addressing the magnetic grain size in a bi-plot of the  $\chi_{\text{lf}}$  and  $\chi_{\text{ARM}}$ . Samples stemming from L5 indicate the smallest magnetic grain sizes where samples stemming from the L2-tephra layers represent the overall largest grain sizes. The majority of all Plevn LPS-samples plot in a mean grain size range of 0.1  $\mu\text{m}$  or less, whereas parts of S4, S0, loess and clay units indicate larger mean grain sizes between 0.1 and 0.2  $\mu\text{m}$ . Figure 4d plots  $\chi_{\text{lf}}$  against  $\chi_{\text{ferri}}$  and confirms that ferrimagnetic minerals control variation of the bulk low-field magnetic susceptibility. In case, that all magnetic susceptibility would be carried by the ferrimagnetic minerals maghemite and magnetite, there would be a 1:1 dependency indicated in this bi-plot. However, this is not the case and indicates, that there are other magnetic minerals such as hematite and potentially goethite present. The largest deviation of the trend line is present in the older paleosols S6 and S5. This magnetic mineral difference is further evidenced by the bi-plot of  $\Delta\chi$  and the S-ratio (Fig. 4e). The clay unit up to L5 loess unit trend over lower S-ratio values (i.e. higher relative proportion of high coercivity minerals, such as hematite) than units above. The L2 tephra samples are characterized by the highest S-ratio, trending higher than units from S4 through S0.

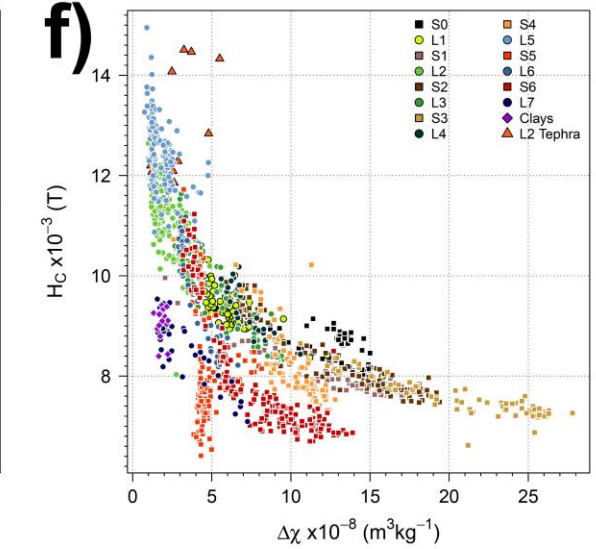
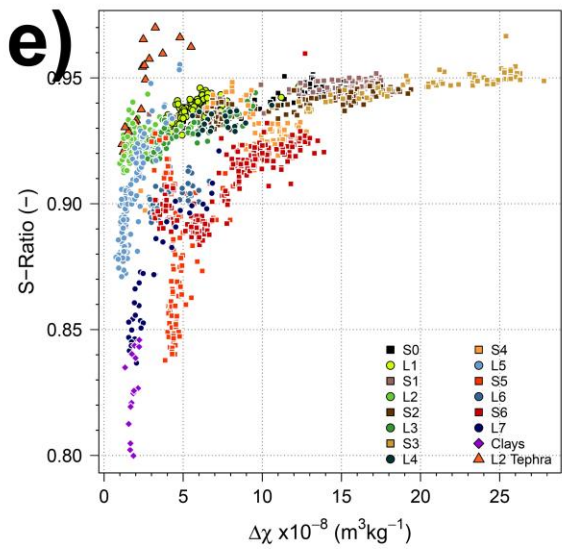
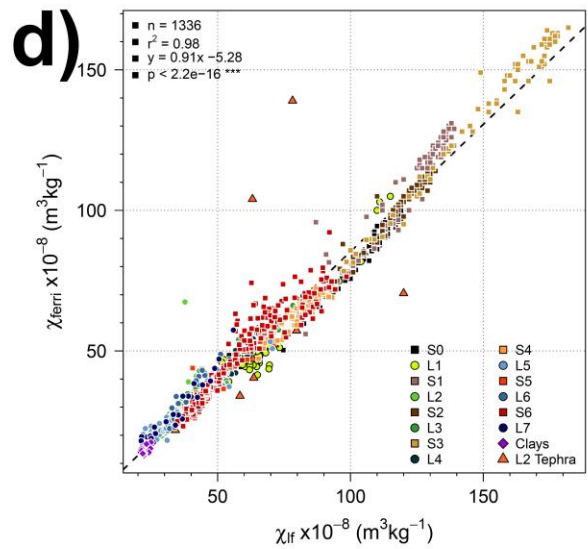
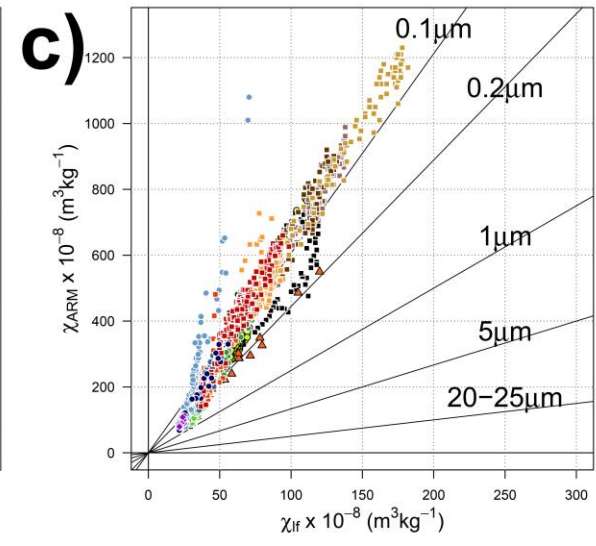
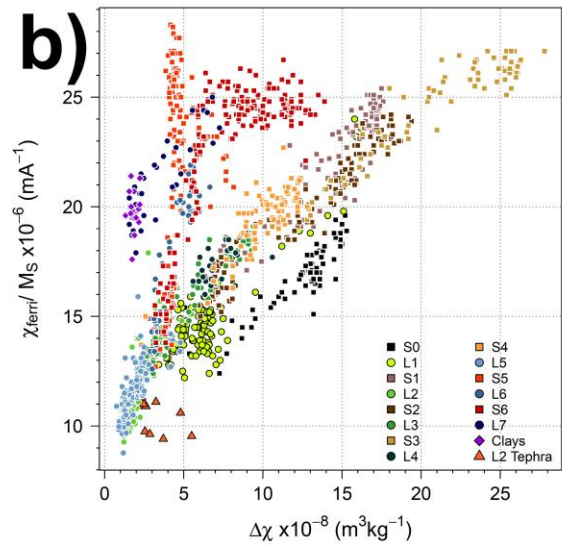
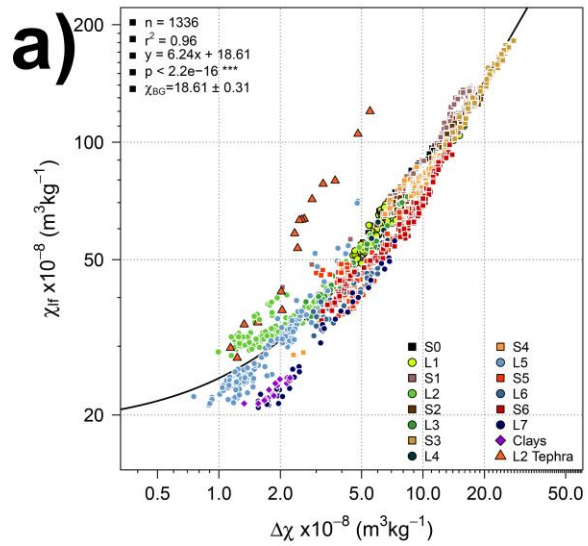




**Figure 4: Standard magnetic parameters applied to all samples. Samples stratigraphical origin can be found in the legend. Panel a) shows the magnetic enhancement plot, b) the comparison of both sensitive to SP particles  $\Delta\chi$  and  $\chi_{\text{ferri}}/M_S$  values, where paleosols of S5 and S6 indicate mineralogical change. Panel c) shows the King plot, indicating absolute grain sizes and shows that the outcropping L2 tephra layer has coarser magnetic grains. Panel d) shows the low-field magnetic susceptibility and ferrimagnetic magnetic susceptibility and reflects that the dominating magnetic susceptibility is carried by ferrimagnetic minerals. Panel e) shows that the stratigraphically lower and older paleosols S5 and S6 are rather dominated by higher hematite and goethite concentrations. Panel f) shows that the coercivity is a negative exponential function of the frequency dependence of magnetic susceptibility and that S5 and S6 paleosols are offsite of the trend provided by loess and paleosol units younger than S5.**

#### **Average ferrimagnetism grain size**

The average ferrimagnetic grain size, tracked with the ARM/IRM<sub>300</sub> ratio, was tested versus several magnetic, colorimetric and mid-infrared derived mineralogical parameters. The plot of ferrimagnetic concentration ( $\chi_{\text{ferri}}$ ) and average ferrimagnetic grain size (Fig 5a)) distinguishes paleosol units above 16 m having higher ferrimagnetic mineral content and high ARM/IRM<sub>300</sub> values, and paleosols and loess units below 16 m having low ferrimagnetic mineral content and the full range of ARM/IRM<sub>300</sub> values with maximum values for S5 and S6 paleosols and minimum values for L5 loess. The highest ferrimagnetic concentration and lowest values of ARM/IRM<sub>300</sub> are observed for the L2 tephra samples.

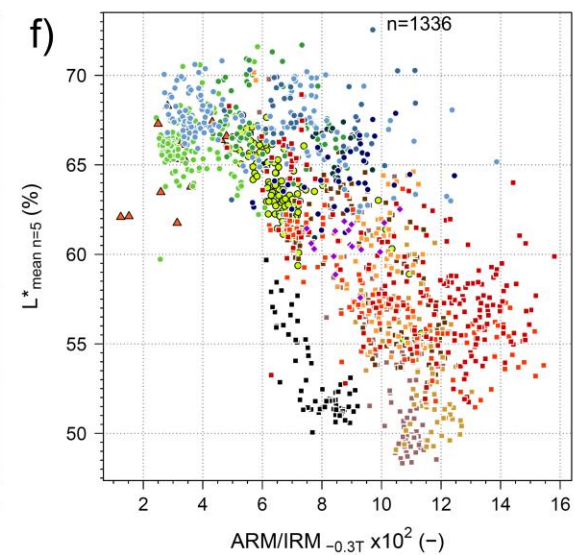
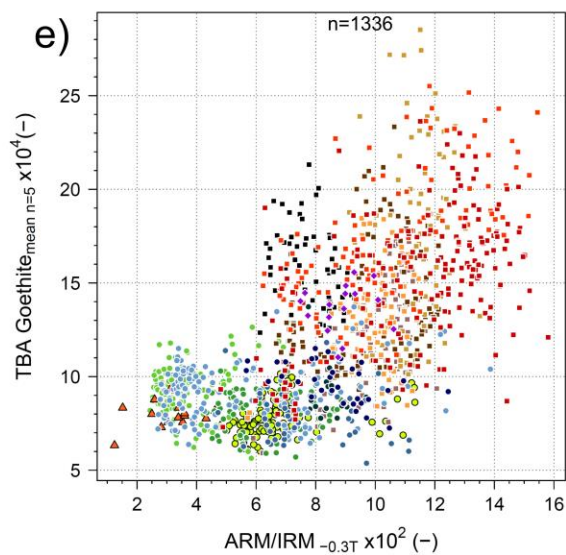
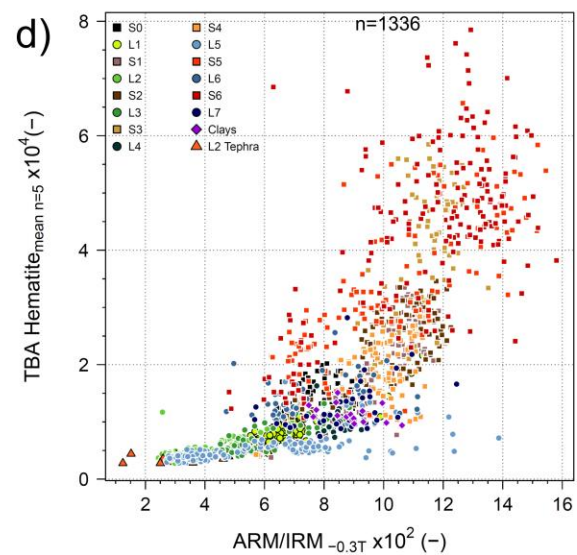
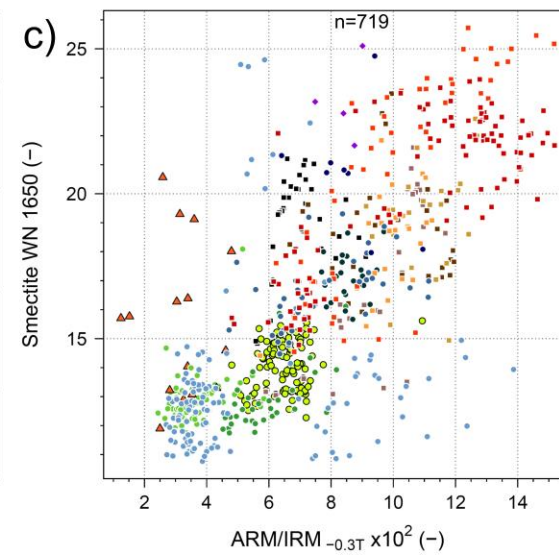
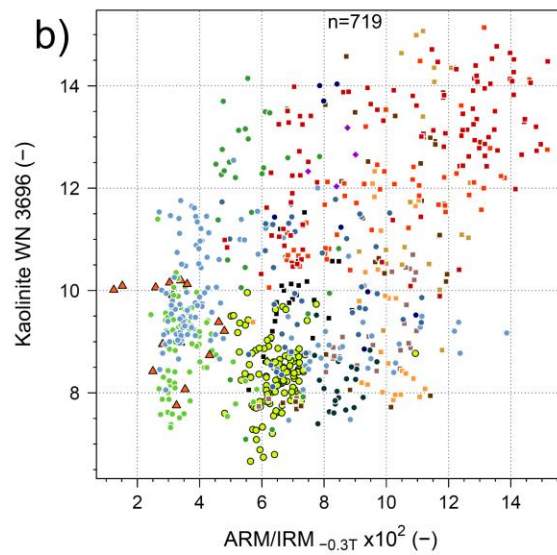
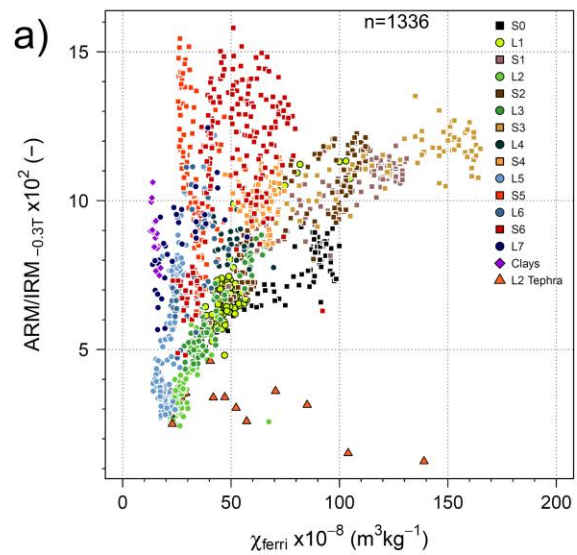


## **Figure 5: Integration of magnetic, colorimetric and mid-infrared derived mineral compositions.**

Combining mid-infra-red results indicating the qualitative content of kaolinite with the average ferrimagnetic grain size provides a rather diffuse relationship with no clearly observable dependence (Fig. 5b). However, smectite content and ARM/IRM<sub>300</sub> (Fig. 5c) seems to be better correlated. This correlation shows also that the outcropping L2-tephra layer seems to stick out in terms that the average ferrimagnetic grain size is rather small but the overall smectite content (which is besides a pedogenesis/seasonality indicator an indicator for weathered tephra glass material) increases significantly. The correlation of TBA<sub>Hema</sub> (hematite content) with the average ferrimagnetic grain size displays an exponential relationship. Samples from all loess units show low TBA<sub>Hema</sub> and ARM/IRM<sub>300</sub> values, whereas intensely weathered reddish paleosols of S6, S5 and S3 units display the highest values for both parameters. In Figure 5 e) the correlation towards TBA<sub>Goeth</sub> is less pronounced than that for TBA<sub>Hema</sub> (Fig. 5d). Overall, in the Figure 5f, the luminance ( $L^*$ ) is correlated to the average ferrimagnetic grain size and a clear negative trend can be observed.

### **High temperature magnetic susceptibility**

The heating and cooling curves are generally non-reversible, indicating, despite the Ar-atmosphere, that alteration and/or neoformation of magnetic minerals has occurred. Possibilities are the transformation of clay minerals into magnetic minerals, and the oxidation or the reduction of iron oxides or oxyhydroxides.. For the majority of the samples investigated, unblocking temperatures ( $T_{UBs}$ ) are in the range of 570-590°C indicative of magnetite (Supplementary Figure 4). Several samples from S2, S3, and S4 interglacial paleosols have lower  $T_{UBs}$  while the lowest  $T_{UBs}$  are observed in S5 paleosol and in the underlying clay unit. Nearly all heating curves show a further decrease in susceptibility beyond the  $T_{UB}$  of magnetite at c. 585°C suggesting the presence of hematite (Supplementary Figure 5).

Meta-stable maghemite transforms to stable hematite during heating (Özdemir and Banerjee, 1984) at about 500°C. Since maghemite is a ferrimagnetic minerals, it has a higher magnetic susceptibility than canted-antiferromagnetic hematite (Hunt et al., 1995; Dunlop and Özdemir, 2013). The transformation of maghemite into hematite consequently leads to a decrease in susceptibility. Relative maghemite content was extracted from heating curves by selecting a maximum in susceptibility reached around 200°C and a minimum in susceptibility reached around 430-500°C and calculating the difference in susceptibility ( $\chi_{Magh}$ ) following (Gao et al.,

2019). The stratigraphic fluctuations of extracted  $\chi_{\text{Magh}}$  contents mimic remarkably well the variations with depth of the frequency dependence of magnetic susceptibility. Since interglacials have relatively moist and warm prevailing climates, the  $\chi_{\text{Magh}}$  could be confirmed as a reliable precipitation indicator at least for the interval between onset of S4 to the top of the profile.  $\chi_{\text{Magh}}$  was then used to tentatively determine absolute mean annual precipitation values (MAPs) following a recent study by (Gao et al., 2019), providing a paleo-precipitation climo-function based on meteorological data from the Chinese Loess Plateau and proposing the following regression function:

$$\text{MAP (mm)} = 102.16 \times \ln(X) + 139.37$$

Given that the paleo-precipitation climo-function was developed from Holocene soil in a different region than the present study, the reconstructed MAP values obtained for the Plevén LPS are compared with a recently conducted study by (Krapp et al., 2021), which provides statistically calculated MAP values for the Plevén LPS location based on different paleoclimatic archives such as e.g., loess-paleosol sequences,  $\delta^{13}\text{C}$  values of speleothems.

However, the comparison between MAP values calculated with aid of the regression function derived from  $\chi_{\text{Magh}}$  and modelled MAP values for the last 800 ky by (Krapp et al., 2021) are in general in well agreement. Precipitation values are both increased during interglacials and low during glacials. The lowest values in both data series can be observed in the rather intense glacials MIS16, MIS12 and MIS6. Hence, the modelled MAP values reflect in Krapp a rather kind of obliquity cyclicity which is not observed in  $\chi_{\text{Magh}}$  data for Plevén since the resolution is not high enough. However, modern MAP values for Plevén are 578 mm, which is closely falling together with  $\chi_{\text{Magh}}$  calculated values for the youngest sample with 528mm at ca 3 ka.

### **IRM acquisition unmixing**

IRM component unmixing provided robust results leading to generally 4 components and a 5<sup>th</sup> component required when a tephra layer is present. In total 263 samples were analyzed and the absolute contributions of each component to the bulk  $M_{\text{RS}}$  is shown in Figure 6. Component #1 (mean Bh of  $22.1 \pm 4.1$  mT) is interpreted as the magnetite/maghemite contribution to the bulk signal. It co-varies well with magnetic susceptibility, which is dominantly influenced by the ferrimagnetic component ( $\chi_{\text{ferri}}$ ), as demonstrated previously. Component #2 (mean Bh of  $85.2 \pm 11.9$  mT) shows an overall increasing trend from the base to the top of the profile. This component is interpreted as weak magnetic / antiferromagnetic iron oxides such as fine-grained hematite. All paleosols have increased C#2 contributions. Component #3 (mean Bh of  $4.9 \pm$

1.9 mT) reflects most likely fine-grained ferrimagnetic / pedogenic and /or MD particles. Higher C#3 contributions are reached in the paleosols and in the tephra layers with the highest C#3 contribution in paleosol S3. Component C4# (mean Bh of  $479.5 \pm 125.9$  mT) is the highest coercivity of remanence component likely associated to hematite and partially magnetized goethite. It is rather ill-defined (broad dispersion) compared to the other components. (Crypto)tephras appear as sharp and high peaks in C#4, indicating the presence of harder coercivity minerals. (Crypto)tephra identification with IRM unmixing seems to be a promising tool for future hunt of these stratigraphic and chronological marker horizons. First investigated in (Laag et al., 2021) and further investigated for this study, the systematic requirement of a 5<sup>th</sup> and well defined component here with an average of  $39.1 \pm 7.6$  mT leads to the identification of further crypto-tephras.

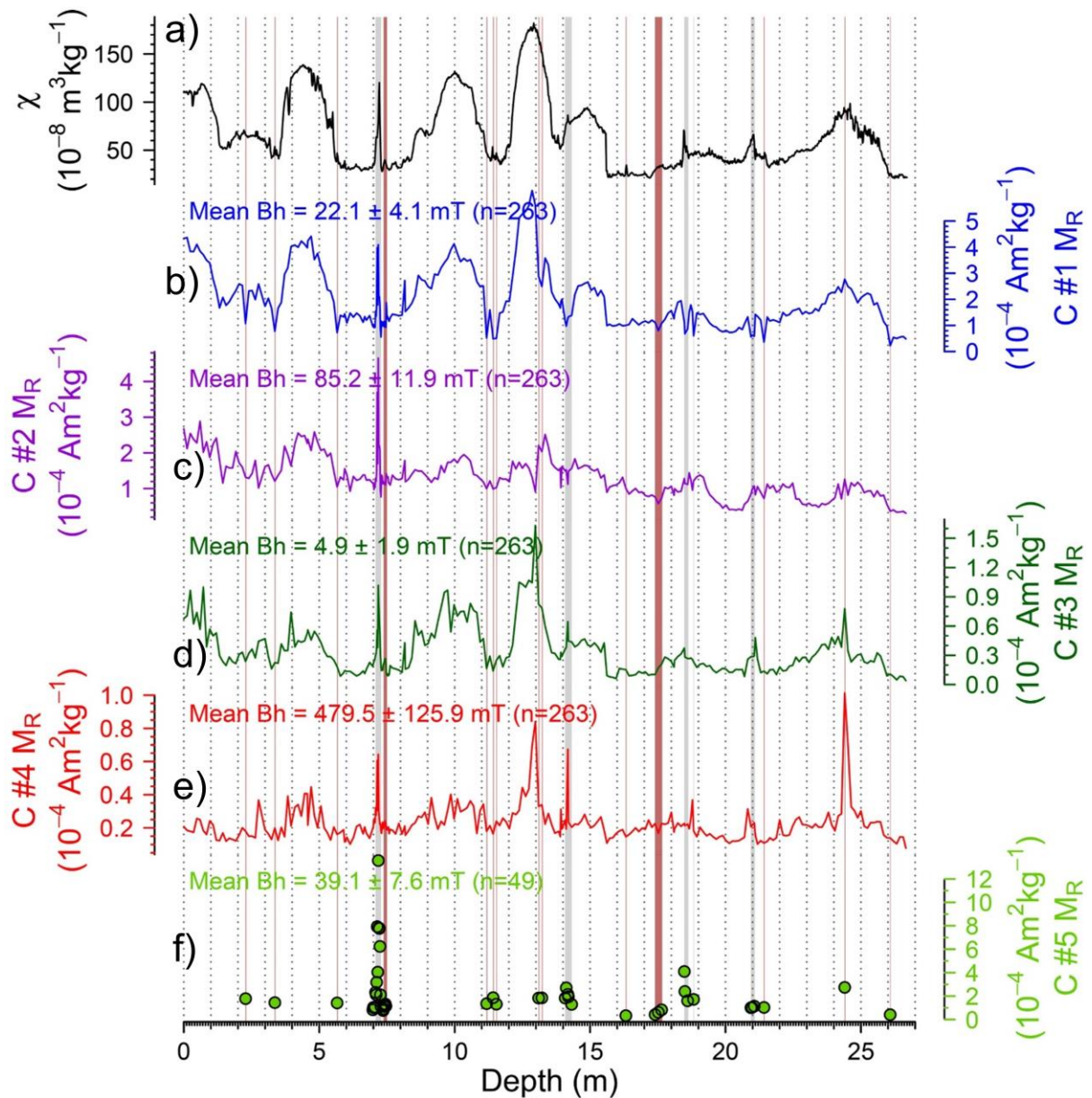


**Figure 6: Stratigraphical presentation IRM component unmixing results.**

The vertical grey bars shown in Figure 6 indicate the 4 (crypto)tephra layers reported in (Jordanova et al., 2022), where the youngest tephra layer presented is an in-field outcropping tephra layer and samples investigated for IRM acquisition and its unmixing are continuously measured and investigated in L2 covering the whole ash deposition of this tephra layer. The other tephra layers at 18.48, 18.80 and 21.00m reflect the same necessity of a 5<sup>th</sup> component. Despite these tephra layers, several other samples required a 5<sup>th</sup> component and are shown as brown vertical bars. Unfortunately, not all 1336 samples were investigated with IRM acquisition experiments but a fraction of n=263 (see supplementary figure 2). This leads to the



non-investigation of samples, which might contain other crypto-tephras. However, taken this information into account, the systematic investigation of IRM acquisition and its unmixing in a consistent resolution might confirm other cryptotephra layer findings, where continuously conducted other magnetic experiments show the same magnetic behavior.

### Colorimetry

Colorimetric experiments provide robust qualitative abundances of hematite, goethite and calcite for the Pleven LPS sequence. In Figure 7, the stratigraphic column,  $\chi_{lf}$ , and the colorimetric parameters Luminance ( $L^*$ , abscissa inverted), redness ( $a^*$ ), extracted goethite and hematite quantitative abundances (displayed as  $TBA_{Goeth}$  and  $TBA_{Hema}$ ) as well as their wavelength peak positions are shown. On the right-hand side of Figure 7, the original (“original”) and enhanced (run 1 & run 2)  $L^*a^*b^*$  data are shown. Overall,  $\chi_{lf}$  and other colorimetric parameters such as  $L^*$ ,  $a^*$ ,  $TBA_{Goeth}$  and  $TBA_{Hema}$  co-vary quasi simultaneously for the depth interval between 0 and 16 m but diverge in their magnitude by comparing different major cycles. In the lower depth interval (16-26.70 m) the  $\chi_{lf}$  appears rather dim but aforementioned colorimetric data expresses high variability with pronounced cyclicity. This cyclicity co-varies with in-field observed alterations between loess and paleosol units and is thus indicated by visualized colorimetric variations on the color-enhanced plot. The paleosol complexes from S1 to S6 vary in the amplitude of the different colorimetric and magnetic parameters. Paleosol complex S6 shows a rather smaller amplitude of  $\chi_{lf}$ , but high amplitudes of  $L^*$ ,  $a^*$ ,  $TBA_{Goeth}$  and  $TBA_{Hema}$ . The highest values are reached in  $TBA_{Hema}$ ,  $a^*$ . The overall highest values of  $TBA_{Goeth}$  and  $\chi_{lf}$  are recorded for paleosol complex S3.



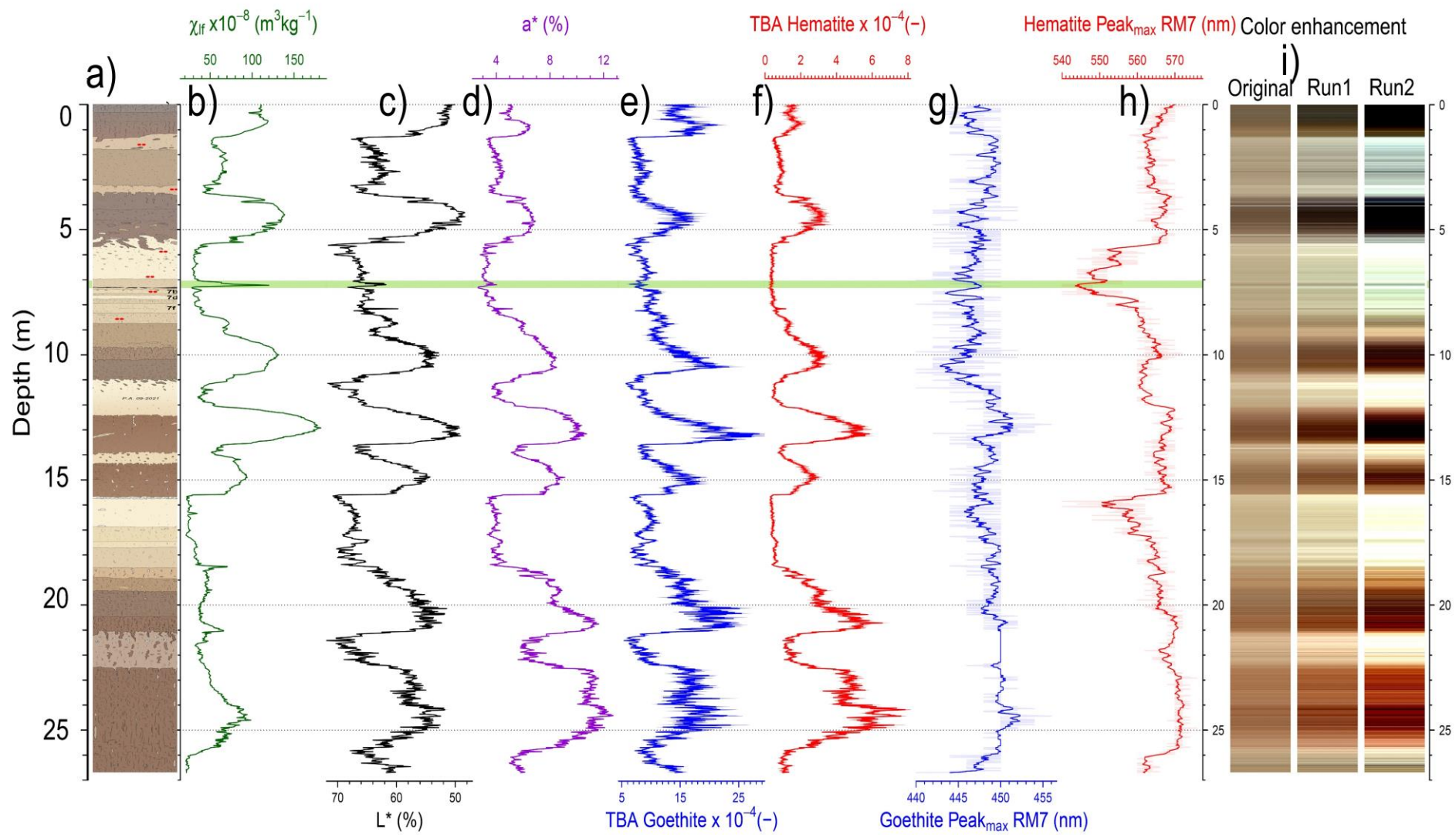


## **Figure 7: Stratigraphical presentation of colorimetric values and color enhancement.**

Shifts in the wavelength position of the absorbance of hematite can indicate either an Al-substitution signal or a grain size related signal. The same holds true for the peak position of goethite. In terms of hematite, the usually indicated range of wavelength-based absorption peak positions is located between 535 and 570 nm in the second derivative of the Kubelka-Munk remission spectra. Differences in the hematite peak position are obvious. Relatively small stoichiometric hematite grains are associated with reddish/yellowish colors with a peak wavelength position of the absorbance between 535 and 550nm (Torrent and Barrón, 2003). Larger hematite grains have a peak position of absorbance between 550 and 570nm, and appear in the color spectrum within the blue-indigo-violet range. (Schwertmann, 1971, 1988) state further that abundances of rather shorter wavelength maxima band positions indicate rather arid conditions. These shifts towards 550nm and below occur during the most intense glacial periods of this record, namely the accumulation of the L5 and L2 loess units. Smaller, but still visible shifts towards smaller wavelengths in the hematite peak waveband positions are found in the L3 and L6 loess packages, indicating the ability of hematite waveband positions able to trace aridity since glacial stages in which loess accumulation is intensified are associated with cold and dry periods. Even the amplitude of shift can be associated by the intensity or harshness of the glacial periods.

### **Granulometry**

Grain size distributions of the Pleven LPS samples show a rather non-typical behavior. First, grain size distributions are multi-modal contrasting with distributions reported from the nearby (~80 km) Harletz LPS (Antoine et al., 2019). Secondly, the typical stratigraphic trends observed in LPS such as increased clays in paleosols and increased coarse silts in loess (e.g. (Antoine et al., 2019), (Wacha et al., 2021)) is disrupted for the Pleven LPS. Clay contents are highly variable and show little correlation with other pedogenic proxies with the exception of youngest portion of the sequence. S1 up to the surface S0 soil follows roughly  $\Delta\chi$ . Taking these initial results into account attempts to include granulometric information in interpretations are considered tentative and less reliable.

Initially, before performing end-member analysis (EMA) different numbers of end-members were tested (n=1-10, Fig. 8a), towards different individual end-member distributions. Criteria for selection of end-members consists of the overall resulting fit of different end-members

compared to the bulk grain size spectrum, the worst as possible-correlation of different end-members compared to each other (indicating overfitting when increasing), and the general overlap of end-members, which might be assigned to the selection of too many endmembers, where 2 or more individual end-members assign rather a single end-member. As manually identified before, the grain size spectra of the Pleven LPS contain 4 to 5 individual endmembers following a Generic Weibull distribution rather than a log-normal distribution. A 5<sup>th</sup> endmember was necessary to be introduced by several samples. Interestingly, the individual end-members do not exactly follow grain size classes mentioned before, this mismatch is most-dominant for finer grain size classes of fine silt and clay.

The result of the a-priori evaluation of end members and underlying distributions reflects for a general Weibull distribution and the selection of 5 end-members the best model to be applied for the Pleven LPS. The selection of 5 end-members has (compared to lower numbers of end members) the highest explained variance and simultaneously the lowest maximum correlation coefficient between single end members. The end member distribution does not follow exactly the grain size classification as indicated in Figure 8b. The End member (EM) #1 covers very well the clay-fraction indicated below 6  $\mu\text{m}$ . EM#2 covers both the larger grain sizes of the clay fraction and the smaller grain sizes of the fine silt fraction. The EM#3 covers both the fine silt and medium silt fractions but with its maximum fractional abundance more inside the medium silt fraction. End member #4 falls inside the coarse silt fraction. The fine sand fraction is represented by end member #5. In Figure 8c the percentages of each end member are shown stratigraphically. For EM#1 there is from the bottom towards the upper end of unit S5 a slight decrease of clay particles recognizable, followed by a low contribution of clay particles in L5. In L5 2 distinct peaks of fine-grained material can be observed which can be traced also in the other end members. End member #3, #4 and #5 reflect a rather coarse grain enhancement in the L5 loess of a similar amplitude compared to the L2 loess unit. Inside the L2 loess, there is the in-field outcropping L2-tephra (marked by the distinct peak in the magnetic susceptibility) and the end member #4 shows a relatively large contribution towards the bulk grain size composition. In general, the coarser end members show in the profile tephra layers such as at 21 m, as well as at 18.48 and 18.80m which were already magnetically identified in (Jordanova et al., 2022).

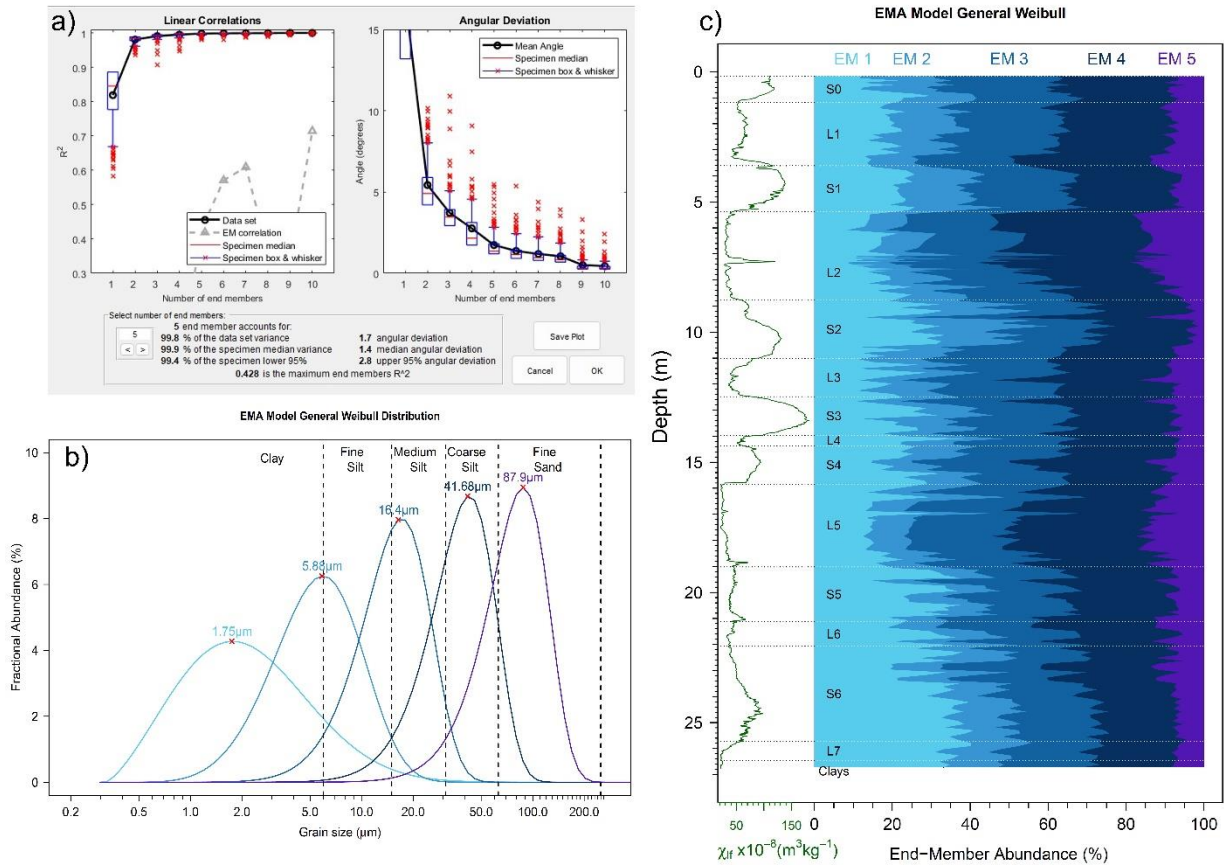


**Figure 8: Grain size end member modeling. A) a-priori analysis of the selection of the end member amount in combination with the underlying distribution model. B). Performed end member analysis and their fractional abundance with grain size classes indicated. In c) the same color coding as used in b) was applied to display the unique end-member abundance and compared to the susceptibility log of the profile.**

However, the grain size intervals are commonly at a 12cm resolution, whereas the magnetic data is measured for each sample at 2cm resolution. It could be that the grain size variations do not always reflect tephra material since it could be oversampled. A higher resolution of grain size measurements equivalent to that of the magnetic and colorimetric measurements will potentially allow a further discrimination perspective between tephra and loess material.

#### ATR-FTIR mid infrared spectrometry

The combination of ATR-FTIR derived calcite and dolomite contents stemming from the extracted magnitude at a wavenumber of  $1428 \text{ cm}^{-1}$  was tested towards the DRS-derived luminance ( $L^*$ ). The underlying assumption is that  $L^*$  (brightness) increases with higher  $\text{CaCO}_3$  contents. Based on 719 investigated samples, we can confirm that the  $L^*$  increases as

expected in well agreement with the ATR-FTIR derived calcite and dolomite content. All loess units express higher  $L^*$  and Calcite and Dolomite values compared to paleosol samples. The Holocene soil unit S0 shows an absence of calcite, meaning that all calcite is completely leached out of this layer. Followed by S5 and S3, additional evidence for paleosols calcite leaching can be shown. Derived smectite and kaolinite contents both increase in paleosols. The maximum values for smectite are reached in the S5 paleosol complex whereas kaolinite maxima are reached in the S6 paleosol complex. Hence, both smectite and kaolinite seem to be more present in S6 and S5 compared to the younger paleosols. Furthermore, smectite contents peak sharply at various depths, which are not association from field investigations with interglacial paleosols.

#### Correlative age model

The correlative age model reported in (Jordanova et al., 2022) is improved here (Fig. 9) following the same approach of identifying major glacial terminations in proxy data and correlating them to well-accepted terminations of the global benthic foraminifera  $\delta^{18}\text{O}$  LR04 stack (Lisiecki and Raymo, 2005). In (Jordanova et al., 2022) glacial terminations were identified from  $\Delta\chi$  data. Here,  $\text{TBA}_{\text{Goeth}}$  and  $\text{TBA}_{\text{Hema}}$  data are used to refine the stratigraphic positions of glacial terminations and are found particularly useful for the older segment of the Pleven LPS sequence. In addition, goethite content derived from  $\text{TBA}_{\text{Goeth}}$  allows a tentative correlation to sub-orbital / millennial scale climate changes for the last interglacial/glacial cycle via the comparison of  $\text{TBA}_{\text{Goeth}}$  with the Greenland Ice Core NGRIP  $\delta^{18}\text{O}$  record (Rasmussen et al., 2014). Arguments for this relationship are presented in the discussion section of this study. Finally, all age-depth tiepoints visualized in Figure 9 are displayed in the supplementary table 2.

A key observation suggested by the improved age model (Fig. 9) is that dust accumulation rates at Pleven varied over time but never stopped completely. Hence, interpretations of pedogenic processes shaping the Pleven LPS record should consider an accretionary soil formation model instead of a down-building soil formation model.



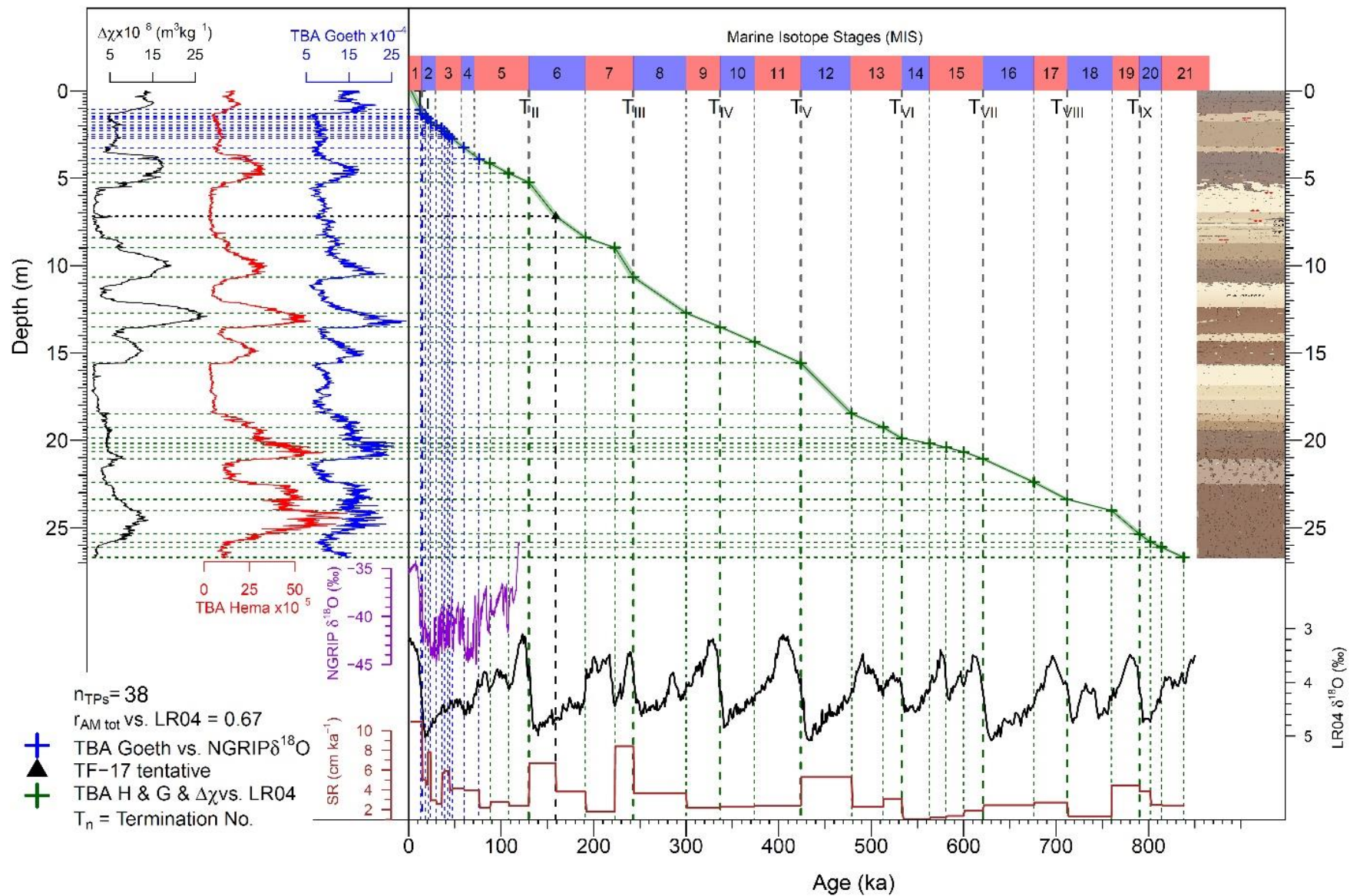


**Figure 9: Refined correlative age model for Pleven. On depth scale, pedogenesis indicating frequency dependence of magnetic susceptibility  $\Delta\chi$ ,  $TBA_{Hema}$  (red) and  $TBA_{Goeth}$  (blue) are shown. Marine Isotope stages (MIS) are indicated in the top on age scale. NGRIP  $\delta^{18}O$  values are displayed in dark-violet. Below, the LR04 stack is shown. Calculated sedimentation rates (SR) are displayed in brown. Blue dotted lines indicate correlations between Pleven and NGRIP, dark green dotted lines display correlations of Pleven towards LR04.**



## Discussion

Tephra layers are important marker horizons and known to be preserved in Eastern European LPSs. Several studies focused on magnetic stratigraphy of thick LPSs recorded in stratigraphically similar levels, as for instance strong peaks in magnetic susceptibility and grain size dependent parameters (Wacha et al., 2011; Marković et al., 2015; Song et al., 2018; Zeeden et al., 2018; Scheidt et al., 2021; Jordanova et al., 2022). In-field outcropping tephra layers have been geochemically investigated and linked to highly explosive volcanic eruptions stemming from the Italian volcanic provinces, such as for the well-known Campanian ignimbrite Y5 (Fitzsimmons et al., 2013), recognized as several decameters thick ash deposits in Romania. The preserved glass shards can be investigated through their geochemical composition and afterwards linked to extensively analyzed and  $^{39}\text{Ar}/^{40}\text{Ar}$  dated tephra-rich records such as the Fucino Basin (Giaccio et al., 2017, 2019; Leicher et al., 2022), Lake Ohrid (Leicher et al., 2021) and Tenaghi Philippon (Vakhrameeva et al., 2018; Wulf et al., 2018) archives. For the first time, we analyzed in the Eastern European Region a continuous, 850-ky-long LPS sequence using a high-sampling resolution multi-proxy approach. Learning from in-field outcropping tephra layers, and assuming that similar explosive silicic eruptions provide similar magnetic signatures, our approach integrates magnetism, colorimetry, mid-infrared spectrometry. We found, that several magnetic parameters are discriminative for the grain size and magnetic mineral assemblage as well as interparametric ratios typical for highly explosive ash deposits. In addition, FTIR-data, especially qualitative Smectite contents potentially weathering products of weathered glass shards are enhanced. Interestingly, our derived hematite contents do not show any response to volcanic ash layers, suggesting a climate-driven variability of this parameter. Our DRS-derived goethite contents appear slightly lowered. From a magnetic point of view, the magnetic susceptibility is increased, the  $H_{CR}$  decreased (indicating rather soft magnetic mineral composition) confirmed by increased S-ratio values.  $IRM_{100mT}$  is nearly always increased in the tephra layers as well as the ARM witnessing rather SD-like grain size distributions. The inter-parametric ratio of  $IRM_{100}/IRM_{300}$  (comparing rather soft magnetic magnetite with magnetite) is increased in tephra-containing samples, as well as  $IRM_{100}/M_S$ . As previously shown in (Laag et al., 2021), highly resolved IRM acquisitions require (with a 5<sup>th</sup> component compared to loess and paleosol samples) an added magnetic fraction with a coercivity of  $B_h = 39 \pm 8$  mT. FORC analyses performed (see supplementary) on loess and paleosol samples as well as on tephra samples confirm a rather SD like grain size assemblage. However, not every suspected tephra layer shows systematic increased/decreased values, which makes tephra discrimination based on the aforementioned parameters still

difficult. This could be caused by either different magnetic minerals and grain size distributions, due to slightly different eruption types and sources/eruptions and ejected material or, caused by mixing effects of material in which the ash layers are embedded in. To overcome that, a regional investigation of already in-field outcropping tephra layers such e.g., in Titel Stari-Slankamen (Song et al., 2018) and comparison with certain tephra records such as e.g., Lake Ohrid (Leicher et al., 2021) can increase the certainty of preserved ashes, derived from the tephra-independent age model applied in Pleven and its chronostratigraphic occurrence in Lake Ohrid. In the supplementary Table 3 we compiled the four already identified tephra layers from (Jordanova et al., 2022) and 51 additional tephra candidates, taking into account the parameters used for the identification, their age derived from our correlative age model and a potential equivalent – if found – from the macroscopic Lake Ohrid tephra record or other closely located records. However, the lake Ohrid tephra list is only focused on the macroscopic tephra, when we found potential candidates which have no potential equivalent in Lake Ohrid, it could be that that tephra is in Lake Ohrid not identified yet, or the tephra stems from another volcanic region than the Italian volcanic provinces and is not preserved in Lake Ohrid, or we falsely identified a climatic signal as a ash layer.

#### The mid Brunhes climate transition

The whole Pleven LPS is bi-parted evidenced by all magnetic, colorimetric, granulometric and mid-infrared mineralogical data. This bi-partition occurs at the same time as the Mid-Brunhes transition, which occurs around 430 ka. The low-field magnetic susceptibility is very low before 430 ka, even in the paleosols S5 and S6, which represent following our age model the marine isotope stages MIS 13-15 and MIS 17-19. Comparable low frequency dependence of magnetic susceptibility and low-field magnetic susceptibility from the Tajik LPS Darai Kalon reflects a similar behavior (Lu et al., 2020; Li et al., 2022). Increased weathering condition prevailing prior the mid-Brunhes climate transition might have caused an increased crystal growth of preexisting SP maghemite and magnetite particles. This could explain the rather low content of SP particles reflected by  $\Delta\chi$  values. However, the SP indicative ratio  $MS/\chi_{ferri}$  does fluctuate with paleosols described for S6 and S6. This parameter nonetheless assumes monomineralogy represented by Ms. This is (compared to  $\Delta\chi$ ) not the case for paleosols older than 430ka. Intense weathering, accompanied by increased precipitation (increased goethite abundance), intensified seasonality, summer heat and mild winter temperatures (indicated by hematite) and a climax state of weathering reached by most increased smectite and thus kaolinite contents evidence extreme weathering intensities during 800-430 ka. This contradicts

globally derived climate conditions stemming from the mid-Brunhes climate transition which reflects, for instance, for the  $\delta D$  record from EPICA dome C rather dimmed seasonality and temperature variability and increased temperature and moisture during the “super-interglacials” post mid Brunhes climate transition. Potentially, local climate conditions and shifts of prevailing climate circulation patterns might have caused this contradicting behavior. The multi-proxy results stemming from Pleven require further research being conducted in closely located LPSs to investigate if the same climatic imprint is preserved.

#### Millennial scale climate change variability

Eastern European LPSs provide valuable records of small-millennial scale climate change constating of Dansgaard-Oeschger events (warm and rather humid periods) and Heinrich events (rather cold and harsh conditions). A few studies conducted on western and eastern European LPSs evidenced the potential of LPS to record millennial scale climate variability triggered by in the NGRIP record preserved short-term climatic events (Shi et al., 2003; Antoine et al., 2009, 2019; Zeeden et al., 2018; Rousseau et al., 2020). In this case study, the variations of qualitative goethite contents ( $TBA_{Goeth}$ ) redraw remarkably short-lived climatic fluctuations like those known from NGRIP, and allow the most recent GICC05 time scale to be applied to the last interglacial-glacial cycle in Pleven (c. the last 100 kyr). The age model for this interval has six major solid anchor points. In the Holocene soil S0, the Younger Dryas and Bølling–Allerød are clearly visible. Hence the most enhanced DO-cycles DO 8 and DO 12 are thus the peaks in Goethite TBA which reach the highest values for the last 60 kyr. Ultimately before the onset of DO 8 (38.22 ka b2k) (Rasmussen et al., 2014), there is a multi-proxy evidence for a widespread and well (radiometrically) dated crypto-tephra, the Campanian Ignimbrite Y5 tephra,  $^{40}Ar/^{39}Ar$  dated to  $39.85 \pm 0.12ka$  (Giaccio et al., 2017). Evidence for this tephra stems from ATR-FTIR derived smectite contents which peak just stratigraphically below the DO8 and hence, the IRM acquisition unmixing reflecting the necessity of a 5<sup>th</sup> component as evidenced to be indicative in eastern European LPSs for tephra layers. However, this stratigraphical position right on the onset of DO8 contradicts other CI-Y5 records, as those shown by (Zeeden et al., 2018). The improved  $\Delta\chi$ -colorimetry-LR04-based age model targeting the onsets of the interglacials assign for the tephra bearing sample a preliminary age of 40.8 ka, which is 1ka absolute difference from its radiometrically dated age. However, the LR04 target ages come with a uncertainty for the last 1 Ma of about  $\pm 4ka$  (Lisiecki and Raymo, 2005). However, this uncommon stratigraphical position of the tephra

layer which we tentatively assign as the CIY5 tephra might be an artefact stemming from the low resolution of the Pleven record.

The combination of  $TBA_{Goeth}$  fluctuations and the NGRIP GICC05 time scale allow the reduction of uncertainty from LR04. Many studies performed in eastern Europe targeting the detection of Dansgaard-Oeschger and Heinrich-like climate events failed because most times only single proxies like magnetic susceptibility and/or grain size data was used. The Pleven multi-proxy study performed here may provide reasons for the non-recording of other studies. By only investigating the strongest expressed DO-cycles 8 and 12 and by comparing to other proxy data, the following explanation can be drawn. The widely applied indicator for strength of pedogenesis (the frequency dependence of magnetic susceptibility)  $\Delta\chi$  shows, compared to  $TBA_{Goeth}$ , no remarkable peaks at the stratigraphic position of DO 8 and DO 12. The same holds true for  $TBA_{Hema}$ . Pedogenesis requires both temperature and humidity, when both increased the  $\Delta\chi$  should increase as well. However, hematite (a widely accepted indicator for increased temperature) does not fluctuate as  $TBA_{Goeth}$ . This leads to the conclusion, that goethite is neo-formed due to available precipitation but insufficient temperatures do not allow pedogenesis (accompanied by the neoformation of SP-particles traced by  $\Delta\chi$ ) to happen. In other words, it was not warm enough but enough precipitation was available allowing the goethite neo-formation only. This explains, why only on magnetism focusing studies do not trace millennial scale climate change in eastern Europe. Arguments for the rather neo-formation instead of eventually occurring provenance changes are visualized in Figure 10.

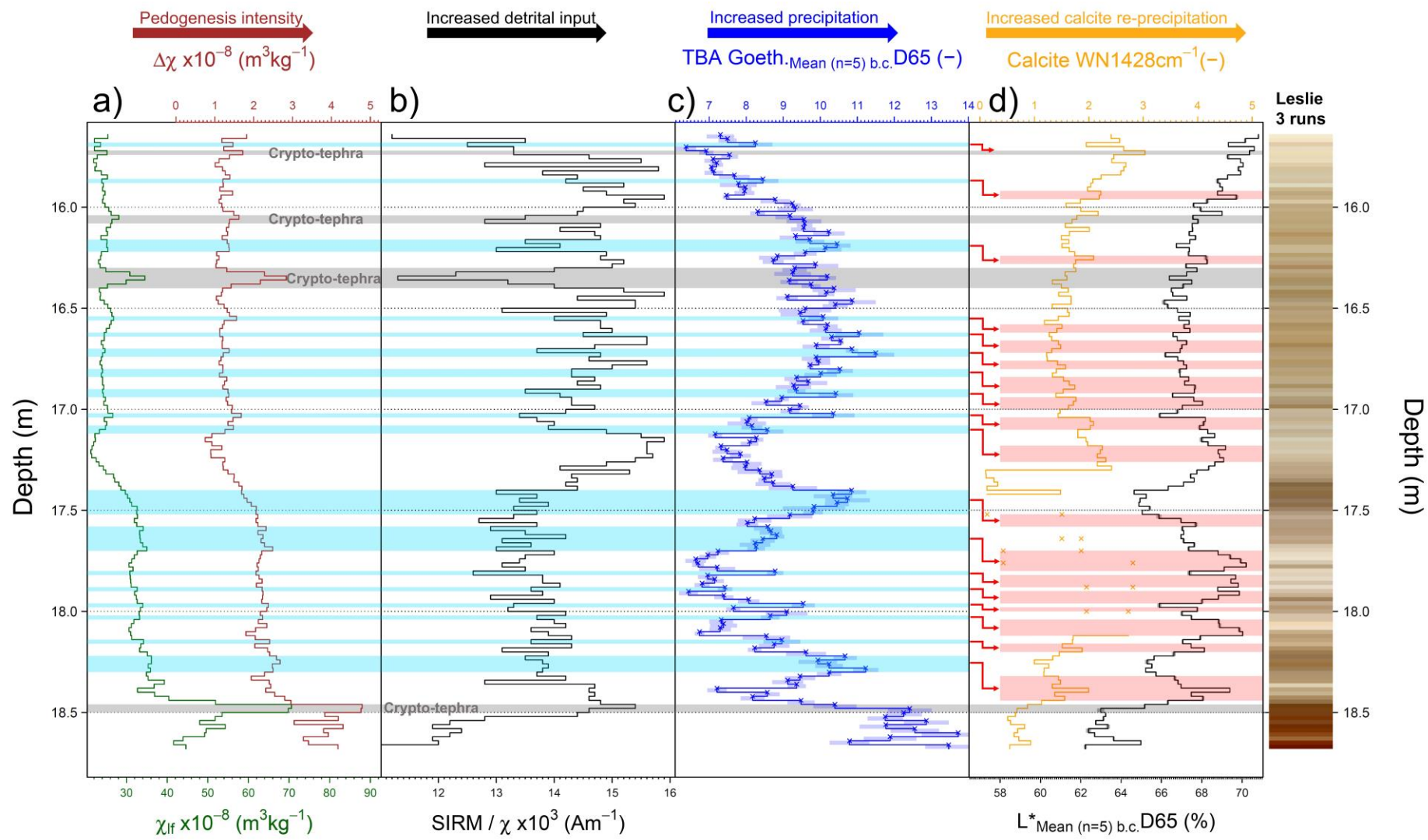


**Figure 10: Indications for the neo-formation of goethite during MIS12. On a depth scale. A) green: low-field magnetic susceptibility ( $\chi_{lf}$ ), red frequency dependence of magnetic susceptibility  $\Delta\chi$ . B) Detrital (coarser) magnetic grain sizes reflected by SIRM/ $\chi$ . C) Precipitation indicative TBAGoeth semi-quantitative content. D) Calcite content (ATR-FTIR-derived orange, Luminance (L\*)-derived: black). Dotted (orange) points indicate not continuously performed measurements. This interval is backed up by L\*. For orientation LESLIE results after 3 color contrast enhancements are shown. Horizontal blue bars indicate peaks in TBAGoeth representing increased precipitation. Horizontal bars in red indicate peaks in calcite which are occurring slightly but systematically shifted to deeper depths indicated with red arrows between c) and d). Grey horizontal bars indicate crypto-tephra layers. Paleoclimatic abstracted interpretations of parameters shown in this figure are indicated on top of the figure with arrows and description. Please notice the very cyclic behavior of ATR-FTIR derived calcite contents, being several centimeters shifted downwards compared to increased goethite contents.**

MIS4 to present

The last glaciation up to present is shown in Figure 11 for 65 to 18 ka and 18 to present in the supplementary figure 8. Since “hard” data from NGRIP is available for these time periods, it is compared with the Iberian Margin foraminifera record and the Hudson ice rafted debris record. Thus, speleothem  $\delta^{13}\text{C}$  values from Italy (Corchia) and Sofular (Turkey) are displayed. Previously mentioned magnetic parameters and smectite contents are shown below as well as goethite and recalculated MAP values from maghemite high-temperature magnetic susceptibility experiments. First of all, the goethite variations fit remarkably well the NGRIP  $\delta^{18}\text{O}$  record. This is not only evident from amplitude variations from stronger and weaker Greenland interstadials but timely also by their individual saw-toothed shape. Every single Dansgaard-Oeschger cycle can be found in the time interval between 65 and 35 ka. The goethite signal is towards younger ages somewhat smeared but peaks inside the Sofular  $\delta^{13}\text{C}$  can be recognized when not present in the  $\delta^{18}\text{O}$  NGRIP record. Thus, the relatively strongest interstadials can be identified in the magnetic parameters of  $\chi_{lf}$ ,  $H_{CR}$  and  $IRM_{-100}$ . Hence, detected rather sharp peaks in magnetic and smectite data fall nearly simultaneously together with prominent tephras such as the Cape Riva Y2, Y3, and the Campanian Ignimbrite. However, two tephras are likely being preserved between 65 and 60 ka, which cannot be found in any literature from Italian volcanic active provinces being ejected. However, some records of the Carpathian and lower Danube Basin reflect in their  $\chi_{lf}$  sometimes one unique or a double

peak. This could indicate that might another volcanic province might have provided tephra material in these regions und thereby indicate for a relatively short time interval a change of source material. The younger time interval (supplementary figure 8), 20-3 ka displays with the same aforementioned parameters the time interval of the MIS 2 to Holocene transition. The onset of the Holocene with the demise of Heinrich event 1 is rather sharp recorded with goethite and smectite. Dimmer transitions are observed by  $IRM_{-100}$ ,  $H_{CR}$  and  $\chi_f$ . These three parameters show thus no further division as reflected by goethite and smectite from 15ka towards younger ages. Smectite and goethite recorded the Bølling Allerød, and thus the younger Dryas. Unfortunately, the ATR-FTIR experiments were not everywhere conducted in a 2 cm resolution, however, goethite variations indicate the presence of the so-called 8.4 and 4.2 ka events, which are with reduced goethite contents appearing in Pleven with comparatively drier conditions. Especially the time interval of the last glacial towards present is known for millennial timescale variability. Evidence for a direct connection between NGRIP and Eastern European LPSs was presented in a few most times single proxy investigations. However, our multi-proxy study in combination with the stratigraphical “falling-together” of crypto-tephras with well-known tephra layers strengthens the evidence for preserved millennial scale variability. Additionally, goethite variations might be together with mid-infrared derived smectite contents a sensitive parameter for detection of millennial scale variability which found for this purpose not yet application in Eastern European LPSs.



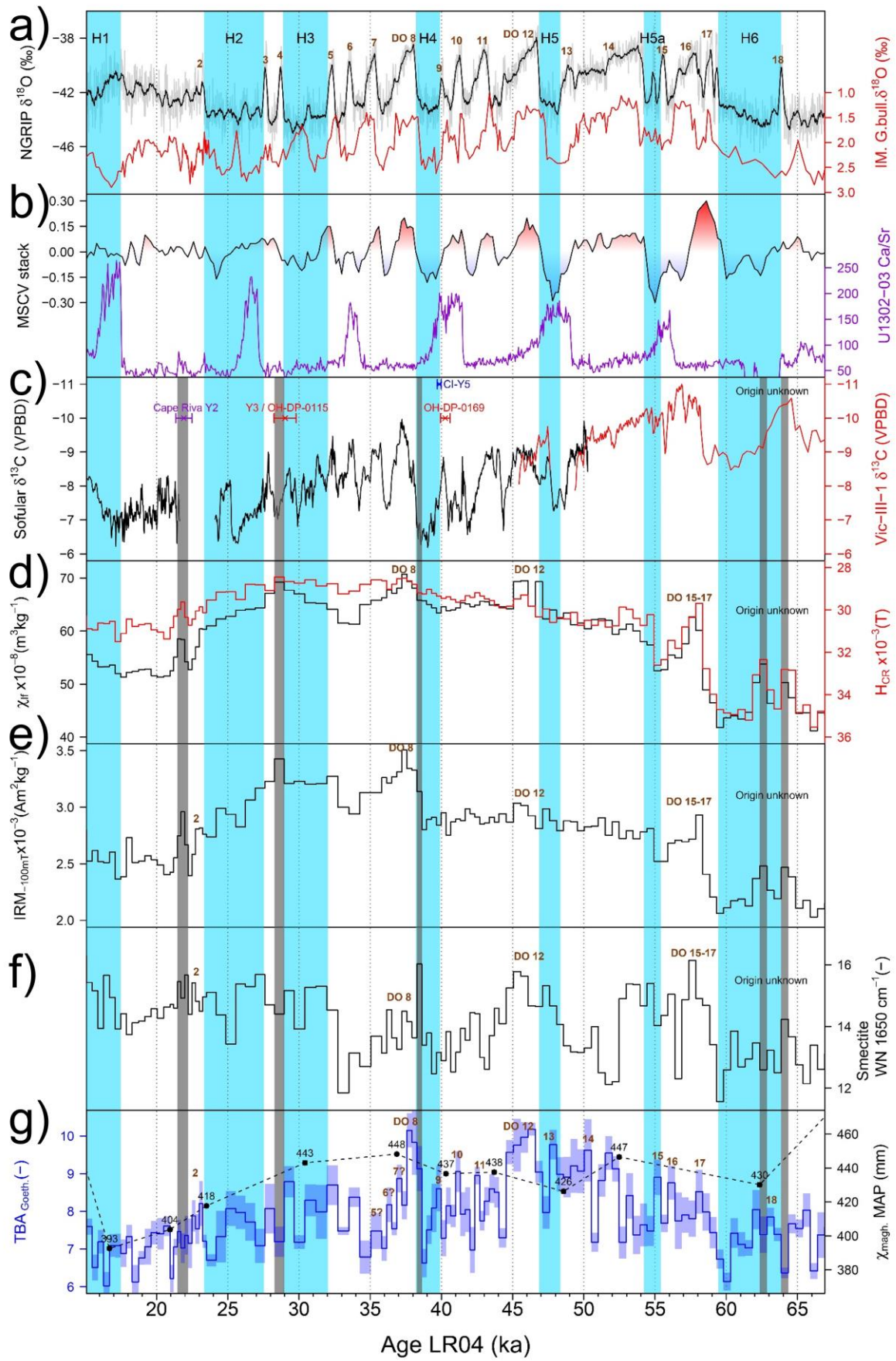


## Figure 11: the time interval 65 to 20 ka and millennial scale climate change variability-.

### MIS 6

In Figure 12 the Iberian Margin *G. bulloides*  $\delta^{18}\text{O}$  (Hodell et al., 2013) record is compared with  $\text{GL}_{\text{SYN}}$  (Barker et al., 2011) to ascertain for older age intervals the reliability of the synthetic Greenland  $\delta^{18}\text{O}$  record. Shown below is the MSCV stack (Sun et al., 2021) and ice rafted debris intensity (Channell et al., 2012). Since  $\delta^{13}\text{C}$  is a reliable proxy for paleoprecipitation (with advantages over  $\delta^{18}\text{O}$  since  $\delta^{18}\text{O}$  indicates both temperature and precipitation), we compare our data towards closely located and available for that time interval speleothem records (see Fig 1 Map of the region), namely Dim cave (Turkey), Abagilet cave ABA 1&2 (southern Hungary, (Koltai et al., 2017) and Corchia Cave (Italy, (Tzedakis et al., 2018) which were extracted from the SISAL data base (Atsawawaranunt et al., 2018; Comas-Bru et al., 2020). Below magnetic parameters are shown such as  $\chi_{\text{lf}}$ , HCR with macroscopic tephtras observed in Lake Ohrid (Leicher et al., 2021) and grey vertical bars which contain the infield outcropping L2 tephra and several more crypto-tephtras. Below the smectite content is shown. Furthermore, the TBAGoeth is shown as well as recalculated mean annual precipitation values by the regression function between maghemite and MAP. The co-variation of calculated MAP values for Pleven and the goethite variation is remarkable. Hence, trends in  $\delta^{13}\text{C}$  and goethite and MAP values are similar. Furthermore, several potential cryptotephtras fall timely together with macroscopic tephtras preserved in Lake Ohrid. Additionally, the timing of demise of the MIS 7 interglacials might be clearer now, since all parameters, especially precipitation indicating variables such as reconstructed MAP values and the rather soft magnetic indicating HCR and smectite contents refine the stratigraphical boundary between rather interglacial conditions from MIS 7a and 7c compared to the onset of harsh and dry glacial conditions with the onset of MIS6.

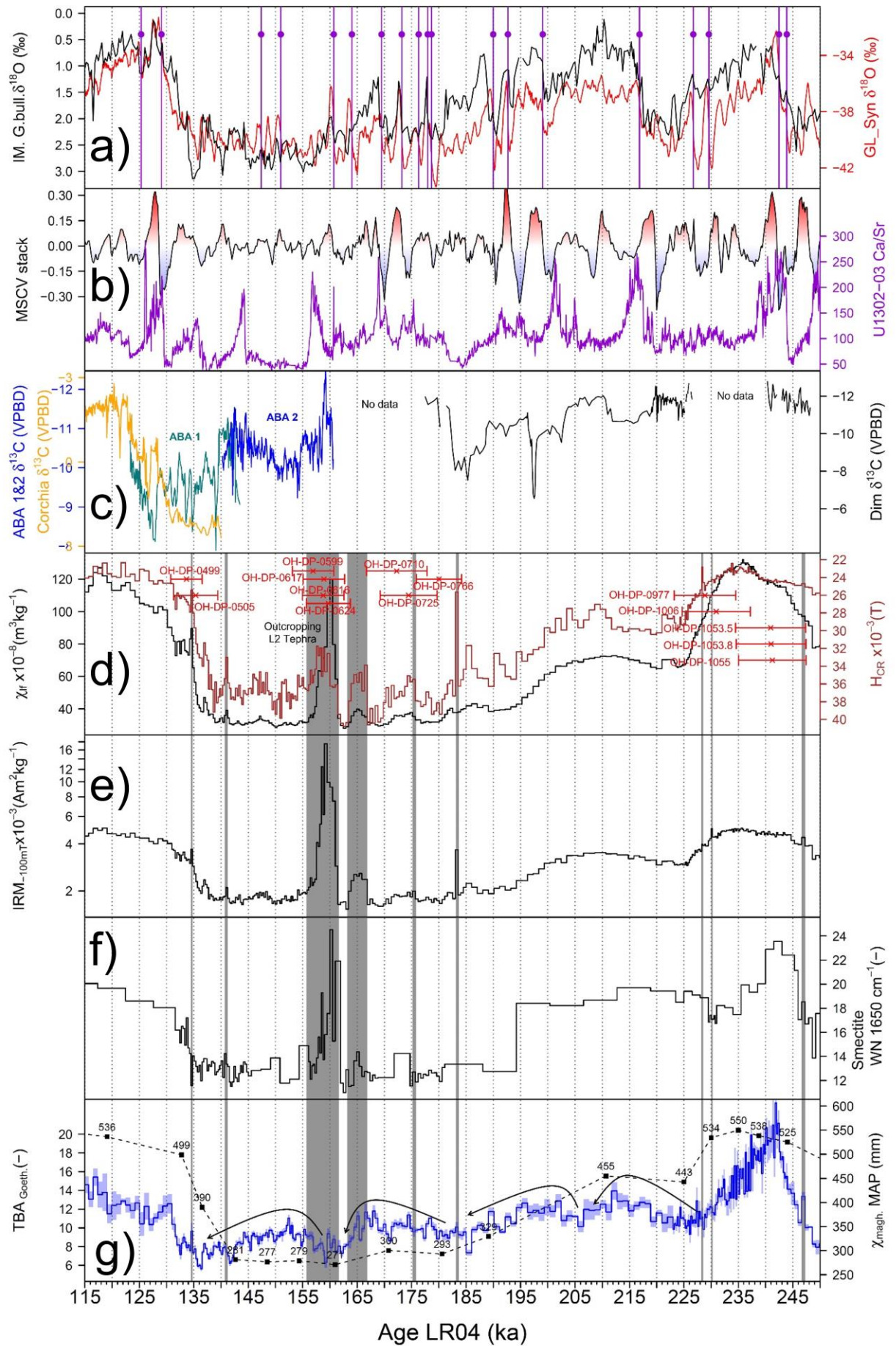




## Figure 12: Climate variability recorded for MIS6 (penultimate glacial).

### MIS12

For the first time, Eastern-European LPS provide evidence for millennial scale climate change during MIS 12. Figure 11 shows a comparison between the synthetic  $\delta^{18}\text{O}$  Greenland record (Barker et al., 2011), the surface water temperature sensitive *Globigerina bulloides* stemming from the Iberian Margin cores (Hodell et al., 2013), the central Mediterranean KC01B borehole planktonic foraminifera composition derived paleoclimate curve (Capotondi et al., 2016) recalculated after (Cita et al., 1977) and given as percentage between -100% (only preferring-loving planktic foraminifera) and +100% (only warm surface water preferring planktic foraminifera) resting on a rather coarse age model (6 tiepoints for the time interval of 504.5 to 287.5 ka) utilizing both the sapropel-stratigraphy adapted from (Konijnendijk et al., 2014) and onsets of MIS12 and MIS9 stemming from the LR04 stack (Lisiecki and Raymo, 2005). The millennial scale climate variability (MSCV) stack was adapted from (Sun et al., 2021) which combines different paleoclimatic archives stemming from the northern hemisphere such as the IODP sites U1308 and 1385 and the (terrestrial and lacustrine) sedimentary records Gulang loess and Lake Ohrid, spread from 23°W to 110°E between 40 and 50°N which covers the Pleven LPS °N latitude. Right below in violet the ratio of Calcium and Strontium stemming from marine cores U1302 and U1303 indicating reliably ice rafted debris events and successfully correlated for the last interglacial/glacial cycle with Heinrich events 1-6 recorded in the NGRIP record (Channell et al., 2012) with a correlative age model derived from LR04 and independently paleomagnetic-dated (via Relative Paleo-Intensity RPI). The sub-graphs below present data stemming from SK18, namely the low-field susceptibility ( $\chi_{lf}$ ). In this plot, macroscopic tephra layers stemming from Lake Ohrid are indicated as red crosses with error bars indicating the age uncertainty as stated in (Leicher et al., 2021). In the figure below, the coercivity of remanence ( $H_{CR}$ ), the FTIR-ATR-derived qualitative smectite content and the  $\text{IRM}_{-100\text{mT}}$  are displayed. All three parameters (and others as shown in the supplementary data file) are either indicative for tephra layers or for paleoclimatic changes. Grey vertical bars show samples which contain with high certainty derived from multi-disciplinary data crypto-tephra layers. Below these four tephra-identifying related figures the qualitative indicator for precipitation is displayed. A mixture of tephra and paleo-climate signal is presumably represented by the hard-IRM (HIRM) representing rather hard magnetic minerals such as hematite and goethite.

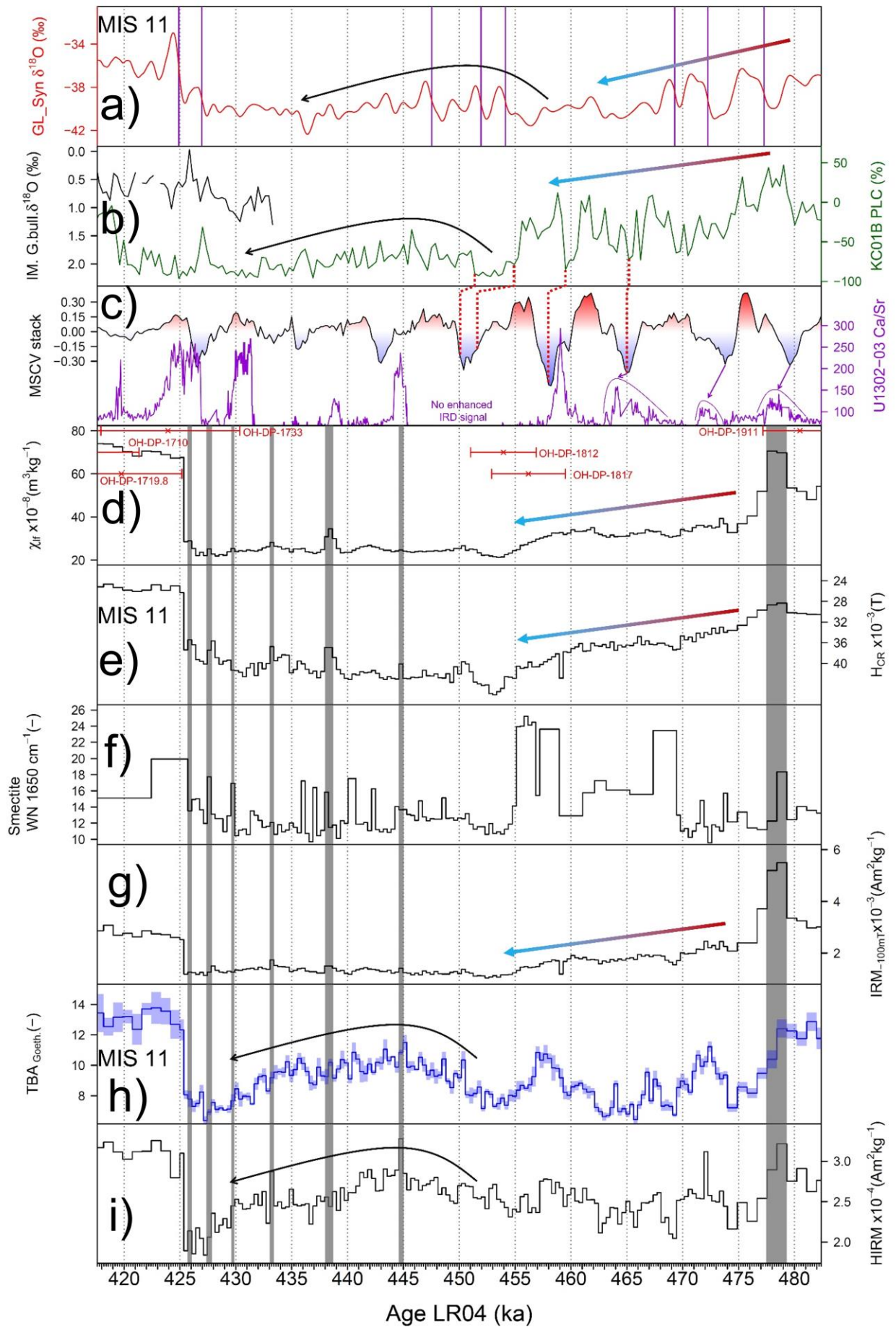


### **Figure 11: Climate variability recorded in MIS12.**

Overall, general trends indicated by the straight red-to-blue colored arrow, and the hump recognized in different datasets indicated by the bended black arrow are obvious. GL<sub>SYN</sub> and KC01B foraminifera compositions are in good agreement, but there is a shift recognizable. This shift can be explained by 1) the age uncertainty stemming from differently applied age models and thus 2) to the selection of tiepoints. However, all features stemming from KC01B foraminifera fluctuations can be correlated very clearly based on shape and intensity variations towards the MSCV stack as indicated by the red dotted lines. Remarkable is the amplitude change from rather high amplitudes represented by the highs and lows of the MSCV stack in the time interval of 480 to 450 ka. This amplitude change compared to the younger time interval of 450 ka towards the onset of MIS 11 (~425 ka) is preserved both in TBA<sub>Goeth</sub> and HIRM, whereas H<sub>CR</sub>, IRM<sub>-100mT</sub> and  $\chi_{lf}$  rather show a decreasing trend of their values towards younger ages. The qualitative smectite content shows even the highest amplitude change between these intervals.

Rather cold intervals similarly to the last glacial (Heinrich events) intervals time-coherent in the northern hemisphere are reflected by minima in the KC01B warm/cold surface water foraminifera, and MSCV stacked lows as well as GL<sub>SYN</sub> lows and further evidence for a northern hemisphere time-coherency is provided by a reliable proxy for ice rafted debris from even further east the Hudson Bay sites U1302-1303. This underlines, that millennial scale variability is rather a quasi-synchronous northern hemisphere phenomenon presumably stemming from the instability of the Laurentide and northern European ice sheets than a regional phenomenon. The coherency of our precipitation indicator TBA Goeth, following not only general trends but also single warming events which is in agreement with KC01B planktic foraminifera indicates a westerly-wind controlled environment. Tephra occurrences like the S5-cryptotephra layer sitting on the demise of MIS 13 pedocomplex observed in Titel-Stari Slankamen and its potential equivalent OH-DP-1911 as well as several cryptotephra layers located at the onset of MIS 11, such as the ones falling timely between 425 and 430 ka potentially correlated with the OH-DP-733 Lake Ohrid Tephra findings underline a rather westerly wind regime. The westerly wind regime is directly triggered with its water vapor by the thermocline circulation in the northern Atlantic. If rather warm water allows evaporation to be transported towards the west, and the Mediterranean sea is heating up in surface waters

e.g., as shown by planktic foraminifera composition of KC01B, which results even in more water saturation in the air transported to further east, the probability of rainfall in Bulgaria will increase which will cause the precipitation indicator  $TBA_{Goeth}$  to increase.

A recent study by (Columbu et al., 2022) evidenced a direct Central Mediterranean rainfall variation triggered by northern latitude temperatures during the last glaciation. With higher northern latitude temperatures the Atlantic moisture availability was increased. This enhanced the strength of the AMOC (Atlantic Meridional Overturning Circulation) causing wetter climate in central Mediterranean region. As observed in the wavelet analysis performed on the Goethite data (supplement Figure 7) for the whole sequence,  $TBA_{Goeth}$  shows in contrast to other parameters like  $TBA_{Hema}$  and magnetic data a strongly expressed obliquity component for nearly the complete last 800 kyrs. Obliquity as the tilt of the Earth's rotation axis ( $22^{\circ}$ - $24.5^{\circ}$  with a periodicity of  $\sim 41$  kyrs) has a direct impact on the latitudinal distribution of top-of-atmosphere incoming solar radiation. A recent study by (Zhang et al., 2022) evidenced for a study performed in the Indo-Pacific region (U1483) a shift of the intertropical convergence zone (ITCZ), which is directly correlated to obliquity minima and maxima. AMOC weakening occurs during low obliquity phases and high north Atlantic sea ice cover. This climatic/thermohaline constellation is expressed by high precipitation  $\delta^{13}C$  values in northern Hemisphere Chinese loess sections. A connection onto this hemispheric transversal link could be the  $\delta D$  record from EPICA Dome C (Jouzel et al., 2007).  $\delta D$  shows a remarkable expressed obliquity component which indicates a 41kyr pattern of positive obliquity linked to higher ice shelf temperatures. This could trigger the northern hemisphere AMOC intensity causing higher precipitation in the central Mediterranean region, even thus transported more to the West by Westerlies. Taking the study (Columbu et al., 2022) for the last Deglaciation as a blueprint for older millennial and glacial interglacial central Mediterranean precipitation fluctuations the obliquity component expressed in Pleven as Goethite increase can be explained both on orbital and millennial scale.



## Obliquity forcing of precipitation in Pleven

In Figure 14, findings addressing other targets than millennial scale climate change variability are presented. The uppermost figure displays the LR04 record with the superimposed assignment of marine isotope stages. Below, the  $\chi_{lf}$  and  $H_{CR}$  are shown. Following plot below shows the  $TBA_{Hema}$  and Smectite content. Vertical bars in orange display previously presented and investigated (crypto-) tephra layers from (Jordanova et al., 2022). Grey bars represent further certainly identified crypto-tephras based on magnetic and smectite characteristics. However, a full vertical bar representation of the tephra list presented in supplementary table 3 would hinder further displayed contents visually. The  $TBA_{Goeth}$  content is compared to the maghemite re-calculated precipitation in the graph below. The further graph below contains a further regression applied to the overall well correlation between maghemite and goethite content, where maghemite derived MAPs were transformed to  $TBA_{Goeth}$  MAPs with maghemite data stemming from the last 430 ka since maghemite is weathered or further oxidized to hematite in the pre-mid-Brunhes paleosols.  $TBA_{Goeth}$  calculated MAP values are presented and compared with mean annual precipitation data from (Krapp et al., 2021). Below is the Chinese Speleothem composite stack compared with the 65°N summer insolation. The two plots below display the high-pass filtered goethite content and  $\delta D$  Antarctica variations excluding the eccentricity signal off the time series. It appears that a rather obliquity-forced signal is prominent in both data sets and that  $\delta D$  Antarctica increases might trigger the precipitation availability in Pleven. The only link between these geographically disconnected sites can be found in the thermohaline and AMOC circulation. Obliquity forced temperature increases on the antarctica ice shelf might have triggered the thermohaline circulation allowing with warm water pulses an increased moisture uptake by the Westerly winds which provided enhanced moisture in Pleven leading to the leaching of the paleosols and the neof ormation of goethite.

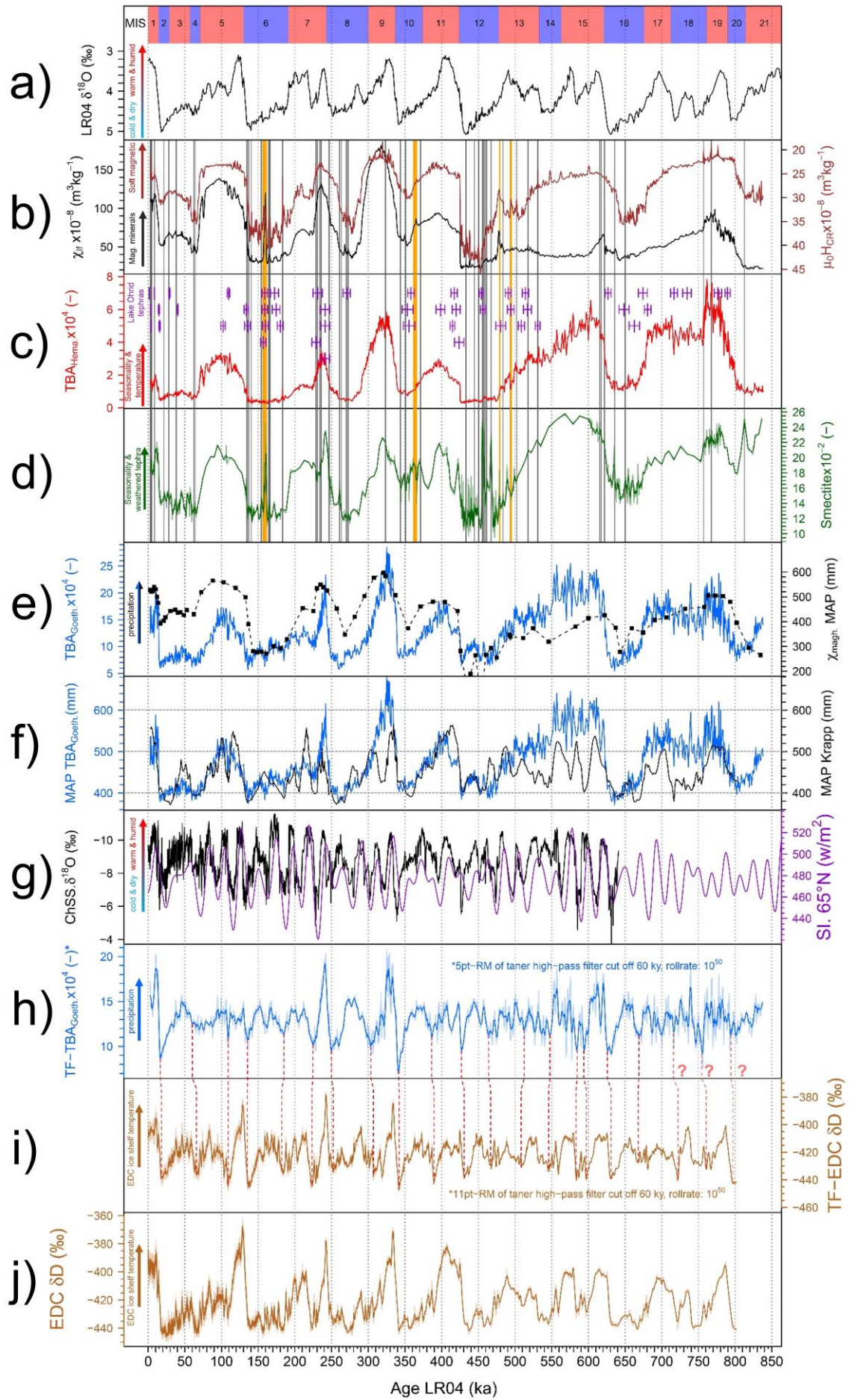


**Figure 14: Integration of all parameters for the last 830 ka. The LR04 stack is shown with marine isotope stages indicated above in red as interglacials and blue as glacials in a). Below, in b) HCR and  $\chi_{lf}$  are shown. Semi-quantitative hematite contents are shown shown in panel c). ATR-FTIR derived smectite contents are displayed in panel d). Panel e) shows in blue the True Band Amplitude (TBA) of goethite and mean annual precipitation (MAP) values derived from maghemite utilizing regression from Gao et al., 2019. Panel f) displays the Krapp MAP modelled data for Pleven and in blue MAP values calculated from the regression of maghemite and goethite. In panel g) the  $\delta^{18}O$  Chinese speleothem stack is shown and compared to the summer insolation at  $65^{\circ}N$ . Below, in panel h) the Taner filtered (high pass with 60ky cut-off and roll rate of  $10^{50}$ ) is shown and compared to the  $\delta D$  (Deuterium, indicative for ice-shelf temperature, panel h)) Antarctica values from EPICA dome C (EDC). Below, in panel j) the original – non filtered  $\delta D$  record from EDC is shown.**

## Conclusion

The detailed multi proxy approach conducted on the Pleven LPS paves the way for further studies to investigate the direct link between global teleconnections of southern and northern hemispheres on different orbital to millennial timescales. The Pleven LPS in Bulgaria witnessed on orbital scale the mid-Brunhes climate transition as one of the first records due to integrated multi-disciplinary experiments conducted on mineral dust accumulated on 27m at Pleven. A precise correlative age model allows the correlation of goethite-recorded precipitation events which re-draw Dansgaard-Oeschger and Heinrich millennial scale variability. The integration of in-depth and continuously applied environmental magnetic and mid-infrared experiments indicate the presence of 55 preserved crypto-tephras which fall in majority together with regional tephra records. For the first time, millennial scale climate change variability can be evidenced from Eastern European LPSs. Further research of neighboring LPSs is necessary to confirm the presence of preserved millennial scale climate variability and the presence of preserved tephra material. Our study might initiate a throughout applicable tephrostratigraphic framework which will allow in the near future the investigation of leads and lags of marine, limnic and terrestrial preserved millennial timescale climate change.

## References

- Antoine, P., Lagroix, F., Jordanova, D., Jordanova, N., Lomax, J., Fuchs, M., et al. (2019). A remarkable Late Saalian (MIS 6) loess (dust) accumulation in the Lower Danube at Harletz (Bulgaria). *Quaternary Science Reviews* 207, 80–100. doi: 10.1016/j.quascirev.2019.01.005.
- Antoine, P., Rousseau, D.-D., Fuchs, M., Hatté, C., Gauthier, C., Marković, S. B., et al. (2009). High-resolution record of the last climatic cycle in the southern Carpathian Basin (Surduk, Vojvodina, Serbia). *Quaternary International* 198, 19–36. doi: 10.1016/j.quaint.2008.12.008.
- Ao, H., Rohling, E. J., Stringer, C., Roberts, A. P., Dekkers, M. J., Dupont-Nivet, G., et al. (2020). Two-stage mid-Brunhes climate transition and mid-Pleistocene human diversification. *Earth-Science Reviews* 210, 103354. doi: 10.1016/j.earscirev.2020.103354.
- Atsawawaranunt, K., Comas-Bru, L., Amirnezhad Mozhdghi, S., Deininger, M., Harrison, S. P., Baker, A., et al. (2018). The SISAL database: a global resource to document oxygen and carbon isotope records from speleothems. *Earth Syst. Sci. Data* 10, 1687–1713. doi: 10.5194/essd-10-1687-2018.
- Barker, S., Knorr, G., Edwards, R. L., Parrenin, F., Putnam, A. E., Skinner, L. C., et al. (2011). 800,000 Years of Abrupt Climate Variability. *Science* 334, 347–351. doi: 10.1126/science.1203580.
- Basarin, B., Buggle, B., Hambach, U., Marković, S. B., Dhand, K. O., Kovačević, A., et al. (2014). Time-scale and astronomical forcing of Serbian loess–paleosol sequences. *Global and Planetary Change* 122, 89–106. doi: 10.1016/j.gloplacha.2014.08.007.
- Bond, G., Heinrich, H., Broecker, W., Labeyrie, L., McManus, J., Andrews, J., et al. (1992). Evidence for massive discharges of icebergs into the North Atlantic ocean during the last glacial period. *Nature* 360, 245–249. doi: 10.1038/360245a0.
- Buggle, B., Hambach, U., Kehl, M., Markovic, S. B., Zoller, L., and Glaser, B. (2013). The progressive evolution of a continental climate in southeast-central European lowlands during the Middle Pleistocene recorded in loess paleosol sequences. *Geology* 41, 771–774. doi: 10.1130/G34198.1.
- Buggle, B., Hambach, U., Müller, K., Zöller, L., Marković, S. B., and Glaser, B. (2014). Iron mineralogical proxies and Quaternary climate change in SE-European loess–paleosol sequences. *CATENA* 117, 4–22. doi: 10.1016/j.catena.2013.06.012.
- Capotondi, L., Girone, A., Lirer, F., Bergami, C., Verducci, M., Vallefucio, M., et al. (2016). Central Mediterranean Mid-Pleistocene paleoclimatic variability and its association with global climate. *Palaeogeography, Palaeoclimatology, Palaeoecology* 442, 72–83. doi: 10.1016/j.palaeo.2015.11.009.
- Channell, J. E. T., Hodell, D. A., Romero, O., Hillaire-Marcel, C., de Vernal, A., Stoner, J. S., et al. (2012). A 750-kyr detrital-layer stratigraphy for the North Atlantic (IODP Sites U1302–U1303, Orphan Knoll, Labrador Sea). *Earth and Planetary Science Letters* 317–318, 218–230. doi: 10.1016/j.epsl.2011.11.029.
- Cita, M. B., Vergnaud-Grazzini, C., Robert, C., Chamley, H., Ciaranfi, N., and d’Onofrio, S. (1977). Paleoclimatic Record of a Long Deep Sea Core from the Eastern Mediterranean. *Quat. res.* 8, 205–235. doi: 10.1016/0033-5894(77)90046-1.

- Columbu, A., Spötl, C., Fohlmeister, J., Hu, H.-M., Chiarini, V., Hellstrom, J., et al. (2022). Central Mediterranean rainfall varied with high northern latitude temperatures during the last deglaciation. *Commun Earth Environ* 3, 181. doi: 10.1038/s43247-022-00509-3.
- Comas-Bru, L., Atsawawaranunt, K., Harrison, S., and SISAL Working Group Members (2020). SISAL (Speleothem Isotopes Synthesis and Analysis Working Group) database version 2.0. doi: 10.17864/1947.256.
- Cornell, R. M., and Schwertmann, U. (2003). *The iron oxides: structure, properties, reactions, occurrences and uses*. John Wiley & Sons.
- Deng, C. (2008). Paleomagnetic and mineral magnetic investigation of the Baicaoyuan loess-paleosol sequence of the western Chinese Loess Plateau over the last glacial-interglacial cycle and its geological implications: BAICAOYUAN LOESS-PALEOSOL SEQUENCE. *Geochem. Geophys. Geosyst.* 9, n/a-n/a. doi: 10.1029/2007GC001928.
- Ding, Z. L., Xiong, S. F., Sun, J. M., Yang, S. L., Gu, Z. Y., and Liu, T. S. (1999). Pedostratigraphy and paleomagnetism of a ~7.0 Ma eolian loess–red clay sequence at Lingtai, Loess Plateau, north-central China and the implications for paleomonsoon evolution. *Palaeogeography, Palaeoclimatology, Palaeoecology* 152, 49–66. doi: 10.1016/S0031-0182(99)00034-6.
- Dunlop, D. J., and Özdemir, Ö. (2013). *Rock magnetism: fundamentals and frontiers*. 1. paperback ed. with corr., 2. ed., reprinted. Cambridge: Cambridge Univ. Press.
- Egli, R. (2013). VARIFORC: An optimized protocol for calculating non-regular first-order reversal curve (FORC) diagrams. *Global and Planetary Change* 110, 302–320. doi: 10.1016/j.gloplacha.2013.08.003.
- Fitzsimmons, K. E., Hambach, U., Veres, D., and Iovita, R. (2013). The Campanian Ignimbrite Eruption: New Data on Volcanic Ash Dispersal and Its Potential Impact on Human Evolution. *PLoS ONE* 8, e65839. doi: 10.1371/journal.pone.0065839.
- Forster, Th., Evans, M. E., and Heller, F. (1994). The frequency dependence of low field susceptibility in loess sediments. *Geophysical Journal International* 118, 636–642. doi: 10.1111/j.1365-246X.1994.tb03990.x.
- Forster, Th., Heller, F., Evans, M. E., and Havlíček, P. (1996). Loess in the Czech Republic: Magnetic properties and paleoclimate. *Stud Geophys Geod* 40, 243–261. doi: 10.1007/BF02300741.
- Frank, U., and Nowaczyk, N. R. (2008). Mineral magnetic properties of artificial samples systematically mixed from haematite and magnetite. *Geophysical Journal International* 175, 449–461. doi: 10.1111/j.1365-246X.2008.03821.x.
- Gao, X., Hao, Q., Oldfield, F., Bloemendal, J., Deng, C., Wang, L., et al. (2019). New High-Temperature Dependence of Magnetic Susceptibility-Based Climofunction for Quantifying Paleoprecipitation From Chinese Loess. *Geochemistry, Geophysics, Geosystems* 20, 4273–4291.
- Gavrilović, B., Sümegi, P., Ćirić, M., Radaković, M. G., Gavrilov, M. B., Mlađan, D., et al. (2019). The Middle and Late Pleniglacial (Weichselian) malacofauna of the Zemun loess–paleosol sequence, Serbia. *PalZ*. doi: 10.1007/s12542-019-00465-y.



- Giaccio, B., Leicher, N., Mannella, G., Monaco, L., Regattieri, E., Wagner, B., et al. (2019). Extending the tephra and palaeoenvironmental record of the Central Mediterranean back to 430 ka: A new core from Fucino Basin, central Italy. *Quaternary Science Reviews* 225, 106003. doi: 10.1016/j.quascirev.2019.106003.
- Giaccio, B., Niespolo, E. M., Pereira, A., Nomade, S., Renne, P. R., Albert, P. G., et al. (2017). First integrated tephrochronological record for the last ~190 kyr from the Fucino Quaternary lacustrine succession, central Italy. *Quaternary Science Reviews* 158, 211–234. doi: 10.1016/j.quascirev.2017.01.004.
- Harrison, R. J., and Feinberg, J. M. (2008). FORCinel: An improved algorithm for calculating first-order reversal curve distributions using locally weighted regression smoothing: FORCINEL ALGORITHM. *Geochem. Geophys. Geosyst.* 9, n/a-n/a. doi: 10.1029/2008GC001987.
- Heinrich, H. (1988). Origin and Consequences of Cyclic Ice Rafting in the Northeast Atlantic Ocean during the Past 130,000 Years. *Quaternary Research* 29, 142–152.
- Heinrich, H., Schmidt, C., Zieme, F., Mikolajewicz, U., and Roettig, C.-B. (2021). Massive deposition of Sahelian dust on the Canary Island Lanzarote during North Atlantic Heinrich Events. *Quat. res.* 101, 51–66. doi: 10.1017/qua.2020.100.
- Hlavatskyi, D., and Bakhmutov, V. (2021). Early–Middle Pleistocene Magnetostratigraphic and Rock Magnetic Records of the Dolynske Section (Lower Danube, Ukraine) and Their Application to the Correlation of Loess–Palaeosol Sequences in Eastern and South-Eastern Europe. *Quaternary* 4, 43. doi: 10.3390/quat4040043.
- Hlavatskyi, D. V., and Bakhmutov, V. G. (2020). Magnetostratigraphy and magnetic susceptibility of the best developed Pleistocene loess-palaeosol sequences of Ukraine: implications for correlation and proposed chronostratigraphic models. *GQ* 64. doi: 10.7306/gq.1544.
- Hodell, D. A., Kanfoush, S. L., Venz, K. A., Charles, C. D., and Sierro, F. J. (2003). The mid-Brunhes transition in ODP sites 1089 and 1090 (subantarctic South Atlantic). *AGU Geophysical Monograph* 137, 113–129.
- Hodell, D., Crowhurst, S., Skinner, L., Tzedakis, P. C., Margari, V., Channell, J. E. T., et al. (2013). Response of Iberian Margin sediments to orbital and suborbital forcing over the past 420 ka: IBERIAN MARGIN PALEOCEANOGRAPHY. *Paleoceanography* 28, 185–199. doi: 10.1002/palo.20017.
- Hunt, C. P., Moskowitz, B. M., and Banerjee, S. K. (1995). “Magnetic Properties of Rocks and Minerals,” in *AGU Reference Shelf*, ed. T. J. Ahrens (Washington, D. C.: American Geophysical Union), 189–204. doi: 10.1029/RF003p0189.
- Jansen, J. H. F., Kuijpers, A., and Troelstra, S. R. (1986). A Mid-Brunhes Climatic Event: Long-Term Changes in Global Atmosphere and Ocean Circulation. *Science* 232, 619–622. doi: 10.1126/science.232.4750.619.
- Jiang, Z., Liu, Q., Roberts, A. P., Dekkers, M. J., Barrón, V., Torrent, J., et al. (2022). The Magnetic and Color Reflectance Properties of Hematite: From Earth to Mars. *Reviews of Geophysics* 60. doi: 10.1029/2020RG000698.

- Jordanova, D., Hus, J., Evlogiev, J., and Geeraerts, R. (2008). Palaeomagnetism of the loess/palaeosol sequence in Viatovo (NE Bulgaria) in the Danube basin. *Physics of the Earth and Planetary Interiors* 167, 71–83. doi: 10.1016/j.pepi.2008.02.008.
- Jordanova, D., Laag, C., Jordanova, N., Lagroix, F., Georgieva, B., Ishlyamski, D., et al. (2022). A detailed magnetic record of Pleistocene climate and distal ash dispersal during the last 800 kyrs - The Suhia Kladenetz quarry loess-paleosol sequence near Pleven (Bulgaria). *Global and Planetary Change* 214, 103840. doi: 10.1016/j.gloplacha.2022.103840.
- Jouzel, J., Masson-Delmotte, V., Cattani, O., Dreyfus, G., Falourd, S., Hoffmann, G., et al. (2007). Orbital and Millennial Antarctic Climate Variability over the Past 800,000 Years. *Science* 317, 793–796. doi: 10.1126/science.1141038.
- Kehl, M., Vlamincx, S., Köhler, T., Laag, C., Rolf, C., Tsukamoto, S., et al. (2021). Pleistocene dynamics of dust accumulation and soil formation in the southern Caspian Lowlands - New insights from the loess-paleosol sequence at Neka-Abelou, northern Iran. *Quaternary Science Reviews* 253, 106774. doi: 10.1016/j.quascirev.2020.106774.
- King, J., Banerjee, S. K., Marvin, J., and Özdemir, Ö. (1982). A comparison of different magnetic methods for determining the relative grain size of magnetite in natural materials: Some results from lake sediments. *Earth and Planetary Science Letters* 59, 404–419. doi: 10.1016/0012-821X(82)90142-X.
- King, J. W., and Channell, J. E. T. (1991). SEDIMENTARY MAGNETISM, ENVIRONMENTAL MAGNETISM, AND MAGNETOSTRATIGRAPHY. *Reviews of Geophysics* 29, 358–370. doi: 10.1002/rog.1991.29.s1.358.
- Koltai, G., Spötl, C., Shen, C.-C., Wu, C.-C., Rao, Z., Palcsu, L., et al. (2017). A penultimate glacial climate record from southern Hungary: PENULTIMATE GLACIAL CLIMATE RECORD FROM SOUTHERN HUNGARY. *J. Quaternary Sci.* 32, 946–956. doi: 10.1002/jqs.2968.
- Költringer, C., Bradák, B., Stevens, T., Almqvist, B., Banak, A., Lindner, M., et al. (2021). Palaeoenvironmental implications from Lower Volga loess - Joint magnetic fabric and multi-proxy analyses. *Quaternary Science Reviews* 267, 107057. doi: 10.1016/j.quascirev.2021.107057.
- Konijnendijk, T. Y. M., Ziegler, M., and Lourens, L. J. (2014). Chronological constraints on Pleistocene sapropel depositions from high-resolution geochemical records of ODP Sites 967 and 968. *nos* 47, 263–282. doi: 10.1127/0078-0421/2014/0047.
- Kosmas, C. S., Curi, N., Bryant, R. B., and Franzmeier, D. P. (1984). Characterization of Iron Oxide Minerals by Second-Derivative Visible Spectroscopy. *Soil Science Society of America Journal* 48, 401–405. doi: 10.2136/sssaj1984.03615995004800020036x.
- Kosmas, C. S., Franzmeier, D. P., and Schulze, D. G. (1986). Relationship among Derivative Spectroscopy, Color, Crystallite Dimensions, and Al Substitution of Synthetic Goethites and Hematites. *Clays and Clay Minerals* 34, 625–634. doi: 10.1346/CCMN.1986.0340602.
- Kotov, S., and Pällike, H. (2018). QAnalySeries – a cross-platform time series tuning and analysis tool. *Geology* doi: 10.1002/essoar.10500226.1.



- Krapp, M., Beyer, R. M., Edmundson, S. L., Valdes, P. J., and Manica, A. (2021). A statistics-based reconstruction of high-resolution global terrestrial climate for the last 800,000 years. *Sci Data* 8, 228. doi: 10.1038/s41597-021-01009-3.
- Kubelka, P., and Munk, F. (1931). An article on optics of paint layers. *Technical Physics* 12, 259–274.
- Laag, C., Hambach, U., Zeeden, C., Lagroix, F., Guyodo, Y., Veres, D., et al. (2021). A detailed paleoclimate proxy record for the Middle Danube Basin over the last 430 kyr: a rock magnetic and colorimetric study of the Zemun loess-paleosol sequence. *Frontiers in Earth Science* 9:600086. doi: 10.3389/feart.2021.600086.
- Laag, C., and Kreutzer, S. (2022). LESLIE - LoESs coLorimetry signal Enhancement: v0.1.0. doi: 10.5281/ZENODO.7257765.
- Laag, C., Lagroix, F., Kreutzer, S., Chapkanski, S., Zeeden, C., and Guyodo, Y. (2022). Measuring and evaluating colorimetric properties of samples from loess-paleosol sequences. *MethodsX*, in press.
- Lagroix, F., and Banerjee, S. K. (2002). Paleowind directions from the magnetic fabric of loess profiles in central Alaska. *Earth and Planetary Science Letters* 195, 99–112. doi: 10.1016/S0012-821X(01)00564-7.
- Leicher, N., Giaccio, B., Pereira, A., Nomade, S., Monaco, L., Mannella, G., et al. (2022). Central Mediterranean tephrochronology between 313 and 366 ka: New insights from the Fucino palaeolake sediment succession. *Boreas*, bor.12610. doi: 10.1111/bor.12610.
- Leicher, N., Giaccio, B., Zanchetta, G., Sulpizio, R., Albert, P. G., Tomlinson, E. L., et al. (2021). Lake Ohrid's tephrochronological dataset reveals 1.36 Ma of Mediterranean explosive volcanic activity. *Sci Data* 8, 231. doi: 10.1038/s41597-021-01013-7.
- Li, Y., Song, Y., Kaskaoutis, D. G., Zhang, X., Chen, X., Shukurov, N., et al. (2022). Atmospheric dust dynamics over Central Asia: A perspective view from loess deposits. *Gondwana Research* 109, 150–165. doi: 10.1016/j.jgr.2022.04.019.
- Lisiecki, L. E., and Raymo, M. E. (2005). A Pliocene-Pleistocene stack of 57 globally distributed benthic  $\delta^{18}\text{O}$  records. *Paleoceanography* 20. doi: 10.1029/2004PA001071.
- Liu, Q., Zhang, C., Torrent, J., Barrón, V., Hu, P., Jiang, Z., et al. (2016). Factors Controlling Magnetism of Reddish Brown Soil Profiles from Calcarenites in Southern Spain: Dust Input or In-situ Pedogenesis? *Front. Earth Sci.* 4. doi: 10.3389/feart.2016.00051.
- Lu, H., Jia, J., Yin, Q., Xia, D., Gao, F., Liu, H., et al. (2020). Atmospheric Dynamics Patterns in Southern Central Asia Since 800 ka Revealed by Loess-Paleosol Sequences in Tajikistan. *Geophysical Research Letters* 47. doi: 10.1029/2020GL088320.
- Marković, S. B., Stevens, T., Kukla, G. J., Hambach, U., Fitzsimmons, K. E., Gibbard, P., et al. (2015). Danube loess stratigraphy — Towards a pan-European loess stratigraphic model. *Earth-Science Reviews* 148, 228–258. doi: 10.1016/j.earscirev.2015.06.005.
- Maxbauer, D. P., Feinberg, J. M., and Fox, D. L. (2016). MAX UnMix: A web application for unmixing magnetic coercivity distributions. *Computers & Geosciences* 95, 140–145. doi: 10.1016/j.cageo.2016.07.009.

- Moskowitz, B. M. (1980). Theoretical grain size limits for single-domain, pseudo-single-domain and multi-domain behavior in titanomagnetite ( $x = 0.6$ ) as a function of low-temperature oxidation. *Earth and Planetary Science Letters* 47, 285–293. doi: 10.1016/0012-821X(80)90045-X.
- Özdemir, Ö., and Banerjee, S. K. (1984). High temperature stability of maghemite ( $\gamma\text{-Fe}_2\text{O}_3$ ). *Geophys. Res. Lett.* 11, 161–164. doi: 10.1029/GL011i003p00161.
- Paterson, G. A., and Heslop, D. (2015). New methods for unmixing sediment grain size data. *Geochem. Geophys. Geosyst.* 16, 4494–4506. doi: 10.1002/2015GC006070.
- R Core Team (2023). R: A Language and Environment for Statistical Computing, R Foundation for Statistical Computing, Vienna, Austria. doi: <https://r-project.org>.
- Rasmussen, S. O., Bigler, M., Blockley, S. P., Blunier, T., Buchardt, S. L., Clausen, H. B., et al. (2014). A stratigraphic framework for abrupt climatic changes during the Last Glacial period based on three synchronized Greenland ice-core records: refining and extending the INTIMATE event stratigraphy. *Quaternary Science Reviews* 106, 14–28. doi: 10.1016/j.quascirev.2014.09.007.
- Rousseau, D.-D., Antoine, P., Boers, N., Lagroix, F., Ghil, M., Lomax, J., et al. (2020). Dansgaard–Oeschger-like events of the penultimate climate cycle: the loess point of view. *Clim. Past* 16, 713–727. doi: 10.5194/cp-16-713-2020.
- Schaetzl, R. J., Bettis, E. A., Crouvi, O., Fitzsimmons, K. E., Grimley, D. A., Hambach, U., et al. (2018). Approaches and challenges to the study of loess—Introduction to the LoessFest Special Issue. *Quat. res.* 89, 563–618. doi: 10.1017/qua.2018.15.
- Scheidt, S., Berg, S., Hambach, U., Klasen, N., Pötter, S., Stolz, A., et al. (2021). Chronological Assessment of the Balta Alba Kurgan Loess-Paleosol Section (Romania) – A Comparative Study on Different Dating Methods for a Robust and Precise Age Model. *Front. Earth Sci.* 8, 598448. doi: 10.3389/feart.2020.598448.
- Scheinost, A. C., Chavernas, A., Barrón, V., and Torrent, J. (1998). Use and Limitations of Second-Derivative Diffuse Reflectance Spectroscopy in the Visible to Near-Infrared Range to Identify and Quantify Fe Oxide Minerals in Soils. *Clays and Clay Minerals* 46, 528–536. doi: 10.1346/CCMN.1998.0460506.
- Schwertmann, U. (1971). Transformation of Hematite to Goethite in Soils. *Nature* 232, 624–625. doi: 10.1038/232624a0.
- Schwertmann, U. (1988). “Occurrence and Formation of Iron Oxides in Various Pedoenvironments,” in *Iron in Soils and Clay Minerals*, eds. J. W. Stucki, B. A. Goodman, and U. Schwertmann (Dordrecht: Springer Netherlands), 267–308. doi: 10.1007/978-94-009-4007-9\_11.
- Shi, C., Zhu, R., Glass, B. P., Liu, Q., Zeman, A., and Suchy, V. (2003). Climate variations since the last interglacial recorded in Czech loess. *Geophys. Res. Lett.* 30, 1562. doi: 10.1029/2003GL017251.
- Song, Y., Guo, Z., Marković, S., Hambach, U., Deng, C., Chang, L., et al. (2018). Magnetic stratigraphy of the Danube loess: A composite Titel-Stari Slankamen loess section over the last one million years in Vojvodina, Serbia. *Journal of Asian Earth Sciences* 155, 68–80. doi: 10.1016/j.jseaes.2017.11.012.

- Sprafke, T., Schulte, P., Meyer-Heintze, S., Händel, M., Einwögerer, T., Simon, U., et al. (2020). Paleoenvironments from robust loess stratigraphy using high-resolution color and grain-size data of the last glacial Krems-Wachtberg record (NE Austria). *Quaternary Science Reviews* 248, 106602. doi: 10.1016/j.quascirev.2020.106602.
- Sümegei, P., Gulyás, S., Molnár, D., Sümegei, B. P., Almond, P. C., Vandenberghe, J., et al. (2018). New chronology of the best developed loess/paleosol sequence of Hungary capturing the past 1.1 ma: Implications for correlation and proposed pan-Eurasian stratigraphic schemes. *Quaternary Science Reviews* 191, 144–166.
- Sun, D., Chen, F., Bloemendal, J., and Su, R. (2003). Seasonal variability of modern dust over the Loess Plateau of China: SEASONAL VARIABILITY OF DUST IN CHINA. *J. Geophys. Res.* 108. doi: 10.1029/2003JD003382.
- Sun, Y., McManus, J. F., Clemens, S. C., Zhang, X., Vogel, H., Hodell, D. A., et al. (2021). Persistent orbital influence on millennial climate variability through the Pleistocene. *Nat. Geosci.* 14, 812–818. doi: 10.1038/s41561-021-00794-1.
- Taylor, S. N., and Lagroix, F. (2015). Magnetic anisotropy reveals the depositional and postdepositional history of a loess-paleosol sequence at Nussloch (Germany): AMS OF NUSSLOCH LOESS-PALEOSOL SEQUENCE. *J. Geophys. Res. Solid Earth* 120, 2859–2876. doi: 10.1002/2014JB011803.
- Torrent, J., and Barrón, V. (2003). The visible diffuse reflectance spectrum in relation to the color and crystal properties of hematite. *Clays and Clay Minerals* 51, 309–317. doi: 10.1346/CCMN.2003.0510307.
- Tzedakis, P. C., Drysdale, R. N., Margari, V., Skinner, L. C., Menviel, L., Rhodes, R. H., et al. (2018). Enhanced climate instability in the North Atlantic and southern Europe during the Last Interglacial. *Nat Commun* 9, 4235. doi: 10.1038/s41467-018-06683-3.
- Udvardi, B., Kovács, I. J., Kónya, P., Földvári, M., Fűri, J., Budai, F., et al. (2014). Application of attenuated total reflectance Fourier transform infrared spectroscopy in the mineralogical study of a landslide area, Hungary. *Sedimentary Geology* 313, 1–14. doi: 10.1016/j.sedgeo.2014.08.005.
- Vakhrameeva, P., Koutsodendris, A., Wulf, S., Fletcher, W. J., Appelt, O., Knipping, M., et al. (2018). The cryptotephra record of the Marine Isotope Stage 12 to 10 interval (460–335 ka) at Tenaghi Philippon, Greece: Exploring chronological markers for the Middle Pleistocene of the Mediterranean region. *Quaternary Science Reviews* 200, 313–333. doi: 10.1016/j.quascirev.2018.09.019.
- Wacha, L., Laag, C., Grizelj, A., Tsukamoto, S., Zeeden, C., Ivanišević, D., et al. (2021). High-resolution palaeoenvironmental reconstruction at Zmajevac (Croatia) over the last three glacial/interglacial cycles. *Palaeogeography, Palaeoclimatology, Palaeoecology* 576, 110504. doi: 10.1016/j.palaeo.2021.110504.
- Wacha, L., Mikulčić Pavlaković, S., Frechen, M., and Crnjaković, M. (2011). The Loess Chronology of the Island of Susak, Croatia. *E&G Quaternary Sci. J.* 60, 153–169. doi: 10.3285/eg.60.1.11.
- Wulf, S., Hardiman, M. J., Staff, R. A., Koutsodendris, A., Appelt, O., Blockley, S. P. E., et al. (2018). The marine isotope stage 1–5 cryptotephra record of Tenaghi Philippon, Greece: Towards a

detailed tephrostratigraphic framework for the Eastern Mediterranean region. *Quaternary Science Reviews* 186, 236–262. doi: 10.1016/j.quascirev.2018.03.011.

Zeeden, C., Hambach, U., Veres, D., Fitzsimmons, K., Obreht, I., Böskén, J., et al. (2018). Millennial scale climate oscillations recorded in the Lower Danube loess over the last glacial period. *Palaeogeography, Palaeoclimatology, Palaeoecology* 509, 164–181. doi: 10.1016/j.palaeo.2016.12.029.

Zeeden, C., Kels, H., Hambach, U., Schulte, P., Protze, J., Eckmeier, E., et al. (2016). Three climatic cycles recorded in a loess-palaeosol sequence at Sendlac (Romania) – Implications for dust accumulation in south-eastern Europe. *Quaternary Science Reviews* 154, 130–142. doi: 10.1016/j.quascirev.2016.11.002.

Zeeden, C., Krauß, L., Kels, H., and Lehmkuhl, F. (2017). Digital image analysis of outcropping sediments: Comparison to photospectrometric data from Quaternary loess deposits at Şanoviţa (Romania) and Achenheim (France). *Quaternary International* 429, 100–107. doi: 10.1016/j.quaint.2016.02.047.

Zhang, P., Xu, J., Holbourn, A., Kuhnt, W., Xiong, Z., and Li, T. (2022). Obliquity Induced Latitudinal Migration of the Intertropical Convergence Zone During the Past ~410 kyr. *Geophysical Research Letters* 49. doi: 10.1029/2022GL100039.

## 5. Synthesis

This thesis focuses on a loess-paleosol sequence located near the northern Bulgarian city of Pleven. This sequence spans the last 850 ky / 950 ky and was studied at a high and continuous resolution using multiple proxies including environmental magnetism, colorimetry, granulometry, and mid-infrared spectroscopy (ATR-FTIR). By combining data from these different experiments, it was possible to identify the mid-Brunhes climate transition (around 430ka), several crypto-tephra layers, and to evidence preserved millennial-scale variability in the glacial marine isotope stages 12, 6, and 4-2.

# 5

### 5.1. Mid Brunhes climate transition (MBT)

The loess-paleosol sequence Pleven evidences for the first time in Eastern European LPSs the mid Brunhes climatic transition (MBT, (Jansen et al., 1986; Candy et al., 2010; Hodell et al., 2013; Yin, 2013; Wang et al., 2014)) before and after 430ka. Several studies targeting marine benthic  $\delta^{18}\text{O}$ , as well as deep sea temperatures and the  $\delta\text{D}$  Antarctic ice record, ascribe the older interglacials (pre- MBT) as lukewarm, which changes rapidly with the onset of the interglacial MIS11, where following younger interglacials as “super” interglacials which were significantly warmer (EPICA community members, 2004; Lisiecki and Raymo, 2005; Jouzel et al., 2007; Lang and Wolff, 2011; Elderfield et al., 2012; Hodell et al., 2013). Essentially this transition is observed globally but not discussed in Eastern European LPSs. The remarkable differences preserved in the Pleven LPS (reduced/altered or intensely undergone weathering of SP particles and its reduced amplitude pre-MPT, the high amounts of hematite and goethite as well as kaolinite and smectite) indicate a rather extremely weathering enhancing environment which needs high precipitation, seasonality and temperature. This contradicts somewhat the globally covering consent that the pre-MTP interglacials were cooler than the post-MPT interglacials. What can be observed is a rather reddish paleosol development pre-MPT and rather brownish/blackish paleosols post-MPT. Regionally closely located LPSs such as Mircea Voda (Romania) and Titel-Stari Slankamen (Serbia) show similar trends based on geochemically derived weathering intensity indices (such as CPA) and clay content ( $>5\mu\text{m}\%$ ) (Bugge et al., 2013) as observed in Pleven. This might indicate a rather locally driven climate. One interesting idea presented in (Bugge et al., 2013) is their relation with precipitation limitation based on the gradual tectonic uplift of the Carpathians and Dinarides throughout the Quaternary. This might hinder with graining importance the Westerly provided moisture to rain down at the Pleven area or larger lower Danube region.

In addition, the weakly expressed MIS11 interglacial (corresponding to the S4 paleosol) might be a result of rather regional climate differences. All magnetic parameters, weathering indicators such as goethite and hematite reflect for MIS11 a rather weakly expressed pedogenesis, since it is globally one of the strongest interglacials of the last 800 ka. The correlation of the June winter precipitation towards the precipitation model by (Krapp et al., 2021) provides a huge discrepancy for MIS11 which is not (that strong) observed in other interglacials. Calcite shows a less solution and is to some extent still present in the MIS11 interglacial. Presumably, CO<sub>2</sub> contents in the atmosphere acts as a driver of calcite solution.

## 5.2. The total time cover of the Pleven LPS – two solutions

The Pleven LPS provides detailed paleoclimatic information over several glacial/interglacial cycles. The start of deposition (maximum age) is not clear yet, but two potential solutions are provided. The first solution leads to the onset of sedimentation around 850 ka ago, stemming from the study performed by (Evlogiev, 2007). All the tie-points stratigraphically originating from levels above the S6 paleosol complex are coherent with global master stacks such as the LR04 benthic oxygen isotope stack (Lisiecki and Raymo, 2005). However, the S6 and L7, as well as the clays recorded as a goethite function of time, lead to another solution which is consistent with the Titel-Stari Slankamen LPS record (Song et al., 2018b) located in Serbia.

The correlative age model is based on the fluctuations of the frequency dependence of magnetic susceptibility, then improved by using hematite and goethite variations. In this case, the maximum age of the sequence has a fundamental pre-condition: the Pleven sequence sits on a Pliocene denudation surface (PDS), arguing for an onset of sedimentation around 820 ka (Evlogiev, 2007, 2019). However, (Evlogiev, 2007) do not provide any arguments or even discussion for the 820 ka onset of sedimentation. Furthermore, several closely to Pleven located LPSs evidentially reflect longer than 820 ka cover such as Koriten (Jordanova and Petersen, 1999a, 1999b), Viatovo (Jordanova et al., 2008), Zimnicea (Radan, 2012), Tuzla (Balescu et al., 2003, 2010) in Romania. Furthermore, nomenclature problems arise from the numbering of the paleosols. In the Serbian composite record Titel-Stari Slankamen (Song et al., 2018b), the high resolution investigation led to the distinct identification of paleosols S6-S8 in the lower part. Below the S8, the Brunhes Matuyama boundary was identified. Taking account the stratigraphic position, the Bulgarian Viatovo and Koriten S6 comprises S6 – S8. The Bulgarian S6 paleosol complex is rather amalgamed but can be disentangled focusing on the Koriten S6, which has on the lower part a peak corresponding to the Titel-Stari Slankamen S8, followed upwards by a less expressed peak associated with the S7 in Titel-Stari Slankamen. The Titel-Stari Slankamen S6 is hence preserved as a small peak in Koriten at c. 29m. The amalgamed paleosols are a common feature of LPSs from the lower Danube Basin. (Evlogiev, 2019) showed in Figure 67 and 68 nicely, that with increasing distance to the Danube River the amalgamation of paleosols increases. However, a definite onset at that age remains speculative, as the age of the PDS could be contested. Underway investigations, such as the exact identification of the paleomagnetic Brunhes-Matuyama boundary at 781 ka, will help clarify the correlation of the lower part of the profile.



My concerns regarding the currently published lower (L7/S6) correlation and onset of sedimentation at 820 ka results from 1) mass accumulation rates which are increased in MIS 19 (a relatively strong interglacial) and 2) the goethite (proxy for paleoprecipitation) fluctuation in comparison with the Titel-Stari Slankamen record located in Serbia and the missing work regarding the Danube history in the lower Danube basin. Regarding the accumulation rates in Pleven, it is not straightforward that all interglacials reflect a decreased accumulation rate which is caused by lesser windspeeds and less available source material because of a relatively higher vegetation cover. However, glacials are characterized by high accumulation rates because of missing vegetation cover and thus increased wind speeds and storm events during glacials. In Figure 10, the dark-blue goethite curve reflects in the lower part of S6 (correlated with the age models of Pleven) towards MIS19 an anomalously high sedimentation rate, even higher than in MIS 16 which is after MIS12 the harshest and best expressed glacial.

Furthermore, there is a fundamental difference of the depositional systems in the Danube Basin north and south of the present-day flow of the Danube including the Dacian Basin and its successor which is the Danube river system which puts Evlogiev's age assignment of sedimentary onset at Pleven (Evlogiev, 2007) taken in (Jordanova et al., 2022) as 820 ka into question. South of the present day Danube, one observes today decametres thick LPS resting on Neogene (mainly Pliocene) denudation surfaces or on Pleistocene strath or accumulation terraces of the Danube and its tributaries draining the North Bulgarian Plain. In contrast, in most areas north of the Danube (the Romanian Plain) the base of LPS is not exposed and where it is exposed the loess deposition starts discordantly or even concordantly on older Pleistocene alluvial or even "loess-like" deposits. A quite contrasting tectonic setting and regime is responsible for this setting: The Lower Danube Basin or late Dacian Basin experienced from the Late Pliocene to Early Pleistocene on a differentiated tectonic history dominated by significant uplift in the south and at the southern and eastern outer margin of the Carpathian Mountains, whereas for wide parts of the Romanian Plain subsidence and hence deposition prevailed (Andreescu et al., 2013; Necea et al., 2013; Van Baak et al., 2015; Evlogiev, 2019). It should be noted that sedimentary units of the Dacian Basin like alluvial fan or lacustrine formations or basal contacts of LPS and are time-transgressive and even intercalations of alluvial facies bodies with LPS occur (Andreescu et al., 2013; Necea et al., 2013; Krézsek and Olariu, 2021). To date, precise numerical ages of the locally different and time-transgressive onset of LPS formation in the Romanian Plain are unknown. Similar to the Bulgarian Plain typical loess is frequently underlain by superimposed partly amalgamated rubified palaeosols

forming stacks of strongly weathered silicate dust deposition named Red Clay Formation (RCF). In contrast to the Chinese Loess Plateau where the transition from Red Clay to typical loess occurs stratiform in the entire plateau in the latest Upper Pliocene, the ages of the top of the RCF in the Lower Danube Basin can range from at least Lower up to Middle Pleistocene (e.g. (Jordanova et al., 2007; Marković et al., 2015; Balescu et al., 2020)).

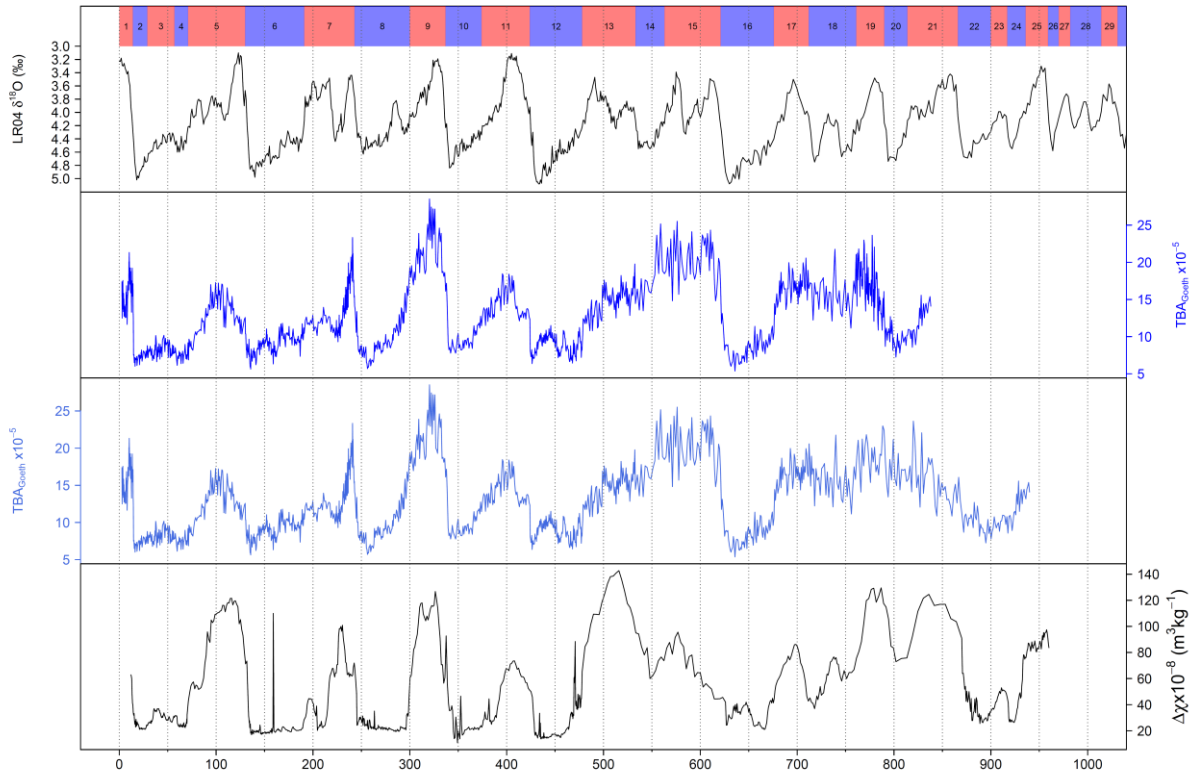


Figure 6: Comparison of two alternative age models for the lower part of the Plevan LPS. Indication for a time cover of 950ka instead of 830ka and the manually tuned Xlf curve of Titel Stari-Slankamen following the description and correlation of (Song et al., 2018b), utilizing the software QAnalySeries (Kotov and Pälke, 2018).

Wavelets analysis of the cyclicities preserved in the goethite proxy record, using the alternative age model, is presented in Figure 11. A weak but rather visible 23 ky frequency is preserved, standing for the combined effects of axial and apsidal precession result in the combined precession. Obliquity is also preserved with a frequency of 41 ky nearly throughout the whole timespan, which was not identified before by application of the initial correlative age model (see supplement of Chapter 3.3.). Another argument for the alternative age model is the indication of the demise of the mid-Pleistocene transition (MPT). The MPT is a gradual change from a 41 ky cyclicity dominated to a 100 ky dominated world, from 1250 to 700 ka. This indeed appears to be the case, as the power of the 100 ky cyclicity of the wavelet spectrum is lower in this interval, relative to the younger 700 to 0 ka interval.

However, the 41 ky cyclicality is rather weakly expressed in the wavelet spectrum. Another component, at the 201 ky cyclicality, could indicate that the transformation from 41ky cycles towards 100ky cycles the balance is rather weighted on 100 ky cycles. Interestingly, in a unique study stemming from the Chinese LPS Luochuan grain size record, (Lu et al., 2003) found in their wavelet analysis a quasi-200 ky cyclicality, dominant in the period before 500 ka, with a transition towards 100 ky for younger ages. The same change in power can be observed in the wavelet spectrum of the goethite fluctuations.

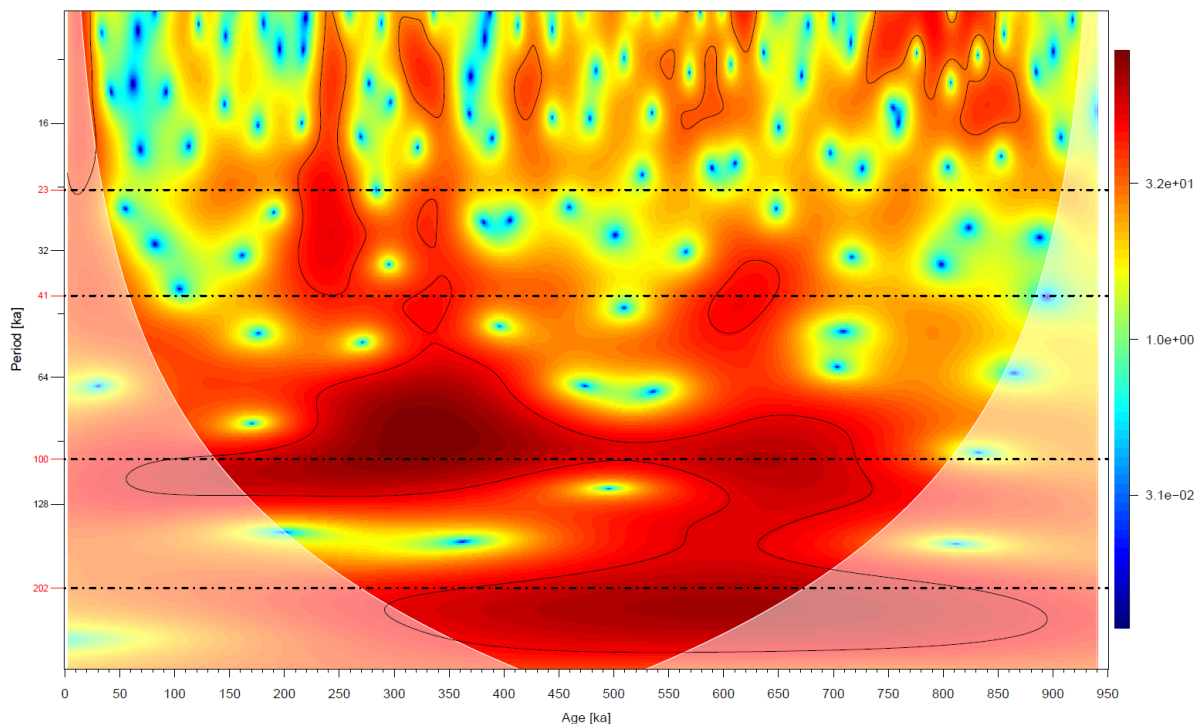


Figure 7: Wavelet analysis of the goethite fluctuation of the Pleven LPS applying the alternative age model solution for the lower part of the Pleven LPS. Orbital cycles' frequencies are indicated with dashed lines. The 80% significance level is indicated by solid black lines.

Further evidence for one or the other solution might be only provided by the stratigraphical location of the last paleomagnetic reversal (Brunhes-Matuyama boundary at ca. 781 ka). Since in the second field campaign more than 600 oriented samples were taken, demagnetization experiments and a throughout paleomagnetic study will hopefully provide records of directions and relative intensity of the paleomagnetic field at Pleven. Such records would likely indicate which age model is the most robust.

### 5.3. Identification of millennial scale climate variability

The identification of millennial scale variability climate change is a challenging task being performed on loess-paleosol sequences. However, several studies evidenced for the last glacial cycle preserved millennial scale climate change being preserved in eastern European LPSs either in grain size fluctuations (Shi et al., 2003) or magnetic parameter variations (Zeeden et al., 2018) or with aid of luminescence dating of weakly developed paleosols (Rousseau et al., 2011; Veres et al., 2018). For the penultimate glacial (MIS6) the close to the Pleven LPS Harletz section provides robust data for preserved millennial scale climate change imprinted in loess (Antoine et al., 2019; Rousseau et al., 2020). Up to today, the evidence for older preserved millennial scale climate change is missing but can be the first time evidenced being preserved in the Pleven LPS as shown with Chapter 3.3. MIS 12 is one of the harshest glacials during the Quaternary and reflects with precipitation sensitive proxies such as colorimetrically derived goethite contents for the younger part of MIS12 Dansgaard-Oeschger-mean duration events following a mean duration of 1.6 ka. However, the Pleven LPS is rather condensed and loess units are relative to other records not thick. However the robust identification of DO-cycles and Heinrich events performed for the last glacial period allow the robust identification of DO-cycles in MIS12 based on goethite variations. However, as I work thus on other, higher resolved LPSs such as Zmajevac (Wacha et al., 2021), I desire to apply the multi proxy approach performed on Pleven to be applied for this Croatian LPS. Loess units are multiple times thicker as in Pleven and allows thus potentially not only the identification of millennial scale climate change variability but also the recognition of internal structures of Dansgaard Oeschger cycles as evidenced for a high sedimentation rate profile located in Romania (Vlasca, (Laag, 2019; Laag et al., 2019b)).

#### 5.4. Multi-proxy (Crypto-)tephra identification in Pleven

Tephra layers provide valuable stratigraphical marker horizons in sedimentary (terrestrial) archives such as loess-paleosol sequences for time intervals older than the last 50 ka and ~250ka which are the dating limits of commonly applied radiometric and dosimetric dating methods  $^{14}\text{C}$  dating and luminescence dating. However, several sedimentary archives cover far older time intervals in the Quaternary in Eastern Europe (Jordanova et al., 2008; Constantin et al., 2015; Marković et al., 2015; Zeeden et al., 2016; Song et al., 2018b; Sümegi et al., 2018; Hlavatskyi and Bakhmutov, 2020, 2021). Age control was established either with aid of paleomagnetic dating or orbital forcing approaches (orbital tuning), or correlations to stacked global target curves such as LR04 (Lisiecki and Raymo, 2005) or for stratigraphically younger part with aforementioned radiometric and dosimetric approaches.

However, the Pleven LPS (with no field nor data evidence for hiatus) is the first terrestrial archive investigated in such a detail based on the applied multi-proxy approach from the disciplines of environmental magnetism, colorimetry, ATR-FTIR and granulometry. Coupled with a very high resolution and the integration of advanced and partly improved methods such as color contrast enhancement, IRM component unmixing and grain size end-member unmixing, this multi-proxy approach leads to a vast number of different parameters and ratios and allowed the detailed study of stratigraphically known crypto-tephra layers and in field widely distributed outcropping tephra layers. The uninterrupted accumulation strengthens further the overall results regarding millennial scale climate variability, the detection of severe changes in prevailing climate systems before and after the mid Brunhes climate event at c. 430 ka and the detection of 55 potential crypto-tephra layers preserved in this archive. Furthermore, the project presented leads to a necessary re-investigation of already acquired and published data as well as a potentially re-sampling of some of the major sites which are major correlation targets. Methodological advances in the discipline of colorimetry enabled a precise record of the qualitative goethite content which appears as a highly moisture sensitive record enabling the detection of millennial scale climate change variability in concert with the NGRIP Dansgaard-Oeschger cycle and Heinrich event record and further evidences millennial scale variability in the penultimate glacial MIS6 and thus not evidence so far in MIS12.

Already measured but so far not further investigated are more than 650 samples based on their anisotropic magnetic susceptibility (AMS). However, initial evaluations of acquired data of these samples which were taken in a second sampling campaign in September 2021, reflect that the degree of anisotropy is relatively low, which potentially hinders a further evaluation

with aim to reconstruct paleo-wind directions indirectly indicating potential source areas of the dust accumulated at Pleven.

However, the aforementioned geochemical fingerprinting applied on volcanic glass shards to trace back and uniquely identify the tephra's origin require the preservation of non-weathered glass shards. This requires several conditions at the location of deposition. The first condition is coupled to the sediment cover which should have happened with high speed, meaning that a high sedimentation rate is required to protect accumulated glass shards with fresh sediment to protect the glass shards from weathering. Another factor is related to turbation. Volcanic glass shards are highly sensitive to mechanical penetration, which is happening due to bioturbation (e.g., by ground penetrating mammals which are commonly occupying LPSs in various depths in the Eastern European region) or plants penetrating surface- or close to the surface exposed glass accumulations. Also the prevailing climate e.g., intense rainfall or temperature changes might have an negative impact on the preservation quality and penetration depth on accumulated glass shards. This explains from a current point of view, why younger (c.39.8ka old) glasses preserved like stemming from the Romanian LPS Urluia were successfully geochemically fingerprinted and correlated towards a major eruption of the super-volcano complex at the Phlegraean fields (Italy). However, older volcanic ash layers previously identified in eastern European LPSs failed in the geochemical fingerprinting approach since the glass shards identified were most of the times already affected by weathering and therefore impossible to investigate via geochemical composition.

FORC diagrams initially presented as a poster at the IAGA-IASPEI conference (Laag et al., 2021b), evidenced higher magnetic interaction in the widespread L2 tephra layers preserved in the Serbian LPS of Zemun (Laag et al., 2021a) and in-field outcropping L2 tephra layer at the Bulgarian LPS Pleven ((Jordanova et al., 2022) and Laag et al., in prep.).

Furthermore, samples reflecting a rather low  $IRM_{-100mT}/M_S$  ratio most likely lose their magnetization easier when the external field is set to 0. This might be explained because these samples have a weaker internal magnetic interaction (which is shown in the poster with the FORCs in (Laag et al., 2021b) and are thus not that efficient to maintain their magnetization.

This enabled me, in this PhD thesis, to use these parameters as indicators identifying tephra layers. First of all we have to understand that all bulk samples taken from loess-paleosol sequences present mixtures of magnetic minerals present in different abundances and grain sizes. A consistent investigation of different magnetic components and magnetic grain sizes

stemming from IRM acquisitions was never applied to LPSs covering time intervals of the Quaternary in that resolution. This rather highly applied resolution leads to the discrimination between pedogenic, source-related and tephra detecting processes. In general, four components reliably discriminated by conducted experiments were identified, and a 5<sup>th</sup> required component initially presented in (Laag et al., 2021a) with a main Bh of 40 mT and indicating in the following tephra layers. These in Pleven identified tephra layers all (when investigated) require a 5<sup>th</sup> component of this specific 40 mT soft mineral magnetic signal.

The novel application of mid-infrared-spectrometry based on a Fourier Transform Attenuated Reflectance Spectrometer first time detailed applied to LPSs provide a very promising bypass of the aforementioned difficulties of geochemical volcanic glass shards fingerprinting.

Based on the rather low sediment accumulation rate and the very likely penetration of pedogenesis towards stratigraphically below located loess units may hinders the identification of short-term geomagnetic excursions serving as independent age control points. However, as mentioned before, there were a huge number of crypto-tephra layers identified based on mineral magnetic, magnetic-granulometric, and smectite content results. The large majority of these crypto-tephra layers were not detected in any of the many conducted studies on LPSs performed in the Eastern European Loess belt. However, several other types of archives such as Lake Ohrid, Tenaghi Philippon, Sulmona, and the Fucino Basin host many tephra layers which are geochemically investigated.

These geochemical investigations allowed to determine a unique geochemical “fingerprint” of each glass-shard rich tephra layer allowing the trace and correlation to not only the source region but even the event of outbreak since every volcanic eruption produces a uniquely composition of minerals traceable by various geochemical quantifying element and mineral composition like the nowadays applied ICP-MS (a laser ablation quantification method). Nevertheless, most of the identified crypto-tephra layers fall (under application of the most recent and here presented correlative age-model) together with radiometrically dated tephra records from the aforementioned other-typed paleoclimatic archives.

The “falling-together” is meant since the age difference of the resulting ages of radiometrically dated tephra layers towards the correlative age model resulting ages for the Pleven LPS are far below the 4ka uncertainty of the correlation target of LR04 (Lisiecki and Raymo, 2005) but are always inside the radiometrically determined  $1\sigma$  uncertainty age range which is sometimes discrepancy by less than 2ka.



The idea is novel, because it is assumed, if the geochemical compounds of glass shards can be determined, spectral analysis of the weathering remains can be individually too, but another method of choice is required able to capture and evaluate weathering remains of volcanic glass shards. ATR-FTIR analysis were successful in addressing aforementioned target ideas. ATR-FTIR analysis have (compared to commonly applied XRD analysis) the advantage to register even amorphous silicates which are tentatively assigned to weathered volcanic glass shards and non-detectable via XRD analysis. Due to my contributing colleagues Dr. Daniel Veres, Dr. Ulrich Hambach (both sent samples stemming from currently investigated LPSs of Romania at Nasturelu and Baneasa), Dr. Luigi Vigliotti (providing confirmed CI-Y5 tephra samples stemming from the Ionian Sea marine cores), Dr. Martin Kehl (provided samples stemming from the Neka-Abelou Iranian LPS where a tephra was even geochemically investigated), Dr. Lara Wacha (provided samples from the Croatian LPS Zmajevac, where based on novel analysis some tephra layers are assumed being preserved), I was able to collect and systematically investigate tephra samples stemming from many LPSs spread in eastern Europe and the Caspian Sea Region and thus reference samples of the (loess) material in which the tephra material are embedded in and thus paleosol material which is still under internal debate having similar magnetic mineralogy and grain size properties such as tephra layers.

However, ATR-FTIR experiments coupled with principal component analysis (PCA) provide very promising initial results. The first three components (hereafter labeled as PC1, PC2, and PC3) show in different constellations the major idea. First of all, the bi-plot of PC1 and PC2 does not provide a clear separation between loess and paleosol samples or tephra samples. However, PC1 seems to split the Iranian tephra samples stemming from the LPS Agh Band from the rest of the 3 three sample groups. PC2 however, seems to separate better between loess and paleosol samples, but tephra samples fall together with loess samples as well as with paleosol samples. Bi-plotting PC1 and PC3 allows a better discrimination of PC3 where loess samples and paleosol samples rather plot with negative values of PC3 and positive values for tephra samples.

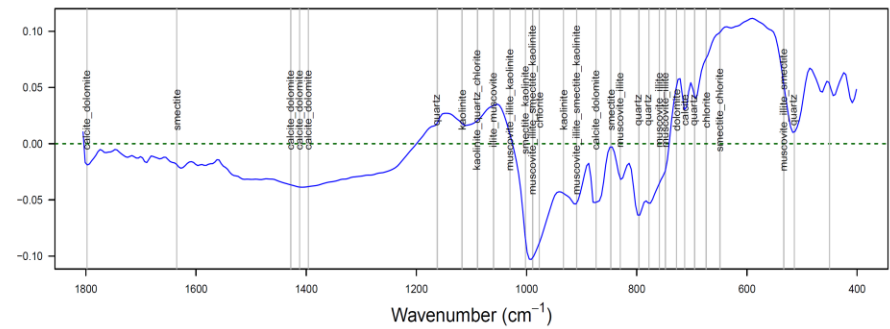
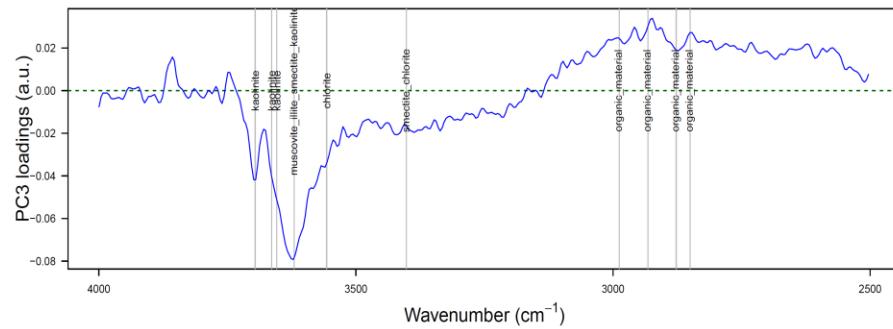
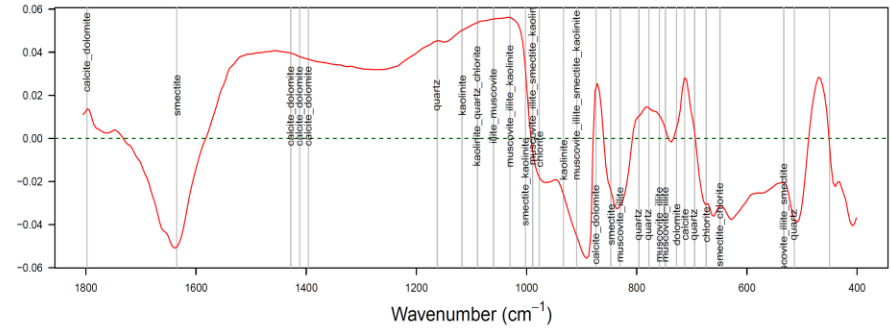
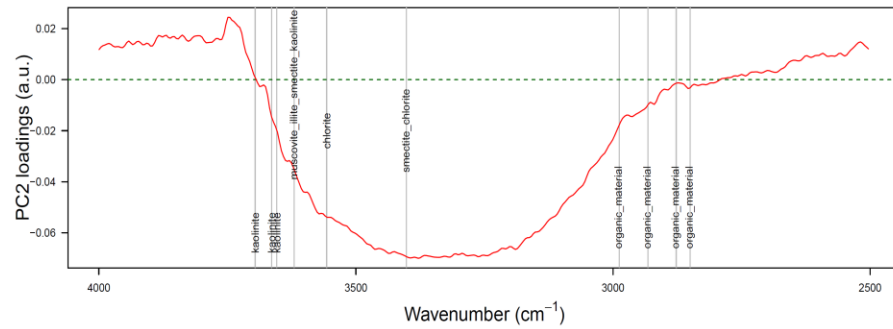
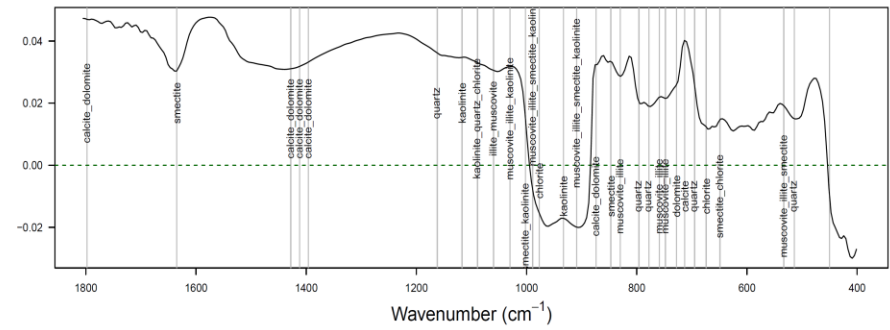
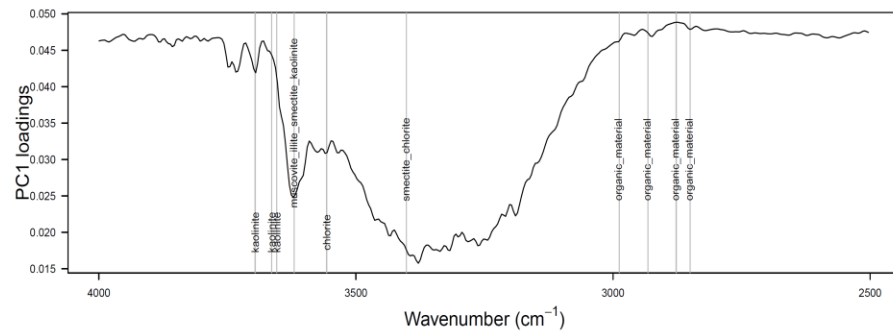


Figure 8: Principal Component Analysis (PCA) loadings for Principal components 1 (black), 2 (red), and 3 (blue). Wavenumber positions are indicated as vertical grey bars.

The next investigation of PC2 and PC3 leads to the desired outcome. PC2 separates paleosol samples (negative loadings) from loess samples (positive loadings) very well. PC3, which explains only 6.5 % of the variance splits with negative values paleosol and loess samples and with positive values nearly all tephra containing samples. What is even more remarkable are two important clusters of tephra falling together. The first cluster in the quadrant II contains samples stemming from the in-field outcropping L2 tephra layer at Pleven, which contains samples from the 2018 (Suhia Kladenetz, SK (Jordanova et al., 2022)) conducted sampling campaign with the samples SK03\_158\_160, SK03\_150\_152 and SK03\_162\_164. Thus, one sample stemming from the 2021 campaign PL21\_L2teph\_lense732 stemming from the in-field outcropping tephra lens of the L2 tephra layer. Hence, the only L2-tephra layer containing stemming from Zemun (Z\_V\_117 (Laag et al., 2021a)) falls within this cluster as well as the L2-tephra layer samples stemming from the novel Romanian LPSs currently under investigation Baneasa (BAN\_01\_tephra) and Nasturelu (NAS\_01\_tephra). From pedostratigraphic investigations, coupled with field notes and their stratigraphical position of this L2 tephra layer, it is assured it is the same tephra layer and underlines therefore the value of application of this method, since it is capable to identify based on their individual ATR-FTIR spectra the identical tephra layer.

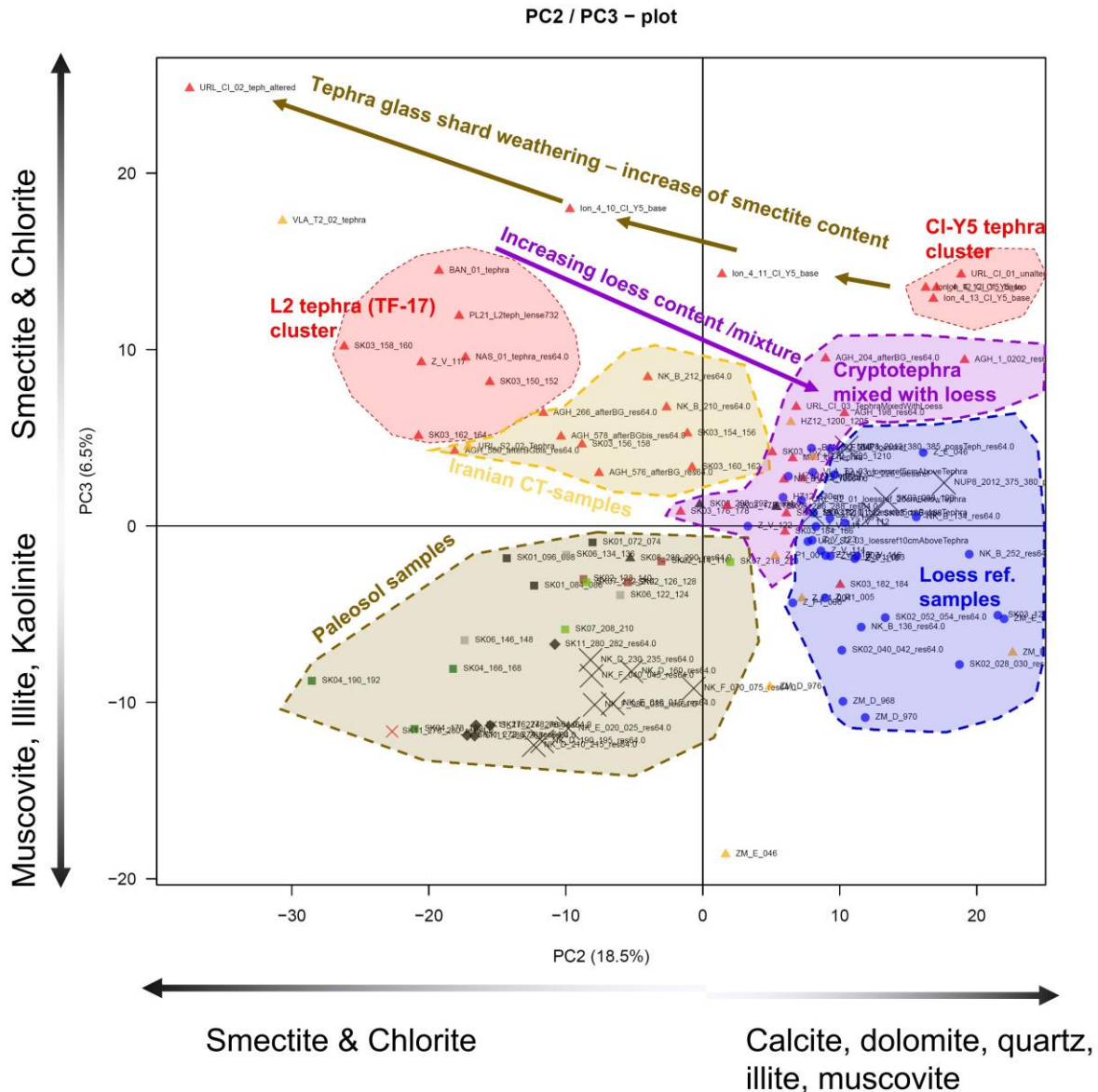


Figure 9: Principal component analysis. PC 2 and 3 enable the discrimination of paleosols, loess and crypto-tephra samples.

Out of curiosity, the well-known and geochemically identified and finger-printed Campanian Ignimbrite Y5 tephra layer was investigated with this method but with aim to 1) separate it, based on its spectral properties from other tephra layers and 2) investigate, if the same tephra layer (assured by geochemical composition) show the same mid-infrared spectral properties even when distinct samples were preserved in different types of archives. In this case, CI-Y5 tephra samples stemming from marine cores (Ionian Sea (Vigliotti, 2015)) and the thick CI-Y5 tephra deposition at the Romanian LPS at Urluia (Fitzsimmons et al., 2013) were investigated. The outcome is more than promising. The cluster found in Quadrant I targets pure-non-weathered tephra material from Urluia (URL-CI\_01\_unaltered, and three samples stemming

from the Ionian Sea marine cores (Ion\_4\_13\_CI-Y5\_base, Ion\_4\_12\_CI\_Y5\_base, Ion\_4\_12\_CI\_Y5\_top). The continuous transition of identified tephra layers towards more positive values in PC2 and decreasing positive values in PC3 may indicate a higher mixture of loess with tephra material. However, he underlines, that this method even is likely independent on the archive conditions where the tephra layers are preserved in.

To summarize, initial analysis of the ATR-FTIR spectra acquired in a high resolution coupled with principal component analysis does not even allow a discrimination in LPSs between loess, paleosol and (crypto-)tephra samples but even discriminates in this example between individual tephra layers. Even more, these tephra layers can be spread and preserved over the whole Balkan area and are still identifiable given different sediment accumulation rates (protecting in various degrees the accumulated volcanic ashes from weathering) or climate conditions during or after deposition (controlling weathering degree of tephra material as well). Even more, the proposed method is capable to identify the geochemically proven equivalent of the same tephra stemming from completely different archives such as shown here LPSs and marine cores.

Reasons for this different principal component characteristics allowing the separation between loess and paleosols and tephra samples as well as the individual tephra separation requires an enhanced investigation of the principal component loadings reasoning the different clusters and separations in the PCA plots. Therefore, as shown below, the loadings per wavelength were investigated which might reflect the reason of mineral abundances preserved as remains after weathering. However, this method needs further refinement. ATR-FTIR experiments in such detail are for now the first time applied to a LPS. Existing data bases and tables so far published are mostly addressing clay-mineralogy wavenumber positions which might not represent weathered materials of crypto-tephra layers. A detailed investigation of mid-infrared spectra for known (identified e.g., with aid of other experiments such as XRD) minerals preserved in a loess-tephra mixture might be a promising approach to better evaluate ATR-FTIR spectra aiming to identify and discriminate/characterize (crypto-) tephra layers in LPSs.

## 5.5. Future work

### 5.5.1. Pleven

There is obviously more research and investigations needed moving forward from this thesis. For the Pleven LPS during the field campaign conducted in September 2021, samples were taken to be dosimetrically dated via luminescence dating. In total, six samples were taken in the loess units representing MIS2, MIS4, and MIS6. The four samples of MIS 6 bracket the in-field outcropping L2 tephra and might confirm the target age of its potential equivalent of TF-17 (dated in Fucino to c. 159 ka). The investigations of the luminescence ages are ongoing and provide independent and absolute age control which might confirm the correctness of the correlative age model. Hence, further potential crypto-tephra candidates found during MIS6 might be confirmed with their associated ages as well. Thus, during the sampling campaign in September 2021, more than 600 oriented samples were taken in order to perform investigations of the anisotropy of magnetic susceptibility (AMS). Samples were taken continuously over the whole profile in 10cm intervals with 2-5 samples from the same depth interval. Paleosol complexes 5 and 6 were taken in 2cm intervals. Thirty five oriented samples were taken horizontally spread over several meters from outcropping tephra material from the L2 tephra. All samples are already measured for AMS, and the evaluation of the data is ongoing. This is the first high resolution AMS data set for Eastern European LPSs. It is envisaged to utilize results from AMS measurements to investigate the magnetic fabric and thus, if possible, to reconstruct paleowind directions. Paleowind directions might provide insights into potential source areas. Thus, the samples stemming from the L2 tephra might point towards its origin and thus gives rise about the AMS of tephric material compared to bracketing loess which might provides insights about the formation of magnetic grains during highly explosive volcanic eruptions.

Hence, oriented samples will be further investigated with aid of demagnetization experiments to reconstruct the Earth's magnetic field strength and direction. Given the correlative age models presented in Chapters 3.1. and 3.3, it is likely that on the base of the profile the geomagnetic reversal (Brunhes-Matuyama Boundary) is preserved. Studies performed on LPSs of the Carpathian and lower Danube basin were already successful in the detection of the Brunhes Matuyama Boundary. This will be an important independent time marker with strengthens further the so-far correlative age model for Pleven. Hence, several geomagnetic excursions are detected over the Quaternary period such as the Mono Lake, Laschamp, post-Blake and Blake as well as the Iceland Basin and Big Lost. Geomagnetic excursions are in sediments not always represented by switches of declination and inclination such as full

reversals but might be identified by a decrease of the relative paleointensity. However, since the latest field campaign did not reach the base as such SK18 did, oriented blocks were taken in 2018, which are currently under investigation by the NIGGG (Bulgaria). Regarding all the identified 55 tephra candidates, which are composed in most cases by more than one sample, complementary highly resolved IRM acquisitions are planned being performed on samples, which were not investigated yet by this experiment. Furthermore, low-temperature magnetic experiments are envisaged being performed on tephra samples from Pleven. These investigations give rise about the precise mineralogical composition of the iron (titanium) iron oxide phases.



### 5.5.2. Nussloch P9

So far non discussed are my attempts to study a LPSs in Western Germany (Nussloch, P9). The Nussloch LPS is one of the most intensely studies profiles of the Rhine Valley loess area. The profile is located above the confluence of Rhine and Neckar rivers. The NUP9 profile is a infilled dry valley which was fed by surrounding loess gredas. Objectives of this study is the determination of the age of the infill, a discrimination of different time intervals of the infill and the investigation of the thick paleosol which had been formed in-situ. The NUP9 profile is nearly 5m thick and might be divided into two parts, a lower part which contains an in-situ formed paleosol and an upper part which is potentially eroded material from the top of the greda. The characterization of the in-situ formed Luvisol is influenced by slope deposits. This intermixture of pedogenesis and slope material supply might be applicable for other LPSs which indicate a tilted stratigraphy. Furthermore, the absolute age control together with the rapid cover of the Luvisol from the top of the greda might allow to investigate the velocity of pedogenesis under in-situ conditions. To answer all mentioned objectives, a multi-proxy investigation of 95 samples taken in 5 cm continuous resolution were taken. Magnetic (susceptibility, hysteresis, backfield experiments, and AMS), colorimetric (DRS), granulometric experiments were performed on all samples. Furthermore, carbon and calcium contents were measured on all samples. The Analysis of all data is in progress as well as the investigation of thin sections. Due to the new colorimetric measurement protocol, the re-measurement of diffuse reflectance spectra for the Nussloch P9 LPS are planned.

### 5.5.3. Zmajevac

The Zmajevac section is located in Croatia and recently investigated (Wacha et al., 2021). It is a 23m-covering loess paleosol sequences which was investigated by high resolution (2cm continuous) grain size experiments applied on all 1012 samples, accompanied by bulk and clay mineralogy as well as low-field and frequency dependent magnetic susceptibility and colorimetric measurements performed continuously but in lower resolution on 111 samples. Absolute dating was performed with aid of luminescence dating and combined with a correlative dating approach performed via the correlation of frequency dependent magnetic susceptibility to LR04 (Lisiecki and Raymo, 2005). The outcome of this approach led to the assumed time cover of the last three interglacial/glacial cycles (see (Wacha et al., 2021), Figs. 9 and 10). Since this publication I was able to measure all remaining samples for magnetic susceptibility and its frequency dependence and further measured hysteresis, and backfield experiments on 250 sample of this sequence. The detailed data now indicates that significantly more time is covered within the Zmajevac LPS (Figure 12). Furthermore, I measured all samples for DRS properties but the extraction of hematite and goethite is still pending. The new DRS protocol (presented in Chapter 2) was not applied for DRS measurements and therefore shall be remeasured. However, the redness ( $a^*$ ) values are presented in Figure 12. However, several arguments rather indicate the time cover of the last 550 ky than 350 ky. Unfortunately, the Zmajevac LPS was not continuously sampled and gaps in data are present in the uppermost weakly developed paleosol, and a more than one meter sampling gap in the third paleosol. This age assignments regarding the longer timespan covered in Zmajevac is not in conflict with the luminescence ages, which are for the older >100 ka minimum ages. Further, the amplitude of the redness and magnetic susceptibility is both the highest in MIS9 and MIS 13, and with respect to MIS11 not that well expressed. Especially the very red appearing MIS 9 and MIS 13 (see the Pleven Hematite curve) are resembled in Zmajevac. Thus MIS 12 is one of the most intense glacial periods. These intensified glacial conditions have increased the dust supply in LPSs and explain why MIS12 assigned here has a thickness of nearly four meters. In Figure 14 the LR04 stack is displayed and marine isotope stages shown above. The two panels below show the redness and the percentage of magnetic susceptibility. Below, the low-field magnetic susceptibility from the Pleven site is shown. The macroscopic tephra layers preserved in Lake Ohrid are indicated in dark violet superimposed on the percentage of magnetic susceptibility of Zmajevac and tephras identified in Pleven are indicated as vertical bars. It is obvious, that in Zmajevac 20 sharp peaks in the magnetic susceptibility can be observed, which

fall in part together with thick tephras preserved in Plevan and macroscopic tephras from Lake Ohrid.

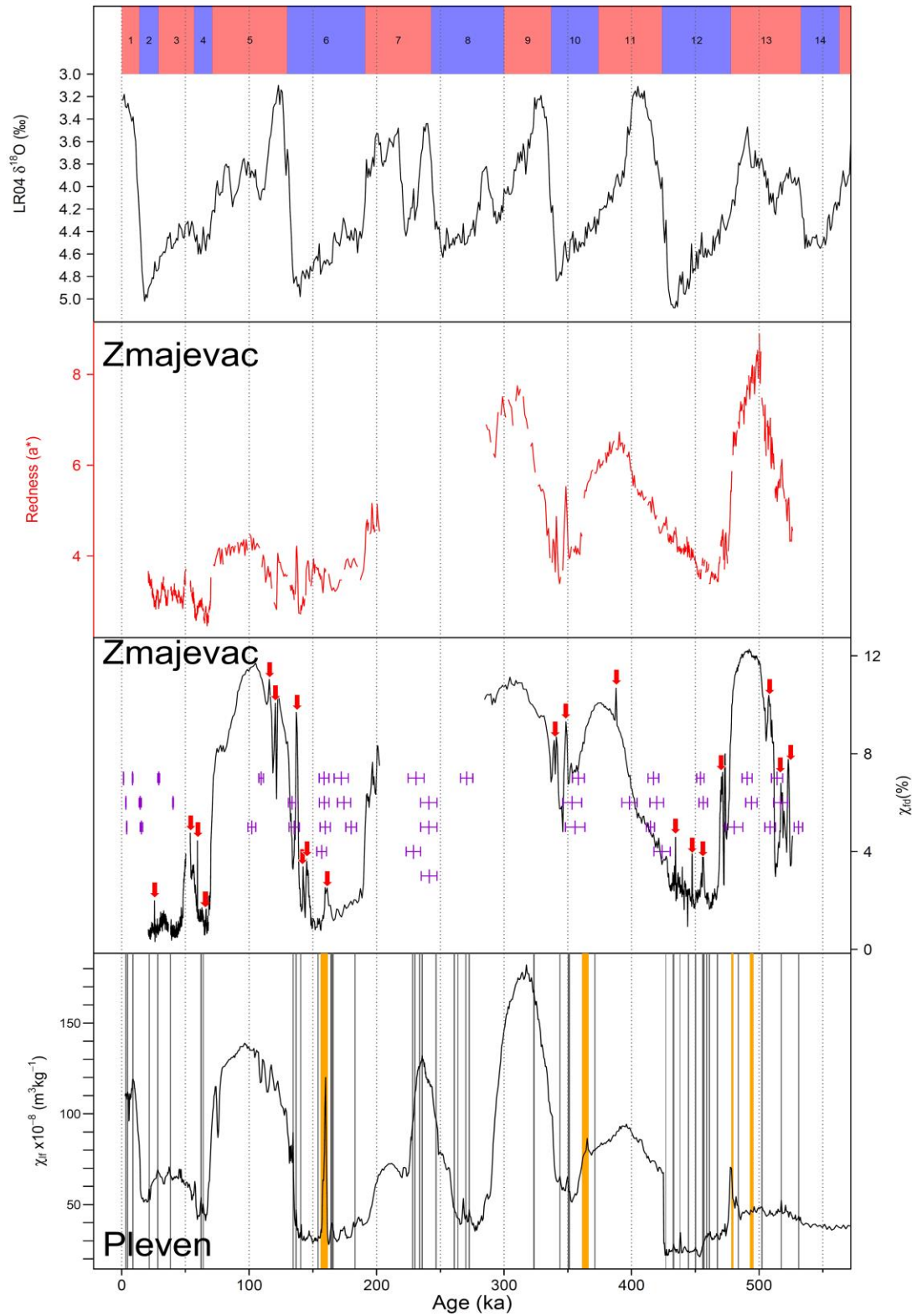


Figure 10: LR04 stack and redness ( $a^*$ ) and percentage of magnetic susceptibility on an alternative age scale.

However, the Zmajevac LPS has thick glacial loess deposits in MIS 12, 6 and 4-2, which are multiple times thicker than in the Pleven LPS. I plan to investigate the Zmajevac LPS further applying the same multi-proxy approach applied for Pleven. Pleven evidenced in rather condensed glacial units the preservation of millennial scale climate variability. The thicker loess units in Zmajevac will potentially provide more detailed insights. Hence, as indicated for now only by the magnetic susceptibility, several peaks might evidence the presence of 20 crypto-tephras contained in Zmajevac. Further magnetic grain size and smectite mid-infrared experiments conducted on these samples might strengthen arguments for preserved crypto-tephras. In case that holds true, Zmajevac becomes a further tephra rich paleoenvironmental archive. Furthermore, the significantly higher sedimentation rates at Zmajevac compared to Pleven might have protected deposited tephra glass shards, which might be able to be geochemically fingerprinted to provide tephrochronological constrains for Eastern European loess paleosol sequences.

## References

- An, Z., Kukla, G. J., Porter, S. C., and Xiao, J. (1991a). Magnetic susceptibility evidence of monsoon variation on the Loess Plateau of central China during the last 130,000 years. *Quat. res.* 36, 29–36. doi: 10.1016/0033-5894(91)90015-W.
- An, Z., Kukla, G., Porter, S. C., and Xiao, J. (1991b). Late quaternary dust flow on the chinese Loess Plateau. *CATENA* 18, 125–132. doi: 10.1016/0341-8162(91)90012-M.
- Andreescu, I., Codrea, V., Lubenescu, V., Munteanu, T., Petculescu, A., Ştiucă, E., et al. (2013). New developments in the Upper Pliocene–Pleistocene stratigraphic units of the Dacian Basin (Eastern Paratethys), Romania. *Quaternary International* 284, 15–29. doi: 10.1016/j.quaint.2012.02.009.
- Antoine, P., Lagroix, F., Jordanova, D., Jordanova, N., Lomax, J., Fuchs, M., et al. (2019). A remarkable Late Saalian (MIS 6) loess (dust) accumulation in the Lower Danube at Harletz (Bulgaria). *Quaternary Science Reviews* 207, 80–100. doi: 10.1016/j.quascirev.2019.01.005.
- Antoine, P., Rousseau, D.-D., Fuchs, M., Hatté, C., Gauthier, C., Marković, S. B., et al. (2009a). High-resolution record of the last climatic cycle in the southern Carpathian Basin (Surduk, Vojvodina, Serbia). *Quaternary International* 198, 19–36. doi: 10.1016/j.quaint.2008.12.008.
- Antoine, P., Rousseau, D.-D., Moine, O., Kunesch, S., Hatté, C., Lang, A., et al. (2009b). Rapid and cyclic aeolian deposition during the Last Glacial in European loess: a high-resolution record from Nussloch, Germany. *Quaternary Science Reviews* 28, 2955–2973. doi: 10.1016/j.quascirev.2009.08.001.
- Ao, H., Rohling, E. J., Stringer, C., Roberts, A. P., Dekkers, M. J., Dupont-Nivet, G., et al. (2020). Two-stage mid-Brunhes climate transition and mid-Pleistocene human diversification. *Earth-Science Reviews* 210, 103354. doi: 10.1016/j.earscirev.2020.103354.
- Balescu, S., Jordanova, D., Forget Brisson, L., Hardy, F., Huot, S., and Lamothe, M. (2020). Luminescence chronology of the northeastern Bulgarian loess-paleosol sequences (Viatovo and Kaolinovo). *Quaternary International* 552, 15–24. doi: 10.1016/j.quaint.2019.04.020.
- Balescu, S., Lamothe, M., Mercier, N., Huot, S., Balteanu, D., Billard, A., et al. (2003). Luminescence chronology of Pleistocene loess deposits from Romania: testing methods of age correction for anomalous fading in alkali feldspars. *Quaternary Science Reviews* 22, 967–973. doi: 10.1016/S0277-3791(03)00056-8.
- Balescu, S., Lamothe, M., Panaiotu, C., and Panaiotu, C. (2010). La chronologie IRSL des séquences loessiques de l'est de la Roumanie. *quaternaire*, 115–126. doi: 10.4000/quaternaire.5488.
- Banerjee, S. K., Hunt, C. P., and Liu, X.-M. (1993). Separation of local signals from the regional paleomonsoon record of the Chinese Loess Plateau: A rock-magnetic approach. *Geophys. Res. Lett.* 20, 843–846. doi: 10.1029/93GL00908.
- Barker, S., Knorr, G., Edwards, R. L., Parrenin, F., Putnam, A. E., Skinner, L. C., et al. (2011). 800,000 Years of Abrupt Climate Variability. *Science* 334, 347–351. doi: 10.1126/science.1203580.

- Beaudette, D., Roudier, P., and Brown, A. (2022). aqp: Algorithms for Qualitative Pedology. version 1.42. Available at: <https://github.com/ncss-tech/aqp>.
- Berg, L. S. (1916). The origin of loess (in Russian). *Izvestiya Russkogo Geograficheskogo Obshchestva* 52, 579–646.
- Berg, L. S. (1964). Loess as a Product of Weathering and Soil Formation. *Israel Program for Scientific Translations, Jerusalem, a section from 'Climate and life' 3*, 207pp.
- Black, B. A., Neely, R. R., and Manga, M. (2015). Campanian Ignimbrite volcanism, climate, and the final decline of the Neanderthals. *Geology* 43, 411–414. doi: 10.1130/G36514.1.
- Bond, G., Heinrich, H., Broecker, W., Labeyrie, L., McManus, J., Andrews, J., et al. (1992). Evidence for massive discharges of icebergs into the North Atlantic ocean during the last glacial period. *Nature* 360, 245–249. doi: 10.1038/360245a0.
- Buggle, B., Hambach, U., Kehl, M., Markovic, S. B., Zoller, L., and Glaser, B. (2013). The progressive evolution of a continental climate in southeast-central European lowlands during the Middle Pleistocene recorded in loess paleosol sequences. *Geology* 41, 771–774. doi: 10.1130/G34198.1.
- Burckle, L. H. (1993). Late quaternary interglacial stages warmer than present. *Quaternary Science Reviews* 12, 825–831. doi: 10.1016/0277-3791(93)90021-D.
- Candy, I., Coope, G. R., Lee, J. R., Parfitt, S. A., Preece, R. C., Rose, J., et al. (2010). Pronounced warmth during early Middle Pleistocene interglacials: Investigating the Mid-Brunhes Event in the British terrestrial sequence. *Earth-Science Reviews* 103, 183–196. doi: 10.1016/j.earscirev.2010.09.007.
- Cao, W., Jiang, Z., Gai, C., Barrón, V., Torrent, J., Zhong, Y., et al. (2022). Re-Visiting the Quantification of Hematite by Diffuse Reflectance Spectroscopy. *Minerals* 12, 872. doi: 10.3390/min12070872.
- Carter, G. F. (1956). On Soil Color and Time. *Southwestern Journal of Anthropology* 12, 295–324.
- Channell, J. E. T., Hodell, D. A., Romero, O., Hillaire-Marcel, C., de Vernal, A., Stoner, J. S., et al. (2012). A 750-kyr detrital-layer stratigraphy for the North Atlantic (IODP Sites U1302–U1303, Orphan Knoll, Labrador Sea). *Earth and Planetary Science Letters* 317–318, 218–230. doi: 10.1016/j.epsl.2011.11.029.
- Channell, J. E. T., Singer, B. S., and Jicha, B. R. (2020). Timing of Quaternary geomagnetic reversals and excursions in volcanic and sedimentary archives. *Quaternary Science Reviews* 228, 106114. doi: 10.1016/j.quascirev.2019.106114.
- Channell, J. E. T., Xuan, C., and Hodell, D. A. (2009). Stacking paleointensity and oxygen isotope data for the last 1.5 Myr (PISO-1500). *Earth and Planetary Science Letters* 283, 14–23. doi: 10.1016/j.epsl.2009.03.012.
- Chauvel, C., Garçon, M., Bureau, S., Besnault, A., Jahn, B., and Ding, Z. (2014). Constraints from loess on the Hf–Nd isotopic composition of the upper continental crust. *Earth and Planetary Science Letters* 388, 48–58. doi: 10.1016/j.epsl.2013.11.045.

- Chen, F. H., Bloemendal, J., Wang, J. M., Li, J. J., and Oldfield, F. (1997). High-resolution multi-proxy climate records from Chinese loess: evidence for rapid climatic changes over the last 75 kyr. *Palaeogeography, Palaeoclimatology, Palaeoecology* 130, 323–335. doi: 10.1016/S0031-0182(96)00149-6.
- Constantin, D., Cameniță, A., Panaiotu, C., Necula, C., Codrea, V., and Timar-Gabor, A. (2015). Fine and coarse-quartz SAR-OSL dating of Last Glacial loess in Southern Romania. *Quaternary International* 357, 33–43. doi: 10.1016/j.quaint.2014.07.052.
- Cornell, R. M., and Schwertmann, U. (2003). *The iron oxides: structure, properties, reactions, occurrences and uses*. John Wiley & Sons.
- Dar, R. A., and Zeeden, C. (2020). Loess-Palaeosol Sequences in the Kashmir Valley, NW Himalayas: A Review. *Front. Earth Sci.* 8, 113. doi: 10.3389/feart.2020.00113.
- Day, R., Fuller, M., and Schmidt, V. A. (1977). Hysteresis properties of titanomagnetites: Grain size and composition dependence. *Physics of the Earth and Planetary Interiors* 13, 260–267.
- Dearing, J. A., Bird, P. M., Dann, R. J. L., and Benjamin, S. F. (1997). Secondary ferrimagnetic minerals in Welsh soils: a comparison of mineral magnetic detection methods and implications for mineral formation. *Geophysical Journal International* 130, 727–736. doi: 10.1111/j.1365-246X.1997.tb01867.x.
- Dearing, J. A., Dann, R. J. L., Hay, K., Lees, J. A., Loveland, P. J., Maher, B. A., et al. (1996). Frequency-dependent susceptibility measurements of environmental materials. *Geophysical Journal International* 124, 228–240. doi: 10.1111/j.1365-246X.1996.tb06366.x.
- Deaton, B. C., and Balsam, W. L. (1991). Visible spectroscopy; a rapid method for determining hematite and goethite concentration in geological materials. *Journal of Sedimentary Research* 61, 628–632. doi: 10.1306/D4267794-2B26-11D7-8648000102C1865D.
- Deng, C., Vidic, N. J., Verosub, K. L., Singer, M. J., Liu, Q., Shaw, J., et al. (2005). Mineral magnetic variation of the Jiaodao Chinese loess/paleosol sequence and its bearing on long-term climatic variability. *J. Geophys. Res.* 110, B03103. doi: 10.1029/2004JB003451.
- Deng, C., Zhu, R., Jackson, M. J., Verosub, K. L., and Singer, M. J. (2001). Variability of the temperature-dependent susceptibility of the Holocene eolian deposits in the Chinese loess plateau: A pedogenesis indicator. *Physics and Chemistry of the Earth, Part A: Solid Earth and Geodesy* 26, 873–878. doi: 10.1016/S1464-1895(01)00135-1.
- Deng, C., Zhu, R., Verosub, K. L., Singer, M. J., and Vidic, N. J. (2004). Mineral magnetic properties of loess/paleosol couplets of the central loess plateau of China over the last 1.2 Myr. *J. Geophys. Res.* 109. doi: 10.1029/2003JB002532.
- Deng, C., Zhu, R., Verosub, K. L., Singer, M. J., and Yuan, B. (2000). Paleoclimatic significance of the temperature-dependent susceptibility of Holocene Loess along a NW-SE transect in the Chinese Loess Plateau. *Geophys. Res. Lett.* 27, 3715–3718. doi: 10.1029/2000GL008462.
- Derbyshire, E., Kemp, R., and Meng, X. (1995). Variations in loess and palaeosol properties as indicators of palaeoclimatic gradients across the Loess Plateau of North China. *Quaternary Science Reviews* 14, 681–697. doi: 10.1016/0277-3791(95)00077-1.



- Dietze, E., and Dietze, M. (2019). Grain-size distribution unmixing using the R package EMMAgeo. *E&G Quaternary Sci. J.* 68, 29–46. doi: 10.5194/egqsj-68-29-2019.
- Ding, Z. L., Derbyshire, E., Yang, S. L., Sun, J. M., and Liu, T. S. (2005). Stepwise expansion of desert environment across northern China in the past 3.5 Ma and implications for monsoon evolution. *Earth and Planetary Science Letters* 237, 45–55. doi: 10.1016/j.epsl.2005.06.036.
- Ding, Z. L., Ren, J. Z., Yang, S. L., and Liu, T. S. (1999a). Climate instability during the penultimate glaciation: Evidence from two high-resolution loess records, China. *J. Geophys. Res.* 104, 20123–20132. doi: 10.1029/1999JB900183.
- Ding, Z. L., Xiong, S. F., Sun, J. M., Yang, S. L., Gu, Z. Y., and Liu, T. S. (1999b). Pedostratigraphy and paleomagnetism of a ~7.0 Ma eolian loess–red clay sequence at Lingtai, Loess Plateau, north-central China and the implications for paleomonsoon evolution. *Palaeogeography, Palaeoclimatology, Palaeoecology* 152, 49–66. doi: 10.1016/S0031-0182(99)00034-6.
- Ding, Z., Rutter, N., Jingtai, H., and Tungsheng, L. (1992). A coupled environmental system formed at about 2.5 Ma in East Asia. *Palaeogeography, Palaeoclimatology, Palaeoecology* 94, 223–242. doi: 10.1016/0031-0182(92)90120-T.
- Doeglas, D. J. (1949). Loess, an eolian product. *Journal of Sedimentary Petrology* 19, 112–117.
- Duller, G. A. T. (2008). *Luminescence Dating: Guidelines on using luminescence dating in archaeology*. Aberystwyth: English Heritage.
- Dunlop, D. J. (1995). Magnetism in rocks. *Journal of Geophysical Research* 100, 2161–2174.
- Dunlop, D. J. (2002a). Theory and application of the Day plot (Mrs/Ms versus Hcr/ Hc 1. Theoretical curves and tests using titanomagnetite data. *J. Geophys. Res.* 107, 2056. doi: 10.1029/2001JB000486.
- Dunlop, D. J. (2002b). Theory and application of the Day plot (Mrs/Ms versus Hcr/ Hc 2. Application to data for rocks, sediments, and soils. *J. Geophys. Res.* 107, 2057. doi: 10.1029/2001JB000487.
- Dunlop, D. J., and Özdemir, Ö. (2013). *Rock magnetism: fundamentals and frontiers*. 1. paperback ed. with corr., 2. ed., reprinted. Cambridge: Cambridge Univ. Press.
- Egli, R., and Winklhofer, M. (2014). Recent developments on processing and interpretation aspects of First-Order Reversal curves (FORC). *Uchenye Zapiski Kazanskogo Universiteta. Seriya Estestvennye Nauki* 156, 14–53.
- Ehlers, J., Gibbard, P. L., and Hughes, P. D. eds. (2011). *Quaternary glaciations - extent and chronology: a closer look*. Amsterdam ; Boston: Elsevier.
- Elderfield, H., Ferretti, P., Greaves, M., Crowhurst, S., McCave, I. N., Hodell, D., et al. (2012). Evolution of Ocean Temperature and Ice Volume Through the Mid-Pleistocene Climate Transition. *Science* 337, 704–709. doi: 10.1126/science.1221294.
- EPICA community members (2004). Eight glacial cycles from an Antarctic ice core. *Nature* 429, 623–628. doi: 10.1038/nature02599.
- Evans, M. E., and Heller, F. (2003). *Environmental Magnetism*. USA: Elsevier Science.

- Evans, M. E., Rutter, N. W., Catto, N., Chlachula, J., and Nyvlt, D. (2003). Magnetoclimatology: Teleconnection between the Siberian loess record and North Atlantic Heinrich events. *Geology* 31, 537–540.
- Evlogiev, Y. (2007). Evidence for the Aeolian Origin of Loess in the Danubian Plain. *Geologica Balcanica* 36, 31–39.
- Evlogiev, Y. (2019). *Quaternary geology and geomorphology of the Danube plain - in Bulgarian*. Sofia: Geological Institute, Bulgarian Academy of Sciences.
- Eyre, J. K. (1997). Frequency dependence of magnetic susceptibility for populations of single-domain grains. *Geophysical Journal International* 129, 209–211. doi: 10.1111/j.1365-246X.1997.tb00951.x.
- Farmer, V. C. (1974). *The infrared spectra of minerals*. London: Mineralogical Society.
- Fedorowicz, S., Lanczont, M., Bogucki, A., Wozniak, P. P., Wroblewski, R., Adamiec, G., et al. (2013). Isotope dating in Roksolany loess profile (in Polish with English summary). in *Loess cover of the North Black Sea Region* (Lublin: Kartpol), 65–68.
- Fedorowicz, S., Wozniak, P. P., Halas, S., Lanczont, M., Paszkowski, M., and Wojtowicz, A. (2012). Challenging K-Ar dating of the Quaternary tephra from Roxolany. in, 102–105.
- Fenn, K., Thomas, D. S. G., Durcan, J. A., Millar, I. L., Veres, D., Piermattei, A., et al. (2021). A tale of two signals: Global and local influences on the Late Pleistocene loess sequences in Bulgarian Lower Danube. *Quaternary Science Reviews* 274, 107264. doi: 10.1016/j.quascirev.2021.107264.
- Fink, J. (1969). Les progres de l' etude de loess en Europe. *Bulletin de l' Association francaise pour l'etude du Quaternaire*, 3–12.
- Fink, J., Haase, G., and Ruske, R. (1977). Bemerkungen zur Lößkarte von Europa 1:2,5 Mio. *Petermanns Geographische Mitteilungen* 2, 81–94.
- Fitzsimmons, K. E., Hambach, U., Veres, D., and Iovita, R. (2013). The Campanian Ignimbrite Eruption: New Data on Volcanic Ash Dispersal and Its Potential Impact on Human Evolution. *PLoS ONE* 8, e65839. doi: 10.1371/journal.pone.0065839.
- Forster, Th., Heller, F., Evans, M. E., and Havlíček, P. (1996). Loess in the Czech Republic: Magnetic properties and paleoclimate. *Stud Geophys Geod* 40, 243–261. doi: 10.1007/BF02300741.
- Frank, U., and Nowaczyk, N. R. (2008). Mineral magnetic properties of artificial samples systematically mixed from haematite and magnetite. *Geophysical Journal International* 175, 449–461. doi: 10.1111/j.1365-246X.2008.03821.x.
- Frechen, M., Horváth, E., and Gábris, G. (1997). Geochronology of Middle and Upper Pleistocene Loess Sections in Hungary. *Quat. res.* 48, 291–312. doi: 10.1006/qres.1997.1929.
- Fu, Y., Hao, Q., Mark, D., Sun, C., Dymock, R., Marković, S. B., et al. (2019). Chances and challenges in tephrochronology of loess: A case study of the Bag tephra in Serbia. in.
- Gao, X., Hao, Q., Oldfield, F., Bloemendal, J., Deng, C., Wang, L., et al. (2019). New High-Temperature Dependence of Magnetic Susceptibility-Based Climofunction for Quantifying

- Paleoprecipitation From Chinese Loess. *Geochemistry, Geophysics, Geosystems* 20, 4273–4291.
- Giaccio, B., Hajdas, I., Isaia, R., Deino, A., and Nomade, S. (2017). High-precision  $^{14}\text{C}$  and  $^{40}\text{Ar}/^{39}\text{Ar}$  dating of the Campanian Ignimbrite (Y-5) reconciles the time-scales of climatic-cultural processes at 40 ka. *Sci Rep* 7, 45940. doi: 10.1038/srep45940.
- Giaccio, B., Leicher, N., Mannella, G., Monaco, L., Regattieri, E., Wagner, B., et al. (2019). Extending the tephra and palaeoenvironmental record of the Central Mediterranean back to 430 ka: A new core from Fucino Basin, central Italy. *Quaternary Science Reviews* 225, 106003. doi: 10.1016/j.quascirev.2019.106003.
- Giaccio, B., Messina, P., Sposato, A., Voltaggio, M., Zanchetta, G., Galadini, F., et al. (2009). Tephra layers from Holocene lake sediments of the Sulmona Basin, central Italy: implications for volcanic activity in Peninsular Italy and tephrostratigraphy in the central Mediterranean area. *Quaternary Science Reviews* 28, 2710–2733. doi: 10.1016/j.quascirev.2009.06.009.
- Gong, Y., Xia, Y., Huang, F., and Yu, H. (2017). Average iron isotopic compositions of the upper continental crust: constrained by loess from the Chinese Loess Plateau. *Acta Geochim* 36, 125–131. doi: 10.1007/s11631-016-0131-5.
- Grahmann, R. (1932). Der Löss in Europa. *Mitteilungen der Gesellschaft für Erdkunde zu Leipzig* 51, 5–24.
- Guo, B., Nie, J., Li, J., Xiao, W., and Pan, F. (2022). Expansion/shrinkage history of the Paratethys Sea during the Eocene: New insights from eolian Red Clay records in the Altyn Mountains, northern China. *Front. Earth Sci.* 10, 1052627. doi: 10.3389/feart.2022.1052627.
- Guyodo, Y., and Valet, J.-P. (1999). Global changes in intensity of the Earth's magnetic field during the past 800 kyr. *Nature* 399, 249–252. doi: 10.1038/20420.
- Haase, D., Fink, J., Haase, G., Ruske, R., Pécsi, M., Richter, H., et al. (2007). Loess in Europe—its spatial distribution based on a European Loess Map, scale 1:2,500,000. *Quaternary Science Reviews* 26, 1301–1312. doi: 10.1016/j.quascirev.2007.02.003.
- Haase, G., Ruske, R., and Fink, J. (1983). Conception, preparation and some results of the Loess Map of Europe on a scale 1:2,5 Million. *INQUA Newsletter* 1, 7–10.
- Hardcastle, J. (1890). On the Timaru loess as a climatic register. *Transactions and Proceedings of the Royal Society of New Zealand* 23, 324–332.
- Hatté, C., Gauthier, C., Rousseau, D.-D., Antoine, P., Fuchs, M., Lacroix, F., et al. (2013). Excursions to C4 vegetation recorded in the Upper Pleistocene loess of Surduk (Northern Serbia): an organic isotope geochemistry study. *Clim. Past* 9, 1001–1014. doi: 10.5194/cp-9-1001-2013.
- Heinrich, H. (1988). Origin and Consequences of Cyclic Ice Rafting in the Northeast Atlantic Ocean during the Past 130,000 Years. *Quaternary Research* 29, 142–152.
- Heller, F., and Evans, M. E. (1995). Loess magnetism. *Rev. Geophys.* 33, 211. doi: 10.1029/95RG00579.
- Heller, F., and Liu, T. (1982). Magnetostratigraphical dating of loess deposits in China. *Nature* 300, 431–433. doi: 10.1038/300431a0.

- Heller, F., and Liu, T. (1984). Magnetism of Chinese loess deposits. *Geophysical Journal International* 77, 125–141. doi: 10.1111/j.1365-246X.1984.tb01928.x.
- Heller, F., and Liu, T. (1986). Palaeoclimatic and sedimentary history from magnetic susceptibility of loess in China. *Geophys. Res. Lett.* 13, 1169–1172. doi: 10.1029/GL013i011p01169.
- Hlavatskyi, D., and Bakhmutov, V. (2021). Early–Middle Pleistocene Magnetostratigraphic and Rock Magnetic Records of the Dolynske Section (Lower Danube, Ukraine) and Their Application to the Correlation of Loess–Palaeosol Sequences in Eastern and South-Eastern Europe. *Quaternary* 4, 43. doi: 10.3390/quat4040043.
- Hlavatskyi, D. V., and Bakhmutov, V. G. (2020). Magnetostratigraphy and magnetic susceptibility of the best developed Pleistocene loess-palaeosol sequences of Ukraine: implications for correlation and proposed chronostratigraphic models. *GQ* 64. doi: 10.7306/gq.1544.
- Hlavay, J. (1978). Characterization of the Particle Size and the Crystallinity of Certain Minerals by IR Spectrophotometry and Other Instrumental Methods—II. Investigations on Quartz and Feldspar. *Clays and Clay Minerals* 26, 139–143. doi: 10.1346/CCMN.1978.0260209.
- Hodell, D. A., Kanfoush, S. L., Venz, K. A., Charles, C. D., and Sierro, F. J. (2003). The mid-Brunhes transition in ODP sites 1089 and 1090 (subantarctic South Atlantic). *AGU Geophysical Monograph* 137, 113–129.
- Hodell, D., Crowhurst, S., Skinner, L., Tzedakis, P. C., Margari, V., Channell, J. E. T., et al. (2013). Response of Iberian Margin sediments to orbital and suborbital forcing over the past 420 ka: IBERIAN MARGIN PALEOCEANOGRAPHY. *Paleoceanography* 28, 185–199. doi: 10.1002/palo.20017.
- Hönisch, B., Hemming, N. G., Archer, D., Siddall, M., and McManus, J. F. (2009). Atmospheric Carbon Dioxide Concentration Across the Mid-Pleistocene Transition. *Science* 324, 1551–1554. doi: 10.1126/science.1171477.
- Horváth, E. (2001). Marker horizons in the loesses of the Carpathian Basin. *Quaternary International* 76–77, 157–163. doi: 10.1016/S1040-6182(00)00099-9.
- Howard, W. R. (1997). A warm future in the past. *Nature* 388, 418–419. doi: 10.1038/41201.
- Howe, H. V. (1971). Memorial to Richard Joel Russell 1895-1971. *GSA Bulletin* 3, 165–174.
- Hrouda, F. (1994). A technique for the measurement of thermal changes of magnetic susceptibility of weakly magnetic rocks by the CH-2 apparatus and KLY-2 Kappabridge. *Geophysical Journal International* 118, 604–612.
- Hu, P., Liu, Q., Heslop, D., Roberts, A. P., and Jin, C. (2015). Soil moisture balance and magnetic enhancement in loess–paleosol sequences from the Tibetan Plateau and Chinese Loess Plateau. *Earth and Planetary Science Letters* 409, 120–132. doi: 10.1016/j.epsl.2014.10.035.
- Hunt, C. P., Moskowitz, B. M., and Banerjee, S. K. (1995). “Magnetic Properties of Rocks and Minerals,” in *AGU Reference Shelf*, ed. T. J. Ahrens (Washington, D. C.: American Geophysical Union), 189–204. doi: 10.1029/RF003p0189.
- Imbrie, J., and Imbrie, J. Z. (1980). Modeling the Climatic Response to Orbital Variations. *Science* 207, 943–953. doi: 10.1126/science.207.4434.943.

- Jansen, J. H. F., Kuijpers, A., and Troelstra, S. R. (1986). A Mid-Brunhes Climatic Event: Long-Term Changes in Global Atmosphere and Ocean Circulation. *Science* 232, 619–622. doi: 10.1126/science.232.4750.619.
- Ji, J., Balsam, W., and Chen, J. (2001). Mineralogic and Climatic Interpretations of the Luochuan Loess Section (China) Based on Diffuse Reflectance Spectrophotometry. *Quat. res.* 56, 23–30. doi: 10.1006/qres.2001.2238.
- Ji, J., Balsam, W., Chen, J. U., and Liu, L. (2002). Rapid and Quantitative Measurement of Hematite and Goethite in the Chinese Loess-paleosol Sequence by Diffuse Reflectance Spectroscopy. *Clays and Clay Minerals* 50, 208–216. doi: 10.1346/000986002760832801.
- Jiang, Z., Liu, Q., Roberts, A. P., Dekkers, M. J., Barrón, V., Torrent, J., et al. (2022). The Magnetic and Color Reflectance Properties of Hematite: From Earth to Mars. *Reviews of Geophysics* 60. doi: 10.1029/2020RG000698.
- Jordanova, D., Hus, J., Evlogiev, J., and Geeraerts, R. (2008). Palaeomagnetism of the loess/palaeosol sequence in Viatovo (NE Bulgaria) in the Danube basin. *Physics of the Earth and Planetary Interiors* 167, 71–83. doi: 10.1016/j.pepi.2008.02.008.
- Jordanova, D., Hus, J., and Geeraerts, R. (2007). Palaeoclimatic implications of the magnetic record from loess/palaeosol sequence Viatovo (NE Bulgaria): Palaeoclimatic implications of the magnetic record. *Geophysical Journal International* 171, 1036–1047. doi: 10.1111/j.1365-246X.2007.03576.x.
- Jordanova, D., and Jordanova, N. (2020). Diversity and peculiarities of soil formation in eolian landscapes – Insights from the mineral magnetic records. *Earth and Planetary Science Letters* 531, 115956. doi: 10.1016/j.epsl.2019.115956.
- Jordanova, D., Laag, C., Jordanova, N., Lagroix, F., Georgieva, B., Ishlyamski, D., et al. (2022). A detailed magnetic record of Pleistocene climate and distal ash dispersal during the last 800 kys - The Suhia Kladenetz quarry loess-paleosol sequence near Pleven (Bulgaria). *Global and Planetary Change* 214, 103840. doi: 10.1016/j.gloplacha.2022.103840.
- Jordanova, D., and Petersen, N. (1999a). Palaeoclimatic record from a loess-soil profile in northeastern Bulgaria-I. Rock magnetic properties. *Geophys. J. Int.* 138, 520–532. doi: 10.1046/j.1365-246X.1999.00874.x.
- Jordanova, D., and Petersen, N. (1999b). Palaeoclimatic record from a loess-soil profile in northeastern Bulgaria-II. Correlation with global climatic events during the Pleistocene. *Geophys. J. Int.* 138, 533–540. doi: 10.1046/j.1365-246X.1999.00873.x.
- Jouzel, J., Masson-Delmotte, V., Cattani, O., Dreyfus, G., Falourd, S., Hoffmann, G., et al. (2007). Orbital and Millennial Antarctic Climate Variability over the Past 800,000 Years. *Science* 317, 793–796. doi: 10.1126/science.1141038.
- Jung, H.-J., Malek, M. A., Ryu, J., Kim, B., Song, Y.-C., Kim, H., et al. (2010). Speciation of Individual Mineral Particles of Micrometer Size by the Combined Use of Attenuated Total Reflectance-Fourier Transform-Infrared Imaging and Quantitative Energy-Dispersive Electron Probe X-ray Microanalysis Techniques. *Anal. Chem.* 82, 6193–6202. doi: 10.1021/ac101006h.
- Käsz, W., and Werner, J. (1962). Farbmessungen an oberschwäbischen Böden. *Geologisches Jahrbuch* 79, 845–862.

- Kehl, M., Sarvati, R., Ahmadi, H., Frechen, M., and Skowronek, A. (2005). Loess paleosoil-sequences along a climatic gradient in Northern Iran. *E&G Quaternary Sci. J.* 55, 149–173. doi: 10.3285/eg.55.1.08.
- Kehl, M., Vlamincx, S., Köhler, T., Laag, C., Rolf, C., Tsukamoto, S., et al. (2021). Pleistocene dynamics of dust accumulation and soil formation in the southern Caspian Lowlands - New insights from the loess-paleosol sequence at Neka-Abelou, northern Iran. *Quaternary Science Reviews* 253, 106774. doi: 10.1016/j.quascirev.2020.106774.
- King, J., Banerjee, S. K., Marvin, J., and Özdemir, Ö. (1982). A comparison of different magnetic methods for determining the relative grain size of magnetite in natural materials: Some results from lake sediments. *Earth and Planetary Science Letters* 59, 404–419. doi: 10.1016/0012-821X(82)90142-X.
- King, J. W., Banerjee, S. K., and Marvin, J. (1983). A new rock-magnetic approach to selecting sediments for geomagnetic paleointensity studies: Application to paleointensity for the last 4000 years. *Journal of Geophysical Research* 88, 5911–5921.
- King, J. W., and Channell, J. E. T. (1991). SEDIMENTARY MAGNETISM, ENVIRONMENTAL MAGNETISM, AND MAGNETOSTRATIGRAPHY. *Reviews of Geophysics* 29, 358–370. doi: 10.1002/rog.1991.29.s1.358.
- Kosmas, C. S., Curi, N., Bryant, R. B., and Franzmeier, D. P. (1984). Characterization of Iron Oxide Minerals by Second-Derivative Visible Spectroscopy. *Soil Science Society of America Journal* 48, 401–405. doi: 10.2136/sssaj1984.03615995004800020036x.
- Kosmas, C. S., Franzmeier, D. P., and Schulze, D. G. (1986). Relationship among Derivative Spectroscopy, Color, Crystallite Dimensions, and Al Substitution of Synthetic Goethites and Hematites. *Clays and Clay Minerals* 34, 625–634. doi: 10.1346/CCMN.1986.0340602.
- Kotov, S., and Pälke, H. (2018). QAnalySeries – a cross-platform time series tuning and analysis tool. *Geology* doi: 10.1002/essoar.10500226.1.
- Krapp, M., Beyer, R. M., Edmundson, S. L., Valdes, P. J., and Manica, A. (2021). A statistics-based reconstruction of high-resolution global terrestrial climate for the last 800,000 years. *Sci Data* 8, 228. doi: 10.1038/s41597-021-01009-3.
- Kreutzer, S., Friedrich, J., Pagonis, V., Laag, C., Rajovic, E., and Schmidt, C. (2021). RLumCarlo: Simulating Cold Light using Monte Carlo Methods. *The R Journal* 13, 351. doi: 10.32614/RJ-2021-043.
- Krészsek, C., and Olariu, C. (2021). Filling of sedimentary basins and the birth of large rivers: The lower Danube network in the Dacian Basin, Romania. *Global and Planetary Change* 197, 103391. doi: 10.1016/j.gloplacha.2020.103391.
- Kubelka, P., and Munk, F. (1931). An article on optics of paint layers. *Technical Physics* 12, 259–274.
- Kukla, G. (1987). LOESS STRATIGRAPHY IN CENTRAL CHINA. *Quaternary Science Reviews* 6, 191–219.
- Kukla, G., and An, Z. (1989). Loess stratigraphy in Central China. *Palaeogeography, Palaeoclimatology, Palaeoecology* 72, 203–225. doi: 10.1016/0031-0182(89)90143-0.

- Kukla, G. J. (1975). "Loess Stratigraphy of Central Europe," in *After the Australopithecines*, eds. K. W. Butzer and G. L. Isaac (DE GRUYTER MOUTON), 99–188. doi: 10.1515/9783110878837.99.
- Kukla, G. J. (1977). Pleistocene land—sea correlations I. Europe. *Earth-Science Reviews* 13, 307–374. doi: 10.1016/0012-8252(77)90125-8.
- Kukla, J. (1970). Correlations between loesses and deep-sea sediments. *Geologiska Föreningen i Stockholm Förhandlingar* 92, 148–180. doi: 10.1080/11035897009453674.
- Laag, C. (2019). Magnetic Stratigraphy in a Late Eemian to Early Würmian Loess-Palaeosol Sequence from SE-Romania - Master's Thesis.
- Laag, C., Hambach, U. F., Botezatu, A., Baykal, Y., Veres, D., Schönwetter, T., et al. (2018). The geographical extent of the "L2-Tephra": a widespread marker horizon for the penultimate glacial (MIS 6) on the Balkan Peninsula. in (Abstract book, INQUA-INTAV International Field Conference and Workshop - Crossing New Frontiers - Tephra Hunt in Transylvania, 111–112, Eds. Hambach, U and Veres, D.). doi: 10.13140/RG.2.2.29686.96325.
- Laag, C., Hambach, U. F., Zeeden, C., Rolf, C., Krawczyk, M., Raczky, J., et al. (2019a). Environmental magnetic, colorimetric, and granulometric screening of a last glacial loess profile from Biały Kościół, lower Silesia: evidence for a harsh periglacial environment. doi: 10.13140/RG.2.2.25487.94881.
- Laag, C., Hambach, U., Veres, D., Zeeden, C., Worm, K., and Rolf, C. (2019b). High resolution paleomagnetic and environmental magnetic data from the last interglacial to glacial transition in a loess-paleosol sequence (LPS) from the Lower Danube (Romania) : Implications for the chronology of the S1 pedocomplex in Eurasian LPSs. *International Workshop on Loess and Archeology : Geoarcheological and paleoenvironmental research in European loess-scapes : Abstract Book / Herausgeber: Prof. Dr. Frank Lehmkuhl Lehrstuhl für Physische Geographie und Geoökologie; Editoren: Dr. Janina Bösken*, pages 68-70. doi: 10.18154/RWTH-2019-10503.
- Laag, C., Hambach, U., Zeeden, C., Lagroix, F., Guyodo, Y., Veres, D., et al. (2021a). A detailed paleoclimate proxy record for the Middle Danube Basin over the last 430 kyr: a rock magnetic and colorimetric study of the Zemun loess-paleosol sequence. *Frontiers in Earth Science* 9:600086. doi: 10.3389/feart.2021.600086.
- Laag, C., and Kreutzer, S. (2022). LESLIE - LoESs coLorimetry signal Enhancement: v0.1.0. doi: 10.5281/ZENODO.7257765.
- Laag, C., Lagroix, F., Kreutzer, S., Chapkanski, S., Zeeden, C., and Guyodo, Y. (2022). Measuring and evaluating colorimetric properties of samples from loess-paleosol sequences. *MethodsX*, in press.
- Laag, C., Yohan Guyodo, Lagroix, F., Veres, D., Wacha, L., and Hambach, U. F. (2021b). Tephra hunt in loess-paleosol sequences – towards an environmental magnetic approach for tephra detection and characterization. doi: 10.13140/RG.2.2.15525.83683.
- Lagroix, F., and Banerjee, S. K. (2002). Paleowind directions from the magnetic fabric of loess profiles in central Alaska. *Earth and Planetary Science Letters* 195, 99–112. doi: 10.1016/S0012-821X(01)00564-7.



- Lang, A., Hatté, C., Rousseau, D.-D., Antoine, P., Fontugne, M., Zöller, L., et al. (2003). High-resolution chronologies for loess: comparing AMS 14C and optical dating results. *Quaternary Science Reviews* 22, 953–959. doi: 10.1016/S0277-3791(03)00035-0.
- Lang, N., and Wolff, E. W. (2011). Interglacial and glacial variability from the last 800 ka in marine, ice and terrestrial archives. *Clim. Past* 7, 361–380. doi: 10.5194/cp-7-361-2011.
- Laskar, J., Fienga, A., Gastineau, M., and Manche, H. (2011). La2010: a new orbital solution for the long-term motion of the Earth. *A&A* 532, A89. doi: 10.1051/0004-6361/201116836.
- Lauer, T., Vlamincq, S., Frechen, M., Rolf, C., Kehl, M., Sharifi, J., et al. (2017). The Agh Band loess-palaeosol sequence – A terrestrial archive for climatic shifts during the last and penultimate glacial–interglacial cycles in a semiarid region in northern Iran. *Quaternary International* 429, 13–30. doi: 10.1016/j.quaint.2016.01.062.
- Lehmkuhl, F., Nett, J. J., Pötter, S., Schulte, P., Sprafke, T., Jary, Z., et al. (2021). Loess landscapes of Europe – Mapping, geomorphology, and zonal differentiation. *Earth-Science Reviews* 215, 103496. doi: 10.1016/j.earscirev.2020.103496.
- Leicher, N., Giaccio, B., Pereira, A., Nomade, S., Monaco, L., Mannella, G., et al. (2022). Central Mediterranean tephrochronology between 313 and 366 ka: New insights from the Fucino palaeolake sediment succession. *Boreas*, bor.12610. doi: 10.1111/bor.12610.
- Leicher, N., Giaccio, B., Zanchetta, G., Sulpizio, R., Albert, P. G., Tomlinson, E. L., et al. (2021). Lake Ohrid's tephrochronological dataset reveals 1.36 Ma of Mediterranean explosive volcanic activity. *Sci Data* 8, 231. doi: 10.1038/s41597-021-01013-7.
- Lepre, C. J., and Olsen, P. E. (2021). Hematite reconstruction of Late Triassic hydroclimate over the Colorado Plateau. *Proc. Natl. Acad. Sci. U.S.A.* 118, e2004343118. doi: 10.1073/pnas.2004343118.
- Li, Y., Shi, W., Aydin, A., Beroya-Eitner, M. A., and Gao, G. (2020). Loess genesis and worldwide distribution. *Earth-Science Reviews* 201, 102947. doi: 10.1016/j.earscirev.2019.102947.
- Liang, L., Sun, Y., Yao, Z., Liu, Y., and Wu, F. (2012). Evaluation of high-resolution elemental analyses of Chinese loess deposits measured by X-ray fluorescence core scanner. *CATENA* 92, 75–82. doi: 10.1016/j.catena.2011.11.010.
- Lisiecki, L. E., and Raymo, M. E. (2005). A Pliocene-Pleistocene stack of 57 globally distributed benthic  $\delta^{18}O$  records. *Paleoceanography* 20. doi: 10.1029/2004PA001071.
- Liu, C., Deng, C., Liu, Q., Zheng, L., Wang, W., Xu, X., et al. (2010). Mineral magnetism to probe into the nature of palaeomagnetic signals of subtropical red soil sequences in southern China. *Geophysical Journal International*. doi: 10.1111/j.1365-246X.2010.04592.x.
- Liu, Q., Banerjee, S. K., Jackson, M. J., Chen, F., Pan, Y., and Zhu, R. (2003). An integrated study of the grain-size-dependent magnetic mineralogy of the Chinese loess/paleosol and its environmental significance: MAGNETIC MINERALOGY OF CHINESE LOESS. *J. Geophys. Res.* 108. doi: 10.1029/2002JB002264.
- Liu, Q., Deng, C., Yu, Y., Torrent, J., Jackson, M. J., Banerjee, S. K., et al. (2005). Temperature dependence of magnetic susceptibility in an argon environment: implications for

- pedogenesis of Chinese loess/palaeosols. *Geophysical Journal International* 161, 102–112. doi: 10.1111/j.1365-246X.2005.02564.x.
- Liu, Q., Roberts, A. P., Larrasoaña, J. C., Banerjee, S. K., Guyodo, Y., Tauxe, L., et al. (2012). Environmental magnetism: Principles and applications. *Rev. Geophys.* 50, RG4002. doi: 10.1029/2012RG000393.
- Liu, Q. S., Torrent, J., Barrón, V., Duan, Z. Q., and Bloemendal, J. (2011). Quantification of hematite from the visible diffuse reflectance spectrum: effects of aluminium substitution and grain morphology. *Clay miner.* 46, 137–147. doi: 10.1180/claymin.2011.046.1.137.
- Liu, T. (1988). *Loess in China*. 2nd ed. Berlin, Heidelberg: Springer Verlag.
- Liu, T., and Chang, T. (1964). The “Huangtu” (loess) of China. *Rept 6th INQUA Congress Warsaw* 4, 503–524.
- Liu, T., Ding Zhongli, Chen Mingyang, and An Zhisheng (1989). The global surface energy system and the geological role of wind stress. *Quaternary International* 2, 43–54. doi: 10.1016/1040-6182(89)90020-7.
- Lohmann, J., and Svensson, A. (2022). Ice core evidence for major volcanic eruptions at the onset of Dansgaard–Oeschger warming events. *Clim. Past* 18, 2021–2043. doi: 10.5194/cp-18-2021-2022.
- Lourens, L. J. (2004). Revised tuning of Ocean Drilling Program Site 964 and KC01B (Mediterranean) and implications for the  $\delta^{18}\text{O}$ , tephra, calcareous nannofossil, and geomagnetic reversal chronologies of the past 1.1 Myr: PLEISTOCENE ASTRONOMICAL TIMESCALES. *Paleoceanography* 19, n/a-n/a. doi: 10.1029/2003PA000997.
- Lowe, D. J., Pearce, N. J. G., Jorgensen, M. A., Kuehn, S. C., Tryon, C. A., and Hayward, C. L. (2017). Correlating tephras and cryptotephras using glass compositional analyses and numerical and statistical methods: Review and evaluation. *Quaternary Science Reviews* 175, 1–44. doi: 10.1016/j.quascirev.2017.08.003.
- Lu, H., Zhang, F., and Liu, X. (2003). Patterns and frequencies of the East Asian winter monsoon variations during the past million years revealed by wavelet and spectral analyses. *Global and Planetary Change* 35, 67–74. doi: 10.1016/S0921-8181(02)00136-4.
- Lyell, C. (1833). *The Principles of Geology*. London: John Murray.
- Machalett, B., Oches, E. A., Frechen, M., Zöller, L., Hambach, U., Mavlyanova, N. G., et al. (2008). Aeolian dust dynamics in central Asia during the Pleistocene: Driven by the long-term migration, seasonality, and permanency of the Asiatic polar front: AEOLIAN DUST DYNAMICS IN CENTRAL ASIA. *Geochem. Geophys. Geosyst.* 9, n/a-n/a. doi: 10.1029/2007GC001938.
- Madejová, J., and Komadel, P. (2001). BASELINE STUDIES OF THE CLAY MINERALS SOCIETY SOURCE CLAYS: INFRARED METHODS. *Clays and Clay Minerals*, 410–432.
- Maher, B. A. (1988). Magnetic properties of some synthetic sub-micron magnetites. *Geophysical Journal* 94, 83–96.
- Maher, B. A. (2011). The magnetic properties of Quaternary aeolian dusts and sediments, and their palaeoclimatic significance. *Aeolian Research* 3, 87–144. doi: 10.1016/j.aeolia.2011.01.005.

- Maher, B. A. (2016). Palaeoclimatic records of the loess/palaeosol sequences of the Chinese Loess Plateau. *Quaternary Science Reviews* 154, 23–84. doi: 10.1016/j.quascirev.2016.08.004.
- Mahmoudian, F., Karimi, A., and Bayat, O. (2022). Soil evolution along an alluvial-loess transect in the Herat Plain, western Afghanistan. *J. Arid Land* 14, 1317–1330. doi: 10.1007/s40333-022-0034-8.
- Makaroglu, Ö., Çağatay, M. N., Nowaczyk, N. R., Pesonen, L. J., and Orbay, N. (2018). Discrimination of Holocene tephra units in Lake Van using mineral magnetic analysis. *Quaternary International* 486, 44–56. doi: 10.1016/j.quaint.2018.03.012.
- Marković, S. B., Hambach, U., Catto, N., Jovanović, M., Buggle, B., Machalett, B., et al. (2009a). Middle and Late Pleistocene loess sequences at Batajnica, Vojvodina, Serbia. *Quaternary International* 198, 255–266. doi: 10.1016/j.quaint.2008.12.004.
- Marković, S. B., Hambach, U., Stevens, T., Kukla, G. J., Heller, F., McCoy, W. D., et al. (2011). The last million years recorded at the Stari Slankamen (Northern Serbia) loess-palaeosol sequence: revised chronostratigraphy and long-term environmental trends. *Quaternary Science Reviews* 30, 1142–1154. doi: 10.1016/j.quascirev.2011.02.004.
- Marković, S. B., Smalley, I. J., Hambach, U., and Antoine, P. (2009b). Loess in the Danube region and surrounding loess provinces: The Marsigli memorial volume. *Quaternary International* 198, 5–6. doi: 10.1016/j.quaint.2009.02.001.
- Marković, S. B., Stevens, T., Kukla, G. J., Hambach, U., Fitzsimmons, K. E., Gibbard, P., et al. (2015). Danube loess stratigraphy — Towards a pan-European loess stratigraphic model. *Earth-Science Reviews* 148, 228–258. doi: 10.1016/j.earscirev.2015.06.005.
- Marsigli, L. F. (1726). *Danubius Pannonico Mysicus; Observationibus Geographicis, Astronomicis, Hydrographicis, Physicis; perlustratus*. The Hague and Amsterdam: Uytwert and Franc Changuion.
- Maxbauer, D. P., Feinberg, J. M., and Fox, D. L. (2016). MAX UnMix: A web application for unmixing magnetic coercivity distributions. *Computers & Geosciences* 95, 140–145. doi: 10.1016/j.cageo.2016.07.009.
- McIntyre, A., Ruddiman, W. F., Karlin, K., and Mix, A. C. (1988). Surface Water Response of the Equatorial Atlantic Ocean to Orbital Forcing. *Paleoceanography* 4, 19–55.
- Menzies, J., and Meer, J. J. M. (2018). “Micromorphology and Microsedimentology of Glacial Sediments,” in *Past Glacial Environments* (Elsevier), 753–806. doi: 10.1016/B978-0-08-100524-8.00036-1.
- Mettig, G. (2020). Umweltmagnetische Eigenschaften quartärer Lössarchive Südtunesiens (Region Matmata), Masters Thesis.
- Milanković, M. (1941). *Kanon der Erdbestrahlung und seine Anwendung auf das Eiszeitenproblem*. Belgrad: Königlich Serbische Akademie.
- Mir, J. A., Dar, R. A., Vinnepand, M., Laag, C., Rolf, C., and Zeeden, C. (2022). Environmental reconstruction potentials of Loess-Paleosol-Sequences in Kashmir through high-resolution proxy data. *Palaeogeography, Palaeoclimatology, Palaeoecology* 601, 111100. doi: 10.1016/j.palaeo.2022.111100.

- Moine, O. (2014). Weichselian Upper Pleniglacial environmental variability in north-western Europe reconstructed from terrestrial mollusc faunas and its relationship with the presence/absence of human settlements. *Quaternary International* 337, 90–113. doi: 10.1016/j.quaint.2014.02.030.
- Morris, R. V., Lauer, H. V., Lawson, C. A., Gibson, E. K., Nace, G. A., and Stewart, C. (1985). Spectral and other physicochemical properties of submicron powders of hematite ( $\alpha\text{-Fe}_2\text{O}_3$ ), maghemite ( $\gamma\text{-Fe}_2\text{O}_3$ ), magnetite ( $\text{Fe}_3\text{O}_4$ ), goethite ( $\alpha\text{-FeOOH}$ ), and lepidocrocite ( $\gamma\text{-FeOOH}$ ). *J. Geophys. Res.* 90, 3126. doi: 10.1029/JB090iB04p03126.
- Muhs, D. R., and Bettis, E. A. III. (2003). "Quaternary loess-paleosol sequences as examples of climate-driven sedimentary extremes.," in *Extreme depositional environments: Mega end members in geologic time*. Special Paper. (Boulder, Colorado: Geological Society of America), 53–74.
- Muhs, D. R., Cattle, S. R., Crouvi, O., Rousseau, D.-D., Sun, J., and Zárata, M. A. (2014). "Loess Records," in *Mineral Dust*, eds. P. Knippertz and J.-B. W. Stuut (Dordrecht: Springer Netherlands), 411–441. doi: 10.1007/978-94-017-8978-3\_16.
- Mullins, C. E. (1977). Magnetic susceptibility of the soil and its significance in soil science - a review. *Journal of soil science* 28, 223–246.
- Namier, N., Gao, X., Hao, Q., Marković, S. B., Fu, Y., Song, Y., et al. (2021). Mineral magnetic properties of loess–paleosol couplets of northern Serbia over the last 1.0 Ma. *Quat. res.*, 1–14. doi: 10.1017/qua.2021.41.
- Necea, D., Fielitz, W., Kadereit, A., Andriessen, P. A. M., and Dinu, C. (2013). Middle Pleistocene to Holocene fluvial terrace development and uplift-driven valley incision in the SE Carpathians, Romania. *Tectonophysics* 602, 332–354. doi: 10.1016/j.tecto.2013.02.039.
- Necula, C. (2006). Rockmagnetic Properties of Loess-paleosol Deposits from Romania: Paleoclimatic Implications. In: *Fizica Atmosferei si a Globului Terestru*.
- Necula, C., Panaiotu, C., Heslop, D., and Dimofte, D. (2013). Climatic control of magnetic granulometry in the Mircea Vodă loess/paleosol sequence (Dobrogea, Romania). *Quaternary International* 293, 5–14. doi: 10.1016/j.quaint.2012.03.043.
- Nie, J., Song, Y., and King, J. W. (2016). A Review of Recent Advances in Red-Clay Environmental Magnetism and Paleoclimate History on the Chinese Loess Plateau. *Front. Earth Sci.* 4. doi: 10.3389/feart.2016.00027.
- Novothy, Á., Frechen, M., Horváth, E., Wacha, L., and Rolf, C. (2011). Investigating the penultimate and last glacial cycles of the Süttő loess section (Hungary) using luminescence dating, high-resolution grain size, and magnetic susceptibility data. *Quaternary International* 234, 75–85. doi: 10.1016/j.quaint.2010.08.002.
- Obrecht, I., Zeeden, C., Hambach, U., Veres, D., Marković, S. B., and Lehmkuhl, F. (2019). A critical reevaluation of palaeoclimate proxy records from loess in the Carpathian Basin. *Earth-Science Reviews* 190, 498–520. doi: 10.1016/j.earscirev.2019.01.020.
- Obruchev, V. A. (1911). The question of the origin of loess - in defense of the aeolian hypothesis (In Russian). *Izvēstiya Tomskago Tekhnologicheskago Instituta* 33, 38–38.

- Obruchev, V. A. (1952). Loess and its significance (in Russian, English translation published as Loess Letter 1986 Supplement 11). *Novyi Mir* 3, 212–233.
- Oches, E. A., and Banerjee, S. K. (1996). Rock-magnetic proxies of climate change from loess - paleosol sediments of the Czech Republic. *Stud Geophys Geod* 40, 287–300. doi: 10.1007/BF02300744.
- Pagonis, V., Kreutzer, S., Duncan, A. R., Rajovic, E., Laag, C., and Schmidt, C. (2020). On the stochastic uncertainties of thermally and optically stimulated luminescence signals: A Monte Carlo approach. *Journal of Luminescence* 219, 116945. doi: 10.1016/j.jlumin.2019.116945.
- Panin, P. G., Filippova, K. G., Bukhonov, A. V., Karpukhina, N. V., Kalinin, P. I., and Ruchkin, M. V. (2021). High-resolution analysis of the Likhvin loess-paleosol sequence (the central part of the East European Plain, Russia). *CATENA* 205, 105445. doi: 10.1016/j.catena.2021.105445.
- Paterson, G. A., and Heslop, D. (2015). New methods for unmixing sediment grain size data. *Geochem. Geophys. Geosyst.* 16, 4494–4506. doi: 10.1002/2015GC006070.
- Pécsi, M. (1990). Loess is not just the accumulation of dust. *Quaternary International* 7–8, 1–21. doi: 10.1016/1040-6182(90)90034-2.
- Pécsi, M., Schweitzer, F., Balogh, J., Balogh, M., Havas, J., and Heller, F. (1995). A new loess-paleosol lithostratigraphical sequence at Paks (Hungary). *Loess inForm* 3, 63–78.
- Peters, C., and Dekkers, M. J. (2003). Selected room temperature magnetic parameters as a function of mineralogy, concentration and grain size. *Physics and Chemistry of the Earth, Parts A/B/C* 28, 659–667. doi: 10.1016/S1474-7065(03)00120-7.
- Pfeifer, L. S., Hinnov, L., Zeeden, C., Rolf, C., Laag, C., and Soreghan, G. S. (2020). Rock Magnetic Cyclostratigraphy of Permian Loess in Eastern Equatorial Pangea (Salagou Formation, South-Central France). *Front. Earth Sci.* 8, 241. doi: 10.3389/feart.2020.00241.
- Pike, C. R., Roberts, A. P., Dekkers, M. J., and Verosub, K. L. (2001). An investigation of multi-domain hysteresis mechanisms using FORC diagrams. *Physics of the Earth and Planetary Interiors* 126, 11–25. doi: 10.1016/S0031-9201(01)00241-2.
- Poulet, A., Horvath, E., Gabris, G., and Juvigné, E. (1999). The Bag Tephra, a widespread tephrochronological marker in Middle Europe: chemical and mineralogical investigations. *Bulletin of Volcanology* 61, 265–272. doi: 10.1007/s004450050275.
- Pujos, A. (1992). Calcaerous nonnofossils of Plio-Pleistocene sediments from the northwestern margin of tropical Africa. *Geological Society Special Publication* 64, 343–359.
- Pye, K. (1987). *Aeolian Dust and Dust Deposits*. London: Academic Press.
- R Core Team (2023). R: A Language and Environment for Statistical Computing, R Foundation for Statistical Computing, Vienna, Austria. doi: <https://r-project.org>.
- Radan, S.-C. (2012). Towards A Synopsis Of Dating The Loess From The Romanian Plain And Dobrogea: Authors And Methods Through Time. *Geo-Eco-Marina* 18. doi: 10.5281/ZENODO.56878.

- Rasmussen, S. O., Bigler, M., Blockley, S. P., Blunier, T., Buchardt, S. L., Clausen, H. B., et al. (2014). A stratigraphic framework for abrupt climatic changes during the Last Glacial period based on three synchronized Greenland ice-core records: refining and extending the INTIMATE event stratigraphy. *Quaternary Science Reviews* 106, 14–28. doi: 10.1016/j.quascirev.2014.09.007.
- Roberts, A. P., Almeida, T. P., Church, N. S., Harrison, R. J., Heslop, D., Li, Y., et al. (2017). Resolving the Origin of Pseudo-Single Domain Magnetic Behavior. *J. Geophys. Res. Solid Earth* 122, 9534–9558. doi: 10.1002/2017JB014860.
- Roberts, A. P., Heslop, D., Zhao, X., and Pike, C. R. (2014). Understanding fine magnetic particle systems through use of first-order reversal curve diagrams: FORC diagrams. *Rev. Geophys.* 52, 557–602. doi: 10.1002/2014RG000462.
- Roberts, A. P., Pike, C. R., and Verosub, K. L. (2000). First-order reversal curve diagrams: A new tool for characterizing the magnetic properties of natural samples. *J. Geophys. Res.* 105, 28461–28475. doi: 10.1029/2000JB900326.
- Rousseau, D. D., Antoine, P., Hatté, C., Lang, A., Zöller, L., Fontugne, M., et al. (2002). Abrupt millennial climatic changes from Nussloch (Germany) Upper Weichselian eolian records during the Last Glaciation. *Quaternary Science Reviews* 21, 1577–1582. doi: 10.1016/S0277-3791(02)00034-3.
- Rousseau, D.-D., Antoine, P., Boers, N., Lagroix, F., Ghil, M., Lomax, J., et al. (2020). Dansgaard–Oeschger-like events of the penultimate climate cycle: the loess point of view. *Clim. Past* 16, 713–727. doi: 10.5194/cp-16-713-2020.
- Rousseau, D.-D., Antoine, P., Gerasimenko, N., Sima, A., Fuchs, M., Hatté, C., et al. (2011). North Atlantic abrupt climatic events of the last glacial period recorded in Ukrainian loess deposits. *Clim. Past* 7, 221–234. doi: 10.5194/cp-7-221-2011.
- Rousseau, D.-D., Sima, A., Antoine, P., Hatté, C., Lang, A., and Zöller, L. (2007). Link between European and North Atlantic abrupt climate changes over the last glaciation. *Geophys. Res. Lett.* 34, L22713. doi: 10.1029/2007GL031716.
- Russell, R. J. (1944). Lower Mississippi valley loess. *Geological Society of America Bulletin* 55, 1–40. doi: 10.1130/GSAB-55-1.
- Sagnotti, L., Speranza, F., Winkler, A., Mattei, M., and Funiello, R. (1998). Magnetic fabric of clay sediments from the external northern Apennines (Italy). *Physics of the Earth and Planetary Interiors* 105, 73–93.
- Sarnthein, M., Tetzlaff, G., Koopmann, B., Wolter, K., and Pflaumann, U. (1981). Glacial and interglacial wind regimes over the eastern subtropical Atlantic and North-West Africa. *Nature* 293, 193–196.
- Sartori, M. (2000). The quaternary climate in loess sediments: evidence from rock and mineral magnetic and geochemical analysis. 231 S. doi: 10.3929/ETHZ-A-004027700.
- Schädel, K., and Werner, J. (1963). Neue Gesichtspunkte zur Stratigraphie des mittleren und älteren Pleistozäns im Rheingletschergebiet. *Eiszeitalter und Gegenwart* 14, 5–26.
- Schatz, A.-K., Zech, M., Buggle, B., Gulyás, S., Hambach, U., Marković, S. B., et al. (2011). The late Quaternary loess record of Tokaj, Hungary: Reconstructing palaeoenvironment, vegetation

- and climate using stable C and N isotopes and biomarkers. *Quaternary International* 240, 52–61. doi: 10.1016/j.quaint.2010.10.009.
- Scheidt, S., Berg, S., Hambach, U., Klasen, N., Pötter, S., Stolz, A., et al. (2021). Chronological Assessment of the Balta Alba Kurgan Loess-Paleosol Section (Romania) – A Comparative Study on Different Dating Methods for a Robust and Precise Age Model. *Front. Earth Sci.* 8, 598448. doi: 10.3389/feart.2020.598448.
- Scheinost, A. C., Chavernas, A., Barrón, V., and Torrent, J. (1998). Use and Limitations of Second-Derivative Diffuse Reflectance Spectroscopy in the Visible to Near-Infrared Range to Identify and Quantify Fe Oxide Minerals in Soils. *Clays and Clay Minerals* 46, 528–536. doi: 10.1346/CCMN.1998.0460506.
- Schmidt, C., Laag, C., Whitehead, M., Profe, J., Tongwa Aka, F., Hasegawa, T., et al. (2022). The complexities of assessing volcanic hazards along the Cameroon Volcanic Line using spatial distribution of monogenetic volcanoes. *Journal of Volcanology and Geothermal Research* 427, 107558. doi: 10.1016/j.jvolgeores.2022.107558.
- Schreuder, L. T., Beets, C. J., Prins, M. A., Hatté, C., and Peterse, F. (2016). Late Pleistocene climate evolution in Southeastern Europe recorded by soil bacterial membrane lipids in Serbian loess. *Palaeogeography, Palaeoclimatology, Palaeoecology* 449, 141–148. doi: 10.1016/j.palaeo.2016.02.013.
- Shackleton, N. J., and Opdyke, N. D. (1976). Oxygen-isotope and paleomagnetic stratigraphy of pacific core V28-239 late Pliocene to latest Pleistocene. *Investigation of late Quaternary paleoceanography and paleoclimatology*, 449–463.
- Shi, C., Zhu, R., Glass, B. P., Liu, Q., Zeman, A., and Suchy, V. (2003). Climate variations since the last interglacial recorded in Czech loess. *Geophys. Res. Lett.* 30, 1562. doi: 10.1029/2003GL017251.
- Smalley, I., and Fagg, R. (2015). John Hardcastle looks at the Timaru loess: Climatic signals are observed, and fragipans. *Quaternary International* 372, 51–57. doi: 10.1016/j.quaint.2014.06.042.
- Smalley, I. J. (1980). *Loess: a partial bibliography*. Norwich: Geo Abstracts.
- Smalley, I. J., Jefferson, I. F., Dijkstra, T. A., and Derbyshire, E. (2001). Some major events in the development of the scientific study of loess. *Earth-Science Reviews* 54, 5–18. doi: 10.1016/S0012-8252(01)00038-1.
- Smalley, I. J., and Marković, S. B. (2014). Loessification and hydroconsolidation: There is a connection. *CATENA* 117, 94–99. doi: 10.1016/j.catena.2013.07.006.
- Smalley, I., Markovic, S. B., O'Hara Dhand, K., and Wynn, P. (2010). A man from Bendery: L.S. Berg as geographer and loess scholar. *Geologos* 16, 111–119.
- Smalley, I., Marshall, J., Fitzsimmons, K., Whalley, W. B., and Ngambi, S. (2019). Desert loess: a selection of relevant topics. *Geologos* 25, 91–102. doi: 10.2478/logos-2019-0007.
- Song, J.-L., Sun, H.-Y., Tian, M.-Z., Zhang, X.-J., Wen, X.-F., and Sun, M. (2018a). Heinrich events recorded in a loess–paleosol sequence from Hexigten, Inner Mongolia. *Geoscience Frontiers* 9, 431–439. doi: 10.1016/j.gsf.2017.03.005.



- Song, Y., Guo, Z., Marković, S., Hambach, U., Deng, C., Chang, L., et al. (2018b). Magnetic stratigraphy of the Danube loess: A composite Titel-Stari Slankamen loess section over the last one million years in Vojvodina, Serbia. *Journal of Asian Earth Sciences* 155, 68–80. doi: 10.1016/j.jseaes.2017.11.012.
- Sprafke, T., and Obreht, I. (2016). Loess: Rock, sediment or soil – What is missing for its definition? *Quaternary International* 399, 198–207. doi: 10.1016/j.quaint.2015.03.033.
- Sprafke, T., Schulte, P., Meyer-Heintze, S., Händel, M., Einwögerer, T., Simon, U., et al. (2020). Paleoenvironments from robust loess stratigraphy using high-resolution color and grain-size data of the last glacial Krems-Wachtberg record (NE Austria). *Quaternary Science Reviews* 248, 106602. doi: 10.1016/j.quascirev.2020.106602.
- Stephenson, A. (1971). Single domain grain distributions I. A method for the determination of single domain grain distributions. *Physics of the Earth and Planetary Interiors* 4, 353–360. doi: 10.1016/0031-9201(71)90018-5.
- Strasser, A., Hilgen, F., and Heckel, P. (2007). Cyclostratigraphy concepts, definitions, and applications. *nos* 42, 75–114. doi: 10.1127/0078-0421/2006/0042-0075.
- Sümeği, P., Gulyás, S., Molnár, D., Sümeği, B. P., Almond, P. C., Vandenberghe, J., et al. (2018). New chronology of the best developed loess/paleosol sequence of Hungary capturing the past 1.1 ma: Implications for correlation and proposed pan-Eurasian stratigraphic schemes. *Quaternary Science Reviews* 191, 144–166.
- Sun, Y., An, Z., Clemens, S. C., Bloemendal, J., and Vandenberghe, J. (2010). Seven million years of wind and precipitation variability on the Chinese Loess Plateau. *Earth and Planetary Science Letters* 297, 525–535. doi: 10.1016/j.epsl.2010.07.004.
- Sun, Y., Clemens, S. C., Morrill, C., Lin, X., Wang, X., and An, Z. (2012). Influence of Atlantic meridional overturning circulation on the East Asian winter monsoon. *Nature Geosci* 5, 46–49. doi: 10.1038/ngeo1326.
- Sun, Y., McManus, J. F., Clemens, S. C., Zhang, X., Vogel, H., Hodell, D. A., et al. (2021). Persistent orbital influence on millennial climate variability through the Pleistocene. *Nat. Geosci.* 14, 812–818. doi: 10.1038/s41561-021-00794-1.
- Sun, Z.-X., Jiang, Y.-Y., Wang, Q.-B., Jiang, Z.-D., Libohova, Z., and Owens, P. R. (2022). Characteristics of a Benchmark Loess–Paleosol Profile in Northeast China. *Agronomy* 12, 1376. doi: 10.3390/agronomy12061376.
- Svirčev, Z., Marković, S. B., Stevens, T., Codd, G. A., Smalley, I., Simeunović, J., et al. (2013). Importance of biological loess crusts for loess formation in semi-arid environments. *Quaternary International* 296, 206–215. doi: 10.1016/j.quaint.2012.10.048.
- Szeberényi, J., Kovács, J., Bradák, B., Barta, G., Csonka, D., Medved'ová, A., et al. (2020). Experiencing new perspectives in the application of reflectance spectroscopy in loess research. *Quaternary International* 552, 36–49. doi: 10.1016/j.quaint.2019.09.035.
- Taylor, S. N., Lacroix, F., Rousseau, D.-D., and Antoine, P. (2014). Mineral magnetic characterization of the Upper Pleniglacial Nussloch loess sequence (Germany): an insight into local environmental processes. *Geophysical Journal International* 199, 1463–1480. doi: 10.1093/gji/ggu331.

- Thiel, C., Horváth, E., and Frechen, M. (2014). Revisiting the loess/palaeosol sequence in Paks, Hungary: A post-IR IRSL based chronology for the 'Young Loess Series.' *Quaternary International* 319, 88–98. doi: 10.1016/j.quaint.2013.05.045.
- Thompson, R., and Oldfield, F. (1986). "Magnetic properties of natural materials," in *Environmental Magnetism* (Dordrecht: Springer Netherlands), 21–38. doi: 10.1007/978-94-011-8036-8\_4.
- Till, J. L., Jackson, M. J., Rosenbaum, J. G., and Solheid, P. (2011). Magnetic properties in an ash flow tuff with continuous grain size variation: A natural reference for magnetic particle granulometry: SUPERPARAMAGNETIC GRAINS IN TUFF. *Geochem. Geophys. Geosyst.* 12, n/a-n/a. doi: 10.1029/2011GC003648.
- Torrent, J., and Barrón, V. (2003). The visible diffuse reflectance spectrum in relation to the color and crystal properties of hematite. *Clays and Clay Minerals* 51, 309–317. doi: 10.1346/CCMN.2003.0510307.
- Torrent, J., Schwertmann, U., and Schulze, D. G. (1980). Iron oxide mineralogy of some soils of two river terrace sequences in Spain. *Geoderma* 23, 191–208. doi: 10.1016/0016-7061(80)90002-6.
- Tutkovskii, P. A. (1899). The question of the method of loess formation (in Russian). *Zemlevedenie* 1–2, 213–311.
- Tutkovskii, P. A. (1900). M. Paul Tutkovskii on the origin of loess. *Scottish Geographical Magazine* 16, 171–174.
- Tutkovskii, P. A. (1910). Das postglaziale Klima in Europa und Nordamerika, die postglazialen Wüsten und die Lössbildung. in *Compte Rendu 11th International Geological Congress Stockholm* (Stockholm), 359–369.
- Tzedakis, P. C., Hooghiemstra, H., and Pälike, H. (2006). The last 1.35 million years at Tenaghi Philippon: revised chronostratigraphy and long-term vegetation trends. *Quaternary Science Reviews* 25, 3416–3430. doi: 10.1016/j.quascirev.2006.09.002.
- Udvardi, B., Kovács, I. J., Kónya, P., Földvári, M., Fűri, J., Budai, F., et al. (2014). Application of attenuated total reflectance Fourier transform infrared spectroscopy in the mineralogical study of a landslide area, Hungary. *Sedimentary Geology* 313, 1–14. doi: 10.1016/j.sedgeo.2014.08.005.
- Újvári, G., Kok, J. F., Varga, G., and Kovács, J. (2016). The physics of wind-blown loess: Implications for grain size proxy interpretations in Quaternary paleoclimate studies. *Earth-Science Reviews* 154, 247–278. doi: 10.1016/j.earscirev.2016.01.006.
- Vaccari, E. (2000). Mining and Knowledge of the Earth in Eighteenth-century Italy. *Annals of Science* 57, 163–180. doi: 10.1080/000337900296236.
- Vaculíková, L., and Plevová, E. (2005). Identification of clay minerals and micas in sedimentary rocks. *Acta Geodynamica et geomaterialia* 2, 167–175.
- Vakhrameeva, P., Koutsodendris, A., Wulf, S., Portnyagin, M., Appelt, O., Ludwig, T., et al. (2021). Land-sea correlations in the Eastern Mediterranean region over the past c. 800 kyr based on macro- and cryptotephra from ODP Site 964 (Ionian Basin). *Quaternary Science Reviews* 255, 106811. doi: 10.1016/j.quascirev.2021.106811.

- Vakhrameeva, P., Wulf, S., Koutsodendris, A., Tjallingii, R., Fletcher, W. J., Appelt, O., et al. (2019). Eastern Mediterranean volcanism during marine isotope stages 9 to 7e (335–235 ka): Insights based on cryptotephra layers at Tenaghi Philippon, Greece. *Journal of Volcanology and Geothermal Research* 380, 31–47. doi: 10.1016/j.jvolgeores.2019.05.016.
- Valet, J.-P., Meynadier, L., and Guyodo, Y. (2005). Geomagnetic dipole strength and reversal rate over the past two million years. *Nature* 435, 802–805. doi: 10.1038/nature03674.
- Van Baak, C. G. C., Mandic, O., Lazar, I., Stoica, M., and Krijgsman, W. (2015). The Slanicul de Buzau section, a unit stratotype for the Romanian stage of the Dacian Basin (Plio-Pleistocene, Eastern Paratethys). *Palaeogeography, Palaeoclimatology, Palaeoecology* 440, 594–613. doi: 10.1016/j.palaeo.2015.09.022.
- van der Marel, H. W., and Beutelspacher, H. (1976). *Atlas of infrared spectroscopy of clay minerals and their admixtures*. Amsterdam ; New York: Elsevier Scientific Pub. Co.
- van Donk, J. (1976). "O18 Record of the Atlantic Ocean for the Entire Pleistocene Epoch," in *Geological Society of America Memoirs* (Geological Society of America), 147–164. doi: 10.1130/MEM145-p147.
- Vandenberghe, J. F., An, Z., Nugteren, G., Lu, H., and van Huissteden, K. (1997). New absolute time scale for the Quaternary climate in the Chinese loess region by grain-size analysis. *Geology* 25, 35–38.
- Vandenberghe, J., Mùcher, H. J., Roebroeks, W., and Gemke, D. (1985). Lithostratigraphy and palaeoenvironment of the Pleistocene deposits at Maastricht–Belvedere, Southern Limburg, The Netherlands. *Mededelingen Rijks Geologische Dienst* 39, 7–18.
- Vandenberghe, J., and Nugteren, G. (2001). Rapid climatic changes recorded in loess successions. *Global and Planetary Change* 28, 1–9. doi: 10.1016/S0921-8181(00)00060-6.
- Vasiljević, D. A., Marković, S. B., Hose, T. A., Ding, Z., Guo, Z., Liu, X., et al. (2014). Loess–palaeosol sequences in China and Europe: Common values and geoconservation issues. *CATENA* 117, 108–118. doi: 10.1016/j.catena.2013.06.005.
- Veres, D., Lane, C. S., Timar-Gabor, A., Hambach, U., Constantin, D., Szakács, A., et al. (2013). The Campanian Ignimbrite/Y5 tephra layer – A regional stratigraphic marker for Isotope Stage 3 deposits in the Lower Danube region, Romania. *Quaternary International* 293, 22–33. doi: 10.1016/j.quaint.2012.02.042.
- Veres, D., Tecsá, V., Gerasimenko, N., Zeeden, C., Hambach, U., and Timar-Gabor, A. (2018). Short-term soil formation events in last glacial east European loess, evidence from multi-method luminescence dating. *Quaternary Science Reviews* 200, 34–51. doi: 10.1016/j.quascirev.2018.09.037.
- Verosub, K. L., Fine, P., Singer, M. J., and TenPas, J. (1993). Pedogenesis and paleoclimate: Interpretation of the magnetic susceptibility record of Chinese loess-paleosol sequences. *Geology* 21, 1011–1014.
- Verosub, K. L., and Roberts, A. P. (1995). Environmental magnetism: Past, present, and future. *J. Geophys. Res.* 100, 2175–2192. doi: 10.1029/94JB02713.

- Vigliotti, L. (2015). Magnetic properties of the Campanian Ignimbrite and the marine Y5 tephra layer. *Geological Society, London, Special Publications* 396, 227–238. doi: 10.1144/SP396.1.
- Vlaminck, S., Kehl, M., Lauer, T., Shahriari, A., Sharifi, J., Eckmeier, E., et al. (2016). Loess-soil sequence at Toshan (Northern Iran): Insights into late Pleistocene climate change. *Quaternary International* 399, 122–135. doi: 10.1016/j.quaint.2015.04.028.
- Wacha, L., Laag, C., Grizelj, A., Tsukamoto, S., Zeeden, C., Ivanišević, D., et al. (2021). High-resolution palaeoenvironmental reconstruction at Zmajevac (Croatia) over the last three glacial/interglacial cycles. *Palaeogeography, Palaeoclimatology, Palaeoecology* 576, 110504. doi: 10.1016/j.palaeo.2021.110504.
- Wacha, L., Mikulčić Pavlaković, S., Frechen, M., and Crnjaković, M. (2011). The Loess Chronology of the Island of Susak, Croatia. *E&G Quaternary Sci. J.* 60, 153–169. doi: 10.3285/eg.60.1.11.
- Wacha, L., Rolf, C., Hambach, U., Frechen, M., Galović, L., and Duchoslav, M. (2018). The Last Glacial aeolian record of the Island of Susak (Croatia) as seen from a high-resolution grain-size and rock magnetic analysis. *Quaternary International* 494, 211–224. doi: 10.1016/j.quaint.2017.08.016.
- Wada, K. (1967). A study of hydroxyl groups in kaolin minerals utilizing selective deuteration and infrared spectroscopy. *Clay miner.* 7, 51–61. doi: 10.1180/claymin.1967.007.1.05.
- Wang, P., Li, Q., Tian, J., Jian, Z., Liu, C., Li, L., et al. (2014). Long-term cycles in the carbon reservoir of the Quaternary ocean: a perspective from the South China Sea. *National Science Review* 1, 119–143. doi: 10.1093/nsr/nwt028.
- Worm, H.-U. (1998). On the superparamagnetic-stable single domain transition for magnetite, and frequency dependence of susceptibility. *Geophys. J. Int.* 133, 201–206. doi: 10.1046/j.1365-246X.1998.1331468.x.
- Worm, H.-U., Ryan, P. J., and Banerjee, S. K. (1991). Domain size, closure domains, and the importance of magnetostriction in magnetite. *Earth and Planetary Science Letters* 102, 71–78. doi: 10.1016/0012-821X(91)90018-D.
- Wu, N., Li, F., and Rousseau, D.-D. (2018). Terrestrial mollusk records from Chinese loess sequences and changes in the East Asian monsoonal environment. *Journal of Asian Earth Sciences* 155, 35–48. doi: 10.1016/j.jseaes.2017.11.003.
- Wulf, S., Hardiman, M. J., Staff, R. A., Koutsodendris, A., Appelt, O., Blockley, S. P. E., et al. (2018). The marine isotope stage 1–5 cryptotephra record of Tenaghi Philippon, Greece: Towards a detailed tephrostratigraphic framework for the Eastern Mediterranean region. *Quaternary Science Reviews* 186, 236–262. doi: 10.1016/j.quascirev.2018.03.011.
- Yang, S., and Ding, Z. (2010). Drastic climatic shift at ~2.8Ma as recorded in eolian deposits of China and its implications for redefining the Pliocene-Pleistocene boundary. *Quaternary International* 219, 37–44. doi: 10.1016/j.quaint.2009.10.029.
- Ye, C., Yang, Y., Fang, X., Zan, J., Tan, M., and Yang, R. (2020). Chlorite weathering linked to magnetic enhancement in Red Clay on the Chinese Loess Plateau. *Palaeogeography, Palaeoclimatology, Palaeoecology* 538, 109446. doi: 10.1016/j.palaeo.2019.109446.

- Yin, Q. (2013). Insolation-induced mid-Brunhes transition in Southern Ocean ventilation and deep-ocean temperature. *Nature* 494, 222–225. doi: 10.1038/nature11790.
- Zech, M., Zech, R., and Glaser, B. (2007). A 240,000-year stable carbon and nitrogen isotope record from a loess-like palaeosol sequence in the Tumara Valley, Northeast Siberia. *Chemical Geology* 242, 307–318. doi: 10.1016/j.chemgeo.2007.04.002.
- Zech, R., Gao, L., Tarozo, R., and Huang, Y. (2012). Branched glycerol dialkyl glycerol tetraethers in Pleistocene loess-paleosol sequences: Three case studies. *Organic Geochemistry* 53, 38–44. doi: 10.1016/j.orggeochem.2012.09.005.
- Zech, R., Zech, M., Marković, S., Hambach, U., and Huang, Y. (2013). Humid glacials, arid interglacials? Critical thoughts on pedogenesis and paleoclimate based on multi-proxy analyses of the loess–paleosol sequence Crvenka, Northern Serbia. *Palaeogeography, Palaeoclimatology, Palaeoecology* 387, 165–175. doi: 10.1016/j.palaeo.2013.07.023.
- Zeeden, C., Hambach, U., Veres, D., Fitzsimmons, K., Obrecht, I., Böskén, J., et al. (2018). Millennial scale climate oscillations recorded in the Lower Danube loess over the last glacial period. *Palaeogeography, Palaeoclimatology, Palaeoecology* 509, 164–181. doi: 10.1016/j.palaeo.2016.12.029.
- Zeeden, C., Kels, H., Hambach, U., Schulte, P., Protze, J., Eckmeier, E., et al. (2016). Three climatic cycles recorded in a loess-palaeosol sequence at Sendlac (Romania) – Implications for dust accumulation in south-eastern Europe. *Quaternary Science Reviews* 154, 130–142. doi: 10.1016/j.quascirev.2016.11.002.
- Zeeden, C., Krauß, L., Kels, H., and Lehmkuhl, F. (2017). Digital image analysis of outcropping sediments: Comparison to photospectrometric data from Quaternary loess deposits at Şanoviţa (Romania) and Achenheim (France). *Quaternary International* 429, 100–107. doi: 10.1016/j.quaint.2016.02.047.
- Zeeden, C., Mir, J. A., Vinneband, M., Laag, C., Rolf, C., and Dar, R. A. (2021). Local mineral dust transported by varying wind intensities forms the main substrate for loess in Kashmir. *E&G Quaternary Sci. J.* 70, 191–195. doi: 10.5194/egqsj-70-191-2021.
- Zhang, R., and Nie, J. (2017). Goethite Concentration Variations in the Red Clay Sequence on the Chinese Loess Plateau. *Geochem. Geophys. Geosyst.* 18, 4179–4185. doi: 10.1002/2017GC007148.
- Zhang, W., Yu, L., Lu, M., Zheng, X., and Shi, Y. (2007). Magnetic properties and geochemistry of the Xiashu Loess in the present subtropical area of China, and their implications for pedogenic intensity. *Earth and Planetary Science Letters* 260, 86–97. doi: 10.1016/j.epsl.2007.05.018.
- Zhang, Y., Guan, L., and Liu, Q. (2018). Liu Tungsheng: A geologist from a traditional Chinese cultural background who became an international star of science. *Journal of Asian Earth Sciences* 155, 8–20. doi: 10.1016/j.jseaes.2017.11.002.
- Zhao, H., Qiang, X., Xu, X., and Sun, Y. (2020). Iron oxide characteristics of the Chinese loess-red clay sequences and their implications for the evolution of the East Asian summer monsoon since the Late Oligocene. *Palaeogeography, Palaeoclimatology, Palaeoecology* 543, 109604. doi: 10.1016/j.palaeo.2020.109604.

- Zhao, H., Sun, Y., and Qiang, X. (2017). Iron oxide characteristics of mid-Miocene Red Clay deposits on the western Chinese Loess Plateau and their paleoclimatic implications. *Palaeogeography, Palaeoclimatology, Palaeoecology* 468, 162–172. doi: 10.1016/j.palaeo.2016.12.008.
- Zhao, M., Beveridge, N. A. S., Shakleton, N. J., Sarnthein, M., and Eglinton, G. (1995). Molecular stratigraphy of cores off northwest Africa: Sea surface temperature history over the last 80 ka. *Paleoceanography* 10, 661–675.
- Zhou, L. P., Oldfield, F., Wintle, A. G., Robinson, S. G., and Wang, J. T. (1990). Partly pedogenic origin of magnetic variations in Chinese loess. *Nature* 346, 737–739. doi: 10.1038/346737a0.
- Zöller, L. ed. (2017). *Die physische Geographie Deutschlands*. Darmstadt: WBG, Wissenschaftliche Buchgesellschaft.
- Zöller, L., Fischer, M., Jary, Z., Antoine, P., and Krawczyk, M. (2022). Chronostratigraphic and geomorphologic challenges of last glacial loess in Poland in the light of new luminescence ages. *E&G Quaternary Sci. J.* 71, 59–81. doi: 10.5194/egqsj-71-59-2022.

## Acknowledgements

I sincerely wanted to thank my both supervisors, **Dr. France Lagroix** and **Dr. Yohan Guyodo**, for their constructive and wholehearted supervision of my PhD thesis. Without your help, my time in Paris would have been much more complicated - whether it was scientific, living, or formal questions. You always encouraged me to think for myself and were there whenever I needed advice or help. As their PhD student, I cannot imagine having had better supervisors. I am grateful for the opportunity to collaborate with you in the future and for the amazing time I spent with France during fieldwork. I am also thankful to Yohan for always being available to listen and offer guidance, whether it was related to mathematics, grain size data evaluation, or tephra identification using magnetic methods such as IRM acquisitions.

I would like to express my gratitude my former supervisor of my Master's thesis, **Dr. Christian Zeeden**, for the constructive discussions we had about LPSs in Eastern and Western Europe. Your active involvement in several LPS projects and the constant exchange of scientific conversations were very helpful and contributed to my development as an early career scientist. Your guidance in broadening my view on terrestrial and limnic archives by involving me in several case studies helped me to understand the larger atmospheric patterns and orbitally driven feedbacks of parameters derived from these archives..

I am deeply grateful to **Dr Sebastian Kreutzer** for his help with the R-related problems I encountered. Sebastian, thank you so much for always being available for in-depth scientific discussions, simplifying my R codes, and strengthening their outcomes. I am also thankful for the beautiful RLumCarlo that you and Dr Christoph Schmidt established and conducted in the USA in late 2019. Those times will not be forgotten.

I sincerely want to thank **Prof. Diana** and **Dr. Neli Jordanova** for involving me in the Pleven LPS project and for the sophisticated exchange we had. I also want to thank you for participating in the intense field work at Pleven and for the amazing stay we had at your home on the last evening.

**Dr. Ulrich Hambach**, my journey with loess began in 2014 when you recommended me for a student assistant position. Shortly after that, I was able to work in your laboratory at the University of Bayreuth, which ignited my passion for terrestrial archives. I was also able to gain experience with various magnetic measurements and the possible interpretations that can be derived from them. You later supervised my Bachelor's thesis with Prof. Ludwig Zöllner and my Master's thesis with Dr. Christian Zeeden. You encouraged me to work with TU Dresden



and get involved with Tunisian LPSs, which provided a unique perspective on the use of proxies to investigate past climate in an area with conditions that differ greatly from those of Eastern European LPSs. Your guidance led me to work at the LIAG lab in Grubenhagen near Hannover and eventually apply for a PhD position at the IPGP in Paris, where I am currently writing this text and completing that chapter. Thank you for always being a critical voice (our common term *advocatus diaboli*) in the background and for sharing your extensive experience in loess-related research in the Carpathian Basin and Lower Danube areas with me.

**Dr. Christoph Schmidt**, I want to thank you for giving me the opportunity to participate in the ULTIMO project funded by DAAD and for the unforgettable trip to Maryland at the beginning of my PhD. I also greatly valued our collaboration on the Cameroon Volcanic Line Mapping project and how we worked together to push it forward. These archives are waiting for an in-depth relative age modeling approach and sedimentary characterization, leading to the newly established paleoenvironmental archive we discovered together from 2019-2022. I hope we can continue this good collaboration to further enhance records and their ability to provide information on past climate changes. Cheers to Lausanne!

**Dr. Lara Wacha**, I just want to say a big thank you for all of your help and support. I am deeply grateful for the opportunity to be a part of your research at Zmajevac and to contribute to the important work that you are doing. Your encouragement and guidance have been invaluable to me, and I am so grateful for the opportunity to present at the Croatian Geological Society. It was a wonderful experience, and I hope to have the chance to participate in more conferences and events like that in the future. I am also looking forward to continuing our collaboration on the Zmajevac, Sarengard, and Susak sequences. These are important archives that hold valuable information about the past, and I am thrilled to be able to work with you to uncover their secrets. I am confident that together we can make significant contributions to our understanding of the Earth's history and the forces that have shaped it over time. I hope to see you at your conference in Dubrovnik for IAS 2023, and I look forward to many more collaborations in the future.

**Stoil Chapkanski**, I wish you all the success, luck, and endurance as you work on your PhD thesis. Working with you has opened up new pathways for loess-related research and tephra identification and characterization using that old mid-infrared spectrometer. I hope that we can continue to work together well and solve stratigraphical issues in LPSs, providing a method for tephra identification beyond traditional geochemical analysis when glass shards are too

weathered. Your kindness and hospitality during my stay at LGP in Meudon made it a very comfortable and enjoyable experience. But we still need to have that beer (which has been waiting for more than a year and is getting numb)!

**Mathias Vinnepand**, I am grateful for the time we have spent together discussing the complex and fascinating topic of Kashmir loess with comparison of the Remagen loess. Your insights and perspectives have been invaluable to me, and I have enjoyed the many deep and thought-provoking discussions we have had about the potential for using and integrating multiple-proxy data to quantify precipitation and temperature. Your expertise and experience in this field have helped me to better understand the challenges and opportunities that lie ahead, and I am grateful for the opportunity to work with you and for the scientific exchange. In the future, my couch is always open for you, and I hope we can continue to have these meaningful conversations and collaborations.

**Dr. Pierre Antoine**, it has been a pleasure to work with you, and I am deeply grateful that you shared your long-term expertise with me regarding loess-paleosol sequences. Your guidance and mentorship have been invaluable to me, and I am thankful for the opportunity to learn from your experience and expertise. Your insights and perspectives have helped me to better understand the complexities of loess-paleosol sequences and the valuable information they contain about the Earth's past climate and environment. Thank you for your support and for being a valuable colleague and mentor.

**Prof. Joshua Feinberg**, I am especially grateful for your willingness to review my thesis. I am also very thankful for the time I spent at the IRM summer school hosted by the Institute for Rock Magnetism in June 2022. In addition, I want to express my gratitude to Dr. Dario Bilardello, **Dr. Peter Solheid**, and **Dr. Maxwell Brown** for the wonderful science school in Minnesota and the valuable insights and teaching content they provided. The entire experience was very pleasantly organized, and I am thankful to all of you for your help and support. Thank you so much!

**Dr. Christine Hatté**, I want to express my sincere gratitude for serving as the second rapporteur for my PhD thesis. Your insights and feedback were invaluable to me, and I appreciate your support and guidance throughout this process.

**Prof. Magali Ader** and **Dr. Simo Spassov**, I am thankful to both of you for serving as examiners of my thesis and defense.

**Bozhurka Georgieva, Daniel Ishlyamski, and Robin Heraibi,** I am grateful for the great time we had together in Pleven and for all of your hard work during the field work we conducted on this LPS. It was a pleasure to work with all of you, and I appreciate the effort and dedication you brought to the project. Your contributions were invaluable, and I am thankful for the opportunity to collaborate with you. Thank you for your support and for making the experience such a memorable one.

**Mme. Assumpta Laag-Uwimanzi,** my dear wife and best friend, I am forever grateful for your love and support. Since the day we met on 05.12.2020, you have been my rock and my constant source of strength. Our marriage on 05. & 06.08.2022 was the happiest day of my life, and I am so thankful to have you as my partner and my soulmate. Your love has sustained me through every challenge and has given me the courage to face whatever comes my way. You have supported me in every situation and have always been there to lift me up when I needed it most. Your love and devotion mean everything to me, and I am so grateful to have you by my side. Thank you for being my everything, my love.

## Appendix

### Appendix A: Supplement for Chapter 3.1.

Appendix A contains supplementary figures and tables for chapter 3.1.

Table 1S: Stratigraphic description of the Pleven (SK18) loess-paleosol sequence.

composite depth (cm)	section name / depth (cm)	horizon	Field description
0 - 30	SK I 0 – 30cm	Ap	fine crumb structure, clay – silty, abundant roots, at 28 – 30cm depth – wheat straw layer, 7.5YR2.5/2 very dark brown, HCl effervescent; lower boundary with E horizon – sharp and clear
30 - 60	SK I 32 – 60cm	B1	fine angular to sub-angular structure, clay – silty, no reaction to HCl, 7.5YR4/4 brown, roots
60 - 100	SK I 62 – 100cm	B2	medium granular structure, silty – clay, 7.5YR3/3 dark brown, lower boundary – gradual, few roots, no reaction to HCl; at 56 – 60cm phytoliths or charcoal pieces (?)
100 - 133	SK I 102 – 132cm	B/C	fine granular structure, silty, roots down to 130cm, 7.5YR5/4 brown, no reaction to HCl
133 - 170	SK I 134 – 170cm	loess L1	granular fine structure, silty, root channels and crotovinas ~ 5mm diameter, fine micellar CaCO <sub>3</sub> , 10YR5/3 brown, HCl effervescent, transition to lower horizon - gradual
170 - 296	SK I 172 – 296cm	incipient soil L1S1	fine granular structure, silty – clay texture, very smooth transition to a darker color at depth. HCl effervescent; at 240cm CaCO <sub>3</sub> concretions ~2cm diameter, irregular very fine CaCO <sub>3</sub> incrustations of root channels and insects' holes; fine roots. Color at 180cm – 10YR4/3, at 250cm – 7.5YR4/3 brown
296 - 356	SK II 0-60cm	loess L1 lower part	structureless, silty – sand texture, fine CaCO <sub>3</sub> concretions, HCl effervescent, color 10YR5/4 yellowish brown; boundary with lower unit - wavy
356 - 386	SK II 60 – 90cm	S1 upper part	mixture of L1 & S1 material, silty texture, crumb structure, color: 10YR5/4 + 10YR4/4, small CaCO <sub>3</sub> concretions, HCl effervescent; shiny mica minerals, small channels of insects (2-3 mm diameter), boundary with lower unit – smooth
386 - 426	SK II 90 – 130cm	S1 Bt1	crumbly structure, silty – clayey, CaCO <sub>3</sub> micellii and small concretions, color 7.5YR3/3 dark brown
426 - 486	SK II 130 – 190cm	S1 Bt2	crumbly structure, more silty than Bt1, color 7.5YR3/4 dark brown

486 - 564	SK II 190 – 268cm	S1 B/C	crumbly, silty texture, many CaCO <sub>3</sub> micellar and fine concretions, boundary with lower unit – wavy, color 7.5YR4/3 brown
564 - 644	SK III 0 – 80cm	loess L2 upper part	structureless, silty with rare sand grains, long thin vertical crotovinas, CaCO <sub>3</sub> concretions with sizes 0.5 – 1cm diameter, color 10YR6/4 light yellowish brown, boundary with upper unit - sharp
644 - 714	SK III 80 – 150cm	loess L2	pure loess, structureless, silty, few CaCO <sub>3</sub> micelii; at 704 – 709cm depth – carbonate concretions of 3-4cm diameter; color 10YR5/4 yellowish brown
714 – 732	SK III 150 – 168cm	tephra layer	hard with stony appearance, silty texture, dense, compacted, medium prismatic structure, color 10YR4/3 brown
732 - 764	SK III 168 – 200cm	L2 lower part	loess, silty – clay texture, structureless, color 10YR5/4 yellowish brown
764 - 832	SK III 200 – 268cm	transition between soil and loess	clayey – silty, few crotovinas, gradual change in texture and color from brown to more reddish; at 796cm – small crotovinas, color 2.5YR5/3 reddish brown
832 – 862	SK IV 0- 30cm	incipient soil	clayey – silty, weak crumbly structure, HCl effervescence, color 10YR5/4 yellowish brown
862 - 875	SK IV 30 – 43cm	incipient soil	inclined layer, clayey, fine platy structure, well defined boundaries with lower and upper units, color 7.5YR4/4 brown; , HCl effervescence
875 - 912	SK IV 43 – 80cm	S2 upper part	crumb structure, silty – clay with few sand grains, color 10YR4/4 dark yellowish brown; , HCl effervescence
912 - 957	SK IV 80 – 125cm	S2 B1	inclined layer, blocky structure, dense clayey unit, fine incrustations with organic matter, color 7.5YR4/4 brown; HCl effervescence
957 - 1002	SK IV 125 – 170cm	S2 B2	silty – clay texture, fine blocky structure, fine pedo-structures, at 959cm – some diffuse CaCO <sub>3</sub> concretions; color 7.5YR3/3 dark brown; , HCl effervescence
1002 - 1022	SK IV 170 – 192cm	S2 B3	dense clayey texture, prismatic structure, dark brown reddish horizon with Mn concretions; CaCO <sub>3</sub> concretions; , HCl effervescence, color 5YR4/4 reddish brown
1022 - 1077	SK V 0 – 55cm	S2 B/C	prismatic structure, silty, 5% abundance of CaCO <sub>3</sub> concretions, micelii, Mn concretions with diameters of 1-2mm; color 5YR4/6 yellowish red
1077 - 1137	SK V 55 – 115cm	loess L3	silty, structureless, 5% abundance of CaCO <sub>3</sub> concretions with diameters up to 1cm; CaCO <sub>3</sub> micelii, holes from biological activities; small crotovinas (diameters up to 1cm); color 10YR5/6 yellowish brown

1137 - 1171	SK VI 0 – 34cm	layer in L3 loess	blocky prismatic structure, clayey, CaCO <sub>3</sub> concretions with diameters up to 3-4cm; color 7.5YR4/4 brown; HCl effervescence
1171 - 1203	SK VI 34 – 66cm	loess L3	silty, structureless, color 10YR5/4 yellowish brown
1203 - 1257	SK VI 66 – 120cm	S3 upper part	crumbly structure, silty – clayey, HCl effervescence, color 7.5YR3/3 dark brown
1257 - 1307	SK VI 120 – 170cm	S3 Bt1	granular structure, clayey – silty, Mn coatings, no HCl reaction; at 1287cm – big CaCO <sub>3</sub> concretion (~4cm diameter)
1307 - 1352	SK VII 0 – 45cm	S3 Bt2	fine prismatic structure, clayey silty, no HCl reaction; small Mn concretions and coatings, color 7.5YR3/4 dark brown
1352 - 1397	SK VII 45 – 90cm	loess L4 altered	granular structure, silty clayey; small and medium sized CaCO <sub>3</sub> concretions; mixing with soil material, color 10YR5/4 yellowish brown, HCl effervescence
1397 - 1457	SK VII 90 – 150cm	S4 B	crumb structure, silty clayey, small CaCO <sub>3</sub> incrustations; HCl effervescence
1457 - 1557	SK VII 150 – 250cm	S4 B1	crumb structure, silty clayey; CaCO <sub>3</sub> fillings of root channels; at 1477cm – big ~3cm CaCO <sub>3</sub> concretion; color 7.5YR4/4 brown; at 1557cm depth – very big (~ 25cm diameter) CaCO <sub>3</sub> concretion
1557 - 1607	SK VIII 0 – 50 cm	S4 B/C	granular structure, silty – sandy; 5% abundance of CaCO <sub>3</sub> concretions; 1% abundance of large crotovinas (diameters of 6 -7 cm); at 1573cm – signs of roots or animal channels.
1607 - 1657	SK VIII 50 – 100cm	loess L5 upper part	structureless, silty; in the upper part – small (2-3mm diameters) CaCO <sub>3</sub> concretions and micellii (fine net); rare (<1%) crotovinas filled with dark soil material; color 10YR5/4 yellowish brown
1657 - 1737	SK VIII 100 – 180cm	pure loess L5	structureless, silty, rare small d<1mm) CaCO <sub>3</sub> concretions, color 10YR5/4 yellowish brown
1737 - 1833	SK VIII 180 – 276cm	S5 upper part	crumb structure, silty – clayey; rare (1% abundance) crotovinas; at 1760 - 1770cm – CaCO <sub>3</sub> layer with small (2-3mm) concretions (abundance of concretions 50%), vertical root channels and animal holes; color 10YR5/4 yellowish brown
1833 - 1847	SK VIII 276 – 290cm	S5	structureless, silty – clayey, mixed with soil material from below; CaCO <sub>3</sub> concretions with abundance of 5%, color 10YR5/4 yellowish brown
1847 - 1879	SK VIII 290 – 322cm	S5 tephra (?)	massive blocky structure; clayey, big CaCO <sub>3</sub> concretions, vertical root channels, smooth boundary with upper unit; color 7.5YR4/6 strong brown; HCl effervescence

1879 - 1919	SK IX 0 – 40cm	S5 B1	fine blocky structure, silty – clayey, small Mn spots, many CaCO <sub>3</sub> concretions with sizes from 5mm up to 5-6cm diameters (abundance 10%); color 7.5YR4/6 strong brown
1919 - 1959	SK IX 40 – 80cm	S5 Bt2	sub-angular massive dense structure, clayey, Mn spots and incrustations, small CaCO <sub>3</sub> concretions (<1% abundance), color 7.5YR4/4 brown
1959 - 2009	SK IX 80 – 130cm	S5 B3	dense angular structure, heavy clayey, frequent larger Mn concretions and incrustations; soft CaCO <sub>3</sub> concretions with abundance of 1%; color 7.5YR4/4 brown
2009 - 2063	SK IX 130 – 184cm	S5 B4	medium size blocky texture, very heavy clayey, frequent Mn concretions and incrustations, large hard CaCO <sub>3</sub> concretions (abundance 5%, diameters 2-3cm), shiny surfaces; color 7.5YR4/6 strong brown
2063 - 2103	SK X 0 – 40cm	S5 B5	sub-angular texture, clayey, large sharp CaCO <sub>3</sub> concretions, increasing in size downward and forming wavy boundary with the loess below, color 7.5YR3/4 dark brown
2103 - 2133	SK X 40 – 70cm	S5 B/C1	crumb texture, silty – clayey, mixture of soil with pale loess-like material, CaCO <sub>3</sub> concretions and micellii, color 5YR4/6 yellowish red
2133 - 2181	SK X 70 – 96cm SK XI 0 – 22cm	S5 B/C2	structureless, silty, pale mixture of CaCO <sub>3</sub> concretions, crotovinas, color 10YR5/4 yellowish brown, boundary with lower unit - transitional
2181 - 2249	SK XI 22 – 90cm	loess L6	structureless, silty, slightly lighter than upper unit, big dark crotovinas and CaCO <sub>3</sub> concretions; reddish – orange spots, color 10YR7/4 very pale brown; lower boundary – irregular wavy
2249 - 2292	SK XI 90 – 133cm	S6 upper part	medium granular structure, silty – clayey, thin Mn coatings, color 5YR4/6 yellowish red
2292 - 2319	SK XI 133 – 160cm	S6 Bt1	prismatic structure, clayey, massive Mn-coatings along planes, color 5YR3/4 dark reddish brown
2319 - 2369	SK XI 160 – 210cm	S6 Bt2	prismatic structure, silty – clayey, massive Mn coatings, large hard irregular CaCO <sub>3</sub> concretions, color 5YR4/6 yellowish red
2369 - 2459	SK XI 210 – 300cm	S6 Bt3	large prismatic structure, clayey, strongly illuviated, Mn coatings and concretions, grey redoximorphic spots near Mn concretions, massive soft CaCO <sub>3</sub> with clear vertical appearance; color 2.5YR3/4 dark reddish brown.
2459 - 2559	SK XII 0 – 100cm	S6 B/C	prismatic structure, clayey – silty, Mn coatings and concretions; massive soft CaCO <sub>3</sub> concretions with diameters of 5-6cm; grey redoximorphic features. At depth (2554 –



			2559cm) - hard CaCO <sub>3</sub> layer. Boundary with lower unit – irregular wavy; color 10YR5/4 yellowish brown.
2559 - 2612	SK XII 100 – 153cm	loess L7 altered	granular loose structure, silty – clayey, CaCO <sub>3</sub> intermixed with thin clay layers, coarse Mn-coated granular voids and large Mn concretions,
2612 - 2669	SK XII 153 – 210cm	clays	clay unit, clayey, CaCO <sub>3</sub> as concretions and vertical fillings, large Mn concretions and Mn coatings along planes, grey redoximorphic features; color 10YR4/4 dark yellowish brown

Table 2S. Tie-points used for the preliminary correlative age models presented in Figure 8.

depth (m) $\Delta\chi$ record	LR04 age (ka)	depth (m) IRM <sub>2T</sub> / $\chi$ record	EDC age (ka)
1.28	15.97	1.68	29.77
2.96	57.09	3.56	68.15
3.56	69.74	5.18	131.97
5.62	135.10	8.76	192.34
8.36	185.06	12.04	277.52
10.78	243.00	14.46	373.16
12.00	276.99	15.58	426.47
13.52	337.88	17.38	477.19
14.00	363.32	22.52	673.58
15.6	426.85	25.60	790.60
17.38	477.60		
21.12	621.89		
22.50	672.31		
25.60	790.60		



Figure 1S: Photograph of the NW wall of the Suhia Kladenetz quarry in August of 2018 showing the complete loess-paleosol sequence and the underlying clays. Loess units L1 to L7 are marked for clarity.

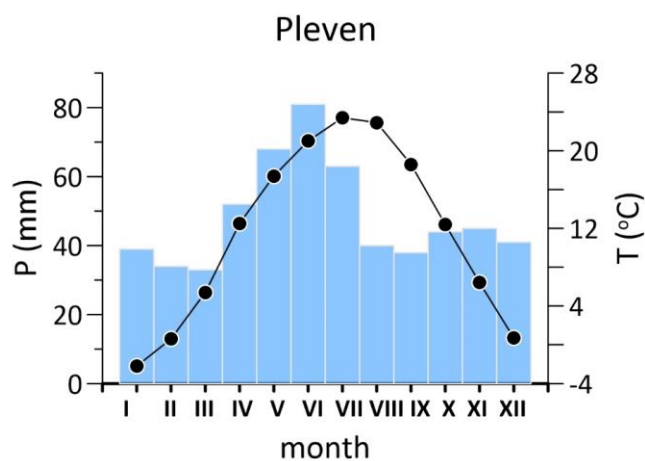


Figure 2 S. Long term (25 years average) average monthly temperature and precipitation at Pleven meteorological station. Temperature data are presented by dots, precipitation – by columns.

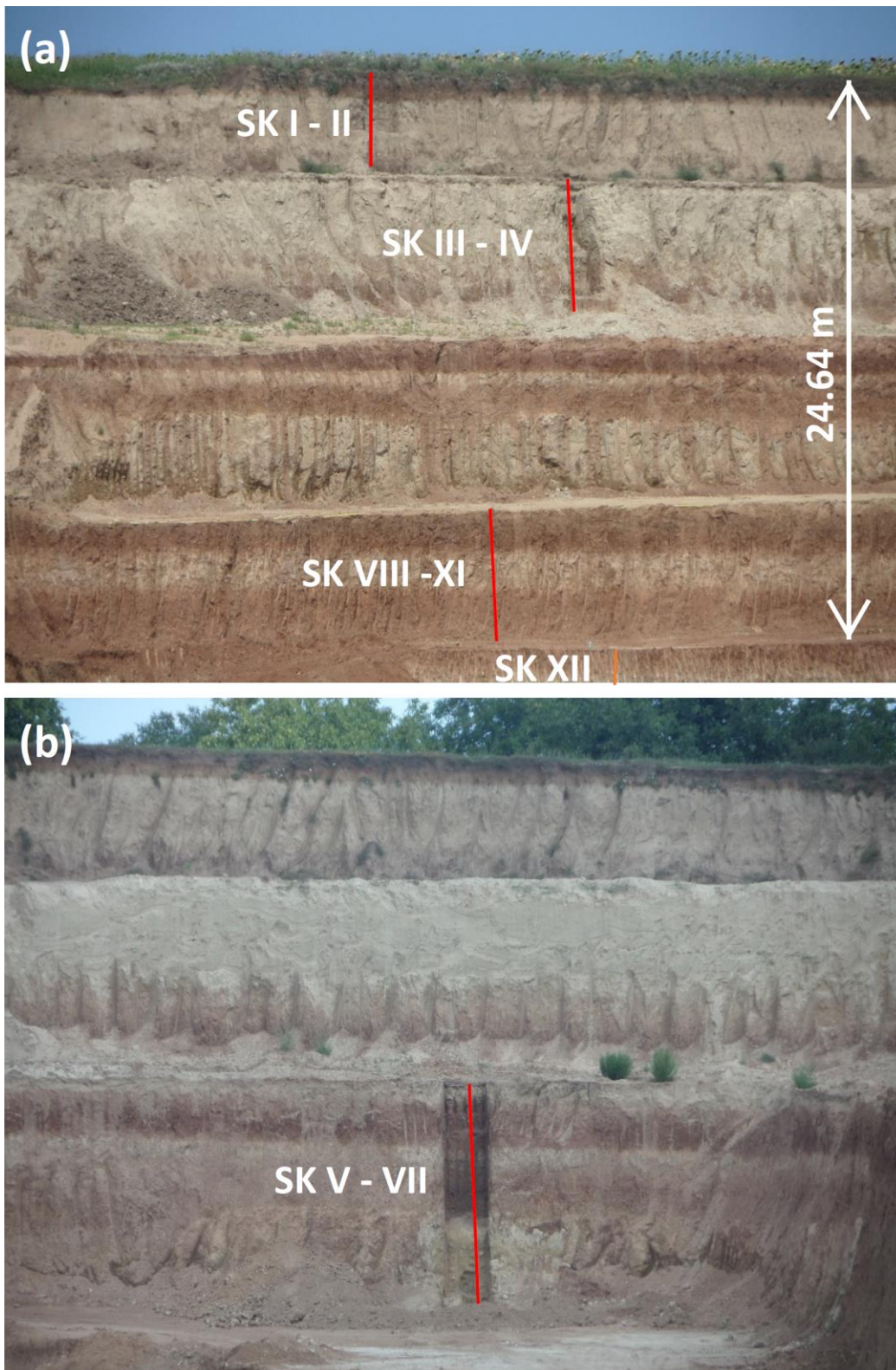


Figure 3S: Photographs of the sampled sub-sections along the quarry steps for (a) sub-sections SK I – II (0 - 5.64 m); SK III – IV (5.64 - 10.24 m); SK VIII – XI (15.60 - 24.64 m); SK XII (24.64 - 26.72 m) on the NW quarry wall and (b) sub-sections SK V - VII (10.24 - 15.60 m) on the E quarry wall.





Figure 4S: Photograph, taken soon after a rainy day, providing field evidence of the textural contrast induced by the visible tephra (marked by dashed stripe) within the L2 loess unit. Loess above the tephra is dry and well drained, while below evidence of water retention is observed.

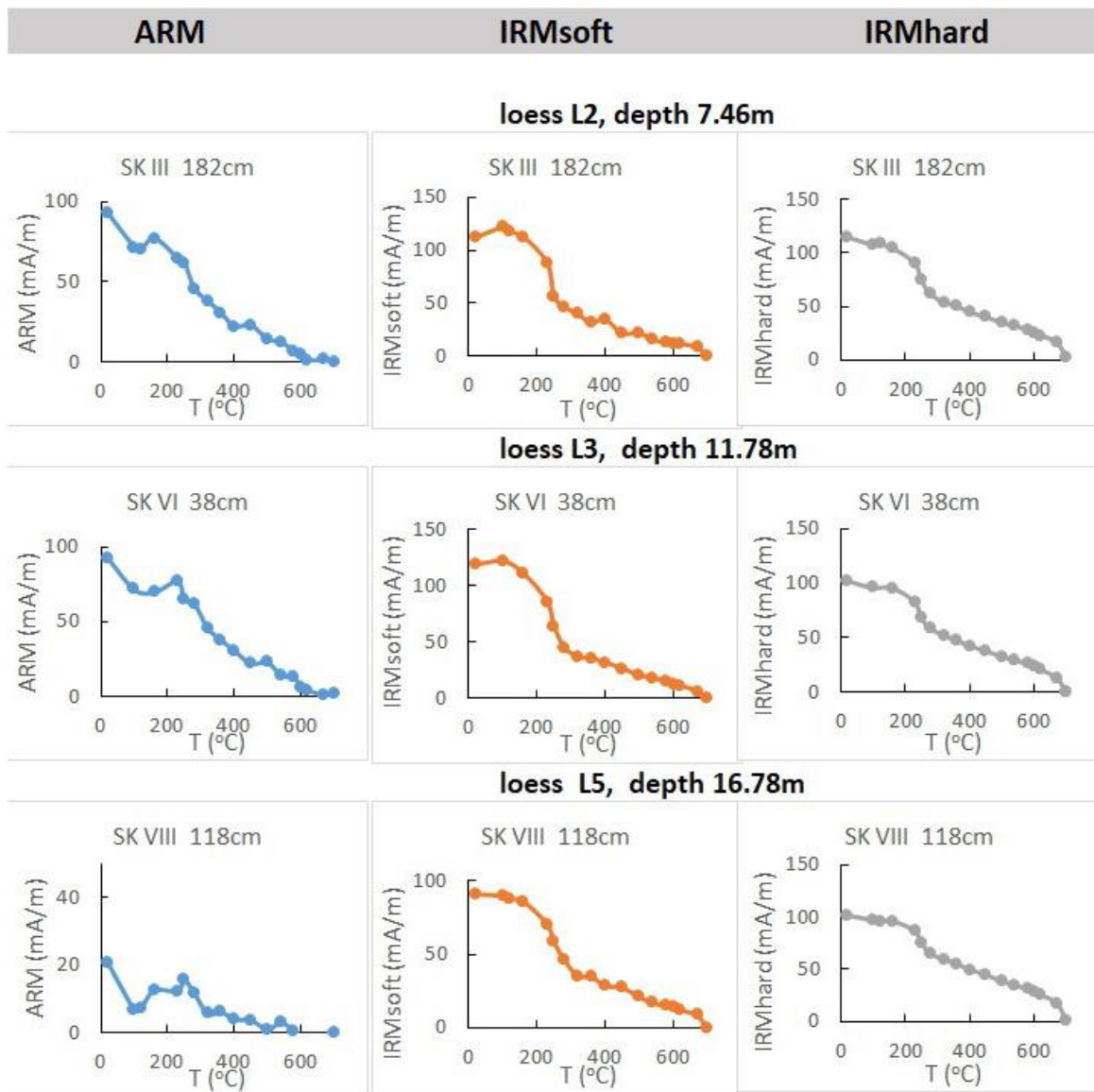


Figure 5S: Examples of thermal demagnetization curves of composite remanence for loess samples (see section 2.1). Left column is ARM component; middle column is  $IRM_{\text{soft}}$  component acquired in 0.1 to 0.2 T fields; right column is  $IRM_{\text{hard}}$  component acquired in 0.2 to 2 T fields.

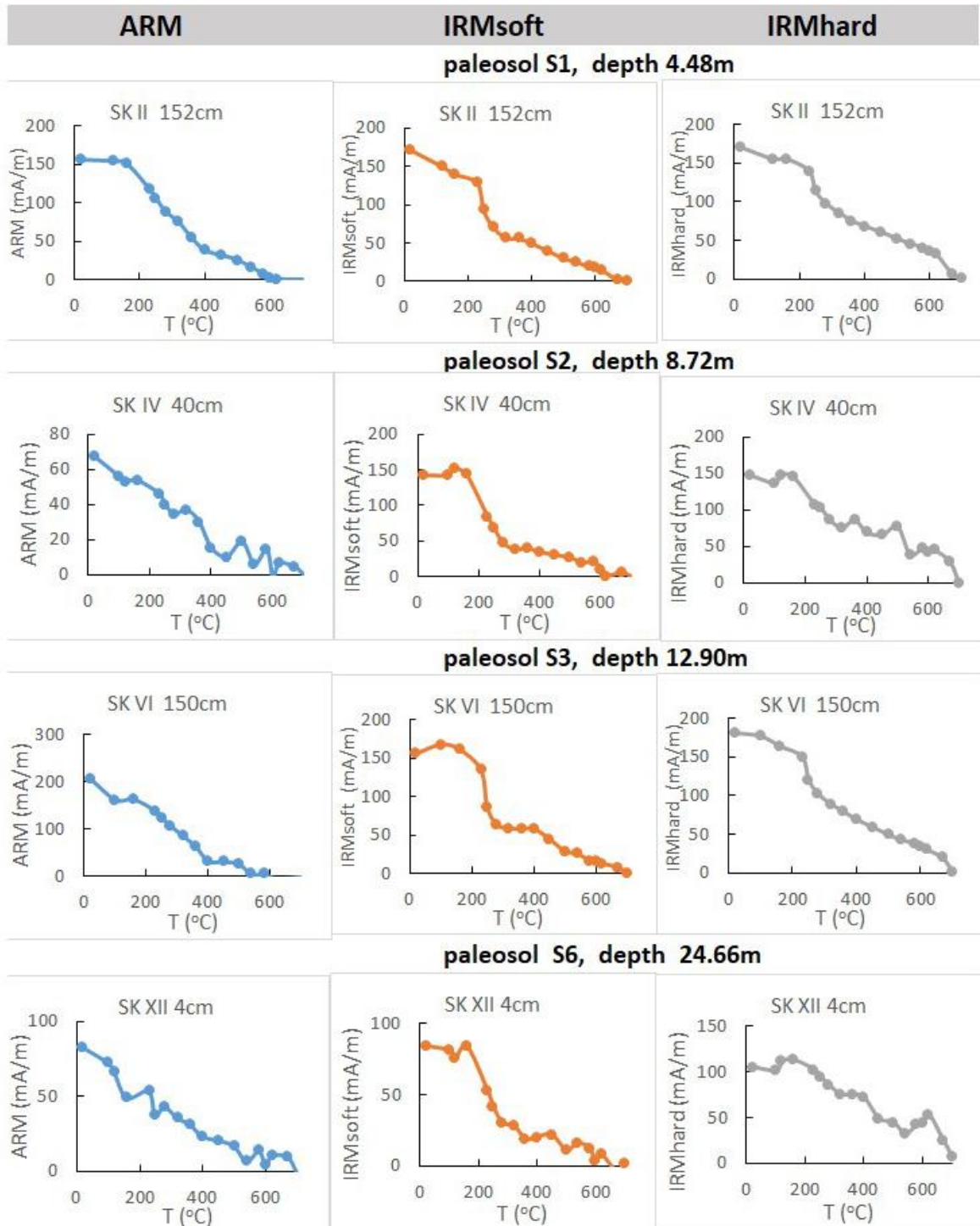


Figure 6S: Examples of thermal demagnetization curves of composite remanence for paleosol samples (see section 2.1). Left column is ARM component; middle column is  $IRM_{soft}$  component acquired in 0.1 to 0.2 T fields; right column is  $IRM_{hard}$  component acquired in 0.2 to 2 T fields.

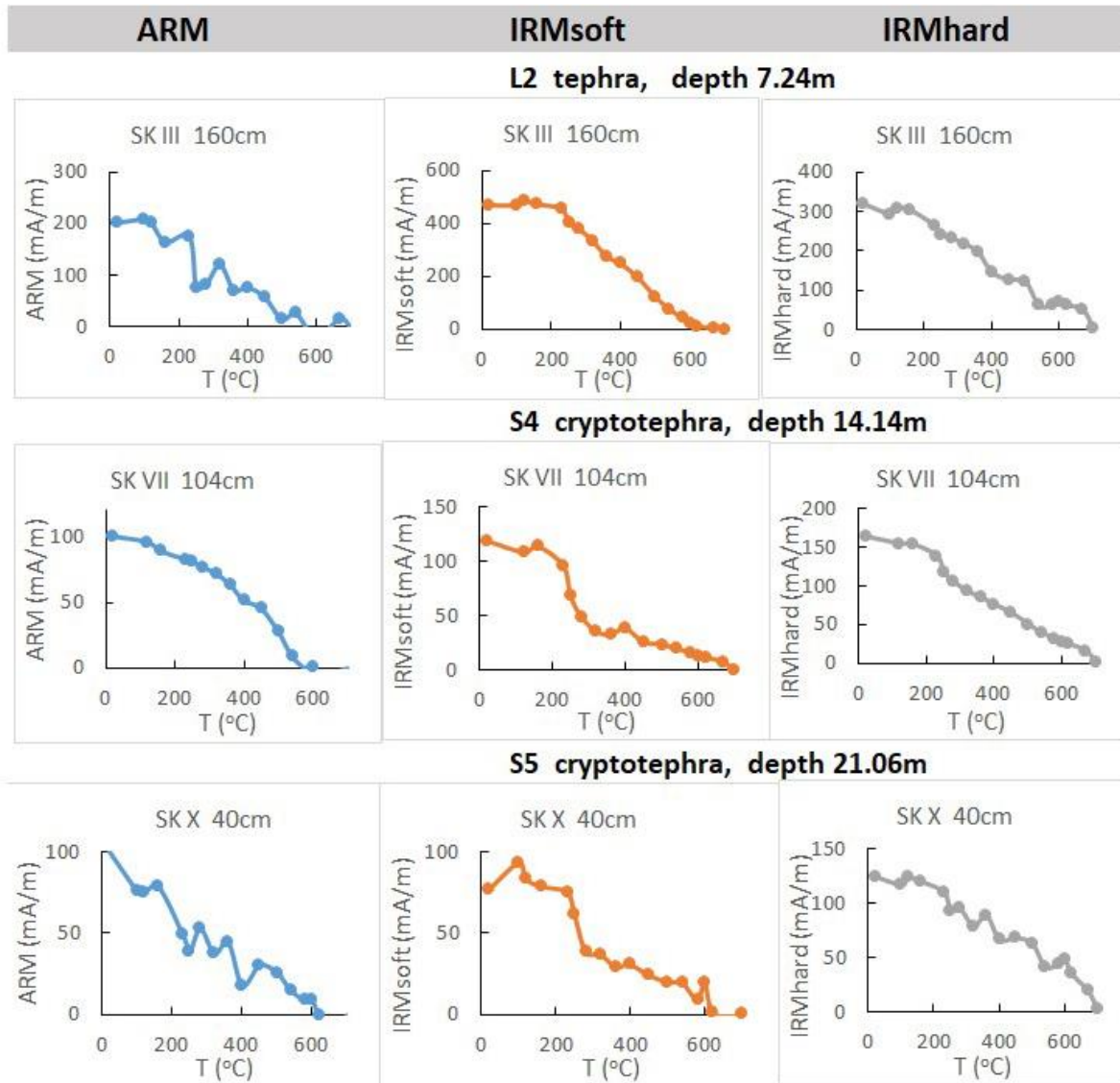


Figure 7S: Examples of thermal demagnetization curves of composite remanence for cryptotephra samples (see section 2.1). Left column is ARM component; middle column is  $IRM_{soft}$  component acquired in 0.1 to 0.2 T fields; right column is  $IRM_{hard}$  component acquired in 0.2 to 2 T fields.



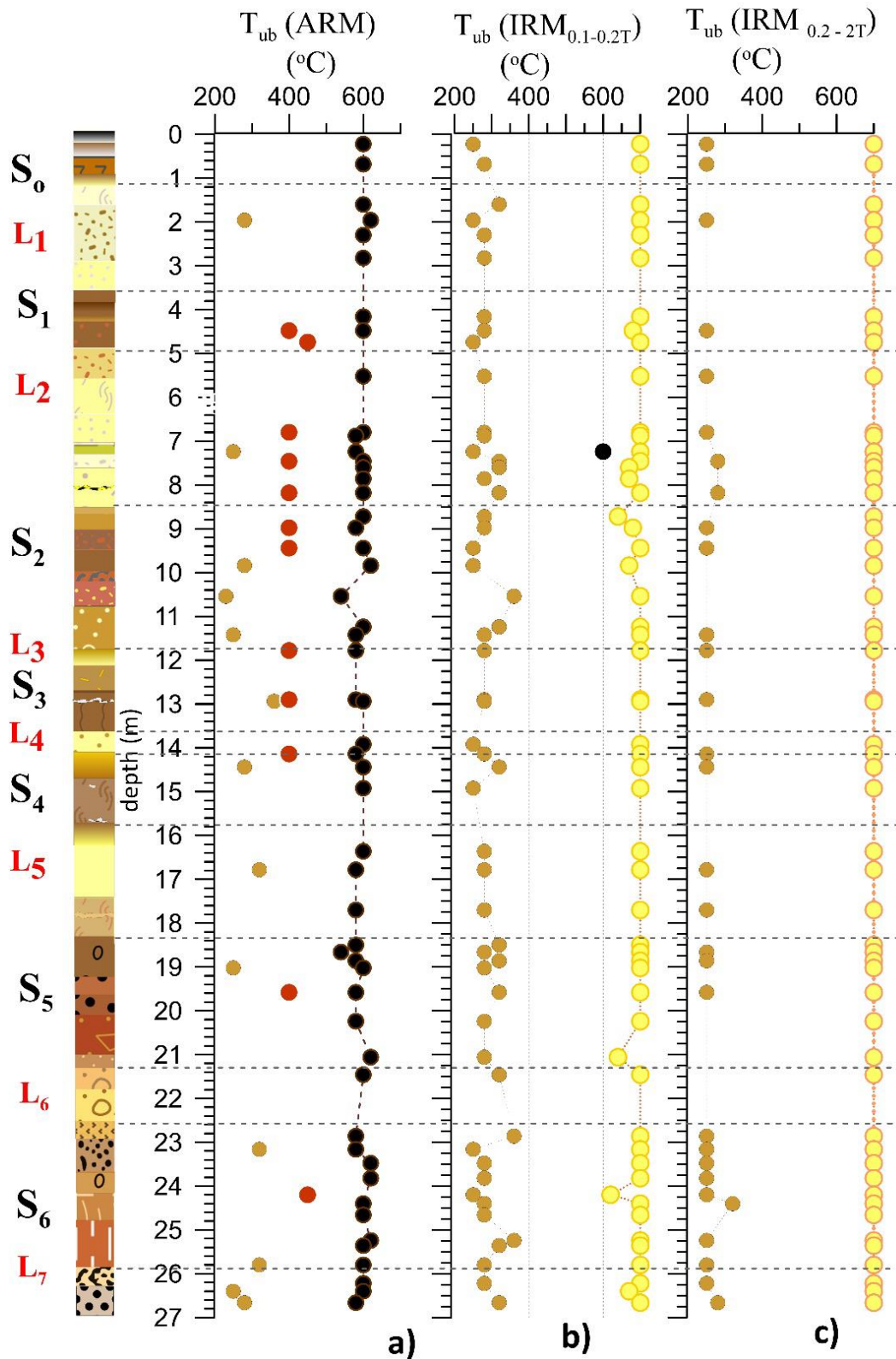


Figure 8S: Unblocking/transformation temperatures determined from thermal demagnetization curves of composite remanences (see section 2.1). Color coding of dots are: brown for maghemite with  $T_b$  of 270 – 360 $^{\circ}\text{C}$ , dark red – for maghemite with  $T_b$  of 400 $^{\circ}\text{C}$ ; black for magnetite and yellow for hematite.



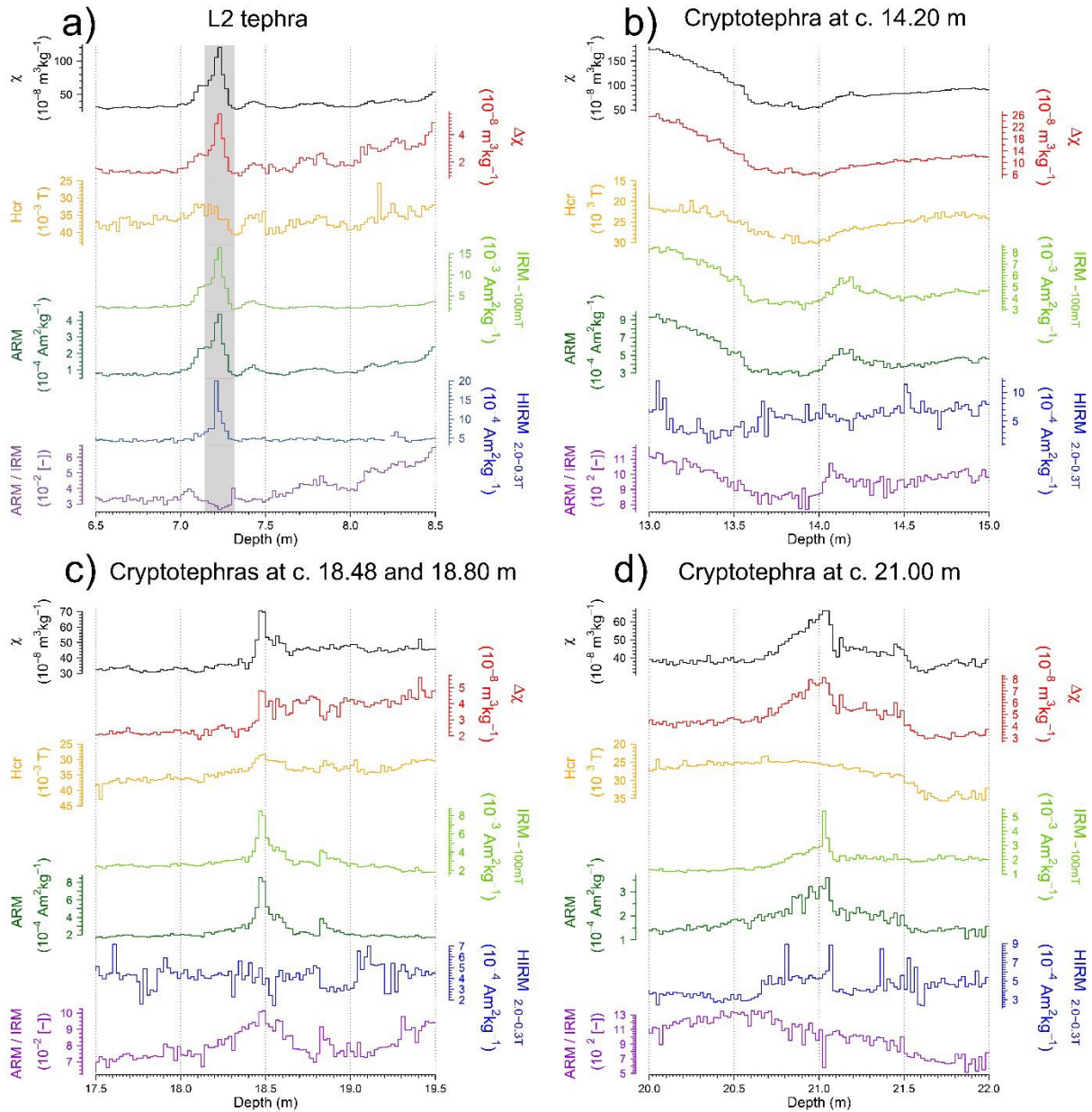
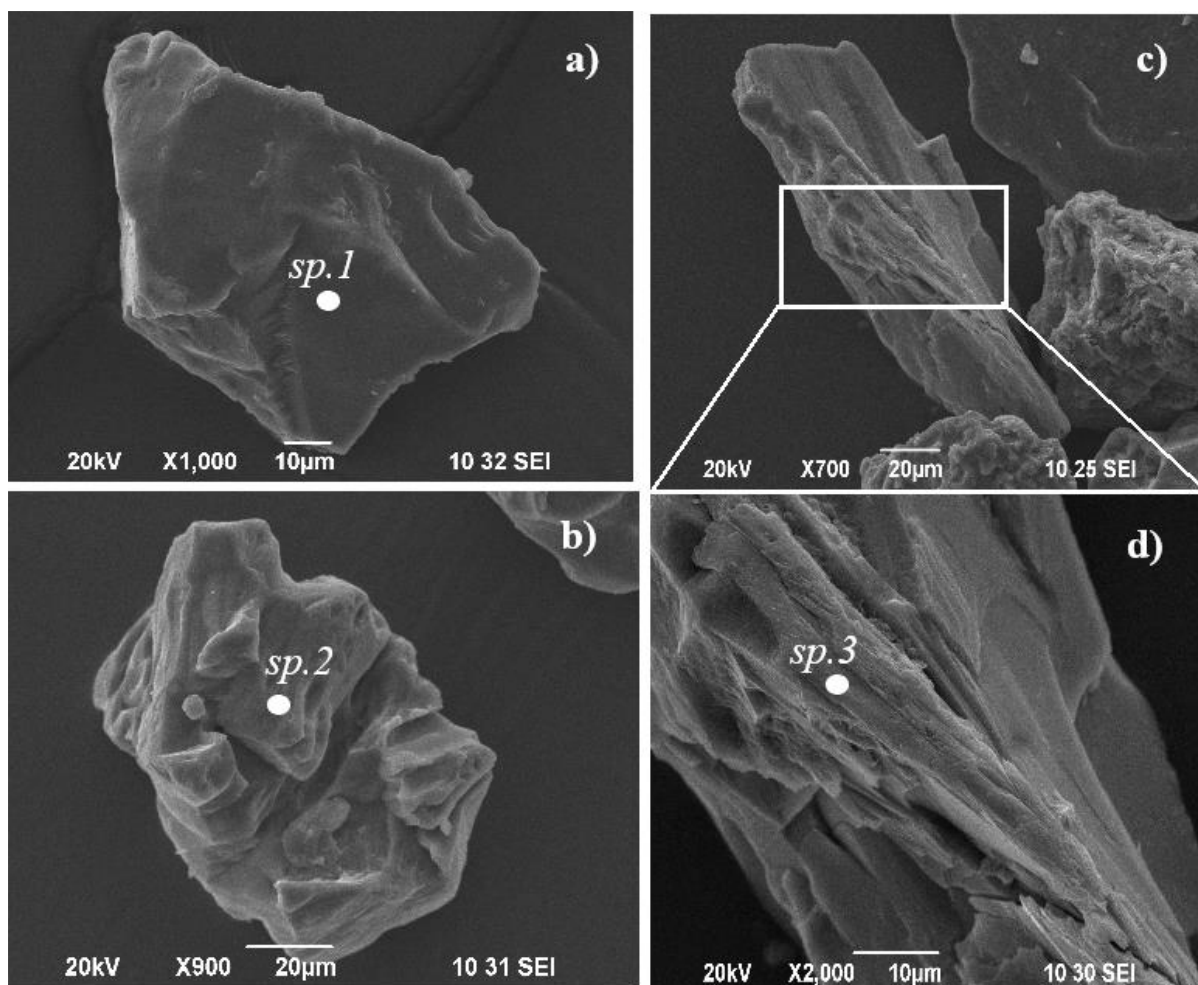


Figure 9S: Variation with depth of magnetic parameters across a 2 m interval centered on (a) the visible tephra in the L2 loess unit (gray shaded interval), (b) the cryptotephra at about 14.10 m depth at the top of the S4 paleosol, (c) the cryptotephra at about 18.48 m depth at the top of the S5 paleosol, and (d) the cryptotephra at about 21.00 m depth at the base of the S5 paleosol.

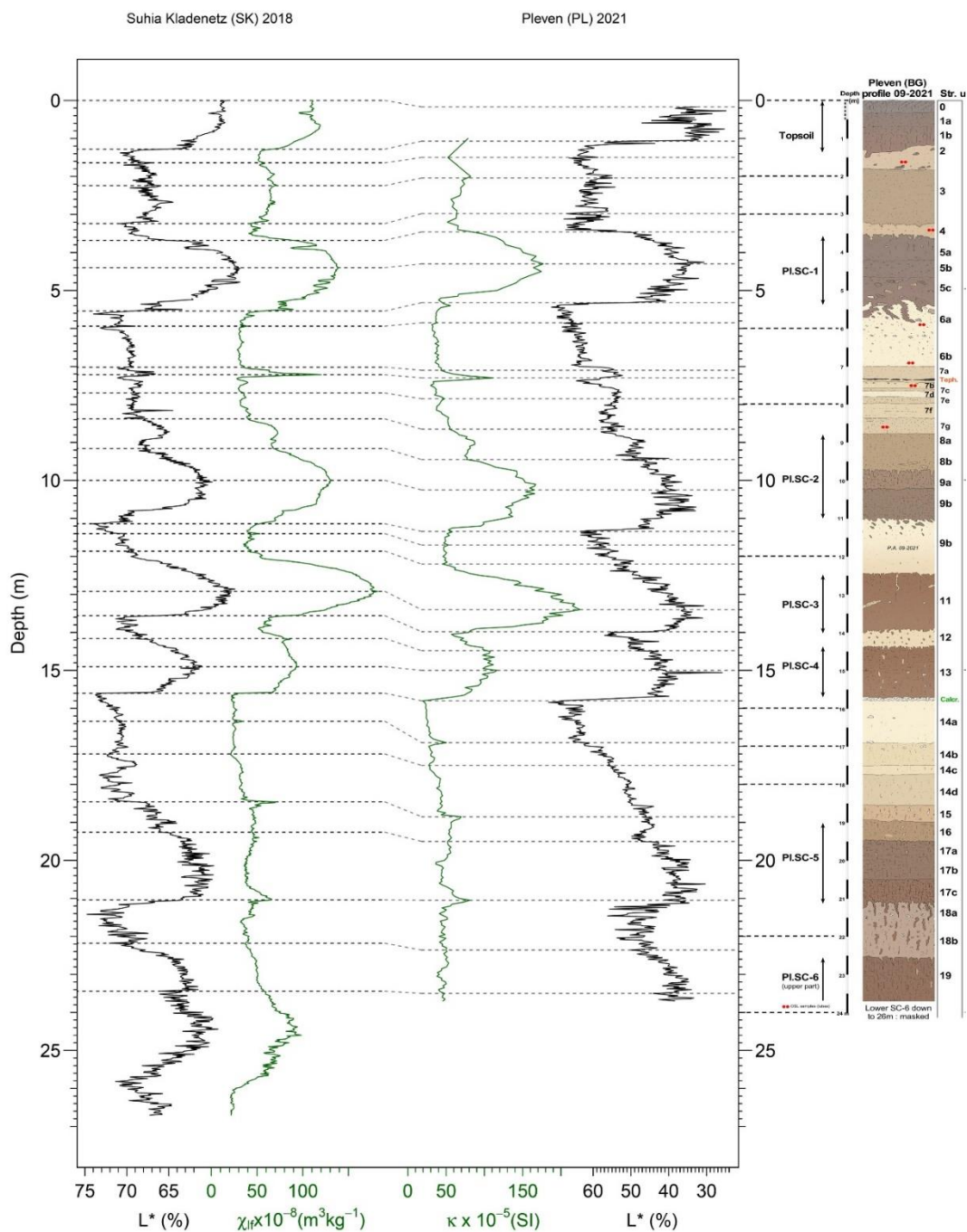


sample	depth (m)	spectrum	Na <sub>2</sub> O	MgO	Al <sub>2</sub> O <sub>3</sub>	SiO <sub>2</sub>	K <sub>2</sub> O	CaO	FeO
SK X 40	21.06	1			2.17	96.34			1.49
SK VIII 288-1	18.48	2	8.38		23.32	62.96		5.34	
SK VIII 288-2	18.48	3		7.04	11.25	72.29	0.37		9.06

Figure 10S: SEM microphotographs (secondary electrons mode) of single grains from cryptotephra layers at 21.06m (a) and 18.48m ( b, c). Zoomed image of the porous microtexture of the elongated clast (c) is shown in d). The obtained elemental compositions (calculated as oxides wt%) through EDS spectra in the points marked are shown in the Table below.

## Appendix B: Supplement for Chapter 3.3.

Appendix B contains supplementary figures and tables for Chapter 3.3, as well as a detailed description of sample preparation for each sample type.



Supplementary figure 1: Comparison of Suhia Kladenetz (SK18) and Pleven (PL2021) sections based on Luminance ( $L^*$ ) and low-field magnetic susceptibility.

## **Sample Boxes and sample treatment**

### **Type A: Plastic boxes (8 cm<sup>3</sup>)**

For magnetic experiments performed at the NIGGG, non-magnetic plastic boxes from the Company Caubère (reference 222, 19x20x20 mm<sup>3</sup>, polystyrene PS) were used to perform magnetic susceptibility measurements. The sample material was after drying carefully homogenized with aid of an agate hand-mortar. After homogenization, sample material was compressed with a hand-stamp in the previously weighted plastic box. The complete mass was weighted again in order to calculate the material mass to mass-normalize acquired magnetic data at NIGGG.

### **Type B: Gelatine Capsules**

Gelatine capsules provided by Quantum Design GmbH (non-magnetic, reference QDS-AGC1) were filled with homogenized material and compressed inside the capsule with a stainless-steel stamp in order to prevent movement of single grains during conducted experiments on a vibrating sample magnetometer. The gelatine caps net mass was noted in order to mass-normalize all magnetic data. The gelatine capsules were closed with thermally high conductivity tape even resistant at high and low temperatures (Quantum Design GmbH reference QDS-ATK1-025). Afterwards, the sealed gelatine capsules were inserted into non-magnetic plastic straws (Quantum Design GmbH, reference QDS-AGC2). In total, 1336 gelatine capsules were prepared and used for magnetic experiments (hysteresis and backfield experiments) on the Vibrating sample magnetometer (VSM). On all samples low-field magnetic susceptibility was measured on a KLY3 kappabridge. On 249 of these samples, additionally highly resolved IRM acquisition curves were measured on the VSM. On 15 of these samples, additional first order reversal curves (FORCs) were acquired on the VSM.

### **Type C: Plastic boxes 4cm<sup>3</sup>**


A total of 1336 samples was prepared in order to measure colorimetric parameters on 4cm<sup>3</sup> half height Caubère boxes (Caubère, reference 221, 4cm<sup>3</sup>, ultra-clear Polystyrene). Since the lids of these samples do not cover from the outside the boxes but inserted inside, the lids of the boxes were impossible to be filled with sample material. Therefore, white Styrofoam was cut into dimensions fitting into the lids. This was necessary in order to maintain compaction of the sample material.

**Type D: Loose material for grain size analysis**

Every 6<sup>th</sup> sample (12-cm resolution) and a continuous 2-cm resolved transect in the L2 loess covering the in-field outcropping L2-tephra was analyzed for grain size distributions. A weighted amount of sample material was filled into plastic tubes containing a hexameta phosphate sodium solution and rotated in an overhead rotator for at least 24 hours. This procedure was used to avoid the formation of aggregates and allowed grain size separation. Following that, wet sieving was performed with a 160  $\mu\text{m}$  mesh wide sieve in order to separate organic remains (e.g., roots) and carbonate concretions and snail shells. This coarse fraction (>160  $\mu\text{m}$ ) was dried in an oven overnight (at 40°C) and its dry mass was weighted and calculated as the weight-percentage of the initial sample. The <160  $\mu\text{m}$  fraction was afterwards measured on a laser granulometer.

**Type E: Loose material for Mid-Infrared Spectrometry experiments**

Loose material was homogenized and measured on a Bruker-Vector 22 ATR-FTIR spectrometer. In total, 719 samples were measured. In order to investigate preferentially glacial units, a 2-cm resolution was applied when enough sample material was left, otherwise the 12-cm resolution (every 6<sup>th</sup> sample) was measured (the same samples which were measured for grain size distributions).

Depth (m)	L/S corr. & Ass.Sy.	unit	description			Soil horizon classification
			color	structure	additional observations	
0.00-0.20	S0 	0	Dark grey brown	clayey-humic silt and blocky (1-2cm)		<b>Ap ploughing horizon of the topsoil</b>
0.22-0.78		1a	brown grey	Compact humic clayey silt, strong blocky to prismatic		Bth horizon of the topsoil
0.80-1.36		1b	dark brown grey clayey silt with	Compact clayey silt, granular structure (2-4 mm aggregates), secondary diffuse large prismatic structure	<ul style="list-style-type: none"> <li>• fully bioturbated</li> </ul>	<b>Bth horizon of the topsoil</b>
		2	yellowish grey	Homogeneous loess	<ul style="list-style-type: none"> <li>• Calcareous</li> <li>• abundant CaCO<sub>3</sub> secondary precipitation around root tracks (≤1mm / pseudomycelium)</li> <li>• The whole unit is strongly affected by bioturbation features from the topsoil (mainly large ø: 10 to 20 cm rodent galleries / crotovinas).</li> </ul>	
		3	grey brownish	Homogeneous compact, lightly humic loess	<ul style="list-style-type: none"> <li>• abundant pseudomycelium</li> <li>• fine granular structure</li> <li>• scattered rodent burrows (crotovinas)</li> <li>• Lower limit intensely deformed by bioturbations</li> <li>• The whole unit corresponds to a cumulic (upbuilding) steppe soil complex.</li> </ul>	
		4	yellowish grey	Homogeneous calcareous loess	<ul style="list-style-type: none"> <li>• scattered pseudomycelium</li> <li>• small root tracks and rodent burrows from unit 3</li> </ul>	

					<ul style="list-style-type: none"> <li>• Lower limit intensely affected by deep bioturbations (up to 20-25 cm in depth).</li> </ul>	
	S1	<b>5 Soil complex PV-SC1 (5a-5c)</b>				
		5a	dark grey brown	Compact clayey silt	<ul style="list-style-type: none"> <li>• abundant pseudomycelium</li> </ul>	<b>Ah horizon / Chernozem</b>
		5b	dark brown to brown reddish	Compact clayey silt	<ul style="list-style-type: none"> <li>• numerous earthworm chambers (1-2cm) (concentrated around - 4.3m depth)</li> <li>• CaCO<sub>3</sub> concretions around 4.2m some insect galleries</li> </ul>	<b>Bth horizon / Interglacial grey-forest soil</b>
		5c	dark grey brown	Compact clayey silt	<ul style="list-style-type: none"> <li>• abundant pseudomycelium</li> <li>• Extremely irregular lower boundary marked by the whole is 100% mixed by bioturbation processes due to rodent burrowing penetrating the underlying loess 6a on about 0.5 m</li> </ul>	<b>Cca horizon / Early interglacial steppe soil</b>
		6a	Beige	homogeneous calcareous loess	<ul style="list-style-type: none"> <li>• scattered pseudomycelium (<math>\leq 1</math>mm)</li> <li>• numerous dark brown to black FeMn dots (<math>\varnothing</math> a few mm)</li> <li>• numerous scattered bioturbations (burrows and root tracks from the overlying soil horizon 5c.</li> </ul>	
		6b	Beige	homogeneous calcareous loess	<ul style="list-style-type: none"> <li>• scattered pseudomycelium (<math>\leq 1</math>mm)</li> <li>• dark brown to black FeMn dots (<math>\varnothing</math> a few mm)</li> <li>• diffuse lower boundary at – 7.05 m.</li> </ul>	
		<b>7 Brownish loess and weak interstadial soils complex</b>				
		7a	Light brown with	homogeneous calcareous silt	<ul style="list-style-type: none"> <li>• scattered pseudomycelium (<math>\leq 1</math>mm)</li> <li>• dark brown to black FeMn dots (<math>\varnothing</math> a few mm)</li> <li>• A 2 to 5 cm thick compact greyish and discontinuous layer is found at – 7.35 m depth in the lower part of this unit (tephra layer)</li> </ul>	<b>Weak “steppe soil” horizon (Bw?)</b>
		7b	Light brownish grey	homogeneous calcareous loess	<ul style="list-style-type: none"> <li>• small CaCO<sub>3</sub> nodules at the top (<math>\varnothing</math>: 1-2cm).</li> </ul>	



		7c	light brown (lightly darker than 7b)	homogeneous calcareous loess	<ul style="list-style-type: none"> <li>• Thin layer</li> </ul>	
		7d	light brownish to beige	Homogeneous calcareous loess		
		7e	brownish	Homogeneous calcareous loess		<b>Weak “steppe soil” horizon?</b>
		7f	light beige	homogeneous calcareous loess	<ul style="list-style-type: none"> <li>• Diffuse lower boundary around -8.35m.</li> </ul>	
		7g	light brownish	Homogeneous loess	<ul style="list-style-type: none"> <li>• abundant small root tracks (herbaceous) underlined by black FeMn coatings</li> </ul>	<b>Weak “steppe soil” horizon</b>
		8&9	Soil complex PV-SC2			
		8a	brown to brown reddish	Compact clayey silt	<ul style="list-style-type: none"> <li>• earthworm chambers (1-2cm)</li> <li>• diffuse lower boundary</li> </ul>	<b>Bw horizon / cambic soil</b>
		8b	light brown	Compact homogeneous clayey silt	<ul style="list-style-type: none"> <li>• Highly bioturbated lower boundary with deep root tracks (+ some frost cracks?) penetrating the underlying soil horizon 9a</li> <li>• Some large burrows at the base.</li> </ul>	
		9a	brown to greyish brown with	Compact clayey silt	<ul style="list-style-type: none"> <li>• numerous FeMn coatings on small root tracks (biopores <math>\leq</math> 1-2mm)</li> <li>• bioturbated lower boundary with root tracks penetrating the underling soil horizon on about 10 cm.</li> </ul>	
		9b	dark brown (lightly reddish)	Highly compact clayey silt with strong prismatic structure (1-2cm large)	<ul style="list-style-type: none"> <li>• FeMn coatings on small root tracks (biopores <math>\leq</math> 1-2mm)</li> <li>• Calcareous nodules (loess “dolls” <math>\varnothing</math>: 1-2cm) close to the base</li> </ul>	

					<ul style="list-style-type: none"> <li>Intensely bioturbated lower boundary (around - 11m depth), with root tracks and numerous rodents' burrows (<math>\varnothing</math>: 5-10cm) penetrating the underling soil horizon.</li> </ul>	
		10	light grey beige	Homogeneous calcareous loess	<ul style="list-style-type: none"> <li>abundant scattered CaCO<sub>3</sub> nodules (1-5cm)</li> <li>larger ones making up to 10 cm large "loess dolls" especially concentrated around - 11.3m</li> <li>Occurrence of numerous root track with dark infilling from the overlying soil Hz 9b in the upper 0.5 of the unit.</li> </ul>	
		11	Soil complex PV-SC3			(Bt to Bth horizon of interglacial forest-steppe soil).
			brown to dark brown	Compact clayey silt (still weakly carbonated) exhibiting a granular texture overprinted by a polyhedral to prismatic structure (2-4 cm aggregates)	<ul style="list-style-type: none"> <li>FeMn black coatings on the surface of the aggregates</li> <li>scattered FeMn small nodules (<math>\varnothing</math> : 2-3mm)</li> <li>abundant earthworm and (or insect) chambers scattered in the lower part</li> </ul>	
			This horizon is characterised by a deep clay illuviation showing two phases			
			1 brown red	clay		
			2 dark brown to black	humic clay coatings	<ul style="list-style-type: none"> <li>Occurrence of shells of large land shells (Cepaea: forest species) scattered around - 13 m (see: O. Moine)</li> <li>Irregular bioturbated lower boundary with roots tracks and rodent burrows</li> </ul>	
		12	light grey beige	Heterogeneous calcareous loess	<ul style="list-style-type: none"> <li>strongly affected by numerous bioturbation features by roots and rodent burrows originating from the overlying soil horizon 11 (<math>\pm</math> 50 % of the whole deposit)</li> <li>Abundant scattered CaCO<sub>3</sub> nodules (1-5cm)</li> <li>Strongly irregular bioturbated lower boundary.</li> </ul>	

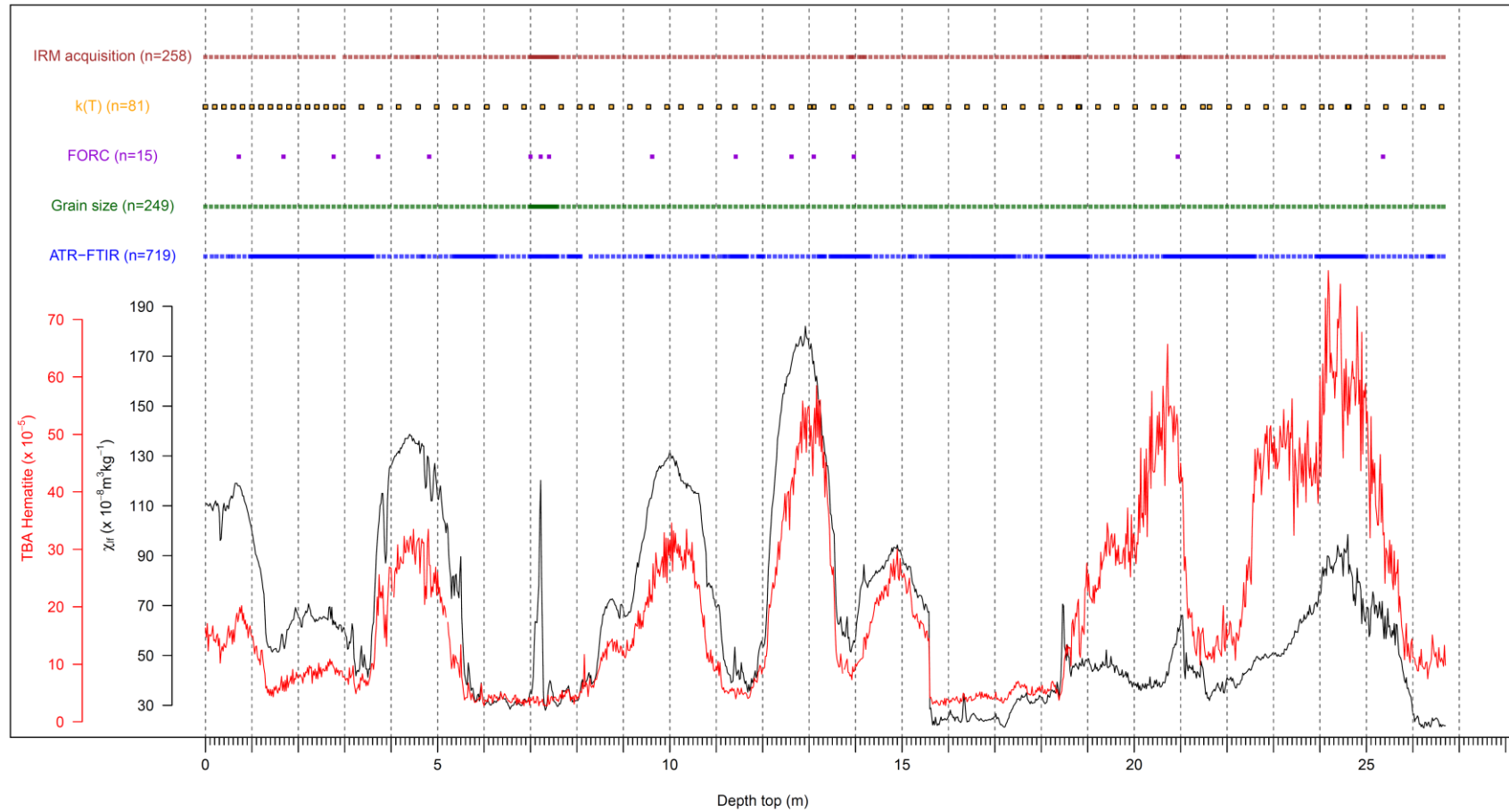
		13	Soil complex PV-SC4			(Bt to Bth horizon of interglacial forest-steppe soil).
			brown-red to dark brown-red	Compact clayey silt (still weakly carbonated) exhibiting a well-marked prismatic structure (4-5 cm aggregates)	<ul style="list-style-type: none"> <li>• FeMn black coatings on the surface of the aggregates, scattered FeMn small nodules (<math>\varnothing</math>: 2-3mm)</li> <li>• earthworm chambers scattered in the lower half part scattered “loess dolls” (3-5cm)</li> <li>• numerous large root (<math>\varnothing</math> 0,5-1 cm) tracks with CaCO<sub>3</sub> infilling in the lower part</li> <li>• Lower boundary underlined by CCA Hz.</li> </ul>	
		CCA	10 cm thick and tabular calcareous concretion horizon making a very good level mark for correlation in the whole quarry.			
		14a	light grey beige	Homogeneous calcareous loess	<ul style="list-style-type: none"> <li>• abundant pseudomycelium</li> <li>• scattered CaCO<sub>3</sub> coatings on root tracks (<math>\varnothing</math>: <math>\leq</math> 5 mm)</li> <li>• a few small “loess dolls” (1-2 cm)</li> <li>• Some burrows infilled by clayey material from soil 13.</li> </ul>	
		14b	Darker grey beige	Homogeneous calcareous loess but more clayey	<ul style="list-style-type: none"> <li>• bigger CaCO<sub>3</sub> nodules (<math>\varnothing</math>: 2-5 cm) than 14a</li> </ul>	
		14c	light grey beige	More homogeneous than 14b and calcareous loess		
		14d	light brown greyish beige	Homogeneous and massive calcareous clayey silt	<ul style="list-style-type: none"> <li>• scattered FeMn coatings on biotubules (fine root tracks: <math>\leq</math> 1mm)</li> <li>• scattered pseudomycelium</li> </ul>	tiny <b>Bw horizon of interstadial steppe soil</b>
		15-17	Soil complex PV-SC5			
		15	light brown	Compact calcareous clayey silt with fine root porosity ( $\varnothing$ : $\leq$ 1mm)	<ul style="list-style-type: none"> <li>• abundant CaCO<sub>3</sub> coatings</li> <li>• FeMn black dots coatings on the surface of the aggregates</li> </ul>	

					<ul style="list-style-type: none"> <li>• scattered FeMn small nodules (<math>\phi</math>: 2-3mm); scattered root tracks</li> <li>• crotovinas infilled by sediment from the overlying horizon 14d.</li> </ul>	
		16	light brown to brownish	calcareous clayey silt with weak fine root porosity ( $\phi$ : $\leq$ 1mm)	<ul style="list-style-type: none"> <li>• abundant CaCO<sub>3</sub> coatings on fine root tracks (<math>\phi</math>: <math>\leq</math> 1mm)</li> <li>• Scattered burrows with darker material reworked from unit 17b.</li> </ul>	
		17a	dark brown-red to dark brown;	clayey silt (still weakly carbonated) deep clayey illuviation (100% of the porosity) showing a well marked prismatic to blocky structure (4-5 cm blocks); (intra-block structure: granular)	<ul style="list-style-type: none"> <li>• FeMn black coatings on the surface of the aggregates</li> <li>• scattered FeMn small nodules (<math>\phi</math>: 2-3mm)</li> <li>• a few scattered “loess dolls” (3-5cm)</li> </ul>	<b>Bt to Bth horizon of interglacial forest-steppe soil</b>
		17b	lightly less coloured, and	weak prismatic structure	<ul style="list-style-type: none"> <li>• Lower horizon of soil 17: only a few FeMn nodules.</li> </ul>	
		17c	dark brown-orange and	clayey silt, deep clayey illuviation (100% of the porosity); showing a well marked prismatic structure (4-5 cm blocks)	<ul style="list-style-type: none"> <li>• abundant FeMn black coatings on the surface of the aggregates and small black FeMn small nodules (<math>\phi</math>: 2-3mm)</li> <li>• a few scattered “loess dolls” (5-10cm) to the base</li> <li>• Lower boundary deeply deformed on almost 0.5m depth by bioturbation: large root tracks (tree roots?) and rodent burrows</li> </ul>	<b>Bt to Bth horizon of interglacial forest-steppe soil</b>
		18a	light brown by	(clayey) calcareous loess silt with very important bioturbation (50% of the outcrop surface)	<ul style="list-style-type: none"> <li>• large subvertical root tracks infilled by brown clayey material from soil 17c</li> <li>• Numerous elongated “loess dolls” in the upper 0.5 m of the horizon.</li> </ul>	

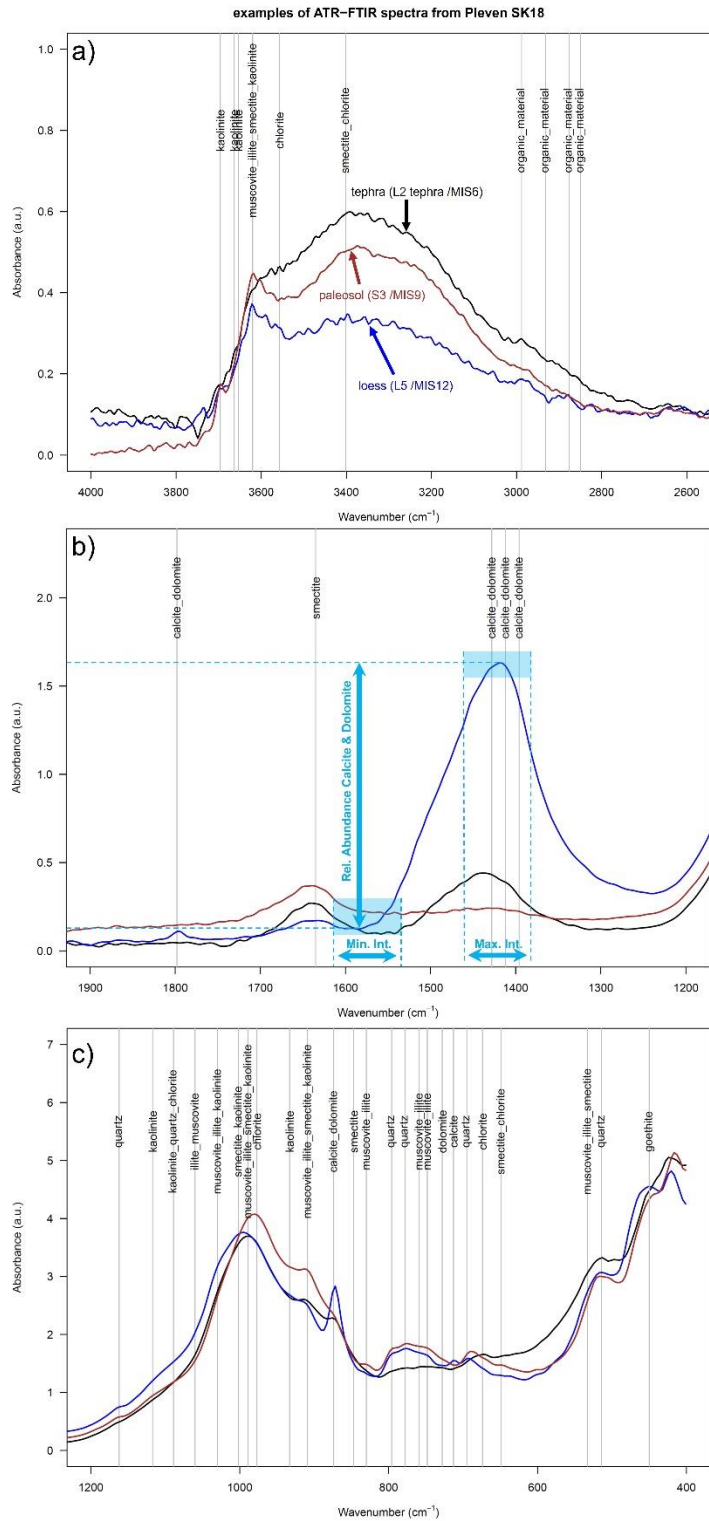
		18b	light brown	(clayey) calcareous loess silt	<ul style="list-style-type: none"> <li>• weaker bioturbation by root tracks</li> </ul>	
		19	Soil complex PV-SC6			<b>Bt horizon of interglacial forest-steppe soil</b>
			brown-red	clayey silt with deep clay illuviation (100% of the porosity); with a diffuse prismatic structure	<ul style="list-style-type: none"> <li>• abundant FeMn black coatings on the surface of the aggregates</li> <li>• small black FeMn small nodules (ø: 2-3mm)</li> <li>• abundant elongated CaCo3 concretions “tubes” formed in subvertical root tracks.</li> </ul>	
			<b>Lower boundary of unit 19 not reached at – 23.70 m depth.</b>			

Supplementary data table 1: Field description

Overview about not-continuously conducted measurements for Pleven Suhia Kladenetz

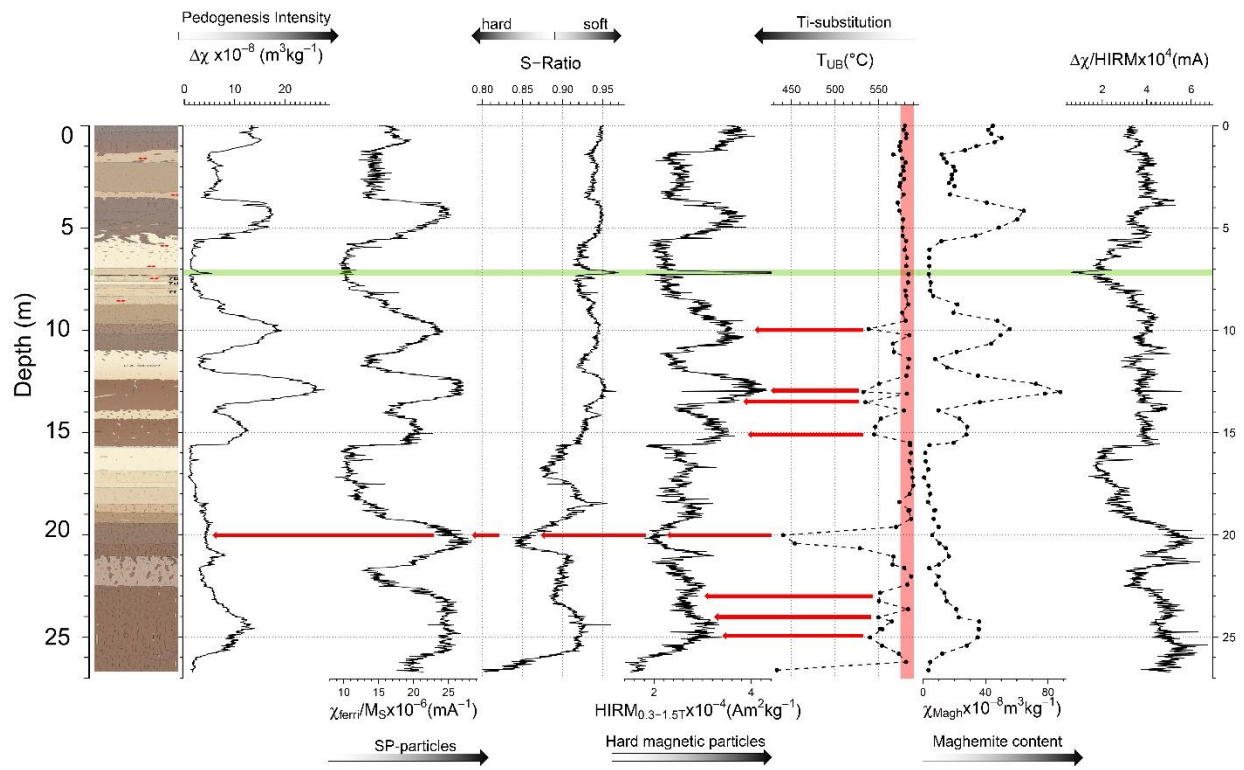


Supplement figure 2: Stratigraphical overview on experiments conducted on sample stemming from the Suhia Kladenetz LPS. Only experiments are shown which were not applied to all 1336 samples, which is the case for hysteresis and backfield, magnetic susceptibility and colorimetric experiments.

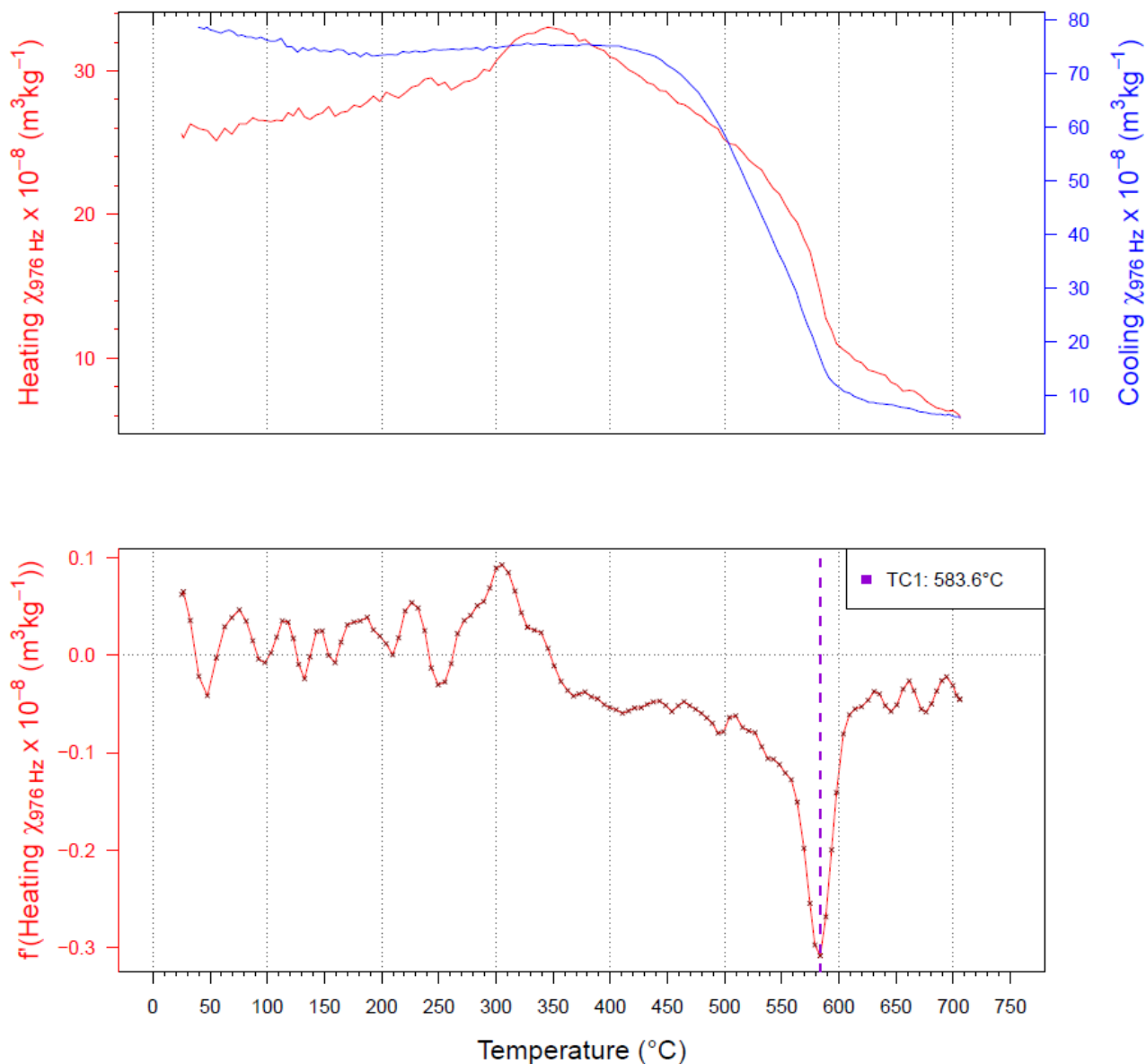


Supplementary figure 3: ATR FTIR spectra schema and mineral abundance extraction.





Supplementary figure 4: From left to right: Frequency dependent magnetic susceptibility  $\Delta\chi$ ,  $\chi_{\text{ferri}}/M_S$  ratio, S-ratio, HIRM, unblocking temperatures  $T_{\text{UB}}$ , maghemite content and  $\Delta\chi/\text{HIRM}$ .



Supplementary Figure 5: High-temperature magnetic susceptibility from room temperature to 700°C (heating, red) and cooling (blue) for a representative sample. Note in the upper figure different y-axes for heating and cooling. The bottom figure shows the first derivative of the heating curve and the lowest value at 583.6°C is indicated as the unblocking temperature.

Supplementary table 2: Age depth model tie points.

Depth top (m)	Age (ka)	Used proxy	Target
1.08	12.6695	TBA_Goethite	NGRIP
1.3	14.6899	TBA_Goethite	NGRIP
1.48	18.2908	TBA_Goethite	NGRIP
1.6	20.9498	TBA_Goethite	NGRIP
1.8	23.5083	TBA_Goethite	NGRIP
1.98	29.6511	TBA_Goethite	NGRIP
2.14	35.8104	TBA_Goethite	NGRIP
2.3	38.6311	TBA_Goethite	NGRIP
2.5	42.0091	TBA_Goethite	NGRIP
2.62	44.0461	TBA_Goethite	NGRIP
2.74	47.108	TBA_Goethite	NGRIP
3.26	59.8059	TBA_Goethite	NGRIP
3.9	76.0143	TBA_Goethite	NGRIP
4.16	88	TBA_Goethite, Hematite, Xfd	LR04
4.72	109	TBA_Goethite, Hematite, Xfd	LR04
5.36	135	TBA_Goethite, Hematite, Xfd	LR04
7.18	159	TBA_Goethite, Hematite, Xfd	LR04
8.24	185	TBA_Goethite, Hematite, Xfd	LR04
9.78	230	TBA_Goethite, Hematite, Xfd	LR04
11.14	252	TBA_Goethite, Hematite, Xfd	LR04
13.6	342	TBA_Goethite, Hematite, Xfd	LR04
15.64	431	TBA_Goethite, Hematite, Xfd	LR04
18.38	475	TBA_Goethite, Hematite, Xfd	LR04
19.96	553	TBA_Goethite, Hematite, Xfd	LR04
21.16	630	TBA_Goethite, Hematite, Xfd	LR04
22.38	672	TBA_Goethite, Hematite, Xfd	LR04
23.44	718	TBA_Goethite, Hematite, Xfd	LR04
23.96	756	TBA_Goethite, Hematite, Xfd	LR04
25.4	794	TBA_Goethite, Hematite, Xfd	LR04
26.7	838	TBA_Goethite, Hematite, Xfd	LR04

Supplementary table 3: Tephras, potential crypto-tephras and crypto-tephra candidates.

Tephra ID	Sample ID	Depth top (m)	Depth bottom (m)	IRM-acq. done	FORC done	X <sub>ir</sub>	ARM/X	IRM <sub>100mT</sub> /IRM <sub>300mT</sub>	IRM <sub>100mT</sub> /M <sub>S</sub>	X <sub>HM</sub>	μ <sub>2</sub> H <sub>2</sub> O <sub>cr</sub>	X <sub>levi</sub>	IRM-100mT	5 <sup>th</sup> IRM comp	FTIR Smectite	Age (ka)	PEQ-T	PEQ-T age (ka)	PEQ-T error (ka)
SK18_T_01	SK_01_004_006	0.04	0.06	✗	✗	✗	✓	✓	✓	✓	✓	✗	✓	○	✗	3.119	OH-DP-0015 [1]	3.29	0.08
SK18_T_02	SK_01_020_022	0.20	0.22	✗	✗	✗	✗	✓	✓	✗	✓	✗	✗	○	✗	4.588	SUL 2-15 [2]	4.75	1.20
SK18_T_03	SK_01_066_068	0.66	0.68	✗	✗	✓	✗	✓	✓	✓	✓	✗	✗	○	✗	8.812	OH-DP-0027 [1]	8.56	0.20
SK18_T_04	SK_01_162_164	1.62	1.64	✗	✗	✓	✓	✓	✓	✓	✓	✓	✓	○	✗	21.206	Cape Riva Y2 [3]	21.92	0.56
	SK_01_164_166	1.64	1.66	✗	✗	✓	✓	✓	✓	✓	✓	✓	✓	○	✓	21.462			
	SK_01_166_168	1.66	1.68	✗	✗	✓	✓	✓	✓	✓	✓	✓	✓	○	✗	21.717			
	SK_01_168_170	1.68	1.70	✓	✓	✓	✗	✓	✓	✓	✓	✗	✓	✗	✓	21.973			
SK18_T_05	SK_01_194_196	1.94	1.96	✗	✗	✓	✗	✓	✓	✓	✓	✓	✓	○	✗	28.286	Y3/OH-DP0115 [1]	29.03	0.77
SK18_T_06	SK_01_228_230	2.28	2.30	✓	✗	✗	✗	✗	✗	✓	✗	✗	✗	✓	✓	38.279	CI-Y5 [4]	39.85	0.14
SK18_T_07	SK_02_038_040	3.34	3.36	✗	✗	✓	✓	✓	✓	✓	✓	✓	✓	○	✓	61.832	TP-05-17.91 [5]	65.145	1.205
	SK_02_040_042	3.36	3.38	✓	✗	✓	✓	✓	✓	✓	✓	✓	✓	✓	✗	62.339			
	SK_02_042_044	3.38	3.40	✗	✗	✓	✓	✓	✓	✓	✓	✓	✓	○	✓	62.845			
SK18_T_08	SK_02_046_048	3.42	3.44	✗	✗	✓	✓	✓	✓	✓	✓	✓	✓	○	✓	63.858	TP-05-17.91 [5]	65.145	1.205
	SK_02_048_050	3.44	3.46	✗	✗	✓	✗	✓	✓	✓	✓	✓	✓	○	✓	64.365			
SK18_T_09	SK_02_254_256	5.50	5.52	✗	✗	✓	✓	✓	✓	✓	✓	✓	✓	○	✗	134.500	OH-DP-0499 [1]	133.66	2.89
SK18_T_10	SK_03_002_004	5.66	5.68	✓	✗	✓	✓	✓	✓	✓	✓	✓	✓	✓	✓	136.833	OH-DP-0505 [1]	135.36	4.06
SK18_T_11	SK_03_028_030	5.92	5.94	✗	✗	✓	✓	✓	✓	✓	✓	✓	✓	✓	✓	140.625	Roxolany (UA) tephra located in upper L2 unit OSL and TL [6,7,8,9]	Above tephra 143.8 ±13.2 ka (OSL) Below tephra 142.0±21.0 ka (TL)	-
	SK_03_030_032	5.94	5.96	✓	✗	✓	✓	✓	✓	✓	✓	✓	✓	✓	✓	140.917			
	SK_03_032_034	5.96	5.98	✗	✗	✓	✓	✓	✓	✓	✓	✓	✓	✓	✓	141.208			
SK18_T_12	SK_03_120_122	6.84	6.86	✗	✗	✗	✓	✓	✓	✓	✓	✗	✓	○	○	154.042	OH-DP-0599 [1]	156.89	3.79
SK18_T_13 OMC* Jordanova et al., 2022 in-field out-cropping tephra layer	SK_03_134_136	6.98	7.00	✓	✗	✓	✓	✓	✓	✗	✓	✓	✓	✓	✗	156.083	OH-DP-0616 [1] Or OH-DP-0617 [1] Or OH-DP-0624 [1]	158.76 Or 158.89 Or 159.71	3.83 Or 3.81 Or 4.03
	SK_03_136_138	7.00	7.02	✓	✓	✓	✓	✓	✓	✓	✓	✓	✓	✓	✗	156.375			
	SK_03_138_140	7.02	7.04	✓	✗	✓	✓	✓	✓	✗	✓	✓	✓	✓	✗	156.667			
	SK_03_140_142	7.04	7.06	✓	✗	✓	✓	✓	✓	✗	✓	✓	✓	✓	✗	156.958			
	SK_03_142_144	7.06	7.08	✓	✗	✓	✓	✓	✓	✗	✓	✓	✓	✓	✗	157.250			
	SK_03_144_146	7.08	7.10	✓	✗	✓	✓	✓	✓	✓	✓	✓	✓	✓	✓	157.542			
	SK_03_146_148	7.10	7.12	✓	✗	✓	✓	✓	✓	✓	✓	✓	✓	✓	✓	157.833			
	SK_03_148_150	7.12	7.14	✓	✗	✓	✓	✓	✓	✓	✓	✓	✓	✓	✓	158.125			
	SK_03_150_152	7.14	7.16	✓	✗	✓	✓	✓	✓	✓	✓	✓	✓	✓	✓	158.417			
	SK_03_152_154	7.16	7.18	✓	✗	✓	✓	✓	✓	✓	✓	✓	✓	✓	✓	158.708			
SK_03_154_156	7.18	7.20	✓	✗	✓	✓	✓	✓	✓	✓	✓	✓	✓	✓	159.000				

	SK_03_156_158	7.20	7.22	✓	✗	✓	✓	✓	✓	✓	✓	✓	✓	✓	✓	159.491			
	SK_03_158_160	7.22	7.24	✓	✓	✓	✓	✓	✓	✓	✓	✓	✓	✓	✓	159.981			
	SK_03_160_162	7.24	7.26	✓	✗	✓	✓	✓	✓	✓	✓	✓	✓	✓	✓	160.472			
	SK_03_162_164	7.26	7.28	✓	✗	✓	✓	✓	✓	✓	✓	✓	✓	✓	✓	160.962			
	SK_03_164_166	7.28	7.30	✓	✗	✓	✓	✓	✓	✗	✓	✓	✓	✓	✓	161.453			
SK18_T_14	SK_03_172_174	7.36	7.38	✓	✗	✓	✓	✓	✓	✗	✓	✓	✓	✓	✗	163.415	?	?	?
	SK_03_174_176	7.38	7.40	✓	✗	✓	✓	✓	✓	✓	✓	✓	✓	✓	✗	163.906			
	SK_03_176_178	7.40	7.42	✓	✓	✓	✓	✓	✓	✗	✓	✓	✓	✓	✓	164.396			
	SK_03_178_180	7.42	7.44	✓	✗	✓	✓	✓	✓	✓	✓	✓	✓	✓	✓	164.887			
	SK_03_180_182	7.44	7.46	✓	✗	✓	✓	✓	✓	✓	✓	✓	✓	✓	✓	165.377			
	SK_03_182_184	7.46	7.48	✓	✗	✓	✓	✓	✓	✗	✓	✓	✓	✓	✗	165.868			
SK18_T_15	SK_03_252_254	8.16	8.18	✓	✗	✗	✗	✓	✓	✗	✓	✓	✓	✗	○	183.038	OH-DP-0766 [1]	180.02	4.14
SK18_T_16	SK_04_108_110	9.40	9.42	✗	✗	✗	✓	✓	✓	✓	✗	✓	○	○	○	228.250	OH-DP-0977 [1]	228.87	5.66
SK18_T_17	SK_04_122_124	9.54	9.56	✗	✗	✗	✓	✓	✓	✓	✓	✓	○	○	○	230.000	OH-DP-1006 [1]	230.93	6.27
SK18_T_18	SK_04_152_154	9.84	9.86	✗	✗	✗	✗	✗	✓	✓	✗	✓	○	○	○	233.750	OH-DP-1053.5 [1]	240.93	6.45
SK18_T_19	SK_04_168_170	10.00	10.02	✗	✗	✓	✗	✓	✗	✓	✓	✓	○	○	○	235.750	OH-DP-1053.8 [1]	240.99	6.41
SK18_T_20	SK_05_050_052	10.74	10.76	✗	✗	✗	✗	✓	✗	✓	✓	✓	○	✓	○	246.601	OH-DP-1055 [1]	241.23	6.18
SK18_T_21	SK_05_094_096	11.18	11.20	✓	✗	✗	✗	✗	✗	✗	✗	✗	✓	✓	○	260.909	?	?	?
SK18_T_22	SK_06_000_002	11.40	11.42	✗	✗	✓	✓	✓	✓	✓	✓	✓	○	✗	○	268.063	OH-DP-1175 [1]	270.64	4.88
	SK_06_002_004	11.42	11.44	✓	✓	✓	✓	✓	✓	✓	✓	✓	✓	✓	○	268.713			
SK18_T_23	SK_06_006_008	11.46	11.48	✗	✗	✓	✓	✓	✓	✓	✓	✓	○	✓	○	270.014	OH-DP-1175 [1]	270.64	4.88
SK18_T_24	SK_06_014_016	11.54	11.56	✓	✗	✓	✓	✗	✓	✓	✗	✓	✓	✓	○	272.615	OH-DP-1175 [1]	270.64	4.88
SK18_T_25	SK_07_000_002	13.10	13.12	✓	✓	✗	✓	✓	✓	✗	✓	✓	✗	✓	○	323.343	TP09-61.35 [10]	324 *est.	NA
SK18_T_26	SK_07_012_014	13.22	13.24	✓	✗	✗	✗	✗	✗	✗	✓	✗	✗	✓	○	327.245	TP09-61.85 [10]	328 *est.	NA
	SK_07_014_016	13.24	13.26	✗	✗	✗	✗	✓	✓	✗	✓	✓	✓	○	✓	327.895			
SK18_T_27	SK_07_058_060	13.68	13.70	✗	✗	✓	✓	✓	✓	✓	✓	✓	○	✗	○	343.835	TF-72 CVZ/RMF [11]	340.8	3.5
SK18_T_28	SK_07_072_074	13.82	13.84	✗	✗	✓	✗	✓	✗	✓	✓	✓	○	✓	○	349.816	TF-75 RMF [11]	349.2	3.6
	SK_07_074_076	13.84	13.86	✓	✗	✓	✓	✗	✗	✗	✗	✗	✗	✗	✗	350.670			
	SK_07_076_078	13.86	13.88	✗	✗	✓	✓	✓	✓	✓	✓	✓	○	✓	○	351.524			
SK18_T_29 OMC* Jordanova et al., 2022	SK_07_098_100	14.08	14.10	✓	✗	✗	✓	✓	✓	✗	✗	✓	✓	✓	○	360.922	TF-81 Or TF-82 or TF-83 or TF84 Or TF-85 [11]	364.5+ -3.0 To 365.9+ -2.9	
	SK_07_100_102	14.10	14.12	✗	✗	✗	✓	✓	✓	✓	✗	✓	○	✓	○	361.777			
	SK_07_102_104	14.12	14.14	✓	✗	✗	✓	✓	✓	✓	✗	✓	○	✓	○	362.631			
	SK_07_104_106	14.14	14.16	✗	✗	✗	✓	✓	✓	✗	✓	✗	○	✓	○	363.485			
	SK_07_106_108	14.16	14.18	✗	✗	✗	✓	✓	✓	✓	✗	✗	○	✓	○	364.340			
	SK_07_108_110	14.18	14.20	✓	✗	✓	✓	✓	✓	✓	✓	✓	✓	✓	○	365.194			
SK_07_110_112	14.20	14.22	✓	✗	✗	✗	✓	✓	✓	✓	✓	✓	✓	✗	366.049				
SK18_T_30	SK_07_122_124	14.32	14.34	✓	✗	✗	✓	✓	✓	✗	✗	✓	✓	○	○	371.175	TP09-66.95 Santorini SAN35[10]	367 * est.	NA

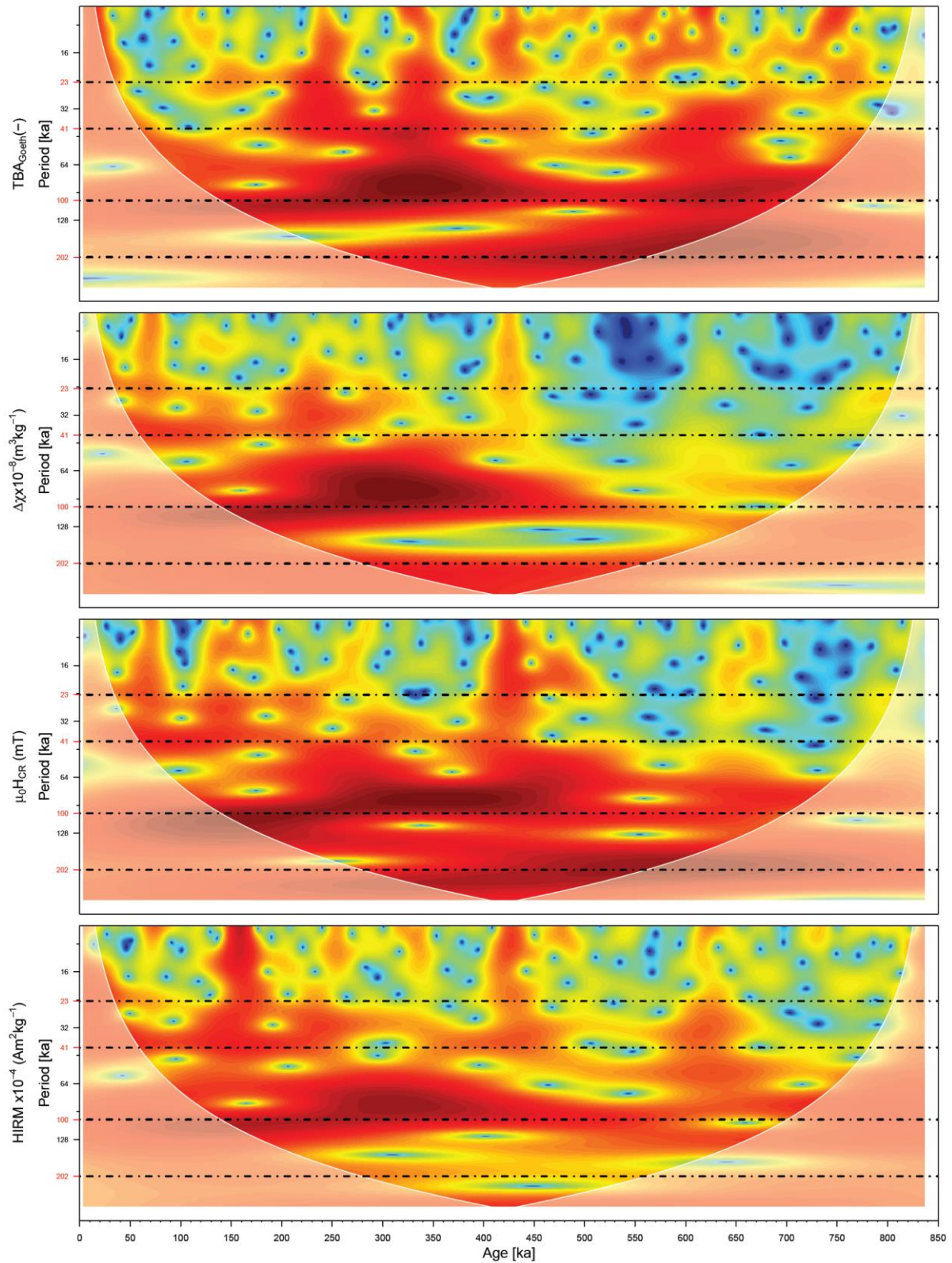
SK18_T_31	SK_07_194_196	15.04	15.06	✓	✗	✗	✗	✗	✓	✗	✗	✗	✓	✗	✗	401.500	OH-DP16.40 [1]	398.37	5.95
SK18_T_32	SK_08_012_014	15.72	15.74	✓	✗	✓	✓	✓	✓	✗	✓	✓	✓	✗	✓	427.450	TP09-75.75 [10] or TP09-75.85 [10]	427 *est. or 428 *est.	NA
	SK_08_014_016	15.74	15.76	✗	✗	✗	✓	✓	✓	✓	✓	✓	✓	○	✓	427.800			
SK18_T_33	SK_08_024_026	15.84	15.86	✓	✗	✓	✓	✗	✗	✗	✗	✓	✗	✗	✓	428.931	TP09-76.05 [10]	430 *est.	NA
SK18_T_34	SK_08_042_044	16.02	16.04	✗	✗	✗	✓	✗	✓	✗	✓	✗	✗	○	✓	432.700	TP09-76.75 [10]	433*est.	NA
	SK_08_044_046	16.04	16.06	✗	✗	✓	✓	✓	✓	✓	✓	✓	✓	○	✓	433.050			
SK18_T_35	SK_08_070_072	16.30	16.32	✗	✗	✓	✓	✗	✓	✗	✓	✗	✗	○	✓	437.600	TP09-77.65 [10] or TP09-77.95 [10]	437 *est. or 438 *est.	NA
	SK_08_072_074	16.32	16.34	✓	✗	✓	✓	✓	✓	✓	✓	✓	✓	✓	✓	437.950			
	SK_08_074_076	16.34	16.36	✗	✗	✓	✓	✓	✓	✓	✓	✓	✓	○	✓	438.414			
	SK_08_076_078	16.36	16.38	✗	✗	✓	✓	✓	✓	✓	✓	✓	✓	○	✓	438.793			
SK_08_078_080	16.38	16.40	✗	✗	✓	✓	✗	✓	✓	✗	✓	✓	✓	○	✗	439.172			
SK18_T_36	SK_08_110_112	16.70	16.72	✗	✗	✓	✗	✓	✓	✓	✓	✗	✓	○	✓	444.600	I24 ODP site 964 (Ionian Sea) [12]	445.1	NA
SK18_T_37	SK_08_142_144	17.02	17.04	✗	✗	✓	✗	✓	✓	✓	✓	✓	✓	○	✓	450.200	I25 ODP site 964 (Ionian Sea) [12]	451.5	NA
SK18_T_38	SK_08_174_176	17.34	17.36	✗	✗	✗	✗	✗	✓	✓	✗	✗	✓	○	✓	455.800	OH-DP-1812 [1]	453.95	2.94
SK18_T_39	SK_08_180_182	17.40	17.42	✓	✗	✗	✗	✗	✗	✓	✗	✗	✗	✗	✗	456.850	OH-DP-1817 Pozzolane Rosse [1] OR I26 ODP site 964 (Ionian Sea) [12]	456.19 or 456.60	3.3 or NA
SK18_T_40	SK_08_192_194	17.52	17.54	✓	✗	✗	✓	✗	✗	✗	✗	✓	✗	✗	✗	458.950	OH-DP-1817 Pozzolane Rosse [1] OR I26 ODP site 964 (Ionian Sea) [12]	456.19 or 456.60	3.3 Or NA
SK18_T_41	SK_08_204_206	17.64	17.66	✓	✗	✗	✗	✗	✗	✓	✗	✗	✓	✗	○	461.050	964B-3H-2-7.5 [13]	461	NA
SK18_T_42	SK_08_240_242	18.00	18.02	✓	✗	✗	✓	✗	✗	✓	✗	✗	✓	✗	✓	467.350	?	?	?
SK18_T_43 OMC* Jordanova et al., 2022	SK_08_282_284	18.42	18.44	✗	✗	✓	✓	✓	✓	✗	✓	✗	✗	○	✗	477.862	964B-3H-2-67.5 13]	477	NA
	SK_08_284_286	18.44	18.46	✗	✗	✓	✓	✓	✓	✓	✓	✓	✓	○	✗	478.241			
	SK_08_286_288	18.46	18.48	✗	✗	✓	✓	✓	✓	✓	✓	✓	✓	○	✓	478.621			
	SK_08_288_290	18.48	18.50	✓	✗	✓	✓	✓	✓	✓	✓	✓	✓	✓	✓	479.000			
SK_08_290_292	18.50	18.52	✓	✗	✓	✓	✓	✓	✓	✓	✓	✓	✓	✓	✗	479.872			
SK18_T_44	SK_08_296_298	18.56	18.58	✗	✗	✓	✓	✓	✓	✗	✓	✓	✓	○	✗	482.487	OH-DP-1911 [1]	480.49	6.84
	SK_08_298_300	18.58	18.60	✗	✗	✓	✓	✓	✓	✓	✓	✓	✓	○	✓	483.359			
	SK_08_300_302	18.60	18.62	✓	✗	✓	✓	✓	✓	✗	✓	✓	✓	✓	✓	484.231			
SK18_T_45	SK_08_320_322	18.80	18.82	✗	✗	✗	✗	✗	✗	✓	✗	✗	✗	○	✗	492.614	OH-DP-1966 [1]	494.05	4.43
	SK_09_000_002	18.82	18.84	✓	✗	✓	✓	✓	✓	✓	✓	✗	✓	✓	✗	493.500			
	SK_09_002_004	18.84	18.86	✗	✗	✗	✓	✓	✓	✓	✗	✓	✗	✓	○	✗			

	SK_09_004_006	18.86	18.88	✗	✗	✗	✓	✓	✓	✗	✓	✗	✓	○	✗	495.273			
SK18_T_46	SK_09_020_022	19.02	19.04	✗	✗	✓	✗	✓	✓	✗	✓	✓	✓	○	○	502.364	?	?	?
SK18_T_47	SK_09_058_060	19.40	19.42	✗	✗	✓	✗	✗	✗	✓	✓	✓	✗	○	○	517.516	OH-DP-2017 [1]	516.87	5.74
SK18_T_48	SK_09_100_102	19.82	19.84	✗	✗	✓	✗	✓	✓	✓	✓	✓	✓	○	○	531.065	OH-DP-2060 [1]	530.86	3.35
SK18_T_49 OMC* Jordanova et al., 2022	SK_10_028_030	20.94	20.96	✓	✓	✓	✓	✗	✗	✓	✗	✓	✓	✓	✓	614.700	I 30 ODP964 [12]	622.8	NA
	SK_10_030_032	20.96	20.98	✗	✗	✓	✓	✗	✗	✓	✗	✓	✓	○	✓	615.750			
	SK_10_032_034	20.98	21.00	✓	✗	✓	✗	✗	✗	✗	✗	✓	✓	✓	✓	616.800			
	SK_10_034_036	21.00	21.02	✗	✗	✓	✓	✗	✗	✓	✗	✓	✓	○	✗	617.850			
	SK_10_036_038	21.02	21.04	✗	✗	✓	✗	✗	✗	✓	✗	✓	✓	○	✗	618.900			
	SK_10_038_040	21.04	21.06	✗	✗	✓	✓	✓	✗	✓	✓	✓	✓	○	✓	619.950			
	SK_10_040_042	21.06	21.08	✓	✗	✓	✗	✗	✗	✓	✗	✓	✓	✓	✓	621.000			
SK18_T_50	SK_10_046_048	21.12	21.14	✗	✗	✓	✗	✗	✗	✓	✓	✓	✓	○	✗	623.463	OH-DP-2439 [1]	626.87	3.98
SK18_T_51	SK_10_076_078	21.42	21.44	✓	✗	✗	✓	✓	✗	✗	✗	✗	✗	✓	✓	635.776	?	?	?
	SK_11_078_080	21.44	21.46	✗	✗	✓	✓	✓	✗	✓	✓	✓	✓	○	✓	636.597			
	SK_11_080_082	21.46	21.48	✗	✗	✓	✗	✓	✗	✓	✓	✓	✓	○	✗	637.418			
	SK_11_082_084	21.48	21.50	✗	✗	✓	✓	✓	✗	✓	✓	✓	✓	○	✗	638.239			
SK18_T_52	SK_11_018_020	21.80	21.82	✗	✗	✓	✓	✓	✓	✓	✓	✓	✓	○	✓	650.030	OH-DP-2512 [1]	648.56	6.76
SK18_T_53	SK_11_238_240	24.00	24.02	✗	✗	✗	✓	✓	✗	✓	✓	✓	✓	○	✓	757.029	?	?	?
SK18_T_54	SK_11_278_280	24.40	24.42	✓	✗	✗	✗	✓	✓	✓	✓	✓	✓	✓	✗	767.314	?	?	?
SK18_T_55	SK_12_146_148	26.08	26.10	✓	✗	✗	✓	✓	✗	✗	✗	✗	✗	✓	✓	812.636	?	?	?

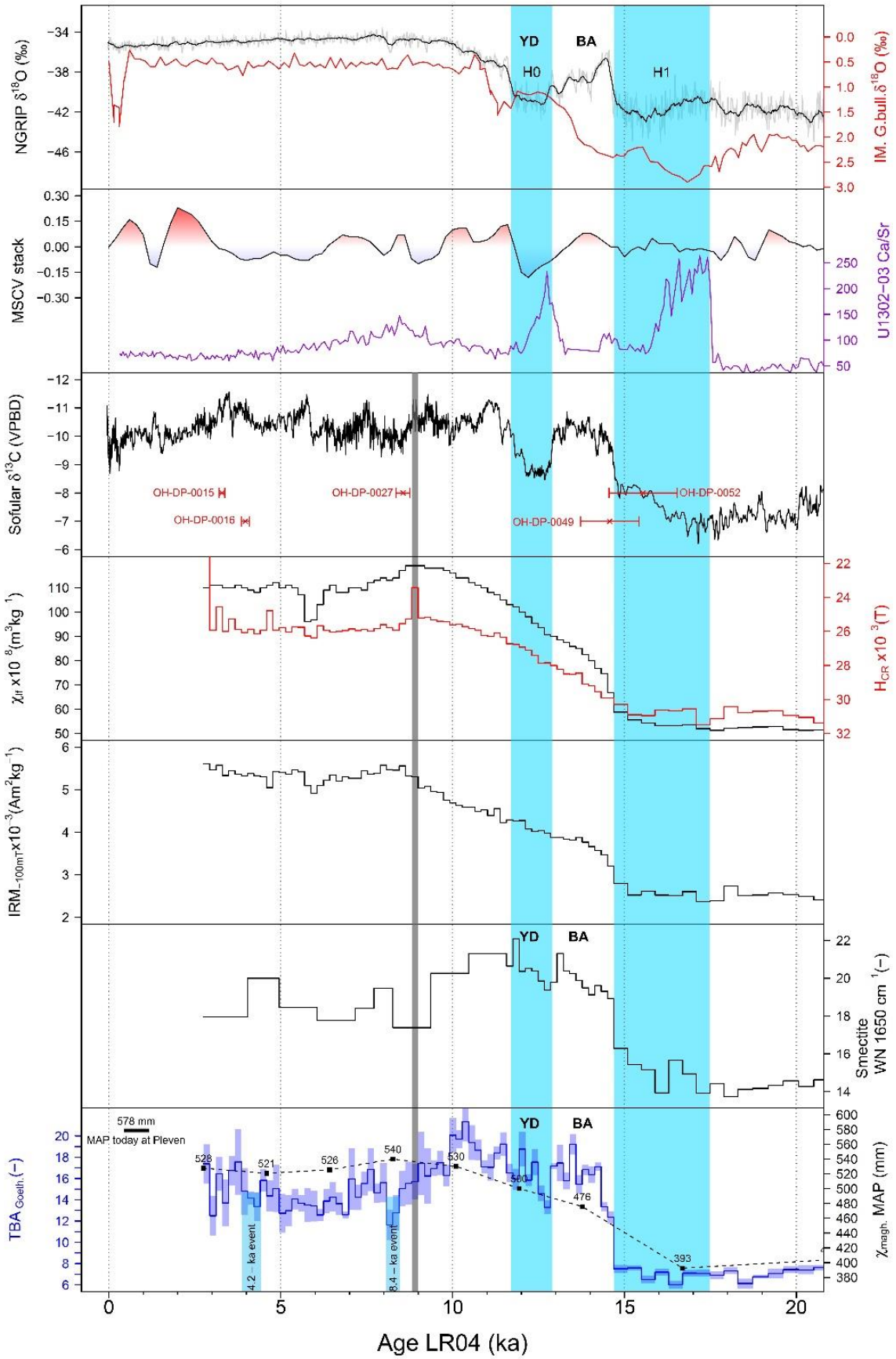
Table 2: The in-field outcropping tephra layer (SK18\_T\_13), crypto-tephra layers identified in (Jordanova et al., 2022) (SK18\_T\_29, SK18\_T\_43, SK18\_T\_49) and other crypto-tephra layer candidates identified in this study. Learning from the in-field outcropping tephra layer SK18\_T\_13 listed magnetic and FTIR data addressing the magnetic mineralogy, magnetic grain size and smectite content were utilized to identify other crypto-tephra layers preserved in the SK LPS. OMS means optically microscopic confirmed (as presented in (Jordanova et al., 2022)). “IRM-acq. done” means that highly resolved IRM acquisitions were measured and component unmixing applied. The same “FORC done” means that FORC experiments were conducted (green checks mean yes, red crosses means no, FORC diagrams can be found in the supplementary material). The following nine columns present magnetic data, where green checks mean that a local value maximum was identified, red crosses indicate no identified local maximum compared to other bracketing samples. Blue circles indicate, that the respective sample was not measured by a regarding experiment and that no statement can be given. The next column contains the regarding age of each sample containing potentially tephra material. In the next column, potential tephra equivalents are listed. [1]OH-staring labels indicate a macroscopic tephra sample presented in (Leicher et al., 2021). SUL stands for Sulmona [2] (Giaccio et al., 2009). The age for the Cape Riva Y2 tephra layer [3] stems from (Fenn et al., 2021), the age for the CI-Y5



tephra [4] from (Giaccio et al., 2017). TP stands for Tenaghi Philippon and TP-05 dates [5] stem from (Wulf et al., 2018). The ages of SK18\_T\_11, which are equivalent to ages [6,7,8,9] presented in (Fedorowicz et al., 2012, 2013) examined with aid of OSL and TL dating were both presented in (Hlavatskyi and Bakhmutov, 2020, 2021) targeting bracketing loess samples were the SK18\_T\_11 tephra or in presented studies “Roxolany L2 tephra” is embedded in. Tenaghi Philippon tephra ages stemming from the 2009 obtained TP09 core [10] are presented in (Vakhrameeva et al., 2019) and are indicated as labels starting with “TP09”. A recent study [11] presented by (Leicher et al., 2022) provides tentative age equivalents for the potential crypto-tephra layers SK18\_T\_27, SK18\_T\_28, and SK18\_T\_29. (Lourens, 2004) provides ages [12] for tephtras found in the Ionian marine core ODP 964 for the SK18 crypto-tephra layers SK18\_T\_36 and SK18\_T\_37, as well as for SK18\_T\_39, SK18\_T\_40, and SK18\_T\_49. (Vakhrameeva et al., 2021) [13] provide for SK18\_T\_41 and SK18\_T\_43 a age identically with the ages derived for these samples from the adjusted age model for the SK LPS. Samples with ages assigned as “?” were not found in any closely located reference tephra-rich archive.



Supplementary figure 5: Wavelet analysis for different magnetic (HIRM,  $H_{CR}$ ,  $\Delta\chi$ ) and colorimetric parameters ( $TBA_{Goeth}$ ).



Supplementary figure 6: The last 20 ka to present recorded.

## Appendix C: Conversions of Colorimetry

Appendix C contains conversion formula applied when transformations between different color spaces are required and how  $L^*$ ,  $a^*$  and  $b^*$  values are calculated.

In the CIE 1931 color space, the chromaticity coordinates ( $x$ ,  $y$ ) of a color are determined by measuring the tristimulus values ( $X$ ,  $Y$ ,  $Z$ ) of the color and then converting them to chromaticity coordinates using the following equations:

$$x = \frac{X}{X + Y + Z}$$

$$y = \frac{Y}{X + Y + Z}$$

In 1976, the CIE introduced this now widely used three-dimensional uniform colour space using the coordinates  $L^*$ ,  $a^*$  and  $b^*$  calculated from tristimulus measurements.

$$L^* = 116 \frac{Y}{Y_n} \times \frac{1}{3} - 16$$

$$a^* = 500 \frac{X}{X_n} \times \frac{1}{3} - \frac{Y}{Y_n} \times \frac{1}{3}$$

$$b^* = 200 \frac{Y}{Y_n} \times \frac{1}{3} - \frac{Z}{Z_n} \times \frac{1}{3}$$

where  $X_n$ ,  $Y_n$ , and  $Z_n$  are the tristimulus values for the relevant standard illuminant and observer. These equations only apply when  $X/X_n$ ,  $Y/Y_n$  and  $Z/Z_n > 0.008856$ . When  $X/X_n$ ,  $Y/Y_n$  and  $Z/Z_n < 0.008856$ , that is, for very dark colours:

$$L^* = 903.3 \frac{Y}{Y_n}$$

$$a^* = 3893.5 \frac{X}{X_n} - \frac{Y}{Y_n}$$

$$b^* = 1557.4 \frac{Y}{Y_n} - \frac{Z}{Z_n}$$

## Appendix D: Publication Zemun

### **A detailed paleoclimate proxy record for the Middle Danube Basin over the last 430 kyr: a rock magnetic and colorimetric study of the Zemun loess-paleosol sequence.**

Christian Laag<sup>1,2,3</sup>, Ulrich Hambach<sup>3,4</sup>, Christian Zeeden<sup>1</sup>, France Lagroix<sup>2</sup>, Yohan Guyodo<sup>2</sup>, Daniel Veres<sup>5</sup>, Mladjen Jovanović<sup>6</sup>, Slobodan B. Marković<sup>6,7</sup>

<sup>1</sup> Section 5: Rock Physics and Borehole Geophysics, Leibniz Institute for Applied Geophysics (LIAG), Hanover, Germany

<sup>2</sup> Université de Paris, Institut de physique du globe de Paris (IPGP), CNRS, Paris, France

<sup>3</sup> Chair of Geomorphology, University of Bayreuth, Bayreuth, Germany

<sup>4</sup> Bayreuth Center of Ecology and Environmental Research (BayCEER), University of Bayreuth, Bayreuth, Germany

<sup>5</sup> Institute of Speleology, Romanian Academy, Cluj-Napoca, Romania

<sup>6</sup> Chair of Physical Geography, Faculty of Sciences, University of Novi Sad, Novi Sad, Serbia

<sup>7</sup> Serbian Academy of Sciences and Arts, Belgrade, Serbia

#### **Status**

- submitted: 28.08.2020
- accepted: 20.04.2021
- published: 25.05.2021 in *Frontiers in Earth Science* 9, 600086, doi: 10.3389/feart.2021.600086

#### **Main findings**

- The Zemun LPS presents a continuous record of dust accumulation from the onset of the interglacial MIS 11 towards the transition of MIS5 to MIS4 (the last 430 -60 ky).
- Between MIS 11 and MIS9, marshy floodplain sediments are preserved containing very coarse grain sizes
- The L2 tephra and Bag tephra was identified with low-field magnetic susceptibility and further characterized with various environmental magnetic experiments
- The detailed analysis of both tephra layers spread the seed of magnetic grain size and IRM acquisition component unmixing (coupled with FORCs) being performed in combination with magnetic concentration parameters to detect cryptotephra layers in other LPSs
- The CIE Lab\* parameters provide reliable indications for organic matter and weathering degree of the paleosols.
- Hysteresis and backfield data confirmed the assumed mineral magnetic and grain size properties acquired during highly explosive silicic eruptions evidenced e.g., by an additional coercivity component necessary for tephra layers with a  $B_h$  of  $\sim 40$  mT.





# A Detailed Paleoclimate Proxy Record for the Middle Danube Basin Over the Last 430 kyr: A Rock Magnetic and Colorimetric Study of the Zemun Loess-Paleosol Sequence

Christian Laag<sup>1,2,3\*</sup>, Ulrich Hambach<sup>3,4</sup>, Christian Zeeden<sup>1</sup>, France Lagroix<sup>2</sup>, Yohan Guyodo<sup>2</sup>, Daniel Veres<sup>5</sup>, Mladjen Jovanović<sup>6</sup> and Slobodan B. Marković<sup>6,7</sup>

<sup>1</sup> Section 5: Rock Physics and Borehole Geophysics, Leibniz Institute for Applied Geophysics (LIAG), Hanover, Germany, <sup>2</sup> Université de Paris, Institut de Physique du Globe de Paris (IPGP), CNRS, Paris, France, <sup>3</sup> Chair of Geomorphology, University of Bayreuth, Bayreuth, Germany, <sup>4</sup> Bayreuth Center of Ecology and Environmental Research (BayCEER), University of Bayreuth, Bayreuth, Germany, <sup>5</sup> Institute of Speleology, Romanian Academy, Cluj-Napoca, Romania, <sup>6</sup> Chair of Physical Geography, Faculty of Sciences, University of Novi Sad, Novi Sad, Serbia, <sup>7</sup> Serbian Academy of Sciences and Arts, Belgrade, Serbia

## OPEN ACCESS

### Edited by:

Julie Fosdick,  
University of Connecticut,  
United States

### Reviewed by:

Giancarlo Scardia,  
São Paulo State University, Brazil  
Jinbo Zan,  
Institute of Tibetan Plateau Research  
(CAS), China  
Chenglong Deng,  
Institute of Geology and Geophysics,  
Chinese Academy of Sciences (CAS),  
China

### \*Correspondence:

Christian Laag  
laag@ipgp.fr

### Specialty section:

This article was submitted to  
Sedimentology, Stratigraphy  
and Diagenesis,  
a section of the journal  
Frontiers in Earth Science

**Received:** 28 August 2020

**Accepted:** 20 April 2021

**Published:** 25 May 2021

### Citation:

Laag C, Hambach U, Zeeden C, Lagroix F, Guyodo Y, Veres D, Jovanović M and Marković SB (2021) A Detailed Paleoclimate Proxy Record for the Middle Danube Basin Over the Last 430 kyr: A Rock Magnetic and Colorimetric Study of the Zemun Loess-Paleosol Sequence. *Front. Earth Sci.* 9:600086. doi: 10.3389/feart.2021.600086

In mid-latitude Eurasia, loess-paleosol sequences (LPS) provide the most widespread sedimentary records of Quaternary paleoenvironmental evolution. In the Middle Danube Basin (MDB), these archives cover at least the last million years of climate history, and occasionally contain archeological findings. The studied Zemun LPS is located on the right bank of the Danube in Northern Serbia. The site was declared as a protected site, based on Paleolithic artifacts found on the riverbank and stemming from unknown stratigraphic levels of the loess cliffs exposed along the Danube. The present study aims to provide a stratigraphic, paleoenvironmental, and temporal context for the Zemun LPS by means of environmental magnetic and colorimetric methods. Our investigations result in a chronostratigraphic scheme allowing direct comparison with other well-established reference records in the MDB and elsewhere. Two potential tephra layers tentatively assigned to the so-called L2 and Bag tephra, which are both widespread in the MDB and beyond were investigated for their bulk magnetic properties. The resulting integrated age model suggests that the Zemun LPS records a detailed history of a quasi-continuous accumulation of mineral dust from Marine Oxygen Isotope Stage (MIS) 11–5a (c. 430–60 ka). The outcome of our integrative approach indicates a continuous aridification over the last four interglacial/glacial cycles and we discuss potential changes in seasonality over time.

**Keywords:** loess-paleosol sequences, environmental magnetism, diffuse reflectance spectrometry, stratigraphy, paleoclimate dynamics

## INTRODUCTION

Over the past decades, many loess-paleosol sequences (LPSs) have been investigated predominantly in the extensive northern hemisphere loess belt (Marković et al., 2015; Schaeztl et al., 2018; Lehmkuhl et al., 2021). Unlike lake and other terrestrial records, which are rather sparsely distributed, the spatial continuity of LPSs makes them valuable archives of past environmental

change in the prevailing climatic past regimes that sustained loess formation and preservation (e.g., Basarin et al., 2014; Marković et al., 2015). Glacial and interglacial cycles, usually associated with shifts in humidity and temperature resulting from long-term variations in orbital parameters of eccentricity, obliquity, and precession driving ice volume (Imbrie and Imbrie, 1980; Heslop et al., 2000; Lisiecki and Raymo, 2005; Sun et al., 2006; Abe-Ouchi et al., 2013), are recorded through the alternation of loess and paleosol horizons, respectively. The paleoclimatic relevance of the quasi-cyclic alternation of loess and paleosols in LPSs of the Chinese Loess Plateau (CLP) was demonstrated in the 1980s through the correlation of magnetostratigraphically dated susceptibility records to the marine oxygen isotope records (Heller and Liu, 1982, 1986), and similarly in the 1990s based on long-term variability in grain size distribution (e.g., Ding et al., 1994). Most of the early work relied on analyses of rock-magnetic parameters, often limited to magnetic susceptibility (Ding et al., 1993) and its frequency dependence. However, quantitative analyses of loess color spectra are also valuable indicators of shifts in mineralogical assemblages, as well as in organic matter content (Ding et al., 2002b; Lukić et al., 2014). Studies of LPSs from the CLP (Ji et al., 2002) and the Danube Basin (Lukić et al., 2014; Obrecht et al., 2016) demonstrated the strength of combining magnetic and colorimetric parameters. While many multi-proxy studies have been performed on archives covering the last glacial cycle, investigations of European LPSs spanning multiple glacial–interglacial cycles are fewer (e.g., Jordanova et al., 2007; Necula et al., 2013; Basarin et al., 2014; Marković et al., 2015; Zeeden et al., 2016; Sümegi et al., 2018; Antoine et al., 2019; Obrecht et al., 2019). In this study, we extend colorimetric data to about 430 kyr with the Zemun LPS record from the Middle Danube Basin (MDB), spanning from Marine Isotope Stage (MIS) 11 to MIS 5a.

Besides a dominating amount of quartz, feldspar, phyllosilicate and carbonate grains, comprising the average composition of the upper continental crust, Eurasian loess consists of heavy minerals and measurable relevant ferromagnetic (s.l.) particles such as a broad variety of iron oxides (Maher, 2016). Rock magnetic investigations allow differentiating magnetic particles formed *in-situ* via pedogenic processes from the initial detrital content of magnetic particles in wind-blown loess. Relevant iron oxides for deciphering between loess and paleosol-units, which are readily detectable and relative concentrations quantifiable by room-temperature magnetic investigations, consists of magnetite, maghemite and hematite (Heller and Evans, 1995). Pedogenesis takes place under relatively warm and humid conditions (Maher, 2016), involving various abiotic and bio-mediated chemical reactions not yet completely understood (e.g., Torrent et al., 2007; sections 2.5.2 and 2.6 in Lagroix et al., 2016) and resulting in the neo-formation of ultra-fine magnetic minerals (Maher and Taylor, 1988; Dearing et al., 1996; Maher, 1998; Torrent et al., 2007; Hu et al., 2013). Pedogenetically neo-formed magnetite/maghemite have magnetic grain sizes ranging from unstable single domain [superparamagnetic (SP)] to stable single domain (SD) sizes, where the SP/SD particle size threshold at room temperature is about 30 nm (e.g., Peters and Dekkers, 2003). SP particles display a frequency dependence of susceptibility, which can be used to quantify their relative

concentration and help discriminate between paleosols (high SP concentration) and loess (low to SP concentration). Weathering of loess can also occur under glacial conditions (Maher, 2011), but it is generally less intense due to increased aeolian sediment accumulation rates and generally drier conditions (Kohfeld and Harrison, 2003). Such weak glacial pedogenic alterations can also be detected by rock magnetic investigations (e.g., Taylor et al., 2014).

In most Eurasian LPSs, magnetic susceptibility values of paleosols are enhanced with respect to loess units (e.g., Maher, 1998, 2016; Marković et al., 2009, 2015) from which a first order (chrono)stratigraphy can be established. For example, Marković et al. (2015) proposed a composite loess stratigraphy nomenclature scheme for the Danube loess belt region to facilitate pan-Eurasian LPS comparisons based on trends in magnetic susceptibility and other chronostratigraphic constrains. The stratigraphic system is based on the “S” (for soil) and “L” (for loess) labeling without any specific regional prefixes as is well established for the Chinese loess stratotype sections (Kukla and An, 1989). In the present study, the proposed composite stratigraphy is used to compare magnetic susceptibility variations of the Zemun LPS, evolving under non-monsoonal controlled (paleo-) climate with that of a monsoonal-dominated loess-paleosol sequence from the CLP (Luochuan, e.g., Hao et al., 2012).

The Zemun site hosts a variety of Middle and Late Paleolithic, and Neolithic artifacts found on the river bank nearby the LPS outcrop and upstream to the northwest (Šarić, 2008). The stratigraphic position within the Zemun LPS of these artifacts is, to date, unknown. However, providing a chronological framework for the protected loess site and establishing a range of environmental conditions these settlements may have been subjected to is important and will be beneficial to future archeological work.

Establishing a reliable chronology for LPSs remains challenging when absolute dating techniques such as luminescence reach their dating limits. Correlative age models are a mean to partly overcome this challenge. For LPS, correlative age models rely on the key process of pedogenic alteration, which induces variations in physical parameters and consequently records the environmental impact of interglacial/glacial cycles. In this study, magnetic susceptibility measurements coupled to diffuse reflectance spectrometry (DRS) analyses provide insights into past changes in environmental conditions. Rock-magnetic parameters provide insight into the source of variations in magnetic susceptibility, and together trace changes in the strength of pedogenesis along the Zemun LPS. Lastly, the developed correlative age model provides a mean to compare DRS and magnetism-based indicators of pedogenesis with global climate stacks (here the LR04 stack; Lisiecki and Raymo, 2005).

Volcanic ashes are often identified in European loess units, but in most cases, these tephra are mixed within aeolian loess or occur as crypto-tephras invisible to the naked eye. As most widespread tephra stem from highly explosive silicic magmas they are rather dominated by volcanic glass instead of by minerals or rock fragments (e.g., Lowe et al., 2017). Therefore, tephra layers are expected to have magnetic grain sizes similar to



rapidly cooled magmatic rocks, characterized by dominantly SD and pseudo-single domain (PSD) particles, representing “frozen” magma at the time of eruption (e.g., Till et al., 2011). Both the magnetic grain size and composition of magnetic minerals contained in the tephra are also expected to contrast with that of the loess in which they are embedded. In the Zemun LPS, two tephra layers were identified through distinguishing magnetic properties similar to previous reports (Marković et al., 2015, 2018). Despite the lack of geochemical and mineralogical constraints, they are tentatively assigned to the so-called L2 and Bag tephra, both widespread regional marker-horizons.

## PROFILE SETTING AND STRATIGRAPHY

The Zemun LPS (N 44.9246°, E 20.3197°) is located in the southern part of the Middle Danube Basin and is exposed by the escarpment of a landslide scar developed in the high cliffs on the right bank of the Danube at the northwestern border of the Belgrade conurbation (Šarić, 2008). The profile belongs to the Srem loess plateau, which is delimited to the East and Northeast by the Danube and to the South by the Sava (**Figure 1A**). The Zemun LPS reveals several loess-paleosol couplets, reflecting warm/humid (interglacial) and cool/dry (glacial) past environmental conditions. The Zemun LPS shows similar litho- and pedo-stratigraphic features as neighboring profiles at Batajnica (Marković et al., 2009) and within the Titel loess plateau (Marković et al., 2015).

Parallel to sampling, the lithology of the sequence was described in the field focusing on loess structure, pedogenic features, and sediment color. Additionally, sediment samples were investigated under the binocular microscope in order to estimate mineralogical compositions and degree of roundness of grains. In loess deposits, aeolian origin is assumed when single grains predominantly show little rounding due to direct source to sink transport, whereas well-rounded grains reflect complex sediment recycling, long term transport and/or fluvial processes. Soil units were described following the *World reference base for soil resources* (IUSS Working Group WRB, 2015<sup>1</sup>), even though we are fully aware that this system is not designed to classify buried soils also referred to as paleosols. Additionally, we follow the concept of accretionary soil formation characteristic of aeolian landscapes of western Eurasian dry steppe regions (Hambach et al., 2019; Jordanova and Jordanova, 2020; Lehmkuhl et al., 2021). These observations combined with results of laboratory analyses (colorimetric and magnetic parameters) form the base for a genetic interpretation of sediment formation.

Field observation of the vertically exposed outcrop wall recognizes four major lithofacies units (**Figure 1**): loess (L4, L3, L2LL1, L2, L1), interstadial-type (embryonic) paleosol (L2SS1), interglacial-type paleosols (S4, S3, S2, S1), and a brownish to blackish, sandy-silty well-bedded unit (marshy floodplain sediment, MFS) outcropping between the lower two interglacial paleosols.

Sampling for sedimentological analysis started at the transition from a basal brownish-yellowish loess unit to the lowermost exposed interglacial pedocomplex (S4) characterized by humus infiltrations in ancient root channels, carbonate concretions (up to 5 cm in diameter) and hydromorphic features, such iron coatings and iron/manganese oxide patches (**Figure 1C**). The basal red-brownish fossil pedocomplex (24.35–22.30 m relative profile depth) is c. 2.05 m thick and can be classified as a Cambisol typical of forest-steppe environments. A gradual transition is observed to the overlying loess unit (L4, 22.25–21.90 m). From 21.85 to 21.70 m, a 0.20 m thick bed of loosely cemented loess can be recognized. At 21.65 m depth, a drastic change in sediment toward sandier material is observed and referred hereafter as marshy floodplain sediment (MFS) (see section “Integrated Stratigraphy”). The MFS persists from 21.65 to 16.50 m with alternation of sandy iron-stained and sandy-silty beds with dark humus rich partly clayey beds dominating.

The subsequent polygenetic light reddish-brown paleosol (S3, 16.45–18.80 m) can be classified as a Phaeozem typical of steppe environments with mild and relatively humid winters. It is built from the bottom to the top by a lower pedogenetically overprinted unit. This is followed by a thin, lightly colored horizon with carbonate nodules and numerous krotovinas likely representing a pedogenetically overprinted loess unit overlain by a pedogenetic horizon with again many krotovinas. A gradual transition to the overlying c. 2.65 m thick yellowish-grayish loess (L3, 13.75–11.10 m) is observed.

The contact between L3 and the pedocomplex above is massively bioturbated and interspersed with carbonate concretions of sub-centimeter to decimeter size. This interglacial-type pedocomplex is c. 3.50 m thick and comprises in its lower part a brownish-blackish to dark grayish c. 2.00 m thick paleosol unit (S2, 11.05–8.70 m), which is classified as a polygenetic steppe soil of Kastanozem to Chernozem type typical of cool mid-latitude steppe environments. The lower strongly developed darker horizon has many carbonate pseudomycelia. Krotovinas are scattered throughout the middle lighter colored horizon and the upper weakly developed interstadial-type paleosol horizon (L2SS1, 8.40–7.35 m). S2 and L2SS1 are separated a thin (~25 cm) pale yellowish loess unit (L2LL1, 8.65–8.45 m), which is bioturbated in its uppermost part transitioning into L2SS1 interstadial paleosol. The overlying pale-yellowish to partly yellowish-grayish loess unit (L2, 7.30–3.60 m) is c. 4.00 m thick and shows numerous fine lamina consisting of sandy loess beds in its middle part. At c. 5.8 m, a 2–3 cm reddish to brownish loose loess layer was observed.

The contact between L2 and the uppermost interglacial pedocomplex (S1, 3.55–0.60 m) is also characterized by massive carbonate concretions and krotovinas. The S1 pedocomplex is c. 2.95 m thick, composed of a lower dark brownish-grayish paleosol overlain by lighter paleosols marking variable degrees of pedogenesis during continued dust deposition. The entire complex can be characterized as a typical Chernozem soil with decreasing intensity of pedogenesis with time. The uppermost horizon of the S1 pedocomplex is rather weakly developed and contains numerous krotovinas.

<sup>1</sup><http://www.fao.org/soils-portal/data-hub/soil-classification/world-reference-base/en/>

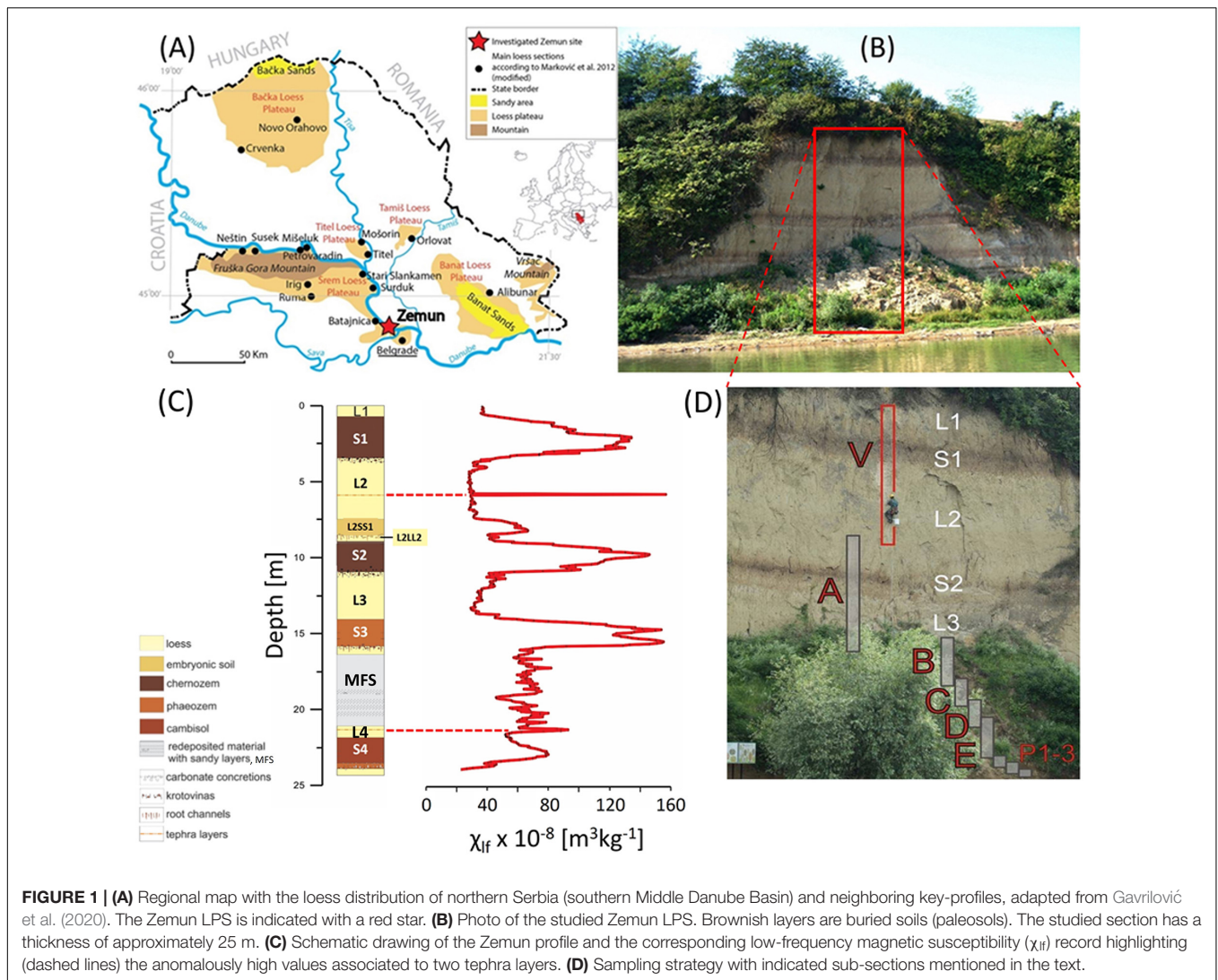


**FIGURE 1 | (A)** Regional map with the loess distribution of northern Serbia (southern Middle Danube Basin) and neighboring key-profiles, adapted from Gavrilović et al. (2020). The Zemun LPS is indicated with a red star. **(B)** Photo of the studied Zemun LPS. Brownish layers are buried soils (paleosols). The studied section has a thickness of approximately 25 m. **(C)** Schematic drawing of the Zemun profile and the corresponding low-frequency magnetic susceptibility ( $\chi_{lf}$ ) record highlighting (dashed lines) the anomalously high values associated to two tephra layers. **(D)** Sampling strategy with indicated sub-sections mentioned in the text.

The uppermost layer of the studied Zemun LPS is composed of pale porous sandy loess (L1, 0.60–0.00 m), which is loosely cemented with a few thin laminated beds of sandy-silt.

With the exception of the MFS sand dominated unit between 21.65 and 16.50 m, the entire sequence consists of coarse primary eolian silt with alternating contributions of fine sand in the pure loess and medium to fine silt in the paleosol units. Similar stratigraphic features can be observed in LPSs close to the Zemun LPS, e.g., from Batajnica (Marković et al., 2009), and the Titel-Stari Slankamen composite profile (Marković et al., 2011, 2015).

## MATERIALS AND METHODS

### Sampling

Sampling was performed from abseiling the wall (subsections V, A) and in dug trenches (subsections B, C, D, E, P 1–3). Subsections V and A cover the uppermost c. 15 m and are c. 2 m apart, whereas subsections B, C, D, E, and P 1–3 are located

between c. 6 and 10 m upstream to the northwest (Figure 1D). All subsections overlap and provide the basis for the construction of the composite profile. After thorough cleaning of the profile, bulk samples were taken with 5 cm spacing for a total of 479 sampling depths. For laboratory analyses described in following section “Room Temperature Susceptibility Measurements”, bulk samples were dried at 30°C for 48 h, homogenized and compressed into non-magnetic 6.4 cm<sup>3</sup> plastic boxes ( $n = 479$ ) and ~1.1 cm<sup>3</sup> gelatin capsules ( $n = 262$ ). Masses of bulk samples within boxes and capsules were measured and recorded.

### Room Temperature Susceptibility Measurements

Magnetic susceptibility measurements were carried out in 2017 at the Environmental and Palaeomagnetic laboratory at the University of Bayreuth. Measurements of low-field mass normalized magnetic susceptibility ( $\chi$ ), performed on all 479 box-samples, were obtained with a Magnon kappa bridge (Magnon, Dassel, Germany—VFSM) operating with a 320 A/m

applied field at low frequency (300 Hz,  $\chi_{lf}$ ) and high frequency (3,000 Hz,  $\chi_{hf}$ ). The absolute frequency dependence of magnetic susceptibility  $\Delta\chi$  is determined from:

$$\Delta\chi = \chi_{lf} - \chi_{hf} [m^3 kg^{-1}]$$

and the percent increase ( $\chi_{fd}$ ) with respect to  $\chi_{lf}$  from:

$$\chi_{fd} = \left( \frac{\chi_{lf} - \chi_{hf}}{\chi_{lf}} \right) \times 100\%$$

(Mullins and Tite, 1973; Dearing et al., 1996; Eyre, 1997).

## Hysteresis Measurements

Hysteresis measurements were performed with a Princeton Measurements Corporation Model 3900 Vibrating Sample Magnetometer (VSM) at the Institut de Physique du Globe de Paris (Paleomagnetism Research Group). A total of 262 samples were investigated across sub-sections of the Zemun profile covering the interval from 12.05 m depth (L3) to the top of the profile continuously ( $n = 240$ ), an interval from 22.25 to 21.50 m continuously ( $n = 16$ ) and 6 other discontinuous intervals within the sandy MFS (Figure 1).

For 6 of 10 samples stemming from the MFS sample preparation required modification to prevent grain movement favored by the higher sand content during hysteresis, FORC and IRM acquisition measurements on the VSM. The preparation consisted in piercing a hole at the base of the capsule to allow air to be released during the filling process. A thin layer of diamagnetic cotton was inserted to prevent single grains to fall through the air-release hole. Between 120 and 170 mg of the coarse grain sediment was added to the capsule and the net-weight measured. Grains were immobilized by adding neoprene gel glue, verified to be diamagnetic (c.  $-3 \times 10^{-8} m^3 kg^{-1}$ ). Complete saturation with glue was confirmed by leaking glue through the air-release hole. The lid was also filled with neoprene glue before sealing the capsules with the temperature resistant tape (see Supplementary Figure 1). Samples were dried overnight.

Prior to hysteresis measurements, the  $\chi$  of each sediment-filled capsule was determined with an AGICO KLY-3 kappabridge operating in a 300 A/m applied field at a frequency of 875 Hz. These low-field susceptibility measurements were used to (1) test whether the gelatine capsule subsamples are representative of the larger box samples, and (2) calculate the ferrimagnetic component of susceptibility ( $\chi_{ferri}$ ) by calculating the difference of the KLY3 bulk low-field susceptibility and the calculated high-field susceptibility ( $\chi_{hifi}$ ) from the slope of the high-field linear segment of the hysteresis loop:

$$\chi_{ferri} = \chi_{lf\ KLY3} - \chi_{hifi}$$

Three experiments were conducted with the VSM. (1) Hysteresis loops were measured in maximum applied fields of  $\pm 1.5$  T over 100 ms measurement times at each applied field step. The applied field increment was set to 5 mT. Experiments began at positive maximum field following a 1 s pause. The following parameters were derived from each hysteresis loop: coercivity

(Hc), saturation magnetization (Ms), saturation remanent magnetization (Mrs) and high-field magnetic susceptibility ( $\chi_{hifi}$ ), calculated from the linear high-field slope of the magnetization above 1.05 T. The ratio between  $\chi_{ferri}$  and Ms can be used to track variations in relative concentration of superparamagnetic (SP) particles assuming a constant magnetic mineral assemblage. (2) The coercivity of remanence (Hcr) was determined from backfield direct current demagnetization of the forward maximum field (1.5 T) isothermal remanent magnetization (IRM). 70 backfield steps were logarithmically spaced over the 0–500 mT range. (3) Backfield direct current demagnetization of the forward maximum field (1.5 T) IRM was also measured using linear 100 mT backfield steps from 0 to 1.5 T. From these data, relative contributions to the total  $IRM_{1.5T}$ , such as the S-ratio are determined, as well as absolute contributions to the total  $IRM_{1.5T}$  within various coercivity windows, such as HIRM, are quantified. The S-ratio was calculated after King and Channell (1991) as follows:

$$S - ratio = \frac{IRM_{-0.3T}}{IRM_{-1.5T}}$$

resulting in values possibly ranging from  $-1$  to  $+1$ , where values decrease from 1 as the relative contribution of hard magnetic minerals (defined here as having a coercivity of remanence greater than 300 mT) to the total  $IRM_{1.5T}$  increases. The hard isothermal remanent magnetization (HIRM) was calculated from the difference in magnetization between the 0.3 T and 1.5 T backfield steps following a forward field magnetization in 1.5 T (e.g., Taylor and Lagroix, 2015; Liu et al., 2016):

$$HIRM = IRM_{-0.3T} - IRM_{-1.5T}$$

The ratios of Hcr/Hc and Mrs/Ms (indicative of a samples mean magnetic grain size) were plotted on a modified Day-Dunlop plot (Day et al., 1977; Dunlop, 2002a,b), tracing differences in loess/paleosol samples and potentially tephra-bearing samples, the latter expected to contain higher PSD and SD content than loess.

## First Order Reversal Curve (FORC) Investigations

FORC investigations were carried out for six samples using the VSM. Specifically, FORCs were acquired on two samples suspected to contain tephra material (ZV 117, 5.80 m profile depth, containing the L2 tephra) and ZP1 001 (21.70 m, containing the Bag tephra, and reflecting the highest magnetic susceptibility signal out of 4 samples (ZP1 001- ZP1 004). To identify differences in magnetic grain size and possible differences in magnetic interactions, FORCs were also carried out on samples representative of loess units bracketing the suspected L2 and Bag tephra occurrences ZV 112 (5.55 m), ZV 126 (6.25 m), ZE 047 (21.65 m), and ZP1 016 (22.45 m). ZE 047 marks the base of the MFS and is hydromorphically overprinted but it is the sample immediately above the suspected Bag tephra sample analyzed (ZP1 001). Samples were exposed to a saturating field of 500 mT, Hu (min, max) were selected after initial test-measurements to  $\pm 80$  mT, and Hc (min, max) to 0 and 100 mT. Averaging



time was set to 300 ms, reducing measurement noise. For each diagram, 150 FORCs were acquired at a field increment of ca. 1.9 mT. For weak samples originating from loess units, 2–9 series of FORC measurements were measured and averaged. The number of FORCs averaged for each sample is reported as *n*-values in **Figure 6**.

FORC data analyses were carried out using FORCinel version 3.06 (Harrison and Feinberg, 2008). The main pre-processing consisted in drift and high-field slope corrections, first point removal, and lower-branch subtraction. FORCs of loess samples, for which multiple FORC were measured, were averaged in FORCinel. FORC diagrams were improved by color rescaling selecting a rectangle area around the central ridge and using the “Autoscale” option. Smoothing was conducted according to the VARIFORC approach (Egli, 2013) with the following smoothing factors: vertical ridge Sc0 = 4, central ridge Sb0 = 3, horizontal smoothing Sc1 = 7, vertical smoothing Sb1 = 7, horizontal and vertical  $\lambda$ das = 0.1, output grid = 1 and central ridge offset = 0. Horizontal profiles were extracted using FORCinextras.

## High-Resolution IRM Acquisition

Complementary to FORC measurements, high-resolution step-wise isothermal remanent magnetizations (IRM) were acquired on the same samples using the VSM. Samples were demagnetized before IRM acquisition. The initial field was set to 15  $\mu$ T, the final field to 1.5 T, using 300 logarithmically spaced measurement steps.

Tentative un-mixing of the IRM acquisition curves was carried out with aid of the MAX UnMix RShiny web-application (Maxbauer et al., 2016). Smoothing factors were set between 0.5 and 0.6, depending on measurement noise. Before using MAX UnMix, first derivatives of the raw IRM acquisition data were calculated, distributions of suspected tephra and bracketing loess samples compared to determine roughly the number and characteristics of geologically realistic components. These components were used in the fitting panel of MAX Unmix, and then refined in the optimization panel by minimizing the residual sum of squares (RSS). Final determination of the components characteristics were obtained in the Error Analysis panel, providing mean values and uncertainties based on 100 Monte-Carlo random re-samplings of 95% of the data.

## Colorimetric Measurements

Initial colorimetric measurements were carried out at the Environmental and Palaeomagnetic laboratory at the University of Bayreuth. Colorimetric analyses have been done in the past decades by visual identification of Munsell color charts (e.g., Tsatskin et al., 1998; Günster et al., 2001; Machalett et al., 2006), but its importance for paleoclimatic reconstruction remained little explored for a long time. These color charts provide alphanumerical indices for each sample by comparing the sampling material with a single-color rectangle. This procedure has some disadvantages (Post et al., 2015) such as subjective evaluation by a researcher and dependence on specific moisture and lighting. Spectrophotometers eliminate these uncertainties (Sun et al., 2011) and provide objective numerical values of luminance ( $L^*$ ), redness ( $a^*$ ) and blueness ( $b^*$ ).  $L^*$  ranges from 0

(black) to 100 (white), whereas  $a^*$  ranges from negative (green) to positive (red) and  $b^*$  from negative (blue) and positive (yellow). The redness  $a^*$  is commonly interpreted as reflecting weathering intensity (Yang and Ding, 2003). These three parameters span a 3-dimensional color sphere and derived Lab-values can be transformed to RGB colors to make their real colors visible (as conducted in **Figure 3**). Furthermore, spectrophotometers provide backscattered intensities of wavelengths each 10 nm from the visible light spectrum (here 400 to 700 nm only). These backscattered spectra are capable of tracing distinct minerals out of a heterogeneous bulk-sample mineral assemblage. An additional advantage is the fast ( $\sim 2$  s per sample) and non-destructive nature of the measurement.

Diffuse Reflective Spectroscopy (DRS) measurements were carried out in 2020 at the Leibniz Institute for Applied Geophysics (LIAG, Grubenhagen) with a Konica Minolta CM 700d spectrophotometer, in 10° observer angle and using the D65 norm-light calibration. An oculus width was obtained with a 0.8 cm open adapter. Backscattered reflectance spectra were converted into 1st derivative values with a newly developed R-script. 1st derivative values were used to calculate the hematite/goethite ratio (HGR), following the same approach described in Wu et al. (2018). HGR was calculated from the ratio of backscattered intensities ( $I$ ) at 565 nm, associated to hematite, and 435 nm, associated to goethite, so that  $HGR = I_{565\text{ nm}} / I_{435\text{ nm}}$  (Barranco et al., 1989; Deaton and Balsam, 1991; Debret et al., 2011). The backscattered intensity bands were selected based on peaks in the 1st derivative spectrum (**Figure 2**). For the transformation of Lab values into RGB colors, a modified R-script (R Core Team, 2020) was used (Zeeden et al., 2017).

## Generation of the Age Model

The age model (**Figure 9**) was constructed by correlating  $\Delta\chi$  variations and the LR04 stack (Lisiecki and Raymo, 2005), reflecting mainly global ice volume by benthic  $\delta^{18}\text{O}$ . Tie-points were selected based on (1) variations in magnetic parameters interpreted to fluctuate predominantly as a function of pedogenic intensity, and (2) similarities in fluctuation and amplitude of magnetic parameters when compared to the LR04 stack and Imbrie and Imbrie ice model (Imbrie and Imbrie, 1980). Identified tephra layers provide additional tie-points. This approach resulted in 13 tie-points (**Table 1**). Two additional tie-points constrain the age model stemming from the two potential tephra layers identified magnetically and compatible with sedimentological observations in the field. For the age model construction, the “astrochron” package version 0.9 (Meyers, 2014) was used for linear interpolation.

## RESULTS

### Magnetic Susceptibility Parameters and Stratigraphical Assignment

Based on the record of magnetic susceptibility with depth, a general pattern with low-frequency susceptibility ( $\chi_{lf}$ ) values being generally low in loess units, and high in paleosols can be observed for the Zemun LPS (**Figure 3** and **Table 2**).

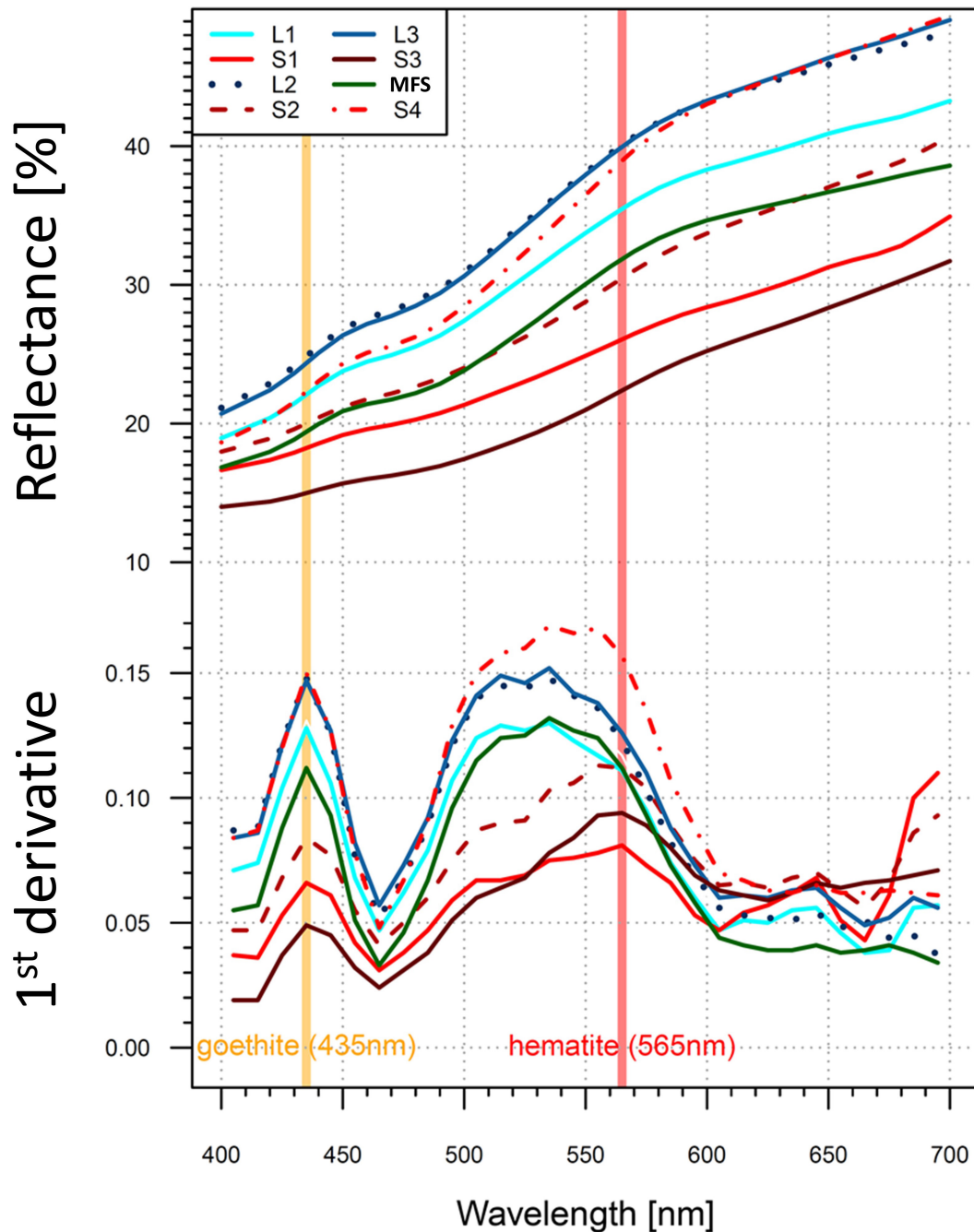


**FIGURE 2** | DRS analysis of selected representative samples from different stratigraphical units of the Zemun LPS. Upper plot displays raw backscattered intensities of wavelengths ranging between 400 and 700 nm in 10 nm intervals. Lower plot displays the first derivatives of backscattered wavelengths. Assumed contributions of hematite and goethite at distinct wavelengths are indicated as orange and red vertical bands, respectively. MFS is the abbreviation for marshy floodplain sediments.

Such a pattern is well known from Eurasian LPS and predominantly reflects past environmental changes between glacials and interglacials during the Pleistocene. Following the stratigraphic nomenclature introduced by Marković et al. (2015), results reveal that the sampled profile extends from a basal S4 pedo-complex, assigned to MIS 11 to the oldest part of the L1 directly overlaying the last interglacial-early glacial pedo-complex S1. Beside distinct elevated magnetic

susceptibilities in interglacial paleosols, the highest  $\chi_{lf}$  value ( $157 \times 10^{-8} \text{ m}^3\text{kg}^{-1}$ ) is observed as a sharp peak at 5.80 m depth within the L2 unit. This peak coincides with the field description of a 2–3 cm reddish to brownish loose loess layer and is stratigraphically and magnetically consistent with the L2 tephra layer described in other LPS regionally (e.g., Laag et al., 2018; Antoine et al., 2019). Mean  $\chi_{lf}$  values of paleosols S3 to S1 decrease slightly from  $\sim 115$  to 100 to  $90 \times 10^{-8} \text{ m}^3\text{kg}^{-1}$ ,

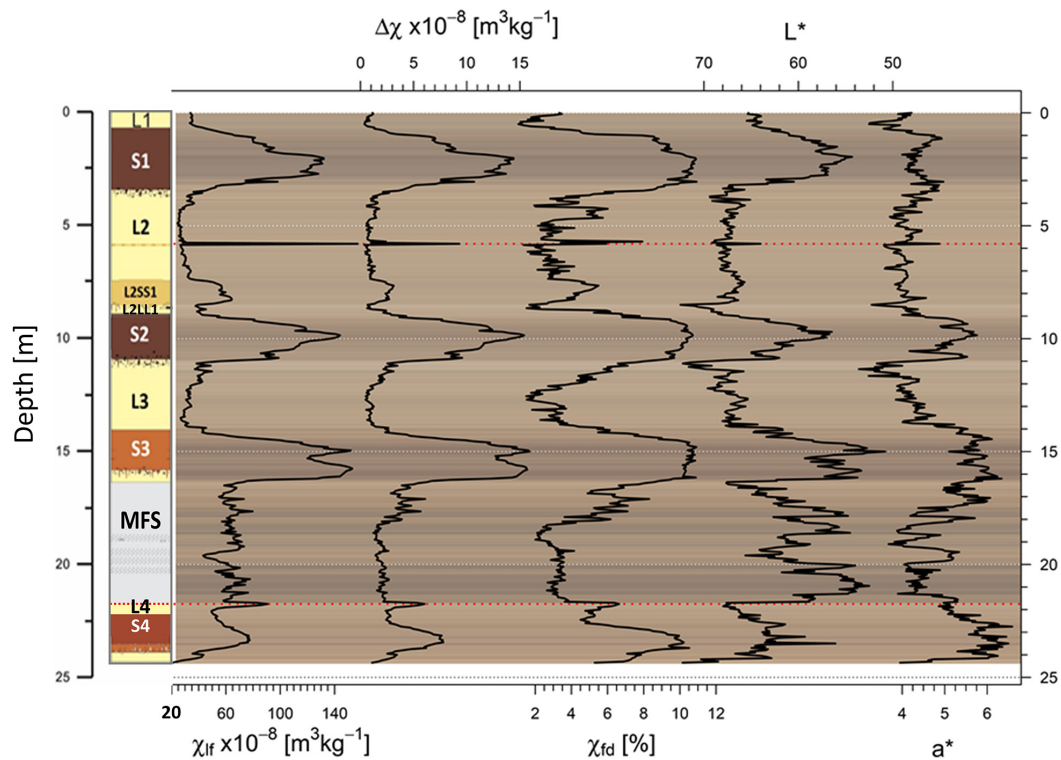


**FIGURE 3** | Stratigraphic view of magnetic susceptibility parameters  $\chi_{lf}$ ,  $\Delta\chi$ ,  $\chi_{fd}$  [%], and selected colorimetric parameters  $L^*$  and  $a^*$ . The variability of magnetic susceptibility parameters with depth reflects the pacing of interglacial (S4–S1) and glacial (L4–L1) cycles. Potential tephra layers (red dotted lines) are referred to as the L2 tephra and to as the Bag tephra. Note that the scale for  $L^*$  is inverted. Lab color values are transformed to RGB colors for each sample and plotted in the background.

**TABLE 1** | Selected tiepoints for age model calculation.

Zemun depth [m]	Age [ka]	Comment
0.50	60.0	LR04
0.50	66.0	LR04
1.65	108.0	LR04
2.70	123.0	LR04
5.80	160.6	L2 tephra / Vico Ignimbrite B
7.65	171.5	LR04
8.55	180.1	LR04
9.90	215.0	LR04
10.85	239.0	LR04
13.80	268.5	LR04
14.95	308.0	LR04
15.85	330.9	LR04
21.80	367.5	Bag Tephra / TF-85
22.60	391.0	LR04
23.45	406.0	LR04

respectively (Table 2 and Figure 3). Mean values of  $\Delta\chi$  also decrease from S3 to S1. The S4 pedocomplex displays mean values of  $\chi_{lf}$ ,  $\Delta\chi$  and  $\chi_{fd}$  % that are much lower than S3–S1. Finally the MFS layer has moderately high  $\chi_{lf}$  values, greater than S4 but less

than S3–S1, which fluctuate over short depth intervals.  $\Delta\chi$  and  $\chi_{fd}$  % values of the MFS are low comparable to loess units.

The magnetic enhancement of the paleosol is readily observable on the  $\Delta\chi$  vs.  $\chi_{lf}$  bi-plot shown in Figure 5A. Depth intervals within the MFS and containing tephra material plot above the main trend line. Two populations are distinctively identified along this trend with one predominantly represented by samples showing no magnetic enhancement characterized by nearly all samples within loess units, and a second reflecting pedogenesis (higher  $\Delta\chi$  and  $\chi_{lf}$ ) are all stemming from paleosol units. The strongest enhancement is expressed in paleosol S3, while S1 and S4 pedocomplexes spread over a wide range of  $\Delta\chi$  and  $\chi_{lf}$ . A background low-frequency magnetic susceptibility of  $24.6 \times 10^{-8} \text{ m}^3\text{kg}^{-1}$  is obtained by fitting a linear regression line through the data excluding the MFS and tephra intervals. This background value is higher than what is observed in Central Asia and China ( $17 \pm 2 \times 10^{-8} \text{ m}^3\text{kg}^{-1}$  Forster et al., 1994) or at Semlac in Romania ( $10 \times 10^{-8} \text{ m}^3\text{kg}^{-1}$  Zeeden et al., 2016) but similar to LPS north of Prague in the Czech Republic ( $22 \times 10^{-8} \text{ m}^3\text{kg}^{-1}$  for Sedlec and  $23 \times 10^{-8} \text{ m}^3\text{kg}^{-1}$  for Zemechy Forster et al., 1996).

## Hysteresis Parameters

Hysteresis loop derived parameters are summarized in Table 3 and plotted in Figures 4, 5. Combining data sets acquired on

**TABLE 2** | Minima, Maxima and Mean values for the different stratigraphic units.

Unit	n	$\Delta\chi \times 10^{-8} [\text{m}^3\text{kg}^{-1}]$			$\chi_{ff} \times 10^{-8} [\text{m}^3\text{kg}^{-1}]$			$\chi_{fd} [\%]$		
		Min	Max	Mean	Min	Max	Mean	Min	Max	Mean
L1	13	0.372	1.19	0.7197	33.50	36.10	34.87	1.073	3.473	2.078
S1	60	0.676	14.40	8.3990	36.20	132.00	88.90	1.766	10.929	8.843
L2*	73	0.360	2.38	0.9840	24.50	29.22	36.70	1.353	7.928	3.355
L2SS1	20	0.912	3.12	2.3450	33.70	64.40	55.16	2.709	5.497	4.228
L2LL1	5	0.624	1.35	0.8484	37.70	50.80	41.64	1.525	2.661	2.005
S2	48	1.090	15.40	9.2760	38.80	144.00	95.54	2.399	10.715	9.233
L3	51	0.471	3.48	1.4100	26.80	49.80	35.52	1.507	7.118	3.813
S3	50	1.020	15.90	10.21	30.20	153.00	103.6	3.365	10.911	9.130
MFS	103	1.200	6.09	2.544	43.40	79.70	63.08	2.010	8.305	4.027
L4	8	2.370	3.280	2.758	49.50	59.90	52.27	4.772	5.617	5.264
S4	42	1.090	7.79	4.599	20.50	77.60	56.89	4.508	10.523	7.813
L2 tephra	1		9.310			157.00			5.935	
Bag tephra	4	4.620	6.030	5.383	74.40	90.70	83.58	6.206	6.643	6.429
Total	479	0.360	15.90	4.540	20.50	157.00	63.98	1.073	10.929	5.872

the box and gelatin capsules subsamples was validated and is demonstrated in the **Supplementary Material (Supplementary Figure 2)** by KLY3  $\chi_{lf}$  vs. VFSM  $\chi_{lf}$  measurements defining a linear fit with an  $r$  of 0.99.

The commonly used magnetic proxy for pedogenic intensity is  $\Delta\chi$ , which increases with increasing degree of pedogenesis is compared to  $\chi_{ferr}/Ms$ , Hc, HIRM and S-ratio in **Figure 4A** through D, respectively. The  $\chi_{ferr}/Ms$  ratio, like  $\Delta\chi$ , track relative changes in SP particle concentration, assuming the mineral assemblage contributing is monomineralic or that proportions between mineral components are constant. The data acquired clearly shows that the magnetic mineral assemblage is not monomineralic but that the soft ferrimagnetic component dominates both Ms (**Figure 5C**) and  $\chi_{ferr}$  (**Figure 5G**). The magnetic mineral assemblage of the MFS and tephra samples do differ in terms of composition, concentration and magnetic grain size with respect to the loess and paleosol units, thus falling off the main trend line correlating ( $r = 0.9$ )  $\chi_{ferr}/Ms$  and  $\Delta\chi$ . At higher pedogenic intensities,  $\chi_{ferr}/Ms$  increases less rapidly than  $\Delta\chi$  suggesting an increased contribution to Ms of a mineral, likely hematite, with a lower saturation magnetization than magnetite and maghemite. **Figure 5I** shows HIRM increasing as  $\Delta\chi$  increases in paleosols corroborating the previous observation. In **Figure 4B**,  $\Delta\chi$  and Hc are displayed, showing for all samples (tephra layers excluded) a negative exponential behavior. Loess and MFS samples reflect the highest coercivities with low amounts of pedogenetically formed SP particles. The tephra samples reflect a diametral behavior, indicating the presence of SP particles but at similar SP concentrations the tephra samples have a higher bulk coercivity due to either a higher proportion of SD and PSD grains and/or of high coercivity minerals. **Figure 4C** confirms the latter and results presented in section “FORC Analysis” supports the former. HIRM and  $\Delta\chi$  correlate positively with a weaker coefficient ( $r = 0.69$ ) than for soft remanence-bearing ferrimagnetic ( $IRM_{-100\text{ mT}}$ ) component (**Figure 5F**,  $r = 0.92$ ), indicating that high-coercivity minerals present are also in paleosols and their concentration increases with increasing

pedogenic intensity (**Figure 4C**). Interestingly, samples from the MFS, L2SS1 and samples stemming from the L4 loess unit also define a linear trend but with a much higher slope where increases in HIRM are associated with only small increases of  $\Delta\chi$ . **Figure 4D** correlates  $\Delta\chi$  and the S-ratio. S-ratio values equal to 1 indicate the presence of only soft magnetic minerals like maghemite and magnetite, whereas reduced values underline the presence of high-coercivity minerals like hematite and goethite. The relative proportion of hard-magnetic minerals contributing to the  $IRM_{1.5T}$  is greater in Zemun loess, especially L2, than in paleosols units. The highest S-ratio values are observed for samples stemming from the MFS and the tephra samples. Excluding MFS and tephra samples, the S-ratio correlates positively with  $\Delta\chi$  with  $r = 0.79$  (**Figure 4D**) indicating that the relative proportion of soft-magnetic minerals contributing to  $IRM_{1.5T}$  increases with increasing degree of pedogenesis. At the same time, absolute concentrations of both soft remanence-bearing (**Figure 5F**) and hard (**Figure 4C**) magnetic mineral components increase individually with increasing pedogenesis.

Finally, hysteresis data presented on a modified Day-Dunlop plot (**Supplementary Figure 3**) reveals that all loess and paleosol samples fall within the PSD range as mean domain size, but samples stemming from the MFS as well as the tephra samples indicate a higher amount of SD particles.

## FORC Analysis

FORC diagrams and extracted horizontal profiles ( $H_u = 0$ ) of the six samples are shown in **Figure 6**. The three samples from the 5.55 to 6.25 m interval (ZV112, ZV117, ZV126) and the 21.65–22.45 m interval (ZE047, ZP1001, ZP1016) are presented separately because their main sediment compositions differ.

FORC diagrams and central ridge profiles of the bracketing loess for each subset interval, are very similar (**Figures 6A,C,D,F**). Samples ZV112 and ZV126 display a FORC diagram globally expected for PSD assemblages, in accordance with hysteresis parameters ( $H_{cr}/H_c = 3.18$  and  $3.29$ ,  $M_{rs}/M_s = 0.14$  and  $0.13$ ). The horizontal profiles are



**TABLE 3** | Summary of derived hysteresis parameters and calculated ratios.

Stratigraphic unit		L1	S1	L2	L2SS1	L2LL1	S2	L3	MFS	L4	L2 tephra	Bag tephra
n samples		13	60	73	20	5	48	20	10	8	1	4
$M_s \times 10^{-3}$ [Am <sup>2</sup> /kg]	Min	21.81	18.16	14.67	19.56	19.44	20.42	19.09	45.65	28.18	100.2	40.88
	Max	27.92	45.92	20.79	36.06	27.49	48.24	27.46	111.85	37.87		46.84
	Mean	24.39	33.45	17.71	30.05	21.87	35.79	22.81	67.40	30.37		44.35
$M_{rs} \times 10^{-3}$ [Am <sup>2</sup> /kg]	Min	3.137	2.501	2.120	2.941	3.117	2.976	2.766	7.785	4.519	17.71	6.763
	Max	3.749	6.615	3.111	5.358	4.038	7.233	3.958	18.2	6.003		7.866
	Mean	3.432	4.769	2.573	4.358	3.338	5.274	3.424	12.04	5.014		7.488
$H_c \times 10^{-3}$ [T]	Min	11.93	7.931	11.97	11.52	11.84	8.377	10.87	13.85	13.03	13.71	11.75
	Max	13.40	11.991	15.09	13.85	13.17	12.338	13.60	17.65	14.07		12.37
	Mean	12.78	9.107	13.78	12.02	12.50	9.409	12.29	15.23	13.44		12.09
$H_{cr} \times 10^{-3}$ [T]	Min	35.91	21.84	38.27	34.22	36.30	23.20	32.46	31.91	36.08	33.03	30.50
	Max	40.86	39.06	46.61	40.41	39.04	37.40	39.90	43.12	39.94		32.15
	Mean	38.35	27.56	42.37	35.90	37.55	28.30	36.87	37.73	37.96		31.33
$\chi_{HKLY3} \times 10^{-8}$ [m <sup>3</sup> /kg]	Min	26.27	27.58	18.31	25.61	30.12	31.82	29.82	46.48	37.94	115.4	53.01
	Max	29.92	94.70	29.83	49.13	40.39	104.72	40.48	77.05	48.35		63.01
	Mean	27.80	64.76	22.53	41.59	33.26	68.74	34.08	52.16	41.09		58.46
$\chi_{hifi} \times 10^{-8}$ [m <sup>3</sup> /kg]	Min	4.340	4.020	4.090	5.000	4.450	3.880	3.770	2.820	4.800	5.660	4.980
	Max	4.860	6.050	5.150	5.630	5.140	6.400	4.890	4.290	5.150		5.130
	Mean	4.637	5.250	4.553	5.441	4.676	5.460	4.511	3.548	4.889		5.055
$\chi_{ferri} \times 10^{-8}$ [m <sup>3</sup> /kg]	Min	21.60	23.40	14.00	20.60	25.70	27.00	25.30	42.20	33.10	110.00	48.00
	Max	25.20	88.90	25.20	43.70	35.30	98.60	36.20	73.60	43.20		57.90
	Mean	23.16	59.51	17.97	36.16	28.60	63.28	29.57	48.60	36.20		53.40
Mrs/Ms	Min	0.1325	0.1326	0.1264	0.1389	0.1469	0.1383	0.1371	0.1484	0.1581	0.1767	0.1654
	Max	0.1509	0.1518	0.1578	0.1523	0.1604	0.1528	0.1574	0.2076	0.1762		0.1719
	Mean	0.1408	0.1424	0.1452	0.1451	0.1532	0.1472	0.1500	0.1808	0.1653		0.1688
Hcr/Hc	Min	2.807	2.664	2.878	2.909	2.879	2.769	2.887	2.278	2.724	2.41	2.561
	Max	3.163	3.257	3.434	3.127	3.077	3.285	3.156	2.648	2.890		2.611
	Mean	3.003	3.019	3.078	2.987	3.005	3.006	3.002	2.475	2.824		2.591
S-ratio	Min	0.9159	0.9153	0.8890	0.9080	0.9143	0.9187	0.9131	0.9491	0.9279	0.9659	0.9472
	Max	0.9394	0.9476	0.9255	0.9327	0.9272	0.9458	0.9339	0.9744	0.9383		0.9518
	Mean	0.9266	0.9346	0.9052	0.9238	0.9201	0.9362	0.9233	0.9642	0.9317		0.9495
HIRM $\times 10^{-5}$ [Am <sup>2</sup> /kg]	Min	21.24	20.86	18.65	25.71	22.58	21.67	21.81	34.05	31.58	58.57	35.16
	Max	26.52	35.35	29.39	40.00	30.88	40.92	28.20	46.01	36.78		38.07
	Mean	24.39	28.70	23.69	31.94	25.81	31.01	25.21	39.81	33.49		36.66
$\chi_{ferri}/M_s \times 10^{-6}$ [m/A]	Min	8.650	11.10	8.770	10.50	12.80	12.90	10.90	5.810	11.40	11.00	11.60
	Max	10.300	21.20	12.400	12.90	13.60	20.70	14.80	9.910	12.50		12.40
	Mean	9.518	17.43	10.114	12.01	13.08	17.27	13.02	7.533	11.94		12.03

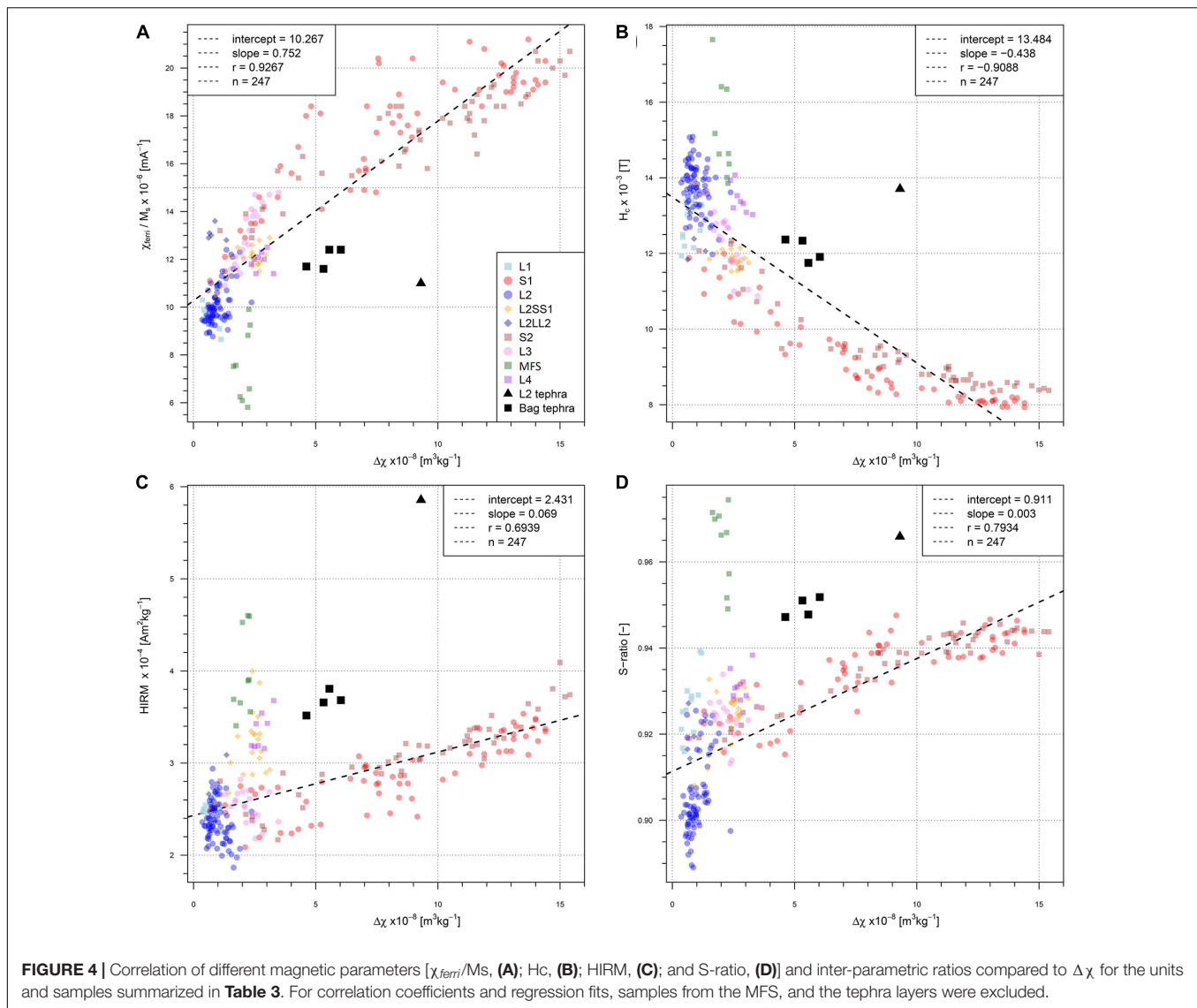
characterized by one main coercivity peak around 10 mT, and a second peak close to  $H_c = 0$ , along with a broad distribution up to about 80–100 mT. The PSD character of the FORC diagrams of samples ZE047 and ZP1016 is less pronounced and also reflected by the main hysteresis parameters ( $H_{cr}/H_c = 2.62$  and  $2.72$ ,  $M_{rs}/M_s = 0.17$  and  $0.17$ ). For these samples, the horizontal profiles are also characterized by a peak around 10 mT, but lack the very low-coercivity peak, probably due to a lesser content in grains either close to the superparamagnetic threshold or in the multidomain range. Sample ZV117 ( $H_{cr}/H_c = 2.46$ ,  $M_{rs}/M_s = 0.17$ ) displays a FORC diagram with a main distribution more elongated along the central ridge axis and shifted to higher  $H_c$  values, making the diagram appear more SD-like than those of the bracketing loess samples (Figure 6B). A similar observation can be made from sample ZP1001

( $H_{cr}/H_c = 2.66$ ,  $M_{rs}/M_s = 0.16$ ), although it is not as prominent as for sample ZV117 (compare Figures 6E,B). This is also seen in the horizontal profiles, where the main distribution peak are broadened and shifted to slightly higher values by 5–10 mT. This indicates the input of additional and non-loessic material.

## High Resolution IRM Acquisition

Detailed IRM acquisitions can provide alternative insights on the coercivity distributions because focusing on remanent magnetizations instead of direct in-field measurements, which is the case for FORCs.

These are therefore differently affected by magnetic particle sizes (for instance, superparamagnetic particles do not carry a remanent magnetization). IRM acquisition curves were obtained for the same six samples that underwent FORC



as shown in **Figures 7A,F**. All six samples fail to saturate by 1.5T, indicating the presence of high-coercivity minerals. Raw coercivity distributions of samples ZV112 and ZV126 (**Figure 7G**) are nearly identical, as expected from both hysteresis parameters and FORC diagrams. Samples ZE047 and ZP1016 are also very similar (**Figure 7G**). The coercivity distribution of all four bracketing loess samples is characterized by two main peaks at about 20–30 mT (1.3–1.5 in log scale) and 60–100 mT (1.8–2.0 in log scale) (**Figures 7C,E,H,J**). The distribution of sample ZV117 (**Figure 7D**) differs significantly from that of samples ZV112 and ZV126 and is dominated by a peak around 45 mT (1.65 in log scale). For sample ZP1001, the distinction with its bracketing loess samples is less marked (**Figure 7I**), similar to observations made from FORC measurements. However, a small additional peak around 35 mT (1.55 in log scale) can be observed. These observations were used as first inputs for the MAX Unmix program. To these, we added a small amount of high-coercivity component to account for the unsaturated

IRM. Results of the unmixing are depicted in **Figures 7C–E,H–J**. Taken separately, each sub-set of loess samples (ZV112 and ZV126; ZE047 and ZP1016) are characterized by similar distribution components. The IRM acquisitions of samples ZV117 and ZP1001 are compatible with models involving the same distribution components as those of the surrounding loess samples, with the addition of the fourth component. As in the case of the FORC measurements, this is more evident for sample ZV117.

### Colorimetric/DRS Analysis

$L^*$  values are generally higher in light loess units meaning brighter colors due to higher amounts of quartz and carbonates than in paleosols, where clays and organic matter decrease the luminance (**Figure 3** and **Table 4**). The highest  $L^*$  value (72.5) is found in the L2SS1 and the lowest  $L^*$  value (50.8) in the S3 pedocomplex. Luminance values follow stratigraphic units from the S3 pedocomplex to the L1 loess at the top of the profile. Below

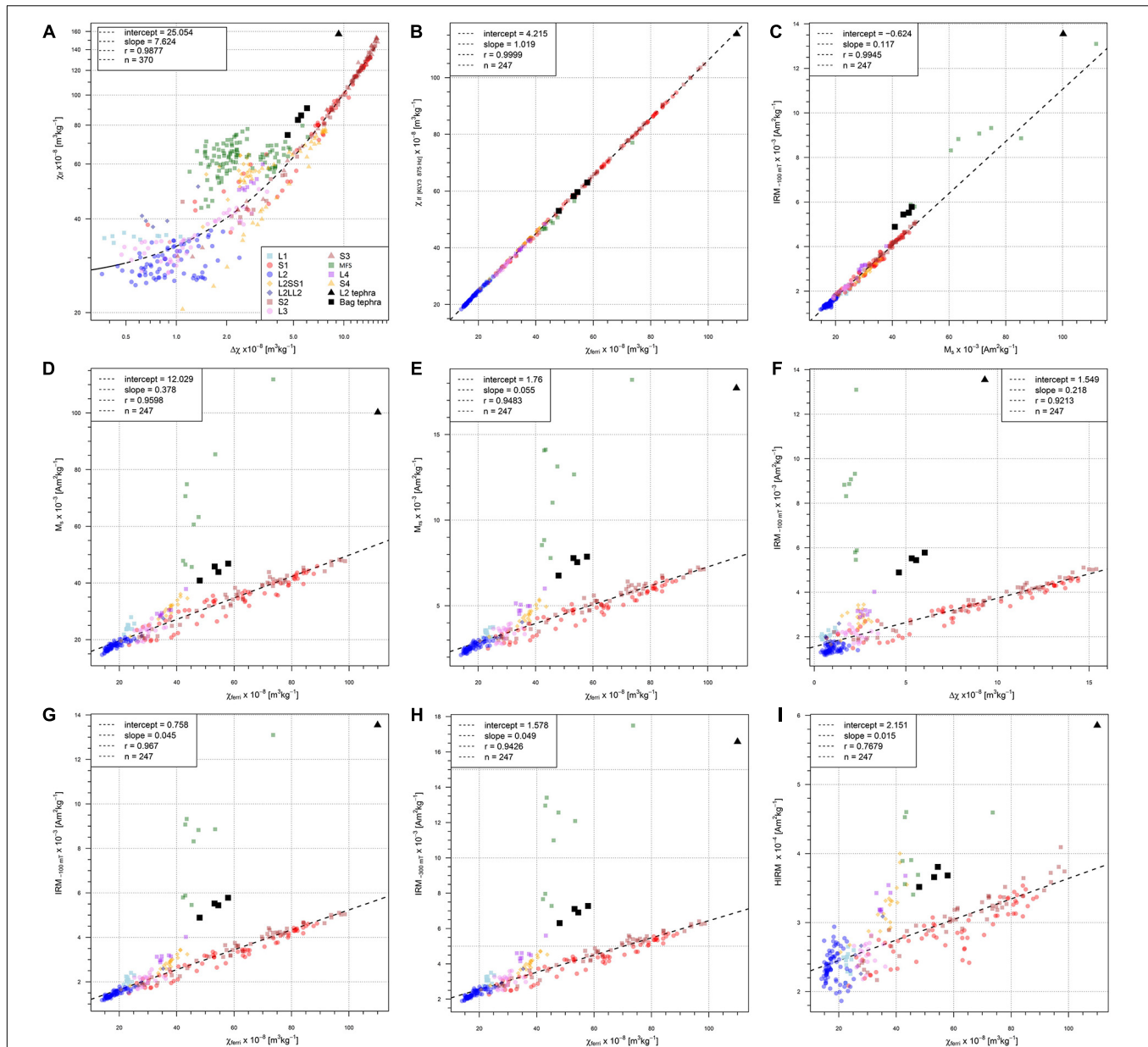
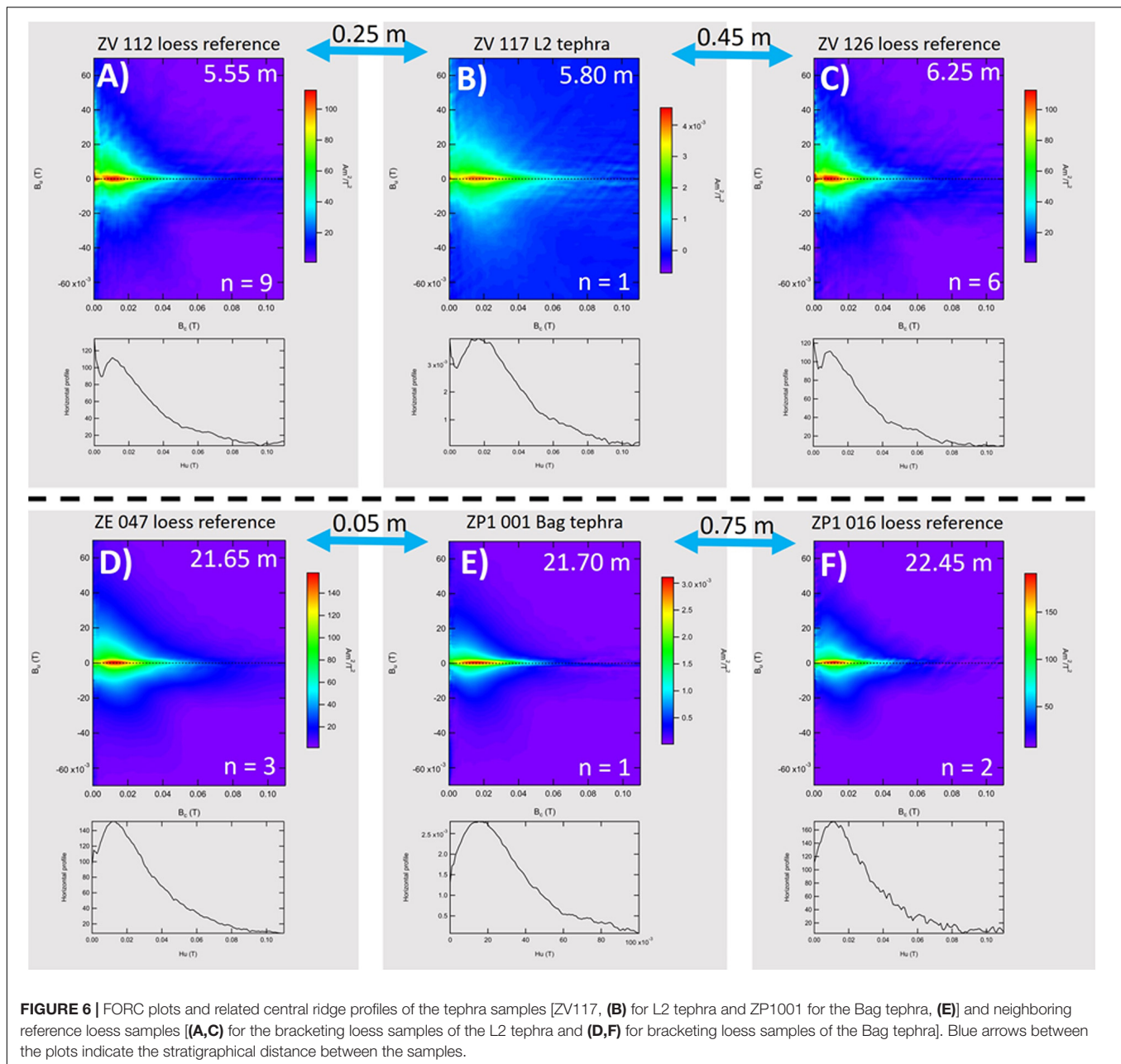


**FIGURE 5** | Scatterplots of environmental magnetic data. Low frequency susceptibility ( $\chi_{lf}$ ) plotted against  $\Delta\chi$  in **(A)** shows the characteristics of magnetic enhancement for the Zemun LPS. Samples stemming from the MFS (marshy floodplain sediments) and the tephra layers are excluded for calculated regression fit and correlation coefficient, resulting in 370 samples out of a total of 479 for **(A)** and 247 samples out of a total of 262 for **(B–I)**.

S3, the correlation of  $L^*$  with the stratigraphy is more complex. The pedocomplex S4 is weakly expressed in the Zemun LPS characterized by a broad range of  $L^*$  values. S4 can be considered as brighter than the other pedocomplexes with brightest values in the lower part at the base of the profile, possibly as a result of carbonate precipitation.

Similar to luminance ( $L^*$ ) values, redness values ( $a^*$ ) also reflect alternations between loess and paleosols (**Figure 3**). However, a clear separation between loess and paleosols is not as obvious for all paleosols from  $a^*$  data. In the L1 loess unit,  $a^*$  values vary between 3.2 and 4.2. Compared to the mean  $a^*$  from

the S1 pedocomplex, redness is reduced in L1 (3.8, in S1 4.4). The mean  $a^*$  of L3 is similar to L2 (4.2) and relatively low with respect to S1. Higher  $a^*$  values are reached in the S3 pedocomplex (mean = 5.7), but the highest  $a^*$  values are reached in the S4 pedocomplex with a mean of 5.8 and a maximum of 6.6. Over the entire profile, a decreasing trend from S4 to S1 samples can be observed with even lower  $a^*$  values for the weakly developed interstadial L2SS1 paleosol. Blueness ( $b^*$ ) values, which are inverse to yellow, are generally low in paleosols and high in loess units. The lowest  $b^*$  values are found in the pedocomplex S1 and the highest  $b^*$  values in the S4 pedocomplex. However, the



pedocomplex S2 (compared to the other pedocomplexes) does not show these well-expressed low values of  $b^*$ . In summary,  $a^*$ , a commonly used pedogenic indicator suggest the highest intensity of pedogenesis is found in S4 which contradicts interpretations based on magnetic proxies and field observations.

DRS derived goethite- and hematite concentrations (1st derivatives of intensities at 435 and 565 nm;  $I_{435}$  and  $I_{565}$ ) and the ratio of hematite to goethite (HGR) mainly follow glacial/interglacial cyclicity. Both  $I_{435}$  nm and  $I_{565}$  nm values are reduced in paleosol complexes and are high in loess units with the exception of S4, which has values characteristic of the loess units (**Table 4**). HGR values are maximum in paleosols and like magnetic susceptibility parameters decrease from S3 to S1.

Luminance ( $L^*$ ) and redness ( $a^*$ ) correlate with  $r \sim -0.3$ , while  $L^*$  and blueness ( $b^*$ ) correlate positively with  $r \sim 0.78$ . HGR correlates with  $L^*$  with  $r \sim -0.82$ , with  $a^*$   $r \sim 0.76$ , and  $b^*$  with  $r \sim -0.5$ .

Additionally, selected colorimetric parameters are tested against magnetic indicators of relative concentration of SP-particles ( $\Delta\chi$  and  $\chi_{ferri}/Ms$ ) and of high-coercive minerals (Hcr and S-ratio) (**Figure 8**). In **Figures 8A–C** test the correlation of  $\Delta\chi$  vs.  $I_{435}$ ,  $I_{565}$  and HGR.  $I_{435}$  correlates strongly negative with  $\Delta\chi$  ( $r = -0.92$ ), indicating a higher amount of goethite in loess units than paleosol units. A weaker but still present negative correlation to  $I_{565}$  ( $r = -0.54$ ) indicates a higher amount of hematite in loess units as well. A strong and positive



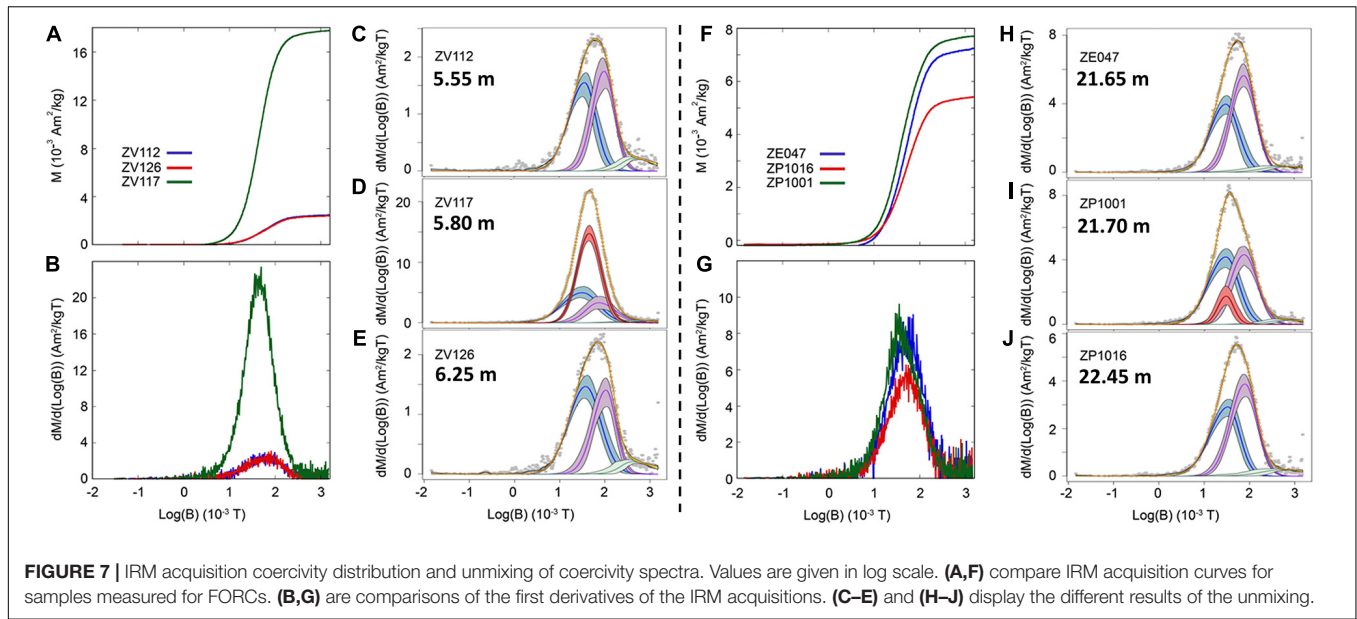


**FIGURE 7** | IRM acquisition coercivity distribution and unmixing of coercivity spectra. Values are given in log scale. **(A,F)** compare IRM acquisition curves for samples measured for FORCs. **(B,G)** are comparisons of the first derivatives of the IRM acquisitions. **(C–E)** and **(H–J)** display the different results of the unmixing.

**TABLE 4** | Summary of colorimetric parameters. HGR is the calculated hematite/goethite ratio.

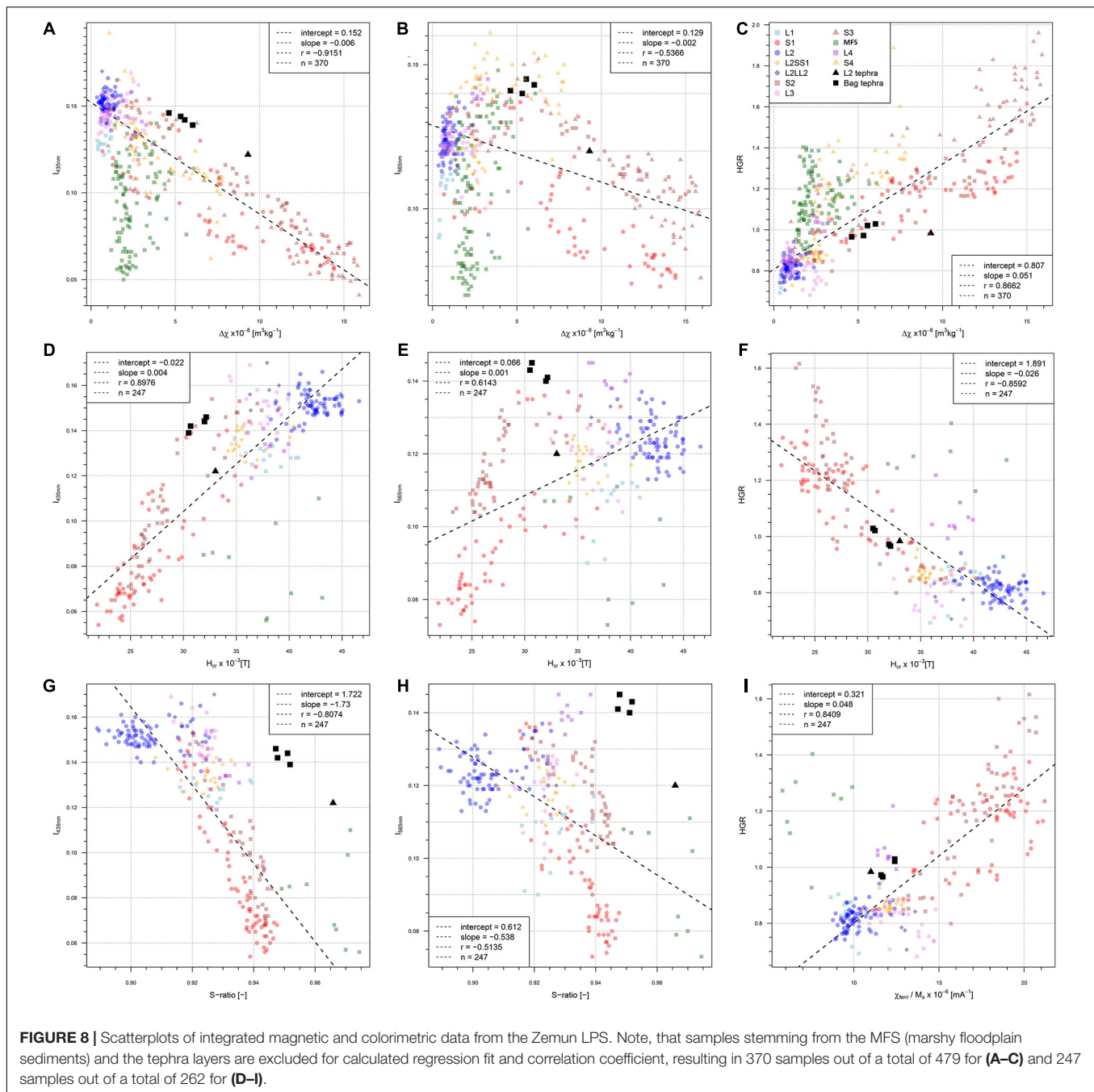
Unit	n	L*			a*			b*			I <sub>435</sub> nm			I <sub>565</sub> nm			HGR		
		Min	Max	Mean	Min	Max	Mean	Min	Max	Mean	Min	Max	Mean	Min	Max	Mean	Min	Max	Mean
L1	12	63.87	65.47	64.60	3.220	4.220	3.832	13.88	15.62	14.85	0.1220	0.1330	0.1281	0.0900	0.1170	0.1061	0.6923	0.9032	0.8285
S1	60	54.31	67.98	59.80	3.560	4.970	4.402	10.01	16.86	12.66	0.0540	0.1530	0.08835	0.07300	0.13700	0.09708	0.8362	1.3750	1.1395
L2	74	65.11	69.38	67.49	3.570	4.690	4.057	14.89	17.47	16.12	0.1360	0.1660	0.1514	0.1130	0.1370	0.1237	0.7419	0.9412	0.8177
L2SS1	20	65.68	68.56	66.79	3.830	4.560	4.061	14.17	15.70	15.16	0.1260	0.1430	0.1353	0.1090	0.1250	0.1177	0.8429	0.9542	0.8703
L2LL1	5	68.50	72.49	70.42	3.280	4.090	3.726	14.31	15.56	15.00	0.1490	0.1700	0.1586	0.1170	0.1330	0.1248	0.7059	0.8418	0.7882
S2	48	56.46	71.43	62.78	3.740	5.760	5.008	12.67	16.04	14.12	0.06500	0.15400	0.10283	0.1030	0.1340	0.1183	0.7987	1.6154	1.2022
L3	51	65.37	72.24	67.72	2.980	4.780	4.072	13.71	16.84	15.42	0.1340	0.1690	0.1471	0.1000	0.1330	0.1216	0.6815	0.9366	0.8283
S3	50	50.81	67.70	58.66	4.760	6.340	5.635	10.25	17.22	14.02	0.04100	0.14800	0.08246	0.07600	0.15200	0.11432	0.9122	1.9600	1.4843
MFS	103	52.49	66.39	59.17	3.680	6.070	4.726	10.28	17.85	14.08	0.05000	0.14000	0.09303	0.0700	0.1480	0.1041	0.8911	1.4035	1.1421
L4	8	64.04	67.24	66.12	4.960	5.840	5.201	16.19	17.01	16.42	0.1190	0.1410	0.1331	0.1380	0.1450	0.1409	0.9929	1.2185	1.0610
S4	42	56.07	72.26	64.09	3.950	6.590	5.791	13.57	18.36	16.40	0.0620	0.1920	0.1193	0.1170	0.1610	0.1442	0.7292	1.8871	1.2460
L2	1	64.00			4.87			17.1			0.122			0.12			0.9836		
tephra																			
Bag	4	67.23	67.96	67.63	4.860	5.130	5.013	16.30	16.68	16.57	0.1390	0.1460	0.1427	0.1400	0.1450	0.1422	0.9658	1.0288	0.9970
tephra																			

correlation of  $\Delta\chi$  with HGR ( $r = 0.87$ ) reflects a relatively higher amount of hematite than goethite in paleosol samples. This is supported by correlations based on magnetic indicators for hard magnetic minerals like hematite and goethite (high Hcr and low S-ratio values) for loess samples reflecting positive correlations for hematite and goethite and a negative correlation with HGR. This underlines the presence of hematite and goethite in loess samples and a relatively higher presence of hematite compared to goethite in paleosol samples. Overall, the variation of HGR and  $I_{565}$  is high in paleosols and low in loess units.  $I_{435}$  varies distinctively less in loess and paleosol samples. The luminance  $L^*$  reflects toward younger samples a continuous evolution of brighter paleosols, where the S3 is the darkest (Figure 3).  $a^*$  decreases as well, even more than  $L^*$ , for all paleosols from S4 to S1 (Figure 3). With respect to the hematite/goethite ratio (HGR),

the decreasing trend is most obvious. While there is a general increase of the colorimetric properties with increasing  $\Delta\chi$ , these are clearly non-linear.

## Age Model

The age model (Figure 9) was constructed based on 15 tie-points listed in Table 1 and shown as dotted lines in Figure 10. Thirteen tie-points are based on synchronizing variations in  $\Delta\chi$  and benthic  $\delta^{18}\text{O}$  values from the LR04 stack (Lisiecki and Raymo, 2005). In total, fifteen tie-points were used including the two identified tephra layers (L2 and Bag tephra). Two additional tie-points correspond to tephra layers demonstrated to be present based on magnetic properties presented in sections “Magnetic Susceptibility Parameters and Stratigraphical Assignment” through “High Resolution IRM Acquisition”,

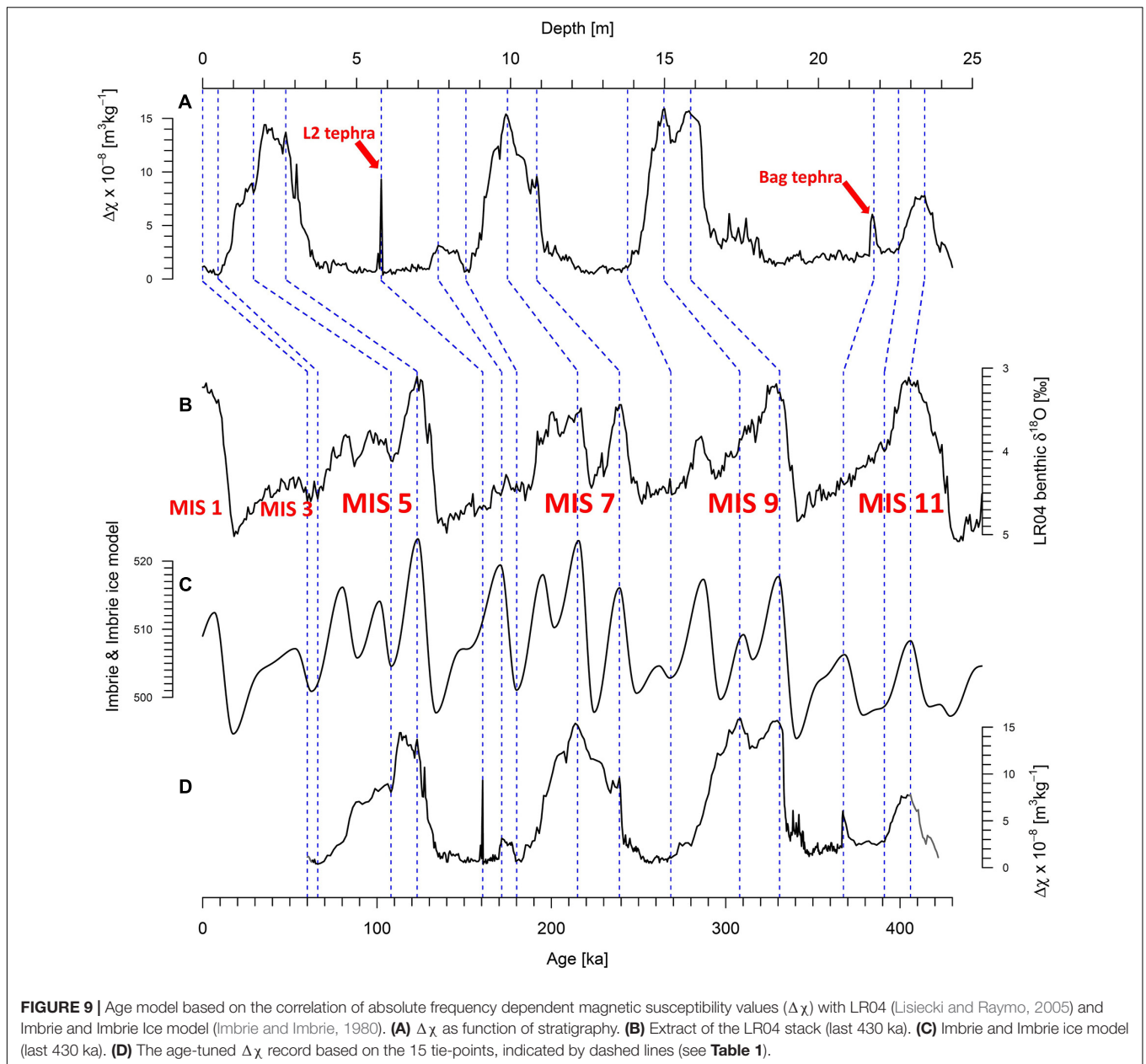


especially evidenced by FORC analysis and IRM unmixing, and compatible with field-based sedimentological observations described in section “Profile Setting and Stratigraphy”.

The L2 tephra is a widespread tephra occurrence within southeastern European loess records (Laag et al., 2018; Avram et al., 2020). Based on its stratigraphic position in several other well-dated profiles, like the neighboring Batajnica LPS (Avram et al., 2020), and the Harletz LPS in Bulgaria (Antoine et al., 2019), the L2 tephra can potentially be correlated to the Vico-Ignimbrite B eruption, dated to  $160.6 \pm 2.0$  ka (Mannella et al., 2019). However, uncertainty remains with the age assignment, because

(1) no geochemical evidence is to our knowledge available to trace back the L2 tephra to a specific eruption and (2) the archives of Lake Ohrid (Wagner et al., 2019) and Fucino Basin (Leicher et al., 2016; Giaccio et al., 2017, 2019) exhibit several prominent tephra layers during MIS 6, which may be assigned to the L2 tephra with ages spanning 150–168 ka. For the present study, we anchored the L2 tephra at 160.6 ka (Table 1) following the hypothesis of a correlation with the Vico-Ignimbrite B eruption and the age provided by Mannella et al. (2019).

The Bag tephra, demonstrated to be contained in the Zemun LPS in 4 samples between 21.85 and 21.70 m depth, has been



associated elsewhere to an eruption originating from the Alban Hill Volcanic region and dated to 350–360 ka (Poulet et al., 1999; Marković et al., 2015). A corresponding tephra layer can be found in the Fucino Basin record (TF-85), which is dated to  $367 \pm 1.6$  ka (Marra et al., 2009, 2019; Giaccio et al., 2012) and thought to originate from the Colli Albani Villa Senni eruption (Marković et al., 2015). We tentatively use this age estimate for the tie-point represented by the Bag tephra at Zemun (**Table 1** and **Figure 9**).

Attempts to extrapolated ages for samples depths above and below the youngest and oldest tie-points lead to an age of 50 ka corresponding to MIS 3 interglacial, which is not contained in the Zemun LPS and therefore too young for the top of the profile. Based on magnetic susceptibility variations, the loess at the top of the profile was likely deposited during the early MIS 4 (~60 ka).

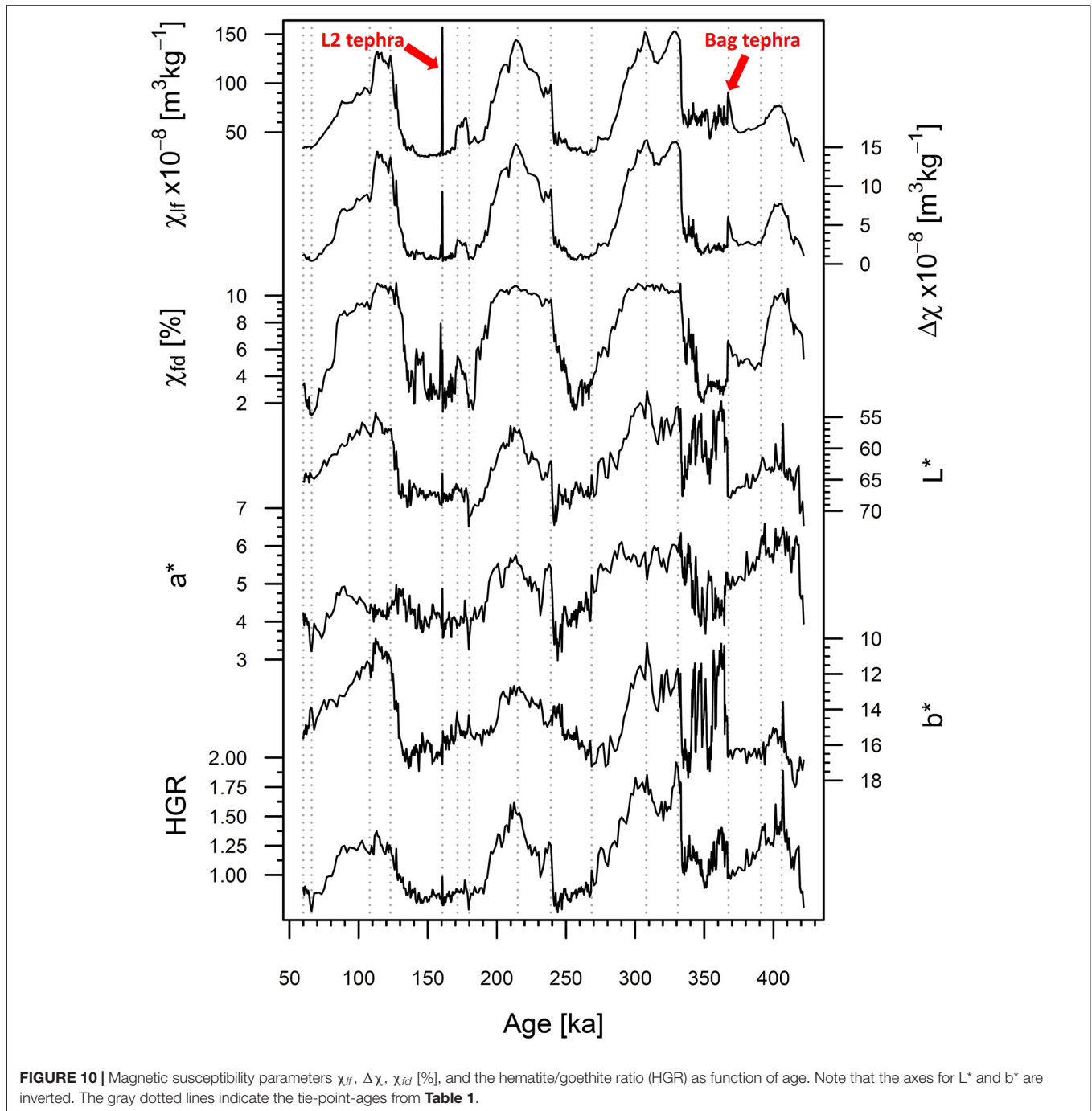
The uncertainty in age extrapolation at the base of the profile is highlighted by the gray shading in **Figure 9**.

## DISCUSSION

### Integrated Stratigraphy

The Zemun LPS comprises four interglacial paleosol complexes, S4 (Cambisol), S3 (forest-steppe soil), and S2 and S1, both considered as steppe soils (Marković et al., 2011; Obrecht et al., 2016). Our correlative age model (**Figure 9**) suggests that the Zemun loess profile covers the time interval from MIS 11 to MIS 5/4, which is additionally constrained by the identification of two widespread tephra layers of known stratigraphic position within





other Danube loess sequences (Marković et al., 2015, 2018). However, the selected correlative tie-points (**Table 1**) include the tephra layers, but do not account for the colorimetric data. The general stratigraphy of loess and intercalated paleosols at the Zemun LPS is in good agreement with independently dated records in the southern MDB, based on luminescence dating and paleomagnetism (Marković et al., 2009, 2011, 2015; Basarin et al., 2014; Song et al., 2018; Avram et al., 2020). It is noteworthy, that uncertainties of the direct correlation of  $\Delta\chi$  to the LR04 stack exist (Zeeden et al., 2018), mainly because of uncertainty in the

exact position of tie points and correlation targets. The stacked LR04 record provides ages for the last 1 Ma with 4 kyr uncertainty (Lisiecki and Raymo, 2005).

The fluvial sediment facies (MFS unit) below S3 is widespread in the southern MDB and is interpreted as an intercalation of marshy floodplain sediments (MFS) consisting of an alternation of sandy iron-stained and sandy-silty beds with dark humus rich partly clayey beds (e.g., Marković-Marjanović, 1970; Gaudenyi et al., 2015). The MFS unit represents overbank deposits of a river system flowing through a steppe/forest steppe landscape laterally

interfingering with aeolian loess. They probably represent relatively short-term intervals of aquatic deposits formed after prominent flooding events. The loess unit L4 in which the MFS are intercalated measures  $\sim 1.1$  m at the neighboring section Batajnica (Marković et al., 2009) and is generally relatively thin in the entire MDB (Marković et al., 2015) and across Eurasia (Song et al., 2018).

Magnetic susceptibility parameters of the Zemun LPS convincingly track the environmental impact of interglacials and glacials during the Middle to Late Pleistocene (Figure 9). All four paleosols (S4–S1) are characterized by elevated values of  $\chi_{lf}$ ,  $\Delta\chi$ , and  $\chi_{fd}$  indicative of higher concentration of magnetic minerals and specifically superparamagnetic particles formed *in-situ* during pedogenesis (Maher and Taylor, 1988). Based on  $\chi_{lf}$ ,  $\Delta\chi$  and  $\chi_{fd}$  parameters, the intensity of pedogenesis increases from S4 (MIS 11) to S1 (MIS 5), to S2 (MIS 7) to S3 (MIS 9).

Colorimetric parameters are used to quantify hematite and goethite (e.g., Scheinost, 1998). The assumption that the HGR reflects changes in goethite remains questionable. Studies from Liu et al. (2008) and Jiang et al. (2018) show that goethite does not play a crucial role for LPS and additionally the process of the neo-formation of goethite is different from processes related to pedogenesis. In contrary, Bilardello et al. (2020) demonstrate in their experimental simulations that a simultaneous neoformation of goethite, hematite and magnetite is possible, and they add further evidence that biogeochemical conditions are a key-controller of the proportions of the neo-formed minerals. Our good correlation of magnetic parameters (Figure 8) like the S-ratio and remanence of coercivity (indicating the presence of hard magnetic minerals) with 1st derivative intensity band values for goethite ( $I_{435\text{ nm}}$ ) indicate the presence of goethite. However, the good correlation of HGR with the pedogenesis indicators ( $\chi_{ferri}/M_s$  and  $\Delta\chi$ ) indicates an overall higher presence of hematite over goethite in the paleosols of the Zemun LPS. This said, the magnetic experiments conducted in the present study do not readily permit the identification of goethite, which is facilitated in low-temperature magnetic experiments (e.g., Lagroix and Guyodo, 2017). Following that, we consider for the Zemun LPS, that the HGR can reflect changes in goethite and/or hematite. Our quantitative colorimetric data show variations that are related to the different soil types. S3, the forest-steppe soil and the most mature paleosol based on magnetic susceptibility parameters and  $\chi_{ferri}/M_s$  has the lowest luminance, which would result from high amounts of mineralized organic matter. With decreasing precipitation, the predominant soils are chernozems, which are represented by S1 and S2. Cambisols are brighter, which is reflected by S4 and its increased luminance ( $L^*$ ).

## Paleoclimatic Implications for the Zemun LPS

The stratigraphic interpretations of both rock magnetic and colorimetric data in combination with the correlative age model provide insights into the environmental evolution of the southern Middle Danube Basin for the last 430 kyr.

All susceptibility parameters ( $\chi_{lf}$ ,  $\Delta\chi$ , and  $\chi_{fd}$  [%]) reflect large and quasi-cyclic fluctuations, generally recording changes

between warm and humid (interglacial), and cool and dry (glacial) conditions (Figure 10). Remarkably, for MIS 9 (paleosol S3) to MIS 5 (paleosol S1) the susceptibility parameters show a similar range of amplitude, whereas in MIS 11 (paleosol S4)  $\Delta\chi$  and  $\chi_{lf}$  are only weakly expressed. For S4, however, the amplitudes of  $\chi_{fd}$  [%] are comparable with S1–S3.

This would suggest that for S4 the intensity of pedogenesis was weaker compared to S3–S1, which is not supported by the general pedogenetic trend in the MDB and Western Eurasia (e.g., Marković et al., 2015, and references therein). Colorimetric data of redness ( $a^*$ ), an indicator for weathering intensity (Yang and Ding, 2003), leads to the opposite conclusion. The  $a^*$  parameter is highest in S4 paleosol (Table 4) suggesting it has the highest intensity of pedogenesis, which is in line with the general paleoenvironmental evolution in the Eurasian loess belt (e.g., Buggle et al., 2013, 2014) and our pedologic interpretation. Both  $I_{435\text{ nm}}$  and  $I_{565\text{ nm}}$  1st derivative intensities are highest in S4 (Figure 8) shows that both high coercivity goethite and hematite are important mineral components in S4. Both are magnetically weak, with mass specific magnetic susceptibilities 3–4 orders of magnitude less than magnetite and maghemite (Hunt et al., 1995). While the absolute concentration of SP particles in S4 is half that of S1 and one third of S3,  $\chi_{fd}$  varies significantly less being 8.2% for S4, 8.9% for S1 and 9.8% for S3 (Table 2). The lower  $\chi_{lf}$  and  $\Delta\chi$  for S4 may simply result from the mineralogy of the neo-formed pedogenic iron mineral, paleoclimate and local biogeochemical conditions favored the formation of hematite and goethite or at least their preservation.

Progressively reduced precipitation and temperature characterize the general climatic trend over the last 430 kyr at Zemun when considering the colorimetric data, gradually leading to more arid climate conditions. A fundamental factor for reduced weathering intensity, indicated by decreasing  $a^*$  values, may be the general aridification as proposed by Marković et al. (2009) and Buggle et al. (2013) for the Middle and Lower Danube Basins. Buggle et al. (2013) proposed the progressive uplift of the Carpathians, Dinarides, and Eastern Alps during the Pleistocene as main cause of this of the aridification trend.

Since, at Zemun, magnetic susceptibility is dominated by ferrimagnetic minerals, maghemite and magnetite (Figure 5B), and colorimetric analyses by hematite, an integrative view of the results from both methods is needed and beneficial. Regarding the formation of magnetite in LPS, the preferred climatic conditions are seasonally alternating wet (reducing) and dry (oxidizing) conditions controlling pedogenetic processes subsequently leading to higher susceptibilities (Maher, 1998). Differences in relative amounts of maghemite and hematite are probably caused by distinct characteristics and seasonality of climatic periods (Maher, 2011). A climate characterized by warm and dry summers in combination with mild and humid winters leads to relatively higher amounts of hematite (Balsam et al., 2004; Liu et al., 2008; Jiang et al., 2018). The interpretation of our results are in good agreement with interpretations from other studies focusing on the Lower and Middle Danube Basin (Buggle et al., 2013, 2014). With regard to the paleosols, a decreasing HGR is associated with a lower seasonality of precipitation and/or a reduction of temperature (Balsam et al., 2004). Based on our

results, we assign HGR as an index for increased heat and dryness during estival periods. With respect to the susceptibility parameters, in interglacial periods the mean precipitation over the year cannot be that different. A similar trend from MIS 9 to MIS 5 is reported by Obreht et al. (2016) from the Stalać LPS, who interpret this as changing influence of different climate systems over western Eurasia.

## Comparison of the Zemun LPS With Titel-Stari Slankamen and Luochuan

Thick loess-paleosols sequences are spread over the northern hemisphere, located in different geomorphological settings which are influenced by diverse prevailing climate regimes (see Schaetzl et al., 2018; Lehmkuhl et al., 2021). To detect similarities and differences in magnetic and colorimetric properties conserved in loess-paleosol sequences, we compare the Zemun LPS with two well-known reference profiles. The Titel-Stari Slankamen LPS (Serbia) covers the last million years and the interval from MIS 11 to present is archived in c. 38 m.

The Luochuan record from the CLP (Hao et al., 2012) covers approximately the last 1.1 million years and the interval MIS 11 to present in c. 30 m of loess/paleosol couplets. For comparison, the low-frequency magnetic susceptibility data (the only data set available for all three LPSs) are shown on an age scale (Figure 11). Generally, the Zemun LPS's long-term  $\chi_{lf}$  variability reflecting interglacial/glacial alternations are in excellent agreement with Titel-Stari Slankamen and Luochuan, even though the latter is located in a monsoon prevailing climate. Indeed, it is well known that different prevailing climate regimes and primary sediment sources affect the  $\chi_{lf}$  values (Maher, 2016; Schaetzl et al., 2018), which are nearly 60% higher in Luochuan than in the both Serbian LPSs. More than doubled  $\Delta\chi$  values in Luochuan compared to Titel-Stari Slankamen (Song et al., 2018) and Zemun indicate that the neo-formation of magnetite/maghemite SP particles during pedogenesis was enhanced at Luochuan, potentially due to more moisture during interglacials. The S4 paleosol at Titel-Stari Slankamen and Zemun shows compared to the S3 paleosol – less prominent values for  $\chi_{lf}$  and  $\Delta\chi$  (Figure 11). In all records, the S3 paleosol appears in the  $\chi_{lf}$  data as a double peak. The timing of onset and demise of the corresponding interglacial MIS 9 (S3) is in better agreement between Zemun and Luochuan than between Zemun and Titel-Stari Slankamen. Variations in  $\chi_{lf}$  for paleosol S2 (MIS 7) are similar for both Zemun and Titel-Stari Slankamen, but the  $\chi_{lf}$  values are 2–3 times higher at Zemun. The S2 pedocomplex at Luochuan displays a clear three folded paleosol based on  $\chi_{lf}$ . Song et al. (2018) correlated the two older paleosols of MIS 7 with the S2 and L2SS1 horizons at Titel-Stari Slankamen. However, comparing Zemun and Titel-Stari Slankamen, a correlation of the S2 pedocomplex with the older two paleosols of Luochuan and a further correlation of the Zemun L2SS1 with the youngest MIS 7 paleosol seems more plausible. Similar to Titel-Stari Slankamen, the S1 of Zemun shows two pedogenetic horizons, a lower strongly expressed paleosol, and a younger, weakly expressed paleosol. This feature is also observable in Titel-Stari Slankamen but differently expressed in Luochuan, where the pedogenic

intensity remains fairly constant throughout the S1 pedocomplex. Age differences for the onsets and demises of the paleosols might result from the applied dating techniques. For Zemun, the correlative age model is based on fluctuation in  $\Delta\chi$  and two tephra marker horizons. For Titel-Stari Slankamen, composite record ages were provided by tuning with aid of an astronomical target, correlating peaks in  $\chi_{lf}$  with June perihelia (Basarin et al., 2014). Ages for the Luochuan LPS were determined by direct correlations of the fluctuations in  $\chi_{lf}$  and isotopic data from deep-sea sediments (Ding et al., 2002a; Sun et al., 2006).

## Tephra Layers as Widespread Marker Horizons Using Magnetic Proxies to Highlight the Presence of Tephra Layers in Loess

In tephrochronology (Lowe, 2011) ash layers of known age and origin can be used as reliable dating tools and correlation targets. This approach plays an increasingly important role in Quaternary stratigraphy (see Abbott et al., 2020 and references therein) as for example, the accuracy of luminescence numerical dating, the choice of method of dating the emplacement time of loess deposits is still impacted by many limiting factors such as large offsets between the different methods currently applied on the same sample (Avram et al., 2020), or even between different grain-size aliquots (e.g., Timar-Gabor et al., 2011; Veres et al., 2018). The most prominent tephra layer preserved in Eastern European loess and archeological deposits is the Campanian Ignimbrite/Y5 tephra (Veres et al., 2013; Giaccio et al., 2017). Dated to c. 40 ka BP, it provides an exceptional tie-point for linking records within MIS 3 and in testing the accuracy of luminescence and radiocarbon dating for loess records (Constantin et al., 2012; Fitzsimmons et al., 2013; Anecitei-Deacu et al., 2014; Obreht et al., 2016, 2017; Scheidt et al., 2021). However, several more tephra layers have been identified in south-eastern European loess profiles (see Marković et al., 2015, 2018) which, if well assessed, not only chronologically but also by their bulk sediment geochemical (see Pötter et al., 2021) and magnetic properties (this work) may serve as important anchor points for more secure lateral stratigraphic correlations (Zeeden et al., 2018). At present, glass shard geochemical data are not available for the two tephra layers identified at Zemun (and elsewhere in the wider region) because all attempts of geochemical fingerprinting have failed due to the strong weathering and alteration of the volcanic products.

Indeed, our integrated approach combining high-resolution FORC analysis and IRM unmixing provide magnetic evidence for the presence of volcanogenic material not only for the L2 tephra, but also for the Bag tephra (Figures 6, 7). Both ZV 117 (L2 tephra) and ZP1 001 (Bag tephra) samples are characterized by a higher relative content of SD and PSD grains than the bracketing loess as well as a distinctive coercivity distribution not present in the bracketing loess. As most volcanic ashes identified in European loess units are mixed with loess or occur as cryptotephra, our approach may provide an excellent screening potential for assessing the tephrostratigraphic potential of loess records beyond the classical glass-shard geochemical analyses.

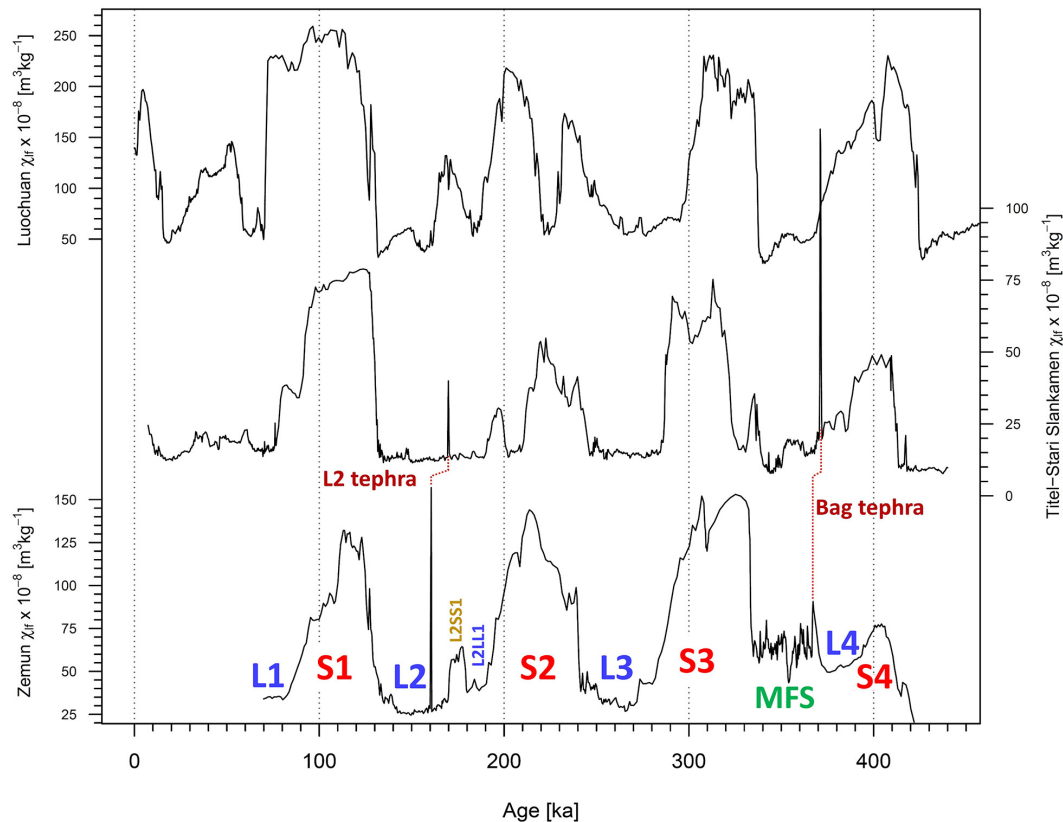


**FIGURE 11** | Comparison of the  $\chi_{Hf}$  record from the LPS at Zemun, Titel-Stari Slankamen, and Luochuan on their individual age scales. Note the very similar chronostratigraphic depiction of the potential tephra layers at Zemun and Titel-Stari Slankamen. Differences in onsets and demises of different paleosol units may result from different age models and applied indirect (correlative) dating. Details are discussed in the text.

## CONCLUSION AND SUMMARY

In this study, we present a new high-resolution loess-paleosol paleoclimate record from the Middle Danube Basin based on the application of environmental magnetic and colorimetric techniques for the last four-interglacial-to-glacial cycles spanning from MIS 11 to MIS 4. Data stemming from the S2 pedocomplex reveals different stages of environmental change during an interglacial, reflected by different coercivities, magnetic grain sizes, and different magnetic mineralogies. The combination of rock-magnetic and colorimetric data for the Zemun loess profile confirms the proposed aridification trend by Marković et al. (2009), Buggle et al. (2013), and Obrecht et al. (2016). Furthermore, our HGR dataset indicates a general decreasing summer heat or dryness over the last 430 kyr in the Middle Danube Basin. Our study shows tracking only the soft ferrimagnetic (magnetite/maghemite) content may not provide a clear interpretation of changes in pedogenic intensity between interglacials, and that colorimetric data, providing insight into hematite and goethite content (high coercivity minerals) in addition are important for reconstructing summer conditions in addition to mean annual soil moisture. For loess samples stemming from the younger L3, L2, and L1 units, both hysteresis data and colorimetric data provide evidence for higher relative concentrations of high-coercivity magnetic minerals (like

hematite and goethite) than in paleosols. The hematite/goethite ratio reflects a relatively higher amount of hematite compared to goethite in paleosol layers. Additionally, the investigation and comparison of FORC and highly resolved IRM acquisitions of potentially tephra bearing and pure loess samples provides further evidence of the deposition of volcanic ashes. Even when volcanic glass shards are too weathered for geochemical investigations, the remaining magnetic signal (increased PSD and SD particles in combination with reduced magnetic interactions) can be clearly identified and used as individual anchor points for future comparison and stratigraphy in the MDB and beyond.

## DATA AVAILABILITY STATEMENT

The original contributions presented in the study are included in the article/**Supplementary Material**, further inquiries can be directed to the corresponding author/s.

## AUTHOR CONTRIBUTIONS

CL, UH, and SM designed the study. CL measured all magnetic and parts of the colorimetric parameters, did the data analysis and interpretation with close advice from CZ, FL, YG, DV, and



UH, and programmed all analytical R-scripts for this study. MJ conducted the sampling. CL, UH, CZ, FL, DV, and YG wrote the manuscript with close advice from all co-authors. All authors contributed significantly to the article.

## ACKNOWLEDGMENTS

We want to thank the Zemun sampling team. We want to thank Kathrin Worm (LIAG Grubenhagen) for the additional colorimetric measurements and Eva Meier (University of

Bayreuth) for language improvements of this manuscript. DV was supported through a fellowship provided by Alexander von Humboldt Foundation. All data will be made available on the Pangaea Data Repository. This is IPGP contribution 4210.

## SUPPLEMENTARY MATERIAL

The Supplementary Material for this article can be found online at: <https://www.frontiersin.org/articles/10.3389/feart.2021.600086/full#supplementary-material>

## REFERENCES

- Abbott, P. M., Jensen, B. J. L., Lowe, D. J., Suzuki, T., and Veres, D. (2020). Crossing new frontiers: extending tephrochronology as a global geoscientific research tool. *J. Quat. Sci.* 35, 1–8. doi: 10.1002/jqs.3184
- Abe-Ouchi, A., Saito, F., Kawamura, K., Raymo, M. E., Okuno, J., Takahashi, K., et al. (2013). Insolation-driven 100,000-year glacial cycles and hysteresis of ice-sheet volume. *Nature* 500, 190–193. doi: 10.1038/nature12374
- Anechitei-Deacu, V., Timar-Gabor, A., Fitzsimmons, K., Veres, D., and Hambach, U. (2014). Multi-method luminescence investigations on quartz grains of different sizes extracted from a loess section in Southeast Romania interbedding the Campanian Ignimbrite ash layer. *Geochronometria* 41, 1–14. doi: 10.2478/s13386-013-0143-4
- Antoine, P., Lacroix, F., Jordanova, D., Jordanova, N., Lomax, J., Fuchs, M., et al. (2019). A remarkable Late Saalian (MIS 6) loess (dust) accumulation in the Lower Danube at Harletz (Bulgaria). *Quat. Sci. Rev.* 207, 80–100. doi: 10.1016/j.quascirev.2019.01.005
- Avram, A., Constantin, D., Veres, D., Kelemen, S., Obrecht, I., Hambach, U., et al. (2020). Testing polymineral post-IR IRSL and quartz SAR-OSL protocols on Middle to Late Pleistocene loess at Batajnica, Serbia. *Boreas* 49, 615–633. doi: 10.1111/bor.12442
- Balsam, W., Ji, J., and Chen, J. (2004). Climatic interpretation of the Luochuan and Lingtai loess sections, China, based on changing iron oxide mineralogy and magnetic susceptibility. *Earth Planet. Sci. Lett.* 223, 335–348. doi: 10.1016/j.epsl.2004.04.023
- Barranco, F. T., Balsam, W. L., and Deaton, B. C. (1989). Quantitative reassessment of brick red lutites: evidence from reflectance spectrophotometry. *Mar. Geol.* 89, 299–314. doi: 10.1016/0025-3227(89)90082-0
- Basarin, B., Bugge, B., Hambach, U., Marković, S. B., Dhand, K. O., Kovačević, A., et al. (2014). Time-scale and astronomical forcing of Serbian loess-paleosol sequences. *Glob. Planet. Change* 122, 89–106. doi: 10.1016/j.gloplacha.2014.08.007
- Bilardello, D., Banerjee, S. K., Volk, M. W. R., Soltis, J. A., and Penn, R. L. (2020). Simulation of natural iron oxide alteration in soil: conversion of synthetic ferrihydrite to hematite without artificial dopants, observed with magnetic methods. *Geochem. Geophys. Geosyst.* 21:e2020GC009037. doi: 10.1029/2020GC009037
- Bugge, B., Hambach, U., Kehl, M., Markovic, S. B., Zoller, L., and Glaser, B. (2013). The progressive evolution of a continental climate in southeast-central European lowlands during the Middle Pleistocene recorded in loess paleosol sequences. *Geology* 41, 771–774. doi: 10.1130/G34198.1
- Bugge, B., Hambach, U., Müller, K., Zöller, L., Marković, S. B., and Glaser, B. (2014). Iron mineralogical proxies and Quaternary climate change in SE-European loess-paleosol sequences. *CATENA* 117, 4–22. doi: 10.1016/j.catena.2013.06.012
- Constantin, D., Timar-Gabor, A., Veres, D., Begy, R., and Cosma, C. (2012). SAR-OSL dating of different grain-sized quartz from a sedimentary section in southern Romania interbedding the Campanian Ignimbrite/Y5 ash layer. *Quat. Geochronol.* 10, 81–86. doi: 10.1016/j.quageo.2012.01.012
- Day, R., Fuller, M., and Schmidt, V. A. (1977). Hysteresis properties of titanomagnetites: grain size and composition dependence. *Phys. Earth Planet. Interiors* 13, 260–267.
- Dearing, J. A., Dann, R. J. L., Hay, K., Lees, J. A., Loveland, P. J., Maher, B. A., et al. (1996). Frequency-dependent susceptibility measurements of environmental materials. *Geophys. J. Int.* 124, 228–240. doi: 10.1111/j.1365-246X.1996.tb06366.x
- Deaton, B. C., and Balsam, W. L. (1991). Visible spectroscopy; a rapid method for determining hematite and goethite concentration in geological materials. *J. Sediment. Res.* 61, 628–632. doi: 10.1306/D4267794-2B26-11D7-8648000102C1865D
- Debret, M., Sebag, D., Desmet, M., Balsam, W., Copard, Y., Mourier, B., et al. (2011). Spectrocolorimetric interpretation of sedimentary dynamics: the new “Q7/4 diagram.” *Earth Sci. Rev.* 109, 1–19. doi: 10.1016/j.earscirev.2011.07.002
- Ding, Z., Rutter, N., and Liu, T. (1993). Pedostratigraphy of Chinese loess deposits and climatic cycles in the last 2.5 Myr. *CATENA* 20, 73–91. doi: 10.1016/0341-8162(93)90030-S
- Ding, Z., Yu, Z., Rutter, N. W., and Liu, T. (1994). Towards an orbital time scale for Chinese loess deposits. *Quat. Sci. Rev.* 13, 39–70. doi: 10.1016/0277-3791(94)90124-4
- Ding, Z. L., Derbyshire, E., Yang, S. L., Yu, Z. W., Xiong, S. F., and Liu, T. S. (2002a). Stacked 2.6-Ma grain size record from the Chinese loess based on five sections and correlation with the deep-sea  $\delta^{18}\text{O}$  record: STACKED QUATERNARY CLIMATE RECORD FROM CHINESE LOESS. *Paleoceanography* 17, 5–1. doi: 10.1029/2001PA000725
- Ding, Z. L., Ranov, V., Yang, S. L., Finaev, A., Han, J. M., and Wang, G. A. (2002b). The loess record in southern Tajikistan and correlation with Chinese loess. *Earth Planet. Sci. Lett.* 200, 387–400. doi: 10.1016/S0012-821X(02)00637-4
- Dunlop, D. J. (2002a). Theory and application of the Day plot (Mrs/Ms versus Hcr/Hc 1. Theoretical curves and tests using titanomagnetite data. *J. Geophys. Res.* 107:2056. doi: 10.1029/2001JB000486
- Dunlop, D. J. (2002b). Theory and application of the Day plot (Mrs/Ms versus Hcr/Hc 2. Application to data for rocks, sediments, and soils. *J. Geophys. Res.* 107:2057. doi: 10.1029/2001JB000487
- Egli, R. (2013). VARIFORC: an optimized protocol for calculating non-regular first-order reversal curve (FORC) diagrams. *Glob. Planet. Change* 110, 302–320. doi: 10.1016/j.gloplacha.2013.08.003
- Eyre, J. K. (1997). Frequency dependence of magnetic susceptibility for populations of single-domain grains. *Geophys. J. Int.* 129, 209–211. doi: 10.1111/j.1365-246X.1997.tb00951.x
- Fitzsimmons, K. E., Hambach, U., Veres, D., and Iovita, R. (2013). The campanian ignimbrite eruption: new data on volcanic ash dispersal and its potential impact on human evolution. *PLoS One* 8:e65839. doi: 10.1371/journal.pone.0065839
- Forster, T., Evans, M. E., and Heller, F. (1994). The frequency dependence of low field susceptibility in loess sediments. *Geophys. J. Int.* 118, 636–642. doi: 10.1111/j.1365-246X.1994.tb03990.x
- Forster, T., Heller, F., Evans, M. E., and Havlíček, P. (1996). Loess in the Czech Republic: magnetic properties and paleoclimate. *Stud. Geophys. Geod.* 40, 243–261. doi: 10.1007/BF02300741
- Gaudenyi, T., Nenadić, D., Stejić, P., Jovanović, M., and Bogičević, K. (2015). The stratigraphy of the Serbian Pleistocene Corbicula beds. *Quat. Int.* 357, 4–21. doi: 10.1016/j.quaint.2014.07.050

- Gavrilović, B., Sümegi, P., Ćirić, M., Radaković, M. G., Gavrilov, M. B., Mlačanin, et al. (2020). The middle and late pleniglacial (Weichselian) malacofauna of the Zemun loess-paleosol sequence, Serbia. *PalZ* 94, 519–531.
- Giaccio, B., Galli, P., Messina, P., Peronace, E., Scardia, G., Sottili, G., et al. (2012). Fault and basin depocentre migration over the last 2 Ma in the L'Aquila 2009 earthquake region, central Italian Apennines. *Quat. Sci. Rev.* 56, 69–88. doi: 10.1016/j.quascirev.2012.08.016
- Giaccio, B., Leicher, N., Mannella, G., Monaco, L., Regattieri, E., Wagner, B., et al. (2019). Extending the tephra and palaeoenvironmental record of the Central Mediterranean back to 430 ka: a new core from Fucino Basin, central Italy. *Quat. Sci. Rev.* 225:106003. doi: 10.1016/j.quascirev.2019.106003
- Giaccio, B., Niespolo, E. M., Pereira, A., Nomade, S., Renne, P. R., Albert, P. G., et al. (2017). First integrated tephrochronological record for the last ~190 kyr from the Fucino Quaternary lacustrine succession, central Italy. *Quat. Sci. Rev.* 158, 211–234. doi: 10.1016/j.quascirev.2017.01.004
- Günster, N., Eck, P., Skowronek, A., and Zöller, L. (2001). Late Pleistocene loess and their paleosols in the Granada Basin, Southern Spain. *Quat. Int.* 7, 241–245. doi: 10.1016/S1040-6182(00)00106-3
- Hambach, U., Veres, D., Constantin, D., Zeeden, C., Pötter, S., Baykal, Y., et al. (2019). “Interglacial, Holocene and recent dust accretion in the Danube Basin and beyond: evidence for uninterrupted dust accumulation in Eurasian dry steppe regions,” in *International Workshop on Loess and Archeology: GEoARChEoLoGICAL and Paleoenvironmental Research in European Loess-scapes: Abstract Book / Herausgeber: Prof. Dr. Frank Lehmkuhl*, ed. J. Böskén (Aachen: Lehrstuhl für Physische Geographie und Geoökologie), 25–27. doi: 10.18154/RWTH-2019-10413
- Hao, Q., Wang, L., Oldfield, F., Peng, S., Qin, L., Song, Y., et al. (2012). Delayed build-up of Arctic ice sheets during 400,000-year minima in insolation variability. *Nature* 490, 393–396. doi: 10.1038/nature11493
- Harrison, R. J., and Feinberg, J. M. (2008). FORCinel: an improved algorithm for calculating first-order reversal curve distributions using locally weighted regression smoothing: FORCINEL ALGORITHM. *Geochem. Geophys. Geosyst.* 9:Q05016. doi: 10.1029/2008GC001987
- Heller, F., and Evans, M. E. (1995). Loess magnetism. *Rev. Geophys.* 33:211. doi: 10.1029/95RG00579
- Heller, F., and Liu, T. (1982). Magnetostratigraphical dating of loess deposits in China. *Nature* 300, 431–433. doi: 10.1038/300431a0
- Heller, F., and Liu, T. (1986). Palaeoclimatic and sedimentary history from magnetic susceptibility of loess in China. *Geophys. Res. Lett.* 13, 1169–1172. doi: 10.1029/GL013i011p01169
- Heslop, D., Langereis, C. G., and Dekkers, M. J. (2000). A new astronomical timescale for the loess deposits of Northern China. *Earth Planet. Sci. Lett.* 184, 125–139. doi: 10.1016/S0012-821X(00)00324-1
- Hu, P., Liu, Q., Torrent, J., Barrón, V., and Jin, C. (2013). Characterizing and quantifying iron oxides in Chinese loess/paleosols: implications for pedogenesis. *Earth Planet. Sci. Lett.* 369–370, 271–283. doi: 10.1016/j.epsl.2013.03.033
- Hunt, C. P., Moskowitz, B. M., and Banerjee, S. K. (1995). “Magnetic properties of rocks and minerals,” in *AGU Reference Shelf*, ed. T. J. Ahrens (Washington, DC: American Geophysical Union), 189–204. doi: 10.1029/RF003p0189
- Imbrie, J., and Imbrie, J. Z. (1980). Modeling the climatic response to orbital variations. *Science* 207, 943–953. doi: 10.1126/science.207.4434.943
- Ji, J., Balsam, W., Chen, J. U., and Liu, L. (2002). Rapid and quantitative measurement of hematite and goethite in the Chinese loess-paleosol sequence by diffuse reflectance spectroscopy. *Clays Clay Minerals* 50, 208–216. doi: 10.1346/000986002760832801
- Jiang, Z., Liu, Q., Roberts, A. P., Barrón, V., Torrent, J., and Zhang, Q. (2018). A new model for transformation of ferrihydrite to hematite in soils and sediments. *Geology* 46, 987–990. doi: 10.1130/G45386.1
- Jordanova, D., Hus, J., and Geeraerts, R. (2007). Palaeoclimatic implications of the magnetic record from loess/paleosol sequence Viatovo (NE Bulgaria): palaeoclimatic implications of the magnetic record. *Geophys. J. Int.* 171, 1036–1047. doi: 10.1111/j.1365-246X.2007.03576.x
- Jordanova, D., and Jordanova, N. (2020). Diversity and peculiarities of soil formation in eolian landscapes – insights from the mineral magnetic records. *Earth Planet. Sci. Lett.* 531:115956. doi: 10.1016/j.epsl.2019.115956
- King, J. W., and Channell, J. E. T. (1991). SEDIMENTARY MAGNETISM, ENVIRONMENTAL MAGNETISM, AND MAGNETOSTRATIGRAPHY. *Rev. Geophys.* 29, 358–370. doi: 10.1002/rog.1991.29.s1.358
- Kohfeld, K., and Harrison, S. P. (2003). Glacial-interglacial changes in dust deposition on the Chinese Loess Plateau. *Quat. Sci. Rev.* 22, 1859–1878. doi: 10.1016/S0277-3791(03)00166-5
- Kukla, G., and An, Z. (1989). Loess stratigraphy in Central China. *Palaeogeogr. Palaeoclimatol. Palaeoecol.* 72, 203–225. doi: 10.1016/0031-0182(89)90143-0
- Laag, C., Hambach, U. F., Botezatu, A., Baykal, Y., Veres, D., Schönwetter, T., et al. (2018). “The geographical extent of the “L2-Tephra”: a widespread marker horizon for the penultimate glacial (MIS 6) on the Balkan Peninsula,” in *Abstract book, INQUA-INTAV International Field Conference and Workshop - Crossing New Frontiers - Tephra Hunt in Transylvania*, eds U. Hambach and D. Veres (Romania: INQUA-INTAV), 111–112. doi: 10.13140/RG.2.2.29686.96325
- Lagroix, F., Banerjee, S. K., and Jackson, M. J. (2016). “Geological occurrences and relevance of iron oxides,” in *Iron Oxides: From Nature to Applications*, ed. D. Faivre (Weinheim: Wiley-VCH), 9–29.
- Lagroix, F., and Guyodo, Y. (2017). A new tool for separating the magnetic mineralogy of complex mineral assemblages from low temperature magnetic behavior. *Front. Earth Sci.* 5:61. doi: 10.3389/feart.2017.00061
- Lehmkuhl, F., Nett, J. J., Pötter, S., Schulte, P., Sprafke, T., Jary, Z., et al. (2021). Loess landscapes of Europe – mapping, geomorphology, and zonal differentiation. *Earth Sci. Rev.* 215:103496. doi: 10.1016/j.earscirev.2020.103496
- Leicher, N., Zanchetta, G., Sulpizio, R., Giaccio, B., Wagner, B., Nomade, S., et al. (2016). First tephrostratigraphic results of the DEEP site record from Lake Ohrid (Macedonia and Albania). *Biogeosciences* 13, 2151–2178. doi: 10.5194/bg-13-2151-2016
- Lisiecki, L. E., and Raymo, M. E. (2005). A Pliocene-Pleistocene stack of 57 globally distributed benthic  $\delta^{18}O$  records. *Paleoceanography* 20:A1003. doi: 10.1029/2004PA001071
- Liu, Q., Barrón, V., Torrent, J., Eeckhout, S. G., and Deng, C. (2008). Magnetism of intermediate hydromagnetite in the transformation of 2-line ferrihydrite into hematite and its paleoenvironmental implications. *J. Geophys. Res.* 113:B01103. doi: 10.1029/2007JB005207
- Liu, Q., Zhang, C., Torrent, J., Barrón, V., Hu, P., Jiang, Z., et al. (2016). Factors controlling magnetism of reddish brown soil profiles from calcarenites in Southern Spain: dust input or in-situ pedogenesis? *Front. Earth Sci.* 4:51. doi: 10.3389/feart.2016.00051
- Lowe, D. J. (2011). Tephrochronology and its application: a review. *Quat. Geochronol.* 6, 107–153.
- Lowe, D. J., Pearce, N. J. G., Jorgensen, M. A., Kuehn, S. C., Tryon, C. A., and Hayward, C. L. (2017). Correlating tephras and cryptotephras using glass compositional analyses and numerical and statistical methods: review and evaluation. *Quat. Sci. Rev.* 175, 1–44. doi: 10.1016/j.quascirev.2017.08.003
- Lukić, T., Basarin, B., Buggle, B., Marković, S. B., Tomović, V. M., Raljić, J. P., et al. (2014). A joined rock magnetic and colorimetric perspective on the Late Pleistocene climate of Orlovat loess site (Northern Serbia). *Quat. Int.* 334–335, 179–188. doi: 10.1016/j.quaint.2014.03.042
- Machalett, B., Frechen, M., Hambach, U., Oches, E. A., Zöller, L., and Marković, S. B. (2006). The loess sequence from Remisowka (northern boundary of the Tien Shan Mountains, Kazakhstan)—Part I: luminescence dating. *Quat. Int.* 15, 192–201. doi: 10.1016/j.quaint.2005.12.014
- Maher, B. A. (1998). Magnetic properties of modern soils and Quaternary loessic paleosols: paleoclimatic implications. *Palaeogeogr. Palaeoclimatol. Palaeoecol.* 137, 25–54.
- Maher, B. A. (2011). The magnetic properties of Quaternary aeolian dusts and sediments, and their palaeoclimatic significance. *Aeolian Res.* 3, 87–144. doi: 10.1016/j.aeolia.2011.01.005
- Maher, B. A. (2016). Palaeoclimatic records of the loess/paleosol sequences of the Chinese Loess Plateau. *Quat. Sci. Rev.* 154, 23–84. doi: 10.1016/j.quascirev.2016.08.004
- Maher, B. A., and Taylor, R. M. (1988). Formation of ultrafine-grained magnetite in soils. *Nature* 336, 368–370.
- Mannella, G., Giaccio, B., Zanchetta, G., Regattieri, E., Niespolo, E. M., Pereira, A., et al. (2019). Palaeoenvironmental and palaeohydrological variability of mountain areas in the central Mediterranean region: a 190 ka-long chronicle from the independently dated Fucino palaeolake record (central Italy). *Quat. Sci. Rev.* 210, 190–210. doi: 10.1016/j.quascirev.2019.02.032

- Marković, S. B., Hambach, U., Catto, N., Jovanović, M., Buggle, B., Machalett, B., et al. (2009). Middle and Late Pleistocene loess sequences at Batajnica, Vojvodina, Serbia. *Quat. Int.* 198, 255–266. doi: 10.1016/j.quaint.2008.12.004
- Marković, S. B., Hambach, U., Stevens, T., Kukla, G. J., Heller, F., McCoy, W. D., et al. (2011). The last million years recorded at the Stari Slankamen (Northern Serbia) loess-palaeosol sequence: revised chronostratigraphy and long-term environmental trends. *Quat. Sci. Rev.* 30, 1142–1154. doi: 10.1016/j.quascirev.2011.02.004
- Marković, S. B., Stevens, T., Kukla, G. J., Hambach, U., Fitzsimmons, K. E., Gibbard, P., et al. (2015). Danube loess stratigraphy — towards a pan-European loess stratigraphic model. *Earth Sci. Rev.* 148, 228–258. doi: 10.1016/j.earscirev.2015.06.005
- Marković, S. B., Stevens, T., Mason, J., Vandenberghe, J., Yang, S., Veres, D., et al. (2018). Loess correlations – between myth and reality. *Palaeogeogr. Palaeoclimatol. Palaeoecol.* 509, 4–23. doi: 10.1016/j.palaeo.2018.04.018
- Marković-Marjanović, J. (1970). Data concerning the stratigraphy and the fauna of the lower and middle pleistocene of Yugoslavia. *Palaeogeogr. Palaeoclimatol. Palaeoecol.* 8, 153–163. doi: 10.1016/0031-0182(70)90008-8
- Marra, F., Bahain, J.-J., Jicha, B. R., Nomade, S., Palladino, D. M., Pereira, A., et al. (2019). Reconstruction of the MIS 5.5, 5.3 and 5.1 coastal terraces in Latium (central Italy): a re-evaluation of the sea-level history in the Mediterranean Sea during the last interglacial. *Quat. Int.* 525, 54–77. doi: 10.1016/j.quaint.2019.09.001
- Marra, F., Karner, D. B., Freda, C., Gaeta, M., and Renne, P. (2009). Large mafic eruptions at Alban Hills Volcanic District (Central Italy): chronostratigraphy, petrography and eruptive behavior. *J. Volcanol. Geothermal Res.* 179, 217–232. doi: 10.1016/j.jvolgeores.2008.11.009
- Maxbauer, D. P., Feinberg, J. M., and Fox, D. L. (2016). MAX UnMix: a web application for unmixing magnetic coercivity distributions. *Comp. Geosci.* 95, 140–145. doi: 10.1016/j.cageo.2016.07.009
- Meyers, S. R. (2014). *astrochron: An R Package for Astrochronology. Version 0.8*. Available online at: <http://www.geology.wisc.edu/~smeyers> (accessed June 17, 2020).
- Mullins, C. E., and Tite, M. S. (1973). Magnetic viscosity, quadrature susceptibility, and frequency dependence of susceptibility in single-domain assemblies of magnetite and maghemite. *J. Geophys. Res.* 78, 804–809. doi: 10.1029/JB078i005p00804
- Necula, C., Panaiotu, C., Heslop, D., and Dimofte, D. (2013). Climatic control of magnetic granulometry in the Mircea Vodă loess/paleosol sequence (Dobrogea, Romania). *Quat. Int.* 293, 5–14. doi: 10.1016/j.quaint.2012.03.043
- Obrecht, I., Hambach, U., Veres, D., Zeeden, C., Böskén, J., Stevens, T., et al. (2017). Shift of large-scale atmospheric systems over Europe during late MIS 3 and implications for Modern Human dispersal. *Sci. Rep.* 7:5848. doi: 10.1038/s41598-017-06285-x
- Obrecht, I., Zeeden, C., Hambach, U., Veres, D., Marković, S. B., Böskén, J., et al. (2016). Tracing the influence of Mediterranean climate on Southeastern Europe during the past 350,000 years. *Sci. Rep.* 6:36334. doi: 10.1038/srep36334
- Obrecht, I., Zeeden, C., Hambach, U., Veres, D., Marković, S. B., and Lehmkuhl, F. (2019). A critical reevaluation of palaeoclimate proxy records from loess in the Carpathian Basin. *Earth Sci. Rev.* 190, 498–520. doi: 10.1016/j.earscirev.2019.01.020
- Peters, C., and Dekkers, M. J. (2003). Selected room temperature magnetic parameters as a function of mineralogy, concentration and grain size. *Phys. Chem. Earth Parts A/B/C* 28, 659–667. doi: 10.1016/S1474-7065(03)00120-7
- Post, D. F., Bryant, R. B., Batchily, A. K., Huete, A. R., Levine, S. J., Mays, M. D., et al. (2015). “Correlations between field and laboratory measurements of soil color,” in *SSSA Special Publications*, eds J. M. Bigham and E. J. Ciolkosz (Madison, WI: Soil Science Society of America), 35–49. doi: 10.2136/sssaspecpub31.c3
- Pötter, S., Veres, D., Baykal, Y., Nett, J. J., Schulte, P., Hambach, U., et al. (2021). Disentangling sedimentary pathways for the Pleniglacial Lower Danube loess based on geochemical signatures. *Front. Earth Sci.* 9:600010.
- Poulet, A., Horvath, E., Gabris, G., and Juvigné, E. (1999). The Bag Tephra, a widespread tephrochronological marker in Middle Europe: chemical and mineralogical investigations. *Bull. Volcanol.* 61, 265–272. doi: 10.1007/s004450050275
- R Core Team (2020). *R: A Language and Environment for Statistical Computing*. Vienna: R Foundation for Statistical Computing.
- Šarić, J. (2008). Paleolithic and mesolithic finds from profile of the Zemun loess. *Starinar* 9–27. doi: 10.2298/STA0858009S
- Schaetzl, R. J., Bettis, E. A., Crouvi, O., Fitzsimmons, K. E., Grimley, D. A., Hambach, U., et al. (2018). Approaches and challenges to the study of loess—introduction to the LoessFest Special Issue. *Quat. Res.* 89, 563–618. doi: 10.1017/qua.2018.15
- Scheidt, S., Berg, S., Hambach, U., Klasen, N., Pötter, S., Stolz, A., et al. (2021). Chronological assessment of the balta alba kurgan loess-paleosol section (Romania) – a comparative study on different dating methods for a robust and precise age model. *Front. Earth Sci.* 8:598448. doi: 10.3389/feart.2020.598448
- Scheinost, A. C. (1998). Use and limitations of second-derivative diffuse reflectance spectroscopy in the visible to near-infrared range to identify and quantify Fe oxide minerals in soils. *Clays Clay Minerals* 46, 528–536. doi: 10.1346/CCMN.1998.0460506
- Song, Y., Guo, Z., Marković, S., Hambach, U., Deng, C., Chang, L., et al. (2018). Magnetic stratigraphy of the Danube loess: a composite Titel-Stari Slankamen loess section over the last one million years in Vojvodina, Serbia. *J. Asian Earth Sci.* 155, 68–80. doi: 10.1016/j.jseas.2017.11.012
- Sümeği, P., Gulyás, S., Molnár, D., Sümeği, B. P., Almond, P. C., Vandenberghe, J., et al. (2018). New chronology of the best developed loess/paleosol sequence of Hungary capturing the past 1.1 ma: implications for correlation and proposed pan-Eurasian stratigraphic schemes. *Quat. Sci. Rev.* 191, 144–166.
- Sun, Y., Clemens, S. C., An, Z., and Yu, Z. (2006). Astronomical timescale and palaeoclimatic implication of stacked 3.6-Myr monsoon records from the Chinese Loess Plateau. *Quat. Sci. Rev.* 25, 33–48. doi: 10.1016/j.quascirev.2005.07.005
- Sun, Y., He, L., Liang, L., and An, Z. (2011). Changing color of Chinese loess: geochemical constraint and paleoclimatic significance. *J. Asian Earth Sci.* 40, 1131–1138. doi: 10.1016/j.jseas.2010.08.006
- Taylor, S. N., and Lagroix, F. (2015). Magnetic anisotropy reveals the depositional and postdepositional history of a loess-paleosol sequence at Nussloch (Germany): AMS OF NUSSLOCH LOESS-PALEOSOL SEQUENCE. *J. Geophys. Res. Solid Earth* 120, 2859–2876. doi: 10.1002/2014JB011803
- Taylor, S. N., Lagroix, F., Rousseau, D.-D., and Antoine, P. (2014). Mineral magnetic characterization of the Upper Pleniglacial Nussloch loess sequence (Germany): an insight into local environmental processes. *Geophys. J. Int.* 199, 1463–1480. doi: 10.1093/gji/ggu331
- Till, J. L., Jackson, M. J., Rosenbaum, J. G., and Solheid, P. (2011). Magnetic properties in an ash flow tuff with continuous grain size variation: a natural reference for magnetic particle granulometry: SUPERPARAMAGNETIC GRAINS IN TUFF. *Geochem. Geophys. Geosyst.* 12:Q07Z26. doi: 10.1029/2011GC003648
- Timar-Gabor, A., Ivascu, C., Vasiliniuc, S., Daraban, L., Ardelean, I., Cosma, C., et al. (2011). Thermoluminescence and optically stimulated luminescence properties of the 0.5P2O5-xBaO-(0.5-x)Li2O glass systems. *Appl. Radiation Isotopes* 69, 780–784. doi: 10.1016/j.apradiso.2011.01.015
- Torrent, J., Liu, Q., Bloemendal, J., and Barrón, V. (2007). Magnetic Enhancement and Iron Oxides in the Upper Luochuan Loess-Paleosol Sequence, Chinese Loess Plateau. *Soil Sci. Soc. Am. J.* 71, 1570–1578. doi: 10.2136/sssaj2006.0328
- Tsatskin, A., Heller, F., Hailwood, E. A., Gendler, T. S., Hus, J., Montgomery, P., et al. (1998). Pedosedimentary division, rock magnetism and chronology of the loess/palaeosol sequence at Roxolany (Ukraine). *Palaeogeogr. Palaeoclimatol. Palaeoecol.* 143, 111–133. doi: 10.1016/S0031-0182(98)00073-X
- Veres, D., Lane, C. S., Timar-Gabor, A., Hambach, U., Constantin, D., Szakács, A., et al. (2013). The Campanian Ignimbrite/Y5 tephra layer – a regional stratigraphic marker for Isotope Stage 3 deposits in the Lower Danube region, Romania. *Quat. Int.* 293, 22–33. doi: 10.1016/j.quaint.2012.02.042
- Veres, D., Tecs, V., Gerasimenko, N., Zeeden, C., Hambach, U., and Timar-Gabor, A. (2018). Short-term soil formation events in last glacial east European loess, evidence from multi-method luminescence dating. *Quat. Sci. Rev.* 200, 34–51. doi: 10.1016/j.quascirev.2018.09.037
- Wagner, B., Vogel, H., Francke, A., Friedrich, T., Donders, T., Lacey, J. H., et al. (2019). Mediterranean winter rainfall in phase with African monsoons during the past 1.36 million years. *Nature* 573, 256–260. doi: 10.1038/s41586-019-1529-0



- WRB 2014/2015. *IUSS Working Group World Reference Base for Soil Resources 2014, Update 2015. International Soil Classification System for Naming Soils and Creating Legends for Soil Maps. World Soil Resources, Reports No. 106*. Rome: FAO.
- Wu, Y., Qiu, S., Fu, S., Rao, Z., and Zhu, Z. (2018). Pleistocene climate change inferred from multi-proxy analyses of a loess-paleosol sequence in China. *J. Asian Earth Sci.* 154, 428–434. doi: 10.1016/j.jseas.2017.10.007
- Yang, S. L., and Ding, Z. L. (2003). Color reflectance of Chinese loess and its implications for climate gradient changes during the last two glacial–interglacial cycles. *Geophys. Res. Lett.* 30:GL018346. doi: 10.1029/2003GL018346
- Zeeden, C., Hambach, U., Obrecht, I., Hao, Q., Abels, H. A., Veres, D., et al. (2018). Patterns and timing of loess-paleosol transitions in Eurasia: constraints for paleoclimate studies. *Glob. Planet. Change* 162, 1–7. doi: 10.1016/j.gloplacha.2017.12.021
- Zeeden, C., Kels, H., Hambach, U., Schulte, P., Protze, J., Eckmeier, E., et al. (2016). Three climatic cycles recorded in a loess-paleosol sequence at Semlac (Romania) – implications for dust accumulation in south-eastern Europe. *Quat. Sci. Rev.* 154, 130–142. doi: 10.1016/j.quascirev.2016.11.002
- Zeeden, C., Krauß, L., Kels, H., and Lehmkuhl, F. (2017). Digital image analysis of outcropping sediments: comparison to photospectrometric data from Quaternary loess deposits at Șanovița (Romania) and Achenheim (France). *Quat. Int.* 429, 100–107. doi: 10.1016/j.quaint.2016.02.047

**Conflict of Interest:** The authors declare that the research was conducted in the absence of any commercial or financial relationships that could be construed as a potential conflict of interest.

Copyright © 2021 Laag, Hambach, Zeeden, Lagroix, Guyodo, Veres, Jovanović and Marković. This is an open-access article distributed under the terms of the Creative Commons Attribution License (CC BY). The use, distribution or reproduction in other forums is permitted, provided the original author(s) and the copyright owner(s) are credited and that the original publication in this journal is cited, in accordance with accepted academic practice. No use, distribution or reproduction is permitted which does not comply with these terms.

## Appendix E: Publication Zmajevac

### **High-resolution palaeoenvironmental reconstruction at Zmajevac (Croatia) over the last three glacial/interglacial cycles**

Lara Wacha<sup>1</sup>, Christian Laag<sup>2,3</sup>, Anita Grizelj<sup>1</sup>, Sumiko Tsukamoto<sup>2</sup>, Christian Zeeden<sup>2</sup>, Danijel Ivanišević<sup>1</sup>, Christian Rolf<sup>2</sup>, Adriano Banak<sup>1</sup>, Manfred Frechen<sup>2</sup>

<sup>1</sup> Croatian Geological Survey, Zagreb, Croatia

<sup>2</sup> Leibniz Institute for Applied Geophysics (LIAG), Hannover, Germany

<sup>3</sup> Université de Paris, Institut de Physique du Globe de Paris (IPGP), CNRS, Paris, France

#### **Status:**

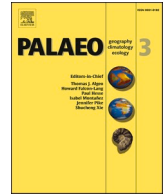
- Submitted: 04.12.2020
- Received in revised form: 18.05.2021
- Accepted: 25.05.2021
- Published in: *Palaeogeography, Palaeoclimatology, Palaeoecology* 567, 110504, <https://doi.org/10.1016/j.palaeo.2021.110504>.

#### **Main findings:**

- The Zmajevac LPS covers four well established paleosols and five thick loess units.
- The magnetic enhancement model indicates high amounts of fine-grained magnetic particles in the paleosols due to neo-formation during pedogenesis.
- Radiometric and correlative dating techniques imply a time range from MIS10 to the Holocene.
- Higher pedogenesis leads to the production of fine (clay) particles and enhances magnetic susceptibility.
- Grain-size derived indicators reflect harsh wind conditions during glacials and calm wind conditions during interglacials and comparable larger grain sizes in the older part of the profile indicate a shift to nearby dust sources.
- The mineral composition of Zmajevac consists mainly of quartz, clay minerals, plagioclase, and calcite.
- The magnetic susceptibility and colorimetric parameters indicate a decrease in summer heat and decreased precipitation availability (increasing aridity) over the last three glacial/interglacial cycles.

Contents lists available at [ScienceDirect](https://www.sciencedirect.com)

## Palaeogeography, Palaeoclimatology, Palaeoecology

journal homepage: [www.elsevier.com/locate/palaeo](http://www.elsevier.com/locate/palaeo)

# High-resolution palaeoenvironmental reconstruction at Zmajevac (Croatia) over the last three glacial/interglacial cycles

Lara Wacha<sup>a,\*</sup>, Christian Laag<sup>b,c</sup>, Anita Grizelj<sup>a</sup>, Sumiko Tsukamoto<sup>b</sup>, Christian Zeeden<sup>b</sup>, Danijel Ivanišević<sup>a</sup>, Christian Rolf<sup>b</sup>, Adriano Banak<sup>a</sup>, Manfred Frechen<sup>b</sup>

<sup>a</sup> Croatian Geological Survey, Sachsova 2, 10 000 Zagreb, Croatia

<sup>b</sup> Leibniz Institute for Applied Geophysics (LIAG), Stilleweg 2, 30655 Hannover, Germany

<sup>c</sup> Université de Paris, Institut de Physique du Globe de Paris (IPGP), CNRS, 1 rue Jussieu, Paris, France

## ARTICLE INFO

Editor: Paul Hesse

## Keywords:

Loess chronology  
Environmental magnetism  
Grain-size analysis  
Clay minerals  
Diffuse reflectance spectrometry

## ABSTRACT

A high-resolution analysis of the Zmajevac loess-palaeosol sequence in East Croatia (Baranja) was performed with the purpose to get new insights into the palaeoenvironmental history during the last three glacial-interglacial cycles. The post-IR infrared stimulated luminescence signal of feldspar, stimulated at 290°C (thereafter pIRIR<sub>290</sub>) was used to establish a reliable chronological framework and revealed intensive sedimentation during (at least) the last 300 kyr, which was five times interrupted by climate optima resulting in the formation of soils (now palaeosols). The environmental magnetic measurements support the obtained luminescence chronology. Further chronological time control was reached by age modelling based on tie points from variations in frequency dependence of magnetic susceptibility and benthic  $\delta^{18}\text{O}$  variations from the LR04 stack of Lisiecki and Raymo (2005). The grain-size record provided information about the environmental conditions and dust accumulation. Additional palaeoenvironmental implications were provided by room temperature magnetic susceptibility and colourimetric analyses and revealed a continuously lower intensity of pedogenesis, coupled with constantly decreasing temperatures and precipitation from the oxygen isotope stage (OIS) 9 to the end of OIS 3. X-ray diffraction of the clay mineral fraction revealed chlorite, smectite and illitic material as dominant mineral phases. While clay minerals from loess are mostly detrital, smectite from palaeosols is partly of a pedogenic origin. The application of our multi-proxy approach, including relative and numerical dating techniques, provided new insights into a highly resolved terrestrial palaeoenvironmental record of Eastern Croatia.

## 1. Introduction

The climate of the last several million years has been influenced by orbital- and millennial-scale fluctuations which are archived in various sediments. The most intensively investigated terrestrial Quaternary sedimentary archives by far are loess-palaeosol sequences (LPSs), which are important deposits genetically linked to major river systems (Smalley et al., 2009) and the extent of the glaciations. Loess-palaeosol sequences may provide detailed data on terrestrial dust accumulation processes and climate changes (Frechen et al., 2003; Marković et al., 2015; Schaetzl et al., 2018). The loess deposits preserved in the Chinese Loess Plateau (CLP) in Central China exhibit a quasi-continuous sediment accumulation during glacial and interglacial cycles during the last

2.4 Ma (Heller and Liu, 1982) and provide a detailed record of climate change in the Asian interior (Kukla, 1987) while the last million years are also recorded in European loess-palaeosol sequences (Antoine et al., 2021; Basarin et al., 2014; Hlavatskyi and Bakhmutov, 2020; Laag et al., 2021a, 2021b; Marković et al., 2015; Schaetzl et al., 2018; Song et al., 2018; Sümegi et al., 2018).

The Danube is the second largest river of Europe and drains an area of ~800,000 km<sup>2</sup> (Sommerwerk et al., 2009) and along with its many tributaries, is also a major transport means of silt i.e. loess material (Smalley et al., 2009). The Danube loess region is an important geo-archive where numerous thick loess-palaeosol sequences have been investigated (Marković et al., 2015; Schaetzl et al., 2018) but often lack absolute and reliable chronologies, especially for the Middle Pleistocene.

\* Corresponding author.

E-mail addresses: [lwacha@hgi-cgs.hr](mailto:lwacha@hgi-cgs.hr) (L. Wacha), [laag@ipgp.fr](mailto:laag@ipgp.fr) (C. Laag), [agrizelj@hgi-cgs.hr](mailto:agrizelj@hgi-cgs.hr) (A. Grizelj), [Sumiko.Tsukamoto@leibniz-liag.de](mailto:Sumiko.Tsukamoto@leibniz-liag.de) (S. Tsukamoto), [Christian.Zeeden@leibniz-liag.de](mailto:Christian.Zeeden@leibniz-liag.de) (C. Zeeden), [divanisevic@hgi-cgs.hr](mailto:divanisevic@hgi-cgs.hr) (D. Ivanišević), [Christian.Rolf@leibniz-liag.de](mailto:Christian.Rolf@leibniz-liag.de) (C. Rolf), [abanak@hgi-cgs.hr](mailto:abanak@hgi-cgs.hr) (A. Banak), [Manfred.Frechen@leibniz-liag.de](mailto:Manfred.Frechen@leibniz-liag.de) (M. Frechen).

<https://doi.org/10.1016/j.palaeo.2021.110504>

Received 4 December 2020; Received in revised form 18 May 2021; Accepted 25 May 2021

Available online 29 May 2021

0031-0182/© 2021 Elsevier B.V. All rights reserved.

A robust chronological framework is mandatory for palaeoenvironmental reconstructions. For that purpose, luminescence dating methods are applied, in particular, the post-IR infrared stimulated luminescence (pIRIR), which is nowadays the most popular dating approach when it comes to dating of older deposits (~300 ka; e.g. Fenn et al., 2020; Wacha et al., 2013). Due to the lack of adequate dating methods for Middle Pleistocene sediments, environmental magnetism is also helpful for placing chronological constraints (e.g. Evans and Heller, 2001; Heller and Liu, 1982 – Chinese loess; Basarin et al., 2014; Laag et al., 2021a, 2021b; Marković et al., 2011; Zeeden et al., 2016 – Danube loess).

Palaeoenvironmental information is obtained by numerous proxy data often in high-resolution which are then compared with global records (LR04 stack; Lisiecki and Raymo, 2005). High-resolution grain size analysis provides data about dust mobilisation, transport and deposition mechanisms (Újvári et al., 2016a; Vandenberghe, 2013) as well as post-depositional conditions related to the climate during and shortly after its deposition (e.g. Schulte and Lehmkuhl, 2018; Vandenberghe et al., 2018). Furthermore, grain size data can be used to qualitatively reconstruct wind intensities and directions (Bokhorst et al., 2011).

Another useful palaeoenvironmental proxy is the magnetic susceptibility ( $\chi$ ) and its frequency dependence ( $\Delta\chi$ ), which is a direct result of the soil-forming processes and the neoformation of magnetic minerals during pedogenesis. In most loess areas of the Eurasian loess belt, both  $\chi$  and  $\Delta\chi$  are increased in buried soils (palaeosols) and relatively low in loess units (e.g. Maher, 1986).  $\chi$  and  $\Delta\chi$  depend strongly on the composition, relative abundance and grain size of different magnetic and paramagnetic minerals inside a bulk sample (e.g. Maher, 2011). The highest values are reached in samples containing the soft magnetic minerals, magnetite and maghemite, which already influence the bulk-samples' signal in amounts of less than 1 (wt)% (e.g. Maher et al., 2003). However, magnetic minerals important for environmental reconstructions like hematite and goethite are barely traceable by  $\chi$ . The magnetic signal is influenced by the magnetic grain size and thus domain state as well, with single domain (SDs), pseudo-single domain (PSDs) and multi-domain (MDs; Liu et al., 2012) grains. Especially the ultrafine super-paramagnetic particles (with a diameter ranging up to 30 nm) are formed in the course of pedogenesis. The neoformation of these superparamagnetic (SP) magnetite/maghemite particles close to the unstable single domain (SP) to stable single domain (SD) grain sizes (30 nm) takes place during pedogenesis (favouring warm and humid conditions) (Heller and Liu, 1982; Peters and Dekkers, 2003).  $\chi$  and  $\Delta\chi$  are used as proxies for palaeoprecipitation (e.g. Hao and Guo, 2005; Heller et al., 1993; Liu et al., 1995; Maher et al., 1994). Here, we use  $\Delta\chi$  for (1) discriminating between warm/moist interglacials and cold/dry glacials, and (2) to compare  $\Delta\chi$  fluctuations with variations in other well-dated master records representing global climate oscillations such as the LR04 stack (Lisiecki and Raymo, 2005).

The combination of magnetic and colourimetric investigations is a valuable tool for unravelling and understanding the different mineralogy and their forming conditions which are a direct result of the environmental impact (e.g. Laag et al., 2021a; Lukić et al., 2014). Different magnetic minerals may record a variety of environmental conditions like precipitation, temperature, and their process-related oscillations in sub-millennial timeframes (e.g. maghemite – Gao et al., 2019). Hence, changes in relative abundances of minerals, as magnetite, maghemite, hematite and goethite are imprints of the palaeoenvironment onto a terrestrial geoarchive. Hematite and goethite cannot be quantified easily through room temperature susceptibility measurements, hence time-consuming as well as complicated measurements are necessary (e.g. low-temperature susceptibility measurements; Lagroix and Guyodo, 2017) to discriminate them. Diffuse reflectance spectrometry (DRS) and the first derivative bands of the backscattered spectra provide numerical indicators for the relative abundance of hematite and goethite (e.g. Wu et al., 2018).

Colour changes in loess are important indicators for both changing concentrations and compositions of clay minerals, organic matter and hematite, controlled by different environmental conditions in terms of precipitation, temperature, and seasonality (Ji et al., 2002). Whereas relative amounts of magnetite and maghemite express high  $\chi$  values in a low concentration (< 1%), hematite and goethite in loess can hardly be detected by fluctuations in  $\chi$ . Investigations of soil-colours were performed during the last decades with Munsell-colour charts, while recent developments for colour-measurements by visible-DRS with spectrophotometers provide objective numerical values to detect small amounts of hematite and goethite inside of bulk-samples (Deaton and Balsam, 1991; Wu et al., 2018).

The clay minerals content and their formation are related to the parent material and source area, transport processes, the weathering regime of the sediment, as well as climate and chemical conditions during their formation (e.g. Taheri et al., 2020; Weaver, 1989). Under arid and cold climates, clay minerals remain relatively unmodified, while humid conditions can significantly alter them. For that reason, they are a powerful tool for interpreting weathering conditions and can be used as a proxy for palaeoclimate reconstructions (e.g. Kovács et al., 2013; Sheldon and Tabor, 2009).

The Danube loess belt preserves palaeoenvironmental records of continuous dust accumulation that extend over the last million years and is characterized by alternating loess formation during glacial times and pedogenesis during interglacial times (e.g. Bradák et al., 2019; Jordanova et al., 2007; Laag et al., 2021b; Marković et al., 2015; Song et al., 2018; Sümegi et al., 2018). These deposits are also the thickest due to the high sediment supply from the Danube and its tributaries and high preservation potential due to pre-existing basin topography (Fitzsimmons et al., 2012; Obrecht et al., 2019). For this reason, numerous multiproxy studies were performed in recent years to understand the significance of LPs and to unravel the data they archive especially related to palaeoclimate (e.g. Laag et al., 2021a; Lukić et al., 2014; Zeeden et al., 2016). Furthermore, the Danube and its tributaries were also the main dispersal corridor (Hauck et al., 2018) for early modern humans during the Upper Palaeolithic which resulted in many Early Upper Palaeolithic sites in the region (Chu, 2018). Detailed stratigraphy of the Danube loess is proposed by (Marković et al., 2015) based on numerous proxy data as well as absolute chronology (Murray et al., 2014; Schmidt et al., 2010). As for loess in eastern Croatia along the Danube, the stratigraphy is based on infrared stimulated luminescence (IRSL; Galović et al., 2009) and post-IR IRSL dating (Wacha et al., 2013; Wacha and Frechen, 2011). Loess along the Drava river, also a tributary of the Danube, was investigated by (Wacha et al., 2018a).

The Zmajevac loess-palaeosol section is probably the most detailed loess record exposed in Baranja (eastern Croatia) and can therefore be used to establish the loess stratigraphy for the area. Furthermore, it is a valuable terrestrial sedimentary archive of palaeoenvironmental changes for the Middle and Upper Pleistocene period. A previous chronological study of the Zmajevac loess-palaeosol sequence was performed by (Galović et al., 2009), where the stratigraphy of the exposed loess and palaeosol horizons was given accompanied with first IRSL dating results. Their ages however, are likely underestimated because these were not corrected for fading (Huntley and Lamothe, 2001; Wintle, 1973). For this study, the same location was excavated and sampled. The Zmajevac loess-palaeosol section was re-investigated through high-resolution sampling and by applying a multi-proxy methodology (high-resolution grain-size analysis, magnetic susceptibility measurements, clay mineral content, and diffuse reflectance spectrometry). Here, we present high-resolution grain-size records supplemented by  $\chi$  and DRS data from the Zmajevac loess section and use the results to unravel the interaction between the palaeoclimate and individual proxies. Furthermore, a more detailed and extended chronological framework is presented by luminescence dating supported by correlative age models.





Fig. 1. Location map with indicated most relevant loess-palaeosol sections in the area mentioned in the text.

## 2. Geological setting and the Zmajevac loess section

The Zmajevac loess-palaeosol section (45.813° N, 18.820° E) is located in Baranja in NE Croatia, which is bordered by the Danube in the east, the Drava in the south and the Hungarian state border in the north-

northwest. Baranja is the SE margin of the Pannonic basin and it is mostly represented by thick sequences of Quaternary sediments which are genetically related to the complex river network and their response to Pleistocene climate changes (Fig. 1). Underlying the Quaternary deposits, Palaeozoic metamorphic rocks and Miocene and Pliocene sediments were

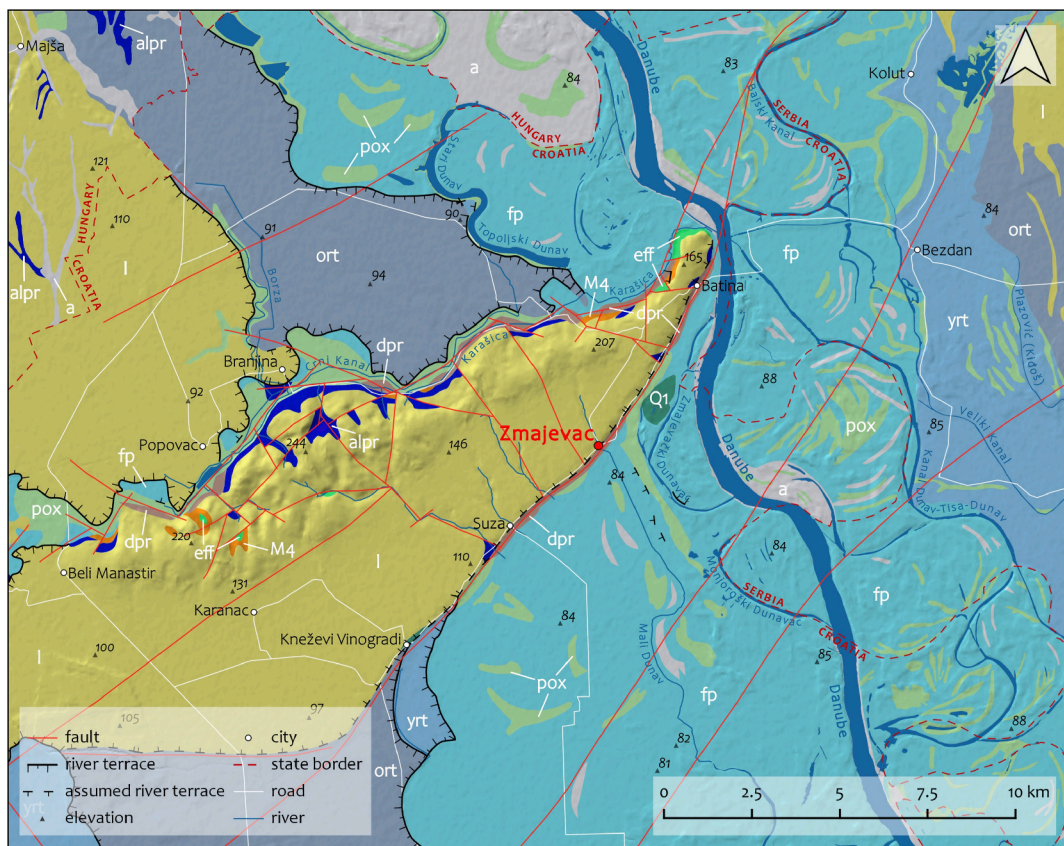


Fig. 2. Geological map of the investigated area (simplified after Gyalog L. and Síkhegyi F. 2005; Píkija et al., 1991a; Trifunović and Strajin, 1995). Legend: Holocene: a - Recent alluvial, beach, ait and bar deposits; yrt - Younger river terrace: Bars and floodplain deposits; dpr - Deluvial - proluvial deposits; pox - Pond and oxbow deposits; Pleistocene: fp - Floodplain deposits; alpr - Alluvial, lake and proluvial deposits; l - Loess and loess-like deposits; ort - Older river terrace: Oxbow, alluvial and loess; Q1 - Unclassified clastites (clay, silt, sand, gravel and peat); Miocene (Badenian): eff - Tuffs, volcanic breccias and basaltic andesite; M4 - Marl, sandy marl, limestones, breccia limestones, sand, sandstones, conglomerates, montmorillonite clay.



determined in deep boreholes, while on the surface mostly Badenian (Miocene) sediments and volcanic rocks can be seen underlying the loess (Pikija et al., 1991a, 1991b, 1995). Except for Bansko brdo (brdo = hill), Baranja is a lowland area, resulting from the alluvial interaction of the rivers Drava, Danube and Karašica (Figs. 1 & 2). The older river terraces are covered by Pleistocene loess and loess-like deposits forming a loess plateau. Bansko brdo is a tectonically uplifted area marked by reverse faults of opposing orientation, on the surface showing Badenian sediments and volcanic rocks covered by loess (Pikija et al., 1991a, 1991b). Baranja is influenced by active tectonics, as evidenced by the present morphostructure and main faults (Hećimović, 2005) some of them forming steep loess cliffs, as seen along the Zmajevac-Batina road (Fig. 2) where the investigated section is exposed (Fig. 3).

The Zmajevac loess-palaeosol section is situated at the outskirts of the Zmajevac settlement, about 6 km away from the Croatian-Serbian state border. It is situated at the fault zone of the Bansko Brdo tectonic unit (Pikija et al., 1991b), at the SE slope of the Bansko Brdo elevated morphostructure (Figs. 1 & 2). The investigated sequence is around 29 m thick. The section starts with an around 3 m thick layer of loess-like sediment, alluvial clayey to sandy silt (Fig. 3). This unit is rich in up to 1 mm Fe—Mn concretions, reddish-brown variegation and redoximorphic features which imply to water saturation. It also shows traces of strong biological activity in the form of bioturbation, krotovinas and root remains (rhizoconcretions). Furthermore, it contains carbonate concretions up to 10 cm. This horizon represents a loess-like sediment probably deposited by aeolian activity in a waterlogged environment, i. e. on the flood plain. In the upper part of this horizon, about 50 cm of loess is present.

The lowest i.e. the oldest exposed palaeosol covering the lowermost loess (Fig. 3), is 250 cm thick and was described by (Galović et al., 2009) as a pedocomplex interrupted by several erosional discontinuities. Furthermore, this pedocomplex was described to be a soil-sediment that was exposed to pedogenesis after redeposition of the soil (Galović, 2014). The lower part of this pedocomplex is enriched with up to 0.5 cm large carbonate concretions, contains krotovinas and has a relatively higher sand content. The palaeosol has a reddish-brown colour. It is covered by a 4 m thick loess layer/horizon on top of which another pedocomplex is developed (Galović, 2014; Galović et al., 2009) which consists of two brown palaeosols intercalated by a 50 cm thick loess layer. The pedocomplex is covered by a laminated sand layer, around 230 cm thick, and shows a sharp and abrupt discontinuity with the layer below. The lower part of the loess covering the laminated sand layer has an increased amount of sand and fines upwards. This loess layer is covered by another brown palaeosol, about 190 cm thick, and shows bioturbation and krotovinas in its upper part. Covering the brown palaeosol is the uppermost, stratigraphically youngest loess horizon which is in its upper part intercalated by a weakly developed, up to 200 cm thick palaeosol. On the top of the section a modern rendzina soil is developed (Galović et al., 2009).

### 3. Methods

#### 3.1. Sampling and sample preparation

During fieldwork in 2015, the previously investigated locations (Galović et al., 2009) were revisited and sampled for a more detailed

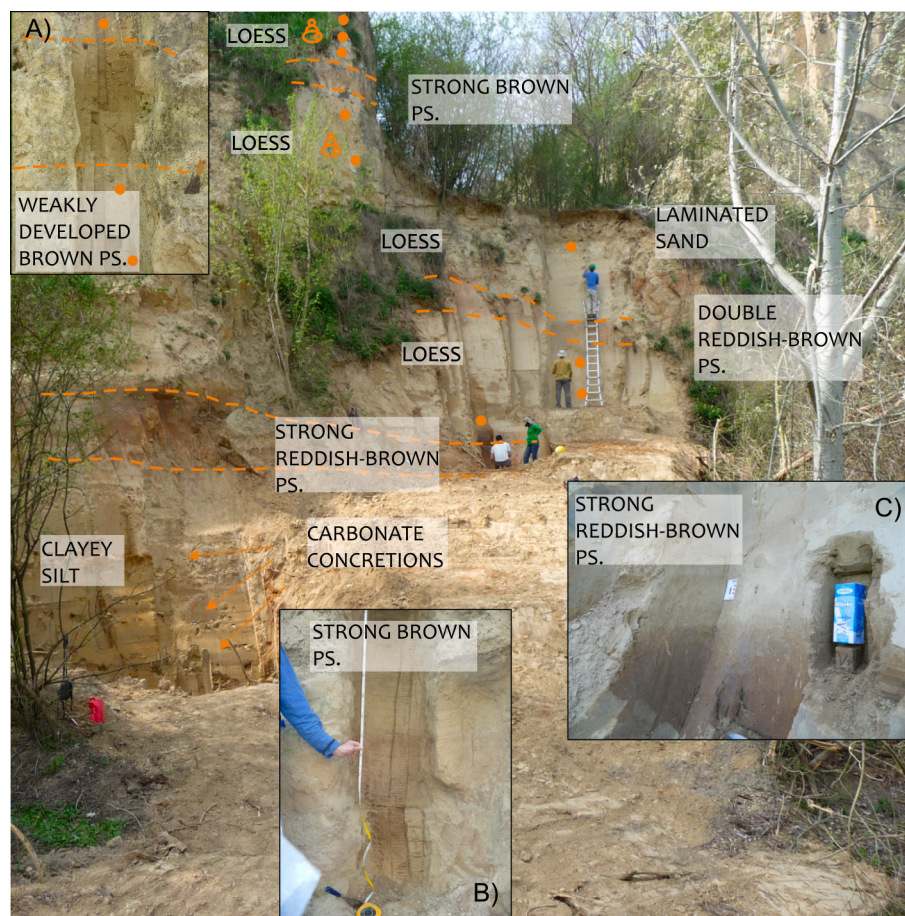


**Fig. 3.** The Zmajevac loess section with indicated individual horizons, stratigraphic marker horizons and sampling locations. A) The youngest, weakly developed brown palaeosol. B) strong brown palaeosol from the upper part of the section. C) The strong reddish-brown palaeosol from the oldest part of the section. (For interpretation of the references to colour in this figure legend, the reader is referred to the web version of this article.)

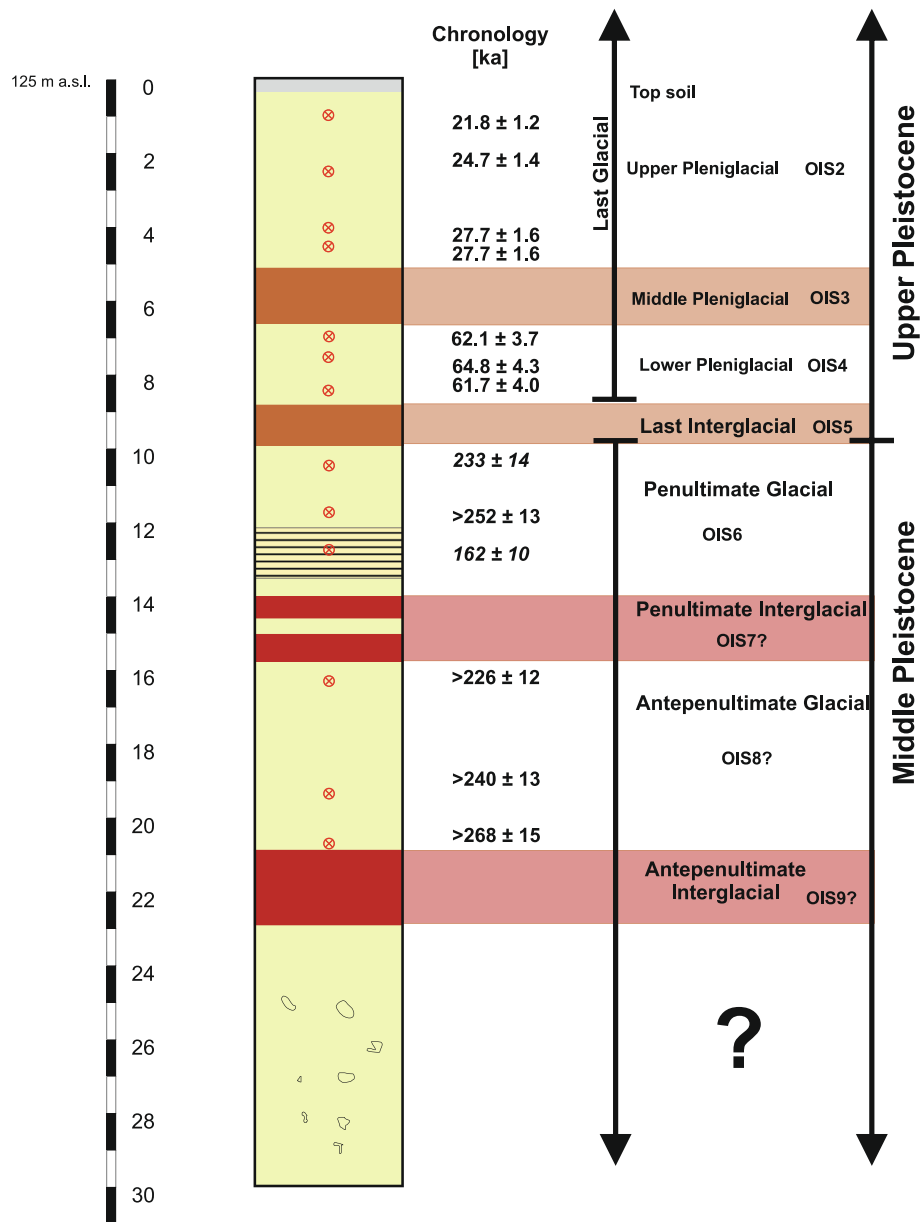


**Fig. 4.** The pIRIR<sub>290</sub> chronology of the Zmajevac loess section. Fading uncorrected ages are given for the Last Glacial loess, minimum ages are given for Penultimate Glacial (and older). The age of the laminated sand horizon was fading corrected (*in italic*).

research. The outcrop was cleaned to remove surface disturbances before any descriptions and sampling. At least 50 cm of the surface was removed from the upper part of the section, while in the lower part heavy-duty cleaning was applied (Fig. 3). Several smaller, nearby subsections were prepared for easier sampling. The profile was described, the thickness of individual horizons was measured and sampled in a 2 cm resolution for grain-size (1026 samples) and 20 cm resolution for  $\chi$  and DRS analyses (115 samples). For luminescence dating 13 samples were collected using PVC and metal light-proof tubes accompanied by an additional sample from the surrounding material for gamma spectrometry. Samples were collected at approximately 80 cm intervals and bracketing the exposed palaeosols. Three samples were collected from the oldest loess, between the lowest pedocomplexes. From the same locations, separate samples for XRD analysis were collected, too. Additional samples were collected from the loess-like silty material below the lowest loess horizon for mineralogical and grain-size analyses. The sampling locations are indicated on Figs. 3 and 4, whereas the depths of the samples for luminescence dating are given in Table 1.

### 3.2. Luminescence dating and experimental details

Laboratory preparation and luminescence measurements were carried out under subdued red light at the luminescence dating laboratory of LIAG (Hannover, Germany). The outer 2 cm of the sample in the tube was removed to avoid possible exposure to light during and after sampling, while the rest was used for further procedure. All samples were treated with 10% HCl to remove the carbonates, Na-oxalate against coagulation and H<sub>2</sub>O<sub>2</sub> to remove organic matter. The material was size separated into the fine silt fraction (4–11  $\mu\text{m}$ ) using several cycles of centrifuging (Frechen et al., 1996). The fine-grained material was mounted on aluminium discs using water and then evaporated. Measurements were performed using automated Risø TL/OSL-DA-15 and -DA20 readers (Bøtter-Jensen et al., 2010) equipped with <sup>90</sup>Sr/<sup>90</sup>Y  $\beta$ -sources, delivering 0.084 and 0.11 Gy s<sup>-1</sup>. Measurements were carried out using infrared (870 ± 40 nm) LEDs. The emitted signal was filtered using the blue filter pack (Schott BG-39 and Corning 7–59).



**Table 1**

Results of gamma spectrometry and dose rate calculations. The error of the cosmic dose rate is 10% of the dose. Water content of  $15 \pm 5\%$  was used for calculations, except for samples 3312 to 3315 where  $20 \pm 10\%$  was used (after Pécsi, 1990). A systematic error of 5% was included.

Sample	Sample Id.	Depth below surface [m]	K (%)	Th (ppm)	U (ppm)	Cosmic dose rate (mGy a-1)	Total dose rate (mGy a-1)
3303	ZMA-1	1	$1.89 \pm 0.01$	$10.23 \pm 0.04$	$3.23 \pm 0.02$	$0.18 \pm 0.02$	$3.99 \pm 0.20$
3304	ZMA-2	2.1	$1.46 \pm 0.01$	$10.09 \pm 0.04$	$3.22 \pm 0.02$	$0.15 \pm 0.02$	$3.56 \pm 0.20$
3305	ZMA-3	4	$1.49 \pm 0.02$	$8.47 \pm 0.05$	$2.72 \pm 0.02$	$0.11 \pm 0.01$	$3.21 \pm 0.18$
3306	ZMA-4	4.7	$1.83 \pm 0.01$	$11.28 \pm 0.04$	$3.48 \pm 0.02$	$0.10 \pm 0.01$	$4.04 \pm 0.21$
3307	ZMA-5	6.8	$1.45 \pm 0.01$	$8.96 \pm 0.04$	$2.71 \pm 0.01$	$0.08 \pm 0.01$	$3.18 \pm 0.18$
3308	ZMA-6	7.6	$1.39 \pm 0.01$	$9.31 \pm 0.03$	$2.81 \pm 0.01$	$0.07 \pm 0.01$	$3.19 \pm 0.18$
3309	ZMA-7	8.5	$1.72 \pm 0.03$	$11.76 \pm 0.09$	$3.84 \pm 0.04$	$0.06 \pm 0.01$	$4.08 \pm 0.22$
3310	ZMA-8	10.5	$1.19 \pm 0.01$	$8.07 \pm 0.03$	$2.40 \pm 0.01$	$0.05 \pm 0.005$	$2.73 \pm 0.17$
3311	ZMA-9	11.8	$1.48 \pm 0.01$	$9.37 \pm 0.04$	$2.38 \pm 0.01$	$0.04 \pm 0.004$	$3.10 \pm 0.17$
3312	ZMA-10	13.9	$1.25 \pm 0.01$	$11.08 \pm 0.04$	$3.16 \pm 0.02$	$0.03 \pm 0.003$	$3.16 \pm 0.23$
3313	ZMA-11	16.5	$1.54 \pm 0.02$	$10.29 \pm 0.06$	$2.50 \pm 0.02$	$0.03 \pm 0.003$	$3.11 \pm 0.21$
3314	ZMA-12	20.4	$1.48 \pm 0.02$	$10.51 \pm 0.06$	$2.66 \pm 0.02$	$0.02 \pm 0.002$	$3.13 \pm 0.21$
3315	ZMA-13	20.7	$1.36 \pm 0.01$	$9.76 \pm 0.03$	$2.55 \pm 0.01$	$0.02 \pm 0.002$	$2.92 \pm 0.21$

### 3.3. Dose rate determination

Samples for gamma spectrometry measurements were dried, weighted (exactly 700 g) and homogenized and then filled into Marinelli-type beakers. They were sealed using parafilm and stored for at least 4 weeks to re-establish equilibrium between radon and its daughter nuclides. Measurements were performed at LIAG in Hannover, Germany. The dose rate was calculated from obtained activities of  $^{238}\text{U}$ ,  $^{232}\text{Th}$  and  $^{40}\text{K}$  (Aitken, 1998). The dose rate conversion factors of Guérin et al. (2011) were applied for dose rate calculations. Alpha efficiency for polymineral fine grains of  $0.08 \pm 0.02$  (Rees-Jones, 1995) was used. The cosmic dose rate was calculated according to Prescott and Stephan (1982) and Prescott and Hutton (1994), and an associated error of 10% is assumed. The water content was assumed to be  $20 \pm 10\%$  and  $15 \pm 5\%$  for the lower (samples 3312–3315) and upper (samples 3303–3311) part of the section, respectively (Pécsi, 1990). The uranium, thorium and potassium concentrations, the cosmic dose and the calculated total dose rates of the samples are given in Table 1.

### 3.4. High-resolution grain-size analysis and end-member modelling

For the high-resolution grain-size analysis the laser diffraction method was used (Beckman-Coulter LS 13320 PID; at LIAG, Hannover). The measurement procedure was the same as presented by Wacha et al. (2018b) and Novothny et al. (2011) i.e. the samples were not chemically treated prior to the measurements, in order not to remove detrital carbonate grains and because the organic content was insignificant in the samples. Reproducibility and reliability test were performed as well as ideal weight tests prior to the measurements. After establishing the most appropriate standard operating protocol the samples were weighted and dispersed for at least 8 h in an overhead tube rotator in a 1% ammonium hydroxide solution. Each sample was measured at least three times and the average was used for the grain-size analysis and further calculations. The granulometric parameters were calculated using the Beckman Coulter particle characterisation software. The U-ratio was calculated according to Vandenberghe et al. (1985) and considers the ratio of the coarse silt and the medium to fine silt fractions ( $16\text{--}44\ \mu\text{m}/5.5\text{--}16\ \mu\text{m}$ ). To decompose the multi-modal grain size distributions into inherent subpopulations, end-member (EM) analysis was performed using the R-package EMMAgeo (Dietze and Dietze, 2019, Version 0.9.7).

### 3.5. Rock-magnetic measurements

For the room-temperature magnetic susceptibility measurements, the samples were dried at  $30\ ^\circ\text{C}$  for 48 h, homogenized, filled in non-magnetic plastic boxes, weighed, compressed and cap sealed to prevent movement of the material. Measurements of magnetic susceptibility ( $\chi$ ) and its frequency dependence ( $\Delta\chi$ ) were performed on a Magnon VFSM kappa-bridge (Magnon International, Dassel, Germany).

The frequency was set to 505 Hz for low frequency ( $\chi_{lf}$ ) and 5050 Hz for high frequency ( $\chi_{hf}$ ) magnetic susceptibility, respectively, and the field was set to 400 A/m.  $\chi_{lf}$  and  $\chi_{hf}$  were normalized as volume susceptibility ( $\kappa$ ) divided by density ( $\rho$ ) to the specific susceptibility with units of  $\text{m}^3\text{kg}^{-1}$  (Thompson and Oldfield, 1986). The frequency dependence was calculated by subtracting  $\chi_{hf}$  from  $\chi_{lf}$ :

$$\Delta\chi = \chi_{lf} - \chi_{hf} \left[ \frac{\text{m}^3}{\text{kg}} \right] \quad (1)$$

and

$$\chi_{fd}[\%] = \frac{\Delta\chi}{\chi_{lf}} \times 100[\%] \quad (2)$$

Since  $\Delta\chi$  is a proxy to determine the relative intensity of pedogenesis by tracking super-paramagnetic particles in the magnetic grain size around 30 nm (Peters and Dekkers, 2003), this parameter was used for comparison to the fluctuations in the LR04 stack following (Laag et al., 2021a). By recognizing similar patterns both in LR04 and  $\Delta\chi$  fluctuations, 12 tie points were selected to create a correlative age model for the whole Zmajevac LPS (Table 2). This age model evaluation was carried out in R (R Core Team, 2021) by using the R-package “astrochron” (Version 0.9, Meyers, 2014). By interpolation between the tie points, for each sample a distinct age was calculated.

### 3.6. Bulk and clay mineralogy

The clay minerals analyses of 19 loess and palaeosol samples were performed using X-ray powder diffraction (XRPD). Preparation for the analyses included carbonate dissolution using acetic acid with ammonium acetate ( $1\ \text{mol}/\text{m}^3$ ) buffer of pH 5 (Jackson, 1956), grinding samples using the McCrone mill and preparation of oriented mounts

**Table 2**

Tie points of the correlative age model derived from the frequency dependency of magnetic susceptibility ( $\Delta\chi$ ) compared to the LR04 stack (Lisiecki and Raymo, 2005) and the ice model by Imbrie and Imbrie (1980).

TP name	depth (m)	Age (ka)
TP_01	0.71	18
TP_02	6.01	52
TP_03	9.41	125
TP_04	10.67	140
TP_05	12.07	192
TP_06	14.17	217
TP_07	14.77	223
TP_08	15.57	240
TP_09	16.97	252
TP_10	18.67	286
TP_11	19.77	317
TP_12	21.57	333

from the  $<2 \mu\text{m}$  fraction. XRPD patterns were recorded on random mounts of bulk samples and oriented mounts. Oriented mounts of the  $<2 \mu\text{m}$  fraction were recorded after the following treatments: a) air drying, b) saturation with  $\text{K}^+$  and  $\text{Mg}^{2+}$  c) ethylene-glycol solvation, d) Mg saturation and glycerol solvation, e) dimethyl sulfoxide (DMSO) solvation, f) heating more than  $\frac{1}{2}$  hour to  $400^\circ\text{C}$  and  $550^\circ\text{C}$  (Moore and Reynolds Jr., 1997; Starkey et al., 1984). A Philips vertical goniometer (type X'Pert) equipped with a Cu tube was used with the following experimental conditions: 45 kV, 40 mA, PW 3018/00 PIXcel detector, primary beam divergence  $1/4^\circ$ , continuous scan (step  $0.02^\circ/2\theta/\text{s}$ ). The interpretation of XRPD and the quantitative analysis of the bulk samples were obtained using HIGH SCORE PLUS (2016) calculation and PDF-4/MINERALS 4.5 (2020) databases. The semi-quantitative analysis of the  $<2 \mu\text{m}$  fraction was performed using the procedure described by (Biscaye, 1965).

### 3.7. Spectrophotometric analysis

Spectrophotometric and diffuse reflectance spectrometry (DRS) measurements were performed with a Konica Minolta spectrophotometer CM 700d at the Leibniz Institute for Applied Geophysics in Hannover, Palaeomagnetic laboratory Grubenhagen. The measurement was performed directly on the filled plastic boxes for magnetic measurements using a lens-open diameter of 0.8 cm, observer angle of  $10^\circ$ , and norm-light source D65. The derived data consist of values from the Lab-colour sphere, providing luminance ( $L^*$ , ranging from 0 (black) to 100 (white)),  $a^*$  (ranging from negative values (green) to positive values (red)), and  $b^*$  (ranging from negative (blue) to positive (yellow)). Additionally, backscattered reflectance values were recorded in the visible light spectrum from 400 to 700 nm in 10 nm intervals. To determine relative abundances of hematite and goethite, 1st derivative values were calculated from sample-wise measured functions of DRS following the approach of Debret et al. (2011), Laag et al. (2021a) and Wu et al. (2018), selecting the first derivative values of 435 nm and 565 nm backscattered intensity values indicative for goethite ( $I_{435}$ ) and hematite ( $I_{565}$ ).

### 3.8. Constructing the correlative age model

Variations in the northern hemisphere climate drive both the intensity of pedogenesis in loess-palaeosol sequences and also the oxygen isotope ratios in the ocean, as evidenced by e.g. the LR04 benthic  $\delta^{18}\text{O}$  stack (Lisiecki and Raymo, 2005). Therefore, this marine stack can be conceptually linked to  $\Delta\chi$  values to provide an age model. This is especially valuable for the older part of the section, where the uncertainty of the pIRIR<sub>290</sub> ages apparently increase and the method reaches its dating limit. Guided by pIRIR<sub>290</sub> ages, selected tie points (see Table 2) were used to quantitatively link the  $\Delta\chi$  values to the age model of the LR04 stack. Data between the tie points were placed on an age scale by linear interpolation.

## 4. Results

Original data of this study discussed in the next chapters (grain-size, end-member modelling, environmental magnetism and DRS data) are available at Mendeley Data (Wacha et al., 2020).

### 4.1. Post-IR IRSL measurements of feldspar

To obtain reliable equivalent doses ( $D_e$ ) used for the calculation of ages, the post-IR IRSL protocol with an elevated temperature stimulation of  $290^\circ\text{C}$  (pIRIR<sub>290</sub>) was used (Thiel et al., 2011). This measuring principle was selected for two reasons. Firstly, it was proven that it is reliable for dating of older material i.e. sediments older than the Last Interglacial (e.g. Li et al., 2018; Murray et al., 2014; Schmidt et al., 2014; Thiel et al., 2011, 2014) and secondly, it was shown that luminescence

signals from feldspars obtained from elevated stimulation temperatures (e.g.  $225$  or  $290^\circ\text{C}$ ) fade less compared to the standard IRSL signal obtained at  $50^\circ\text{C}$ . Fading (anomalous fading – Spooner, 1994; Wintle, 1973) is an athermal loss of signal with time observed in feldspar grains, which causes age underestimation. It can be circumvented by testing the samples for fading (Auclair et al., 2003) and correcting them using procedures proposed by Huntley and Lamothe (2001) for younger samples and Lamothe et al. (2003) or Kars et al. (2008) for older samples.

The elevated temperature post-IR IRSL (or pIRIR) measurements of the polymineral fine-grained fraction were performed as presented for the first time by Thiel et al. (2011) and subsequently successfully used at many other study sites (e.g. Thiel et al., 2014; Wacha et al., 2016, 2018a). This protocol utilizes a preheat of  $320^\circ\text{C}$  for 60s, before an IR stimulation for 100 s on  $50^\circ\text{C}$  and a subsequent IR stimulation on a significantly higher temperature, i.e. on  $290^\circ\text{C}$  for 200 s. The first IR stimulation step is used for recombination of the near-neighbour trap/centre pairs which are prone to fading while the IR stimulation at  $290^\circ\text{C}$  allows the more stable distant trap/centre pairs to recombine (Thiel et al., 2014).

The measured signals were analysed using Analyst 4.31.9 (Duller, 2015). The  $D_e$  values were obtained by integrating the first 3 to 5 s (depending on the sample) of the IRSL decay curve after fitting the dose response curve to a single saturating exponential. The signal of the final 50 s (for younger samples) and 15 s (for older samples) of the decay curve were used for background subtraction. Representative dose response and decay curves for the pIRIR<sub>290</sub> signal of a young (3304) and an old (3315) sample are given in Fig. 5. Most tested aliquots and aliquots used for  $D_e$  measurements showed recycling ratio close to  $1 \pm 0.1$  and recuperation values  $<3\%$ . Dose recovery tests were performed to all stratigraphically youngest samples (3303–3309) and to sample 3314 from the lower part of the section. The dose recovery test is useful to check whether a given dose can be recovered successfully. In case the measured to given dose ratio is close to unity ( $\pm 10\%$ ), the measurement protocol is considered to be appropriate and the sample datable. Doses were recovered from previously bleached aliquots (four hours in a SOL2 solar simulator) to which a dose similar to the natural was given. Residuals were also measured on bleached aliquots and were subtracted from the dose recovery ratios. The dose recovery ratios are satisfactory for the younger samples while the older samples show overestimation. Poor dose recovery tests and high residual doses for the pIRIR<sub>290</sub> signal in samples close to saturation were reported in several studies (e.g. Schatz et al., 2012; Thiel et al., 2014; Wacha et al., 2018a).

To investigate whether our samples are prone to fading and whether this could cause age underestimation, fading tests were performed on three aliquots of four youngest (3303–3306) and three oldest samples (3312, 3313 and 3315). Fading tests were performed according to Auclair et al. (2003) which understands repeated measurements of the sensitivity corrected luminescence intensity after increasing storage times. The given doses were  $\sim 100$  Gy for younger and  $\sim 200$  Gy for older samples. Since the data were significantly scattered, we calculated a mean fading rate ( $g_{2\text{days}}$ -values) for each fading experiment. The young samples yielded a negative fading rate ( $-0.61 \pm 0.36\%/decade$ ), which is consistent to zero with  $2\text{-}\sigma$  uncertainty. For the older samples (3312, 3313 and 3315), the calculated fading rate is  $0.83 \pm 0.33\%/decade$ . For the six older samples (3310–3315) the natural signal saturation ratio was calculated for both without fading correction,  $(n/N)_{\text{nat}}$ , and after the fading correction,  $(n/N)_{\text{corrected}}$  following Lamothe et al. (2003) (Table 3). After the fading correction, all samples except 3310 and 3312 are also close to saturation, showing  $(n/N)_{\text{corrected}} > 0.86$ , which means that the  $D_e$  values of these samples are above  $2D_0$  after the fading correction and indistinguishable from saturation. For these samples, the minimum age calculated from  $2D_0$  divided by the dose rate, was given as the final age estimate (Table 3). Only the sample 3310 and 3312 gave a finite fading corrected age of  $233 \pm 14$  ka and  $162 \pm 10$  ka, respectively (Table 3, values in italic).

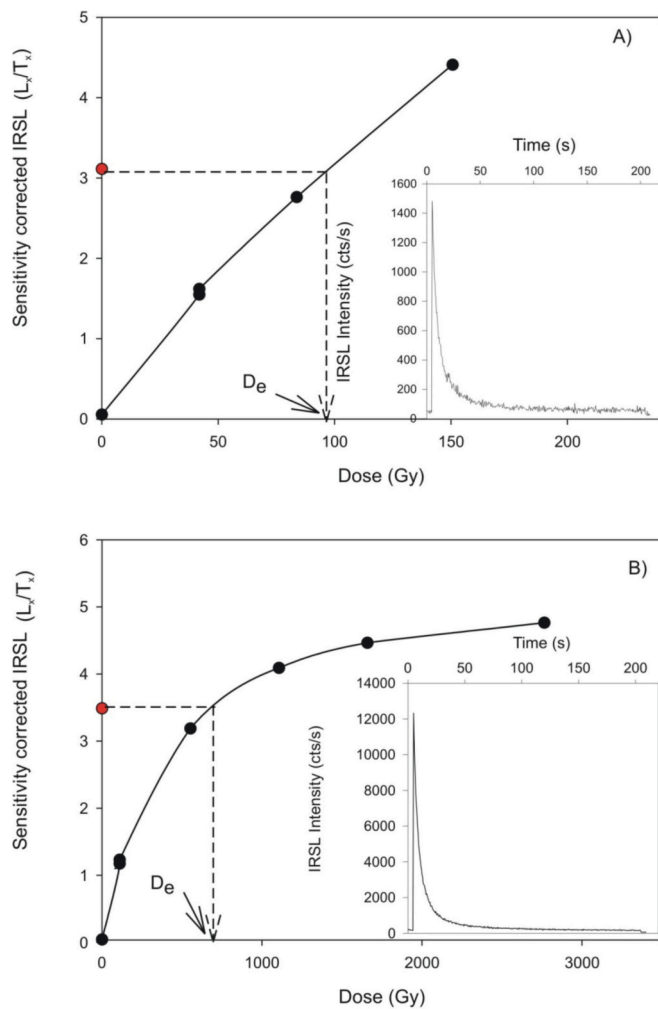


Fig. 5. Decay and Growth curves of an aliquot of a young (3304) and an old (3315) sample.

The chronological framework of the Zmajevac loess section discussed within this paper is based mainly on the fading uncorrected pIRIR<sub>290</sub> ages, especially for the younger part of the section. The samples older than the last interglacial, which were close to saturation, gave dose recovery tests overestimation and a small fading rate, which implies to the possibility of even older ages. For these samples, the minimum age was considered. For samples 3310 and 3312, which did not show saturation of the signal, the age was corrected for fading. The obtained ages and the stratigraphy of the Zmajevac section is given in Fig. 4.

#### 4.2. Grain size properties

A selection of most representative differential grain-size curves of the measured samples are given in Fig. 6. The shapes of the presented frequency distribution curves of selected loess samples are in accordance with typical loess grain-size curves from the region, e.g. from Hungary (Novothny et al., 2011; Újvári et al., 2016a) or Croatia (Wacha et al., 2018a). The curve of the loess-like material at the bottom of the section is identical to the curves of selected loess samples (Fig. 6a) and are mostly unimodal with a tail in the fine-grain fraction. Some samples show a small peak in the fine sand part of the curve (Fig. 6a). Such grain-size distribution is characteristic for loess (Pécsi, 1993; Pye, 1987; Vandenberghe, 2013 – sediment type 1.b., subgroup 1.b.2). Compared to the loess curves, the palaeosol curves are polymodal with a larger proportion in the fine-grained part (<10 μm) which is due to the

**Table 3** Summary of  $D_e$  values, measuring properties, dose rates and calculated pIRIR<sub>290</sub> ages. The fading rates (g-values) of measured samples are given and sample 3312 was corrected for fading (in *italic*). Saturation ratio (n/N) of older samples was checked and a minimum age based on  $2D_0$  values was calculated for samples 3311, 3313–3315.

Sample	Sample ID	$D_e$ (Gy)	Aliquots	Dose recovery	Residuals (Gy)	Dose rate (mGy/ka)	Fading uncorrected age (ka)	$(n/N)_{nat}$	$g_{2days}$ (%/decade)	$(n/N)_{corr}$	$2D_0$ (Gy)	Age min (ka)
ZMA-1	3303	86.85 ± 1.88	8/8	0.92 ± 0.05	9	3.98 ± 0.20	21.80 ± 1.2	-	-0.62	-	-	-
ZMA-2	3304	87.88 ± 1.35	8/8	0.97 ± 0.14	7	3.56 ± 0.20	24.70 ± 1.4	-	-0.62	-	-	-
ZMA-3	3305	89.09 ± 1.48	8/8	0.98 ± 0.05	9	3.21 ± 0.18	27.74 ± 1.6	-	-0.62	-	-	-
ZMA-4	3306	111.76 ± 3.13	8/8	0.93 ± 0.03	10	4.04 ± 0.21	27.65 ± 1.6	-	-0.62	-	-	-
ZMA-5	3307	197.83 ± 3.73	8/8	0.97 ± 0.07	12	3.18 ± 0.18	62.13 ± 3.7	-	-	-	-	-
ZMA-6	3308	206.95 ± 6.78	12/12	0.98 ± 0.02	12	3.19 ± 0.18	64.81 ± 4.3	-	-	-	-	-
ZMA-7	3309	251.69 ± 8.33	5/5	1.32 ± 0.11	22	4.08 ± 0.22	61.73 ± 4.0	-	-	-	-	-
ZMA-8	3310	524.11 ± 36.26	9/9	-	-	2.73 ± 0.17	194 ± 17	0.79	-	0.85	663 ± 6	233 ± 14
ZMA-9	3311	722.10 ± 23.20	5/5	-	-	3.10 ± 0.17	210 ± 14	0.81	-	0.87	782 ± 7	>252 ± 13
ZMA-10	3312	487.94 ± 38.30	6/6	-	-	3.16 ± 0.23	139 ± 10	0.69	0.83	0.74	793 ± 11	162 ± 10
ZMA-11	3313	868.90 ± 32.73	5/5	-	-	3.11 ± 0.21	252 ± 20	0.89	0.83	0.95	740 ± 5	>226 ± 12
ZMA-12	3314	822.03 ± 38.63	10/10	1.71 ± 0.08	3	3.13 ± 0.21	227 ± 17	0.85	-	0.91	790 ± 11	>240 ± 13
ZMA-13	3315	797.79 ± 40.32	4/4	-	-	2.92 ± 0.21	225 ± 16	0.81	0.83	0.87	823 ± 1.4	>268 ± 15

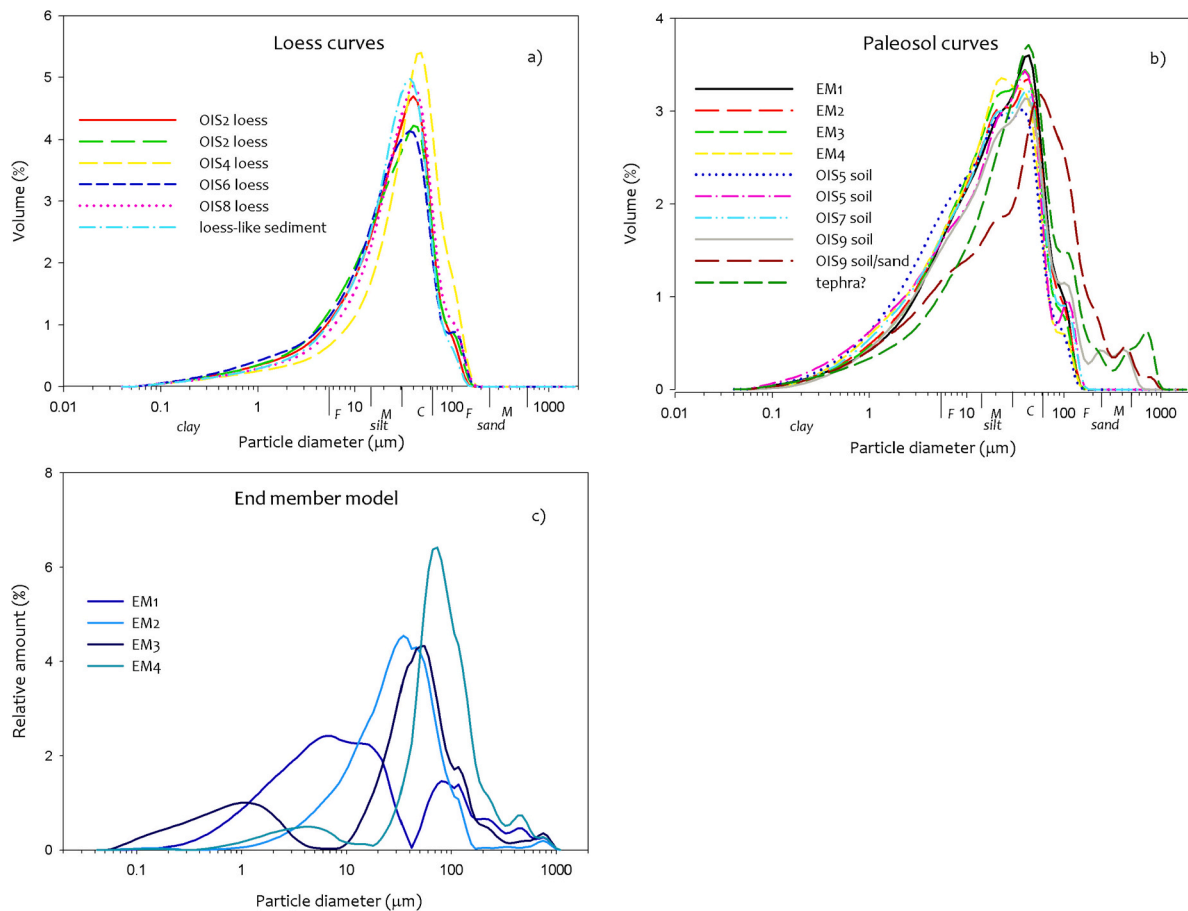


**Fig. 6.** The grain size curves of selected loess and palaeosols samples. a) Loess grain-size curves from loess horizons representing glacial periods (OIS2, 4, 6 and 8). The curve of the sample collected from the loess-like sediment at the base of the Zmajevac section is presented for comparison; b) Grain-size curves of different palaeosols representing interglacial (OIS 5, 7 and 9) and interstadial periods (OIS3). The curve of the distinguishable peak in grain-size on Fig. 4 is presented, as well. The peak could represent a tephra layer. c) Four endmembers obtained using the EMMAgeo package for end member modelling (Dietze and Dietze, 2019). The brighter the colour, the coarser are the grains.

increased amount of clay size particles resulting from soil-forming processes. The palaeosol curves show the same dominant mode (40  $\mu\text{m}$ ) as the loess but also show a second, less prominent peak at  $\sim 20 \mu\text{m}$  (Fig. 6b). A fine-grained population in loess sediments with the modal grain-size of 25–31  $\mu\text{m}$  (1.b.3 subgroup) was recognized by Vandenberghe (2013) in European loess as well as in Red Clays in China and Europe. Several smaller peaks are recognized in the sand fraction. The oldest samples i.e. the OIS9 palaeosol shows several peaks in the sand part and a general increase in the grain size. Its mode is shifted towards the fine and medium sand content while some amount of coarser sand is present as well (Fig. 6b). According to Vandenberghe (2013), the 1.b loess sediments are the most common type of loess sediments, and were deposited during most severe cold periods, and provide an orbital signal. Furthermore, he concluded that they were transported in short-term, near-surface to low suspension clouds. Vandenberghe (2013) also assumed a general source region of all 1.b components to be fluvio-glacial and alluvial plains and alluvial fans of rivers originating from glaciated mountainous areas (e.g. the Danube and the Drava originating from the Alpine region). These rivers were the main sediment carriers during glacial-interglacial changes. The vertical distribution of the mean grain size (Ms) of the Zmajevac section is given in Fig. 7. A general fining upwards trend is recognized within the record. The Ms. of the entire section ranges from 19.7  $\mu\text{m}$  to 79.3  $\mu\text{m}$ , with an average value of 33.5  $\mu\text{m}$  while the median grain-size (Md) ranges from 12.5  $\mu\text{m}$  to 45.5  $\mu\text{m}$ , with an average value of 24.4  $\mu\text{m}$ . Both average values represent the medium silt fraction. The mean value curve pattern (Fig. 7) is similar to the  $>63 \mu\text{m}$  curve pattern which implies that silt-sized particles

predominate in the sediment. The content of particles  $<5.5 \mu\text{m}$  (clay-sized particles) ranges from 9.4% to 30.8%, with an average value of 17.6%. The content of the sand fraction ( $>160 \mu\text{m}$ ) is up to 13%. Coarse sand (630–2000  $\mu\text{m}$ ), present in small amounts (up to 2%), is present only in the OIS 9 palaeosol. A more prominent increase of coarser grain sizes is visible within the OIS9 soil and the covering loess as well as in the OIS5-4 transition and OIS4 loess. An increase in grain-size during OIS6-4 compared to OIS2 was also recognized in the Süttő section in Hungary (Novothy et al., 2011) and in the Surduk section in Serbia (Antoine et al., 2009). Within the OIS8 loess, there is a pronounced peak in the mean grain size and coarse fraction (Fig. 7), which may relate to a tephra layer.

The U-ratio is a useful proxy for discriminating cold periods (high U-ratio), characterized by a dynamic aeolian environment (strong winds), from warm periods (low U-ratio), with weak winds (Vandenberghe et al., 1985). The U-ratio obtained from the Zmajevac samples range from 1.5 to 5.2 which is relatively high compared to some loess sections in the region (Obrecht et al., 2014, 2016; Vandenberghe et al., 2014). The U-ratio is highest for the OIS4 loess as well as for OIS8 loess (Fig. 7) which could imply to the accumulation of coarser grain sizes probably due to increased aridity and stronger wind activity. But it is more likely that the proximity of the Danube as a sediment source had an important influence in the contribution of coarser grain sizes (e.g. Zeeden et al., 2016). This is also supported by the laminated horizon intercalated within the penultimate glacial loess. The clay content ( $<5.5 \mu\text{m}$ ) spans from 9.4 to 30.8% with highest rates related to the palaeosol layers and is a result of weathering and soil-forming processes (e.g. Taheri et al., 2020).



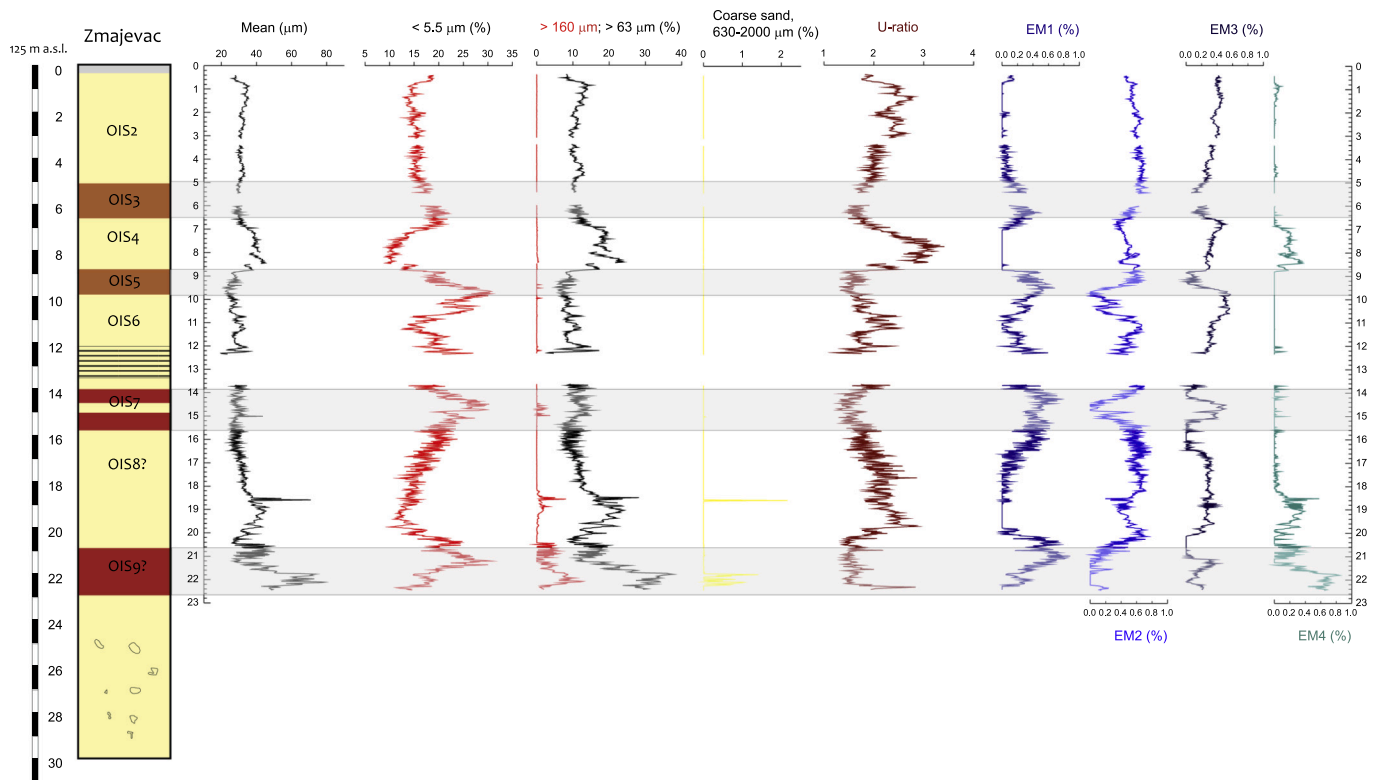


Fig. 7. Variations with depth of the grain-size content and some grain-size parameters. The samples were taken in 2 cm resolution. The loess-palaeosol section of Zmajevac is given on the left with the interpreted stratigraphy based on pIRIR<sub>290</sub> ages presented in Fig. 5. Loadings of the four endmembers obtained from end member modelling (Dietze and Dietze, 2019) are given for comparison.

#### 4.3. End-member modelling analysis

EM modelling uses 4 EMs here, reflecting variations in grain sizes for distinct grain size distributions. The modelled end-members are shown on Fig. 6c which displays the contribution of all grain size classes to the modelled EMs. EM1 has two major contribution groups of two grain size classes of the fine and medium silt particles. EM1 shows another, less pronounced peak in the very fine sand range. EM2 and EM3 reflect grain size classes ranging in the medium and coarse silt fraction, however, EM3 has an additional component of fine particles (clay size particles). EM4 comprises the highest contribution of coarser grain sizes including very fine and fine sand. The contributions of EMs through time, derived from the integrated age model are plotted on Fig. 7 for comparison with grain size proxies.

#### 4.4. Bulk and clay mineralogy

Table 4 shows the quantitative mineral composition of the analysed bulk samples. The main mineral components of the analysed loess and palaeosol samples are quartz and clay minerals while plagioclase is present in a lesser quantity. Calcite and/or dolomite are present in a smaller quantity in all samples except in the sample collected from the double reddish-brown palaeosol (sample ZmF 220–230). In some samples, a negligible number of amphiboles and K-feldspar are also present. Table 4 also shows the semi-quantitative composition of the fraction of less than 2 µm. Illitic material, chlorite and smectite are present in all samples while kaolinite and quartz are present in all samples in a lesser quantity. These findings are in general agreement with observations made by Újvári et al. (2012) with samples stemming from the Carpathian Basin. Vermiculite is uncertainly determined in only a few samples (Table 4). An example of parallel XRD patterns of an oriented and treated sample of the strong reddish-brown palaeosol is given in Supplement 2 (sample ZmG 200–210).

#### 4.5. Rock magnetic properties

As is common for Eurasian loess deposits,  $\chi_{lf}$  and  $\Delta\chi$  are increased in palaeosols and low in pure loess units. The highest  $\chi_{lf}$  and  $\Delta\chi$  values are present in OIS 9, while OIS 7, OIS 5, and OIS 3 are less expressed. The lowest susceptibility values in a soil formation phase are reached in the palaeosol in OIS 3. The palaeosol of OIS 7 is bipartite and shows a general pattern known from other loess-palaeosol sections in the Danube region (e.g. Marković et al., 2009; Újvári et al., 2014b; Zeeden et al., 2016). The younger sub-palaeosol reflects higher susceptibilities than the older part. Magnetic enhancement is well expressed in palaeosol samples. However, pure loess units show no or little enhancement. The background-susceptibility (BGS) of  $18.0 \times 10^{-8} [\text{m}^3\text{kg}^{-1}]$  (Fig. 8) obtained from the Zmajevac section is in excellent agreement with  $18.2 \times 10^{-8} [\text{m}^3\text{kg}^{-1}]$  from Dunaszekcső, Hungary (Újvári et al., 2016a), with  $16.1 \times 10^{-8} [\text{m}^3\text{kg}^{-1}]$  for the Semeac loess section from south-east Romania (Zeeden et al., 2016; Fig. 8) and in good agreement with BGSs calculated from north of Prague ( $22 \times 10^{-8} [\text{m}^3\text{kg}^{-1}]$ ) and Zemechy ( $23 \times 10^{-8} [\text{m}^3\text{kg}^{-1}]$ ) (Forster et al., 1996) as well as Zemun ( $24.6 \times 10^{-8} [\text{m}^3\text{kg}^{-1}]$ ) (Laag et al., 2021a). These values are in accordance with the BGS values of  $17 \pm 2 \times 10^{-8} \text{ m}^3\text{kg}^{-1}$  proposed by (Forster et al., 1994) for central Asian and Chinese Loess-Palaeosol sequences (Fig. 8). In conclusion, the magnetic susceptibility can be regarded as an excellent recorder of the intensity of pedogenesis here.

#### 4.6. Colourimetric analysis

The parameters luminance ( $L^*$ ) and redness ( $a^*$ ) from the Lab color-sphere fluctuate synchronously with changes in the stratigraphy of the Zmajevac section.  $L^*$  values are low in palaeosols, and may be reduced by mineralized organic matter, while  $a^*$  values are high in palaeosols, indicating intense weathering. Both colorimetric parameters fluctuate with the beat of the alternation of interglacials and glacials. For calculations of

**Table 4**  
Quantitative mineral composition of bulk samples (in wt%) and semi-quantitative results of analyses of the <2 µm fraction. tr - Mineral is probably present, but cannot be confirmed with certainty.

Bulk sample	<2 µm												
	Quartz	Plagioclase	Feldspar	Dolomite	Amphibole	Calcite	Clay minerals	Quartz	Illitic material	Smectite	Chlorite	Kaolinite	Vermiculite
ZmA 100-110	36	20	tr	19		9	16	30	47	11	7	5	
ZmA 200-210	37	11	tr	19		12	21	27	51	11	8	3	
ZmB 390-400	33	16		19		7	25	17	55	16	7	5	
ZmB 470-780	32	18		13		6	31	17	53	15	9	6	
ZmC 640-650	33	15	tr	7	tr	19	26	21	48	17	12	3	
ZmC 740-750	33	16		14		12	25	24	47	15	9	5	
ZmC 800-810	31	16		20		11	22	21	51	14	8	6	?
ZmD 842-852	34	17	tr	16		9	24	24	50	14	8	4	
ZmD 950-960	38			10		20	32	40	40	12	8	tr	tr
ZmE 90-100	33	14		20		12	21	55	24	8	8	5	
ZmF 10-20	38	19				3	40	46	33	11	10	tr	
ZmF 90-100	33	10	tr			25	32	52	21	13	11	3	
ZmF 220-230	40	15				45	45	41	35	14	10	tr	?
ZmG 80-90	31	17		10		13	29	50	32	9	7	2	
ZmG 135-145	38	14		3		11	34	33	48	11	8	tr	
ZmG 200-210	40	12		10		13	35	34	46	10	10	tr	tr
ZmH 1/2	37	18	tr	10		11	24	57	24	7	8	4	
ZmH 2/1	35	11		18		11	25	36	40	10	11	4	
ZmH 4/1	35	20	tr	3	tr	4	38	47	28	12	9	4	

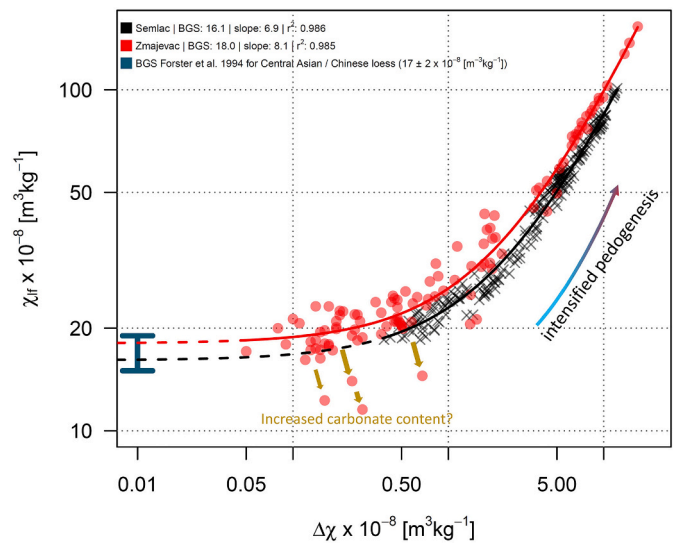


**Fig. 8.** Enhancement plot of all Zmajevac samples compared to data from Semlac (Romania, Zeeden et al., 2016). Background-susceptibility (BGS) is comparable similar to Semlac samples and falls inside the BGS proposed by Forster et al. (1994) for Central Asian and Chinese loess. 4 samples might reflect increased carbonate contents.

correlation values, all samples ( $n = 109$ ) were included. The  $L^*$  value is always reduced in OIS9, OIS7, OIS5 and OIS3 and reflects local minima in the palaeosol layers. The minimum of  $L^*$  is reached in the palaeosol correlated to the OIS9. Overall, an increasing trend of  $L^*$  over the whole profile is recognizable. A similar pattern in intensity and trend is observable by investigating the fluctuation of the  $a^*$  value, reaching its maximum in the palaeosol OIS9. However, the  $a^*$  value is in the palaeosols correlated to OIS 5 and OIS 3 not that highly expressed compared to the  $L^*$  value. The values of  $L^*$  and  $a^*$  correlate with  $r = -0.69$ ,  $p(a) < 2.2 \times 10^{-16}$ . The negative correlation is explained by the decrease of the  $L^*$  value, representing more organic matter in the palaeosols, and increase of  $a^*$ , assigned as indicator for weathering. On the contrary, the blueness ( $b^*$ ) barely follow the alteration of palaeosols and loess units, but shows in distinct intervals (0.0–6.0 m, 14.50–15.50 m, 18–21 m) similar trends.  $L^*$  and  $b^*$  reflect no correlation ( $r = 0.095$ ,  $p(a) = 0.3192$ ), while  $a^*$  and  $b^*$  reflect a weak correlation ( $r = 0.36$ ,  $p(a) = 7.26 \times 10^{-05}$ ). First derivative intensity values of the diffuse reflectance spectra at 435 nm ( $I_{435}$ , indicative for goethite) and 565 nm ( $I_{565}$ , indicative for hematite) reflect similar patterns in intensity and trend like  $a^*$  and  $L^*$ . However,  $I_{435}$  is low and  $I_{565}$  is increased in the palaeosol layers.  $L^*$  and  $I_{435}$  correlate with  $r = 0.95$ ,  $p(a) < 2.2 \times 10^{-16}$ , and negatively with  $a^*$  with  $r = -0.76$ ,  $p(a) < 2.2 \times 10^{-16}$ . No or weakly expressed correlation is observed with  $b^*$  leading to  $r = 0.18$ ,  $p(a) = 0.05599$ . On the contrary,  $I_{565}$  and  $b^*$  correlate with  $r = 0.64$ ,  $p(a) = 3.228 \times 10^{-14}$ . A weak negative correlation is observed by correlating  $L^*$  and  $I_{565}$ , leading to  $r = -0.26$ ,  $p(a) = 0.00548$ . The  $a^*$  reflects a strong correlation to  $I_{565}$ , yielding to  $r = 0.87$ ,  $p(a) < 2.2 \times 10^{-16}$ . The resulting correlations of  $a^*$  and  $I_{565}$  indicate the traceability of redness of hematite by both colorimetric parameters, where hematite seems to appear also under weathering conditions. The negative correlation of  $L^*$  and  $I_{565}$  hints that more hematite is present in loess-units than in palaeosol units, which is in general agreement with recent findings from Laag et al. (2021a). Resulting from the ratio of  $I_{565}$  and  $I_{435}$ , we calculated the widely used hematite/goethite ratio (HGR, e.g. Laag et al., 2021a; Wu et al., 2018) and tested its correlation to the mentioned colorimetric parameters from the Lab colorsphere. HGR is high in palaeosols and low in loess units. In OIS9, HGR reaches its maximum and decreases from palaeosol to palaeosol towards the top of the profile. HGR correlates with  $L^*$  with  $r = -0.76$ ,  $p(a) < 2.2 \times 10^{-16}$ , with  $a^*$  with  $r = 0.95$ ,  $p(a) < 2.2 \times 10^{-16}$ , and with  $b^*$  very weakly with  $r = 0.14$  and  $p(a) = 0.1254$ .

## 5. Discussion

### 5.1. Chronology and stratigraphy of Zmajevac

A previous geochronological study of the Zmajevac loess section (Galović et al., 2009) was based on IRSL data. The results implied that at least two glacial cycles are archived at Zmajevac. The oldest obtained age of the lowermost dated sample at Zmajevac was  $217 \pm 22$  ka (Galović et al., 2009). Nevertheless, the obtained ages were ambiguous and the correlation with other nearby dated sections was not straightforward. It should be also considered that within the study of Galović et al. (2009) the multiple aliquot additive dose (MAAD) protocol was used for obtaining the equivalent doses ( $D_e$ ) as well as no fading corrections were performed. Hence the obtained data must be underestimated. Nevertheless, the data presented within this study partly support the first reconstructions by Galović et al. (2009) and give a more detailed and robust chronological framework.

The presented pIRIR<sub>290</sub> ages clearly show that at Zmajevac, a sedimentary archive of at least three glacial-interglacial cycles is exposed. The Zmajevac loess section starts with a horizon of clayey silt rich in carbonate concretions on top of which a strong rubified brown palaeosol is developed. The age of this loess-like horizon is not known; it can be correlated to the Middle Pleistocene ( $> 280$  ka; OIS9 or older). The lowermost palaeosol was covered with loess which gave uncorrected pIRIR<sub>290</sub> ages of  $225 \pm 16$  ka (sample 3315),  $227 \pm 17$  ka (sample 3314) and  $252 \pm 20$  ka (sample 3313) (Fig. 4). However, after the fading correction, the natural pIRIR<sub>290</sub> signal of the samples are indistinguishable from saturation and only the minimum age can be given,  $>268 \pm 15$  ka (sample 3315),  $>240 \pm 13$  ka (sample 3314) and  $> 226 \pm 12$  ka (sample 3313). Nevertheless, when all data are considered we tentatively propose this soil to correlate to OIS 9 and the oldest loess to OIS 8.

Above the oldest loess horizon, the double reddish-brown palaeosol is exposed. Based on the obtained pIRIR<sub>290</sub> ages, the age of this soil complex is ambiguous. Below the double palaeosol (sample 3313) an uncorrected age of  $252 \pm 20$  ka (corrected minimum age of  $>226 \pm 12$  ka) was obtained from the loess. Above this soil complex laminated sand is exposed which gave a fading corrected pIRIR<sub>290</sub> age of  $162 \pm 10$  ka (sample 3312). This age seems underestimated when compared with surrounding data. This age can also be correlated to OIS6, implying that the surrounding ages obtained from loess are overestimated. However, it was shown in many studies that pIRIR<sub>290</sub> dating protocol applied on loess samples gave reliable ages for older samples ( $>OIS6$ ) useful for stratigraphic interpretations and correlation deposits (e.g. Thiel et al., 2014). The loess above the sand gave uncorrected ages of  $210 \pm 14$  ka (sample 3311, fading corrected age) and  $233 \pm 14$  ka (sample 3310, below the brown palaeosol, corrected minimum age of  $>243 \pm 14$  ka). It is not quite clear what is the reason for this age inversion. A similar discrepancy of the age of the laminated horizon was observed by Fenn et al. (2020) for the Erdut section. Fenn et al. (2020) recorded an age overestimation of a sample collected from the top of the laminated sediment, which they explain due to its fluvial origin of the sand causing partial bleaching. As described in Fenn et al. (2020), it is very likely that the sand was reworked, insufficiently bleached during deposition (fluvial transport) and recently bioturbated and thus the obtained age underestimated. Nevertheless, the age of the laminated sediment from Zmajevac of  $162 \pm 10$  ka (fading corrected age; sample 3313) correlates well with results from nearby Erdut section and implies the same conclusion as Fenn et al. (2020), a temporary shift to fluvial sedimentation. Similar was also recorded at Stari Slankamen (Marković et al., 2011).

A double palaeosol is exposed at the Šarengrad II section in Croatia. Based on pIRIR<sub>225</sub> ages the double palaeosol at Šarengrad II was tentatively correlated to the OIS7 (Wacha et al., 2013). Similar double soil complex is also reported in the Danube loess region; the V-S2 in the Serbian loess stratigraphy (Marković et al., 2013, 2015) and the BD<sub>1</sub>-BD<sub>2</sub> in the Hungarian loess stratigraphy (Thiel et al., 2014; Újvári et al., 2016a) and is correlated to OIS7. Based on our results, for which we

acknowledge that they are ambiguous in this part of the section, we also tentatively correlate the double palaeosol to OIS7 (Fig. 4). The fading corrected age of  $233 \pm 14$  ka (sample 3310) and fading uncorrected age of  $210 \pm 14$  ka (sample 3311) obtained from the loess covering the laminated sand can be correlated to at least OIS6, i.e. to the Penultimate Glacial or any older glacial. But when the minimum age of  $>252 \pm 13$  ka (sample 3311) is considered a correlation to OIS8 is more appropriate. Nevertheless, the data clearly shows evidence of erosional processes within this loess horizon (laminated sand horizon and reduced thickness of the covering palaeosol-OIS5). A more detailed record of OIS6 loess is exposed at Erdut (Fenn et al., 2020) giving pIRIR<sub>225</sub> ages ranging from  $137 \pm 6$  ka to  $158 \pm 8$  ka. Above the Penultimate Glacial loess (OIS6) at Zmajevac, a strong brown palaeosol is exposed bracketed with pIRIR<sub>290</sub> ages of  $233 \pm 14$  ka (fading corrected age, sample 3310) and  $61.7 \pm 4.0$  ka (sample 3309; Fig. 4). These results place the brown palaeosol into OIS5. A single thick brown palaeosol correlating to OIS5 is also exposed at the Gorjanović loess section in Vukovar (Wacha and Frechen, 2011) but the soil there has a significant thickness compared to the Zmajevac OIS5 soil. A single soil pedocomplex (S1 palaeosol after Marković et al., 2009) is correlated with the complete OIS5 period in the Danube loess stratigraphy (Marković et al., 2015). Furthermore, the results from Zmajevac are very similar when compared to the fading corrected pIRIR<sub>225</sub> ages from the Gorjanović loess section in Vukovar (Wacha and Frechen, 2011). In Vukovar ages around 64 ka were obtained above the OIS5 palaeosol, same as in Zmajevac (Fig. 4) but significantly younger ages were obtained for the Penultimate Glacial (OIS6) loess ( $141 \pm 11$  ka; Wacha and Frechen, 2011). The somewhat older ages of the Penultimate Glacial loess from Zmajevac directly below the OIS5 soil could be due to age overestimation but could also imply erosion, possibly due to fluvial activity and/or erosion due to its ridge position. A larger discontinuity was also recognized at the Paks loess section in Hungary (Thiel et al., 2014) where the OIS4 loess and the OIS5 soil are completely missing. However, this is not the case with the Paks cores (Novothy et al., 2020) where the last interglacial palaeosol is preserved. The difference between the Paks outcrop and core record is very likely due to their position, the Paks section being in a slope position prone to erosion. The Last Glacial loess from Zmajevac gave ages ranging from  $64.8 \pm 4.3$  ka to  $21.8 \pm 1.2$  ka (Fig. 4). Within the Last Glacial loess, a weakly developed brown palaeosol is intercalated. It is bracketed by pIRIR<sub>290</sub> ages of  $62.1 \pm 3.7$  ka obtained below and  $27.6 \pm 1.6$  ka above the palaeosol. These ages imply that soil-forming processes happened during the OIS3. In the wider area, OIS3 is characterized by soil formation and weakly developed soils (LIS1 in Serbian loess stratigraphy; Marković et al., 2015) or humic and weakly developed soil horizons (e.g. Novothy et al., 2011; Újvári et al., 2014b) are often recognized within the Last Glacial loess. The ages of the youngest exposed loess range from  $21.8 \pm 1.2$  ka to  $27.6 \pm 1.6$  ka. The obtained results also revealed that deposits younger than 20 ka are missing, which was also observed in the nearby section of Dunaszekcső (Újvári et al., 2014a, 2016b, 2017). The age of the uppermost sample is  $21.8 \pm 1.2$  ka above which the recent soil is exposed. It is very likely that loess younger than 20 ka was pedogenetically altered to form the modern soil (Rubinić et al., 2018) but erosion and agricultural activity could be the reason for the hiatus, too. The age-depth plot resulting from the correlative age model and the pIRIR<sub>290</sub> ages is given in Fig. 9 while the comparison of the independently developed age models is given in Fig. 10. Fig. 9 shows the underestimation of the (Galović et al., 2009) data, especially in the older part and the dating limit of the older samples. Nevertheless, within error limits, the ages can be used as a chronological framework and for stratigraphic interpretations. To reliably establish a correlative age model, several assumptions are taken into considerations, including guidance by luminescence data, experience in the proxy patterns of soils and importantly field experience. The age model can be assumed to be correct on glacial/interglacial and possibly obliquity timescales. However, we can also expect imperfections due to (a) uncertainty of the LR04 stack on the order of 4 ka (Lisiecki and Raymo, 2005), (b) uncertainty in



the tie points due to the low-resolution magnetic susceptibility data (on the order of several ka up to  $\sim 20$  ka), and (c) probably not uniform sedimentation rates between tie points. In addition, the tie point at the end of MIS 7 may be shifted towards younger ages, but the rather low-resolution  $\chi$  data do not allow an unambiguous assignment.

## 5.2. Palaeoenvironmental evolution derived from the grain size record and the EMM

At the base of the Zmajevac loess-palaeosol section loess-like sediments are exposed on top of which the oldest (OIS9) palaeosol is formed. This palaeosol has an increased sand content which implies, same as the loess-like sediment below, that approximately during the antepenultimate glacial (OIS8) the environment in the area transitioned from an alluvial plain environment of the rivers Drava and Danube into a plateau-like, stable, aeolian depositional environment. The high contribution of EM4 indicates abundant local material. The evidence of the aeolian influence is the relatively constant influx of silt in the grain-size record (average Ms.  $33.5 \mu\text{m}$ ; the dominance of the silt fraction and the consistent presence of EM2 and EM3). The increased sand content in the lower part of the section, besides the vicinity of the alluvial source, may also be related to stronger winds during the OIS8. Regarding the pedogenesis, the clay content and EM1 is here considered a direct result of the pedogenesis. Our data clearly show the differentiation between cold glacial periods and the overprint of warmer climate on loess, evidenced as palaeosols. The OIS3 soil, however, shows only weak pedogenic overprinting, compared to older soils. This is a common feature in Eurasian loess with different soil formation intensity (Bronger, 1975), which is consistently weaker than interglacial soil formation. The U-ratio shows different values for loess and for palaeosols, which also indicates a difference in wind strengths over the last  $\sim 330$  ka. The U-ratio values of OIS8 reflect first a rapid increase of wind strength towards younger samples until  $\sim 20$  m, then a gentle decrease, indicating a progressively weakening wind strength. Wind intensities from OIS7 and 6 remain on a quasi-comparable low level. Thus, the variations of the U-ratio values remain lower in the palaeosols compared to the loess units,

indicating more constant wind intensities. Lower U-ratios in palaeosols could also be the result of post-depositional alterations due to pedogenesis. Inside the loess units from OIS 8, 6 and 4, high varying U-ratios may indicate strong wind events, which appear in a somehow cyclical shape. The overall trend of the U-ratio values from OIS6 reflect a slightly decreasing trend as well as in OIS8, but much weaker expressed. OIS4 is indicating first a rapid increase of wind intensity (between 8.5 and 9 m), then a kind of plateau where wind intensities remain strong between 8.5 and 7.5 m, followed by a well-expressed drop in wind intensities (between 7.5 and 6.5 m). However, the availability of coarser grain sizes in the lower part of the section also influences the U-ratio and interpreting the U-ratio as a result of wind strength only would be oversimplification. OIS4 U-ratio values are comparably high, similar to U-ratio values from Süttő (Novothy et al., 2011) but do not reflect any periodicity like in Süttő. The OIS2 loess seems quite uniform if the mean grain-size values are considered (Fig. 7). However, when the total sand content and the U-ratio are taken into consideration one can recognize a slight coarsening upwards trend. This is opposite of what is seen for OIS 8 and OIS4. Similar was also recognized within OIS2 loess from Süttő (Novothy et al., 2011) and Surduk (Antoine et al., 2009). OIS2 loess reflects, opposite to all other loess units, an increasing trend of wind intensities from older to younger samples. The Last Glacial Maximum (LGM - OIS2) is a period with highest mass accumulation rates in Europe (Frechen et al., 2003), due to the availability of the source material as well as the cold, dry and arid climate. Following these observations, the Zmajevac LPS provides insights into past wind intensity changes with more unstable conditions during glacials and more stable wind intensities during interglacials.

We interpret EM1 as representing mainly fine clay particles formed during pedogenesis which is also supported by a good correlation with  $\chi_{fd}$  (%) (see eq. 2) to EM1 scores. The coarse component may be due to aggregation, or due to fine sand input during these intervals. The intermediate EM2 and EM3 may be interpreted as grains provided by longer-distance transport and exclusively aeolian transportation. They could also imply to local supply. EM2 is finer than EM3 and could therefore imply to even more distant sources compared to EM3. EM3 is

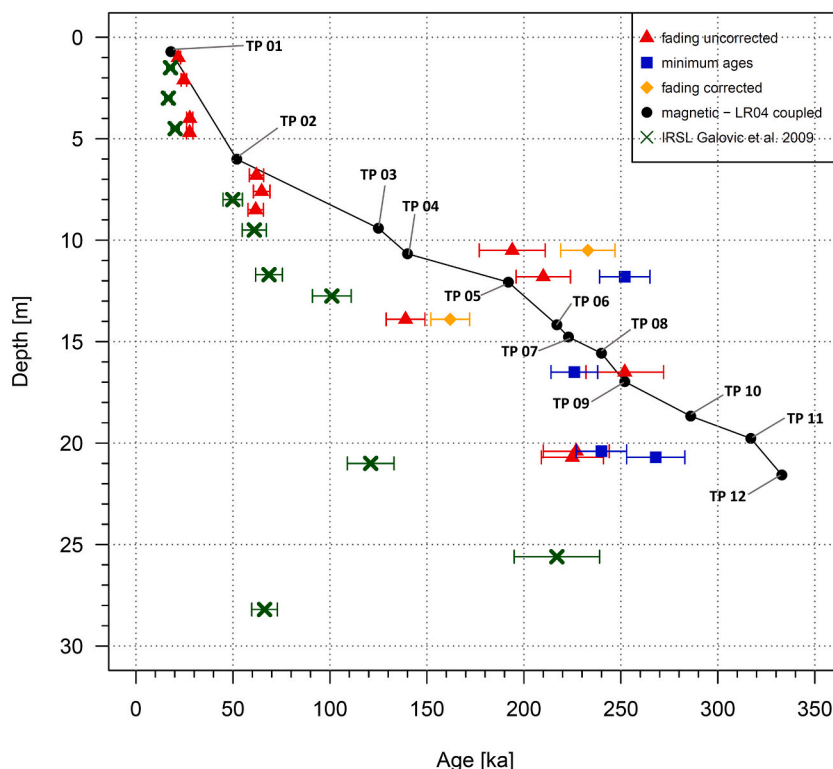


**Fig. 9.** Comparison of the independently developed age models for the Zmajevac LPS. Red triangles - fading-uncorrected pIRIR<sub>290</sub> ages, blue squares - the minimum pIRIR<sub>290</sub> ages; green crosses - IRSL ages from Galović et al. (2009); black filled circles - independently correlated tiepoints from Table 1. The lines in between reflect the interpolation for all samples in between the tie points. The tie points are given in Table 2. (For interpretation of the references to colour in this figure legend, the reader is referred to the web version of this article.)

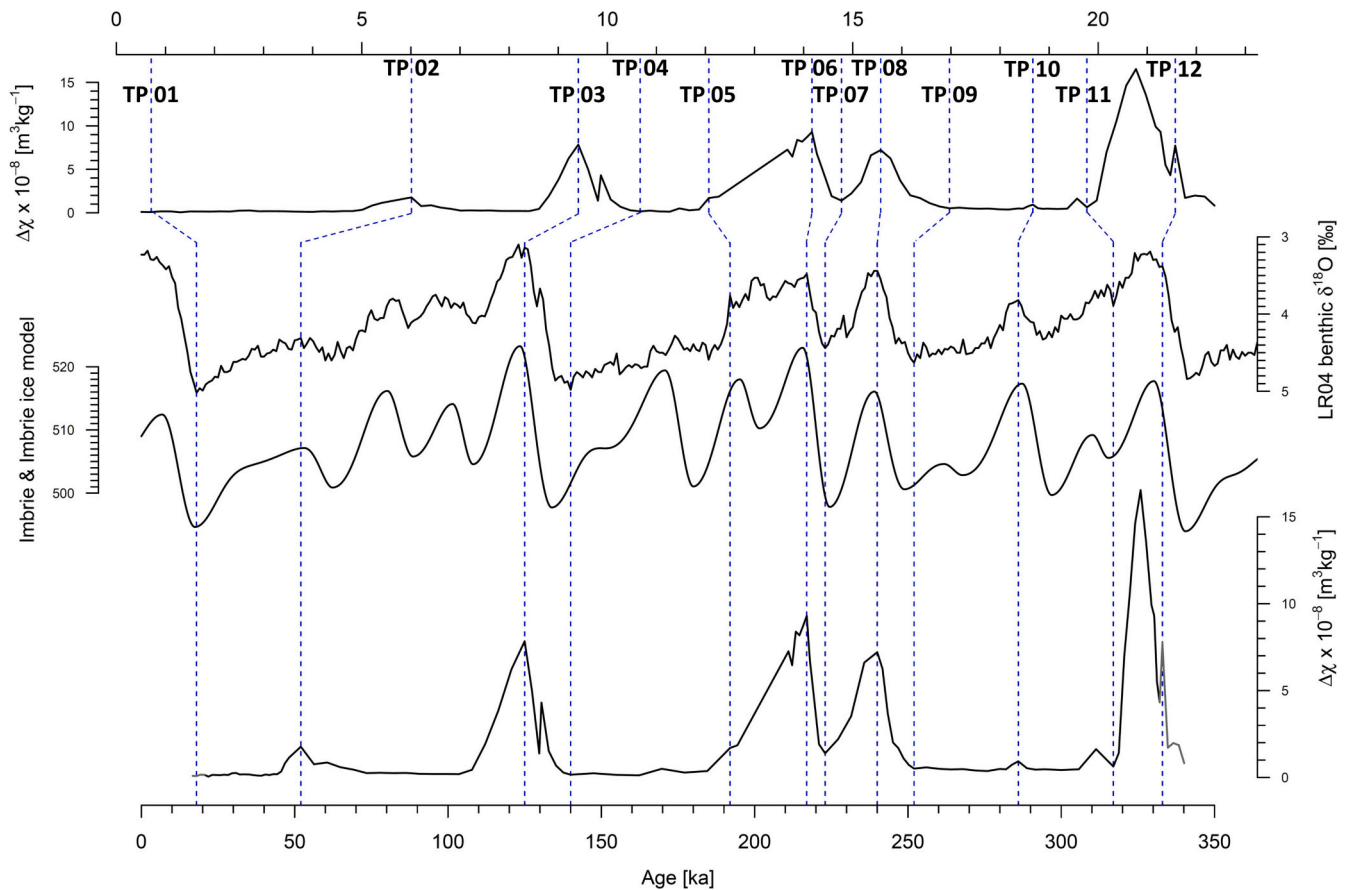


**Fig. 10.** The correlative age model based on the correlation between frequency dependent magnetic susceptibility  $\Delta\chi$  and the LR04 stack and Imbrie and Imbrie (1980) ice model. The tie points are indicated as dashed blue lines and are compiled and labelled in Table 2. (For interpretation of the references to colour in this figure legend, the reader is referred to the web version of this article.)

interpreted as related to silt sources in the wider area (from the direct vicinity to several km) because of its clay contribution and also fine sand component. The negative correlation of EM2 with  $L^*$  reflect low EM scores in palaeosols. Generally, dark sediment colours (low  $L^*$ ) indicate the presence of palaeosol formation and can be correlated with EM2. The applied age model reflects the dependence of increased magnetic susceptibility ( $\chi_{fd}$ ) and its frequency dependence ( $\chi_{fd}$  [%]) where large amounts of fine particles are detectable in consistent stratigraphic units. EM3 also correlates well with the clay content and the U-ratio values (Fig. 7). EM4 reflects coarse grains accumulated predominantly during glacial conditions. Especially OIS 4, OIS6 and OIS8 reflect high amounts of these coarse grain sizes. At the bottom of the Zmajevac LPS, the relative amount of coarse grains is highest. During glacial conditions, intensified wind strength is assumed triggering the increased input of coarse grains to the Zmajevac LPS. Additionally, potential sources (close to the geographical location of the Zmajevac LPS) may be available for uptake, probably alluvial deposits related to the Danube and Drava rivers in the vicinity, because a stabilizing vegetational cover is missing due to too cold and dry environmental conditions during the glacials.

### 5.3. Clay minerals and hematite and goethite content as indicators of provenance and climate

Mineralogical data suggest that the dominant association for loess-palaeosol sequences in Croatia, in particularly Zmajevac is garnet, minerals from the epidote-zoisite group, chlorite and amphiboles (Banak et al., 2013; Galović, 2014). Similar is in the wider Pannonian basin (Thamó-Bozsó et al., 2014). The main mineral phases in the clay mineral fraction are illitic material, smectite and chlorite (Table 4). An almost

identical mineral composition of the clay mineral fraction of two loess samples from the area of Zmajevac was also obtained by Újvári et al. (2012). The vertical distribution along the Zmajevac section is fairly uniform and their mineralogical composition is typical for loess-palaeosol sequences in the area (Marković et al., 2004; Újvári et al., 2012; Varga et al., 2011). The presence of the illitic material and chlorite, which are well represented throughout the profile, could imply to an environment which was cold(er) with reduced chemical weathering and hence limited soil formation (Fanning et al., 1989; Wilson, 1999). A somewhat lesser amount of chlorite was detected in the Last Interglacial brown palaeosol, which probably together with a larger amount of smectite and the absence of feldspar implies to a warmer and more humid environment during the Last Interglacial. Kaolinite is uniformly, but only in subordinate amounts, distributed along the analysed profile with no obvious differences in quantity between loess and palaeosol (Table 4) which could suggest that kaolinite is mainly detrital. This is consistent with the fact that samples mainly contain kaolinite forming intercalation compounds with DMSO or well-crystallized kaolinites. Namely, according to Durn et al. (2014 and references therein) kaolinite that does not intercalate with DMSO is predominantly of paedogenic origin, while kaolinite that forms intercalations with DMSO is inherited from the kaolinite-containing parent rock. Table 4 shows that smectite is more abundant in palaeosol samples as well as in Penultimate Glacial loess, compared to other loess samples, i.e. there is an increased smectite content in the older part of the section. The presence of increased smectite content in the Penultimate Glacial loess and -Interglacial palaeosols probably indicates multiple reworking and resedimentation of these horizons. Generally, there are two main sources of smectite in soils; smectite can be of detrital origin or it can form by alteration of

volcanic material, micas, feldspars and various Fe—Mg silicates (Millot, 1964; Taheri et al., 2020; Weaver, 1989). It can also form by neoformation, by precipitation directly from the solution. According to (Weaver, 1989), climatic and topographic conditions necessary for the formation of smectite are low relief and/or low permeability, low rainfall and low temperature. A part of the smectite in the analysed palaeosols probably has a detrital origin, but a part could have been created by the alteration of mica and/or feldspars, and/or the amphibole-pyroxene group of minerals. The reason for the very low content or the complete absence of vermiculite in the analysed samples (Table 4) could be their alteration into smectite. Dioctahedral vermiculite is more common in soils than trioctahedral vermiculite (Jackson, 1957). Due to continued weathering of minerals such as biotite, trioctahedral vermiculite can be altered in dioctahedral form, but since the charge is usually lowered it alters into smectite (Weaver, 1989). These results are in accordance with (Bronger, 2003) who reported that high amounts of vermiculite are present in loess-palaeosol sequences from Central Asia, whereas in loess-palaeosol sections from Hungary, Serbia and Croatia illite and smectite are dominant mineral phases. Markovic et al. (2004), Galović et al. (2006), Varga et al. (2011) and Újvári et al. (2012; 2014) also presented a similar clay minerals composition (illite, chlorite and smectite) determined in studied loess-palaeosol sequences from Hungary, Serbia and Croatia.

Since the initial work of Deaton and Balsam (1991), distinct back-scattered wavelengths are indicative for the relative abundance of hematite and goethite (e.g. Wu et al., 2018), both high coercive magnetic minerals. This dependence was shown by a recent study from Laag et al. (2021a), by showing high correlations between the mentioned wavelength bands with high-coercivity magnetic parameters. For hematite the favoured forming conditions are precisely investigated and characterized, providing valuable information about the past in terms of temperature, precipitation, and seasonality regimes. Hematite contains only the oxidized form of iron. Its formation is favoured by both a short period of limited precipitation and high temperatures (Maher, 1998).

The limit of precipitation is considered as the ideal formation condition, and usually is below 350 mm/year (Ji et al., 2001, 2002). In relation to magnetite and maghemite, the enhancement of hematite content is positively influenced by a longer warmer and dryer period following a shorter period of soil wetness. It forms most effectively when the period of soil wetting is too short to produce significant contents of magnetite and maghemite, which leads (regarding the mentioned conditions) to reduced magnetic susceptibility (Ji et al., 2001). Additionally, a rapid release of iron under neutral or slightly acidic conditions influences the formation of hematite positively, which forms probably from dehydration of ferrihydrite (Balsam et al., 2004). The determination of goethite content follows the same procedure as hematite with other back-scattered wavelengths. However, the climatic interpretation of the goethite content is more uncertain because formation conditions occur in wide temperature and precipitation regimes. Commonly, the goethite formation is connected to lower temperatures and/or higher (less seasonal) precipitation than favoured by the formation of hematite. Additionally, the goethite formation is favoured under higher organic matter content, lower pH and increased aluminium concentration (Balsam et al., 2004).

Diffuse reflectance spectrometry provides insights into relative abundances of hematite and goethite, whose favoured conditions for neoformation is well-known. Luminance ( $L^*$ ) reflects darkness in palaeosols and bright colours in pure, unweathered loess units and correlates negatively with  $\Delta\chi$  values. The high  $L^*$  values in loess represent higher amounts of bright minerals like quartz and carbonates. Darker material (reduced  $L^*$ ) is commonly found in palaeosols, mostly influenced by weathered organic matter and changed mineral composition. Generally, in Fig. 11 the frequency dependent susceptibility, goethite (green), and hematite (red) are displayed on an age scale produced by the age model comparing LR04 and depth-based  $\Delta\chi$  values. Reflectance values, indicating goethite abundance, show correlation with  $\Delta\chi$  values ( $r = -0.81$ ,  $p(a) < 2.2e-16$ ,  $n = 109$ ). Generally, goethite abundances are the lowest, where palaeosols are indicated by high  $\Delta\chi$

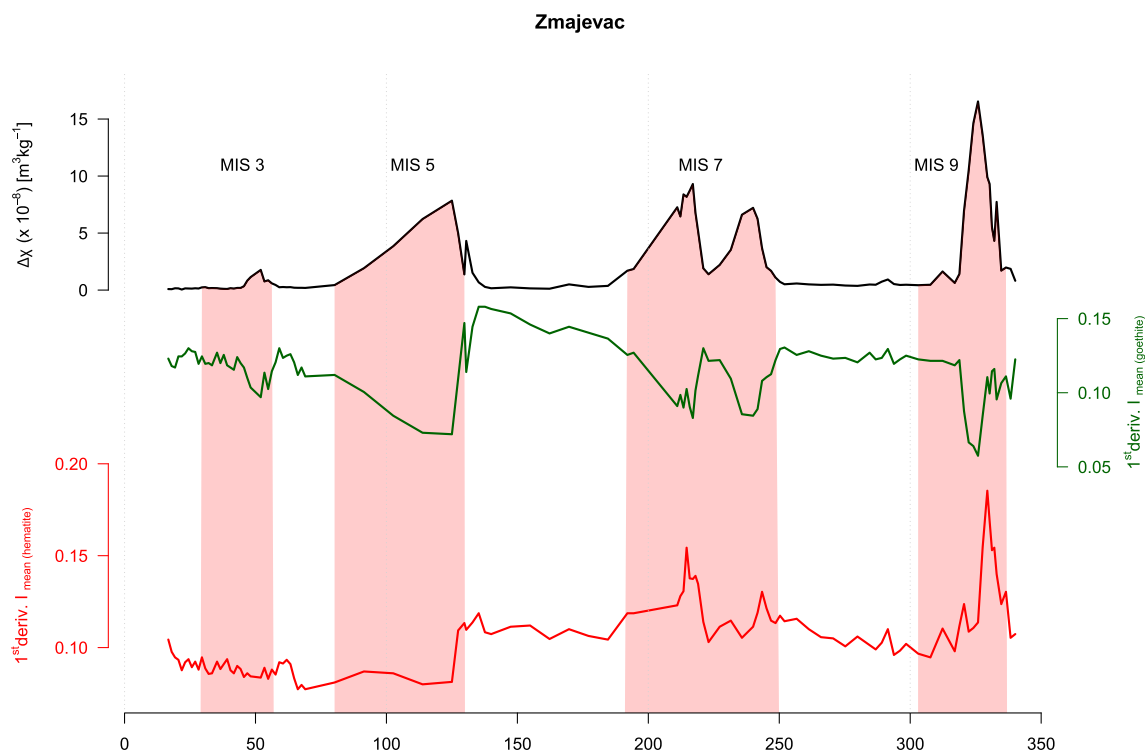


**Fig. 11.** Frequency dependence of magnetic susceptibility ( $\Delta\chi$ , black), first derivative of DRS intensity wavelength 435 nm (green, indicative for goethite) and 565 nm (red, indicative for hematite) on an age scale derived from the tie points of the correlative age model (Table 1). (For interpretation of the references to colour in this figure legend, the reader is referred to the web version of this article.)

values. Hematite is increased in warm (uneven) OISs, except for OIS3 and 5, and decreases from the oldest samples to the youngest ones. The highest abundance of hematite is in OIS9 palaeosol. Goethite fluctuations of OIS 7 are divided into an older (badly expressed) peak and younger peak, which are well expressed and timed, where the  $\Delta\chi$  values are the highest. A clear and permanent drop in hematite content appears at the beginning of OIS 5, where the lowest hematite contents are displayed, which is unusual and interesting regarding the palaeoclimatic implications during OIS 5. In OIS 3, the hematite content is increasing again. Commonly, OIS 9 and 5 are the most intense interglacials in the last 350 kyr (PAGES, 2016). At Zmajevac OIS 9 fits this pattern, whereas OIS 5 does not. The decreasing trend from older to younger samples of the HGR was observed in the Zemun LPS (Laag et al., 2021a) and interpreted as decreasing of summer temperatures. While at Zemun a very slight decreasing trend of susceptibility parameters is observed in palaeosols from older to younger samples, Zmajevac indicates an overall, clearly visible decreasing trend.

## 6. Conclusion

The Zmajevac loess-palaeosol section was re-examined in high resolution to get insight into the palaeoclimatic history of the region and to update the chronological framework. A detailed and robust chronology is given, established based on post-infra-red stimulated luminescence (IRSL) dating with luminescence signals registered at 290 °C (post-IR IRSL<sub>290</sub> or pIRIR<sub>290</sub>). The obtained results show that, contrary to previous interpretations, at least three glacial-interglacial cycles are preserved at Zmajevac. While the pIRIR<sub>290</sub> ages of the older samples are somewhat ambiguous, the younger samples are in stratigraphic order. The correlative age model, which is based on  $\Delta\chi$  to LR04 correlations, generally supports the luminescence-based stratigraphy of Zmajevac.

Changes in grain-size were analysed with respect to supposed atmospheric dynamics of the area and the palaeoclimate. Four grain size EMs were identified. We interpret EM1 as representing mainly fine silt and clay particles formed during pedogenesis which is also supported by a good correlation with  $\chi_{fd}$  (%). The intermediate EM2 and EM3 may be interpreted as grains provided by longer-distance transport and exclusively aeolian entrainment. EM4 reflects coarse grains accumulated predominantly under glacial conditions. The EM-s distinguish grain-size subpopulations which may imply variations in the provenance of the material. Amplitude and variations of the U-ratio inside palaeosol- and loess units indicate differences in wind intensity and changes of individual and high-intensity wind events in interglacials and glacials as well as changes in the distance to the source area. Loess units witness increased wind intensities with intercalated high-intensity events whereas palaeosols, in contrast, reflect milder, less windy and more stable conditions. Besides the wind intensity, the increase in grain size visible in the older part of the section also indicates the shorter distance of the source area, which are the nearby alluvial deposits of the Drava and Danube.

The mineralogical composition of the Zmajevac section consists dominantly of quartz, clay minerals, plagioclase and calcite. The distribution of the clay minerals is fairly uniform, consisting dominantly of smectite, illitic material and chlorite, which is comparable with earlier studies of loess-palaeosol sequences in the SE part of Central Europe/Danube loess region. The presence of the increased smectite content in the Penultimate Glacial loess and -Interglacial palaeosols probably indicates multiple reworking and re-sedimentation in this part of the section. Smectite in palaeosols is probably in part of a detrital origin, but a part likely originated from micas and feldspars as a result of weathering.

Changes both in magnetic susceptibility and colourimetric parameters indicate a strong decrease of summer heat and seasonality over the last three interglacial/glacial cycles. Additionally, the decreasing susceptibility parameters may indicate an increased limitation of the palaeoprecipitation. The reason for this decreasing trend remains

questionable and we propose to investigate the Zmajevac section for further colourimetric and rock-magnetic parameters to find an explanation for this trend. The combination of grain size analysis with further colourimetric and rock-magnetic investigations may reveal a direct link of temperature, precipitation and wind-strength seasonality, possibly linked to small millennial-scale climatic changes.

Supplementary data to this article can be found online at <https://doi.org/10.1016/j.palaeo.2021.110504>.

## Declaration of Competing Interest

The authors declare that they have no known competing financial interests or personal relationships that could have appeared to influence the work reported in this paper.

## Acknowledgements

This research was funded by the Croatian Science Foundation (HRZZ, UIP-2013-11-4425 *Standardisation and Applied Investigation of Quaternary Sediments in Croatia*). Special thanks to technicians from S3 and S5 from LLAG, for all the laboratory work; Gudrun Drewes, Astrid Jaeckel, Petra Posimowski, Sonja Riemenschneider and Kathrin Worm. Thanks to Mihovil Brlek for help during sampling. This is IGP contribution 4219.

## References

- Aitken, M., 1998. *An Introduction to Optical Dating*. Oxford University Press, Oxford.
- Antoine, P., Rousseau, D.-D., Fuchs, M., Hatté, C., Gauthier, C., Marković, S.B., Jovanović, M., Gaudenyi, T., Moine, O., Rossignol, J., 2009. High-resolution record of the last climatic cycle in the southern Carpathian Basin (Surduk, Vojvodina, Serbia). *Quat. Int.* 198, 19–36. <https://doi.org/10.1016/j.quaint.2008.12.008>.
- Antoine, P., Coutard, S., Bahain, J., Lochet, J., Hérisson, D., Govaal, E., 2021. The last 750 ka in loess-palaeosol sequences from northern France: environmental background and dating of the western European Palaeolithic. *J. Quat. Sci.*, jqs.3281 <https://doi.org/10.1002/jqs.3281>.
- Auclair, M., Lamothe, M., Huot, S., 2003. Measurement of anomalous fading for feldspar IRSL using SAR. *Radiat. Meas.* 37, 487–492. [https://doi.org/10.1016/S1350-4487\(03\)00018-0](https://doi.org/10.1016/S1350-4487(03)00018-0).
- Balsam, W., Ji, J., Chen, J., 2004. Climatic interpretation of the Luochuan and Lingtai loess sections, China, based on changing iron oxide mineralogy and magnetic susceptibility. *Earth Planet. Sci. Lett.* 223, 335–348. <https://doi.org/10.1016/j.epsl.2004.04.023>.
- Banak, A., Pavelić, D., Kovačić, M., Mandić, O., 2013. Sedimentary characteristics and source of loess in Baranja (Eastern Croatia). *Aeolian Res.* 11, 129–139. <https://doi.org/10.1016/j.aeolia.2013.08.002>.
- Basarin, B., Bugle, B., Hambach, U., Marković, S.B., Dhand, K.O., Kovačević, A., Stevens, T., Guo, Z., Lukić, T., 2014. Time-scale and astronomical forcing of Serbian loess-palaeosol sequences. *Glob. Planet. Chang.* 122, 89–106. <https://doi.org/10.1016/j.gloplacha.2014.08.007>.
- Biscaye, P.E., 1965. Mineralogy and Sedimentation of recent Deep-Sea Clay in the Atlantic Ocean and Adjacent Seas and Oceans. *Geol. Soc. Am. Bull.* 76, 803. [https://doi.org/10.1130/0016-7606\(1965\)76\[803:MASORD\]2.0.CO;2](https://doi.org/10.1130/0016-7606(1965)76[803:MASORD]2.0.CO;2).
- Bokhorst, M.P., Vandenberghe, J., Sümegei, P., Lanczont, M., Gerasimenko, N.P., Matviishina, Z.N., Marković, S.B., Frechen, M., 2011. Atmospheric circulation patterns in central and eastern Europe during the Weichselian Pleniglacial inferred from loess grain-size records. *Quat. Int.* 234, 62–74. <https://doi.org/10.1016/j.quaint.2010.07.018>.
- Bötter-Jensen, L., Thomsen, K.J., Jain, M., 2010. Review of optically stimulated luminescence (OSL) instrumental developments for retrospective dosimetry. *Radiat. Meas.* 45, 253–257. <https://doi.org/10.1016/j.radmeas.2009.11.030>.
- Bradák, B., Seto, Y., Nawrocki, J., 2019. Significant pedogenic and palaeoenvironmental changes during the early Middle Pleistocene in Central Europe. *Palaeogeogr. Palaeoclimatol. Palaeoecol.* 534, 109335. <https://doi.org/10.1016/j.palaeo.2019.109335>.
- Bronger, A., 1975. Paläoböden als Klimazeugen — Dargestellt an Löß-Boden-Abfolgen des Karpatenbeckens. *E & G Quat. Sci. J.* 26, 131–154. <https://doi.org/10.3285/eg.26.1.08>.
- Bronger, A., 2003. Correlation of loess-palaeosol sequences in East and Central Asia with SE Central Europe: towards a continental Quaternary pedostratigraphy and paleoclimatic history. *Quat. Int.* 106–107, 11–31. [https://doi.org/10.1016/S1040-6182\(02\)00159-3](https://doi.org/10.1016/S1040-6182(02)00159-3).
- Chu, W., 2018. The Danube Corridor Hypothesis and the Carpathian Basin: Geological, Environmental and Archaeological Approaches to Characterizing Aurignacian Dynamics. *J. World Prehist.* 31, 117–178. <https://doi.org/10.1007/s10963-018-9115-1>.
- Core Team, R., 2021. R: A Language and Environment for Statistical Computing. R Foundation for Statistical Computing, Vienna, Austria. <https://r-project.org>.



- Deaton, B.C., Balsam, W.L., 1991. Visible spectroscopy; a rapid method for determining hematite and goethite concentration in geological materials. *J. Sediment. Res.* 61, 628–632. <https://doi.org/10.1306/D4267794-2B26-11D7-8648000102C1865D>.
- Debret, M., Sebag, D., Desmet, M., Balsam, W., Copard, Y., Mourier, B., Susperrigui, A.-S., Arnaud, F., Bentaleb, I., Chapron, E., Lallier-Vergès, E., Winiarski, T., 2011. Spectrocolorimetric interpretation of sedimentary dynamics: The new “Q7/4 diagram”. *Earth Sci. Rev.* 109, 1–19. <https://doi.org/10.1016/j.earscirev.2011.07.002>.
- Dietze, E., Dietze, M., 2019. Grain-size distribution unmixing using the R package EMMAGEO. *E & G Quat. Sci. J.* 68, 29–46. <https://doi.org/10.5194/egqsj-68-29-2019>.
- Duller, G.A.T., 2015. The analyst software package for luminescence data. *Ancient TL* 33, 35–42.
- Durn, G., Čorić, R., Tadej, N., Barudžija, U., Rubinić, V., Husnjak, S., 2014. Bulk and clay mineral composition indicate origin of terra rossa soils in Western Herzegovina. *Geol. Cro.* 67, 171–183. <https://doi.org/10.4154/GC.2014.13>.
- Evans, M.E., Heller, F., 2001. Magnetism of loess/paleosol sequences: recent developments. *Earth Sci. Rev.* 54, 129–144. [https://doi.org/10.1016/S0012-8252\(01\)00044-7](https://doi.org/10.1016/S0012-8252(01)00044-7).
- Fanning, D.S., Keramidas, V.Z., El-Desoky, M.A., 1989. Micas. In: Dixon, J.B., Weed, S.B. (Eds.), *SSSA Book Series. Soil Science Society of America, Madison, WI, USA*, pp. 551–634. <https://doi.org/10.2136/sssabookser1.2ed.c12>.
- Fenn, K., Durcan, J.A., Thomas, D.S.G., Banak, A., 2020. A 180 ka record of environmental change at Erdut (Croatia): a new chronology for the loess–paleosol sequence and its implications for environmental interpretation. *J. Quat. Sci.* 35, 582–593. <https://doi.org/10.1002/jqs.3201>.
- Fitzsimmons, K.E., Marković, S.B., Hambach, U., 2012. Pleistocene environmental dynamics recorded in the loess of the middle and lower Danube basin. *Quat. Sci. Rev.* 41, 104–118. <https://doi.org/10.1016/j.quascirev.2012.03.002>.
- Forster, Th., Evans, M.E., Heller, F., 1994. The frequency dependence of low field susceptibility in loess sediments. *Geophys. J. Int.* 118, 636–642. <https://doi.org/10.1111/j.1365-246X.1994.tb03990.x>.
- Forster, Th., Heller, F., Evans, M.E., Havlíček, P., 1996. Loess in the Czech Republic: magnetic properties and paleoclimate. *Stud. Geophys. Geod.* 40, 243–261. <https://doi.org/10.1007/BF02300741>.
- Frechen, M., Schweitzer, U., Zander, A., 1996. Improvements in sample preparation for the fine grain technique. *Ancient TL* 14, 15–17.
- Frechen, M., Oches, E., Kohfeld, K., 2003. Loess in Europe — Mass accumulation rates during the last Glacial Period. *Quat. Sci. Rev.* 22, 1835–1857. [https://doi.org/10.1016/S0277-3791\(03\)00183-5](https://doi.org/10.1016/S0277-3791(03)00183-5).
- Galović, L., 2014. Geochemical archive in the three loess/paleosol sections in the Eastern Croatia: Zmajevac I, Zmajevac and Erdut. *Aeolian Res.* 15, 113–132. <https://doi.org/10.1016/j.aeolia.2014.07.004>.
- Galović, L., Mileušnić, M., Peh, Z., Durn, G., Halamić, J., 2006. Mineralogical and geochemical characteristics of loess/paleosol section in Šarengrad, Srijem, Croatia. In: Vlahović, I., Tibljaš, D., Durn, G., Biševac, V. (Eds.), *Abstract Book - 3rd Mid-European Clay Conference – MECC06*, p. 46. Faculty of Science, Faculty of Mining, Geology and Petroleum Engineering, Zagreb.
- Galović, L., Frechen, M., Halamić, J., Durn, G., Romić, M., 2009. Loess chronostratigraphy in Eastern Croatia — A luminescence dating approach. *Quat. Int.* 198, 85–97. <https://doi.org/10.1016/j.quaint.2008.02.004>.
- Gao, X., Hao, Q., Oldfield, F., Bloemendal, J., Deng, C., Wang, L., Song, Y., Ge, J., Wu, H., Li, F., Han, L., Fu, Y., Guo, Z., 2019. New high-temperature dependence of magnetic susceptibility-based climofunction for quantifying paleoprecipitation from Chinese Loess. *Geochem. Geophys. Geosyst.* 20, 4273–4291.
- Guérin, G., Mercier, N., Adamiec, G., 2011. Dose-rate conversion factors: update. *Ancient TL* 29, 5–8.
- Gyalog, L., Síkhgyei, F., 2005. Geological Map of Hungary, M=1:100 000. Geological Institute of Hungary, Budapest.
- Hao, Q., Guo, Z., 2005. Spatial variations of magnetic susceptibility of Chinese loess for the last 600 kyr: implications for monsoon evolution. *J. Geophys. Res.* 110, B12101. <https://doi.org/10.1029/2005JB003765>.
- Hauk, T.C., Lehmkuhl, F., Zeeden, C., Bösen, J., Thiemann, A., Richter, J., 2018. The Aurignacian way of life: contextualizing early modern human adaptation in the Carpathian Basin. *Quat. Int.* 485, 150–166. <https://doi.org/10.1016/j.quaint.2017.10.020>.
- Hećimović, I., 2005. Morphostructural Fabric of Baranja. In: Velić, I., Vlahović, I., Biondić, R. (Eds.), *Abstracts Book. Presented at the 3rd Croatian Geological Congress, Croatian Geological Survey, Zagreb*, pp. 5–6.
- Heller, F., Liu, T., 1982. Magnetostratigraphical dating of loess deposits in China. *Nature* 300, 431–433. <https://doi.org/10.1038/300431a0>.
- Heller, F., Shen, C.D., Beer, J., Liu, X.M., Liu, T.S., Bronger, A., Suter, M., Bonani, G., 1993. Quantitative estimates of pedogenic ferromagnetic mineral formation in Chinese loess and palaeoclimatic implications. *Earth Planet. Sci. Lett.* 114, 385–390. [https://doi.org/10.1016/0012-821X\(93\)90038-B](https://doi.org/10.1016/0012-821X(93)90038-B).
- Hlavatskyi, D.V., Bakhmutov, V.G., 2020. Magnetostratigraphy and magnetic susceptibility of the best developed Pleistocene loess-paleosol sequences of Ukraine: implications for correlation and proposed chronostratigraphic models. *Geol. Q.* 64. <https://doi.org/10.7306/gq.1544>.
- Huntley, D.J., Lamothe, M., 2001. Ubiquity of anomalous fading in K-feldspars and the measurement and correction for it in optical dating. *Can. J. Earth Sci.* 38, 1093–1106. <https://doi.org/10.1139/e01-013>.
- Imbrie, J., Imbrie, J., 1980. Modeling the Climatic Response to Orbital Variations. *Science* 207, 943–953. <https://doi.org/10.1126/science.207.4434.943>.
- Jackson, M.L., 1956. *Soil Chemical Analysis – Advanced Course*. Published by the author, Wisconsin.
- Jackson, M.L., 1957. Frequency distribution of clay minerals in major great soil groups as related to the factors of soil formation. *Clay Clay Miner.* 6, 133–143. <https://doi.org/10.1346/CCMN.1957.0606111>.
- Ji, J., Balsam, W., Chen, J., 2001. Mineralogical and climatic interpretations of the Luochuan Loess Section (China) based on diffuse reflectance spectrophotometry. *Quat. Res.* 56, 23–30. <https://doi.org/10.1006/qres.2001.2238>.
- Ji, J., Balsam, W., Chen, J.U., Liu, L., 2002. Rapid and quantitative measurement of hematite and goethite in the Chinese Loess-paleosol sequence by diffuse reflectance spectroscopy. *Clay Clay Miner.* 50, 208–216. <https://doi.org/10.1346/000986002760832801>.
- Jordanova, D., Hus, J., Geeraerts, R., 2007. Palaeoclimatic implications of the magnetic record from loess/paleosol sequence Viatovo (NE Bulgaria): palaeoclimatic implications of the magnetic record. *Geophys. J. Int.* 171, 1036–1047. <https://doi.org/10.1111/j.1365-246X.2007.03576.x>.
- Kars, R.H., Wallinga, J., Cohen, K.M., 2008. A new approach towards anomalous fading correction for feldspar IRSL dating — Tests on samples in field saturation. *Radiat. Meas.* 43, 786–790. <https://doi.org/10.1016/j.radmeas.2008.01.021>.
- Kovács, J., Raucsik, B., Varga, A., Újvári, G., Varga, G., Ottner, F., 2013. Clay mineralogy of red clay deposits from the central Carpathian Basin (Hungary): implications for Plio-Pleistocene chemical weathering and palaeoclimate. *Turk. J. Earth Sci.* 22, 414–426.
- Kukla, G., 1987. Loess stratigraphy in central China. *Quat. Sci. Rev.* 6, 191–219.
- Laag, C., Hambach, U., Zeeden, C., Lagroix, F., Guyodo, Y., Veres, D., Jovanović, M., Marković, S.B., 2021a. A detailed paleoclimate proxy record for the Middle Danube Basin over the last 430 kyr: a rock magnetic and colorimetric study of the Zemun loess-paleosol sequence. *Front. Earth Sci.* <https://doi.org/10.3389/feart.2021.600086>, 9 (May).
- Laag, C., Jordanova, D., Lagroix, F., Jordanova, N., Guyodo, Y., 2021b. A New Reference Loess-Paleosol Archive Spanning the Last 850 Kyr near Pleven (Bulgaria): First Results. <https://doi.org/10.5194/egusphere-egu21-6381>. EGU 2021, Vienna.
- Lagroix, F., Guyodo, Y., 2017. A New tool for separating the magnetic mineralogy of complex mineral assemblages from low temperature magnetic behavior. *Front. Earth Sci.* 5, 61. <https://doi.org/10.3389/feart.2017.00061>.
- Lamothe, M., Auclair, M., Hamzaoui, C., Huot, S., 2003. Towards a prediction of long-term anomalous fading of feldspar IRSL. *Radiat. Meas.* 37, 493–498. [https://doi.org/10.1016/S1350-4487\(03\)00016-7](https://doi.org/10.1016/S1350-4487(03)00016-7).
- Li, Y., Tsukamoto, S., Frechen, M., Gabriel, G., 2018. Timing of fluvial sedimentation in the Upper Rhine Graben since the Middle Pleistocene: constraints from quartz and feldspar luminescence dating. *Boreas* 47, 256–270. <https://doi.org/10.1111/bor.12266>.
- Lisiecki, L.E., Raymo, M.E., 2005. A Pliocene-Pleistocene stack of 57 globally distributed benthic  $\delta^{18}O$  records. *Paleoceanography* 20. <https://doi.org/10.1029/2004PA001071>.
- Liu, X., Rolph, T., Bloemendal, J., Shaw, J., Liu, T., 1995. Quantitative estimates of paleoprecipitation at Xifeng, in the Loess Plateau of China. *Palaeogeogr. Palaeoclimatol. Palaeoecol.* 113, 243–248. [https://doi.org/10.1016/0031-0182\(95\)00053-0](https://doi.org/10.1016/0031-0182(95)00053-0).
- Liu, Q., Roberts, A.P., Larrasoana, J.C., Banerjee, S.K., Guyodo, Y., Tauxe, L., Oldfield, F., 2012. Environmental magnetism: principles and applications. *Rev. Geophys.* 50, RG4002. <https://doi.org/10.1029/2012RG000393>.
- Lukić, T., Basarin, B., Bugle, B., Marković, S.B., Tomović, V.M., Raljić, J.P., Hrnjak, I., Timar-Gabor, A., Hambach, U., Gavrilov, M.B., 2014. A joined rock magnetic and colorimetric perspective on the Late Pleistocene climate of Orlovat loess site (Northern Serbia). *Quat. Int.* 334–335, 179–188. <https://doi.org/10.1016/j.quaint.2014.03.042>.
- Maher, B.A., 1986. Characterisation of soils by mineral magnetic measurements. *Phys. Earth Planet. Inter.* 42, 76–92. [https://doi.org/10.1016/S0031-9201\(86\)80010-3](https://doi.org/10.1016/S0031-9201(86)80010-3).
- Maher, B.A., 1998. Magnetic properties of modern soils and Quaternary loessic paleosols: paleoclimatic implications. *Palaeogeogr. Palaeoclimatol. Palaeoecol.* 137, 25–54.
- Maher, B.A., 2011. The magnetic properties of Quaternary aeolian dusts and sediments, and their palaeoclimatic significance. *Aeolian Res.* 3, 87–144. <https://doi.org/10.1016/j.aeolia.2011.01.005>.
- Maher, B.A., Thompson, R., Zhou, L.P., 1994. Spatial and temporal reconstructions of changes in the Asian palaeomonsoon: a new mineral magnetic approach. *Earth Planet. Sci. Lett.* 125, 461–471. [https://doi.org/10.1016/0012-821X\(94\)90232-1](https://doi.org/10.1016/0012-821X(94)90232-1).
- Maher, B.A., Alekseev, A., Alekseeva, T., 2003. Magnetic mineralogy of soils across the Russian Steppe: climatic dependence of pedogenic magnetite formation. *Palaeogeogr. Palaeoclimatol. Palaeoecol.* 201, 321–341. [https://doi.org/10.1016/S0031-0182\(03\)00618-7](https://doi.org/10.1016/S0031-0182(03)00618-7).
- Marković, S., Kostić, N.S., Oches, E.A., 2004. Paleosols in the Ruma loess section (Vojvodina, Serbia). *Revi. Mex. Ciencias Geol.* 21, 79–87.
- Marković, S.B., Hambach, U., Catto, N., Jovanović, M., Bugle, B., Machalet, B., Zöller, L., Glaser, B., Frechen, M., 2009. Middle and Late Pleistocene loess sequences at Batajnica, Vojvodina, Serbia. *Quat. Int.* 198, 255–266. <https://doi.org/10.1016/j.quaint.2008.12.004>.
- Marković, S.B., Hambach, U., Stevens, T., Kukla, G.J., Heller, F., McCoy, W.D., Oches, E.A., Bugle, B., Zöller, L., 2011. The last million years recorded at the Stari Slankamen (Northern Serbia) loess-paleosol sequence: revised chronostratigraphy and long-term environmental trends. *Quat. Sci. Rev.* 30, 1142–1154. <https://doi.org/10.1016/j.quascirev.2011.02.004>.
- Marković, S.B., Hambach, U., Stevens, T., Jovanović, M., O'Hara-Dhand, K., Basarin, B., Lu, H., Smalley, I., Bugle, B., Zech, M., Svirčev, Z., Sümege, P., Milojković, N., Zöller, L., 2013. Loess in the Vojvodina region (Northern Serbia): an essential link between European and Asian Pleistocene environments. *Neth. J. Geosci.* 91, 173–188. <https://doi.org/10.1017/S0016774600001578>.

- Marković, S.B., Stevens, T., Kukla, G.J., Hambach, U., Fitzsimmons, K.E., Gibbard, P., Bugge, B., Zech, M., Guo, Z., Hao, Q., Wu, H., O'Hara Dhand, K., Smalley, I.J., Újvári, G., Sümegi, P., Timar-Gabor, A., Veres, D., Sirocko, F., Vasiljević, D.A., Jary, Z., Svensson, A., Jović, V., Lehmkuhl, F., Kovács, J., Svirčev, Z., 2015. Danube loess stratigraphy — Towards a pan-European loess stratigraphic model. *Earth Sci. Rev.* 148, 228–258. <https://doi.org/10.1016/j.earscirev.2015.06.005>.
- Meyers, S.R., 2014. *astrochron: An R Package for Astrochronology* Version 0.8.
- Millot, G., 1964. *Géologie des argiles*. Masson and Cie, Paris.
- Moore, D.M., Reynolds Jr., R.C., 1997. *X-Ray Diffraction and the Identification and Analysis of Clay Minerals*. Oxford University Press, Oxford.
- Murray, A.S., Schmidt, E.D., Stevens, T., Buylaert, J.-P., Marković, S.B., Tsukamoto, S., Frechen, M., 2014. Dating Middle Pleistocene loess from Stari Slankamen (Vojvodina, Serbia) — Limitations imposed by the saturation behaviour of an elevated temperature IRSL signal. *CATENA* 117, 34–42. <https://doi.org/10.1016/j.catena.2013.06.029>.
- Novothy, Á., Frechen, M., Horváth, E., Wacha, L., Rolf, C., 2011. Investigating the penultimate and last glacial cycles of the Süttő loess section (Hungary) using luminescence dating, high-resolution grain size, and magnetic susceptibility data. *Quat. Int.* 234, 75–85. <https://doi.org/10.1016/j.quaint.2010.08.002>.
- Novothy, Á., Barta, G., Végh, T., Bradák, B., Surányi, G., Horváth, E., 2020. Correlation of drilling cores and the Paks brickyard key section at the area of Paks, Hungary. *Quat. Int.* 552, 50–61. <https://doi.org/10.1016/j.quaint.2019.09.012>.
- Obrecht, I., Bugge, B., Catto, N., Marković, S.B., Bösel, S., Vandenberghe, D.A.G., Hambach, U., Svirčev, Z., Lehmkuhl, F., Basarin, B., Gavrilov, M.B., Jović, G., 2014. The Late Pleistocene Belotinac section (southern Serbia) at the southern limit of the European loess belt: Environmental and climate reconstruction using grain size and stable C and N isotopes. *Quat. Int.* 334–335, 10–19. <https://doi.org/10.1016/j.quaint.2013.05.037>.
- Obrecht, I., Zeeden, C., Hambach, U., Veres, D., Marković, S.B., Bösen, J., Svirčev, Z., Bavec, N., Gavrilov, M.B., Lehmkuhl, F., 2016. Tracing the influence of Mediterranean climate on Southeastern Europe during the past 350,000 years. *Sci. Rep.* 6, 36334. <https://doi.org/10.1038/srep36334>.
- Obrecht, I., Zeeden, C., Hambach, U., Veres, D., Marković, S.B., Lehmkuhl, F., 2019. A critical reevaluation of palaeoclimate proxy records from loess in the Carpathian Basin. *Earth Sci. Rev.* 190, 498–520. <https://doi.org/10.1016/j.earscirev.2019.01.020>.
- PAGES, Past Interglacials Working Group, 2016. Interglacials of the last 800,000 years. *Rev. Geophys.* 54, 162–219. <https://doi.org/10.1002/2015RG000482>.
- Pécsi, M., 1990. Loess is not just the accumulation of dust. *Quat. Int.* 7–8, 1–21. [https://doi.org/10.1016/1040-6182\(90\)90034-2](https://doi.org/10.1016/1040-6182(90)90034-2).
- Pécsi, M., 1993. Quaternary and loess research. In: Bassa, L., Keresztesi, Zs, Lóczy, D. (Eds.), *Presented at the Loess in Form 2*. Hungarian Academy of Science, Budapest, pp. 1–82.
- Peters, C., Dekkers, M.J., 2003. Selected room temperature magnetic parameters as a function of mineralogy, concentration and grain size. *Phys. Chem. Earth Parts A/B/C* 28, 659–667. [https://doi.org/10.1016/S1474-7065\(03\)00120-7](https://doi.org/10.1016/S1474-7065(03)00120-7).
- Pikija, M., Šikić, K., Trifunović, S., 1991a. Basic Geological Map 1:100 000, Sheet Mohač L 34-7474 (2015).
- Pikija, M., Šikić, K., Trifunović, S., 1991b. Basic Geological Map, Explanatory notes, Sheet Mohač L 34-74.
- Pikija, M., Šikić, K., Sarkotić-Šlat, M., Magaš, N., 1995. *Geologija hrvatskog dijela Baranje*. In: Vlahović, I., Velčić, I., Šparica, M. (Eds.), *First Croatian Geological Congress*. Presented at the First Croatian Geological Congress, Opatija, October 18–21, Proceedings, 2. Institute of Geology & Croatian Geological Society, Zagreb, Opatija, pp. 447–451.
- Prescott, J.R., Hutton, J.T., 1994. Cosmic ray contributions to dose rates for luminescence and ESR dating: large depths and long-term time variations. *Radiat. Meas.* 23, 497–500. [https://doi.org/10.1016/1350-4487\(94\)90086-8](https://doi.org/10.1016/1350-4487(94)90086-8).
- Prescott, J.R., Stephan, L.G., 1982. The contribution of cosmic radiation to the environmental dose for thermoluminescent dating — latitude, altitude and depth dependences. *PACT* 6, 17–25.
- Pye, K., 1987. *Aeolian Dust and Dust Deposits*. Academic Press, London.
- Rees-Jones, J., 1995. Optical dating of young sediments using fine-grain quartz. *Ancient TL* 9–14.
- Rubinić, V., Galović, L., Lazarević, B., Husnjak, S., Durn, G., 2018. Pseudogleyed loess derivatives — the most common soil parent materials in the Pannonian region of Croatia. *Quat. Int.* 494, 248–262. <https://doi.org/10.1016/j.quaint.2017.06.044>.
- Schaetzl, R.J., Bettis, E.A., Crouvi, O., Fitzsimmons, K.E., Grimley, D.A., Hambach, U., Lehmkuhl, F., Marković, S.B., Mason, J.A., Owczarek, P., Roberts, H.M., Rousseau, D.-D., Stevens, T., Vandenberghe, J., Zárate, M., Veres, D., Yang, S., Zech, M., Conroy, J.L., Dave, A.K., Faust, D., Hao, Q., Obrecht, I., Prud'homme, C., Smalley, I., Tripaldi, A., Zeeden, C., Zech, R., 2018. Approaches and challenges to the study of loess—Introduction to the LoessFest special issue. *Quat. Res.* 89, 563–618. <https://doi.org/10.1017/qua.2018.15>.
- Schatz, A.-K., Buylaert, J.-P., Murray, A., Stevens, T., Scholten, T., 2012. Establishing a luminescence chronology for a palaeosol-loess profile at Tokaj (Hungary): a comparison of quartz OSL and polymineral IRSL signals. *Quat. Geochronol.* 10, 68–74. <https://doi.org/10.1016/j.quageo.2012.02.018>.
- Schmidt, E.D., Machalet, B., Marković, S.B., Tsukamoto, S., Frechen, M., 2010. Luminescence chronology of the upper part of the Stari Slankamen loess sequence (Vojvodina, Serbia). *Quat. Geochronol.* 5, 137–142. <https://doi.org/10.1016/j.quageo.2009.09.006>.
- Schmidt, E.D., Tsukamoto, S., Frechen, M., Murray, A.S., 2014. Elevated temperature IRSL dating of loess sections in the East Eifel region of Germany. *Quat. Int.* 334–335, 141–154. <https://doi.org/10.1016/j.quaint.2014.03.006>.
- Schulte, P., Lehmkuhl, F., 2018. The difference of two laser diffraction patterns as an indicator for post-depositional grain size reduction in loess-paleosol sequences. *Palaeogeogr. Palaeoclimatol. Palaeoecol.* 509, 126–136. <https://doi.org/10.1016/j.palaeo.2017.02.022>.
- Sheldon, N.D., Tabor, N.J., 2009. Quantitative paleoenvironmental and paleoclimatic reconstruction using paleosols. *Earth Sci. Rev.* 95, 1–52. <https://doi.org/10.1016/j.earscirev.2009.03.004>.
- Smalley, I., O'Hara-Dhand, K., Wint, J., Machalet, B., Jary, Z., Jefferson, I., 2009. Rivers and loess: the significance of long river transportation in the complex event-sequence approach to loess deposit formation. *Quat. Int.* 198, 7–18. <https://doi.org/10.1016/j.quaint.2008.06.009>.
- Sommerwerk, N., Hein, T., Schneider-Jacoby, M., Baumgartner, C., Ostojić, A., Siber, R., Bloesch, J., Paunović, M., Tockner, K., 2009. The Danube River Basin. In: *Rivers of Europe*. Elsevier, pp. 59–112. <https://doi.org/10.1016/B978-0-12-369449-2.00003-5>.
- Song, Y., Guo, Z., Marković, S., Hambach, U., Deng, C., Chang, L., Wu, J., Hao, Q., 2018. Magnetic stratigraphy of the Danube loess: a composite Titel-Stari Slankamen loess section over the last one million years in Vojvodina, Serbia. *J. Asian Earth Sci.* 155, 68–80. <https://doi.org/10.1016/j.jseaeas.2017.11.012>.
- Spooner, N.A., 1994. The anomalous fading of infrared-stimulated luminescence from feldspars. *Radiat. Meas.* 23, 625–632. [https://doi.org/10.1016/1350-4487\(94\)90111-2](https://doi.org/10.1016/1350-4487(94)90111-2).
- Starkey, H.C., Blackmon, P.D., Hauff, P.L., 1984. The routine mineralogical analysis of clay-bearing samples (No. 1563). In: *U. S. Geological Survey Bulletin*. <https://doi.org/10.3133/b1563>.
- Sümegi, P., Gulyás, S., Molnár, D., Sümegi, B.P., Almond, P.C., Vandenberghe, J., Zhou, L., Pál-Molnár, E., Töröcsik, T., Hao, Q., Smalley, I., Molnár, M., Marsi, I., 2018. New chronology of the best developed loess/paleosol sequence of Hungary capturing the past 1.1 ma: implications for correlation and proposed pan-Eurasian stratigraphic schemes. *Quat. Sci. Rev.* 191, 144–166.
- Taheri, M., Khormali, F., Wang, X., Amini, A., Landi, A., Wei, H., Kehl, M., Chen, F., 2020. Clay mineralogy and geochemistry of the Lower Pleistocene Loess in the Iranian Loess Plateau (Agh Band section) and implications for its provenance and paleoclimate change. *Quat. Int.* 552, 91–99. <https://doi.org/10.1016/j.quaint.2019.09.011>.
- Thamó-Bozsó, E., Kovács, L.Ó., Magyari, Á., Marsi, I., 2014. Tracing the origin of loess in Hungary with the help of heavy mineral composition data. *Quat. Int.* 319, 11–21. <https://doi.org/10.1016/j.quaint.2013.04.030>.
- Thiel, C., Buylaert, J.-P., Murray, A., Terhorst, B., Hofer, I., Tsukamoto, S., Frechen, M., 2011. Luminescence dating of the Stratzing loess profile (Austria) — Testing the potential of an elevated temperature post-IR IRSL protocol. *Quat. Int.* 234, 23–31. <https://doi.org/10.1016/j.quaint.2010.05.018>.
- Thiel, C., Horváth, E., Frechen, M., 2014. Revisiting the loess/paleosol sequence in Paks, Hungary: A post-IR IRSL based chronology for the 'Young Loess Series'. *Quat. Int.* 319, 88–98. <https://doi.org/10.1016/j.quaint.2013.05.045>.
- Thompson, R., Oldfield, F., 1986. *Magnetic Properties of Natural Materials*, in: *Environmental Magnetism*. Springer Netherlands, Dordrecht, pp. 21–38. [https://doi.org/10.1007/978-94-011-8036-8\\_4](https://doi.org/10.1007/978-94-011-8036-8_4).
- Trifunović, S., Strajin, V., 1995. *Basic Geological Map of Serbia, 1:100 000, Sheet Mohač. Savezno ministarstvo za privrednu SRJ, Beograd.*
- Újvári, G., Varga, A., Ramos, F.C., Kovács, J., Németh, T., Stevens, T., 2012. Evaluating the use of clay mineralogy, Sr–Nd isotopes and zircon U–Pb ages in tracking dust provenance: an example from loess of the Carpathian Basin. *Chem. Geol.* 304–305, 83–96. <https://doi.org/10.1016/j.chemgeo.2012.02.007>.
- Újvári, G., Molnár, M., Novothy, Á., Páll-Gergely, B., Kovács, J., Várhegyi, A., 2014a. AMS 14C and OSL/IRSL dating of the Dunaszekcső loess sequence (Hungary): chronology for 20 to 150 ka and implications for establishing reliable age–depth models for the last 40 ka. *Quat. Sci. Rev.* 106, 140–154. <https://doi.org/10.1016/j.quascirev.2014.06.009>.
- Újvári, G., Varga, A., Raucsik, B., Kovács, J., 2014b. The Paks loess-paleosol sequence: a record of chemical weathering and provenance for the last 800ka in the mid-Carpathian Basin. *Quat. Int.* 319, 22–37. <https://doi.org/10.1016/j.quaint.2012.04.004>.
- Újvári, G., Kok, J.F., Varga, G., Kovács, J., 2016a. The physics of wind-blown loess: implications for grain size proxy interpretations in Quaternary paleoclimate studies. *Earth Sci. Rev.* 154, 247–278. <https://doi.org/10.1016/j.earscirev.2016.01.006>.
- Újvári, G., Molnár, M., Páll-Gergely, B., 2016b. Charcoal and mollusc shell 14 C-dating of the Dunaszekcső loess record, Hungary. *Quat. Geochronol.* 35, 43–53. <https://doi.org/10.1016/j.quageo.2016.05.005>.
- Újvári, G., Stevens, T., Molnár, M., Demény, A., Lambert, F., Varga, G., Jull, A.J.T., Páll-Gergely, B., Buylaert, J.-P., Kovács, J., 2017. Coupled European and Greenland last glacial dust activity driven by North Atlantic climate. *Proc. Natl. Acad. Sci. U. S. A.* 114, E10632–E10638. <https://doi.org/10.1073/pnas.1712651114>.
- Vandenberghe, J., 2013. Grain size of fine-grained windblown sediment: a powerful proxy for process identification. *Earth Sci. Rev.* 121, 18–30. <https://doi.org/10.1016/j.earscirev.2013.03.001>.
- Vandenberghe, J.F., Múcher, H.J., Roebroeks, W., Gemke, D., 1985. *Lithostratigraphy and palaeoenvironment of the Pleistocene deposits at Maastricht-Belvédère, southern Limburg, The Netherlands*. *Meded. Rijks Geol. Dienst* 39, 7–29.
- Vandenberghe, J., Marković, S.B., Jovanović, M., Hambach, U., 2014. Site-specific variability of loess and palaeosols (Ruma, Vojvodina, northern Serbia). *Quat. Int.* 334–335, 86–93. <https://doi.org/10.1016/j.quaint.2013.10.036>.
- Vandenberghe, J., Sun, Y., Wang, X., Abels, H.A., Lü, X., 2018. Grain-size characterization of reworked fine-grained aeolian deposits. *Earth Sci. Rev.* 177, 43–52. <https://doi.org/10.1016/j.earscirev.2017.11.005>.

- Varga, A., Újvári, G., Raucsik, B., 2011. Tectonic versus climatic control on the evolution of a loess–paleosol sequence at Beremend, Hungary: an integrated approach based on paleoecological, clay mineralogical, and geochemical data. *Quat. Int.* 240, 71–86. <https://doi.org/10.1016/j.quaint.2010.10.032>.
- Wacha, L., Frechen, M., 2011. The geochronology of the “Gorjanović loess section” in Vukovar, Croatia. *Quat. Int.* 240, 87–99. <https://doi.org/10.1016/j.quaint.2011.04.010>.
- Wacha, L., Galović, L., Koloszar, L., Magyari, Á., Chikán, G., Marsi, I., 2013. The chronology of the Šarengrad II loess-palaeosol section (Eastern Croatia). *Geol. Cro.* 66, 191–203. <https://doi.org/10.4154/GC.2013.18>.
- Wacha, L., Vlahović, I., Tsukamoto, S., Kovačić, M., Hasan, O., Pavelić, D., 2016. The chronostratigraphy of the latest Middle Pleistocene aeolian and alluvial activity on the Island of Hvar, eastern Adriatic, Croatia. *Boreas* 45, 152–164. <https://doi.org/10.1111/bor.12141>.
- Wacha, L., Matoš, B., Kunz, A., Lužar-Oberiter, B., Tomljenović, B., Banak, A., 2018a. First post-IR IRSL dating results of Quaternary deposits from Bilogora (NE Croatia): implications for the Pleistocene relative uplift and incision rates in the area. *Quat. Int.* 494, 193–210. <https://doi.org/10.1016/j.quaint.2017.08.049>.
- Wacha, L., Rolf, C., Hambach, U., Frechen, M., Galović, L., Duchoslav, M., 2018b. The Last Glacial aeolian record of the Island of Susak (Croatia) as seen from a high-resolution grain-size and rock magnetic analysis. *Quat. Int.* 494, 211–224. <https://doi.org/10.1016/j.quaint.2017.08.016>.
- Wacha, L., Laag, C., Grizelj, A., Tsukamoto, S., Zeeden, C., Ivanišević, D., Rolf, C., Banak, A., Frechen, M., 2020. Zmajevac data. <https://doi.org/10.17632/RNVRZFXGFM.1>.
- Weaver, C.E., 1989. *Clays, Muds, and Shales*. Elsevier, Amsterdam.
- Wilson, M.J., 1999. The origin and formation of clay minerals in soils; past, present and future perspectives. *Clay Miner.* 34, 7–25.
- Wintle, A.G., 1973. Anomalous Fading of Thermo-luminescence in Mineral Samples. *Nature* 245, 143–144. <https://doi.org/10.1038/245143a0>.
- Wu, Y., Qiu, S., Fu, S., Rao, Z., Zhu, Z., 2018. Pleistocene climate change inferred from multi-proxy analyses of a loess-paleosol sequence in China. *J. Asian Earth Sci.* 154, 428–434. <https://doi.org/10.1016/j.jseas.2017.10.007>.
- Zeeden, C., Kels, H., Hambach, U., Schulte, P., Protze, J., Eckmeier, E., Marković, S.B., Klasen, N., Lehmkühl, F., 2016. Three climatic cycles recorded in a loess-palaeosol sequence at Semeac (Romania) – Implications for dust accumulation in south-eastern Europe. *Quat. Sci. Rev.* 154, 130–142. <https://doi.org/10.1016/j.quascirev.2016.11.002>.



## Appendix F: R-package LESLIE

R (R Core Team, 2023) is an open source programming language (like e.g., Python) and software environment for data manipulation, statistical analysis and visualization. It offers hence a custom development statistical software packages and data analysis packages designed for very specific tasks. R is thus a object-oriented language which uses therefore objects like vectors, matrices, lists and data frames to store and manipulate data. R also places great emphasis on functions, which are reusable pieces of code that can be called with different arguments to accomplish a particular task.

R has a large and active user community, which means that there are many open accessible resources available online for e.g., troubleshooting, as well as a vast number of packages (collections of R functions, data, and compiled code) that can be easily downloaded and used to extend the functionality of R. R Studio is a IDE (integrated development environment) for R, providing a user-friendly interface while working with R. It makes the writing and debugging code of R easier, since there are syntax highlighting and bug-highlighters implemented.

The own progress in R and neglection of Python is that R is specifically designed to perform statistical analysis and data manipulation. For these purposes, a vast number of built-in functions and packages are available. Hence, for users with a statistical background, R is easier to use than Python. However, Python is a more-general-purpose programming language, which can be used for a wider range of tasks such as web-development or geoinformation systems such as ArcGIS which are built on and designed to interoperable with Python. The wider range of usage makes it a more popular programming language and more resources are based on a larger active community available.

Coupled with the stronger focus of R on statistical analysis and data visualization, the need of the researcher's development of own packages is required to solve specific tasks. One of this tasks is required to perform colorimetric enhancement. Therefore, a novel R package was programmed and named LESLIE (standing for LoESs coLorimetry sIgnal Enhancement) (Laag and Kreutzer, 2022).

## The LESLIE R Package

The application of the LESLIE R package is designed as user-friendly as possible. To utilize the LESLIE package and LESLIE R-shiny application we recommend for newbies in R following steps (bold text is meant to be copied in your R-script):



1. Download & install the most recent version of R for Windows or Mac

```
if(!require("devtools"))  
  install.packages("devtools")  
devtools::install_github("https://github.com/CLaag/LESLIE@main")
```

2. Open R-Studio and open a new R-script
3. Call the LESLIE package to be activated in the library

```
library(LESLIE)
```

4. Load randomly created colorimetric ( $L^*$ ,  $a^*$ ,  $b^*$ ) data (comes with the LESLIE package)

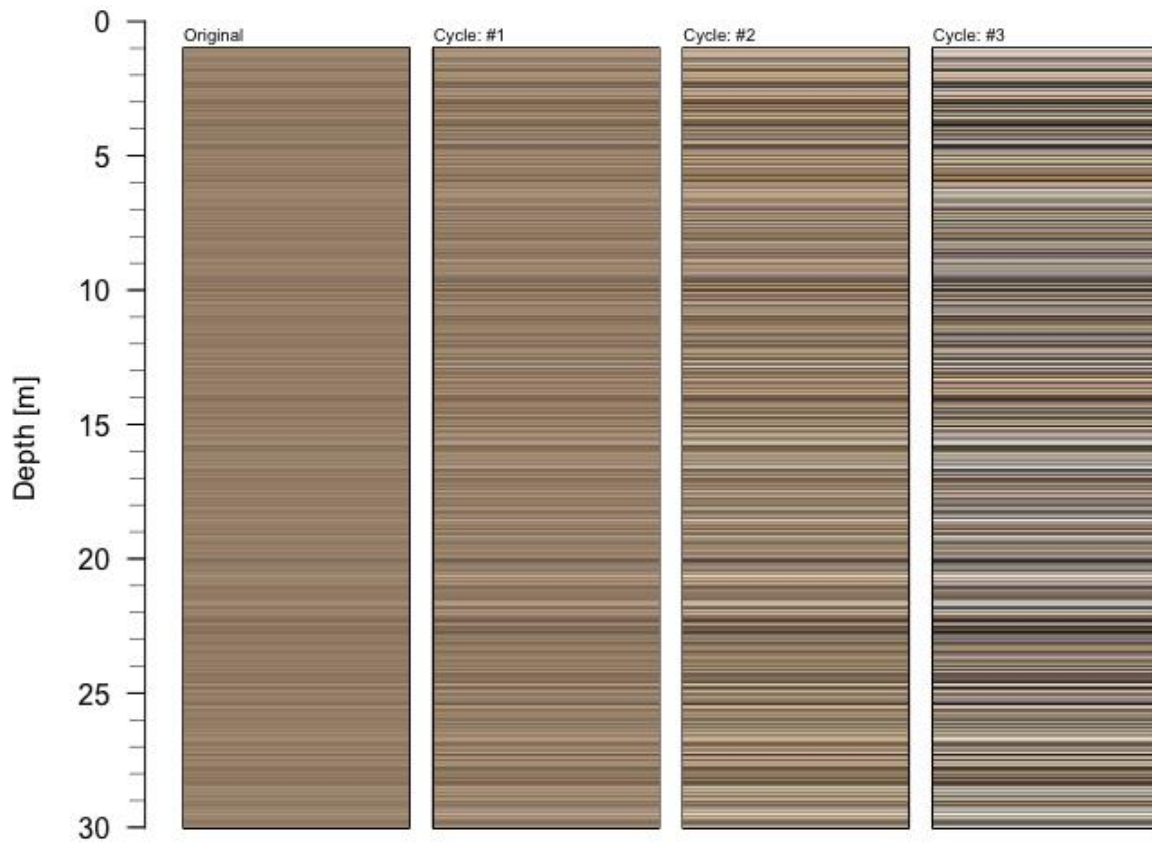
```
data(LESLIE_profile, envir = environment())
```

5. Plot the example data with original data on the left and three enhancement cycles following towards the right

```
plot_colProfile(LESLIE_profile, cycles = 1:3)
```

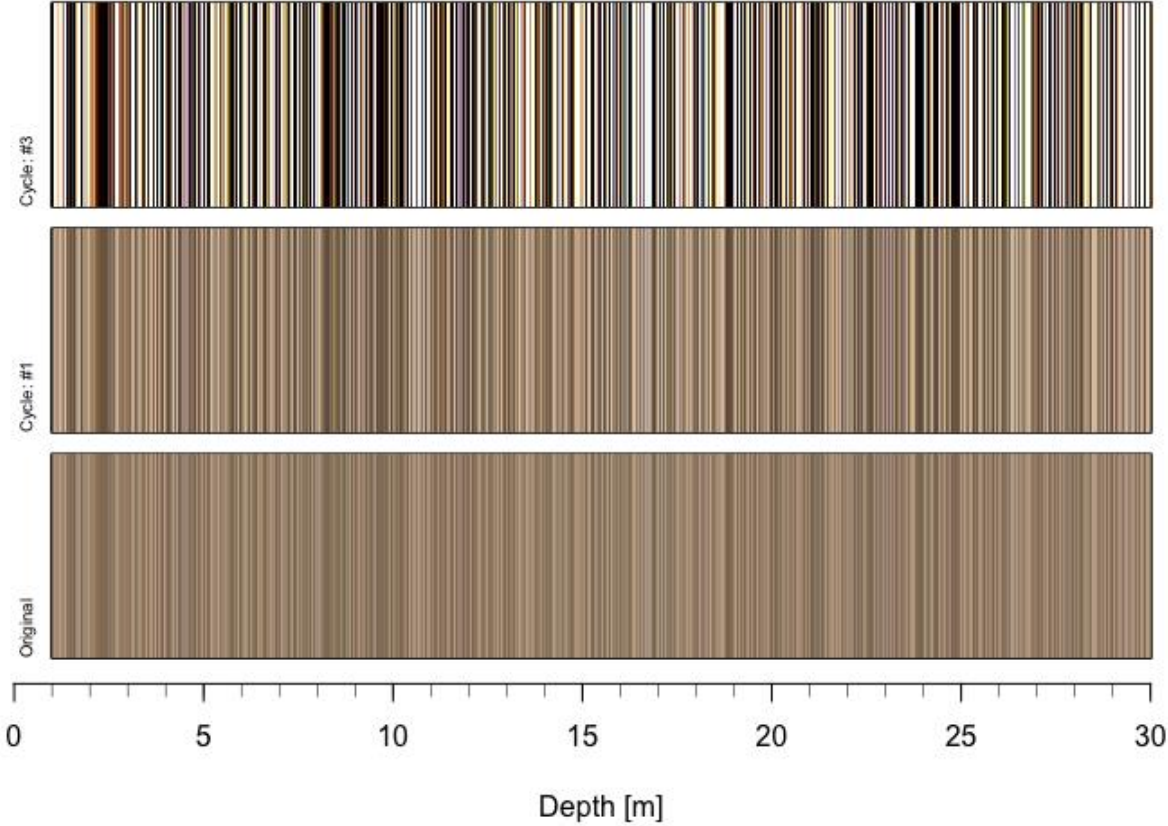
**# plot\_colProfile is the function to plot the colorimetric profile based on provided  $L^*a^*b^*$  data (here example data). Of course, you can enter your own data. Therefore, we recommend that you check out the input data-format of the example data. A additional description of your input data-format can be found in the help section. To assess it, click left with your cursor into the "plot\_colProfile" function and press "F1". That opens the help panel and gives you detailed advice.**

The result looks like the figure below:



6. In case you want to change the orientation (e.g., also exchange the depth scale and replace it by an age scale you can modify the code by adding the orientation parameter as follows:  
`plot_colProfile(LESLIE_profile, cycles = c(1,3), orientation = "landscape")`

The result looks like :



## The LESLIE R-shiny application

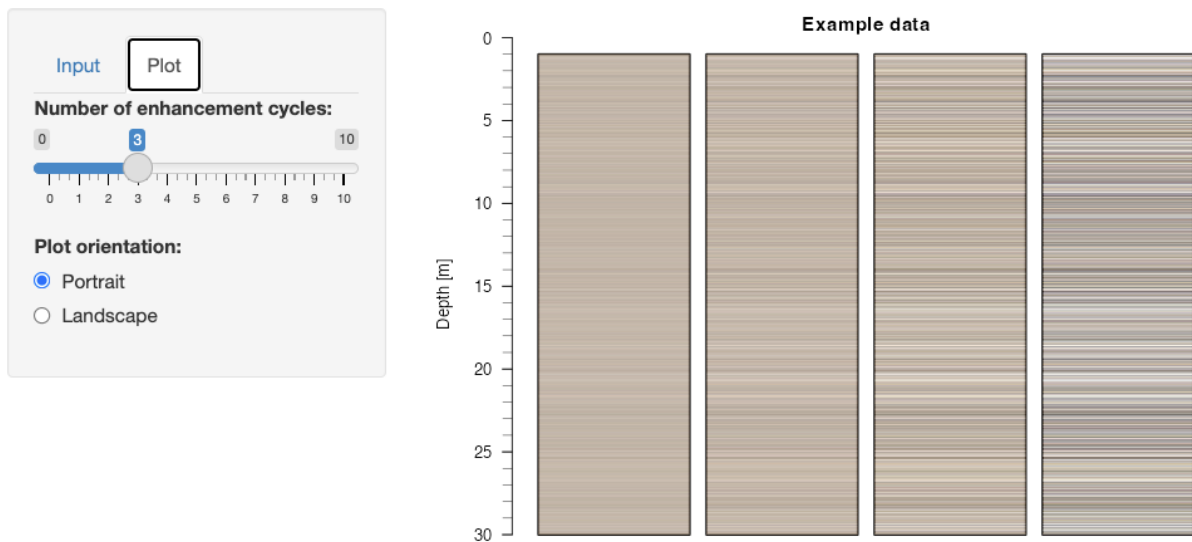
In case one user is not very sure about parameter-modification, we provide now an even easier solution inviting users to play around with their data or the provided example data. Therefore, after following steps 1-4 from the before explained pathway, one just enters

```
app_LESLIE()
```

to open the interactive shiny app inside the R-studio environment.

This allows the use of buttons and shifters to manipulate the data and the interactive surface looks like this:

### LoESs coLorimetry signal Enhancement



### Objectives of LESLIE

LESLIE was initially designed to contrast-enhance and visualize measured  $L^*$ ,  $a^*$  and  $b^*$  data. However, as detailed explained in (Laag et al., 2022) we aim to integrate different functions such as the box-correction procedure as well as goethite and hematite extraction based on diffuse reflectance data provided by spectrophotometers. Hence, conversion tools between different observer angles, applied standard illuminants from different colorimetric systems are envisaged to be provided by LESLIE. As known from still conducted studies and past-decades covering studies, a vast amount of colorimetric data was presented tabularly as Munsell color alpha numerical values. Initial tests of transfer-functions applying the conversion between Munsell and Lab values show, that a color-visualization of in field and in laboratory established Munsell colors can be re-calculated and presented in a manner as shown above. Furthermore, the recalculation of reflectance spectra allowing the extraction of qualitative hematite and goethite contents based on this conversion and transformation of Lab data into Absorbance values may be possible in future. This will allow even older and not accessible anymore archives to be evaluated by climatic highly sensitive minerals such as goethite and hematite. By conducting colorimetric measurements following the approach presented in (Laag et al., 2022) and utilizing the acquired data to undergo color contrast enhancement with the LESLIE R-Package (Laag and Kreutzer, 2022), several assumed tephra layers (based on aforementioned magnetic properties) are providing quietly diverging colors from surrounding loess material which is thus not similar to pedogenetically modified units. Running e.g., three enhancement cycles and plotting results stratigraphically, (crypto-)tephra samples visibly differentiate with rather greyish – olive-greenish -or slight grey-violet colors. Exaggerating the application of enhancement cycles, e.g., performing 20 enhancement cycles lead for the majority of tephra layers to colorimetric end members providing fire-brick red and dark violet colors. An explanation cannot be given so far explaining colorimetrically or mineralogically this phenomenon but it might be efficient to create a DRS data base of minerals contained in highly explosive tephtras and loess and paleosols and compare with multivariate statistics the probable cause of fire-brick red and dark violet colors represented by (crypto-) tephra layers.



## Appendix G: R-code VSM haRvesteR

The VSM Harvester is a novel R-script, which enables to manipulate large data sets measured on a Vibrating Sample Magnetometer. However, this script was uniquely designed to manipulate and re-assemble data performed on the MicroMag 3900 VSM located at the Institute de Physique du Globe de Paris with a very specific output data format and specific measurement settings. However, open-available software targeting vast numbers of samples measured on this device and calculating resulting magnetic parameters is so far missing and the establishment of an R-package, allowing other experimental settings and output formats is desired. However, for now only a static R-script is available but has the advantage to provide all required data within seconds, shows data measurement errors and e.g., forgotten to be analyzed samples.

### Structure and working process of the code

The R code is separated into part A, B, and C. Part A targets a folder, where the measurement data is stored in. For all VSM experiments performed in the presented studies, the VSM experiments consists of three unique sub-experiments. The first experiments is a hysteresis loop, the second experiment a HCR experiment and the third experiment a HCR experiment in distinct 100 mT steps towards -1.5T. The experiments were performed right after each other and specific data-type names such as “.lp” for the hysteresis loop data, “.hcr” for the logarithmic HCR experiment and “.s” for the static 100mT steps were given. The R-code initially checks, if for each sample all three experiments were conducted and provides a positive answer if fulfilled or a warning message, in case not. Then, three different functions addressing the specific position of alphanumeric strings are applied to extract initial magnetic parameter by performed experiment.

`VSM_extract_lp` is a function which browses through all “.lp” data files and compiles mass-normalized data for all parameters to be calculated stemming from hysteresis loop experiments, simultaneously assuring that the sample ID is maintained (in case sample ID zeroing was applied) and no mixing up takes place. The stored and calculated / transformed data stemming from the hysteresis loop experiments contains then the sample ID, the net-mass, the slope correction (which was transformed from  $\text{Am}^2\text{Tkg}$  into  $\text{m}^3\text{kg}^{-1}$  units),  $M_S$  (saturation magnetization),  $M_R$  (remanent saturation magnetization) and  $H_C$  (coercivity).

`VSM_extract_Hcr` is a function determined to exactly extract the x-axis intercept to determine  $H_{CR}$ . It searches at a distinct text position for the  $H_{CR}$  value and stores it per sample ID in a new data frame.

VSM\_extract\_s extracts all remanence values acquired in 100mT steps between 0 and 1.5T and stores them followed the sample IDs in a new data frame.

Part B of the code compiles all acquired and when necessary mass normalized data in columns, where each row represents each unique sample ID. It assigns new column headers with the values' parameters unit. The result is a full data frame containing each parameter, in case necessary mass normalized where each column represents a determined parameter and each row represents one unique sample.

In Part C, the final composition of all samples takes place. Here also inter-parametric ratios are calculated such as  $M_{RS}/M_S$ ,  $H_{CR}/H_C$ , the s-ratio and the HIRM. All these values are in a following step exported as a .csv data table, where the user is allowed to change the name of the table. Hence, automatically a text-file is created, explaining each parameter and ratio and its abbreviations used in the headers of each column.

```
##### VSM HaRvester #####  
##### programmed by Christian Laag #####  
## Paleomagnetism Research Group, Institut de Physique du Globe de Paris #####  
## Usage and handover only with written permission and citation #####  
### this is version 0.0.6 #####
```

```
setwd(dirname(rstudioapi::getActiveDocumentContext())$path))
```

```
data.path <- getwd()
```

```
#install.packages("stringr") ### for package installation unblock by removing "#"  
#install.packages("dplyr") ### same here, after installation block again
```

```
library(stringr)  
library(dplyr)
```

```
#by executing the following lines, you can test if your data input is ok - the  
result of the test will be written into the console
```

```
if(length(list.files(data.path, pattern = '\\.lp', full.names = TRUE))==  
  length(list.files(data.path, pattern = '\\.hcr', full.names = TRUE))&  
  length(list.files(data.path, pattern = '\\.hcr', full.names =  
TRUE))==length(list.files(data.path, pattern = '\\.s', full.names = TRUE))){  
  print("Your data looks fine. You can continue.")  
} else {  
  print("There is a problem with your data. For a sample there are varying numbers  
of measurements.")  
}
```

```
VSM_extract_lp <- function(filename) {  
  data.raw <- read.fwf(filename, widths = c(31,21))  
  data.form <- as.data.frame(data.raw)
```

```

data.sort <- data.form[c(13,48,60,61,62),2]
data.sort <- as.numeric(data.sort)
data.prep <- as.data.frame(t(data.sort))
colnames(data.prep) <- c("mass.kg", "sl.corr.Am2Tkg", "Ms.Am2kg", "Mr.Am2kg",
"Hc.T")

data.prep$sl.corr.micAm2T <- abs(data.prep$sl.corr.Am2T*10000*4*pi*10^-11)
data.prep$chi_hifi.m3kg <- data.prep$sl.corr.micAm2T/data.prep$mass.kg

return(data.prep)
}

filename_lp <- list.files(data.path, pattern = '\\.lp', full.names = TRUE)
output_lp <- lapply(filename_lp, VSM_extract_lp)
data_frame_comp_lp <- bind_rows(output_lp, .id = "column_label")
data_frame_comp_lp <- data_frame_comp_lp[,-c(3,7)]

VSM_extract_Hcr <- function(filename) {

data.raw_Hcr <- read.fwf(filename, widths = c(31,21))
data.form_Hcr <- as.data.frame(data.raw_Hcr)
data.sort_Hcr <- data.form_Hcr[c(59,61),2]
data.sort_Hcr <- as.numeric(data.sort_Hcr)
data.prep_Hcr <- as.data.frame(t(data.sort_Hcr))
colnames(data.prep_Hcr) <- c("NL_rem.Am2", "Hcr.T")
return(data.prep_Hcr)
}

filename_Hcr <- list.files(data.path, pattern = '\\.hcr', full.names = TRUE)
output_Hcr <- lapply(filename_Hcr, VSM_extract_Hcr)
data_frame_comp_Hcr <- bind_rows(output_Hcr, .id = "column_label")
data_frame_comp_Hcr$NL_rem.Am2kg <-
data_frame_comp_Hcr$NL_rem.Am2/data_frame_comp_lp$mass.kg

VSM_extract_s <- function(filename) {
data.raw_s <- read.fwf(filename, widths = c(31,21))
data.form_s <- as.data.frame(data.raw_s)
data.sort_s <- data.form_s[c(59),2]
data.sort_s <- as.numeric(data.sort_s)
data.prep_s <- as.data.frame(t(data.sort_s))
colnames(data.prep_s) <- c("L_rem.Am2kg")
return(data.prep_s)
}

filename_s <- list.files(data.path, pattern = '\\.s', full.names = TRUE)
output_s <- lapply(filename_s, VSM_extract_s)
data_frame_comp_s <- bind_rows(output_s, .id = "column_label")
data_frame_comp_s$L_rem.Am2kg <-
data_frame_comp_s$L_rem.Am2kg/data_frame_comp_lp$mass.kg

all_data_s <- lapply(filename_s, readLines)
selected_lines_s <- lapply(all_data_s, "[",94:109)
separated_cols_s <- lapply(selected_lines_s, function(x) read.table(text = x, sep
= ",",))
names(separated_cols_s) <- filename_s
data_frame_comp_s_B <- bind_rows(separated_cols_s, .id = "column_label")

data_frame_comp_s_B$V1 <- rep(seq(0,1.5, 0.1), length(filename_s))

```

```

mass.list <- matrix(data=NA, ncol=length(filename_s),nrow =
length(unique(data_frame_comp_s_B$V1)))
#####
mass.list.new <- rep(data_frame_comp_lp$mass.kg,
each=length(unique(data_frame_comp_s_B$V1)))

#####

data_frame_comp_s_B$rem_Am2.kg <-data_frame_comp_s_B$V2/mass.list.new
data_frame_comp_s_B <- data_frame_comp_s_B[,c(1,2,4)]

remanence_neg0.0T <- subset(data_frame_comp_s_B, data_frame_comp_s_B$V1 == 0.0)
remanence_neg0.1T <- subset(data_frame_comp_s_B, data_frame_comp_s_B$V1 == 0.1)
remanence_neg0.2T <- subset(data_frame_comp_s_B, data_frame_comp_s_B$V1 == 0.2)
remanence_neg0.3T <- subset(data_frame_comp_s_B, data_frame_comp_s_B$V1 > 0.29 &
data_frame_comp_s_B$V1 < 0.31)
remanence_neg0.4T <- subset(data_frame_comp_s_B, data_frame_comp_s_B$V1 == 0.4)
remanence_neg0.5T <- subset(data_frame_comp_s_B, data_frame_comp_s_B$V1 == 0.5)
remanence_neg0.6T <- subset(data_frame_comp_s_B, data_frame_comp_s_B$V1 > 0.59 &
data_frame_comp_s_B$V1 < 0.61)
remanence_neg0.7T <- subset(data_frame_comp_s_B, data_frame_comp_s_B$V1 > 0.69 &
data_frame_comp_s_B$V1 < 0.71)
remanence_neg0.8T <- subset(data_frame_comp_s_B, data_frame_comp_s_B$V1 == 0.8)
remanence_neg0.9T <- subset(data_frame_comp_s_B, data_frame_comp_s_B$V1 == 0.9)
remanence_neg1.0T <- subset(data_frame_comp_s_B, data_frame_comp_s_B$V1 == 1.0)
remanence_neg1.1T <- subset(data_frame_comp_s_B, data_frame_comp_s_B$V1 == 1.1)
remanence_neg1.2T <- subset(data_frame_comp_s_B, data_frame_comp_s_B$V1 > 1.19 &
data_frame_comp_s_B$V1 < 1.21)
remanence_neg1.3T <- subset(data_frame_comp_s_B, data_frame_comp_s_B$V1 == 1.3)
remanence_neg1.4T <- subset(data_frame_comp_s_B, data_frame_comp_s_B$V1 > 1.39 &
data_frame_comp_s_B$V1 < 1.41)
remanence_neg1.5T <- subset(data_frame_comp_s_B, data_frame_comp_s_B$V1 == 1.5)

s_experiment <-
  cbind(remanence_neg0.0T$rem_Am2.kg,
    remanence_neg0.1T$rem_Am2.kg*(-1),
    remanence_neg0.2T$rem_Am2.kg*(-1),
    remanence_neg0.3T$rem_Am2.kg*(-1),
    remanence_neg0.4T$rem_Am2.kg*(-1),
    remanence_neg0.5T$rem_Am2.kg*(-1),
    remanence_neg0.6T$rem_Am2.kg*(-1),
    remanence_neg0.7T$rem_Am2.kg*(-1),
    remanence_neg0.8T$rem_Am2.kg*(-1),
    remanence_neg0.9T$rem_Am2.kg*(-1),
    remanence_neg1.0T$rem_Am2.kg*(-1),
    remanence_neg1.1T$rem_Am2.kg*(-1),
    remanence_neg1.2T$rem_Am2.kg*(-1),
    remanence_neg1.3T$rem_Am2.kg*(-1),
    remanence_neg1.4T$rem_Am2.kg*(-1),
    remanence_neg1.5T$rem_Am2.kg*(-1))
s_experiment <- as.data.frame(s_experiment)

colnames(s_experiment) <- c("rem_Am2.kg_at0.0T",
  "rem_Am2.kg_at0.1T",
  "rem_Am2.kg_at0.2T",

```

```

"rem_Am2.kg_at0.3T",
"rem_Am2.kg_at0.4T",
"rem_Am2.kg_at0.5T",
"rem_Am2.kg_at0.6T",
"rem_Am2.kg_at0.7T",
"rem_Am2.kg_at0.8T",
"rem_Am2.kg_at0.9T",
"rem_Am2.kg_at1.0T",
"rem_Am2.kg_at1.1T",
"rem_Am2.kg_at1.2T",
"rem_Am2.kg_at1.3T",
"rem_Am2.kg_at1.4T",
"rem_Am2.kg_at1.5T")

```

```

data.final <- cbind(data_frame_comp_lp, data_frame_comp_Hcr[,c(3,4)],
data_frame_comp_s$L_rem.Am2kg, s_experiment)

```

```

colnames(data.final) <-
c(
"sampleID",
"mass.kg",
"Ms.Am2kg",
"Mr.Am2kg",
"Hc.T",
"chi_hifi.m3kg",
"Hcr.T",
"NL_rem.Am2kg",
"L_rem.Am2kg",
"rem_Am2.kg_at0.0T",
"rem_Am2.kg_at0.1T",
"rem_Am2.kg_at0.2T",
"rem_Am2.kg_at0.3T",
"rem_Am2.kg_at0.4T",
"rem_Am2.kg_at0.5T",
"rem_Am2.kg_at0.6T",
"rem_Am2.kg_at0.7T",
"rem_Am2.kg_at0.8T",
"rem_Am2.kg_at0.9T",
"rem_Am2.kg_at1.0T",
"rem_Am2.kg_at1.1T",
"rem_Am2.kg_at1.2T",
"rem_Am2.kg_at1.3T",
"rem_Am2.kg_at1.4T",
"rem_Am2.kg_at1.5T"
)

```

```

filename_final <- list.files(data.path, pattern = '\\.s', full.names = FALSE)
sampleID_help<- str_split_fixed(filename_final, ".s", 2)
sampleID <- sampleID_help[,1]

```

```

data.final$sampleID <- sampleID

```

```

data.final$Mr_Ms_rat <- data.final$Mr.Am2kg/data.final$Ms.Am2kg
data.final$Hcr_Hc_rat <- data.final$Hcr.T/data.final$Hc.T

```

```

data.final$sratio <- data.final$rem_Am2.kg_at0.3T/data.final$rem_Am2.kg_at1.5T

```

```

data.final$HIRM.Am2.kg <- data.final$rem_Am2.kg_at1.5T-
data.final$rem_Am2.kg_at0.3T

#plot(seq(1,length(data.final$HIRM.Am2.kg),1), abs(data.final$HIRM.Am2.kg),
type="l")

fileConn<-file("VSM_readme_v.0.0.6.txt")
writeLines(c("VSM HaRvesterR - Version 0.0.6 - coded by",
            "Christian Laag - Institut de Physique du Globe de Paris -
Palaeomagnetism Research Group",
            "" ,
            "" ,

"=====
=====)",
            "Dear User, thank you for using the R VSM Harvester version 0.0.6",
            "By using this script, please cite as follows:
Laag, C. (2023): VSM_HaRvester v.0.0.6:
A solution for extracting VSM parameters of large sample sets",
            "explanation for the headers of the HaRvester-table:",

"
-----",
            "SampleID.....The sample ID of the measured sample.",
            "mass.kg.....The netto mass of a single sample",
            "Ms.Am2kg.....The saturation magnetization (mass normalized)",
            "Mr.Am2kg.....The saturation remanence (mass normalized)",
            "Hc.T.....The coercivity (attention: given in Tesla)",
            "Hcr.T.....The coercivity of remanence (attention: given in
Tesla)",
            "chi_hifim3kg.....The high-field susceptibility derived from the
slope correcture for paramagnetic contributions and mass normalized",
            "NL_rem.Am2kg.....Remanence measured during determining Hcr (mass
normalized), for quality assessment to be compared with L_rem.Am2kg",
            "L_rem.Am2kg.....Remanence measurement during the stepwise
backfield application - qualitiy assessment:the difference of NL_rem.Am2kg and
L_rem.Am2kg should be as small as possible, changes could indicate the presence of
SP particles",
            "rem_Am2kg.....at 0.0 to 1.5 Tesla measured backfield steps (mass
normalized)",
            "Mr_Ms_rat.....The ratio of Mr and Ms as preparation for the
Dunlop plot",
            "Hcr_Hc_rat.....The ratio of Hcr and Hc as preparation for the
Dunlop plot",
            "sratio.....The ratio of backfield IRM at -300 and -1500 mT",
            "HIRM.....Hard IRM: The difference of above mentioned IRMs,
both backfield"), fileConn)
close(fileConn)

write.table(data.final, "latest_SK11_VSM_params_by_HaRvesteRv0.0.5.csv", row.names
= F, sep=";")

```

### Objectives of the VSM harvester

As stated in the introductory paragraph, the VSM harvester provides a solid base to evaluate, and mass normalize VSM derived experiments' magnetic parameters. However, this rather static script is only applicable to the device used at IPGP and the precise settings applied to the three applied experiments. Programming an R-package regrading device independent and setting independent decisions may help in future to skip long lasting manually-typed Excel sheets and helps to over-time consuming processes to achieve desired data.



## Appendix H: Contributions to international conferences

<p><b>2023</b></p>	<ul style="list-style-type: none"> <li>• <b>Laag, C.</b>, Guyodo, Y., Chapkanski, S., Lagroix, F. (2023): <b>Convener</b> of Special Session 12.4 at the International Association of Sedimentologists 2023, Dubrovnik, Croatia: Tephra and cryptotephra layer detection and identification through multiproxy data integration.</li> <li>• <b>Laag, C.</b>, Lagroix, F., Guyodo, Y., Jordanova, D., Jordanova, N., Ishlyamski, D., Georgieva, B., Saulnier-Copard, S., Chapkanski, S., Moine, O., Antoine, P. (2023): Mid-Brunhes Climate Transition and millennial-timescale climate change preserved in a 800 kyrs loess-paleosol sequence from the Suhia Kladenetz quarry (Pleven, Bulgaria): a multidisciplinary study. <b>INQUA XXI, Rome, Italy.</b></li> <li>• Dar, R., Zeeden, C., Mir, J., Vinnepand, M., Rolf, C., <b>Laag, C.</b>, Tsukamoto, S. (2023): High-resolution multiproxy data from a last interglacial loess paleosol sequence in Kashmir. <b>INQUA XXI, Rome, Italy.</b></li> <li>• Zeeden, C., Hambach, U., Rolf, C., Obreht, I., Marković, S.B., Schulte, P., Veres, D., Kehl, M., <b>Laag, C.</b>, Vinnepand, M., Lehmkuhl, F. (2023): Magnetic susceptibility properties in loess-paleosol sequences over Eurasia. <b>INQUA XXI, Rome, Italy.</b></li> <li>• <b>Laag, C.</b>, Guyodo, Y., Lagroix, F., Chapkanski, S., Jordanova, D., Jordanova, N. (2023): Tephra identification and discrimination in loess-paleosol sequences integrating rock magnetism and mid-infrared spectrometry experiments. <b>EGU General Assembly 2023, Vienna, Austria.</b></li> </ul>
<p><b>2022</b></p>	<ul style="list-style-type: none"> <li>• <b>Laag, C.</b>, Lagroix, F., Guyodo, Y., Jordanova, D., Jordanova, N., Ishlyamski, D., Georgieva, B., Saulnier-Copard, S., Chapkanski, S., Moine, O., Antoine, P. (2022): Millennial-timescale climate change over the last 800 kyrs evidenced by magnetic, colorimetric and ATR-FTIR data from the Suhia Kladenetz quarry loess-paleosol sequence (Pleven, Bulgaria). <b>GeoMin Colone Sept. 2022, co-convener of session 5.4: Palaeomagnetic and rock magnetic approaches applied to sedimentary sequences.</b></li> <li>• Jordanova, D., Jordanova, N., <b>Laag, C.</b>, Lagroix, F., Georgieva, B., Ishlyamski, D., Guyodo, Y. (2022): Loess-paleosol sequence from central north Bulgaria as a unique detailed archive of the Middle – Late Pleistocene environmental change in SE Europe. <b>Castle Meeting 2022, Trakošćan, Croatia, to be held 28.08.-03.09.2022.</b></li> </ul>
<p><b>2021</b></p>	<ul style="list-style-type: none"> <li>• <b>Laag, C.</b>, Jordanova, D., Lagroix, F., Jordanova, N., Guyodo, Y., Georgieva, B., Ishlyamski, D. (2021): Dust flux and global ice volume variations enable correlative age modelling for an 800 kyrs covering loess-paleosol sequence at Pleven (Bulgaria). <b>PMAG 2021 conference</b>, oral talk, 03.11.2021, Gif sur Yvette, France.</li> <li>• Jordanova, D., Jordanova, N., <b>Laag, C.</b>, Lagroix, F., Guyodo, Y. (2021): High-resolution magnetic archive of the dynamic interplay of past climatic and dust sedimentation changes during the middle and late Pleistocene in central North Bulgaria, lower Danube area. <b>DUST2021 conference</b>, Monopoly, Italy, 04.-07.10.2021.</li> <li>• Schmidt, C., <b>Laag, C.</b>, Whitehead, M., Kereszturi, G., Profe, J. (2021): The complexities assessing volcanic hazards along the Cameroon Volcanic Line using spatial distribution of monogenetic volcanoes. <b>19<sup>th</sup> Swiss Geoscience Meeting</b>, Geneva, 19.-20.11.2021.</li> <li>• Zeeden, C., Mir, J.A., Vinnepand, M., Rolf, C., <b>Laag, C.</b>, Dar, R.A. (2021): High-resolution Proxy Data from Kashmir Loess Imply Predominant Local Dust Sources and Confirm Climate Sensitivity of the Loess-Palaeosol Sequences. <b>vDEUQUA2021.</b></li> <li>• Ryzner, K., Zeeden, C., Lauer, T., Kehl, M., <b>Laag, C.</b>, Vinnepand, M., Rolf, C. (2021): Magnetic fabric of the Agh Band loess-paleosol section (Northern Iran) – investigating past wind dynamics. <b>vDEUQUA 2021</b></li> <li>• Schmidt, C., <b>Laag, C.</b>, Profe, J. (2021): Distribution of monogenetic volcanism along the Cameroon Line. <b>Spatial Data Science</b> 08.-11.06.2021, Lausanne, Switzerland.</li> </ul>

	<ul style="list-style-type: none"> <li>• <b>Laag, C.</b>, Guyodo, Y., Lagroix, F., Veres, D., Wacha, L., Hambach, U. (2021): Tephra hunt in loess-paleosol sequences – towards an interdisciplinary approach for tephra detection and characterization. <b>International Association of Geomagnetism and Aerometry</b>, Hyderabad, India, 21.08.-27.08.2021.</li> <li>• <b>Laag, C.</b>, Wacha, L., Ryzner, K., Zeeden, C., Rolf, C., Lagroix, F., Guyodo, Y., Tsukamoto, S., Frechen, M. (2021): 350 kyrs of increasing aridity reflected by geophysical proxies from the LPS of Zmajevac, Croatia. <b>35<sup>th</sup> IAS Meeting of Sedimentology</b>, June 2021.</li> <li>• <b>Laag, C.</b>, Jordanova, D., Lagroix, F., Jordanova, N., Guyodo, Y., Saulnier Copard, S., Antoine, P. (2021): 850 kyrs of paleoclimate evolution from magnetic and granulometric data of the Pleven loess-paleosol sequence. <b>35<sup>th</sup> IAS Meeting of Sedimentology, June 2021</b>.</li> <li>• Zeeden, C., Vinnepand, M., Ryzner, K., Rolf, C., <b>Laag, C.</b>, Abadi, M.S., Radaković, M.G., Gavrilov, M.B., Marković, S.B. (2021): Relationships between meteorological data and soil properties: quantifying precipitation and aridity in the Middle Danube Basin through geophysical proxies. <b>European Geoscience Union</b>, April 2021, oral presentation.</li> <li>• <b>Laag, C.</b>, Jordanova, D., Lagroix, F., Jordanova, N., Guyodo, Y. (2021): A new reference loess-paleosol archive spanning the last 850 kyrs near Pleven (Bulgaria) - first results. European Geoscience Union, April 2021, oral presentation &amp; poster.</li> <li>• Schmidt, C., <b>Laag, C.</b>, Profe, J. (2021): Distribution of monogenetic volcanism along the Cameroon Line. <b>European Geoscience Union</b>, oral presentation.</li> </ul>
2020	<ul style="list-style-type: none"> <li>• <b>Laag, C.</b>, Hambach, U., Zeeden, C., Lagroix, F., Jovanović, M., Marković, S.B. (2020): Integrating magnetic susceptibility and colorimetric parameters for paleoenvironmental reconstructions from loess-paleosol sequences: A case study from northern Serbia for the last 430 ka. <b>American Geophysical Union (AGU)</b>, oral presentation, 16.12.2020.</li> <li>• Pfeifer, L., Hinnov, L., Zeeden, C., Rolf, C., <b>Laag, C.</b>, Soreghan, G.S. (2020): Ten Million Years of Paleoclimatic Variability Recorded in Permian Loessite of Eastern Equatorial Pangea. <b>AGU Fall Meeting</b>, 01.-17.12.2020 online.</li> <li>• Pfeifer, L., Hinnov, L., Zeeden, C., Rolf, C., <b>Laag, C.</b>, Soreghan, G.S. (2020): Milankovitch-scale paleoclimatic variability recorded in Permian loessite (south-central France). <b>Virtual GeoUtrecht</b> conference, 24.-26.8.2020.</li> <li>• <b>Laag, C.</b>, Zeeden, C., Hambach, U., Jovanovic, M., Markovic, S.B. (2020): Advantages in integrating rock-magnetic and colorimetric measurements for palaeoenvironmental reconstructions on loess-palaeosol sequences: A case study from northern Serbia for the last 430 ka. <b>Virtual GeoUtrecht</b> conference, 24.-26.8.2020.</li> <li>• <b>Laag, C.</b>, Hambach, U., Veres, D., Zeeden, C., Worm, K., Rolf, C. (2020): High resolution paleomagnetic and environmental magnetic data from the last interglacial to glacial transition in a loess-paleosol sequence (LPS) from the Lower Danube (Romania) – Implications for the Chronology of the S1 pedocomplex in Eurasian LPSs. Oral Presentation, <b>Quaternaire 12</b>, Paris.</li> <li>• <b>Laag, C.</b>, Zeeden, C., Rolf, C., Worm, K., Lauer, T., Kehl, M., Lehndorff, E., Khormali, F. (2020): Palaeoenvironmental- and palaeomagnetic stratigraphy for a 250-ka covering, quasi continuous dust accumulation. <b>Quaternaire 12</b>, Paris. Poster presentation.</li> <li>• Hambach, U., Veres, D., Constantin, D., Zeeden, C., Pötter, S., Obreht, I., <b>Laag, C.</b>, Böskén, J., Schulte, P., Markovic, S.-B., Lehmkuhl, F., Timar-Gabor, A. (2020): Evidence for uninterrupted glacial and interglacial dust accumulation in Eurasian dry steppe regions. <b>Quaternaire12</b>, 3.-5.2.2020, Paris, France.</li> <li>• <b>Laag, C.</b>, Hambach, U., Zeeden, C., Jovanovic, M., Marković, S. (2020): Combined rock-magnetic and colorimetric stratigraphy for a 430-ka covering loess-palaeosol sequence in the vicinity of Belgrade, Northern Serbia. <b>EGU sharing geoscience online</b> poster presentation.</li> </ul>

	<ul style="list-style-type: none"> <li>• Zeeden, C., <b>Laag, C.</b>, Camps, P., Guyodo, Y., Hambach, U., Just, J., Lurcock, P., Rolf, C., Satolli, S., Scheidt, S., Wouters, S. (2020): Towards data interchangeability in paleomagnetism. <b>European Geoscience Union</b>, online poster presentation.</li> <li>• Wouters, S., Boulvain, F., Crucifix, M., da Silva, A.-C., <b>Laag, C.</b>, Sinnesael, M., Zeeden, C., Zivanovic, M., Devleeschouwer, X. (2020): Data reversibility in geology: applications in litho-, magneto- and cyclostratigraphy, <b>EGU General Assembly</b>, 3.-8.5.2020.</li> </ul>
<b>2019</b>	<ul style="list-style-type: none"> <li>• <b>Laag, C.</b>, Hambach, U., Veres, D., Zeeden, C., Worm, K., Rolf, C. (2019): High resolution paleomagnetic and environmental magnetic data from the last interglacial to glacial transition in a loess-paleosol sequence (LPS) from the Lower Danube (Romania) – Implications for the Chronology of the S1 pedocomplex in Eurasian LPSs. Poster presentation at <b>Workshop on Loess and Archaeology</b>, Aachen, Germany</li> <li>• Hambach, U., Veres, D., Constantin, D., Zeeden, C., Pötter, S., Baykal, Y., Obreht, I., <b>Laag, C.</b>, Böskén, J., Schulte, P., Stevens, T., Marković, S., Lehmkuhl, F., Timar-Gabor, A. (2019): Interglacial, Holocene and recent dust accretion in the Danube Basin and beyond – evidence for uninterrupted dust accumulation in Eurasian dry steppe regions, Co-author in oral presentation at <b>Workshop on Loess and Archaeology</b>, Aachen, Germany</li> <li>• Zeeden, C., Hambach, U., Necula, C., Jordanova, D., Panaiotu, C., Rolf, C., Veres, D., Obreht, I., Chu, W., <b>Laag, C.</b>, Marković, S., Lehmkuhl, F., Kaboth-Bahr, S. (2019): A European loess stack and its timing (in progress) in the context of human evolution. Co-author in oral presentation at <b>Workshop on Loess and Archaeology</b>, Aachen, Germany</li> <li>• Veres, D., Hambach, U., Pötter, S., Obreht, I., Zeeden, C., Böskén, J., Baykal, Y., <b>Laag, C.</b>, Timar-Gabor, A., Stevens, T., Lehmkuhl, F., Marković, S. (2019): Disentangling millennial-scale variability in south-eastern European loess-paleosol sequences. Co-author in oral presentation at <b>Workshop on Loess and Archaeology</b>, Aachen, Germany</li> <li>• <b>Laag, C.</b>, Hambach, U., Krawczyk, M., Raczky, J., Jary, Z., Zöller, L. (2019): Environmental magnetic and colorimetric screening of a last glacial loess profile from Lower Silesia: evidence for a harsh periglacial environment. <b>INQUA</b> poster presentation, funding by DEUQUA</li> <li>• Schmidt, C., <b>Laag, C.</b>, Profe, J., Richter, T., Tchouankoue, J.P. (2019): The morphometry of scoria cones as an indicator of their relative age – Results from the Cameroon Volcanic Line. <b>EGU 2019</b> presentation.</li> </ul>
<b>2018</b>	<ul style="list-style-type: none"> <li>• <b>Laag, C.</b>, Hambach, U., Botezatu, A., Baykal, Y., Veres, D., Schönwetter, T., Viola, T., Zeeden, C., Radaković, M.G., Obreht, I., Jovanović, M., Böskén, J., Lehmkuhl, F., Marković, S.B. (2018): The geographical extent of the “L2-Tephra”: a widespread marker horizon for the penultimate glacial (MIS 6) on the Balkan Peninsula, <b>INQUA-INTAV international field conference</b>, Romania; abstract &amp; poster presentation, funding by BayHOST</li> </ul>
<b>2017</b>	<ul style="list-style-type: none"> <li>• <b>Laag, C.</b> (2017): “A scientific concept for NOAH (North Sea Observation and Assessment of Habitats)”, presentation at <b>KüNO Conference Rostock</b> (coastMap-focus group meeting)</li> </ul>

## Data availability statement

All data presented in this thesis is either already made available or will be made available in open source repositories such as Pangaea or Zenodo.